SYNTHESIS AND CHARACTERIZATION OF NON-HEME 3d METAL COMPOUNDS FOR SELECTED APPLICATIONS

A THESIS SUBMITTED IN PARTIAL FULFILLMENT FOR THE DEGREE OF

DOCTOR OF PHILOSOPHY

IN CHEMISTRY

IN THE SCHOOL OF CHEMICAL SCIENCES
GOA UNIVERSITY

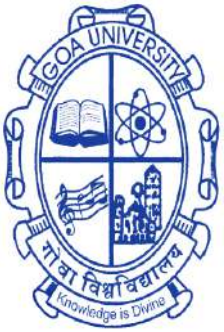

By

Mr. JEFFREY LAURO VIEGAS
Goa University
Goa

August 2025

DECLARATION

I, Mr. Jeffrey Lauro Viegas hereby declare that this thesis represents work which has been carried out by me and that it has not been submitted, either in part or full, to any other University or Institution for the award of any research degree.

Place: Taleigao Plateau.

Date : Mr. Jeffrey L. Viegas

CERTIFICATE

I hereby certify that the above Declaration of the candidate, Mr. Jeffrey Lauro Viegas is true and the work was carried out under my supervision.

Prof. Sunder N. Dhuri
School of Chemical Sciences
Goa University, Goa.

ACKNOWLEDGEMENT

The work presented in this thesis would not have been possible without the support and goodwill of many people who stood by me throughout my research journey. I gratefully acknowledge their contributions and extend my sincere thanks to all of them.

First and foremost, I express my deepest gratitude to my research supervisor, Prof. Sunder N. Dhuri, from the School of Chemical Sciences (SCS), Goa University, for invaluable guidance, scholarly insight, constant encouragement, and patience. Working under your mentorship has been a privilege; this thesis would not have taken shape without your continuous support and trust.

I am especially thankful to Prof. V. M. S. Verenkar (Dean), Dr. Bidhan Shinkre (Vice- Dean, Research) and Dr. Digamber Porob (Vice- Dean, Academics) for their encouragement, constructive suggestions, and many insightful discussions. I acknowledge the School of Chemical Sciences for providing access to research facilities. I also thank my subject experts, Prof. V. M. S. Verenkar and Prof. M. S. Majik for their thoughtful feedback and well-wishes. I sincerely thank Goa University for providing this platform to pursue research. I am grateful to the Vice-Chancellor and Registrar of Goa University for their administrative support. I also acknowledge the administrative staff (AR- PG) of Goa University for their assistance.

Gratitude to the helping hands in research work: Dr. Venkatesha Hathwar (School of Physical and Applied Sciences, Goa University) for his inputs on crystal structure solving and helping with the Le- Bail method for powder diffraction, BITS Pilani, Goa for powder diffraction analysis. Prof. W. Nam, Ewa Women's University, South Korea, Dr. Dipika Karmalkar and Ms. Madhuri Nilajkar for ESI-MS and EPR measurements. Dr. Elaine Dias for inputs in SQUID analysis. Mr. Vishnu Chari for his collaboration in computational chemistry.

My heartfelt thanks to all the present and former teachers of School of Chemical Sciences Goa University and St. Xavier's College, Mapusa Goa, for cultivating my research interest in chemistry.

My heartfelt thanks to the non-teaching staff of the School of Chemical Sciences, Goa University, for timely help. I am indebted to my lab mates, Dr. Dattaprasad Narulkar, Dr. Sarvesh Harmalkar, Dr. Luann D'souza, Nikita Harmalkar, Milagrina D'souza, Disha Gauns, V. Swapna, Medha Gaude and Jocelyn Kuate Njomkam for their cheerful company, prompt help, and many scientific discussions and trainings. I also thank my senior and junior colleagues for their guidance, encouragement, and good wishes. I am thankful to all my colleagues at Carmel College of Arts, Science and Commerce for Women, Nuvem Goa, and Directorate of Higher Education for their constant support and wishes. I owe my appreciation to some special ones who have left an indelible mark in this journey: Luann, Mangala, Disha, Nikita, Vipul, Anson and Fr. Doel.

I am indebted to Carmel College of Arts, Science and Commerce for Women, Nuvem Goa, and Directorate of Higher Education for providing me with study leave for a period of two years to complete my research work.

I remain deeply grateful to my family, my spouse, my children and to my well-wishers and friends for their unwavering support, patience, and love throughout this period.

Above all, I owe it to the Almighty for granting me the wisdom, health, and strength to undertake this research and bring it to completion.

... Jeffrey Viegas

Dedicated to my family!!

CONTENTS

LIST OF SCHEMES

CHAPTER 5

LIST OF TABLES

CHAPTER 3

SECTION I

SECTION II

CHAPTER 4

SECTION I

SECTION II

CHAPTER 5

LIST OF FIGURES

CHAPTER 1

CHAPTER 2

CHAPTER 3

SECTION I

CHAPTER 4

SECTION I

CHAPTER 5

SECTION I

SECTION II

List of Abbreviation

Abbreviations (General)

sMMO	-	Soluble methane monooxygenase
CPO	-	Chloroperoxidase
CYP	-	Cytochrome P450
Fe–BLM	-	Bleomycin–iron
DNA	-	Deoxyribonucleic acid
MnSOD	-	Manganese superoxide dismutase
MnCAT	-	Manganese catalase
RNR	-	Ribonucleotide reductase
dNTP	-	Deoxyribonucleoside triphosphate
MCM	-	Methylmalonyl-CoA mutase
MetH	-	Methionine synthase
NHase	-	Nitrile hydratase
Ure	-	Urease
H_2ase	-	[NiFe]-hydrogenase
CODH/ACS	-	Carbon monoxide dehydrogenase/acetyl-CoA synthase
LAC	-	Laccase
TYR	-	Tyrosinase
CcO	-	Cytochrome *c* oxidase
CuNiR	-	Copper nitrite reductase
CA	-	Carbonic anhydrase
ADH	-	Alcohol dehydrogenase
CPA	-	Carboxypeptidase A
TauD	-	Taurine/α-ketoglutarate dioxygenase
ROS	-	Reactive oxygen species
OEC	-	Oxygen-evolving complex
MIOX	-	Myo-inositol oxygenase
PSII	-	Photosystem II
PhIO	-	Iodosylbenzene
m-CPBA	-	Metachloroperbenzoic acid
CAN	-	Ceric ammonium nitrate
HAT	-	H-atom abstraction
PHS	-	Phenoxazinone synthase
SP	-	Square pyramidal
TBP	-	Trigonal bipyramidal
2-PPA	-	2-phenylpropinaldehyde
OAP	-	2-aminophenol
3,5-DTBC	-	3,5-di-*tert*-butylcatechol
APX	-	2-aminophenoxazine-3-one

3,5-DTBQ	-	3,5-di-*tert*-butyl-*o*-quinone
TBAH	-	Tetrabutylammonium hydroxide
IPNS	-	Isopenicillin N synthase
CDO	-	Cysteine dioxygenase
EgtB	-	Ergothioneine-biosynthetic enzyme
MDO	-	Mercaptopropionate dioxygenase
PCS	-	Primary coordination sphere
SCS	-	Secondary coordination sphere
MLCT	-	Metal to ligand charge transfer
HAA	-	Hydrogen atom abstraction
NACs	-	Nitroaromatic compounds
NB	-	Nitrobenzene
p-NT	-	p-nitrotoluene
o-NT	-	o-nitrotoluene
p-NP	-	p-nitrophenol
o-NP	-	o-nitrophenol
DNP	-	2,4-dinitrophenol
TNP	-	2,4,6-trinitrophenol
RET	-	Resonance energy transfer
NiRs	-	Nitrite reductases
CuNiRs	-	Copper containing NiRs
NOSs	-	Nitric oxide synthases
NOO	-	Nitric oxide oxidase

Abbreviations (Instrumentation techniques)

XRD	-	X-ray Diffraction
IR	-	Infrared
NMR	-	Nuclear magnetic resonance
UV–Vis	-	UV-Visible
ESI-MS	-	Electron spray ionization mass spectroscopy
EPR	-	Electron paramagnetic resonance
VSM	-	Vibrating Sample Magnetometer
GC	-	Gas chromatography
DEPT	-	Distortionless Enhancement by Polarization Transfer
MALDI-TOF	-	Matrix-assisted Laser Desorption Ionization Time-of-flight
FID	-	Flame Ionization Detector
PL	-	Photoluminescence
PXRD	-	Powder X- ray diffraction
TGA	-	Thermogravimetric Analysis
DTG	-	Derivative Thermogravimetry
SQUID	-	Superconducting Quantum Interference Device
ZFC	-	Zero-field-cooled

FC	-	Field-cooled
CSD	-	Cambridge Structural Database
DFT	-	Density functional theory

Abbreviations (Ligands)

12-TMC	-	1, 4, 7, 10-tetramethyl-1, 4, 8, 11-tetraazacyclododecane
13-TMC	-	1, 4, 7, 10-tetramethyl-1, 4, 8, 11-tetraazacyclotetradecane
14-TMC	-	1, 4, 8, 11-tetramethyl-1, 4, 7, 10-tetraazacyclotridecane
15-TMC	-	1, 4, 8, 12-tetramethyl-1, 4, 8, 12-tetraazacyclopentadecane
N4Py	-	N, N-bis(2-pyridylmethyl)-N-bis(2-pyridyl)methylamine
Bn-tpen	-	N-benzyl-N, N', N'-tris(2-pyridylmethyl)ethane-1,2-diamine
BQCN	-	N,N'-dimethyl-N,N'-bis(8-quinolyl)cyclohexanediamine
TPA	-	Tris-(2-pyridylmethyl)-amine
BQEN	-	N, N′-Dimethyl-N, N′-bis(8-quinolyl)ethane-1,2-diamine
BQMEN	-	N, N′-Dimethyl-N, N′-bis(8-quinolylmethyl)ethane-1,2-diamine
BQCN	-	N,N'-dimethyl-N,N'-bis(8-quinolyl)cyclohexanediamine
BPMCN	-	N,N-bis(2-pyridylmethyl)-N,N-dimethyl-trans-1,2-diaminocyclohexane
N4Py	-	N, N-bis(2-pyridylmethyl)-N-bis(2-pyridyl)methylamine
Bn-TPEN	-	N-benzyl-N,N',N'-tris(2-pyridylmethyl)ethane-1,2-diamine
TAML	-	Tetra amido macrocyclic ligand
$mL5^2$	-	(N-methyl-N,N',N'-tris(2-pyridylmethyl)ethane-1,2-diamine)
$imL5^2$	-	(N-methyl-N,N,N'-tris((1-methyl-4-imidazolyl)methyl)ethane-1,2-diamine)
TQA	-	Tris(quinolin-2-ylmethyl)amine
QBPA	-	1-(pyridin-2-yl)-N-(pyridin-2-ylmethyl)-N-(quinolin-2-ylmethyl)methanamine
TATM	-	1,4,8,11-tetramethyl-1,4,8,11-tetraazacyclotetradecane
TAPM	-	1,5,9,13-tetramethyl-1,5,9,13-tetraazacyclohexadecane
TMG_3tren	-	2',2",2"-(nitrilotris(ethane-2,1-diyl))tris(1,1,3,3-tetramethylguanidine)

SYNOPSIS

SYNTHESIS AND CHARACTERIZATION OF NON-HEME 3d METAL COMPOUNDS FOR SELECTED APPLICATIONS

General Introduction

The thesis entitled "Synthesis and Characterization of Non-heme 3d Metal Compounds for Selected Applications" encompasses synthesis, characterization, and selective applications of several novel 3d metal compounds stabilized by non-heme nitrogen and sulfur donor ligands.

Enzymes are involved in the majority of biological processes. Nature has capitalized on the unique properties of metal ions by encapsulating them with various protein matrices and tailoring these to perform a wide range of specific functions related to biological processes. Metals such as manganese (Mn), iron (Fe), cobalt (Co), nickel (Ni), copper (Cu) and zinc (Zn) that have biological significance are prominent examples in the field of biomimetic chemistry [1-5]. As Ronald Breslow noted, biomimetic chemistry is a branch of science that reflects human endeavors spanning decades, which involve creating new innovations inspired by natural processes [6,7]. The primary objective of the study is to characterize newly synthesized compounds, while also exploring their biomimetic functions in different reactions.

Investigating enzymatic reactions in detail is complicated by the short lifespan of intermediate compounds within the catalytic cycle; therefore, it is not always evident which reactive species is responsible for the transformations or which characteristics of the active site influence the rate-determining step of the reaction. Biomimetic models were employed to comprehend the functional characteristics of these metal-containing active sites, which included a metal with a comparable coordination environment [8-13]. Biomimetic models offer valuable insights into how ligands affect the chemical properties and reactivity of the oxidant, including its first and second coordination spheres, as well as the reaction mechanism and rate constants. Numerous critical oxidative transformations and metabolic reactions are highly regio- and stereospecific, and it is thought that selectivity is influenced by the second coordination sphere effects on the protein. Steric and electronic effects are two crucial tuning parameters which reveal the reactivity profiles of these systems, with a subtle distinction existing between the two influences. Specifically, a more precise positioning of the oxidant and substrate in the rate-

determining transition state reduces the reaction barrier. Consequently, an ideal balance between steric and electronic factors facilitates the optimal positioning of the oxidant and substrate in the rate-determining transition state, which in turn impacts the reactivity of high-valent reaction intermediates [14,15]. Over the past few decades, numerous bioinorganic chemistry groups have been actively engaged in the modelling of metalloenzymes, as a result of which this field has been extensively researched in the recent past [16-20]. Building on the research of several groups in this area, we concentrated on creating novel nonheme ligands (**Scheme 1**) and their 3d metal compounds for targeted uses. The nonheme ligands utilized in this research were either synthesized in accordance with a previously documented procedure or via the implementation of a novel synthetic approach. The various non-heme 3d metal compounds analyzed in this research are shown in **Scheme 2**.

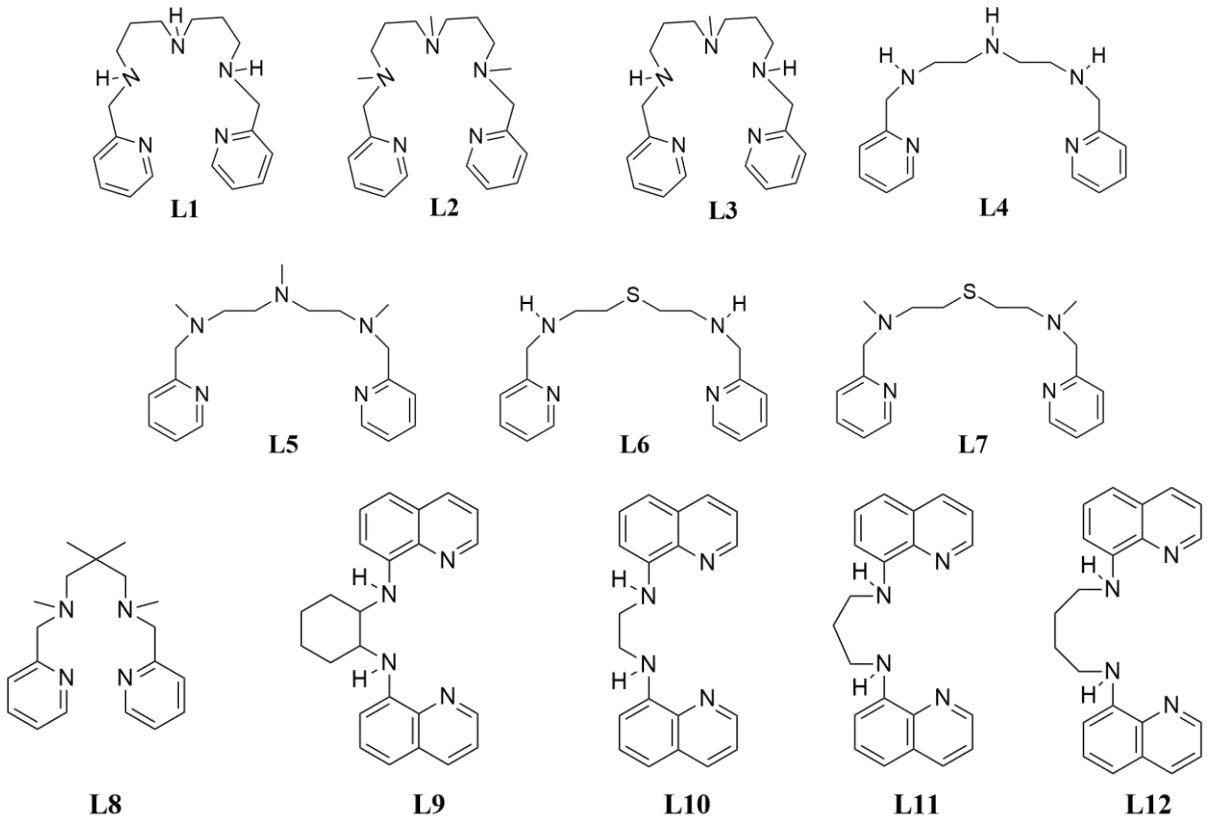

Scheme 1: Schematic representation of the pentadentate and tetradentate nonheme ligands, **L1-L12**, examined in this study.

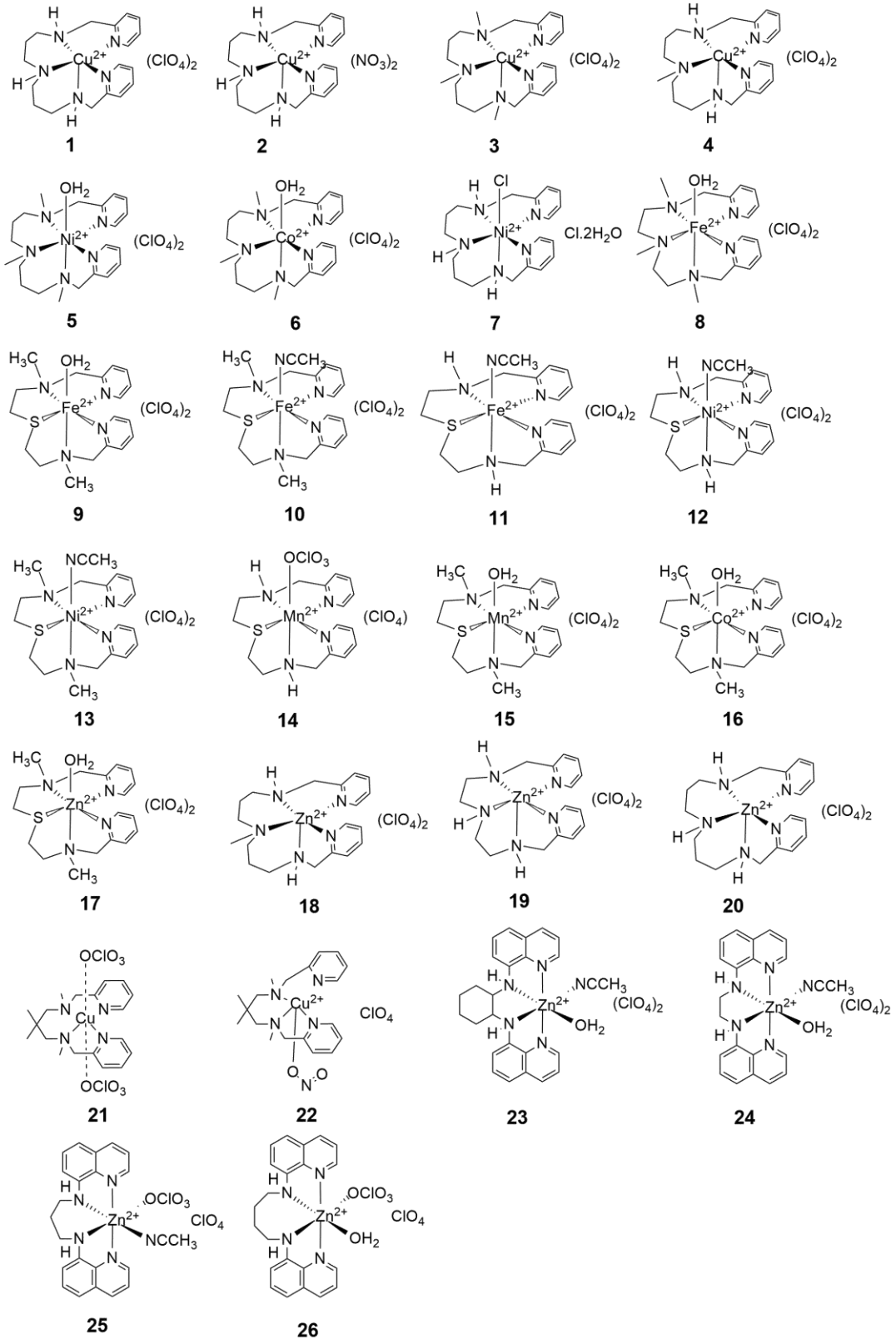

Scheme 2: Schematic representation of the novel compounds **1-26** investigated in the thesis.

The content of this thesis is organized into five chapters. A concise, section-by-section summary of the findings is provided below.

Chapter 1: Introduction

This chapter provides a concise introduction to the research topic, highlighting the aims and objectives of the study along with a general literature review.

Chapter 2: Materials and Methods

Chapter 2 outlines the particulars of all the materials used in the research and includes the general procedures for the synthesis, purification, and characterization of ligands and metal compounds. The specific instrumental and technical details of the instruments employed in the different characterizations are also examined. An overview of the methodologies utilized in this work is presented in **Scheme 3**.

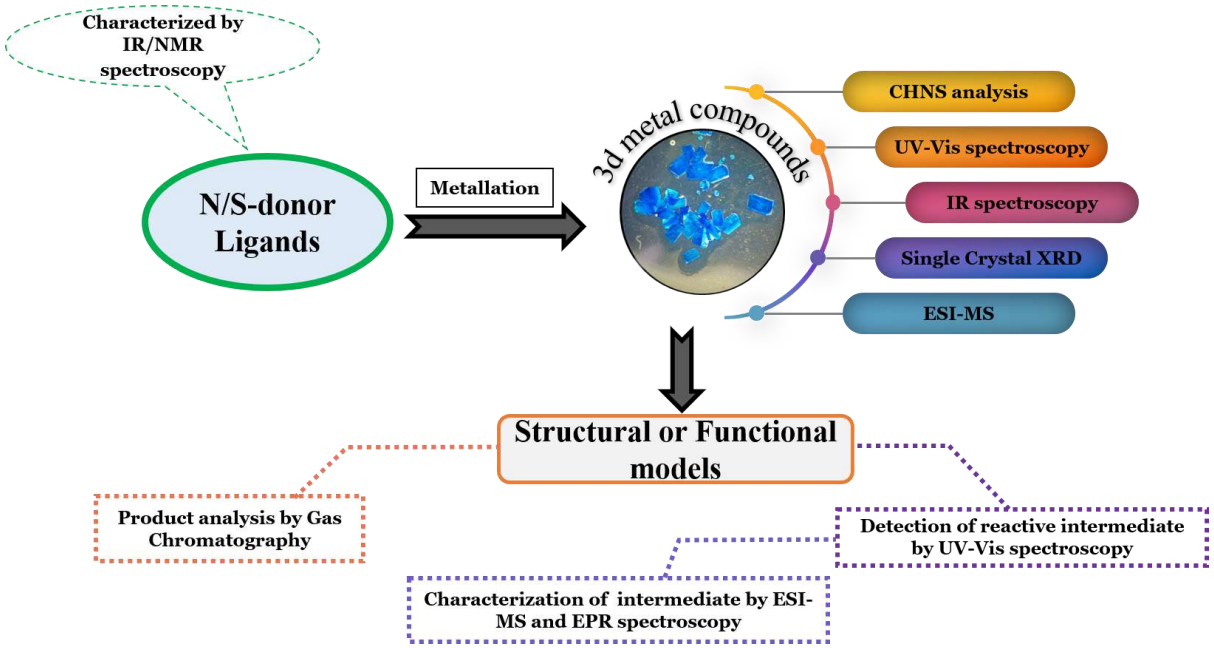

Scheme 3: Schematic representation of the general techniques and work strategy utilized in this present work.

Chapter 3

Section I: Influence of methyl substitution on structural parameters and catalytic mimicking activity of Cu(II) compounds.

The synthesis of mononuclear Cu(II) compounds **1-4** with nonheme pentadentate ligands **L1-L3** is the main focus of Section I in Chapter 3.The ligands **L2** and **L3** reported in this study are *N*-methylated analogues of the non-methylated pyridyl amine ligand **L1**. Our group reported the new pentadentate ligands **L2** and **L3** for the first time, characterizing them using NMR spectroscopy. Compounds **1-4** were synthetized and characterized using various techniques

including IR, ESI-MS, TG-DTG, SQUID and UV-Visible spectroscopy. Structural analysis of compounds **1-4** by SCXRD revealed that the compounds crystalize in monoclinic crystal system with the asymmetric unit built from one unique Cu(II) ion, a discrete pentadentate ligand and two independent perchlorate ions (**Figure 1**). The computed τ_5 values for the compounds indicate a notable geometrical alteration caused at the coordination center by the methylation of amine nitrogen atoms.

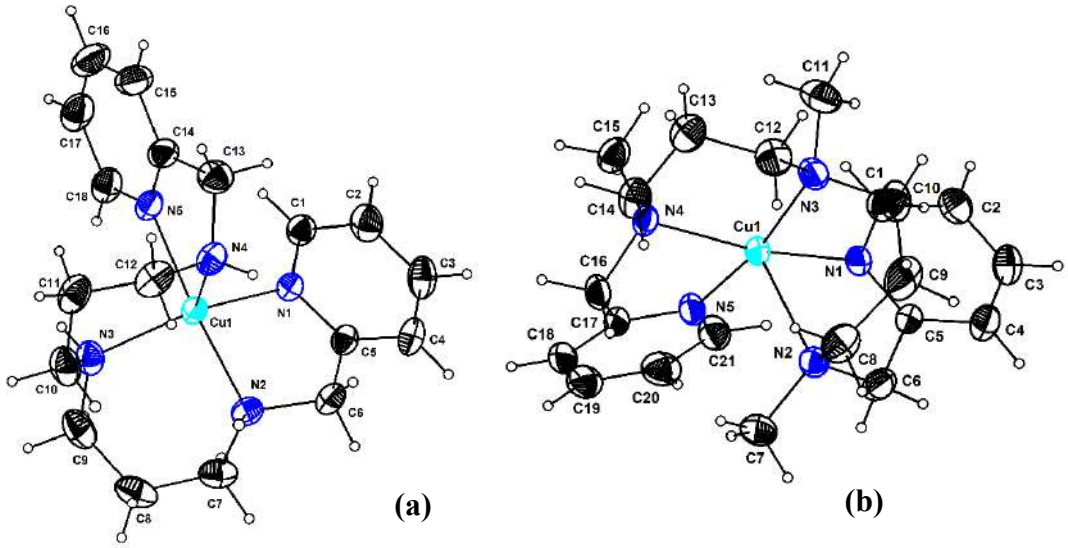

Figure 1: Crystal Structure of compounds a) $[Cu(L1)]^+$ **1**, and b) $[Cu(L2)]^+$ **3** with atom labelling scheme. Thermal ellipsoids are drawn at 50% probability except for the H atoms, which are shown as spheres of arbitrary radii.

We investigated the application of these Cu(II) compounds for the phenoxazinone synthase and catecholase-like mimicking reactivities by using 2-aminophenol (OAP) and 3,5- di-*tert*-butylcatechol (3,5-DTBC) [21,22] and the results are discussed in this section.

Section II: Synthesis, characterization and reactivity studies of non-heme Ni(II) and Co(II) compounds

The work done in Section I prompted us to delve into more model compounds of alternative 3d metals employing the same series of aminopyridyl ligands. Ni(II) and Co(II) compounds are frequently employed in literature as biomimetic models [23,24]. The three new compounds $[Ni(L2)(H_2O)](ClO_4)_2$ **5**, $[Co(L2)(H_2O)](ClO_4)_2$ **6**, and $[Ni(L1)(Cl)]\ Cl{\cdot}2H_2O$ **7** were prepared and analyzed using C,H,N analysis, ESI-MS, VSM, IR, and UV-Visible spectroscopy. Compounds **5** and **6** are isostructural, as indicated by single-crystal X-ray diffractometry.

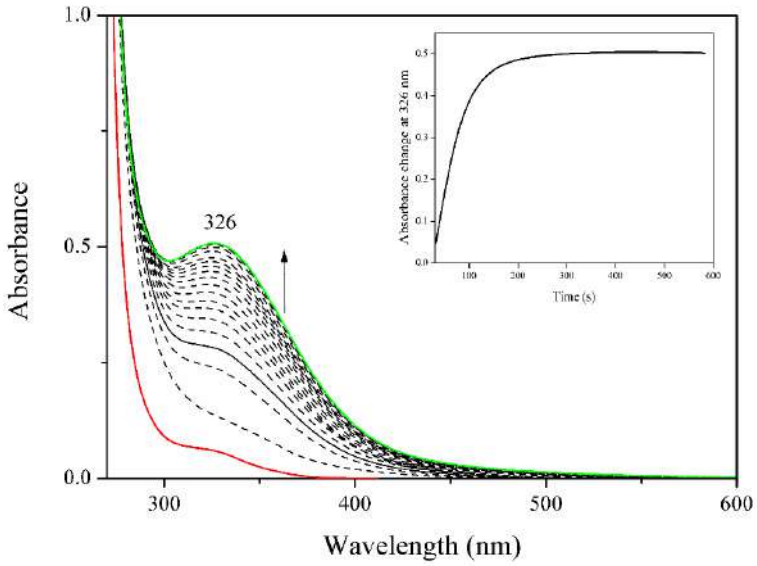

Figure 2: UV-Visible spectral changes after addition of H_2O_2 in the presence of TBAH (tetrabutylammonium hydroxide) at 15°C. Inset shows time trace monitored at 326 nm for the formation of peak.

The generation of reactive intermediates from compounds **5-7** was assessed by their reaction with the artificial oxidant H_2O_2 in basic conditions using TBAH. We successfully detected the intermediate related to compound **5** with a UV-Visible spectrophotometer (**Figure 2**). This intermediate was subsequently utilized in the aldehyde deformylation reaction. An elaborate account of the detailed investigation is provided in the thesis.

Chapter 4

Section I: Rational design of bioinspired novel pentadentate Fe(II) compounds : reactivity towards oxidation reactions

Metalloenzymes that activate oxygen possess distinctive structures and characteristics, enabling them to catalyze a wide variety of chemical reactions in nature under physiological conditions. A number of these metalloenzymes use iron that is attached to the protein at its active site. The active site of metalloenzymes often exhibits unique properties due to sulfur ligation, be it the equatorial sulfur/thiol ligation in nonheme iron enzymes or the axial cysteinate ligand in cytochrome P450s [25,26]. To comprehend how sulfur ligation interacts with iron compounds and its influence on the structural, spectroscopic, and intrinsic properties of the active species as well as the catalysis of substrates, we conducted a systematic study and designed a few N- and S-based bioinspired ligand frameworks **L4-L7**.

This section highlights the synthesis and characterization of the newly developed nonheme ligands **L6** and **L7**, where one of the amine functional groups in the parent ligands **L4** and **L5** is replaced with a thioether sulfur functional group. The novel Fe(II) compounds $[Fe(L5)(H_2O)](ClO_4)_2$ **8**, $[Fe(L7)(H_2O)](ClO_4)_2$ **9**, $[Fe(L7)(CH_3CN)](ClO_4)_2$ **10**, and $[Fe(L6)(CH_3CN)](ClO_4)_2$ **11** were synthesized and characterized by various techniques including C,H,N,S analysis, ESI-MS, IR, and UV-Visible spectroscopy. Compounds **8-11** were further characterized using single-crystal XRD, and the analysis uncovered unique structural characteristics, which are detailed further in this section.

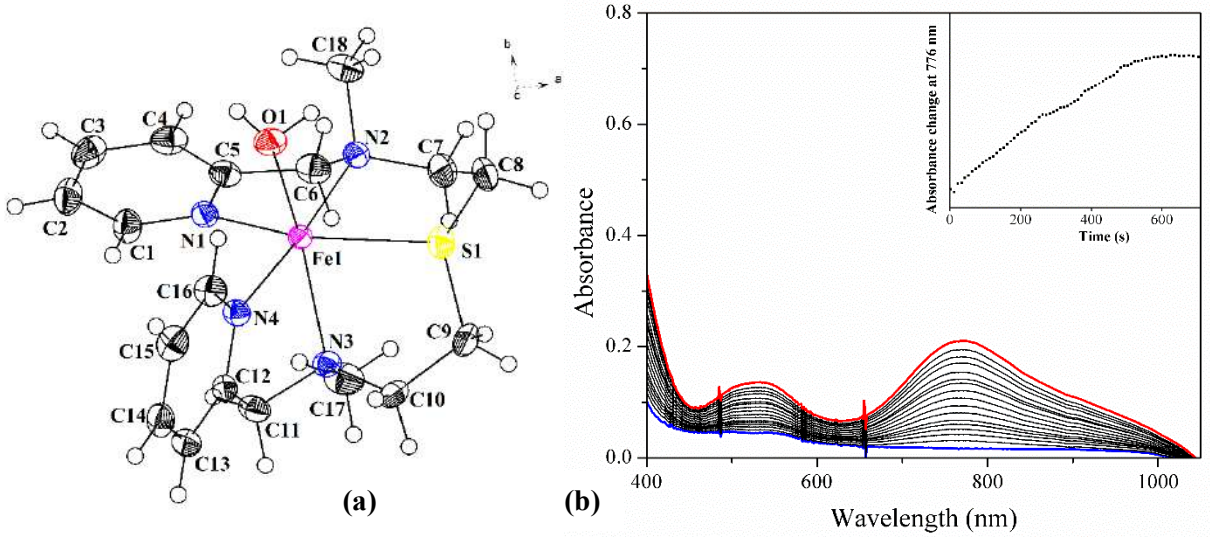

Figure 3: a) The crystal structure of $[Fe(L7)(H_2O)]^{2+}$ **9** with atom labels. Thermal ellipsoids are drawn at 50 % probability except for the H atoms which are shown as spheres of arbitrary radii. **b**) UV-Visible spectral changes after the reaction of **9** (1mM) and PhIO (1.1equiv.) in CH_3CN at −10°C. Inset: time course monitored at 776 nm for the formation of the peak.

The treatment of compounds **8** and **9** with 1.1 equiv. of iodosylbenzene (PhIO) in CH_3CN at -10°C resulted in the formation of new species **8a** and **9a**, as evidenced by the appearance of the new bands at 780 and 776 nm respectively in its UV-Vis spectrum (**Figure 3**). Given the stability of the newly discovered species, we were able to examine their reactivity with various organic substrates, as detailed in this thesis.

Section II: Synthesis and spectroscopic study of 3d metal compounds bearing N/S-donor ligands

Biomimetic inorganic chemistry has shown numerous examples illustrating how slight alterations in denticity and stereoelectronic properties significantly impact the performance of model systems [27]. The 3d metal compounds are considered as candidates due to their

abundance and redox characteristics. Investigations in Section I led us to further explore model compounds of alternative 3d metals utilizing the same series of ligands.

Section II of Chapter 4 discusses the synthesis of the seven new compounds, $[Ni(L6)(CH_3CN)](ClO_4)_2$ **12**, $[Ni(L7)(CH_3CN)](ClO_4)_2$ **13**, $[Mn(L6)](ClO_4)_2$ **14**, $[Mn(L7)(H_2O)](ClO_4)_2$ **15**, $[Co(L7)(H_2O)](ClO_4)_2$ **16**, $[Zn(L7)(H_2O)](ClO_4)_2$ **17** and $[Zn(L3)](ClO_4)_2$ **18**, which were prepared by the reaction of $M(ClO_4)_2.6H_2O$ salt and the corresponding ligand. These compounds were characterized by various techniques including C,H,N analysis, ESI-MS, IR, and UV-Visible spectroscopy. Compounds **12-18** were studied in detail using single-crystal XRD, revealing distinctive structural properties that are discussed in this section.

Section III: Ligand backbone influenced luminescent properties of Zn(II) compounds for detection of nitroaromatic compounds

Aminopyridine-based multidentate ligands have proven more acceptable in contemporary coordination chemistry due to their reactivity and stability being governed by a delicate interplay of electronic and structural properties [28]. Minor alterations to the ligand's structure can have a significant effect on its properties. Compounds of non-transition metals, such as Zn^{2+} and $Cd^{2+,}$ display notable luminescence in comparison to compounds of other transition metals, which in turn makes them suitable for a range of applications [29]. Hence, this research focused on the structural, spectroscopic, and photophysical characteristics of two Zn(II) compounds, $[Zn(L4)](ClO_4)_2$ **19** and $[Zn(L1)](ClO_4)_2$ **20**.

We investigated the sensing powers of **19** and **20** in relation to various NACs, specifically nitrobenzene (NB), o-nitrotoluene (o-NT), p-nitrotoluene (p-NT), o-nitrophenol (o-NP), p-nitrophenol (p-NP), 2,4-dinitrophenol (DNP), and 2,4,6-trinitrophenol (TNP) (**Figure 4**).

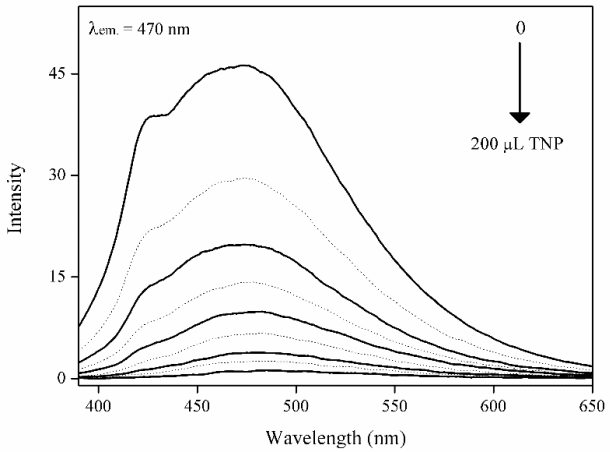

Figure 4: The decay of fluorescence emission peak of **1** ($\lambda_{ex.}$ = 370 nm) upon gradual addition of 1 mM of trinitrophenol (TNP).

The findings of this work encapsulated the selectivity of Zn(II) compounds as a reagent for chemical sensing in the detection of TNP and DNP. The Stern-Volmer plot showed non-linear characteristics with K_{sv} values significantly higher than those of other NACs, indicating its exclusive quenching ability. The distinct influence of varying ligand topology is evident in the reactivity patterns of compounds **19** and **20** with different NACs.

Chapter 5

Section I: Synthesis and characterization of novel tetradentate Cu(II) compounds and its reactivity

The conversion of nitrites (NO_2^-) to nitric oxide (NO) at Cu/Fe centers is a crucial process within the nitrogen cycle and provides a vital pathway for NO production. Over the past few years, several *in vitro* functional models have been developed and studied in order to gain a deeper understanding of NO_2^- reduction chemistry. Here, we endeavored to synthesize the novel Cu^{II}-nitrito compound as a functional model [30,31]. This section covers the synthesis and characterization of a newly developed tetradentate ligand **L8**, and its subsequent chelation with copper(II). The obtained compound, $[Cu(L8)](ClO_4)_2$ **21** was thoroughly characterized by C,H,N analysis, IR, ESI-MS and UV-Visible spectroscopy.

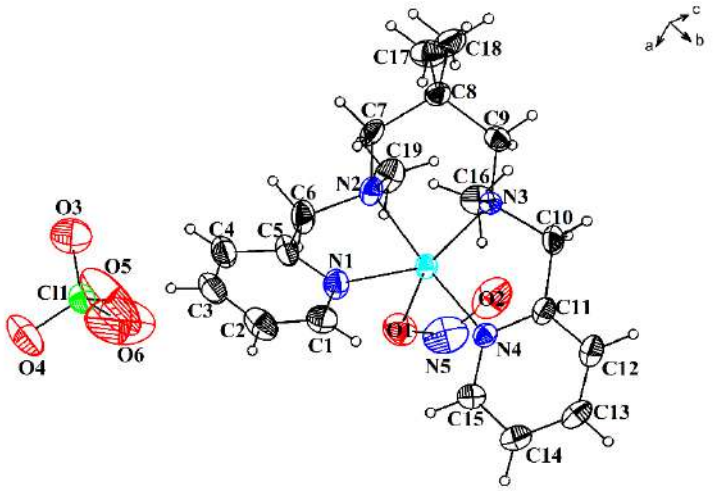

Figure 5: The crystal structure of $[Cu(L8)(NO_2^-)](ClO_4)$ **22** with atom labels. Thermal ellipsoids are drawn at 50 % probability except for the H atoms which are shown as spheres of arbitrary radii.

Further, in order to investigate the NO_2^- reactivity we synthesized the Cu^{II}-nitrito compound $[Cu(L8)(NO_2^-)](ClO_4)$ **22** (**Figure 5**) as functional model by addition of 1 equiv. of $NaNO_2$ to compound **21**. The analysis of a single crystal of compound **22** showed that the central copper(II) ion is bonded to four nitrogen atoms of ligand **L8**, and the fifth coordination site is

filled with the oxygen of a nitrite ion. The detailed investigation of the acid-catalyzed conversion of NO_2^- to NO at the Cu^{II} center in Cu^{II} -nitrito compound **22** is presented in this section.

Section II: Synthesis and spectroscopic study of tetradentate quinoline based Zn(II) compounds

Bis-quinoline derived ligands constitute a category of nonheme ligands that have been employed to synthesize model compounds and require detailed examination to fully comprehend their spectroscopic, structural, and chemical characteristics [32,33]. Chapter 5, Section II, explores uninvestigated Zn(II) compounds of non-heme tetradentate quinoline-based ligands. Four new compounds $[Zn(L9)(H_2O)(CH_3CN)](ClO_4)_2$ **23**, $[Zn(L10)(H_2O)(CH_3CN)](ClO_4)_2$ **24**, $[Zn(L11)(H_2O)(ClO_4)](ClO_4)$ **25** and $[Zn(L12)(H_2O)(ClO_4)](ClO_4)$ **26** have been prepared by reaction of $Zn(ClO_4)_2.6H_2O$ with ligands **L9-L12**. Single crystal X-ray diffractometry of compounds **23-26** showed that they possess an octahedral geometry. Compounds **12-18** were studied in detail using single-crystal XRD, revealing distinctive structural properties that are discussed in this section. A thorough examination of the structural framework showed that the unique structural characteristics arose from modifications to the ligand backbone, as detailed in this section.

References

[1] W. Sun and Q. Sun, *Acc. Chem. Res.*, 2019, **52**, 2370-2381.

[2] X. Zang, A. Chandra, Y. Lee, R. Cao, K. Ray and W. Nam, *Chem. Soc. Rev.*, 2021, **50**, 4804.

[3] A. Rajeev, M. Balamurugan and M. Sankaralingam, *ACS Catal.*, 2022, **12**, 9953-9982.

[4] J. Chen, W. Song, Y. Lee, W. Nam and B. Wiang, *Coord. Chem. Rev.*, 2023, **477**, 214945.

[5] G. Mukherjee, J. K. Satpathy, U.K. Bagha, M. Q. Mubarak, C. V. Sastri and S. P. Visser, 2022, *ACS Catal.*, 2021, **11**, 9761-9797.

[6] R. Breslow, *Acc. Chem.Res*., 1995, **28**, 146.

[7] R. Breslow, *J. Biological. Chem*., 2009, **284**, 1337.

[8] M. Costas, M. P. Mehn, M. P. Jensen and L. Que, Jr., *Chem. Rev.*, 2004, **104**,939 –986.

[9] P. C. A. Bruijnincx, G. van Koten and R. J. M. Klein Gebbink, *Chem. Soc. Rev*., 2008, **37**, 2716 –2744.

[10] S. V.K ryatov, E. V. Rybak-Akimova and S. Schindler, *Chem. Rev.*, 2005, **105**, 2175 – 2226.

[11] Y. Lu, N. Yeung, N. Sieracki and N.M. Marshall, *Nature*, 2009, **460**, 855–862.

[12] T. Devi, Y-M. Lee, W. Nam and S. Fukuzumi, *Coord. Chem. Rev.*, 2020, **410**, 213219.

[13] X.X. Li, S.S. Xue, X. Lu, M.S. Seo, Y.M. Lee, W.S. Kim, K. Bin Cho and W. Nam, *Inorg. Chem.*, 2021, **60**, 4058–4067.

[14] P. E. Gormisky and C. White, J. Am. Chem. Soc., 2013,135,14052-14055

[15] S. Jana, P. De, C. Dey, S. G. Dey, A. Dey and S. S. Gupta, Chem. Sci., 2023, 14, 10515.

[16] W. Nam, *Acc. Chem. Res*., 2007, **40**, 522

[17] S. N. Dhuri, Y-M. Lee, M. S. Seo, J. Cho, D. D. Narulkar, S. Fukuzumi and W. Nam, *Dalton Trans.*, 2015, **44**, 7634.

[18] M. Guo, Y-M. Lee, S. Fukuzumi and W. Nam, *Coord. Chem. Rev.*, 2021, **435**, 213807.

[19] A. J. Jasniewski and L. Que, Jr., *Chem. Rev.*, 2018, **118**, 2554-2592.

[20] H. M. Neu, R. A. Baglia and D. P. Goldberg, *Acc. Chem. Res.*, 2015, **48**, 2754-2764.

[21] S.S. Harmalkar, V.R. Chari, R.K. Kunkalekar and S.N. Dhuri, *New J. Chem.*, 2023, **47**, 1852–1860.

[22] S. Kumari, A.K. Mahato, A. Maurya, V.K. Singh, N. Kesharwani, P. Kachhap, I. O. Koshevoy and C. Haldar, *New J. Chem.*, 2017, **41**, 13625–13646.

[23] M. Sankaralingam, M. Balamurugan, M. Palaniandavar, P. Vadivelu and C. H. Suresh, *Chem. Eur. J.*, 2014, **20**, 11346 – 11361.

[24] D. Kim, J. Cho,Y-M. Lee, R. Sarangi, and W. Nam, *Chem. Eur. J.,* 2013, **19**, 14112 – 14118.

[25] T. L. Poulos and A. H. Follmer, *Acc. Chem. Res.*, 2022, **55**, 373−380.

[26] J. K. Satpathy, R. Yadav, U. K. Bagha, D. Kumar, C. V. Sastri and Sam P. de Visser, *Inorg. Chem.*, 2024, **63**, 6752−6766.

[27] G. Mukherjee, A. Alili, P. Barman, D. Kumar, C. V. Sastri and S. P. de Visser, *Chem. Eur. J.*, 2019, **25**, 5086.

[28] A. G. Blackman, *Polyhedron,* 2019, **161**, 1–33.

[29] M. Shyamal, A. Panja, A. Sah, *Polyhedron*, 2014, **69**, 141-148.

[30] B. C. Sanders, S. M. Hassan and Todd C. Harrop, *J. Am. Chem. Soc.*, 2014, **136**, 10230−10233.

[31] P. Bhardwaj, Kulbir, T. Devi and P. Kumar, *Inorg. Chem. Front.,* 2023, **10**, 7285.

[32] J. England, G. J. P. Britovsek, N. Rabadia and A. J. P. White, *Inorg. Chem.*, 2007, **46**, 3752−3767.

[33] D. Hong, S. Mandal, Y. Yamada, Y-M. Lee, W. Nam, A. Llobet and S. Fukuzumi, *Inorg. Chem.*, 2013, **52**, 9522−9531.

Publications

1. Synthesis and characterization of a copper (II) compound with a new N3Py2 core ligand: Influence of methyl substitution on structural parameters and catalytic mimicking activity. **Jeffrey, L. V**.; Sunder, N. D.; ***J.*** *Mol. Struct.,* **2023**, *1288,* 135719.

2. Ligand Backbone Influenced Luminescent Properties of Mononuclear Zn(II)-N3Py2 Compounds: Synthesis, Structures and Nitroaromatics Detection. **Jeffrey, L. V**.; Vishnu R. C.; Sunder, N. D.; ***J.*** *Mol. Struct.,* **2024**, *9, e202402704*.

Manuscripts under preparation

1. Synthesis, characterization and catalytic application of tetradentate amino-pyridyl appended Cu(II) compounds.
2. Influence of equatorial sulfur coordination in nonheme Fe(II) compounds on the reactivity.

Papers presented at conferences

1. "Synthesis, characterization and catalytic application of pentadentate copper (II) compounds." at International Conference on "Advance Materials: Properties and Applications" held on 20-24 February, 2023, organised by Goa University.
2. "Synthesis, characterization and catalytic fate of copper(II) compounds towards oxidation reaction." at International Conference on "Modern Trends in Inorganic Chemistry" held on 14-17 December, 2023, organised by IISc Bangalore.
3. "Synthesis, characterization and reactivity of non-heme manganese compound" at 6th symposium on "Advanced Biological Inorganic Chemistry" held on 7-11 January, 2024, organised by IACS-Kolkata and TFIR-Mumbai.
4. "Tuning the reactivity of copper(II) compounds as biomimetic catalysts", National conference on Advances in material science, organized by Department of Chemistry & Cluster research centre of Government college of Arts and Science and Commerce, Khandola, Feb. 09-10, 2024.

Seminars/Workshops/Webinars attended

[1] Attended two-day workshop on Raman Spectroscopy organized by School of Chemical Sciences and School of Physical and Applied Sciences Goa University on 26-27 August 2024

[2] Attended Webinar on “Unlock the Potential of the CSD to Teach Chemistry and Crystallography” by CCDC on 6 June 2024.

[3] Attended Workshop on “Innovating, Designing, Modeling, Characterization and Simulation of Materials and Bio-Molecule using in Silico Solution Suite, Atomistic Simulation Advanced Platform (ASAP) and J-OCTA” jointly organized by Goa University, Directorate of Research Development and Resource Mobilization (DRDRM) and Directorate of Internships, Incubation and Industry Partnership (DI3P) from 18- 19 January 2024.

[4] Attended one day seminar on “Recent Advances in Bio-Inorganic Chemistry” organized by BITS Pilani KK Birla Goa Campus, on 29 December 2023.

[5] Attended workshop on “Materials Characterization using Powder X-ray Diffraction” organized by School of Chemical Sciences Goa University on 7-8 December 2023.

[6] Attended the one-day National Seminar on Recent Trends in Applied Organic Synthesis at the School of Chemical sciences, Goa University on 26 November 2022.

[7] Attended a three- day workshop on X-ray Crystallography at the School of Chemical Sciences, Goa University from 21-23 July 2022.

[8] Attended the 2D-SAGE webinar talk by Prof. Giulia Grancini at SCS, Goa University through Google meet on 10 March 2022.

[9] Attended the 2D-SAGE webinar talk by Dr. Aditya Sadhanala at SCS, Goa University through Google meet on 21 January 2022.

[10] Attended one-day Seminar on “Recent Advances in Chemical Sciences” organized by School of Chemical Sciences, Goa University on 17 December 2019.

[11] Attended two- day Workshop on Material Science organized by University of Porto, University of Coimbra and Goa University held from 18- 19 November 2019.

[12] Attended the one-day seminar on “Recent trends in Structural Chemistry” organized by the Department of Chemistry, Goa University on 16 February 2019.

CHAPTER 1

CHAPTER 1

General Introduction

Over millions of years, evolution and natural selection has shaped living things into efficient molecular machines, each equipped with specialized tools for essential biochemical tasks. Nature uses the right tool for each job. Many of these tools are proteins that hold metal ions, called metalloproteins. A special group of metalloproteins, metalloenzymes, speed up many key reactions in cells under gentle, life-friendly conditions. The metal ions can switch between oxidation states. This lets metalloenzymes run important redox reactions with high control. Scientists try to learn from these natural systems[1].

Bioinorganic chemistry, at the interface of chemistry and biology, seeks to understand how metal ions embedded within protein frameworks achieve such reactivity and how these principles can be translated into well-defined synthetic systems[2,3]. A productive route to this understanding is biomimetic chemistry, the design of small molecule models that capture the key structural and functional features of enzymatic active sites. Breslow coined "biomimetic chemistry" to describe inventing new chemistry inspired by what nature already does[4–6]. The term "biomimetics," from the Greek *bios* (life) and *mimesis* (imitation), dates to the 1960s[7]. Rather than reproducing full protein architectures, biomimetic studies apply principles derived from nature to craft synthetic compounds that deliver comparable function. A central aim is to decipher metalloenzyme mechanisms well enough to create artificial catalysts.

Thirteen elements are widely recognized as essential for life: the alkali or alkaline earth metals Na, K, Mg and Ca, and the d-block metals V, Cr, Mn, Fe, Co, Ni, Cu, Zn and Mo, which support biological function in humans and other organisms. *d*-block transition metals play special roles in catalysis, signaling, transport, structure, and sensing. Some are essential at trace levels, while others such as iron, which mediates O_2 transport, electron transfer, and oxidation chemistry, can be abundant. Of the elements essential to life, seven are typically 3d metals in cationic form: Fe, Mn, Cu, Co, V, Ni (redox-active) and Zn (a Lewis acid and structural template)[8,9]. Biologically important 3d metals, anchor a wide array of metalloenzymes that inspire biomimetic design. Iron is indispensable, occurring in soluble methane monooxygenase (sMMO), chloroperoxidase (CPO), cytochrome P450

(CYP), and the bleomycin–iron compound (Fe–BLM), where it mediates C–H hydroxylation, peroxidation, and DNA cleavage[10–12]. Manganese is likewise prevalent in manganese superoxide dismutase (MnSOD), manganese catalase (MnCAT) and the manganese-dependent class Ib ribonucleotide reductase (RNR), governing reactive-oxygen control and dNTP biosynthesis. Cobalt appears in corrinoid (B_{12}) enzymes such as methylmalonyl-CoA mutase (MCM) and methionine synthase (MetH), and in non-heme systems like nitrile hydratase (NHase)[13–18]. Nickel sits at the cores of urease (Ure), [NiFe]-hydrogenase (H_2ase) and carbon monoxide dehydrogenase/acetyl-CoA synthase (CODH/ACS), catalyzing urea hydrolysis, H_2 interconversion and CO/CO_2 transformations[19–21]. Copper features in laccase (LAC) and tyrosinase (TYR), multicopper oxidases that couple O_2 reduction to substrate oxidation, as well as cytochrome *c* oxidase (CcO) and copper nitrite reductase (CuNiR), which mediate respiratory O_2 reduction and NO_2^- to NO conversion[22–25]. Zinc, typically as catalytic or structural Zn(II), is exemplified by carbonic anhydrase (CA), alcohol dehydrogenase (ADH) and carboxypeptidase A (CPA), effecting CO_2 hydration, alcohol/aldehyde interconversion and peptide bond hydrolysis[26–28].

Systematic investigation of enzymatic reactivity provides a practical blueprint for chemists to design and synthesize tailored, 3d metal based small molecules. Because many catalytic intermediates are short lived and air sensitive, their generation and manipulation demand careful technique. This work focuses on designing synthetic compounds that reproduce natural function, guided by insights from biology. Central to this approach is a deep understanding of metalloenzymes, whose metal cofactors promote transformations that are otherwise difficult under mild conditions[29]. The primary coordination sphere (direct ligation) defines geometry and redox properties, whereas the secondary sphere i.e. non-coordinating residues and the local environment, exerts decisive control through electrostatics, hydrogen bonding, van der Waals interactions and hydrophobic effects. Even subtle mutations in these outer sphere elements can markedly reshape activity and selectivity. Because numerous residues surround many enzymatic active sites, extracting clear structure–function parameters from the native proteins are challenging; consequently, simplified model systems capturing key features of the biological site are invaluable[30]. These models enable straightforward links between structure and reactivity and allow systematic tuning in ways that are rarely feasible in the full protein context.

Given the breadth of prior work, this introductory chapter provides only a concise backdrop to the advances in bioinorganic chemistry, while the detailed literature survey pertinent to the present study is organized chapter wise in Chapters III–V. This thesis investigates a series of new 3d metal compounds, Mn, Fe, Co, Ni, Cu and Zn, stabilized by non-heme ligands. These compounds are thoroughly characterized and evaluated in enzyme inspired model reactions and in selected sensing applications.

Heme iron enzymes feature a porphyrinoid macrocycle bound to Fe at the center, whereas non-heme enzymes employ iron coordinated by non-porphyrinoid ligands[31]. Accordingly, "heme ligands" and "non-heme ligands" refer to porphyrinoid and non-porphyrinoid scaffolds, respectively. Representative oxygenase's include cytochrome P450 (heme) and taurine/α-ketoglutarate dioxygenase (TauD, non-heme) (**Figure 1.1**), for which Fe(IV/V)=O species are invoked as key intermediates in alkane C–H activation[32]. While heme systems have been extensively explored, recent emphasis has shifted toward non-heme compounds.

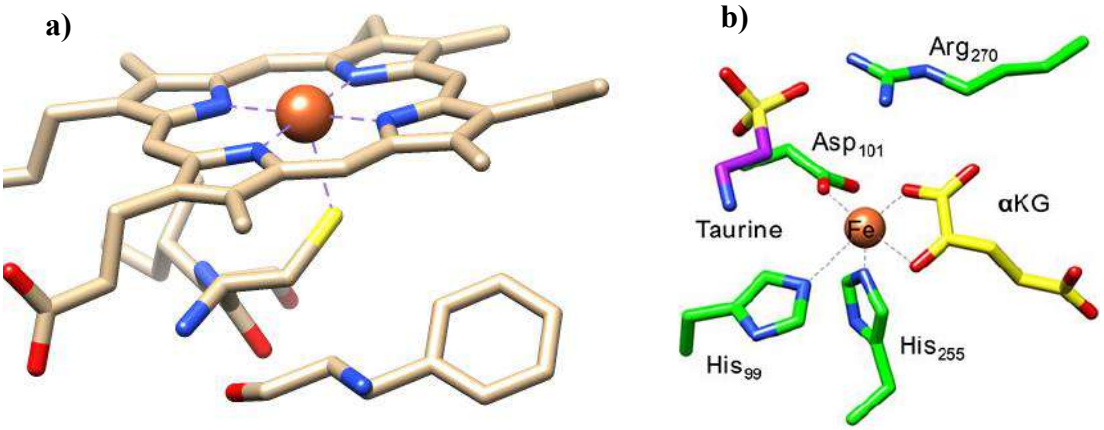

Figure 1.1 *Representative structural snapshots of (a) cytochrome P450 and (b) taurine/α-ketoglutarate dioxygenase, derived from PDB entries 5G5J and 1OS7 respectively.*

Earth's biosphere evolved under an oxidizing atmosphere, and molecular oxygen has been pivotal to the emergence and sustenance of aerobic life. Dioxygen is an especially effective oxidant because its ground state is triplet, bearing two unpaired electrons (i.e., diradical character). Consequently, many biological oxidations proceed via the thermodynamically favorable four electron reduction of O_2 to H_2O, the universal solvent of living systems. In nature, metalloenzymes commonly mediate O_2 activation to

accomplish diverse oxidative transformations. Upon coordination to a metal center, O_2 can be stepwise reduced to a spectrum of reactive oxygen species (ROS)[33,34]. The general synthetic manifold for accessing such metal oxygen intermediates in model systems is summarized in **Scheme 1.1**, proceeds via stepwise O_2 activation[35]. Initial binding of ground-state dioxygen at the metal center furnishes M–superoxo species. When superoxide does not directly participate in substrate oxidation, one-electron reduction affords M–peroxo, which upon protonation yields M–hydroperoxo. Subsequent O–O bond cleavage (homolytic or heterolytic) produces the high-valent M–oxo unit.

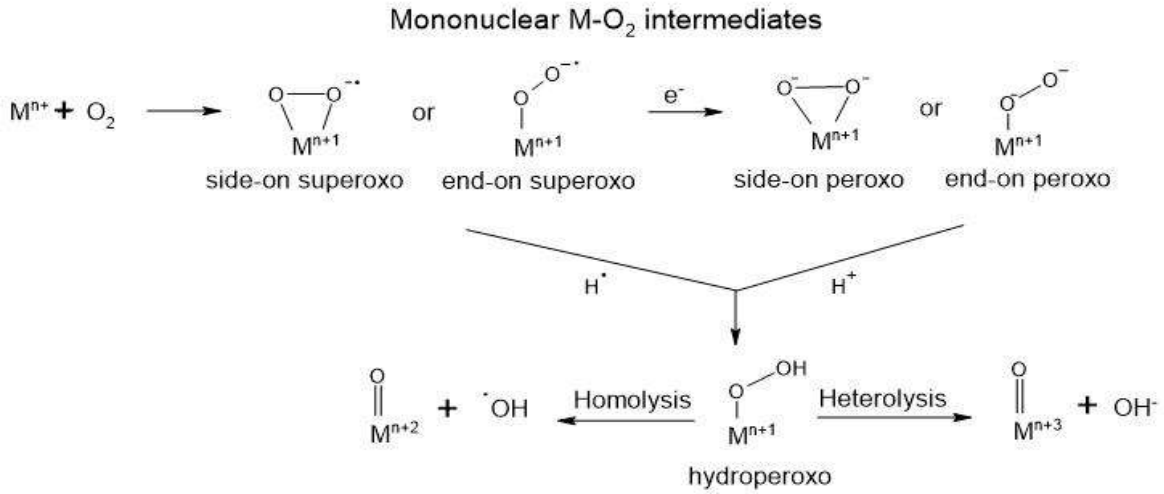

Scheme 1.1 *The synthetic routes showing formation of reactive intermediates in the enzymatic reactions by the reaction of the dioxygen with mononuclear metal centre at the active sites.*

These four high valent metal-oxygen intermediates have been identified, with spectroscopic support in enzymes. Illustrative examples include Mn(IV)=O within the oxygen-evolving complex (OEC) of photosystem II, which promotes the four electron oxidation of water to O_2[36–38]. Mononuclear nonheme Fe(IV)=O species have been implicated in α-KG-dependent oxygenases such as prolyl-4-hydroxylase[39] and taurine dioxygenase[40], in pterin-dependent hydroxylases (e.g., phenylalanine[41] and tyrosine[42] hydroxylases), and in halogenases enzymes including cytochrome C_3 halogenases[43,44] and $SyrB_2$ halogenases[45,46]. Manganese peroxo intermediates have been associated with manganese ribonucleotide reductase[47], MndD[48], Mn-SOD[49,50], and again the OEC in photosynthesis, supported by complementary spectroscopic and computational evidence. Metal hydroperoxo species are also

documented, for example, a high spin Fe(III)–OOH (S = 5/2) in benzoate 1,2-dioxygenase (EPR/Mössbauer)[51], and an end-on Fe(III)–OOH captured crystallographically in carbazole 1,9a-dioxygenase from the Rieske family[52]. Additional reactive motifs include a di-iron(III)–superoxo in myo-inositol oxygenase (MIOX), which converts myo-inositol to D-glucuronate via activation of O_2 at a mixed-valent Fe(II/III) site[53], and a Mn(III)–superoxo (S = 5/2) observed in Mn-substituted HPCD (Mn-HPCD)[48].

Inspired by these biological blueprints, chemists have developed small, well-defined transition-metal models that form and utilize such intermediates in the laboratory. The protein environment is structurally diverse, with metal ions bound to heteroatom donors (N/O/S) and small ligands embedded within a large macromolecular matrix[54]. To emulate this, synthetic systems use multidentate ligands that recreate the primary and secondary spheres around the metal. Ligand choice governs steric, electronic, redox properties, and flexibility, thereby influencing accessible oxidation and spin states and ultimately reactivity[55]. This tunability underpins the surge of interest in non-heme ligand platforms, which can be systematically modified while maintaining robustness under oxidative conditions and stabilizing high valent states required for biomimetic chemistry.

Several non-heme ligand families have been especially influential (**Scheme 1.2**). Tetramethylated cyclam macrocycles of varying ring size (12-, 13-, 14-, 15-TMC) stabilize a broad range of 3d metal intermediates[56]. Pentadentate scaffolds such as N4Py[57] and Bn-tpen[58] support high valent metal-oxo species, in some cases even at room temperature. By contrast, certain tetradentate ligands (e.g., BQCN, TPA) stabilize Mn(IV)=O and Fe(IV)=O only at cryogenic temperatures[59], whereas the pentadentate analogues (Bn-tpen, N4Py) yield Fe(IV)=O and Mn(IV)=O intermediates that persist at ambient conditions[60,61]. Macrocycle ring size also modulates reactivity: 13-TMC-supported Fe(IV)=O outperforms 14-TMC analogues in oxidation, and 12-TMC-supported Co(III)–peroxo is more reactive than its 13-TMC counterpart in aldehyde deformylation[62]. In addition, redox-inactive Lewis acids (e.g., $Ca^{2+,}$ $Sc^{3+,}$) enhance activity by stabilizing key states or facilitating O–O chemistry[63–66]. Inspired by PSII, where Ca^{2+} is proposed to assist O–O bond formation at the Mn–Ca site[67–70], studies

show Sc^{3+} can boost Fe(IV)=O and Mn(IV)=O oxidations[71,72], with single-crystal XRD confirming Sc^{3+} binding to an Fe(IV)=O unit [68].

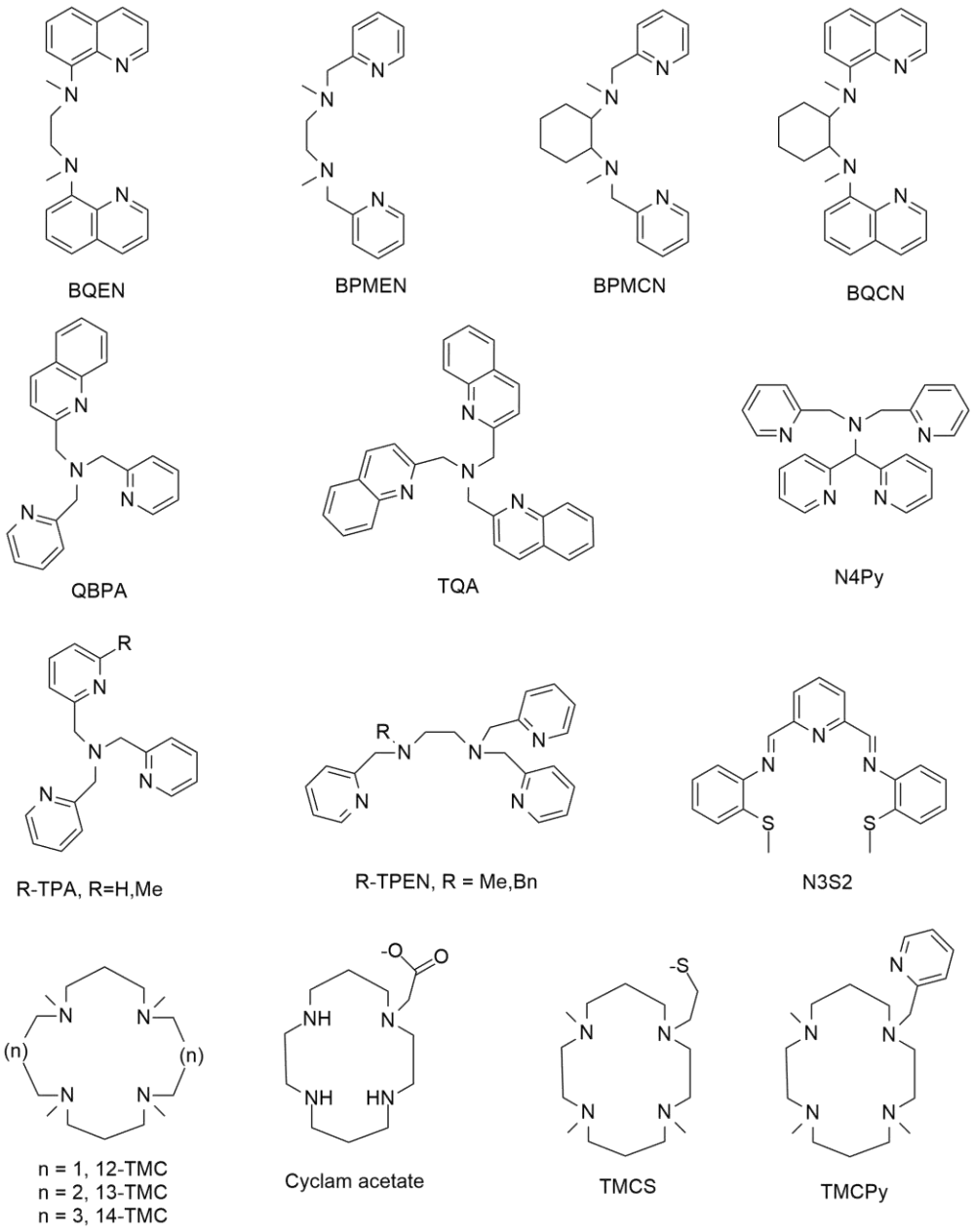

Scheme 1.2 *The structure of non-heme ligands that are frequently employed for stabilizing high valent metal-O_2 species.*

Biologically, high-valent species arise from O_2 and its reduced forms or water. In the laboratory, diverse oxidants are used, including peracids, PhIO, KO_2, *m*-CPBA, CAN/H_2O and H_2O_2[73]. The first synthetic, spectroscopically characterized Fe(III)–superoxo was generated by bubbling O_2 into a THF solution of Fe(II)(BDPP) at −80°C[74], and an end-

on Mn(III)–superoxo has likewise been prepared using O_2. Water has served as an oxygen source in several cases[75–77]. H_2O_2 offers a greener route to intermediates, while PhIO is a versatile two-electron oxygen donor; historically, ozonolysis of an Fe-cyclam acetate provided an early Fe(IV)=O example[78].

Ligand architecture plays an important role in tuning function in non-heme 3d compounds. Multidentate N/S/O-donor scaffolds define geometry (octahedral, trigonal bipyramidal, square planar/pyramidal), enforce chelation and rigidity, and modulate metal center electronics, thereby stabilizing specific oxidation and spin states. Macrocyclic amines, polypyridyl and bis-quinoline frameworks are frequently deployed to access high valent metal-oxygen adducts and to tune reaction pathways for O–O bond cleavage and H-atom abstraction (HAT). Secondary sphere elements such as proximal H-bond networks, charged or Lewis-acidic groups and sterically defined pockets further influence substrate binding, transition state stabilization and product release. In addition, exogenous ligands (axial donors, counter-anions) and medium effects (solvent, pH, ionic strength) can pivot reactivity between nucleophilic, electrophilic and radical pathways. Experimentally, building a faithful and useful model requires (i) rational ligand synthesis, (ii) controlled metalation to access targeted oxidation states and (iii) comprehensive physicochemical characterization. Against this backdrop, the present thesis focuses on the synthesis and characterization of non-heme 3d metal compounds tailored for selected applications spanning oxidative catalysis and small molecule activation. Emphasis is placed on establishing structure, property and reactivity relationships by systematic variation of ligand topology (denticity, donor set, rigidity), steric profile and electronic tuning.

The objectives of the present investigation are as follows

1. Design and synthesis of novel as well as known non-heme ligands that are robust and capable of stabilizing 3d metals across multiple oxidation states, with built-in handles for secondary sphere modulation.
2. The characterization of the ligands using IR and NMR spectroscopy.
3. Preparation of non-heme 3d metal compounds using synthesised ligands under controlled metalation conditions to access targeted geometries and spin states.

4. Comprehensive characterization using CHN analysis, IR, UV–Vis spectroscopic techniques, ESI-MS spectrometry, single-crystal X-ray diffraction and where applicable, EPR and VSM.
5. Investigate enzyme-mimetic reactivity of the complexes through representative model transformations using artificial oxidants.
6. Reactivity assessment in selected applications, including oxidative C–H activation, aldehyde deformylation and nitrite reduction to nitric oxide, with product analysis by GC and appropriate methods.
7. Examine extended properties of the systems, including analytical sensing application.

References

1 A. W. Foster, T. R. Young, P. T. Chivers and N. J. Robinson, *Curr. Opin. Chem. Biol.*, 2022, **66**, 102095.

2 *J. Am. Chem. Soc.*, 2010, **132**, 14689–14693.

3 E. L. Que, *Curr. Opin. Chem. Biol.*, 2022, **69**, 102159.

4 R. Breslow, *Acc. Chem. Res.*, 1995, **28**, 146–153.

5 R. Breslow, *Isr. J. Chem.*, 1979, **18**, 187–191.

6 R. Breslow, *Chem. Soc. Rev.*, 1972, **1**, 553.

7 J. F. . Vincent, O. A. Bogatyreva, N. R. Bogatyrev, A. Bowyer and A.-K. Pahl, *J. R. Soc. Interface*, 2006, **3**, 471–482.

8 C. Andreini, I. Bertini, G. Cavallaro, G. L. Holliday and J. M. Thornton, *JBIC J. Biol. Inorg. Chem.*, 2008, **13**, 1205–1218.

9 R. J. P. Williams and J. J. R. Fraústo da Silva, *Coord. Chem. Rev.*, 2000, **200**–**202**, 247–348.

10 R. Banerjee, J. C. Jones and J. D. Lipscomb, *Annu. Rev. Biochem.*, 2019, **88**, 409–431.

11 I. G. Denisov, T. M. Makris, S. G. Sligar and I. Schlichting, *Chem. Rev.*, 2005, **105**, 2253–2278.

12 J. Stubbe and J. W. Kozarich, *Chem. Rev.*, 1987, **87**, 1107–1136.

13 J. Azadmanesh and G. E. O. Borgstahl, *Antioxidants (Basel, Switzerland)*, DOI:10.3390/antiox7020025.

14 J. W. Whittaker, *Arch. Biochem. Biophys.*, 2012, **525**, 111–120.

15 T. B. Ruskoski and A. K. Boal, *J. Biol. Chem.*, 2021, **297**, 101137.

16 R. Mascarenhas, H. Gouda, M. Ruetz and R. Banerjee, *Methods Enzymol.*, 2022, **668**, 309–326.

17 R. Banerjee and S. W. Ragsdale, *Annu. Rev. Biochem.*, 2003, **72**, 209–247.

18 Z. Cheng, Y. Xia and Z. Zhou, *Front. Bioeng. Biotechnol.*, DOI:10.3389/fbioe.2020.00352.

19 L. Mazzei, F. Musiani and S. Ciurli, *JBIC J. Biol. Inorg. Chem.*, 2020, **25**, 829–845.

20 H. Ogata, W. Lubitz and Y. Higuchi, *J. Biochem.*, 2016, **160**, 251–258.

21 Y. Kung and C. L. Drennan, in *The Biological Chemistry of Nickel*, The Royal Society of Chemistry, 2017, pp. 121–148.

22 S. M. Jones and E. I. Solomon, *Cell. Mol. Life Sci.*, 2015, **72**, 869–883.

23 S. Zolghadri, A. Bahrami, M. T. Hassan Khan, J. Munoz-Munoz, F. Garcia-Molina, F. Garcia-Canovas and A. A. Saboury, *J. Enzyme Inhib. Med. Chem.*, 2019, **34**, 279–309.

24 S. Yoshikawa and A. Shimada, *Chem. Rev.*, 2015, **115**, 1936–1989.

25 S. Horrell, D. Kekilli, R. W. Strange and M. A. Hough, *Metallomics*, 2017, **9**, 1470–1482.

26 C. T. Supuran, *Biochem. J.*, 2016, **473**, 2023–2032.

27 D. S. Auld and T. Bergman, *Cell. Mol. Life Sci.*, 2008, **65**, 3961–3970.

28 A. V. Kilshtain and A. Warshel, *Proteins Struct. Funct. Bioinforma.*, 2009, **77**, 536–550.

29 Y. Lu, N. Yeung, N. Sieracki and N. M. Marshall, *Nature*, 2009, **460**, 855–862.

30 A. J. . Kirby and F. Hollfelder, *From enzyme models to model enzymes*, Royal Society of Chemistry, 2009.

31 S. Sahu and D. P. Goldberg, *J. Am. Chem. Soc.*, 2016, **138**, 11410–11428.

32 Y. Morimoto, J. Park, T. Suenobu, Y.-M. Lee, W. Nam and S. Fukuzumi, *Inorg. Chem.*, 2012, **51**, 10025–10036.

33 J. M. McCord, *Am. J. Med.*, 2000, **108**, 652–659.

34 J. M. McCord, *J. Nutr.*, 2004, **134**, 3171S-3172S.

35 K. Ray, F. F. Pfaff, B. Wang and W. Nam, *J. Am. Chem. Soc.*, 2014, **136**, 13942–13958.

36 J. P. McEvoy and G. W. Brudvig, *Chem. Rev.*, 2006, **106**, 4455–4483.

37 T. J. Meyer, M. H. V. Huynh and H. H. Thorp, *Angew. Chemie Int. Ed.*, 2007, **46**, 5284–5304.

38 V. L. Pecoraro and W.-Y. Hsieh, *Inorg. Chem.*, 2008, **47**, 1765–1778.

39 L. M. Hoffart, E. W. Barr, R. B. Guyer, J. M. Bollinger and C. Krebs, *Proc. Natl. Acad. Sci.*, 2006, **103**, 14738–14743.

40 P. J. Riggs-Gelasco, J. C. Price, R. B. Guyer, J. H. Brehm, E. W. Barr, J. M. Bollinger and C. Krebs, *J. Am. Chem. Soc.*, 2004, **126**, 8108–8109.

41 A. J. Panay, M. Lee, C. Krebs, J. M. Bollinger and P. F. Fitzpatrick, *Biochemistry*, 2011, **50**, 1928–1933.

42 B. E. Eser, E. W. Barr, P. A. Frantom, L. Saleh, J. M. Bollinger, C. Krebs and P. F. Fitzpatrick, *J. Am. Chem. Soc.*, 2007, **129**, 11334–11335.

43 D. P. Galonić, E. W. Barr, C. T. Walsh, J. M. Bollinger and C. Krebs, *Nat. Chem. Biol.*, 2007, **3**, 113–116.

44 D. Galonić Fujimori, E. W. Barr, M. L. Matthews, G. M. Koch, J. R. Yonce, C. T. Walsh, J. M. Bollinger, C. Krebs and P. J. Riggs-Gelasco, *J. Am. Chem. Soc.*, 2007, **129**, 13408–13409.

45 S. D. Wong, M. Srnec, M. L. Matthews, L. V. Liu, Y. Kwak, K. Park, C. B. Bell III, E. E. Alp, J. Zhao, Y. Yoda, S. Kitao, M. Seto, C. Krebs, J. M. Bollinger and E. I. Solomon, *Nature*, 2013, **499**, 320–323.

46 M. L. Matthews, C. M. Krest, E. W. Barr, F. H. Vaillancourt, C. T. Walsh, M. T. Green, C. Krebs and J. M. Bollinger, *Biochemistry*, 2009, **48**, 4331–4343.

47 J. A. Cotruvo, T. A. Stich, R. D. Britt and J. Stubbe, *J. Am. Chem. Soc.*, 2013, **135**, 4027–4039.

48 W. A. Gunderson, A. I. Zatsman, J. P. Emerson, E. R. Farquhar, L. Que, J. D. Lipscomb and M. P. Hendrich, *J. Am. Chem. Soc.*, 2008, **130**, 14465–14467.

49 C. Bull, E. C. Niederhoffer, T. Yoshida and J. A. Fee, *J. Am. Chem. Soc.*, 1991, **113**, 4069–4076.

50 A. S. Hearn, C. Tu, H. S. Nick and D. N. Silverman, *J. Biol. Chem.*, 1999, **274**, 24457–24460.

51 M. D. Wolfe, D. J. Altier, A. Stubna, C. V. Popescu, E. Münck and J. D. Lipscomb, *Biochemistry*, 2002, **41**, 9611–9626.

52 Y. Ashikawa, Z. Fujimoto, Y. Usami, K. Inoue, H. Noguchi, H. Yamane and H. Nojiri, *BMC Struct. Biol.*, 2012, **12**, 15.

53 G. Xing, Y. Diao, L. M. Hoffart, E. W. Barr, K. S. Prabhu, R. J. Arner, C. C. Reddy, C. Krebs and J. M. Bollinger, *Proc. Natl. Acad. Sci.*, 2006, **103**, 6130–6135.

54 T. Joshi, B. Graham and L. Spiccia, *Acc. Chem. Res.*, 2015, **48**, 2366–2379.

55 M. Swart and M. Gruden, *Acc. Chem. Res.*, 2016, **49**, 2690–2697.

56 J. Cho, R. Sarangi and W. Nam, *Acc. Chem. Res.*, 2012, **45**, 1321–1330.

57 Y. Lee, S. N. Dhuri, S. C. Sawant, J. Cho, M. Kubo, T. Ogura, S. Fukuzumi and W. Nam, *Angew. Chemie Int. Ed.*, 2009, **48**, 1803–1806.

58 H. Yoon, Y. Morimoto, Y.-M. Lee, W. Nam and S. Fukuzumi, *Chem. Commun.*, 2012, **48**, 11187.

59 S. C. Sawant, X. Wu, J. Cho, K. Cho, S. H. Kim, M. S. Seo, Y. Lee, M. Kubo, T. Ogura, S. Shaik and W. Nam, *Angew. Chemie Int. Ed.*, 2010, **49**, 8190–8194.

60 J. Kaizer, E. J. Klinker, N. Y. Oh, J.-U. Rohde, W. J. Song, A. Stubna, J. Kim, E. Münck, W. Nam and L. Que, *J. Am. Chem. Soc.*, 2004, **126**, 472–473.

61 X. Wu, M. S. Seo, K. M. Davis, Y.-M. Lee, J. Chen, K.-B. Cho, Y. N. Pushkar and W. Nam, *J. Am. Chem. Soc.*, 2011, **133**, 20088–20091.

62 J. Cho, R. Sarangi, H. Y. Kang, J. Y. Lee, M. Kubo, T. Ogura, E. I. Solomon and W. Nam, *J. Am. Chem. Soc.*, 2010, **132**, 16977–16986.

63 F. F. Pfaff, S. Kundu, M. Risch, S. Pandian, F. Heims, I. Pryjomska-Ray, P. Haack, R. Metzinger, E. Bill, H. Dau, P. Comba and K. Ray, *Angew. Chemie Int. Ed.*, 2011, **50**, 1711–1715.

64 W. W. Y. Lam, S.-M. Yiu, J. M. N. Lee, S. K. Y. Yau, H.-K. Kwong, T.-C. Lau, D. Liu and Z. Lin, *J. Am. Chem. Soc.*, 2006, **128**, 2851–2858.

65 S.-M. Yiu, Z.-B. Wu, C.-K. Mak and T.-C. Lau, *J. Am. Chem. Soc.*, 2004, **126**, 14921–14929.

66 C. G. Miller, S. W. Gordon-Wylie, C. P. Horwitz, S. A. Strazisar, D. K. Peraino, G. R. Clark, S. T. Weintraub and T. J. Collins, *J. Am. Chem. Soc.*, 1998, **120**, 11540–11541.

67 P. Gatt, S. Petrie, R. Stranger and R. J. Pace, *Angew. Chemie Int. Ed.*, 2012, **51**, 12025–12028.

68 Y. Umena, K. Kawakami, J.-R. Shen and N. Kamiya, *Nature*, 2011, **473**, 55–60.

69 J. S. Kanady, E. Y. Tsui, M. W. Day and T. Agapie, *Science (80-.).*, 2011, **333**, 733–736.

70 Y. J. Park, J. W. Ziller and A. S. Borovik, *J. Am. Chem. Soc.*, 2011, **133**, 9258–9261.

71 J. Park, Y. Morimoto, Y.-M. Lee, W. Nam and S. Fukuzumi, *J. Am. Chem. Soc.*, 2011, **133**, 5236–5239.

72 J. Chen, Y.-M. Lee, K. M. Davis, X. Wu, M. S. Seo, K.-B. Cho, H. Yoon, Y. J.

Park, S. Fukuzumi, Y. N. Pushkar and W. Nam, *J. Am. Chem. Soc.*, 2013, **135**, 6388–6391.

73 S. Fukuzumi, T. Kojima, Y.-M. Lee and W. Nam, *Coord. Chem. Rev.*, 2017, **333**, 44–56.

74 C.-W. Chiang, S. T. Kleespies, H. D. Stout, K. K. Meier, P.-Y. Li, E. L. Bominaar, L. Que, E. Münck and W.-Z. Lee, *J. Am. Chem. Soc.*, 2014, **136**, 10846–10849.

75 H. Kotani, T. Suenobu, Y.-M. Lee, W. Nam and S. Fukuzumi, *J. Am. Chem. Soc.*, 2011, **133**, 3249–3251.

76 D. Wang, K. Ray, M. J. Collins, E. R. Farquhar, J. R. Frisch, L. Gómez, T. A. Jackson, M. Kerscher, A. Waleska, P. Comba, M. Costas and L. Que, *Chem. Sci.*, 2013, **4**, 282–291.

77 M. J. Collins, K. Ray and L. Que, *Inorg. Chem.*, 2006, **45**, 8009–8011.

78 C. A. Grapperhaus, B. Mienert, E. Bill, T. Weyhermüller and K. Wieghardt, *Inorg. Chem.*, 2000, **39**, 5306–5317.

CHAPTER 2

CHAPTER 2

2.1 Introduction

Chapter 2 sets out the experimental foundation of this work, built on carefully designed protocols and systematic observation. It consolidates the procedures used to design ligand architecture and assemble the target metal compounds. The technical aspects and key operating parameters of the instruments employed for structural, spectroscopic, kinetic, and application-oriented studies are also discussed. An integrated overview of these synthetic routes and characterization steps is summarized in **Scheme 2.1**.

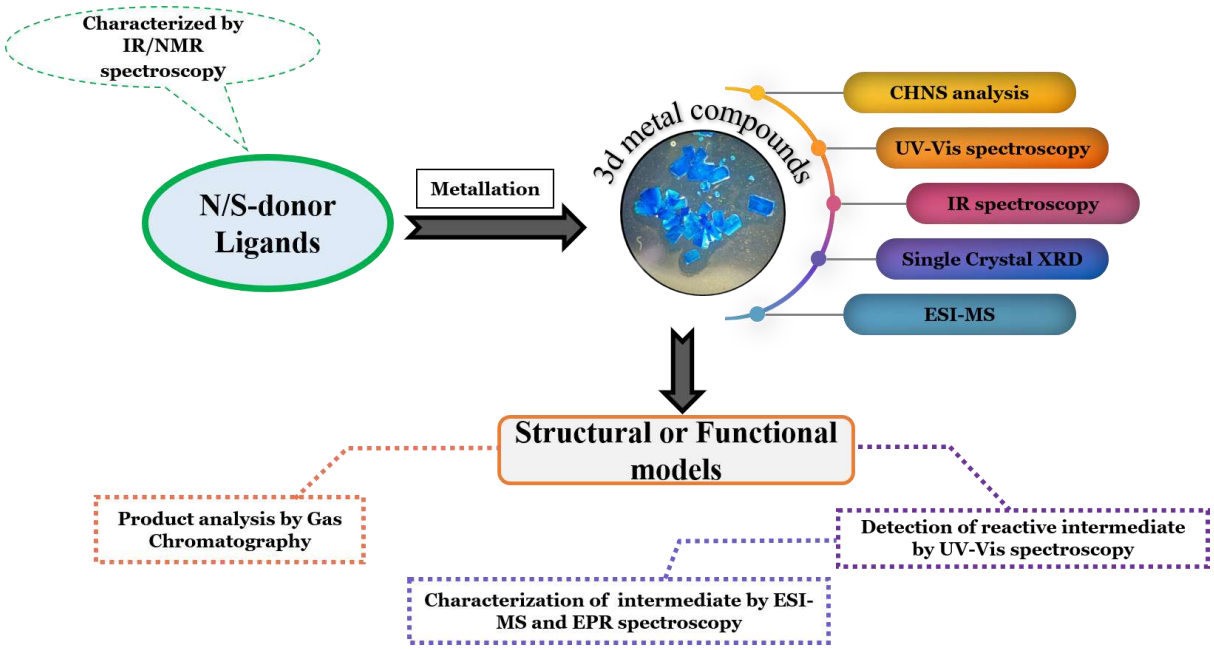

Scheme 2.1 *Diagrammatic illustration of the general techniques and work strategy used in this present work.*

2.2 Experimental section

2.2.1 Chemicals and solvents

All the chemicals employed were of analytical reagent grade and were used without further purification unless specified. Iodometric titrations were used to measure the precise amount of peroxide in commercially available 30% H_2O_2[1]. Solvents were dried according to established protocols[2] and distilled under nitrogen atmosphere prior to use. Purified solvents were transferred into pre-dried glassware under vacuum. All glassware was thoroughly dried either by prolonged heating in a hot oven before use.

2.2.2 Synthesis of metal perchlorate hexahydrate $M(ClO_4)_2.6H_2O$

The 3d-metal compounds described in this study were obtained by reacting non-heme ligands with the corresponding metal perchlorate salts. The hexahydrate salts, $M(ClO_4)_2 \cdot 6H_2O$, were prepared according to a reported method[1]: an aqueous suspension of the metal carbonate was treated dropwise with 70% aqueous perchloric acid under stirring until CO_2 evolution ceased. The mixture was filtered to remove any residual carbonate, and the clear filtrate was slowly evaporated to afford crystalline metal perchlorates. The isolated salts, $Mn(ClO_4)_2 \cdot 6H_2O$ (pale pink), $Ni(ClO_4)_2 \cdot 6H_2O$ (green), $Co(ClO_4)_2 \cdot 6H_2O$ (reddish-pink) and $Cu(ClO_4)_2 \cdot 6H_2O$ (dark blue), were obtained as crystalline solids.

Caution: *Perchlorates salts are potential explosive and should be handled in small quantity with care.*

2.2.3 Synthesis of iodosylbenzene (PhIO)

Iodosylbenzene (PhIO) was prepared following a reported method[3]. Finely powdered iodosobenzene diacetate (3.2 g, 0.010 mol) was placed in a 100 mL vessel under vigorous stirring, and 15 mL of 3N NaOH was added dropwise over ~5 min. Any agglomerates that formed initially were broken up with a spatula for ~15 min, and the mixture was then left to stand for a further 45 min to complete the conversion. Water (10 mL) was added to the suspension and stirred vigorously, the crude PhIO was collected by vacuum filtration. The solid was triturated with 20 mL of water, refiltered, and washed thoroughly with an additional 20 mL of water before drying under vacuum to give a yellow solid. Final purification was achieved by trituration with 10 mL of chloroform, followed by filtration and air-drying.

2.2.4 Synthesis strategy employed for the synthesis of ligands

The aminopyridine based ligands were prepared by the condensation of a primary amine and pyridine-2-carboxaldehyde to give Schiff base imine, which was then reduced by sodium borohydride to give the non-methylated aminopyridine ligands as shown in **Scheme 2.2**. We have further reported the synthesis of novel N-methylated aminopyridine ligands from the non-methylated precursors following the Eschweiler-Clarke reaction[4,5] (**Scheme 2.3**).

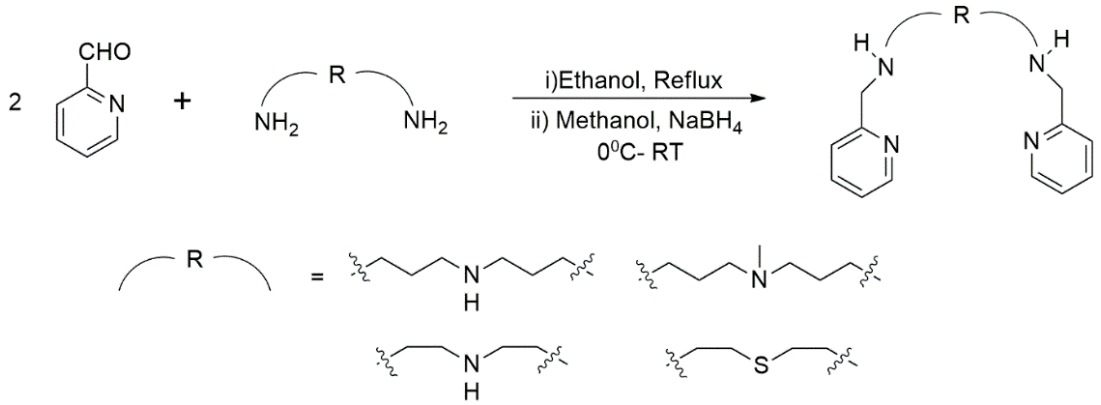

Scheme 2.2 *Synthetic route employed to synthesize non-methylated aminopyridine ligands.*

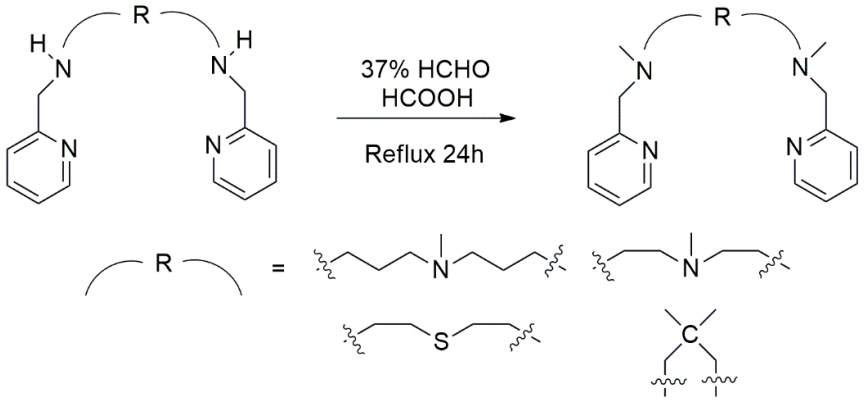

Scheme 2.3 *Synthetic route employed to synthesize methylated aminopyridine ligands.*

Quinoline-based ligands were prepared using a generalized synthetic protocol. The corresponding primary amines were reacted with 8-hydroxyquinoline via The modified Bucherer reaction, initially reported by Nielsen and co-workers[6] (**Scheme 2.4**). Minor adjustments to the workup substantially improved the isolated yields.

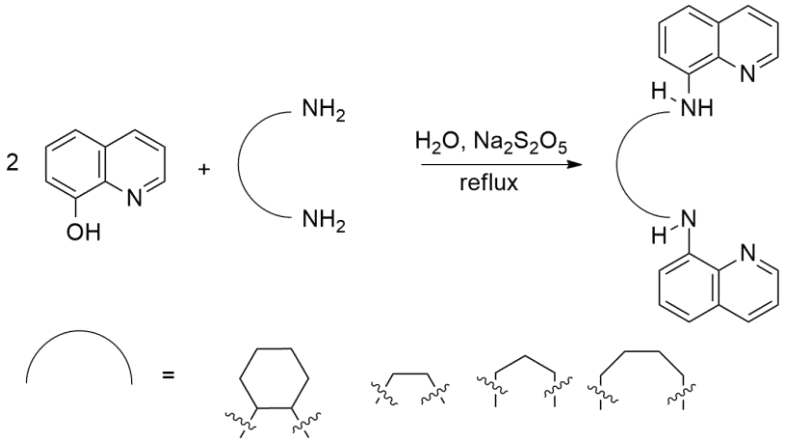

Scheme 2.4 *Synthetic route employed to synthesize non-methylated quinoline-based ligands.*

2.2.5 Reaction setup for the synthesis of metal compounds

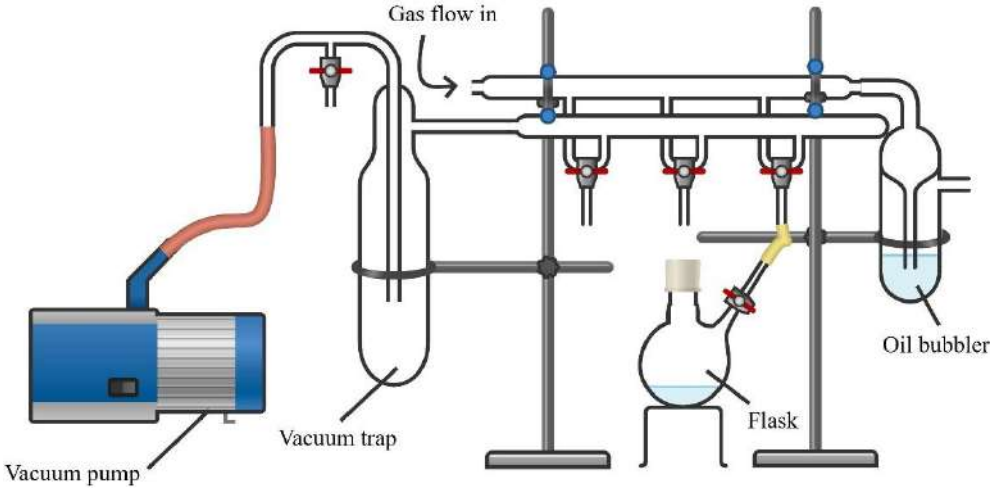

Figure 2.1 *Schlenk line setup for the synthesis of metal compounds under inert atmosphere.*

The Schlenk line setup used for synthesis of compounds is illustrated in **Figure 2.1**. All glassware (Schlenk flasks, adapters, syringes) was oven dried and assembled under a positive flow of dry N_2. The round bottom Schlenk flask containing the metal perchlorate solution was sealed with a septum and connected to the dual manifold via a two-way stopcock. The assembly was evacuated and backfilled with N_2; this pump and purge cycle was repeated 4 times to remove residual oxygen and moisture to establish an inert atmosphere. Where required, solvents were pre-dried and degassed.

With the metal solution stirring, the ligand solution was introduced dropwise by syringe through the septum. Addition rates were kept slow to minimize local concentration gradients and to control heat release; the internal pressure was relieved via a needle vent to maintain a gentle N_2 overpressure. After complete addition, the mixture was stirred for approximately 5 h, maintaining the inert atmosphere throughout. Crystallization was achieved by slow diffusion of diethyl ether into the reaction mixture. Throughout, a slight positive N_2 pressure was maintained, and all transfers were performed by syringe or cannula to avoid air ingress.

2.3 Instrumentation techniques

2.3.1 Infrared spectroscopy (IR)

The infrared (IR) region of the electromagnetic spectrum is conventionally divided into three parts: near-IR (14,000–4,000 cm^{-1}), mid-IR (4,000–400 cm^{-1}), and far-IR (400–10 cm^{-1}). In IR spectroscopy, a molecule absorbs radiation at frequencies characteristic of its structure; absorption occurs when the incident frequency matches that of a normal vibrational mode (i.e., is resonant). In this work, IR spectroscopy was used primarily to characterize the ligands and their metal complexes, and to track multistep ligand syntheses via changes in functional group signatures[7]. Upon coordination to a metal centre, diagnostic ligand bands often shift to lower wavenumbers. When perchlorate served as the counter anion, its distinctive IR bands also corroborated successful metalation. Spectra were collected in the 4,000–400 cm^{-1} range on a Shimadzu IRPrestige-21 FT-IR spectrometer (4 cm^{-1} resolution) using KBr pellets prepared from finely ground samples and on an Alpha II transmittance FT-IR instrument.

2.3.2 Nuclear magnetic resonance (NMR) spectroscopy

Nuclear magnetic resonance (NMR) spectroscopy probes how magnetically active nuclei respond to a strong external field and radiofrequency excitation; in such a field, nuclei behave like tiny bar magnets and resonate at characteristic frequencies dictated by their chemical environment[8]. We used NMR to confirm the structures of the synthesized ligands and to assess their purity. ^{1}H, ^{13}C, and DEPT spectra were acquired on a Bruker Avance III 400 MHz instrument with the samples dissolved in $CDCl_3$.

2.3.3 Elemental analysis (CHN)

Elemental (CHNS) analysis was used to determine the mass percentages of carbon, hydrogen, nitrogen, and sulfur in each sample. For measurement, a known amount of material was weighed into a tin foil capsule, sealed, and placed in the instrument's loading assembly. Using sulfanilamide as the calibration standard, CHN measurements were performed on an Elementar vario MICRO cube (CHNS) analyzer to verify the composition and assess the purity of the synthesized ligands and metal compounds.

2.3.4 UV-Visible spectroscopy

Ultraviolet–visible (UV–Vis) spectroscopy quantifies how a sample absorbs UV and visible light and is widely used to characterize materials. According to the Beer Lambert law, absorbance (A) varies linearly with the concentration of the absorbing species and the optical path length. In this study, UV–Vis measurements served to probe the electronic structures of the metal compounds and to characterize species formed during reactions. All spectra were recorded in 1 cm quartz cuvettes. The generation of metal–oxygen reactive intermediates was monitored by UV–Vis spectroscopy: upon addition of oxidants, these intermediates displayed bands that were clearly distinct from those of the precursor compounds. Their stability was assessed by following the time dependent absorbance at the diagnostic λ_{max}. Kinetic information (rate constants) was obtained under pseudo-first-order conditions by fitting the change in absorbance at λ_{max} at controlled temperatures. Spectra were collected on an Agilent 8453 UV–Vis spectrophotometer equipped with a liquid-nitrogen cryostat (Unisoku) and a temperature controller.

2.3.5 Electron spray ionization mass spectroscopy (ESI-MS)

Mass spectrometry was employed to characterize both the metal compounds and, where possible, transient solution-phase intermediates. Acetonitrile solutions were analyzed by electrospray ionization (ESI-MS) using Applied Biosystem Matrix-assisted Laser Desorption Ionization Time-of-flight (MALDI-TOF) spectrometer and on a Thermo Finnigan (San Jose, CA, USA) LCQ^{TM} Advantage MAX quadrupole ion trap via direct infusion using a syringe pump (20 μL min^{-1}). The spray potential was typically 4.7 kV, and the capillary temperature was adjusted to suit the thermal stability of each sample.

2.3.6 Electron paramagnetic resonance (EPR) spectroscopy

A subfield of absorption spectroscopy known as electron paramagnetic resonance (EPR) studies how paramagnetic materials absorb microwave-frequency radiation to cause changes in the magnetic energy levels of electrons with unpaired spins. The foundation of ESR is the fact that molecules, atoms, ions, or molecular fragments with an odd number of electrons display distinctive magnetic characteristics. The resonance condition and the spectrum depends on the local environment (e.g., ligand field, geometry, and nearby

nuclei). EPR therefore serves as a sensitive probe for identifying paramagnetic centers and extracting information about their electronic structure and surroundings[9]. The X-band EPR measurements were performed on a JEOL X-band spectrometer (JESFA100) at liquid nitrogen temperature (77 K).

2.3.7 Single crystal X-ray diffractometry

Single crystals appropriate for structural analysis were obtained using the vapor diffusion of diethyl ether into an acetonitrile solution of metal compounds and slow evaporation techniques. The Bruker D8 Quest Eco X-ray diffractometer was used to determine the single crystal structure of the compounds[10]. At room temperature (RT), intensity values were obtained using monochromatic light (MoKα = 0.7107 Å). The frames were integrated, absorption correction was carried out, and the unit cell was ascertained using the APEX4 software suite (Version 2021.10-0). SHELXS was used to solve the structures, and SHELXL was used for further modifications. Anisotropic refinement was used for all non-hydrogen atoms. The hydrogen bonding parameters were determined by the WinGX Single Crystal Suite. "Diamond 2: Crystal and Molecular Structure Visualization" and "Mercury 4.2" softwares were used to create crystal pictures.

2.3.8 Gas chromatography (GC)

The Shimadzu GC 2014 with an HP capillary column (30 m x 0.25 mm x 2.5 μM) and an FID detector was used to quantify the organic products in the catalytic reactions. The products' peak areas and retention times were then compared with the standard curves that were produced using authentic samples. Decane was used as an internal standard.

2.3.9 Photoluminescence (PL) spectroscopy

The luminescence characteristics of the compounds were investigated using photoluminescence spectroscopy[11]. The Cary Eclipse Fluorescence Spectrophotometer (G9800A) from Agilent Technologies, which uses xenon flash lamp technology, was used to acquire the photoluminescence spectra.

2.3.10 Powder X- ray diffraction (PXRD)

Powder X-ray diffraction is an analytical method that can provide information about the unit cell dimensions, purity assessment, studying polymorphism and used for phase identification of a crystalline material. The diffraction pattern was obtained employing a RIGAKU ULTIMA IV and RIGAKU SMARTLAB diffractometer using Cu-Kα radiations.

2.3.11 Thermogravimetric studies

Thermogravimetric Analysis (TGA) and Derivative Thermogravimetry (DTG) are two methods for examining a material's thermal characteristics. TGA measures the change in weight of a sample as it is heated or cooled whereas DTG is the first derivative of the TGA curve, which indicates the rate of weight change with respect to temperature or time. TGA and DTG were determined using the Netzsch STA 409 analyser.

2.3.12 Vibrating Sample Magnetometer (VSM) and Superconducting Quantum Interference Device (SQUID)

Magnetic susceptibility describes how strongly a material becomes magnetized when it is placed in an external magnetic field. If the response is positive i.e. the magnetization aligns with the field, the material is paramagnetic; if the response is negative i.e. it opposes the field, the material is diamagnetic[12]. Field dependent magnetization measurements including zero-field-cooled (ZFC) and field-cooled (FC) protocols were carried out between 5 and 300 K under an applied field of 100 Oe (M-T) with S700X SQUID magnetometer, Cryogenic Limited and The Quantum Design, USA make Versalab Cryogen free VSM with 3 Tesla Magnet and temperature range of 50-400 K.

The following chapters have covered the specific synthetic procedures as well as the ligand and new metal compound characterization used in this investigation. **Scheme 2.5** and **Scheme 2.6** shows the chemical structures of the ligands **L1-L12** and metal compounds **1-26** respectively.

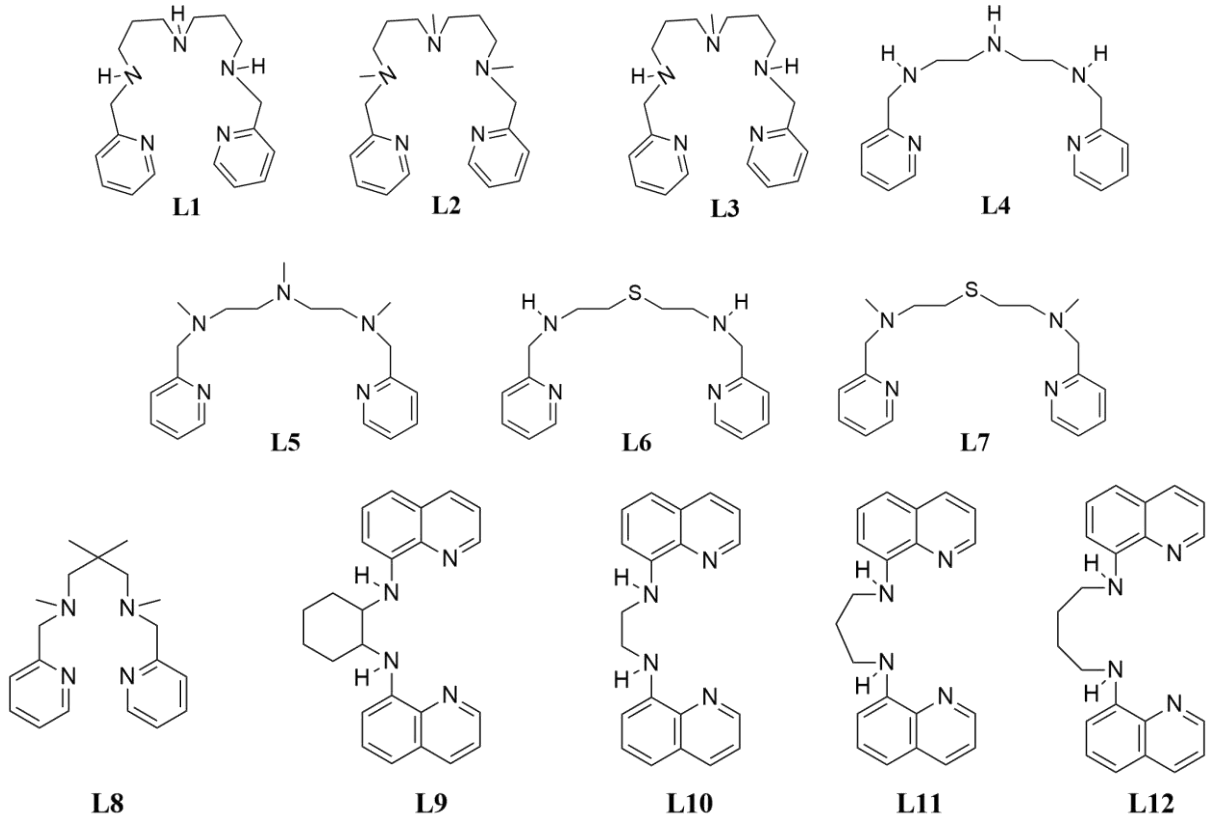

Scheme 2.5 *The chemical structures of all the ligands in this study.*

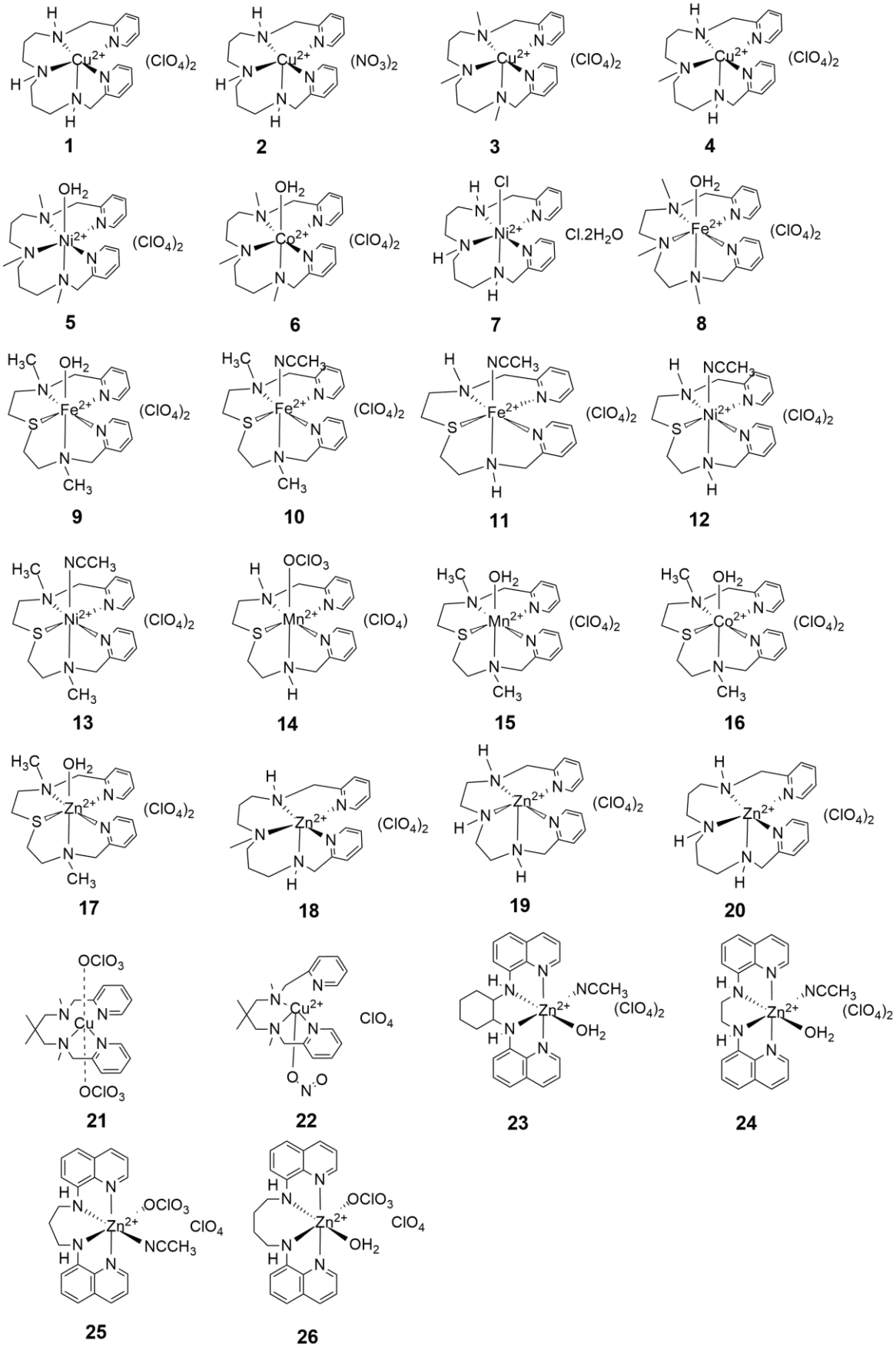

Scheme 2.6 *Chemical structures of the new compounds* ***1-26*** *discussed in the subsequent Chapters of the thesis.*

References

1 A. I. . Vogel, J. Mendham, R. C. . Denney, J. D. . Barnes and M. . Thomas, *Vogel's quantitative chemical analysis*, Pearson, 2009.

2 W. L. F. . Armarego, *Purification of laboratory chemicals*, Butterworth-Heinemann, 2017.

3 H. Saltzman and J. G. Sharefkin, *Org. Synth.*, 1963, **43**, 60.

4 D. D. Narulkar, A. K. Srivastava, R. J. Butcher, K. M. Ansy and S. N. Dhuri, *Inorganica Chim. Acta*, 2017, **467**, 405–414.

5 S. H. Pine, *J. Chem. Educ.*, 1968, **45**, 118.

6 J. England, G. J. P. Britovsek, N. Rabadia and A. J. P. White, *Inorg. Chem.*, 2007, **46**, 3752–3767.

7 K. Nakamoto, *Infrared and Raman Spectra of Inorganic and Coordination Compounds, Part B: Applications in Coordination, Organometallic, and Bioinorganic Chemistry Part 2 of Infrared and Raman Spectra of Inorganic and Coordination Compounds*, John Wiley & Sons, 6th edn., 2009.

8 J. Keeler, *Understanding NMR spectroscopy*, John Wiley and Sons, 2010.

9 M. M. Roessler and E. Salvadori, *Chem. Soc. Rev.*, 2018, **47**, 2534–2553.

10 J. Li and J. Sun, *Acc. Chem. Res.*, 2017, **50**, 2737–2745.

11 T. S. . Teets and F. Keutsch, *Photoluminescence*, American Chemical Society, 2021.

12 S. Mugiraneza and A. M. Hallas, *Commun. Phys.*, 2022, **5**, 95.

CHAPTER 3

CHAPTER 3

Section I: Influence of methyl substitution on structural parameters and catalytic mimicking activity of Cu(II) compounds

3.1 Introduction and literature

Pentaammine compounds of transition metals have held a significant position in the historical and evolutionary development of coordination chemistry. The synthesis of $[Co(NH_3)_5H_2O]^{3+}$, $[Co(NH_3)_5Cl]^{2+}$, and $[Co(NH_3)_5NO_2]^{2+}$ in the mid-1800s exhibited how altering one ligand could influence the color of the resulting compound[1]. The 19th century signified the commencement of mechanistic and kinetic investigations of ligand exchange reactions and electron transfer reactions employing pentaamine compounds[2–4]. Pentadentate pentaamine ligands represent a logical extension of the pentaamine unit. However, such ligands have been relatively rare and underutilized until the last two decades. Over the course of this period, extensive research employing such ligands has been conducted[5].

Aminopyridyl ligands are the most commonly used type of pentadentate ligands. Nitrogen based pentadentate aminopyridyl ligands are a group of multidentate ligands that are defined by their capacity to form bonds with metal centers via five different donor atoms, usually incorporating multiple pyridine units and amine groups. A significant amount of interest has been focused on these ligands within coordination chemistry due to their robust metal-binding abilities, varied coordination geometries, and adjustable electronic characteristics, ultimately enabling their application in catalysis, biomimetic simulations, and materials science research[6–8].

Structurally, pentadentate aminopyridyl ligands are composed of pyridine rings connected to central nitrogen atoms via flexible or rigid linkers, often secondary or tertiary amines, which create a stable chelating framework that facilitates coordination with a range of metal ions. These structural configurations result in stable metal compounds with distinct coordination geometries, commonly taking on trigonal bipyramidal or square pyramidal structures, which are vital for regulating the electronic and steric surroundings around the metal centre. Modifications to these ligand structure enable researchers to make precise

adjustments to their electronic and spatial properties, thereby allowing for the optimization of ligand frameworks to achieve improved catalytic performance and selectivity[9–13].

Although significant research has been carried out, additional investigation into pentadentate aminopyridyl ligands is still required to fully take advantage of their chemical flexibility and to gain a more profound understanding of their structure activity correlations. In our endeavor to design new N3Py2 type N-donor ligands, we herein report the synthesis and characterization of new ligands **L2** = N^1,N^3-dimethyl-N^1-(3-(methyl(pyridin-2-ylmethyl)amino)propyl)-N^3-(pyridin-2-ylmethyl)propane-1,3-diamine) and **L3** = N^1-methyl-N^3-(pyridin-2-ylmethyl)-N^1-(3-((pyridin-2-ylmethyl)amino)propyl)propane-1,3-diamine prepared by methylation of **L1** = N^1-(pyridin-2-ylmethyl)-N^3-(3-((pyridin-2-ylmethyl)amino)propyl)propane-1,3-diamine at normal laboratory conditions.

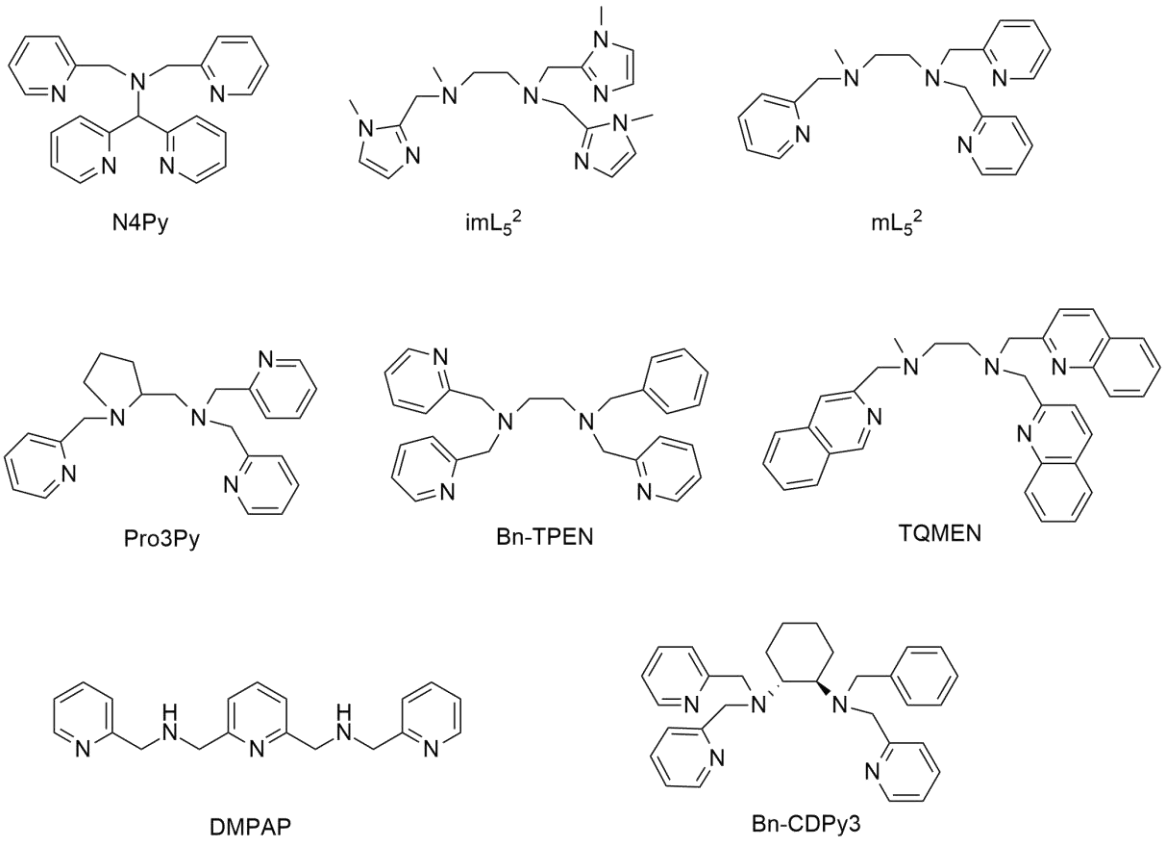

Scheme 3.1 *Diverse set of pentadentate aminopyridyl ligands supporting transition metal compounds.*

The transition metalloenzymes play critical roles in biological processes. Several reports on biomimetic model compounds containing N-donor coordination suppliers have shown an insight into the structure-function properties[14–21]. The impetus to design novel ligands and transition metal compounds appears from their potential to understand the correlation of their geometric and electronic structure with their reactivity. The copper-based coordination compounds are known for their diverse applications[22–25]. Several copper compounds have been known as biomimetic models of metalloenzymes[26,27]. The coinage transition metal copper is a well-known essential element in biology. Its compounds can catalyze various biochemical redox reactions such as methane monooxygenase, catechol oxidase, superoxide dismutase, and phenoxazinone synthase[28–31]. Phenoxazinone synthase (PHS) is a multicopper oxidase enzyme produced by *Streptomyces antibioticus*. A hexameric copper active site can catalyze an oxidative coupling of substituted 2-aminophenols to phenoxazinone chromophore in the biosynthesis of actinomycin D, a naturally synthesized antineoplastic agent[32,33]. The design and development of numerous small molecule catalysts bearing amine and polypyridyl ligands have helped the bioinorganic chemist to understand the structure-activity synergy at the active site[34–39]. The metal compounds, ligand architecture, and coordination geometry, are known to control the reactivity and stability of such compounds[40–46]. Copper(II) ions tend to form common tetrahedral, octahedral, square pyramidal, and trigonal bipyramidal geometry compounds, all of which are tetragonally distorted[47]. The pentadentate N-donor ligands form square pyramidal and trigonal bipyramidal copper(II) compounds. Addison and co-workers showed connectivity between SP and TBP with intermediate geometries in copper compounds[48].

In this work, we are presenting thoroughly characterized four copper(II) compounds **1-4**, stabilized by novel pentadentate aminopyridyl ligand architectures, showing the influence of ligand architecture and geometry on the phenoxazinone synthase and catecholase-like activity.

Section II: Synthesis, characterization and reactivity studies of non-heme Ni(II) and Co(II) compounds

Research into the chemistry of first row transition metal compounds that incorporate nonheme N-donor ligands is an area of growing interest[49,50]. In metalloenzymes, metal active sites are crucial for facilitating biochemical reactions[51]. Transition metals from the 3d series exhibit a range of properties making them abundant and available for various applications, due to their ability to form a variety of coordination numbers and adopt flexible geometries. Cobalt and nickel, which are late transition metals, have received less attention in biomimetic research owing to their limited applications in the field of biology. Substantial research has been conducted in recent years to comprehend the functions of high valent cobalt and nickel oxygen intermediates in various biomimetic reactions[52–56].

A large number of Nickel(II) compounds have been studied for their role as the models for several metalloenzymes. They displayed good efficiency in electrolytic water oxidation[57], hydrogen gas generation and oxygen gas evolution[58,59]. Biomimetic non-heme systems have gained significant attention in recent years due to their potential to function as oxidizing agents. Akita and co-workers have investigated the reactivity of a nickel(II)-alkylperoxo complex, [Ni(OO*t*Bu)(TpiPr)], when it reacts with a series of para-substituted benzaldehydes, resulting in the formation of the corresponding benzoato adducts[60]. Further research by Nam and co-workers has provided a high-resolution crystal structure of a side-on nickel(III)-peroxo complex containing a 12-membered macrocyclic ligand, $[Ni^{III}(O_2)(12\text{- TMC})]^+$. Investigations have been conducted using both 2-PPA and CCA as substrates, yielding acetophenone and cyclohexene as a result of a nucleophilic aldehyde deformylation reaction. The reactivity of nickel-oxygen adducts is influenced by the ring size of the supporting ligands[61], as well as electronic and steric effects[62,63]. Cho and his colleagues have synthesized a nickel(III)-peroxo complex using the Me_6-trien ligand, which is analogous to the macrocyclic 12-TMC ligand, and discovered that an open-chain nickel-oxygen intermediate complex is more reactive than its macrocyclic counterpart towards aldehyde deformylation[64].

Investigations into the interaction of cobalt complexes with dioxygen have been extensive, resulting in the synthesis of $Co\text{-}O_2$ species that serve as chemical models of dioxygen

carrier proteins, such as haemoglobin and myoglobin[65,66]. Currently, many Cobalt-Oxygen species stabilised by non-heme ligands have been identified using spectroscopic methods and a smaller number have been characterised by X-ray crystallography, with their reactivity having been studied in a range of oxidation reactions.

Extensive examination of cobalt schiff base complexes in the presence of dioxygen revealed their potential for the catalytic oxidation of organic substrates such as phenols and olefins. These Oxidative studies proposed an end-on Co(III)-superoxo intermediate as the key species involved in the reactions. It is proposed that this species abstracts a hydrogen atom from the substrates through the weak C-H or O-H bonds[67,68]. Researchers led by Nam characterised a cobalt(III)-peroxo complex incorporating the tetradentate TMC ligand and examined its reactivity in deformylation reactions with various aldehydes[69]. Further research concentrated on how variations in the TMC ring's size affected cobalt(III)-peroxo complexes reactivity in the aldehyde deformylation reaction. Specifically, two mononuclear cobalt(III)-peroxo complexes were examined: those with tetradentate 12-TMC and 13-TMC ligands. A larger ring size resulted in an oxidant that was more reactive towards nucleophilic addition to aldehydes[70]. Reports on cobalt(III)-hydroperoxo species are scarce in comparison to those on the Co(III)-peroxo species[71]. The end-on Co(III)-hydroperoxo species have been found to form through the protonation of Co(III)-peroxo species in acidic conditions[72].

Section I of our studies has focused on the synthesis, characterisation, and catalytic reactivity of copper(II) complexes incorporating the pentadentate ligands **L1**, **L2**, and **L3**. Despite significant amounts of research on nonheme Ni(II) and Co(II) compounds, our current understanding indicates that there is still potential in designing novel topological ligands that aid in stabilizing Ni-O_2 and Co-O_2 intermediates. This section focuses on 3d transition metal compounds, specifically those of Ni(II) and Co(II). The Ni(II) and Co(II) compounds synthesised from the pentadentate ligands **L1** and **L2** have been characterised and their potential role in the formation of stable reactive intermediates for biomimetic purposes has been studied.

3.2 Experimental details

The details of procedures which are employed for the synthesis of ligands **L1**, **L2** and **L3** along with four Cu(II) compounds $[Cu(L1)](ClO_4)_2$ **1**, $[Cu(L1)](NO_3)_2$ **2**, $[Cu(L2)](ClO_4)_2$ **3** and $[Cu(L3)](ClO_4)_2$ **4** and their characterization have been described in this section. The **Scheme 3.2** shows structures of ligands and the Cu(II) compounds that are synthesized in this study.

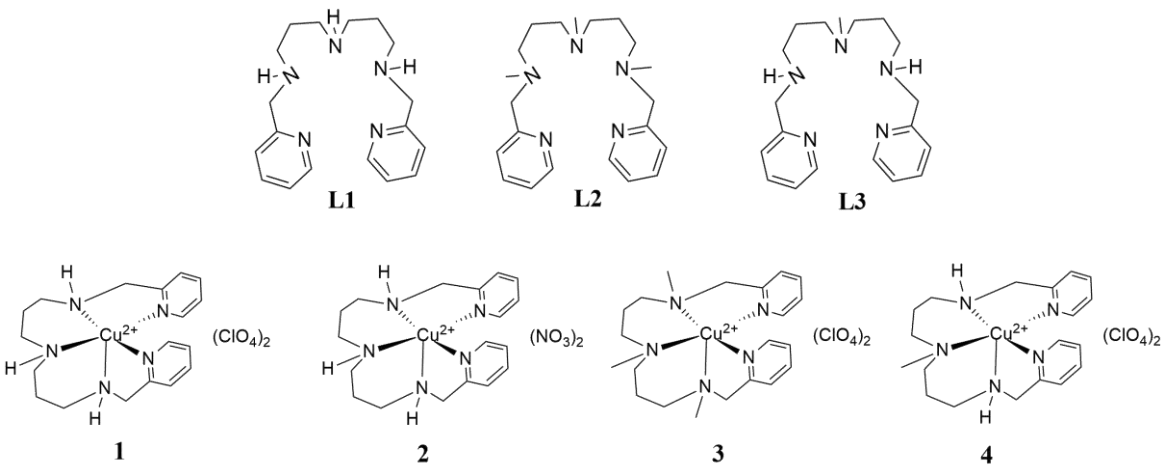

Scheme 3.2 *Structure of the ligands employed in this work and the corresponding Cu(II) compounds.*

3.2.1 Synthesis of ligands L1, L2 and L3

The synthesis of **L1** was reported elsewhere, followed with modifications[73]. A solution of bis(3-aminopropyl) amine (1.8 g, 14.0 mmol) in ethanol (5 mL) was added dropwise to a solution of pyridine-2-carboxaldehyde (3.0 g, 28.0 mmol) in ethanol (15 mL) and refluxed, with stirring, for 5 h. The mixture was cooled to room temperature and evaporated under reduced pressure to produce semisolid imine. The imine was redissolved in ice-cold methanol (20 mL) and to this solution $NaBH_4$ (0.48g, 12.8 mmol) was added slowly, after which the mixture was stirred overnight. The solvent was then removed under vacuum, and the distilled water (20 mL) was added to the crude product flask. Yellow viscous oil of **L1** was extracted with three aliquots of 30 mL of ethyl acetate. The yield of **L1** was 3.6g (11.48 mmol), 85 %. *Anal. Calc.* for **L1** $C_{18}H_{27}N_5$ (%): C, 68.97; H, 8.63; N, 22.34. *Found:* C, 68.26; H, 8.45; N, 21.92. IR (KBr, cm^{-1}): 3298 υ(NH); 3053-2816 υ(CH).

Ligand **L2** was synthesized by methylation of the reported **L1**[74]. The ice-cold aqueous solution of **L1** (3g, 9.5 mmol) was combined with formaldehyde solution (37%, 22.0 mL) and formic acid (85%, 15.0 mL) and refluxed for 24 h. An aqueous NaOH (2.0 M) was added until the pH was above 12. A brown oil was extracted with three 30 mL aliquots of chloroform and dissolved in HCl solution (pH ~ 1). The acidic mixture was basified with aqueous NaOH, and the reddish-brown product **L2** was then extracted with six 20 mL aliquots of diethyl ether. The yield of **L2** was 2.7g (7.59 mmol), 79 %. *Anal. Calc.* for **L2** $C_{21}H_{33}N_5$ (%): C, 70.95; H, 9.36; N, 19.70. *Found:* C, 70.04; H, 8.95; N, 19.03. IR (KBr, cm^{-1}): 3007-2895 υ(CH); ^{1}H NMR ($CDCl_3$, ppm): δ 8.54 (d, 2H, *J* = 4.8 Hz), δ 7.65 (t, 2H, *J* = 7.6 Hz), δ 7.42 (d, 2H, *J* = 8.0 Hz), δ 7.15 (t, 2H, *J* = 6.0 Hz), δ 3.64 (s, 4H), δ 2.44 (t, 4H), δ 2.36 (t, 4H), δ 2.24 (s, 6H), δ 2.20 (s, 3H), δ 1.70 (qui, 4H),^{13}C NMR ($CDCl_3$, ppm): δ 159.4, δ 149.0, δ 136.4, δ 123.0, δ 121.9, δ 63.9, δ 55.9, δ 55.6, δ 42.4, δ 42.2, δ 25.1.

Ligand **L3** was synthesized by similar protocol as in **L1** wherein 3,3′-Diamino-*N*-methyldipropylamine (2.0 g, 14.0 mmol) instead of Bis(3-aminopropyl) amine was reacted ethanolic solution of pyridine-2-carboxaldehyde (3.0 g, 28.0 mmol). The yield of **L3** was 3.6g (1.11 mmol), 80 %. *Anal. Calc.* for **L3** $C_{19}H_{29}N_5$ (%): C, 69.69; H, 8.93; N, 21.39. *Found:* C, 70.15; H, 9.27; N, 21.81. IR (KBr, cm^{-1}): 3007-2895 υ(CH); ^{1}H NMR ($CDCl_3$, ppm): δ 8.55 (d, 2H, *J* = 4.4 Hz), δ 7.66 (t, 2H, *J* = 7.6 Hz), δ 7.31 (d, 2H, *J* = 7.6 Hz), δ 7.17 (t, 2H, *J* = 6.4 Hz), δ 3.88 (s, 4H), δ 2.69 (t, 4H), δ 2.41 (t, 4H), δ 2.20 (s, 3H), δ 1.74 (qui, 4H),^{13}C NMR ($CDCl_3$, ppm): δ 159.3, δ 149.1, δ 136.4, δ 122.3, δ 121.9, δ 55.9, δ 55.0,δ 48.0, δ 42.0, δ 27.2.

3.2.2 Synthesis of Cu(II) compounds $[Cu(L1)](ClO_4)_2$ 1, $[Cu(L1)](NO_3)_2$ 2, $[Cu(L2)](ClO_4)_2$ 3 and $[Cu(L3)](ClO_4)_2$ 4

$[Cu(L1)](ClO_4)_2$ **1** was synthesized with a modification of the reported procedure[74]. A solution of **L1** (0.42 g, 1.37 mmol) in acetonitrile (5 mL) was added slowly to the stirring solution of $Cu(ClO_4)_2.6H_2O$ (0.50 g, 1.37 mmol) in acetonitrile (2 mL) at room temperature. The mixture was stirred for ~8 h. Diethyl ether (10 mL) was added to the resulting dark blue color solution, and the mixture was kept undisturbed for crystallization. The blue crystals formed after two days were isolated by filtration and dried in the air. The yield of **1** was 0.62g (1.07 mmol), 80 %. *Anal. Calc.* for **1** C_{18} H_{27} Cl_2 Cu N_5 O_8 (%): C, 37.54; H, 4.73; N, 12.16. *Found:* C, 37.10; H, 3.95; N, 12.23. IR (KBr, cm^{-1}): 3217

υ(NH); 3053-2816 υ(CH); 1093, 621 υ(ClO_4); UV-Vis data, λ_{max}, CH_3CN/nm (ε/dm^3 mol^{-1} cm^{-1}): 280 (2722) and 690 (75). ESI-MS: m/z = 188.0 (calc. 188.0) for $[Cu(L1)]^{2+}$ and m/z = 475.1 (calc. 475.1) for $[Cu(L1)(ClO_4)]^+$.

Compound **2** was prepared by similar protocol as in **1** wherein $Cu(NO_3)_2.3H_2O$ (0.50 g, 2.06 mmol) instead of $Cu(ClO_4)_2.6H_2O$ was reacted with **L1** (0.64 g, 2.06 mmol) in acetonitrile. Yield of **2** was 0.86g (1.73 mmol), 85(%). *Anal. Calc.* for **2** C_{18} H_{27} Cu N_7 O_6 (%): C, 43.15; H, 5.43; N, 19.57. *Found:* C, 43.58; H, 5.98; N, 20.18. IR (KBr, cm^{-1}): 3208 υ(NH); 3071-2878 υ(CH); 1384 υ(NO_3); UV-Vis data (CH_3CN, λ_{max}, nm, ϵ): 280 (2722) and 690 (83). ESI-MS: m/z = 188.6 (calc. 188.3) for $[Cu(L1)^{2+}$ and m/z = 438.6 (calc. 438.4) for $[Cu(L1)(NO_3)]^+$.

A solution of **L2** (0.48 g, 1.37 mmol) in acetonitrile (5 mL) was added slowly to the stirring solution of $Cu(ClO_4)_2.6H_2O$ (0.50 g, 1.37 mmol) in acetonitrile (2 mL) at room temperature. The mixture was stirred for ~ 8 h. Diethyl ether (10 mL) was added to the resulting dark blue color solution, and the mixture was kept undisturbed for crystallization. The blue crystals formed after two days were isolated by filtration and dried in the air. The yield of **3** was 0.64 g (1.03 mmol), 77.0 %. *Anal. Calc.* for **3** C_{21} H_{33} Cl_2 Cu N_5 O_8 (%): C, 40.82; H, 5.38; N, 11.33. *Found:* C, 40.58; H, 5.05; N, 11.95. IR (KBr, cm^{-1}): 3007-2895 υ(CH); 1093, 621 υ(ClO_4); UV-Vis data, λ_{max}, CH_3CN/nm (ε/dm^3 mol^{-1} cm^{-1}): 275 (2665) and 610 (45). ESI-MS: m/z = 209.1 (calc. 209.1) for $[Cu(L2)]^{2+}$ and m/z = 517.0 (calc. 517.0) for $[Cu(L2)(ClO_4)]^+$.

L3 (0.45g, 1.37 mmol) was dissolved in acetonitrile (2 mL) and added to the stirring solution of $Cu(ClO_4)_2.6H_2O$ (0.50g, 1.37 mmol) in acetonitrile at room temperature. The mixture was stirred for 5 h and filtered. The product was isolated by evaporation of solvent and recrystallization of the residue from minimum volume of acetonitrile by the gradual addition of diethyl ether to obtain the compound as a blue solid. Crystals of diffractable quality were obtained by slow diffusion of diethyl ether to acetonitrile solution of the compound. The yield of **4** was 0.68 g (1.16 mmol), 85.0 %. *Anal. Calc.* for **4** $C_{19}H_{29}Cl_2CuN_5O_8$ (%): C, 38.68; H, 4.96; N, 11.87. *Found:* C, 38.92; H, 5.07; N, 11.24. IR (KBr, cm^{-1}): 3007-2895 υ(CH); 1093, 621 υ(ClO_4); UV-Vis data, λ_{max}, CH_3CN/nm (ε/dm^3 mol^{-1} cm^{-1}): 286 (2893) and 720 (115). ESI-MS: m/z = 215.7 (calc. 215.6) for $[Cu(L3)(CH_3CN)]^{2+}$ and m/z = 489.2 (calc. 489.1) for $[Cu(L3)(ClO_4)]^+$.

3.2.3 Catalytic oxidation

Compounds **1** - **4** were tested in the oxidation of model substrates 2-aminophenol (OAP) and 3,5-di-*tert*-butylcatechol (3,5-DTBC). In a typical catalytic reaction, the compound (1 x 10^{-4} M) dissolved in dioxygen-saturated methanolic solution was reacted with OAP (1 x 10^{-3} M) at 25°C for 2 h. The time dependent reaction progress was monitored using UV-Vis spectrophotometer. After two hours, the evaporation of the solvent yielded a reddish-brown residue which was then infused on Shimadzu GC 2014 equipped with HP capillary column (30 m x 0.25 mm x 2.5 μM) and an FID detector using methanol as eluent. The oxidation of 3,5-DTBC was examined spectrophotometrically by reacting 100 equivalents of 3,5-DTBC with catalyst (1 x 10^{-4} M) in methanol for two hours. The quinone was purified by column chromatography using a 10% mixture of ethyl acetate and hexane as eluent.

3.3 Results and discussions

3.3.1 Synthesis and characterization of L1, L2 and L3

Martell and co-workers first synthesized the bis-pyridine ligand **L1** in 1978, wherein the Schiff base was subsequently hydrogenated with a palladium catalyst. A similar diimine reduction method with Zn has also been reported[5]. In the current work, we have synthesized **L1** starting from its diimine precursor, followed by the standard $NaBH_4$ reduction (**Scheme 3.3**).

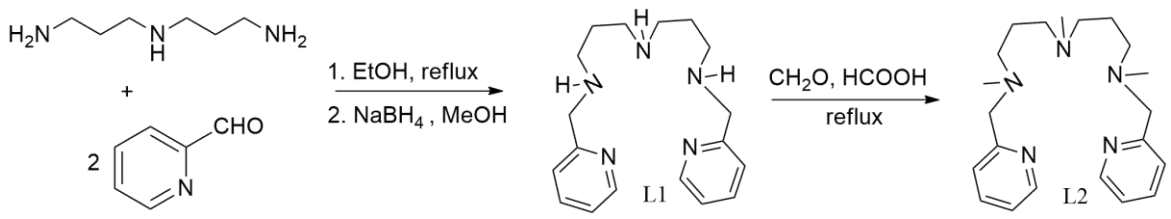

Scheme 3.3 *Synthesis of ligands **L1** and **L2**.*

We have further reported the synthesis of new pentadentate N-methylated pyridyl amine ligands **L2** and **L3**. **L2** is prepared from the non-methylated precursor **L1** via the Eschweiler-Clarke reaction (**Scheme 3.3**)[75]. Whereas **L3** is synthesized by reductive amination of Bis(3-aminopropyl) amine with pyridine-2-carboxaldehyde (**Scheme 3.4**).

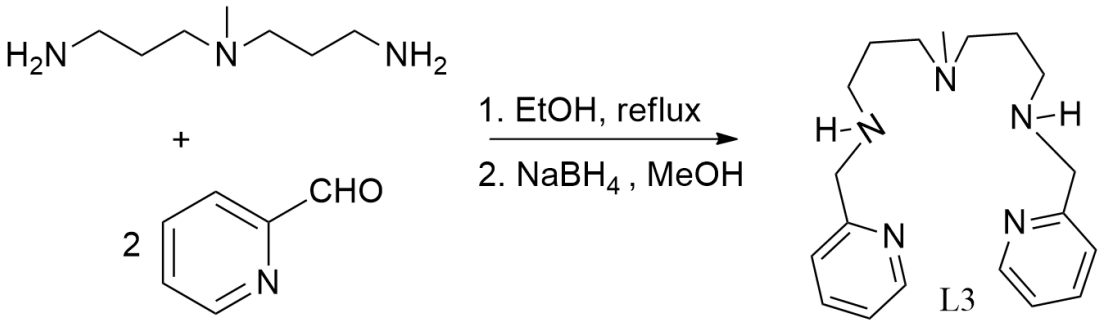

Scheme 3.4 *Synthesis of ligand* ***L3****.*

IR spectra of ligands **L1- L3** were recorded in the region 4000 – 400 cm^{-1}. The overlaid IR spectra (**Figure 3.1**) show features attributed to the ligand formation. The IR spectrum of **L1** exhibits N-H stretching vibration in the region 3290-3350 cm^{-1}, while similar peaks were not observed in the IR spectrum of methylated analog. Medium-to-weak absorptions observed between 2890-3040 cm^{-1} were characteristic of C-H stretching vibrations of organic ligands[76].

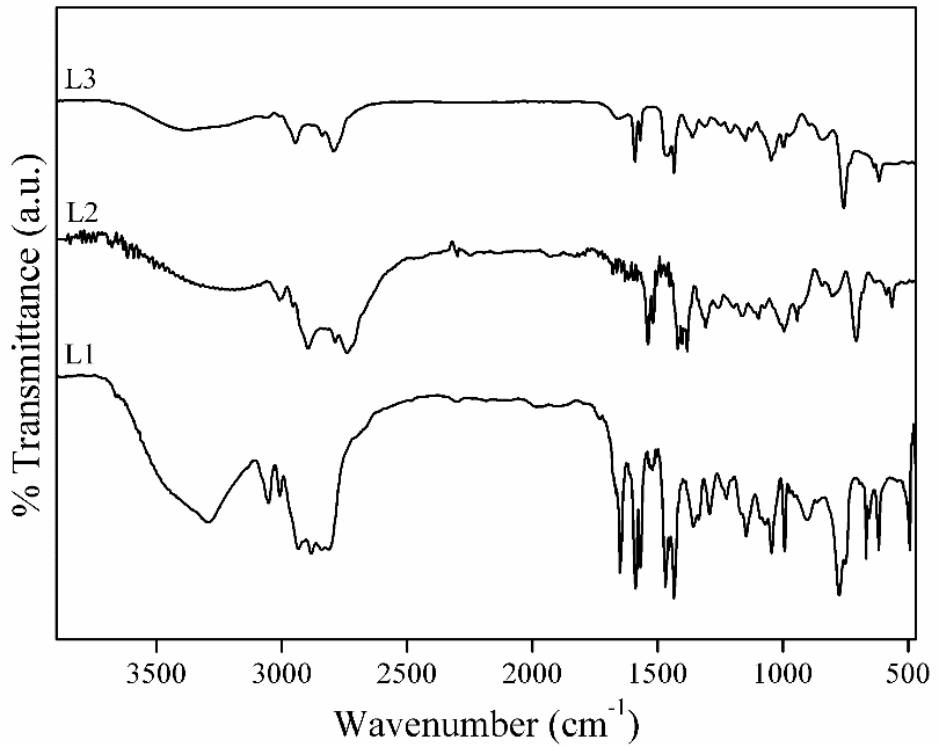

Figure 3.1 *IR spectra of the ligands* ***L1****,* ***L2*** *and* ***L3****.*

The structure of the ligands was confirmed by ^{1}H, ^{13}C and DEPT NMR spectroscopy and the corresponding peaks were assigned in the corresponding NMR spectra as depicted in **Figure 3.2-3.7**.

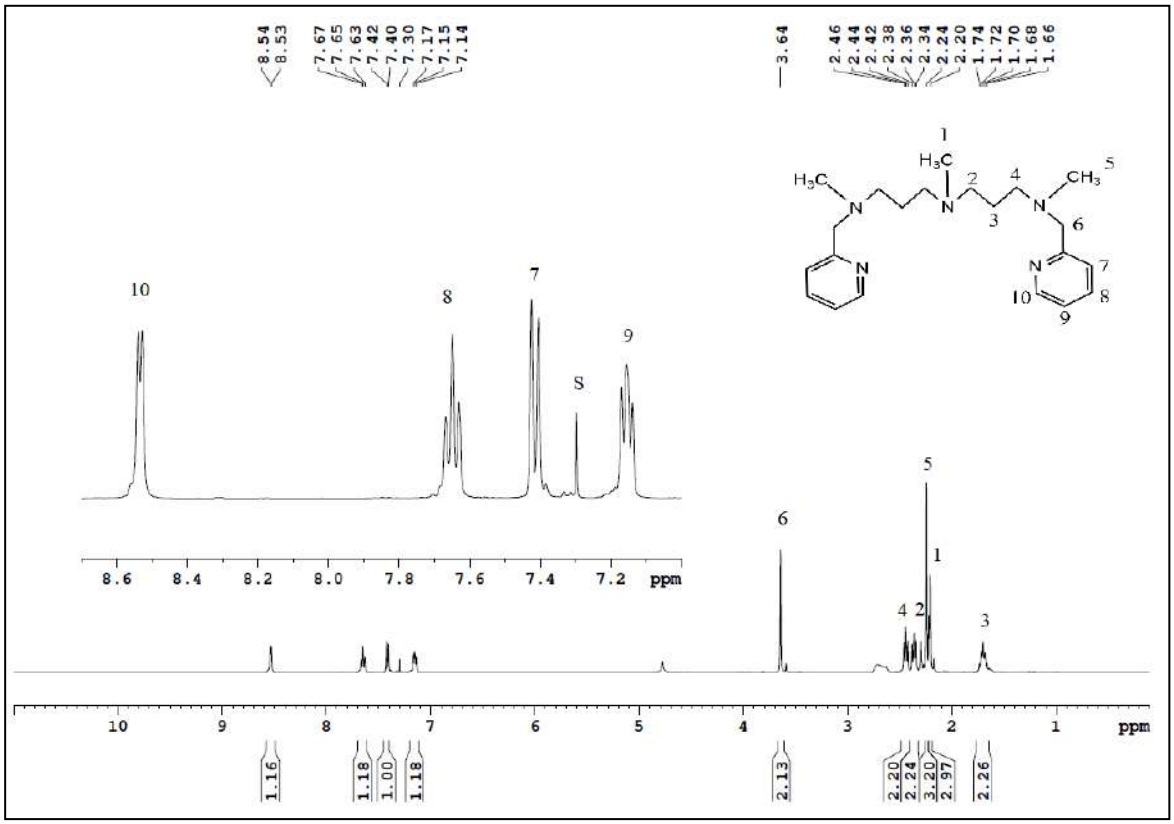

Figure 3.2 *The [1]H NMR spectrum of* ***L2*** *recorded in $CDCl_3$ (S stands for solvent peak).*

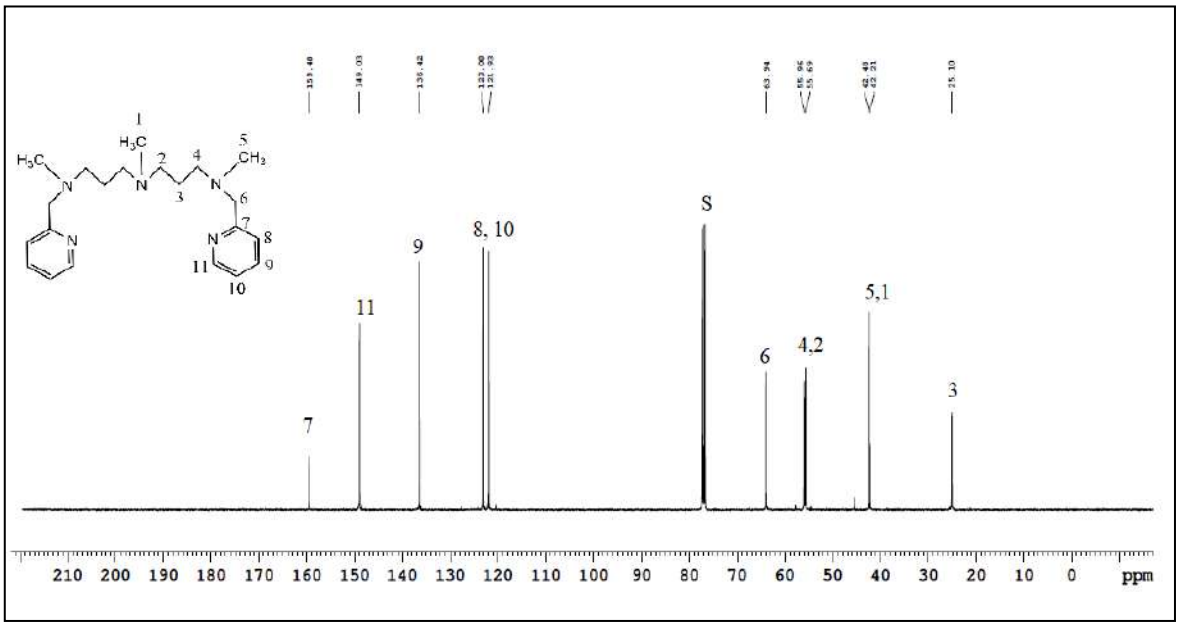

Figure 3.3 *The [13]C NMR spectrum of* ***L2*** *recorded in $CDCl_3$ (S stands for solvent peak).*

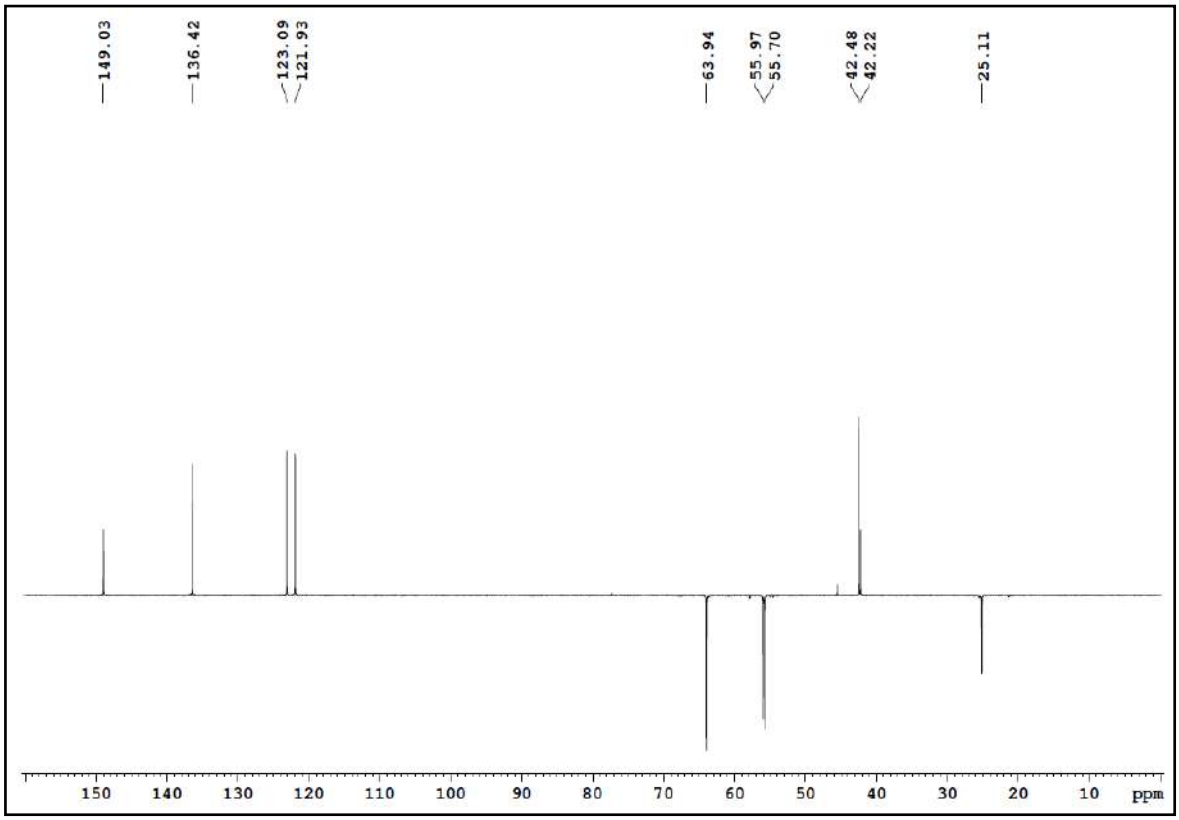

Figure 3.4 *The DEPT spectrum of* ***L2*** *recorded in* $CDCl_3$.

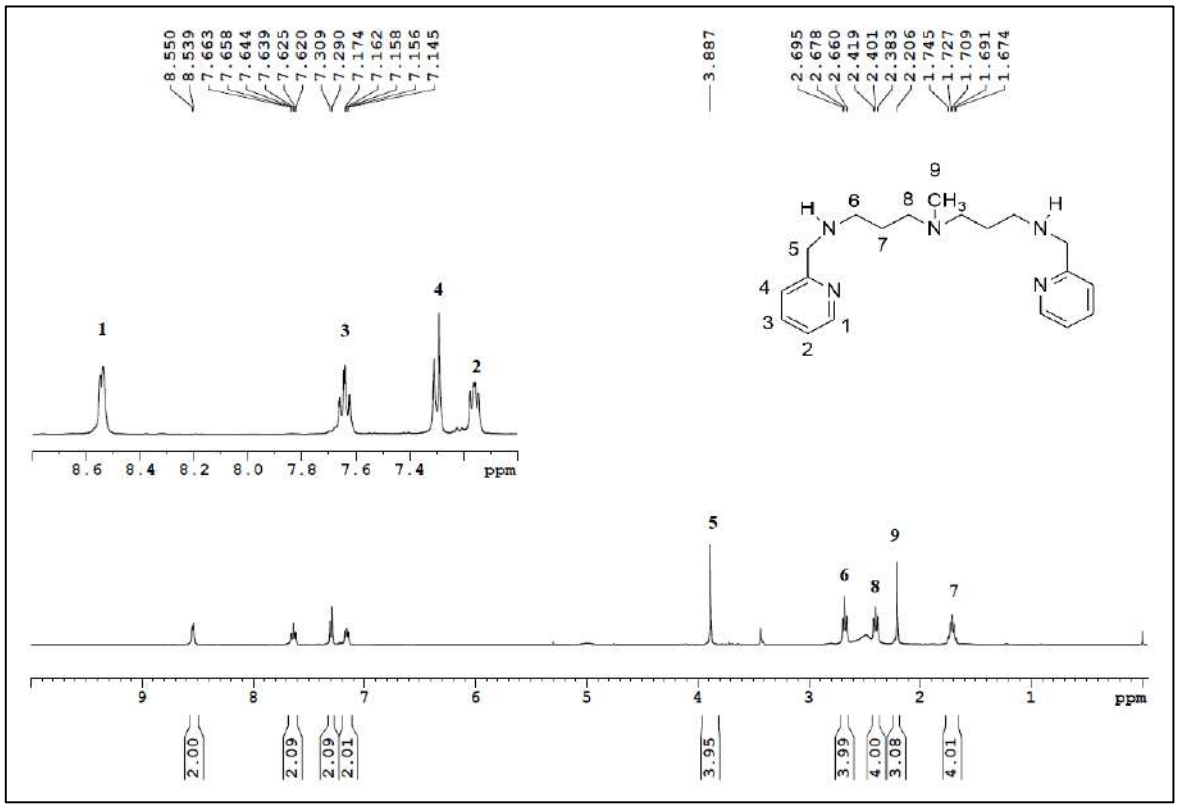

Figure 3.5 *The* ^1H *NMR spectrum of* ***L3*** *recorded in* $CDCl_3$.

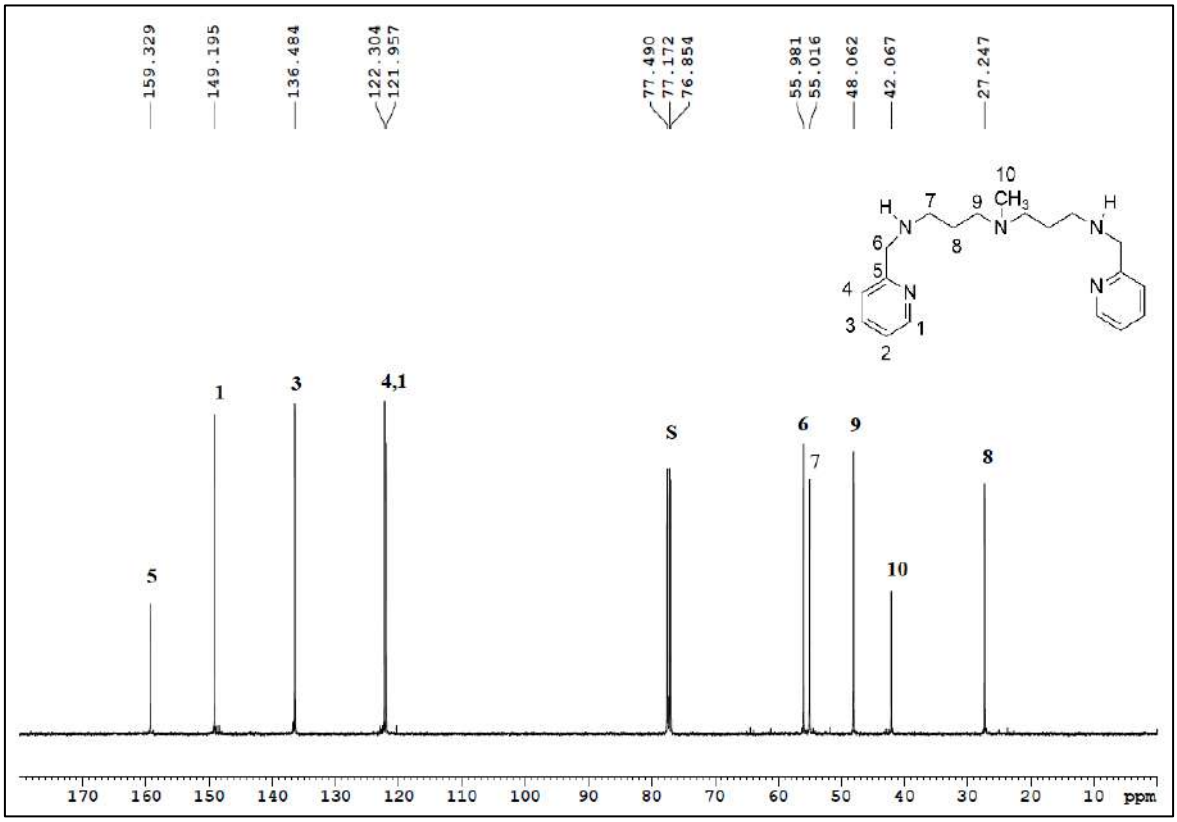

Figure 3.6 *The ^{13}C NMR spectrum of* ***L3*** *recorded in $CDCl_3$ (S stands for solvent peak).*

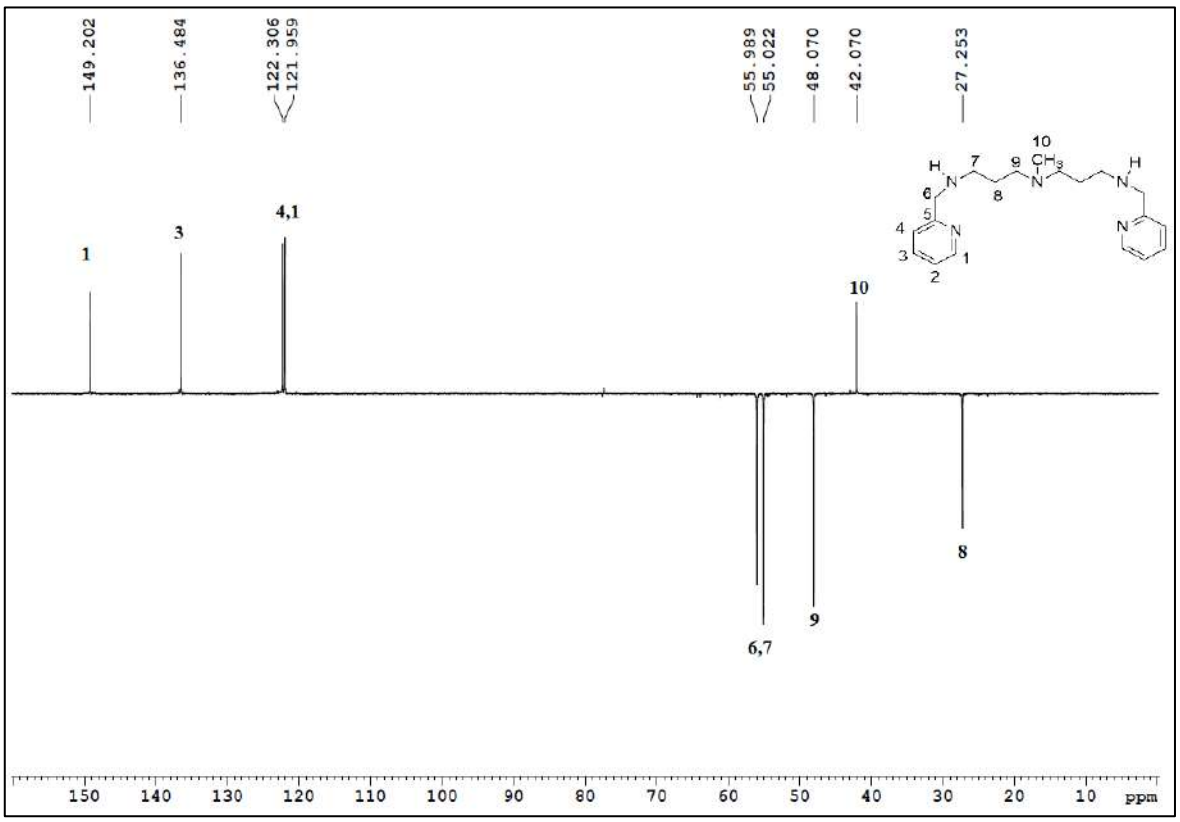

Figure 3.7 *The DEPT spectrum of* ***L3*** *recorded in $CDCl_3$.*

3.3.2 Infrared (IR) spectroscopic analysis of compounds 1-4

The bands due to O-H vibrations are absent in the IR spectra of compounds **1-4**, indicating the absence of water molecules, thus giving the first hint of pentadentate coordination with copper(II). The spectra showed C-H stretching vibration in the region 3100-2800 cm^{-1} due to incorporating ligands. In **1**, **3** and **4**, the well-resolved absorption bands at ~ 1090 cm^{-1} and ~ 620 cm^{-1} are observed for uncoordinated perchlorate anions[77,78] (**Figure 3.8**), whereas **2** exhibited a peak at 1384 cm^{-1} due to nitrate anion[79].

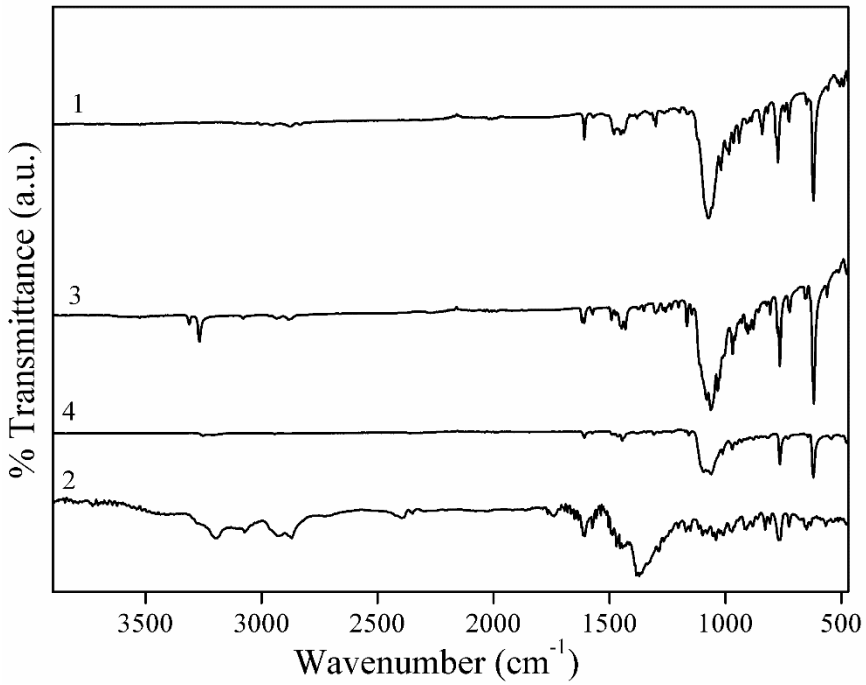

Figure 3.8 *The overlaid infrared spectra of compounds **1-4**.*

3.3.3 UV-Visible spectra of compounds 1-4

UV-Vis spectra for compounds **1-4** were recorded in CH_3CN. The pentadentate ligand-based Cu(II) compounds with a typical square pyramidal geometry exhibit $d_{xz}, d_{xy} \rightarrow d_{z^2}$ transition bands in the 550-670 nm region, i.e., a high-energy peak with a low-energy shoulder. The intense band observed in the high energy region are assigned to the Cu(II)-pyridine charge transfer band (260-315 nm)[80]. The weaker *d-d* bands observed in the 500-1000 nm region and their patterns can suggest the exact nature of pentacoordinate geometry[81,82]. A broad band centered at ~690 nm in compound **1** and **2**; and ~720 nm in compound **4** indicates a significant distortion (**Figure. 3.9**).The high-intensity band at ~ 610 nm and shoulder at ~ 800 nm could be attributed to the effects of distortion in compound **3**.

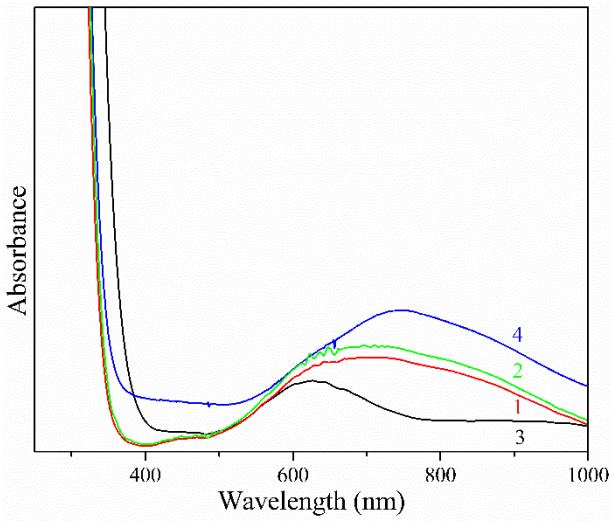

Figure 3.9 *UV-Vis spectra recorded in CH_3CN for compounds* ***1-4*** *(5 mM) shows the visible region exposing the d-d bands.*

3.3.4 ESI-Mass spectrometry

Electrospray mass spectra (ESI-MS) of compounds **1-4** were studied in acetonitrile. ESI-MS spectrum of **1** exhibits mass peaks at *m/z* = 188.0 (calc. *m/z* 188.3) for $[Cu(L1)]^{2+}$ and *m/z* = 475.1 (calc. *m/z* 475.1) for $[Cu(L1)(ClO_4)]^{+}$ fragments. On the other hand, the ESI-MS spectrum of **2** exhibits two major mass peaks at *m/z* = 188.6 (calc. *m/z* 188.3) and *m/z* = 438.6 (calc. *m/z* 438.4), which can be assigned to $[Cu(L1)]^{2+}$ and $[Cu(L1)(NO_3)]^{+}$ species, respectively (**Figure 3.10**). Similarly the ESI-MS spectrum of **3** shows fragmentation peaks at *m/z* = 209.1 (calc. *m/z* 209.1) for $[Cu(L2)]^{2+}$ and *m/z* = 517.0 (calc. *m/z* 517.0) for $[Cu(L2)(ClO_4)]^{+}$. The peaks observed at *m/z* = 215.9 (calc. *m/z* 215.6) and *m/z* = 489.3 (calc. *m/z* 489.1) in ESI-MS spectrum of **4** can be attributed to $[Cu(L3)(CH_3CN)]^{2+}$ and $[Cu(L3)(ClO_4)]^{+}$ species respectively (**Figure 3.11**).

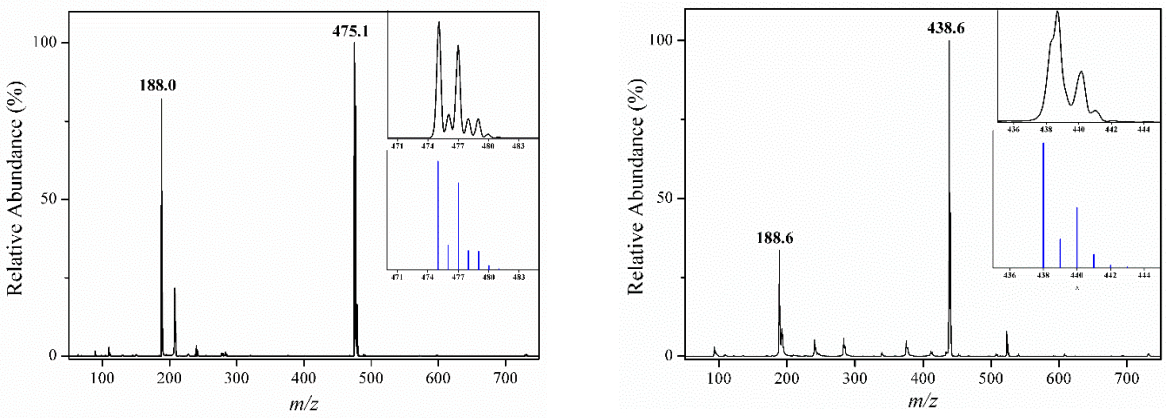

Figure 3.10 *ESI-MS spectrum of* ***1*** *(left) and* ***2*** *(right) recorded in acetonitrile solvent. The inset shows the isotope distribution patterns for the prominent peaks in black with stimulated pattern in blue colour.*

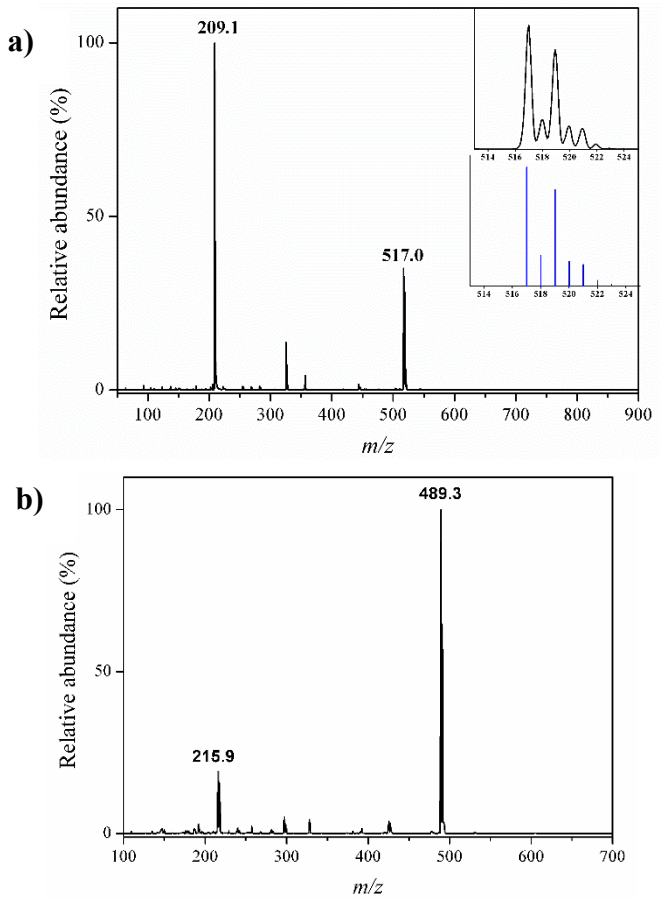

Figure 3.11 *ESI-MS spectrum of **3** (a) and **4** (b) recorded in acetonitrile solvent.*

3.3.5 Crystal structure and geometrical analysis of compounds 1- 4

All four compounds **1-4** were obtained as crystalline solids. Single crystals of $[Cu(L1)](ClO_4)_2$ **1**, $[Cu(L1)](NO_3)_2$ **2**, $[Cu(L2)](ClO_4)_2$ **3** and $[Cu(L3)](ClO_4)_2$ **4** suitable for structure determination were obtained by slow diffusion of diethyl ether into the CH_3CN solution of the respective compounds. Our CSD search indicated that the crystal structure of **1** was earlier reported[74]. However, for comparing the crystal structure data of **1**, we have reinvestigated the crystal structure and reactivity of compound **1** prepared by our method. The summary of technical details of data acquisition and selected refinement results for **1** and **2** are given in **Table 3.1** and for **3** and **4** are given in **Table 3.2**. At the same time, the desired bond lengths and angles are provided in **Table 3.3**, **Table 3.5**, **Table 3.6 and Table 3.8** for **1-4** respectively. Compounds **1**, **2** and **3** crystallize in the centrosymmetric monoclinic space group $P2_1/n$ whereas **4** in monoclinic space group $P2_1/c$ with all the atoms located at general positions. An asymmetric unit of **1-4** is made up of one unique Cu(II) ion, a discrete pentadentate ligand (**L1** in **1** and **2**; **L2** in **3**; **L3** in **4**), and two independent counter ions (ClO_4^- in **1**,**3** and **4**; NO_3^- in **2**). The independent anions

balance the charge neutrality of the cationic core without coordinating with the Cu(II) ion (**Figure 3.12-3.15**). Despite of apparent resemblance in their asymmetric unit, they show different coordination geometries due to changes at N-donor. Crystallographic analysis of compound **1** revealed it to be identical to the previously published structure[74].

Table 3.1 *Technical details and structure refinement parameters of* ***1*** *and* ***2****.*

Compound	**1**	**2**
Empirical formula	$C_{18}H_{27}Cl_2CuN_5O_8$	C_{18} H_{27} Cu N_7 O_6
Formula weight	575.90	501.02
Temperature	296(2) K	296(2) K
Wavelength	0.71073 Å	0.71073 Å
Crystal system	Monoclinic	Monoclinic
Space group	$P2_1/n$	$P2_1/n$
Unit cell dimensions	a = 8.2978(4) Å	a = 8.1442(7) Å
	b = 14.7237(7) Å	b = 13.8364(11) Å
	c = 19.4686(9) Å	c = 19.4561(16) Å
	α = 90°	α = 90°
	β = 92.263(2)°	β = 90.978(3)°
	γ = 90°	γ = 90°
Volume	2376.71(19) $Å^3$	2192.1(3) $Å^3$
Z	4	4
Density (calculated)	1.609 mg/m^3	1.518 mg/m^3
Absorption coefficient	1.198 mm^{-1}	1.047 mm^{-1}
F(000)	1188	1044
Theta range for data collection	2.708 to 28.295°	2.695 to 26.598°
Completeness to theta	99.9%	99.9%
Index ranges	-11≤ h ≤11	-10≤ h ≤10
	-19≤ k≤19	-17≤ k≤17
	-25≤ l≤25	-24≤ l≤24
Reflections collected	35004	46401
Independent reflections	5895(R_{int}= 0.0387)	4590 (R_{int}= 0.0340)
Refinement method	Full-matrix least-squares on F^2	Full-matrix least-squares on F^2
Absorption correction	Semi- empirical from equivalents	Semi- empirical from equivalents
Data/restraints/parameters	5895 / 0 / 319	4590 / 0 / 301
Goodness-of-fit on F^2	1.043	1.038
Final *R*indices[I>2sigma(I)]	R1= 0.0372, wR2= 0.0854	R1= 0.0471, wR2= 0.1361
R indices (all data)	R1= 0.0636, wR2= 0.1023	R1= 0.0612, wR2= 0.1527
CCDC No.	2244556	2386737

Table 3.2 *Technical details and structure refinement parameters of* ***3*** *and* ***4****.*

Compound	**3**	**4**
Empirical formula	$C_{21}H_{33}Cl_2CuN_5O_8$	$C_{19}H_{29}Cl_2CuN_5O_8$
Formula weight	617.97	589.92
Temperature	296(2) K	296(2) K
Wavelength	0.71073 Å	0.71073 Å
Crystal system	Monoclinic	Monoclinic
Space group	$P2_1/n$	$P2_1/c$
Unit cell dimensions	a = 8.3095(3)Å	a = 14.1336(5) Å
	b = 34.3277(13)Å	b = 10.5927(4) Å
	c = 9.4567(4)Å	c = 17.9410(6) Å
	α = 90°	α = 90°
	β = 100.7640(10)°	β = 111.5030(10)°
	γ = 90°	γ = 90°
Volume	2650.02(18) $Å^3$	2499.05(15) $Å^3$
Z	4	4
Density (calculated)	1.549 mg/m^3	1.568 mg/m^3
Absorption coefficient	1.080mm^{-1}	1.141 mm^{-1}
F(000)	1284	1220
Theta range for data collection	2.565 to 28.272°	2.277 to 28.419°
Completeness to theta	99.8%	100%
Index ranges	-11≤ h ≤11	-18≤ h ≤18
	-45≤ k≤45	-14≤ k≤14
	-12≤ l≤12	-23≤ l≤24
Reflections collected	24038	72769
Independent reflections	6565 (R_{int}= 0.0439)	6246 (R_{int}= 0.0742)
Refinement method	Full-matrix least-squares on F^2	Full-matrix least-squares on F^2
Absorption correction	Semi- empirical from equivalents	Semi- empirical from equivalents
Data/restraints/parameters	6565/0/337	6246 / 0 / 320
Goodness-of-fit on F^2	1.079	1.009
Final Rindices[I>2sigma(I)]	R1= 0.0751, wR2= 0.1882	R1= 0.054, wR2= 0.1350
R indices (all data)	R1= 0.1102, wR2= 0.2108	R1= 0.0986, wR2= 0.1567
CCDC No.	2244555	2386753

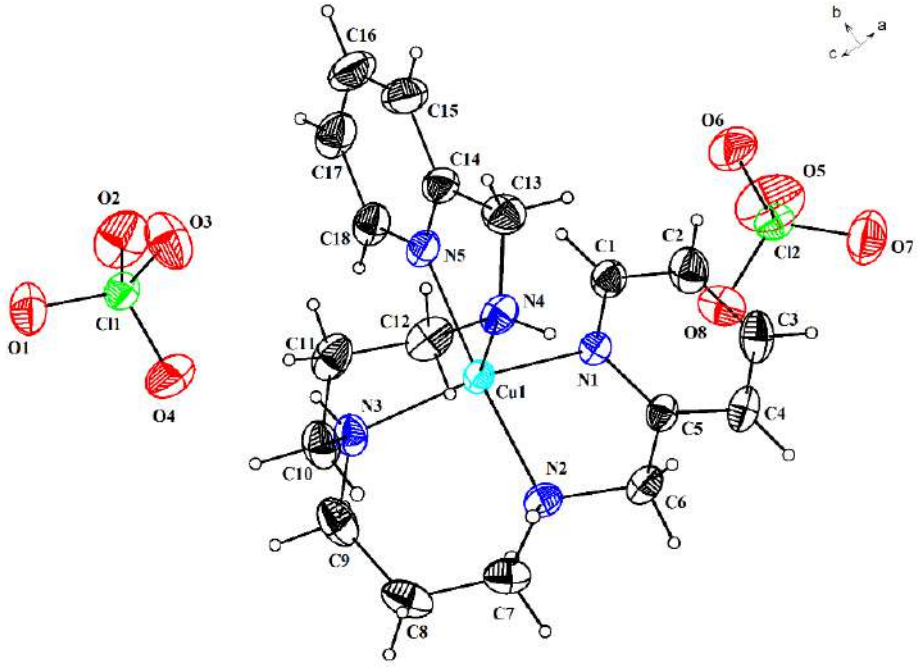

Figure 3.12 *Crystal structure of **1** showing atom labelling scheme. The thermal ellipsoids are drawn at a 30 % probability level for all the atoms except for the H atoms, which are shown as spheres of arbitrary radii.*

Table 3.3 *Selected bond lengths (Å) and angles (°) for **1**.*

Bond lengths (Å)			
Cu(1)-N(1)	2.017(2)	Cu(1)-N(2)	2.023(2)
Cu(1)-N(3)	2.028(2)	Cu(1)-N(5)	2.032(2)
Cu(1)-N(4)	2.225(2)		
Bond angles (°)			
N(1)-Cu(1)-N(2)	82.97(9)	N(1)-Cu(1)-N(3)	153.78(10)
N(2)-Cu(1)-N(3)	91.94(10)	N(1)-Cu(1)-N(5)	93.25(8)
N(2)-Cu(1)-N(5)	175.72(9)	N(3)-Cu(1)-N(5)	92.34(10)
N(1)-Cu(1)-N(4)	106.05(9)	N(2)-Cu(1)-N(4)	98.62(9)
N(3)-Cu(1)-N(4)	100.14(10)	N(5)-Cu(1)-N(4)	80.47(9)

Table 3.4 *Hydrogen bonding parameters (Å, º) for **1**.*

D-H···A	**D-H/ Å**	**H···A/ Å**	**D···A/ Å**	**D-H···A/º**	**Symmetry code**
N3-H6 ···O4	0.79(0)	2.402(1)	3.075(1)	143.72(0)	x, y, z
C13-H13B ···O4	0.970(1)	2.611(2)	3.561(3)	166.29(0)	x+1, y, z
N4-H5···O8	0.817(0)	2.501(2)	3.195(2)	143.38(0)	x, y, z
C6-H6AB ···O8	0.97(0)	2.682(1)	3.471(1)	138.72(0)	x, y, z
C18-H18 ···O6	0.930(0)	2.676(1)	3.457(1)	141.98(0)	x-1, y, z
C7-H7AB···O7	0.970(1)	2.677(2)	3.615(3)	162.85(0)	x-1, y, z

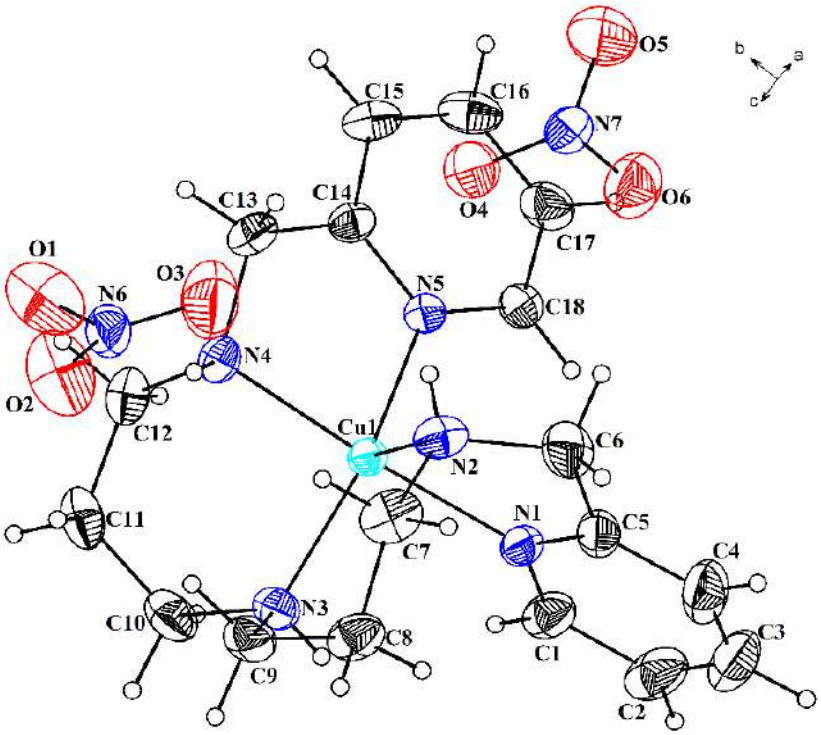

Figure 3.13 *Crystal structure of* ***2*** *showing atom labelling scheme. The thermal ellipsoids are drawn at a 30 % probability level for all the atoms except for the H atoms, which are shown as spheres of arbitrary radii.*

Table 3.5 *Selected bond lengths (Å) and angles (°) for* ***2****.*

Bond lengths (Å)			
Cu(1)-N(1)	2.038(3)	Cu(1)-N(2)	2.219(3)
Cu(1)-N(3)	2.022(3)	Cu(1)-N(5)	2.023(3)
Cu(1)-N(4)	2.026(3)		
Bond angles (°)			
N(1)-Cu(1)-N(2)	80.42(12)	N(3)-Cu(1)-N(1)	92.01(12)
N(3)-Cu(1)-N(2)	100.44(13)	N(5)-Cu(1)-N(1)	93.66(11)
N(5)-Cu(1)-N(2)	104.40(11)	N(3)-Cu(1)-N(5)	155.11(13)
N(4)-Cu(1)-N(1)	176.10(11)	N(4)-Cu(1)-N(2)	100.10(12)
N(3)-Cu(1)-N(4)	91.69(13)	N(5)-Cu(1)-N(4)	82.46(11)

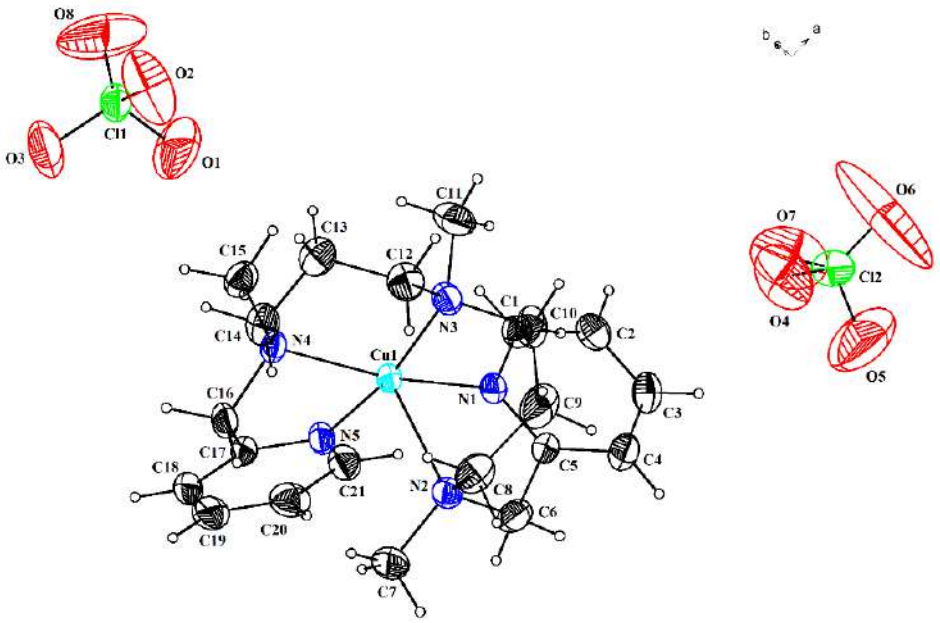

Figure 3.14 *Crystal structure of **3** showing atom labelling scheme. The thermal ellipsoids are drawn at a 30 % probability level for all the atoms except for the H atoms, which are shown as spheres of arbitrary radii.*

Table 3.6 *Selected bond lengths (Å) and angles (°) for **3**.*

Bond lengths (Å)			
Cu(1)-N(1)	2.064(4)	Cu(1)-N(4)	2.067(4)
Cu(1)-N(2)	2.302(4)	Cu(1)-N(5)	2.042(4)
Cu(1)-N(3)	2.088(4)		
Bond angles (°)			
N(5)-Cu(1)-N(1)	91.47(16)	N(5)-Cu(1)-N(4)	80.64(17)
N(1)-Cu(1)-N(4)	162.05(16)	N(5)-Cu(1)-N(3)	169.90(17)
N(1)-Cu(1)-N(3)	91.62(16)	N(4)-Cu(1)-N(3)	93.64(17)
N(5)-Cu(1)-N(2)	96.28(16)	N(1)-Cu(1)-N(2)	79.39(15)
N(4)-Cu(1)-N(2)	117.31(15)	N(3)-Cu(1)-N(2)	93.74(17)

Table 3.7 *Hydrogen bonding parameters (Å, º) for **3**.*

D-H···A	**D-H/ Å**	**H···A/ Å**	**D···A/ Å**	**D-H···A/º**	**Symmetry code**
C6-H6AB··· O5	0.97(0)	2.638(0)	3.514(0)	150.3(0)	x-1/2, -y+1/2, z+1/2
C4-H4··· O5	0.93(0)	2.539(0)	3.275(0)	136.28(0)	x-1/2, -y+1/2, z+1/2
C10-H10A··· O5	0.97(1)	2.536(1)	3.478(2)	163.80(0)	x, y, z+1
C11-H11B··· O7	0.960(1)	2.551(1)	3.438(2)	153.7(0)	x, y, z+1
C3-H3··· O4	0.93(0)	2.54(0)	3.211(1)	129.42(0)	x, y, z
C16-H16A··· O3	0.97(0)	2.439(0)	3.346(0)	155.61(0)	-x, y-1, -z+2
C15-H15C··· O3	0.96(0)	2.690(1)	3.530(1)	146.34(0)	-x, y-1, -z+2
C13-H13B··· O1	0.97(0)	2.533(0)	3.206(0)	126.51(0)	x, y, z
C15-H15A··· O2	0.96(0)	2.654(1)	3.269(1)	122.27(0)	x, y, z-1
C1-H1··· O2	0.93(0)	2.468(0)	3.354(0)	159.38(0)	x, y, z-1
C14-H14A··· O7	0.97(0)	2.47(0)	3.418(0)	165.57(0)	x-1, y, z+1

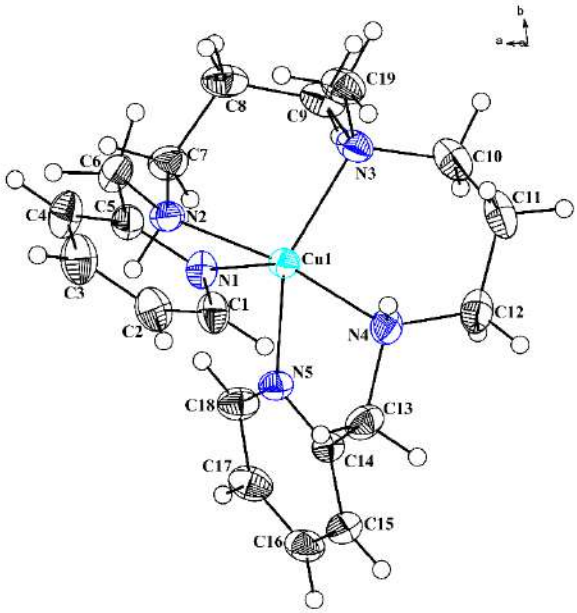

Figure 3.15 *Crystal structure of* ***4*** *showing atom labelling scheme. The thermal ellipsoids are drawn at a 30 % probability level for all the atoms except for the H atoms, which are shown as spheres of arbitrary radii. The perchlorate anions are omitted for clarity.*

Table 3.8 *Selected bond lengths (Å) and angles (°) for* ***4****.*

Bond lengths (Å)			
Cu(1)-N(4)	2.015(3)	Cu(1)-N(3)	2.113(3)
Cu(1)-N(2)	2.021(3)	Cu(1)-N(1)	2.207(3)
Cu(1)-N(5)	2.111(3)		
Bond angles (°)			
N(4)-Cu(1)-N(2)	169.12(13)	N(5)-Cu(1)-N(3)	130.62(11)
N(4)-Cu(1)-N(5)	80.88(12)	N(4)-Cu(1)-N(1)	92.88(12)
N(2)-Cu(1)-N(5)	95.04(11)	N(2)-Cu(1)-N(1)	78.84(11)
N(4)-Cu(1)-N(3)	96.15(13)	N(5)-Cu(1)-N(1)	108.95(11)
N(2)-Cu(1)-N(3)	94.15(12)	N(3)-Cu(1)-N(1)	120.42(11)

Table 3.9 *Hydrogen bonding parameters (Å, º) for* ***4****.*

D-H···A	**D-H/ Å**	**H···A/ Å**	**D···A/ Å**	**D-H···A/º**	**Symmetry code**
N2-H2 ···O4	0.980(0)	2.076(1)	3.027(1)	162.95(0)	x, y, z
N4-H1B ···O5	0.815(0)	2.352(1)	3.149(1)	165.68(0)	x, y, z
C11-H11A···O5	0.970(0)	2.625(1)	3.480(1)	147.12(0)	x, y, z
C19-H19B ···O5	0.960(0)	2.644(1)	3.587(1)	167.46(0)	x, y, z
C13-H13B ···O8	0.970(0)	2.365(1)	3.312(1)	165.25(0)	-x, -y, -z+1
C10-H10A···O6	0.970(1)	2.517(1)	3.404(3)	152.06(0)	x, -y+1/2, z+1/2
C9-H9A···O7	0.970(1)	2.618(1)	3.544(3)	159.76(0)	x, -y+1/2, z+1/2

The two unique perchlorate ions in compound **1** display an extensive network of hydrogen bonding. The predominant intermolecular H-bonding interactions arising from N3-H6···O4 and N4-H5···O8, accompanied by several C-H···O interactions, renders additional stability to compound **1** (**Figure 3.16** and **Table 3.4**). The oxygen atoms: O1, O2, O3, O4, O5, and O7 of the tetrahedral $(ClO_4)^-$ units are involved in C-H···O interactions resulting in an extended network in compound **3** (**Figure 3.16** and **Table 3.7**).

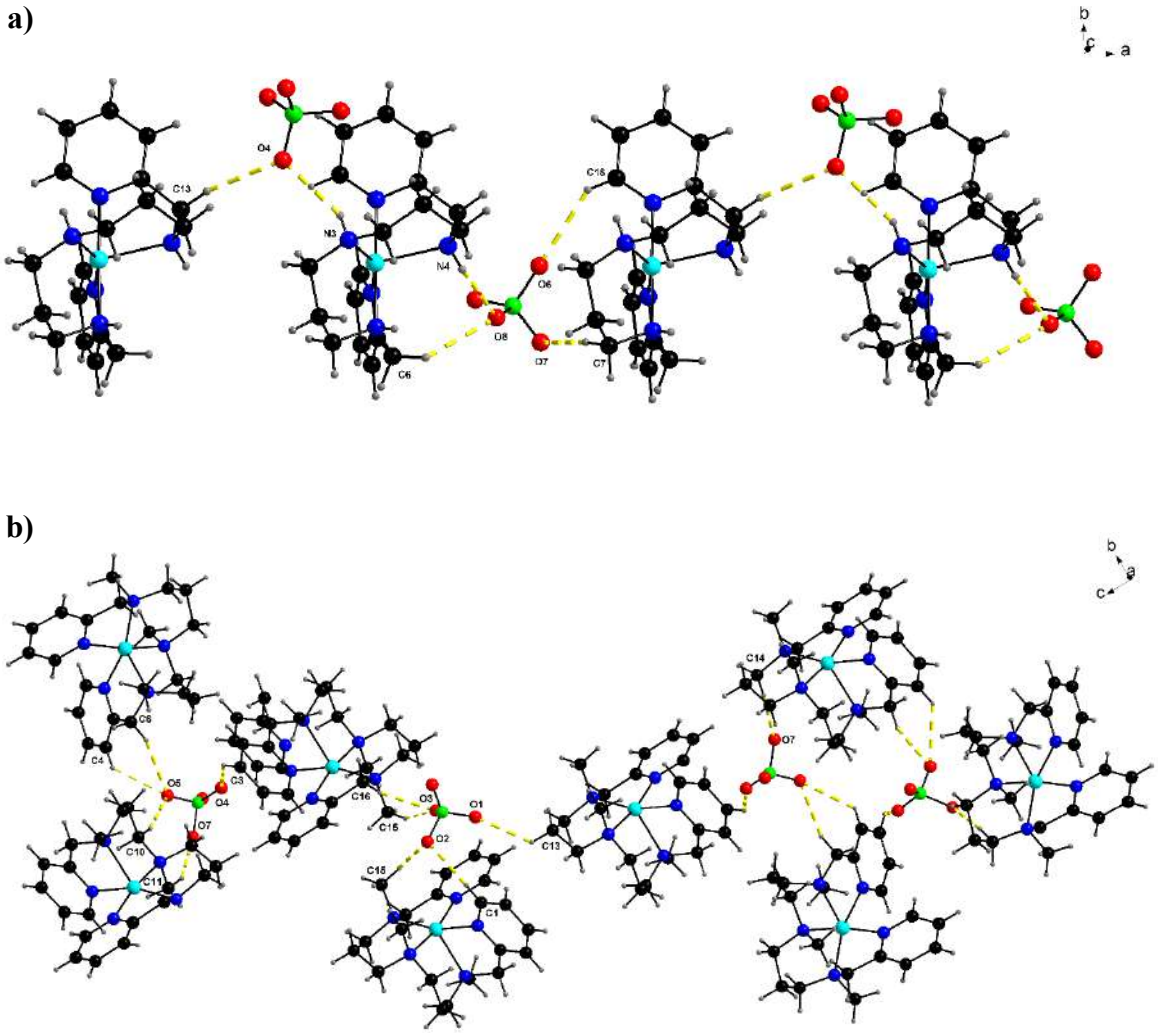

Figure 3.16 *Hydrogen bonding interactions in* ***1*** *(a)* ***3*** *(b) with atom labeling scheme of atoms involved in hydrogen bonding.*

The geometries of five-coordinated metal compounds lie on a continuum between a square pyramid and a trigonal bipyramid. Addison and co-workers clearly defined and quantified this continuum using the geometric parameter τ, according to the equation $\tau = (\beta - \alpha)/60$, where $\beta > \alpha$ are the two most prominent coordinate angles[48]. Since such structural parameters were also calculated for four-coordinate compounds, the symbol τ was modified to τ_5[83]. For perfect square pyramidal, τ_5 is 0, while it becomes 1.0 for ideal trigonal bipyramidal geometry; however, Allan and co-workers have also presented τ_5 values greater than 1.0[84,85]. The calculated τ_5 values for compounds **1** compared with **2** suggest a significant structural change induced upon the coordination center by methylation of amine nitrogen atoms.

In compound **1**, N4 is the apical bond, and the atoms N1, N2, N3, and N5 form the base of the square pyramid. The basal Cu-N bond lengths lie in the range (2.017-2.032 Å), whereas the apical Cu-N4 bond is slightly longer, 2.225 Å, as is typical for SP Cu(II) geometries (**Figure 3.12** and **Table 3.3**). Based on the calculation, the two relevant angles β and α are N2-Cu1-N5 (175.72°) and N1-Cu1-N3 (153.78°), respectively, which gave τ_5 = 0.36. Similarly, Compound **2** exhibited distorted square pyramidal geometry (**Figure 3.13**) as revealed from lower τ value of 0.34 calculated from $\tau = (\beta - \alpha)/60$; β and α are N(4)-Cu(1)-N(1) (176.10°) and N(3)-Cu(1)-N(5) (155.11°) respectively. In compound **3** (**Figure 3.14**) the equatorial positions of square pyramidal geometry are occupied by N1, N3, N4, and N5, while N2 occupies the axial position. The τ_5 value calculated from the bond angles N5-Cu1-N3 (169.90°) and N1-Cu1-N4 (162.05°) was found to be 0.13, which indicates a slight divergence from the ideal square pyramidal geometry. The τ value of 0.64 calculated for compound **4** indicates a geometry that is intermediate between the two ideal square pyramidal and trigonal bipyramidal geometries. Thus, suggesting that the compound **4** is leaning more towards trigonal bipyramidal geometry, but still indicating some distortion.

Table 3.10 *Structural parameters for Cu(II) compounds supported by pentadentate ligands.*

Compound	τ (distortion index)
1	0.36
2	0.34
3	0.13
4	0.64

3.3.6 X-ray powder diffraction

We recorded powder X-ray diffraction patterns to confirm the phase purity of the crystalline compounds **1-4** with that of the bulk material. The experimental powder patterns of **1-4** were compared with the simulated PXRD pattern obtained from single crystal structure data of **1** using Mercury 4.0 software[86]. The experimental and simulated powder patterns matched, suggesting that the bulk and single crystal phase are identical (**Figure 3.17-3.20**).

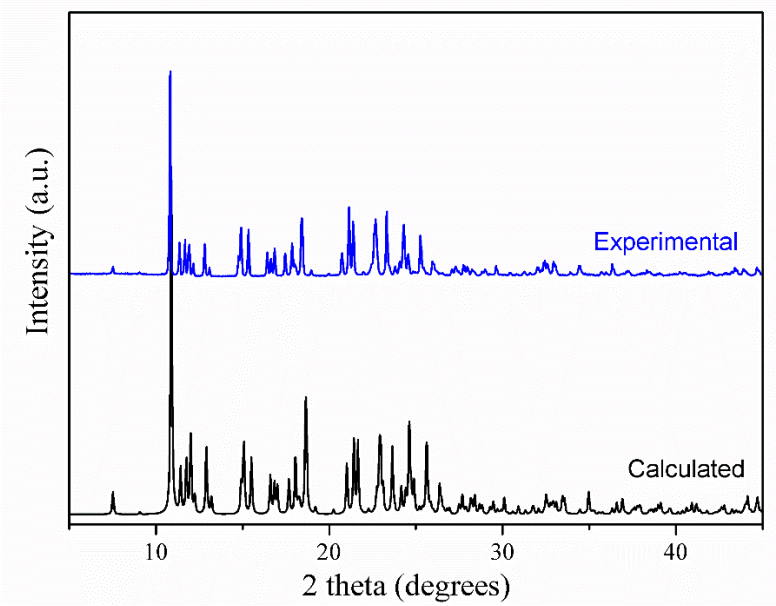

Figure 3.17 *The experimental and calculated PXRD patterns of* ***1****.*

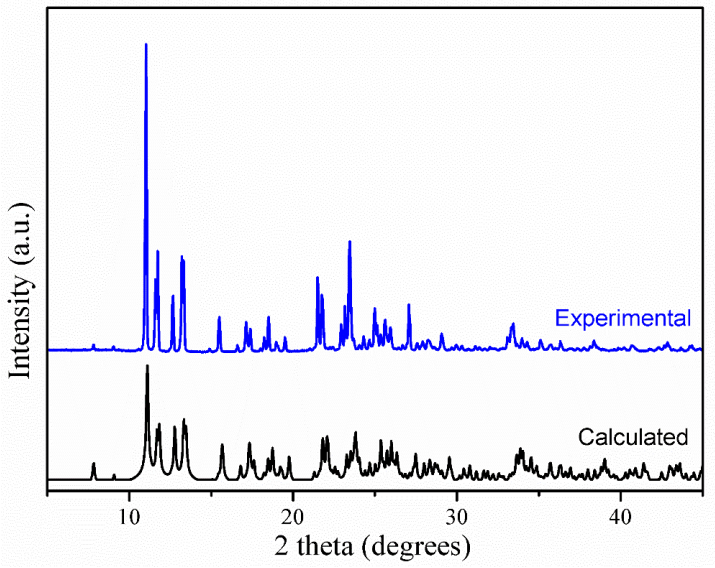

Figure 3.18 *The experimental and calculated PXRD patterns of* ***2****.*

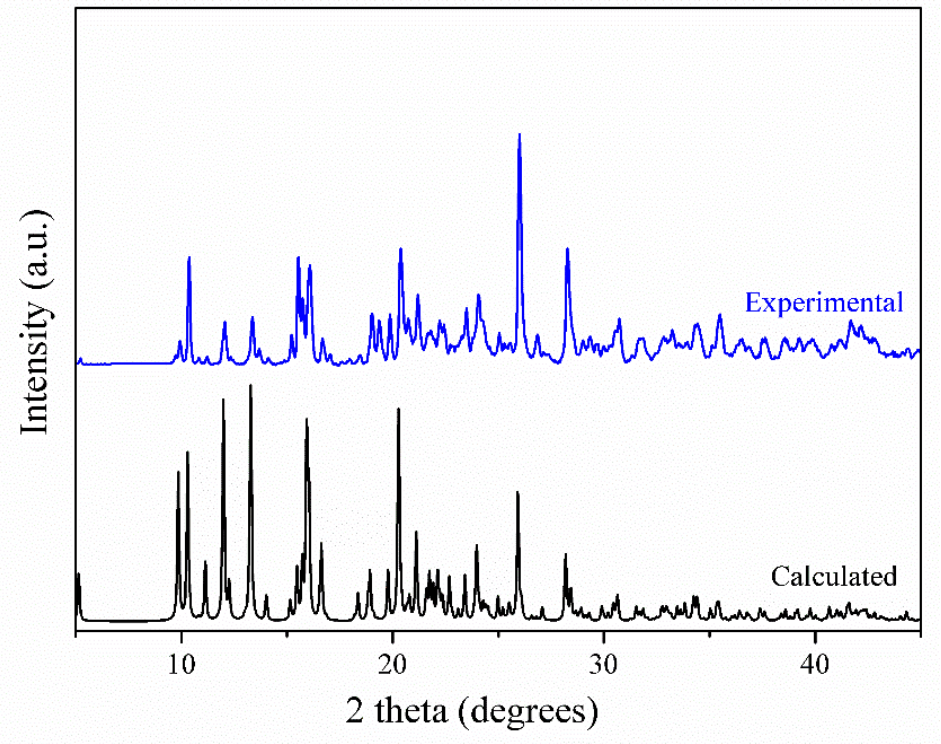

Figure 3.19 *The experimental and calculated PXRD patterns of* ***3****.*

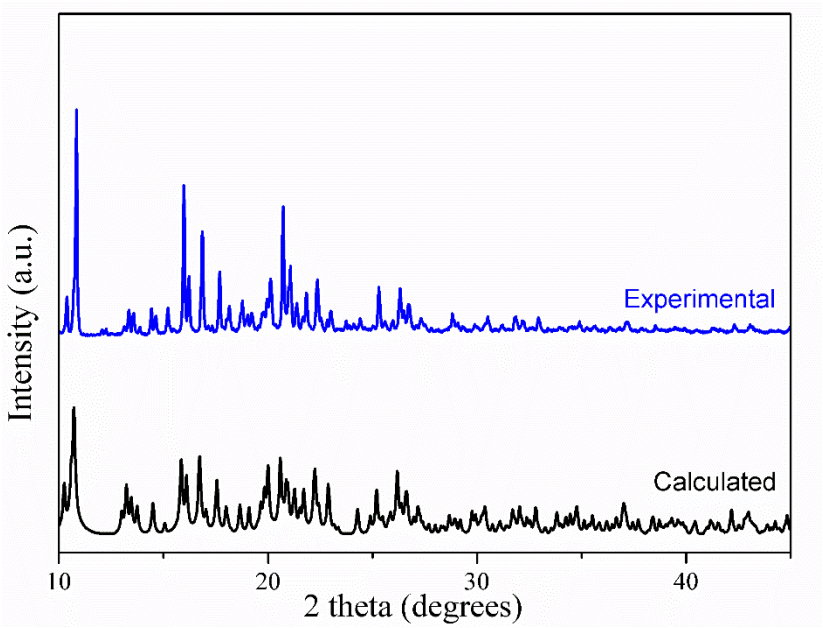

Figure 3.20 *The experimental and calculated PXRD patterns of* ***4****.*

3.3.7 Magnetic studies of 1 - 4.

The magnetic properties of compound **1-4** were studied by temperature-dependent magnetic susceptibility (χM) measurements on the finely powdered samples under an applied magnetic field of 100 Oe in the temperature range of 5 -300K. The resulting magnetization (emu/g) vs. temperature plots for compounds **1-4** revealed simple paramagnetic behavior (**Figure 3.21-3.24**)[87].

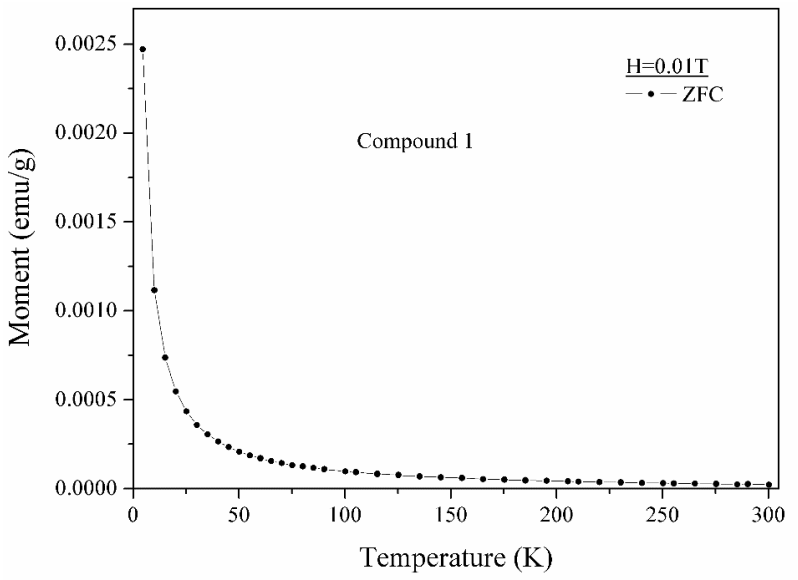

Figure 3.21 *Plot of Magnetic moment vs. Temperature for* ***1*** *under an applied field of 100 Oe between 5 to 300 K.*

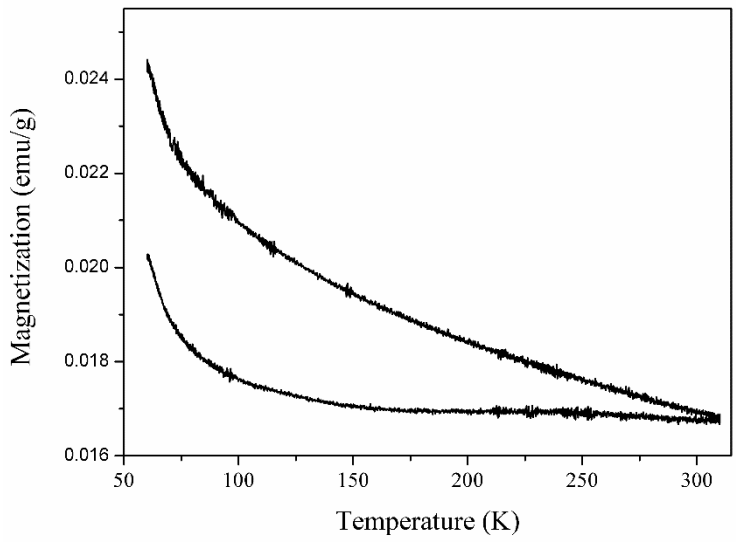

Figure 3.22 *Plot of Magnetic moment vs. Temperature for* ***2*** *under an applied field of 100 Oe between 50 to 300 K.*

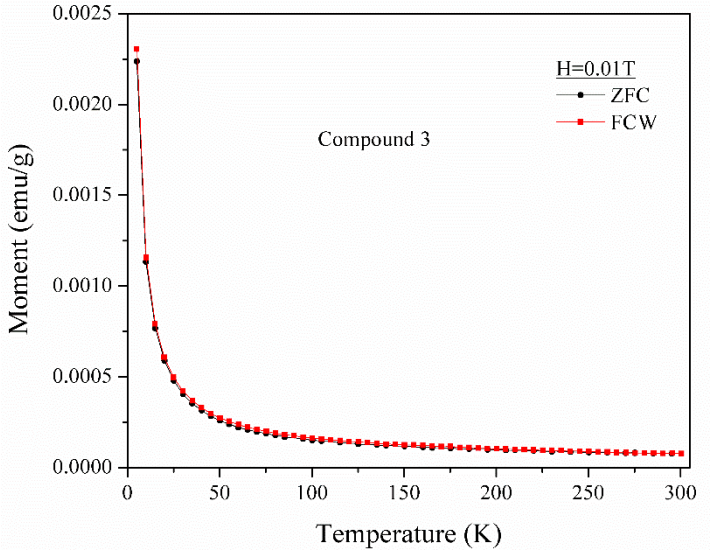

Figure 3.23 *Plot of Magnetic moment vs. Temperature for* ***3*** *under an applied field of 100 Oe between 5 to 300 K.*

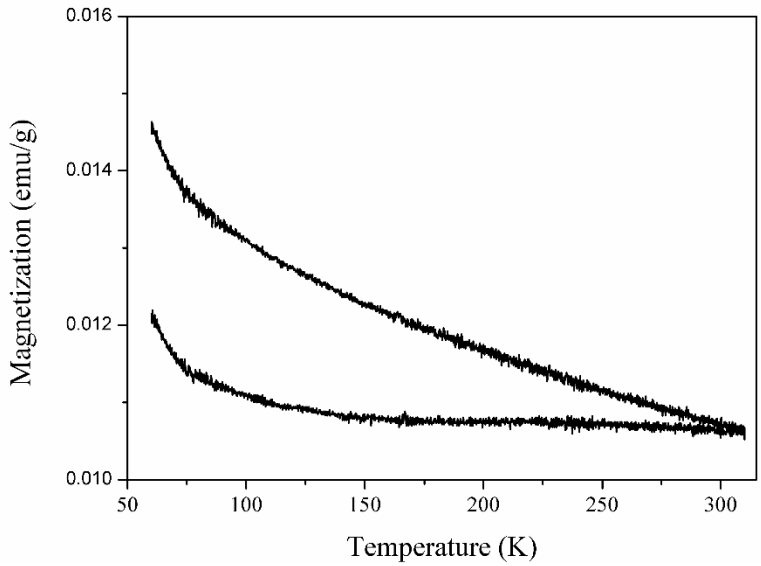

Figure 3.24 *Plot of Magnetic moment vs. Temperature for* ***4*** *under an applied field of 100 Oe between 50 to 300 K.*

3.3.8 Thermogravimetric and EPR studies of 1 and 3

Thermogravimetric (TG) plots of compounds **1** and **3** obtained between 30-400 ºC under a nitrogen atmosphere are displayed in **Figure 3.25**. The slight difference in the thermal stability of compounds **1** and **3** can be attributed to the nature of the ligands (**L1** and **L2**) coordinated with the copper (II) ion. The decrease in weight observed above 200 ºC indicates the absence of lattice water or solvent in its formula unit and the decomposition of the ligand.

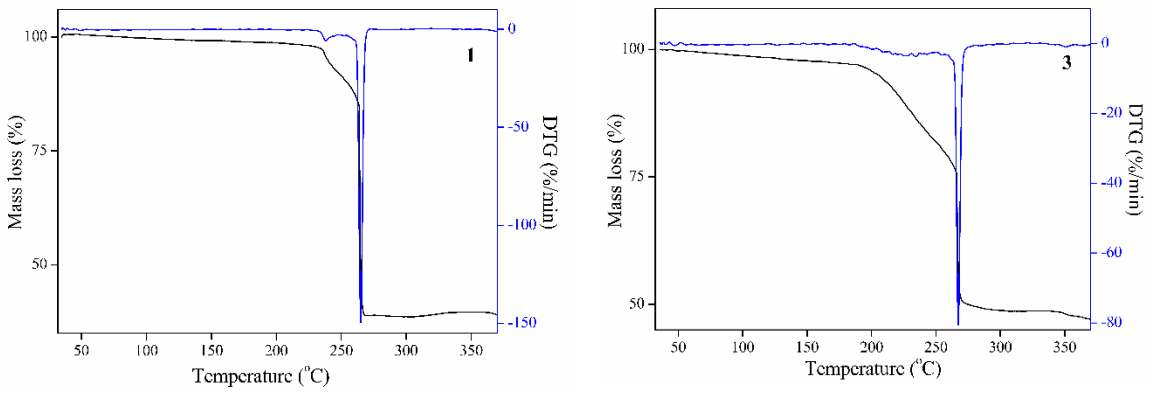

Figure 3.25 *Thermogravimetric (TG) and derivative thermogravimetric (DTG) measurements of compounds **1** (left) and **3** (right).*

The EPR spectra for Compounds **1** and **3** were recorded as frozen acetonitrile solutions at 77 K. Both **1** and **3** showed a broad pseudo isotropic band at 312 mT (**Figure 3.26**), with g_{iso} values of 2.07 and 2.06, respectively, and no observable hyperfine structure. Similar observations were reported for the known square-pyramid compounds[74,88–90].

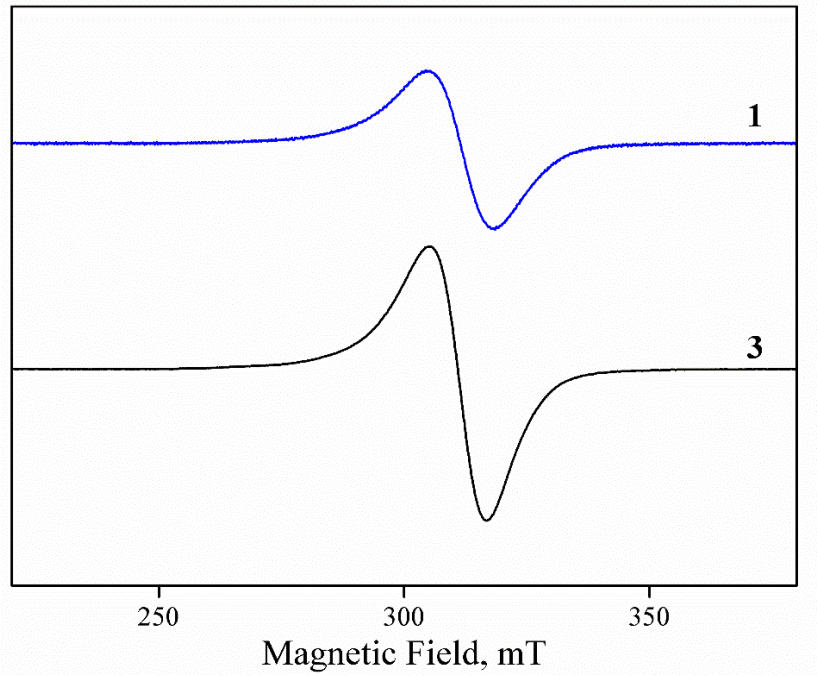

Figure 3.26 *EPR spectra of frozen sample of **1** and **3** recorded 77K in CH_3CN.*

3.3.9 Catalytic activity

As compounds **1**-**4** were phase pure, thermal stable, and structurally different in terms of τ_5 values, we considered investigating their enzyme-mimicking properties using 2-aminophenol (OAP) and 3,5-di-*tert*-butylcatechol (3,5-DTBC) for phenoxazinone synthase and catecholase activity. The dioxygen-saturated methanolic solutions (1 x 10^{-4} M) of **1**-**4** were treated with OAP (1 x 10^{-3} M) at 25°C. The time-dependent spectrophotometrically studies exhibited a gradual growth of the signature peak at 432 nm, indicating the formation of phenoxazinone chromophore[91]. The colorless solution of OAP changing to intense brown reveal its catalytic oxidation to the corresponding 2-aminophenoxazine-3-one (APX). The oxidation product was quantified by gas chromatography, and the yields were 30 (±3) %, 30 (±3) %, 73 % (±5) and 10 (±2) % for compounds **1**, **2**, **3** and **4** respectively. The appearance of a base peak at *m/z* 213.0 in ESI-MS spectrometry and the ^{1}H NMR ($CDCl_3$, ppm): δ 7.77 (d, 1H), δ 7.46-7.35 (m, 3H), δ 6.48 (s, 1H), δ 6.42 (s, 1H), δ 5.13 (br, s, 2H), analysis of the product helped in confirming the formation of APX product. The comparative experiments without a catalyst do not show significant peak intensity growth at 432 nm under identical conditions.

The kinetic experiments have been performed to understand the catalytic efficacy of copper (II) compounds **1** (**Figure 3.28**) and **3** (**Figure 3.27**) in the oxidation of OAP. For this study, a fixed concentration of 1 x 10^{-4} M solutions of **1** and **3** was reacted with varying substrate concentrations in methanol to maintain the pseudo-first-order kinetics. All the kinetic studies were carried out at 25°C. The experiments were monitored at a wavelength of 432 nm for a time span of 10 min. The non-linear plot of the initial rate of a reaction (v_o) versus substrate concentration indicates rate saturation kinetics for both compounds **1** (**Figure 3.30**) and **3** (**Figure 3.29**).

The Michealis-Menten approach was used to analyze the data and obtain the kinetic parameters like maximum rate of reaction (V_{max}), Michealis binding constant (K_m), and turnover number (K_{cat}), which are listed in **Table 3.11**. Comparing compound **1** with **3**, we observed a higher catalytic efficiency K_{cat} (4.34 x 10^5 h^{-1}) for **3** than **1** K_{cat} (3.67 x 10^4 h^{-1}) in methanol.

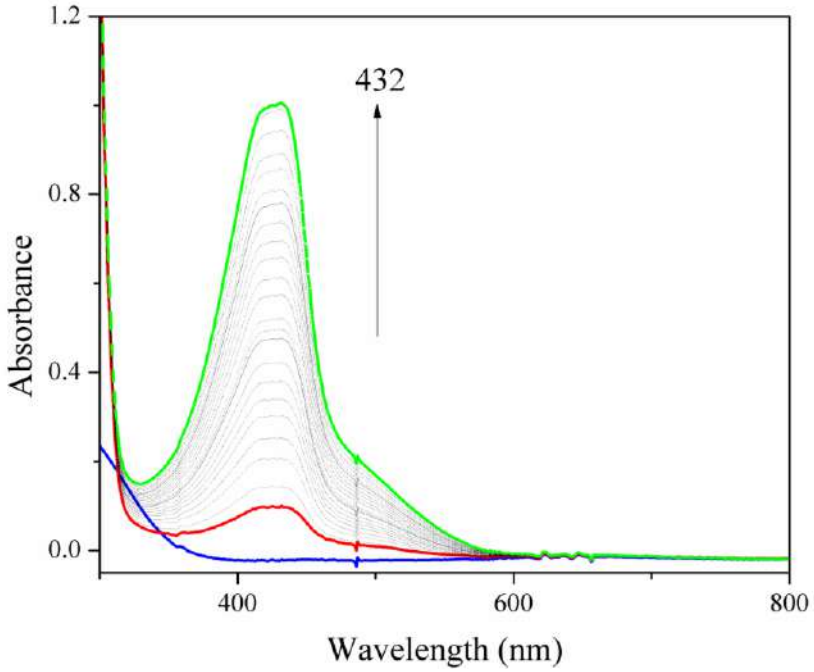

Figure 3.27 *The UV-Vis spectral profile exhibiting the growth of phenoxazine band (432 nm) over time upon addition of 10^{-3} M 2-aminophenol to 10^{-4} M methanolic solution of compound* ***3*** *at 25°C.*

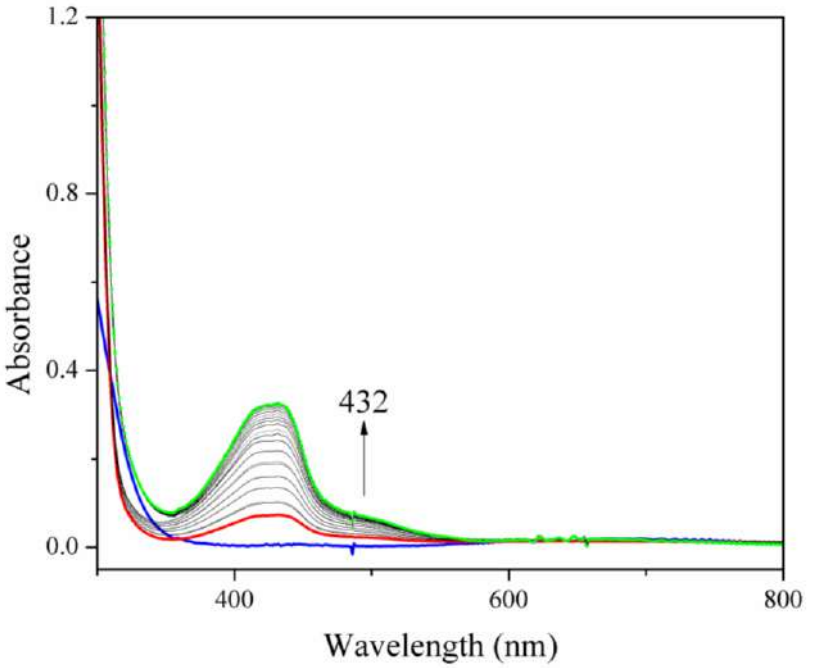

Figure 3.28 *The UV-Vis spectral profile exhibiting the growth of phenoxazine band (432 nm) over time upon addition of 10^{-3} M 2-aminophenol to 10^{-4} M methanolic solution of compound* ***1*** *at 25°C.*

Table 3.11 *Kinetic parameters comparison for phenoxazinone synthase-like activity of compounds* ***1*** *and* ***3****.*

Compound	V_{max} (Ms^{-1})	K_m (M)	K_{cat} (h^{-1})
1	10.21 $x10^{-4}$	2.62 $x10^{-4}$	3.67 x 10^4
3	12.06 $x10^{-3}$	2.05 $x10^{-3}$	4.34 x 10^5

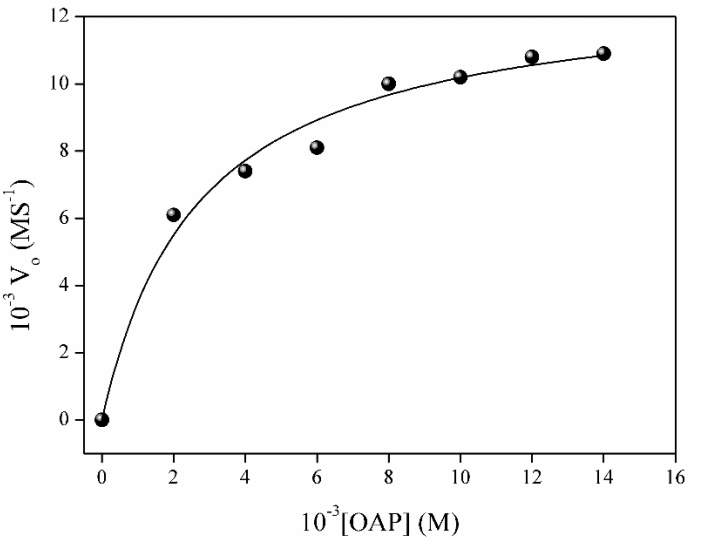

Figure 3.29 *Plot of rate vs [OAP] in the presence of* ***3*** *in methanol.*

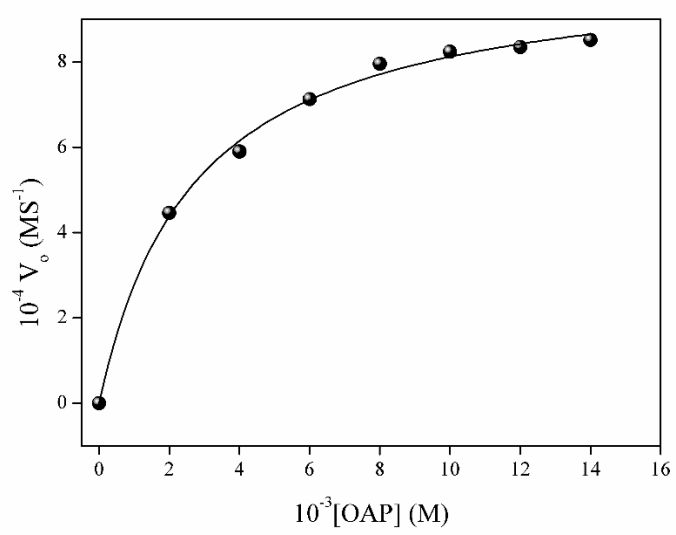

Figure 3.30 *Plot of rate vs. [OAP] in the presence of* ***1*** *in methanol.*

For catecholase activity studies, we have examined the efficiency of **1**-**4** in the oxidation of 3,5-di-*tert*-butylcatechol (3,5-DTBC). 3,5-DTBC is known to form a very stable oxidized product 3,5-di-*tert*-butyl-*o*-quinone (3,5-DTBQ) due to low quinone-catechol

reduction potential[92]. The time-dependent spectral changes for a period of 2 h after the addition of catalyst (1 x 10^{-4} M) and 100 equivalents of 3,5-DTBC in methanol were monitored by UV-Visible spectroscopy. The growth of the characteristic peak of 3,5-DTBQ at 398 nm in methanol was observed (**Figure 3.31** for **3** and **Figure 3.32** for **1**), which is due to the oxidation of 3,5-DTBC in presence of the catalyst (**1** and **2**) [93]. The color of the solution gradually turned deep brown that indicated the formation of 3,5-DTBQ. However, the oxidative conversion of 3,5-DTBC substrate alone in methanol was found to be negligible. The 3,5-DTBQ was purified by column chromatography, and the product was isolated as a solid. The melting point (110° C) of the isolated *o*-quinone product was the same as that reported literature[93]. The ^{1}H NMR spectrum in $CDCl_3$ of the isolated *o*-quinone product same as reported[93]. The yields for **1**-**4** were 35 (±2) %, 32 (±2) %, 85 (±5) and 5 (±2) %, respectively. The first-order catalytic reaction was observed with an initial rate of 2.7 x10^{-3} s^{-1} for compound **3** and 3.4 x10^{-5} s^{-1} for compound **1**.

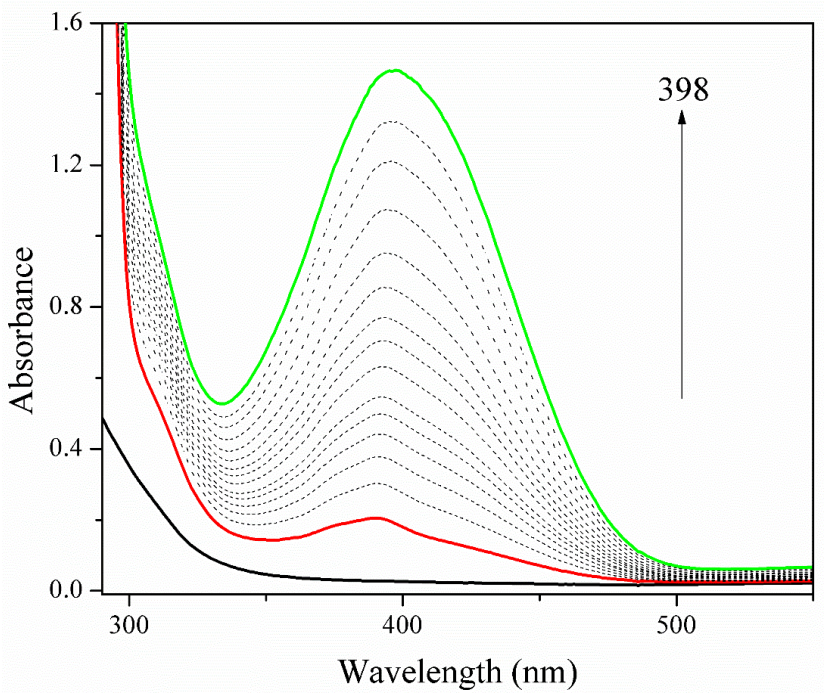

Figure 3.31 *The UV-Vis spectral profile showing an increase of 3,5-DTBQ band at 398 nm on addition of 100 equivalents of 3,5-DTBC to the solution of* ***3*** *in MeOH.*

Thus, the product yields and reactivity studies of **1**-**4** with OAP and 3,5-DTBC was clearly visible based on the topology of ligands **L1**, **L2** and **L3** in **1**-**4**. In **3** all three N's are methylated, making it sterically hindered, less distorted and more reactive; on the other hand, **1** and **2** has all three secondary N's making it topologically a different environment around the Cu(II) ion and show greater distortion as compared to analogous methylated

compound **3**. Compound **4** exhibits highest distortion form ideal square pyramidal geometry among compounds **1-4**, and show negligible reactivity. Ligand topology in various metal compounds has always been a factor in olefin oxidation, C-H activation, and other oxygenation reactions[94–96].

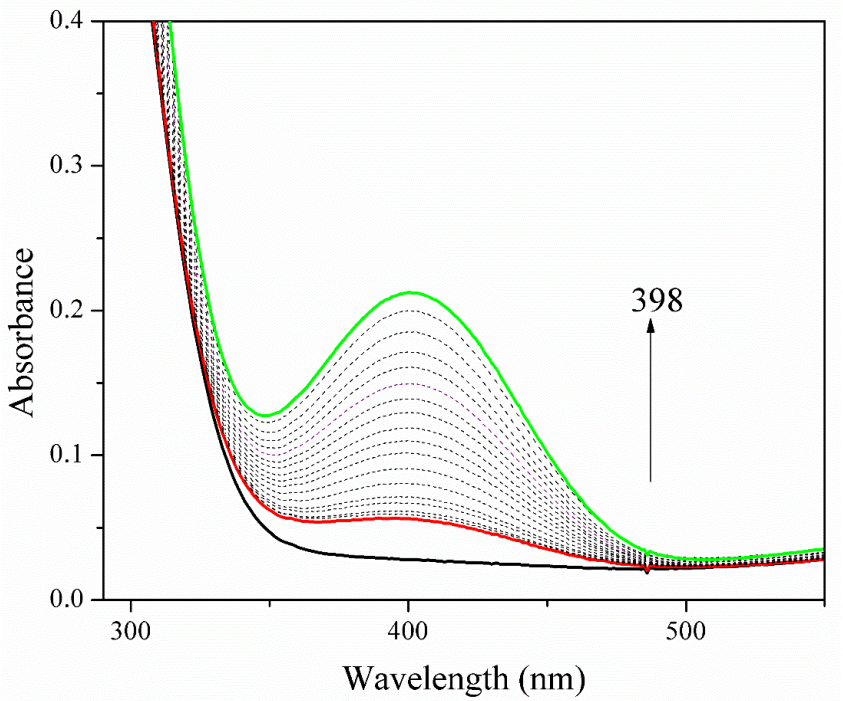

Figure 3.32 *The UV-Vis spectral profile showing an increase of 3,5-DTBQ band at 398 nm on addition of 100 equivalents of 3,5-DTBC to the solution of **1** in MeOH.*

3.4 Conclusion

In this study we have successfully synthesized novel ligands **L2** and **L3**, as well as the previously reported ligand **L1**, using a newly developed method. **L1**, **L2**, and **L3** were then utilized for the synthesis and analysis of four mononuclear copper(II) compounds, $[Cu(L1)](ClO_4)_2$ **1**, $[Cu(L1)](NO_3)_2$ **2**, $[Cu(L2)](ClO_4)_2$ **3** and $[Cu(L3)](ClO_4)_2$ **4**. The four compounds were identified through a combination of analytical methods. Compounds **1-4** were studied using single crystal X-ray diffraction. These compounds crystallize in a centrosymmetric monoclinic crystal system and exhibit geometries typical of five-coordinated metal compounds, ranging from a square pyramidal to a trigonal bipyramidal, with **4** exhibiting the greatest distortion from the ideal square pyramidal geometry among them. We then examined the applications of compounds **1-4** in phenoxazinone synthase and catecholase activity. The findings indicate that compound **3** outperformed the others in both activities. Research has indicated that the ligand topology of molecules **L1**, **L2**, and **L3** plays a significant role in the reactivity of compounds **1-4**.

Section II

Synthesis, characterization and reactivity studies of non-heme Ni(II) and Co(II) compounds

3.5 Experimental details

Detailed procedures for the synthesis of compounds of nickel(II) and cobalt(II) derived from ligands **L1** and **L2** are outlined in this section. The structures of compounds $[Ni(L2)(H_2O)](ClO_4)_2$ **5**, $[Co(L2)(H_2O)](ClO_4)_2$ **6** and $[Ni(L1)(Cl)]$ $Cl.2H_2O$ **7**, which were synthesized and characterized, are illustrated in **Scheme 3.5** for their potential use in catalytic reactions.

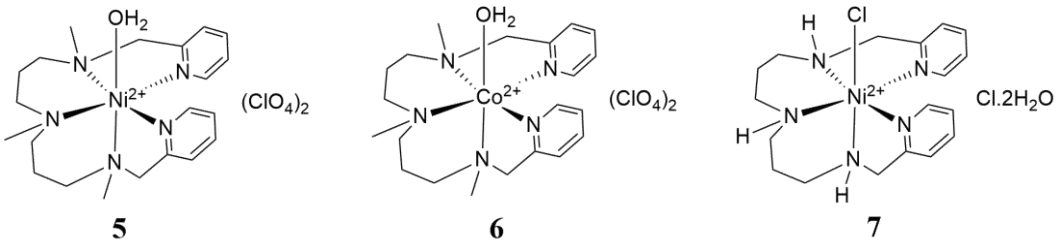

5 **6** **7**

Scheme 3.5 *Structure of the Ni(II) and Co(II) compounds used in this work.*

3.5.1 Synthesis of Ni(II) and Co(II) compounds $[Ni(L2)(H_2O)](ClO_4)_2$ 5, $[Co(L2)(H_2O)](ClO_4)_2$ 6 and $[Ni(L1)(Cl)]$ $Cl.2H_2O$ 7.

Acetonitrile solution of **L2** (0.49 g, 1.37 mmol) was added dropwise to the stirring solution of $Ni(ClO_4)_2.6H_2O$ (0.50 g, 1.37 mmol) in acetonitrile (2 mL) under the N_2 atmosphere at room temperature. The mixture was stirred for ~ 8 h. Diethyl ether (10 mL) was added to the resulting dark blue color solution, and the mixture was kept undisturbed for crystallization. The blue crystals formed after two days were isolated by filtration and dried in the air. The yield of **5** was 0.71 g (1.12 mmol), 82.0 %. *Anal. Calc.* for **5** C_{21} H_{35} Cl_2 Ni N_5 O_9 (%): C, 39.96; H, 5.59; N, 11.10. *Found:* C, 39.48; H, 5.02; N, 11.89. IR (KBr, cm^{-1}): 3460 υ(OH); 3007-2895 υ(CH); 1094, 620 υ(ClO_4); UV-Vis data, λ_{max}, CH_3CN/nm (ε/dm^3 mol^{-1} cm^{-1}): 275 (2682), 592 (42) and 977 (28). ESI-MS: m/z = 207.1 (calc. 207.0) for $[Ni(L2)]^{2+}$ and m/z = 512.5 (calc. 512.3) for $[Ni(L2)(ClO_4)]^+$.

Compound **6** was synthesized via a similar protocol as described in **5**; **L2** (0.49 g, 1.37 mmol) was reacted with $Co(ClO_4)_2.6H_2O$ (0.5 g, 1.37 mmol) in acetonitrile under a N_2

atmosphere. The reddish-pink crystalline compound **6** was obtained. The yield of **6** was 0.75 g (1.19 mmol), 77.0 %. *Anal. Calc.* for **6** C_{21} H_{35} Cl_2 Co N_5 O_9 (%): C, 39.95; H, 5.59; N, 11.09. *Found:* C, 39.31; H, 5.09; N, 11.63. IR (KBr, cm^{-1}): 3460 υ(OH); 3007-2895 υ(CH); 1093, 620 υ(ClO_4); UV-Vis data, λ_{max}, CH_3CN/nm (ε/dm^3 mol^{-1} cm^{-1}): 275 (2671), 505 (38) and 961 (19). ESI-MS: m/z = 207.5 (calc. 207.2) for $[Co(L2)]^{2+}$ and m/z = 513.5 (calc. 513.9) for $[Co(L2)(ClO_4)]^+$.

L1 (0.65 g, 2.1 mmol) was dissolved in CH_3CN (2 mL) and added to the stirring CH_3CN solution of $NiCl_2.6H_2O$ (0.5g, 2.1 mmol) at room temperature. The mixture was stirred for 4 h and filtered. To the resulting dark blue solution, diethyl ether (10 mL) was added and the mixture was kept undisturbed for crystallization. The blue crystals formed after two days were isolated by filtration and dried in air. The yield of **7** was 0.82 g (1.71 mmol), 83 %. *Anal. Calc.* for **7** C_{18} $H_{31}Cl_2$ Ni N_5O_2 (%): C, 45.13; H, 6.52; N, 14.62. *Found:* C, 45.10; H, 6.40; N, 14.55. IR (KBr, cm^{-1}): 3435 υ(OH); 3010-2850 υ(CH); UV-Vis data, λ_{max}, CH_3CN/nm (ε/dm^3 mol^{-1} cm^{-1}): 280 (2793), 576 (39) and 931 (27). ESI-MS: m/z = 406.4 (calc. 406.1) for $[Ni(L1)(Cl)]^+$

3.5.2 Reactivity of 5-7 with H_2O_2 in presence of TBAH

Adding 10 equivalents of 30% hydrogen peroxide (H_2O_2) and 5 equivalents of tetrabutylammonium hydroxide (TBAH) to the 0.5 mM solution of **3** in 2ml of CH_3CN resulted in an intense band at 326 nm in the UV-Vis spectrum. This species exhibited kinetic stability. Following the intermediate solution, the addition of 40 equivalents of 2-PPA caused the peak at 326 nm to decay. The products resulting from the reaction assessed through GC analysis indicated the major product of the reaction with 2-PPA was acetophenone.

3.6 Results and discussions

3.6.1 Synthesis and characterization of 5 and 6

The reaction of **L2** with metal salts, specifically $Ni(ClO_4)_2.6H_2O$ and $Co(ClO_4)_2.6H_2O$ in CH_3CN at an equimolar concentration yielded us two new compounds, namely $[Ni(L2)(H_2O)](ClO_4)_2$ **5** and $[Co(L2)(H_2O)](ClO_4)_2$ **6**, as shown in **Scheme 3.6**. The compounds were unambiguously formulated as $[Ni(L2)(H_2O)](ClO_4)_2$ **5** and $[Co(L2)(H_2O)](ClO_4)_2$ **6** based on IR, C,H,N analysis, and UV-Vis spectroscopy results

combined with data from ESI-MS. Compounds **5** and **6** were subsequently analyzed by single-crystal X-ray structure determination.

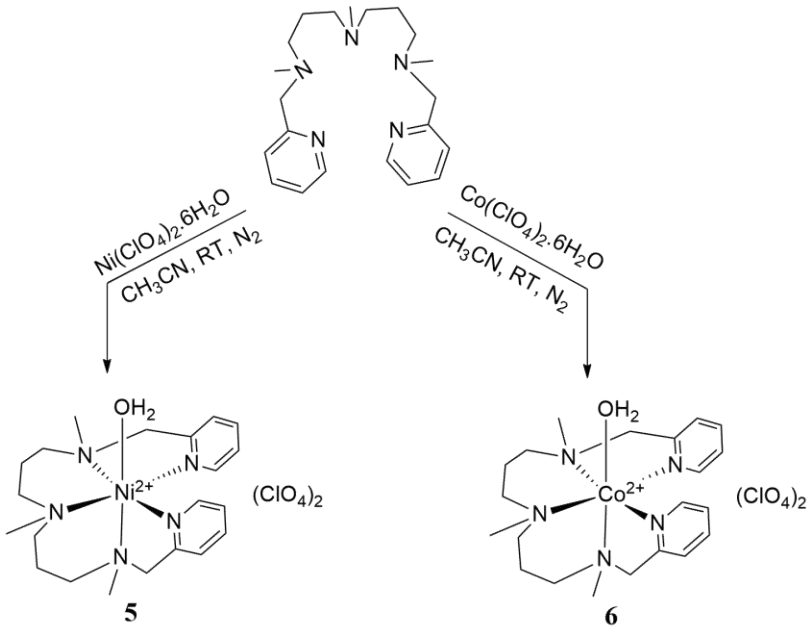

Scheme 3.6 *Synthetic protocol for the Ni(II) and Co(II) compounds of ligand* ***L2****.*

3.6.2 Infrared (IR) spectroscopic analysis of compounds 5 and 6

The Infrared spectra of compounds **5** and **6**, as overlaid, are illustrated in **Figure 3.33**. A broad band centered at ~3460 cm^{-1} have been attributed to the O-H vibration of a water molecule. Further, the well pronounced absorption peaks at 1090 cm^{-1} and 621 cm^{-1} indicates uncoordinated perchlorate ions[77,78].

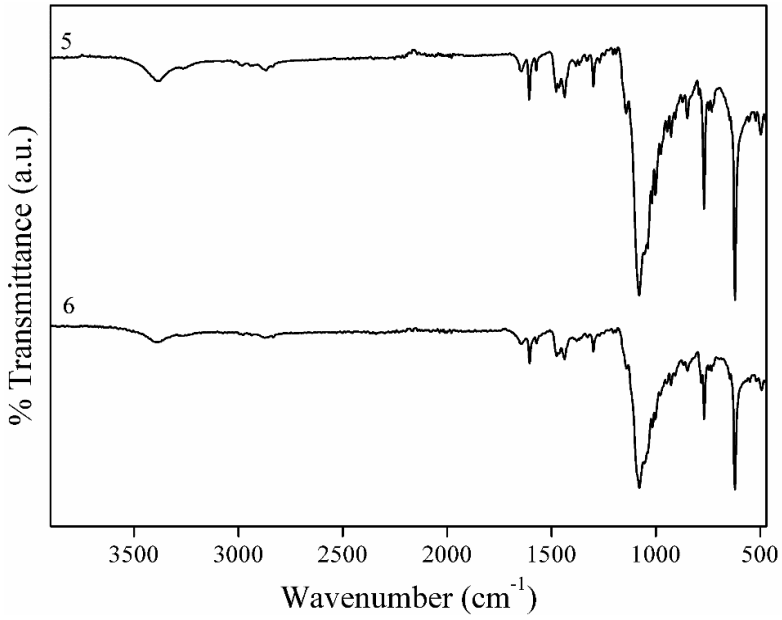

Figure 3.33 *Overlaid Infrared spectra of compounds* ***5*** *and* ***6****.*

3.6.3 ESI-Mass spectrometry

The ESI-MS spectra of compounds **5** and **6** are presented in **Figure 3.34**. The mass spectrum obtained by electrospray ionization mass spectrometry (ESI-MS) of compound **5** dissolved in acetonitrile exhibited two distinct mass peaks at *m/z* values of 207.1 (calc. *m/z* 207.0) and 512.5(calc. *m/z* 512.6). These peaks were attributed to the $[Ni(L2)]^{2+}$ and $[Ni(L2)(ClO_4)]^{+}$ species respectively. Whereas the peaks observed at m/z values of 207.5(calc. *m/z* 207.3) and 513.5(calc. *m/z* 513.5) can be assigned to $[Co(L2)]^{2+}$ and $[Co(L2)(ClO_4)]^{+}$ species respectively.

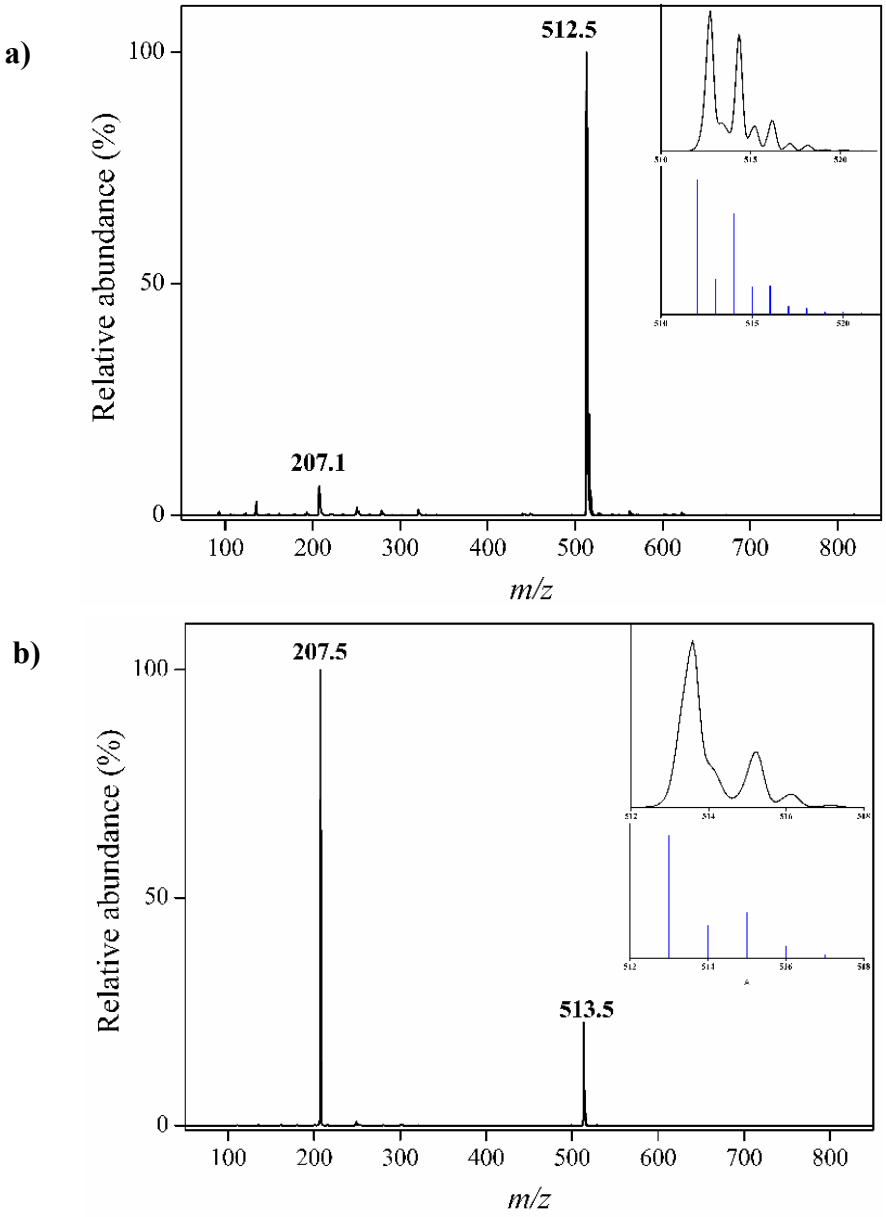

Figure 3.34 *ESI-MS spectrum of* ***5*** *(a) and* ***6*** *(b) recorded in acetonitrile solvent. The inset shows the isotope distribution patterns for the prominent peaks in black with stimulated pattern in blue colour.*

3.6.4 Crystal structure and geometrical analysis of compounds 5 and 6

Single crystals of compounds **5** and **6**, suitable for X-ray crystallography, were grown by slowly diffusing diethyl ether into their solutions of acetonitrile. The technical details of data acquisition and selected refinement results for **5** and **6** are listed in **Table 3.12**. The selected bond lengths and bond angles for **5** and **6** are listed in **Table 3.13** and **Table 3.15**. In our X-ray structural analysis, compounds **5** and **6** are seen to be isostructural. Compounds **5** and **6** crystallize in monoclinic space groups, specifically $P2_1/c$ and $P2_1/n$ respectively. The crystal structures of both compounds feature a centrally positioned metal(II) ion, specifically nickel(II) in compound **5** and cobalt(II) in compound **6**, along with a pentadentate **L2** ligand and a water molecule, as well as two crystallographically independent perchlorate ions, as depicted in **Figure 3.35** and **Figure 3.36** respectively. The octahedral $[MN_5O]^{2+}$ unit, where M is either Ni(II) or Co(II), shows slight distortion. This distortion is caused by the presence of two types of nitrogen donor atoms, with two being from the pyridyl part and three from the tertiary amine backbone, as well as a water molecule. The distortion in the octahedral structure is visibly apparent from the cis angles of (N-Ni-N and N-Co-N), which span a range of 83.43(11)-104.65(11)° in sample **5** and 78.37(14)-107.44(13)° in sample **6**, and similarly, the trans angles vary between 167.25(10)-171.85(12)° in **5** and 166.25(15)-169.85(15)° in **6** (**Table 3.13** and **Table 3.15**). In both compounds, the pyridyl nitrogen atoms are oriented in a syn arrangement, and the triamine section occupies the facial position of the octahedral structure. Analogous donor atom dispositions were also observed in compounds incorporating pentadentate ligands derived from pyrrole[37,97]. Reports have also described triamine nitrogens occupying the meridional positions of the octahedron. The perchlorates in compounds **5** and **6** function solely as counter anions for the cations $[Co(L2)]^{2+}$ and $[Ni(L2)]^{2+}$ and do not engage in bonding with cobalt(II) or nickel(II) ions (**Figure 3.35** and **Figure 3.35**). However, the perchlorate anions contribute significantly to the formation of the extended network via their oxygen atoms, which include O6 and O8 in structure **5**, and O6 and O7 in structure **6**; these oxygen atoms participate in weak hydrogen bonding with a water molecule, as shown in **Table 3.14** and **Table 3.16**. The three-dimensional network structures, which are composed of Cl-O···H contacts, $[MN_5O]^{2+}$ motifs, and perchlorate anions, are illustrated in **Figure 3.37** and **Figure 3.38**. Two O-Cl-O and two H-O-H molecules are connected through hydrogen bonds to create a 12-membered ring structure within compounds **5** and **6**. Structural data clearly indicates that the primary source of

hydrogen bonding is the coexistence of a water molecule and perchlorate ions in compounds **5** and **6**. The presence of water in the crystal structures of **5** and **6** can be accounted for despite the use of acetonitrile as the solvent, due to the employment of metal perchlorate hexahydrates in the synthesis process. Water molecules were also incorporated in other nickel(II) compounds, despite the reactions being conducted in methanol[98–100].

Table 3.12 Technical details and structure refinement parameters of **5** and **6**.

Compound	**5**	**6**
Empirical formula	$C_{21}H_{35}Cl_2NiN_5O_9$	$C_{21}H_{35}Cl_2CoN_5O_9$
Formula weight	631.15	631.37
Temperature	296(2) K	296(2) K
Wavelength	0.71073 Å	0.71073 Å
Crystal system	Monoclinic	Monoclinic
Space group	$P2_1/c$	$P2_1/n$
Unit cell dimensions	a = 9.331(2) Å	a = 8.6089(4) Å
	b = 33.424(7) Å	b = 34.7926(15) Å
	c = 8.6936(19) Å	c = 9.4193(4) Å
	α = 90°	α = 90°
	β = 104.045(6)°	β = 102.8400(10)°
	γ = 90°	γ = 90°
Volume	2630.4(19) $Å^3$	2750.8(2) $Å^3$
Z	4	4
Density (calculated)	1.594 mg/m^3	1.525 mg/m^3
Absorption coefficient	1.001 mm^{-1}	0.875 mm^{-1}
F(000)	1320	1316
Theta range for data collection	2.331 to 28.391°	2.508 to 26.374°
Completeness to theta	99.7%	99.9%
Index ranges	-12≤ h ≤12	-10≤ h ≤10
	-44≤ k≤44	-43≤ k≤43
	-11≤ l≤11	-11≤ l≤11
Reflections collected	84615	35102
Independent reflections	6542(R_{int}= 0.0484)	5611 (R_{int}= 0.034)
Refinement method	Full-matrix least-squares on F^2	Full-matrix least-squares on F^2
Absorption correction	Semi- empirical from equivalents	Semi- empirical from equivalents
Data/restraints/parameters	6542 / 0 / 390	5611 / 1 / 352
Goodness-of-fit on F^2	1.228	1.058
Final *R*indices[I>2sigma(I)]	R1= 0.0637, wR2= 0.1283	R1= 0.0676, wR2= 0.1900
R indices (all data)	R1= 0.0682, wR2= 0.1305	R1= 0.0840, wR2= 0.2073
CCDC No.	2386748	2386736

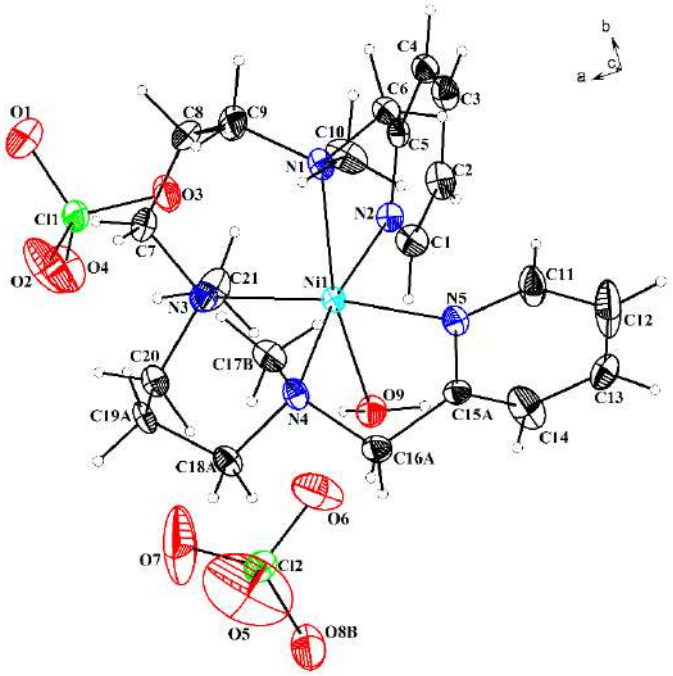

Figure 3.35 *Crystal structure of* ***5*** *showing atom labelling scheme. The thermal ellipsoids are drawn at a 50 % probability level for all the atoms except for the H atoms, which are shown as spheres of arbitrary radii.*

Table 3.13 *Selected bond lengths (Å) and angles (°) for* ***5****.*

Bond lengths (Å)			
Ni(1)-N(5)	2.111(3)	Ni(1)-N(2)	2.116(3)
Ni(1)-O(9)	2.143(3)	Ni(1)-N(4)	2.174(3)
Ni(1)-N(3)	2.202(3)	Ni(1)-N(1)	2.331(3)
Bond angles (°)			
N(5)-Ni(1)-N(2)	92.61(12)	N(5)-Ni(1)-O(9)	83.43(11)
N(2)-Ni(1)-O(9)	89.54(11)	N(5)-Ni(1)-N(4)	79.83(11)
N(2)-Ni(1)-N(4)	171.30(12)	O(9)-Ni(1)-N(4)	85.35(11)
N(5)-Ni(1)-N(3)	171.85(12)	N(2)-Ni(1)-N(3)	93.77(11)
O(9)-Ni(1)-N(3)	91.55(11)	N(4)-Ni(1)-N(3)	93.40(12)
N(5)-Ni(1)-N(1)	90.49(11)	N(2)-Ni(1)-N(1)	79.52(10)
O(9)-Ni(1)-N(1)	167.25(10)	N(4)-Ni(1)-N(1)	104.65(11)
N(3)-Ni(1)-N(1)	95.65(11)		

Table 3.14 *Hydrogen bonding parameters (Å, º) for* ***5****.*

D-H···A	**D-H/ Å**	**H···A/ Å**	**D···A/ Å**	**D-H···A/º**	**Symmetry code**
O9-H9A··· O8A	0.851(1)	1.994(4)	2.820(4)	163.46(2)	1-x, 1-y, 1-z
O9-H9B··· O6	0.851(2)	2.091(3)	2.801(5)	140.59(1)	x, y, z

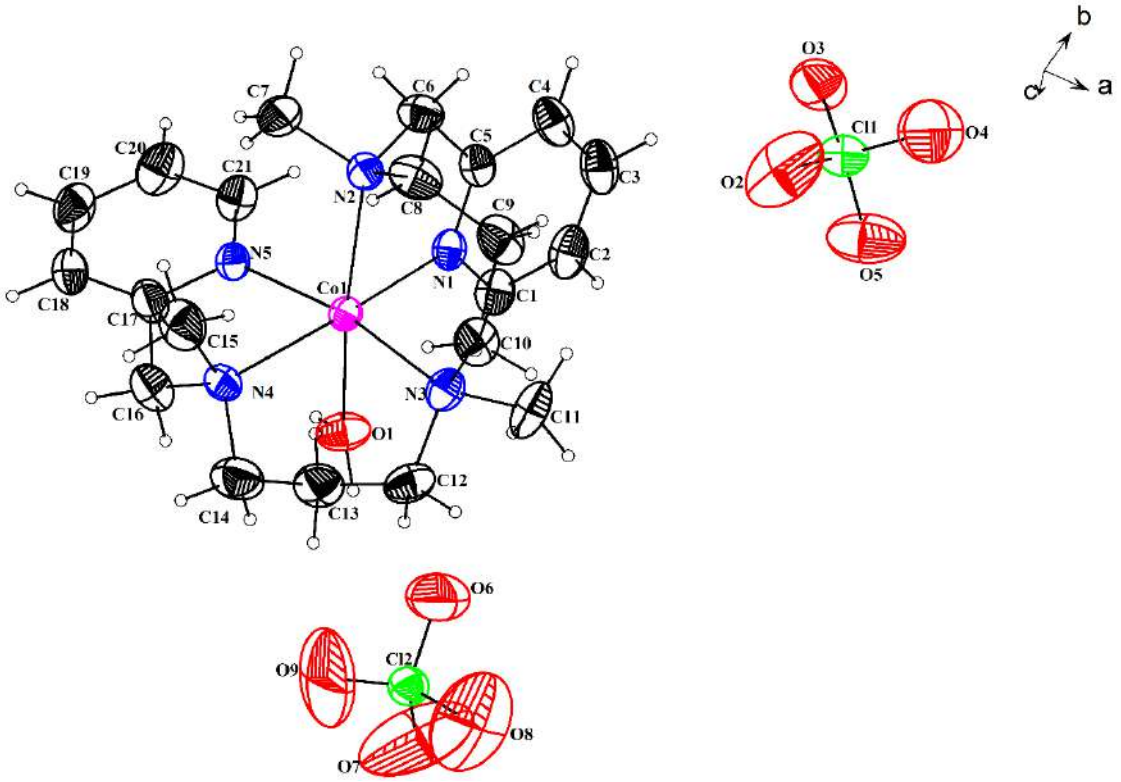

Figure 3.36 *Crystal structure of* ***6*** *showing atom labelling scheme. The thermal ellipsoids are drawn at a 30 % probability level for all the atoms except for the H atoms, which are shown as spheres of arbitrary radii.*

Table 3.15 *Selected bond lengths (Å) and angles (°) for* ***6****.*

Bond lengths (Å)			
Co(1)-N(1)	2.155(4)	Co(1)-N(5)	2.163(3)
Co(1)-O(1)	2.198(3)	Co(1)-N(4)	2.219(4)
Co(1)-N(3)	2.230(4)	Co(1)-N(2)	2.316(4)
Bond angles (°)			
N(1)-Co(1)-N(5)	92.44(14)	N(1)-Co(1)-O(1)	88.37(16)
N(5)-Co(1)-O(1)	84.04(15)	N(1)-Co(1)-N(4)	169.10(14)
N(5)-Co(1)-N(4)	78.37(14)	O(1)-Co(1)-N(4)	84.88(16)
N(1)-Co(1)-N(3)	95.84(15)	N(5)-Co(1)-N(3)	169.85(15)
O(1)-Co(1)-N(3)	90.32(16)	N(4)-Co(1)-N(3)	92.75(15)
N(1)-Co(1)-N(2)	78.51(13)	N(5)-Co(1)-N(2)	92.36(13)
O(1)-Co(1)-N(2)	166.25(15)	N(4)-Co(1)-N(2)	107.44(13)
N(3)-Co(1)-N(2)	95.04(15)		

Table 3.16 *Hydrogen bonding parameters (Å, º) for* ***6****.*

D-H···A	**D-H/ Å**	**H···A/ Å**	**D···A/ Å**	**D-H···A/º**	**Symmetry code**
O1-H1A··· O7	0.793(0)	2.014(0)	2.797(1)	169.54(0)	1-x, 1-y, 1-z
O1-H5··· O6	0.892(0)	2.054(0)	2.762(1)	135.47(0)	x, y, z

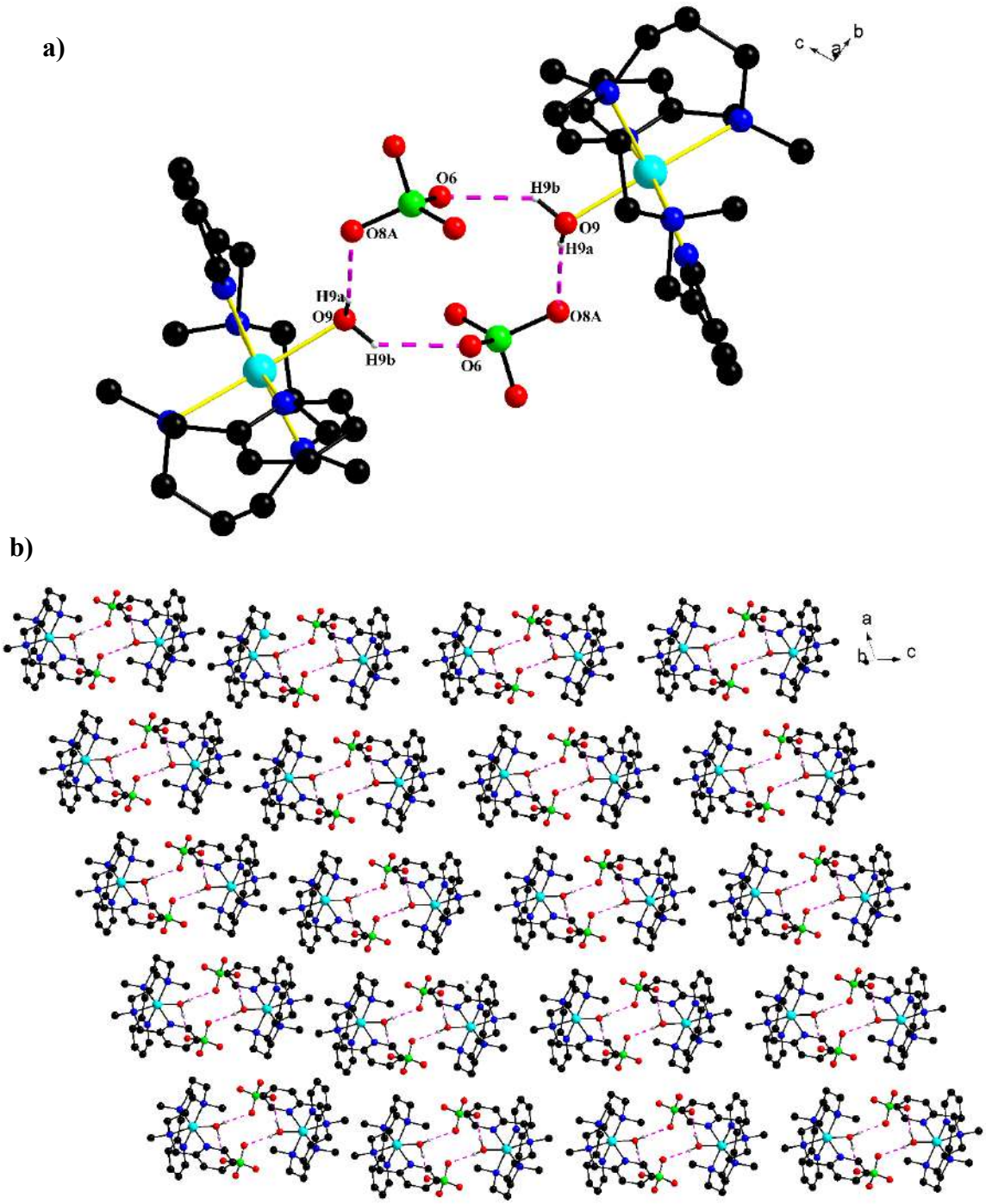

Figure 3.37 *(a) The cyclic structure formed due to hydrogen bonding interactions in* ***5*** *with atom labelling scheme of atoms involved in hydrogen bonding. Hydrogen atoms attached to carbon are omitted for clarity (b) The enlarged view of a network of hydrogen bonding in* ***5*** *showing the symmetric organisation of* $[Ni(L2)(H_2O)]^{2+}$ *cations and perchlorate anions.*

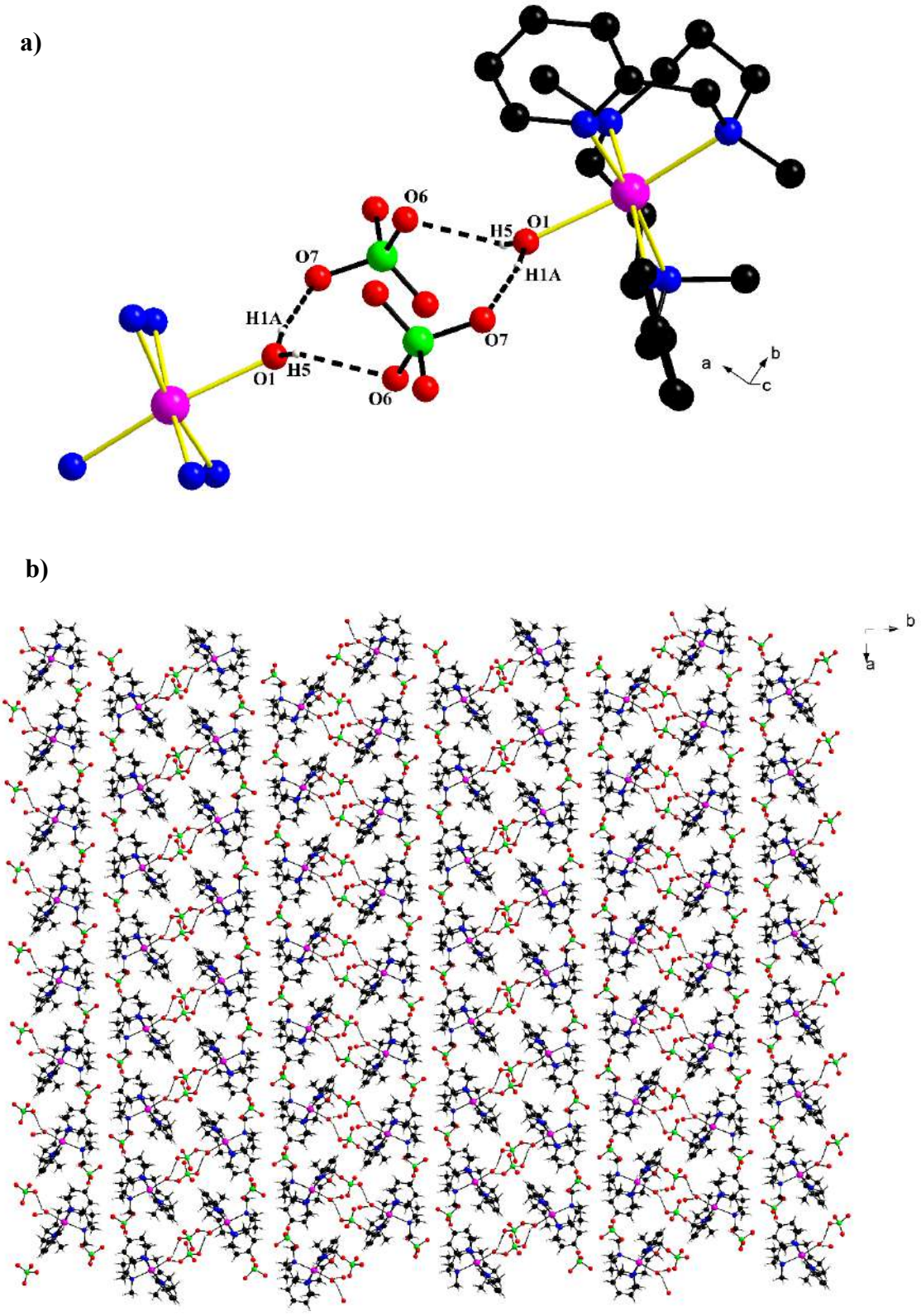

Figure 3.38 *(a) The cyclic structure formed due to hydrogen bonding interactions in* ***6*** *with atom labelling scheme of atoms involved in hydrogen bonding. Hydrogen atoms attached to carbon are omitted for clarity (b) The enlarged view of a network of hydrogen bonding in* ***6*** *showing the symmetric organisation of* $[Co(L2)(H_2O)]^{2+}$ *cations and perchlorate anions.*

3.6.5 Magnetic studies of 5 and 6

Compounds **5** and **6** had their magnetic properties examined through magnetic susceptibility (χM) measurements, which were taken at varying temperatures, on finely powdered samples under a magnetic field of 100 Oe between 5 and 300K. The plots of magnetization (emu/g) versus temperature for compounds **5** and **6** showed straightforward paramagnetic properties (**Figure 3.39** and **Figure 3.40**).

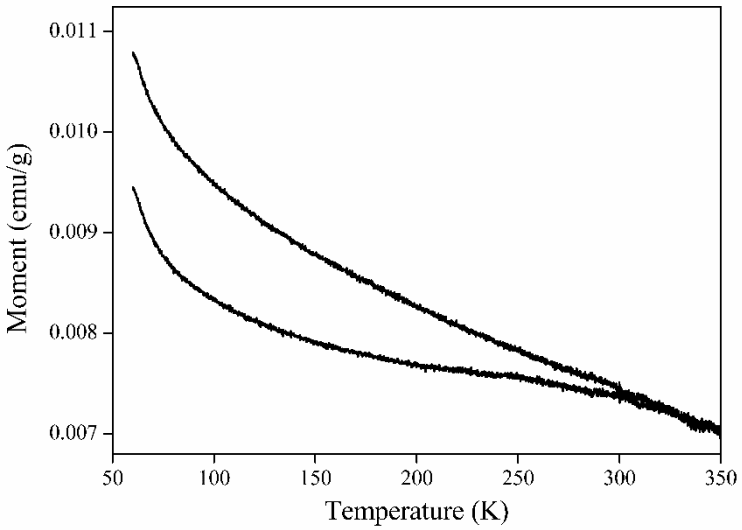

Figure 3.39 *Plot of Magnetic moment vs. Temperature for* ***5*** *under an applied field of 100 Oe between 50 to 300 K.*

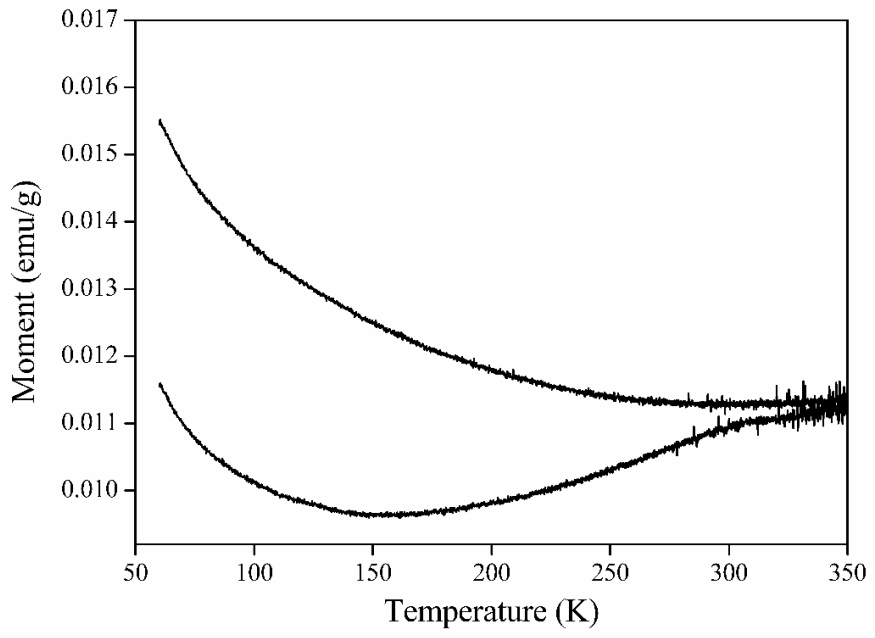

Figure 3.40 *Plot of Magnetic moment vs. Temperature for* ***6*** *under an applied field of 100 Oe between 50 to 300 K.*

3.6.6 Synthesis and characterization of 7

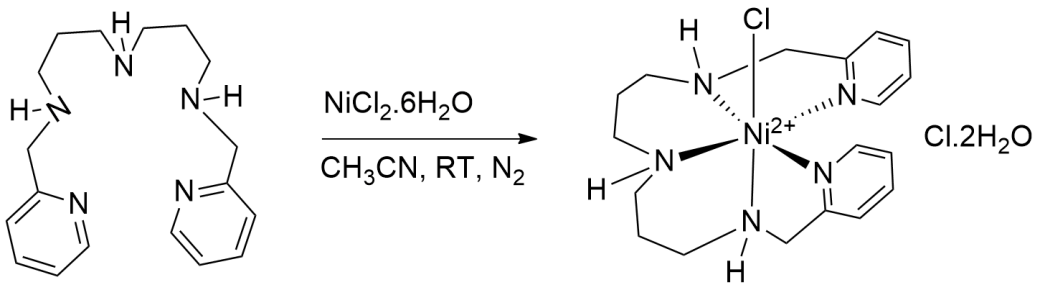

Scheme 3.7 *Synthetic protocol for the Ni(II) compound of ligand* ***L1****.*

The synthetic strategy employed to obtain compound **7** is shown in **Scheme 3.7**. The stoichiometric addition of **L1** and nickel chloride in acetonitrile afforded blue crystalline powder of **7**. IR spectrum of compound **7** exhibit broad peak at 3435 cm^{-1} which can be attributed to the O-H stretching vibration of water. The bands in the range 3010-2850 cm^{-1} are exhibited due to the C-H streching vibrations[78] (**Figure 3.41**).

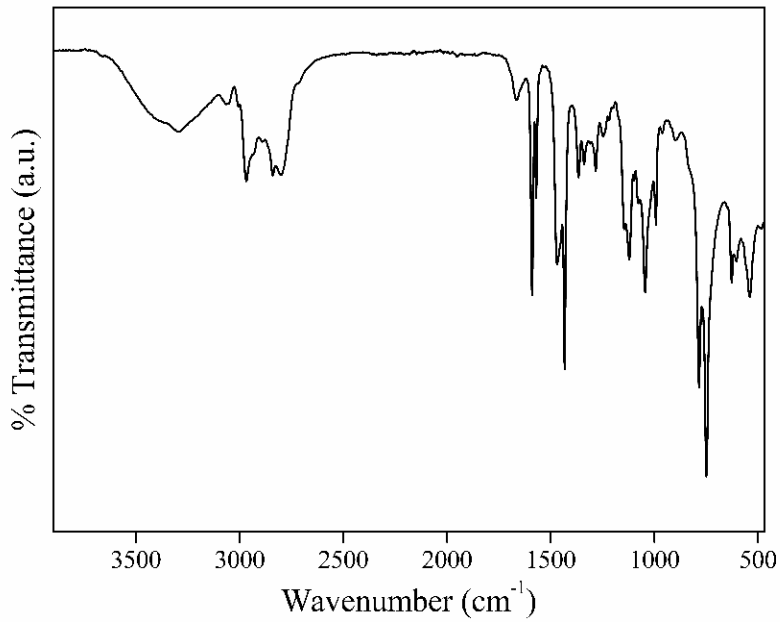

Figure 3.41 *Infrared spectrum of compound 7.*

The mass spectrum of compound **7** was analyzed in acetonitrile solution, which was obtained via electrospray ionization. The formation of the fragmentation peak at *m/z* = 406.4 was evident from electrospray-ionization mass spectrometry (ESI-MS). The peak at 406.4 is assignable to $[Ni(L1)(Cl)]^+$ (calculated = 406.4) according to its mass (**Figure**

3.42).The powder pattern derived from experimental data was compared to the simulated PXRD pattern obtained from single crystal data for compound **7** using the Mercury 4.0 software[86]. The experimental and simulated powder patterns showed a match, implying that the bulk and single crystal phases are the same, as demonstrated in **Figure 3.43**.

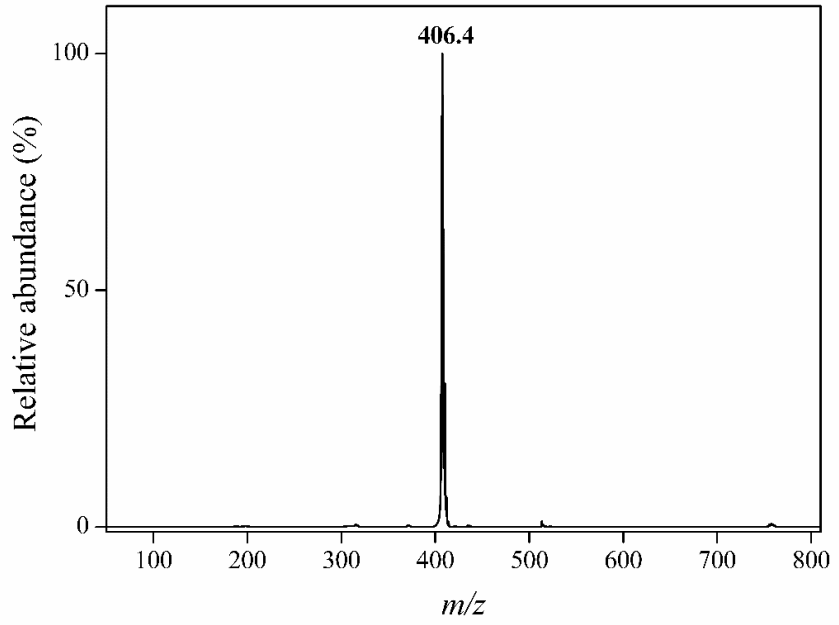

Figure 3.42 *ESI-MS spectrum of 7 recorded in acetonitrile solvent.*

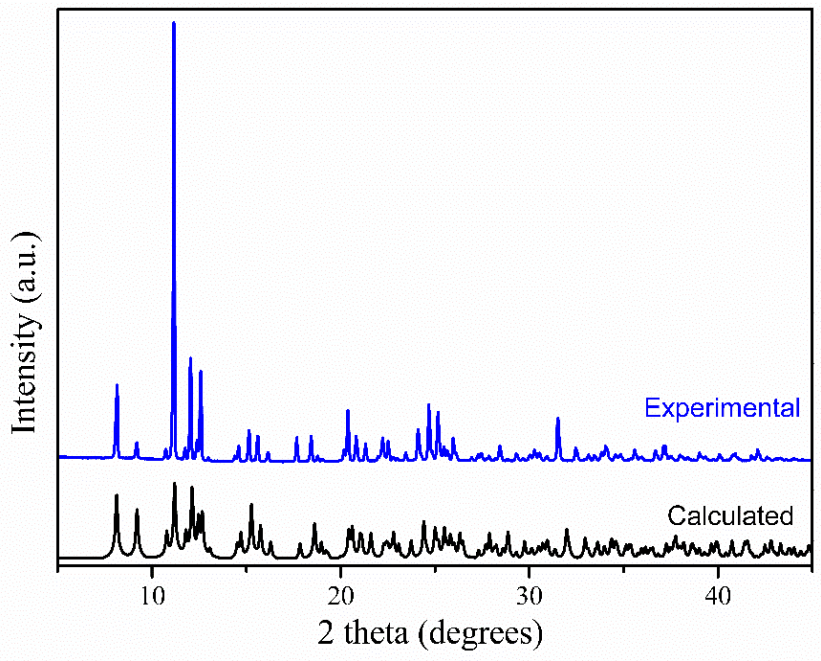

Figure 3.43 *The experimental and calculated PXRD patterns of 7.*

3.6.7 Crystal structure description of 7

We were able to grow single crystals of the compounds **7** by using slow diffusion crystallization techniques, where **7** was crystallized into blue block shaped crystals upon slow diffusion of diethylether in a CH_3CN solution of the compound. The single crystal X-ray crystallographic (SCXRD) data analysis revealed that compound **7** crystallize in the centrosymmetric monoclinic space group $P2_1/c$. The technical specifications of data collection and the chosen refinement parameters for compound **7** can be found in **Table 3.18** and the selected bond lengths and angles are listed in **Table 3.17**.

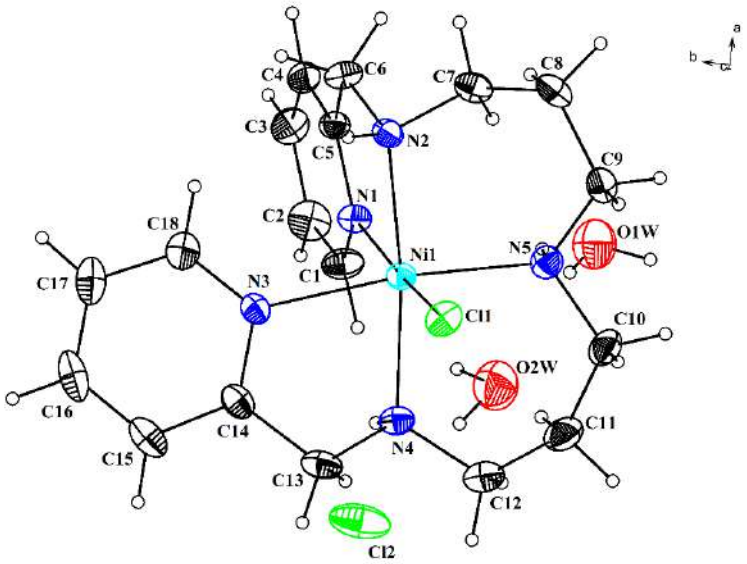

Figure 3.44 *Crystal structure of **7** showing atom labelling scheme. The thermal ellipsoids are drawn at a 50 % probability level for all the atoms except for the H atoms, which are shown as spheres of arbitrary radii.*

Table 3.17 *Selected bond lengths (Å) and angles (°) for **7**.*

Bond lengths (Å)			
Ni(1)-N(1)	2.119(4)	Ni(1)-N(5)	2.154(4)
Ni(1)-Cl(1)	2.4786(13)	Ni(1)-N(4)	2.112(4)
Ni(1)-N(3)	2.158(4)	Ni(1)-N(2)	2.112(4)
Bond angles (°)			
N(2)-Ni(1)-N(4)	172.86(16)	N(2)-Ni(1)-N(1)	80.34(14)
N(4)-Ni(1)-N(1)	98.75(15)	N(2)-Ni(1)-N(5)	94.22(15)
N(4)-Ni(1)-N(5)	92.88(16)	N(1)-Ni(1)-N(5)	91.40(15)
N(2)-Ni(1)-N(3)	94.03(15)	N(4)-Ni(1)-N(3)	78.83(15)
N(1)-Ni(1)-N(3)	86.53(14)	N(5)-Ni(1)-N(3)	171.04(15)
N(2)-Ni(1)-Cl(1)	90.38(11)	N(4)-Ni(1)-Cl(1)	90.02(11)
N(1)-Ni(1)-Cl(1)	170.08(10)	N(5)-Ni(1)-Cl(1)	92.77(12)
N(3)-Ni(1)-Cl(1)	90.67(10)		

The asymmetric unit of **7** has a distinct cationic core, chloride as a counter ion, and two lattice water molecules, as illustrated in the figure. The unique cationic core is built from one independent Ni(II) ion, along with **L1**, which functions as a pentadentate ligand and one coordinated chloride ion, leading to an octahedral geometry around the Ni(II) ion.

Table 3.18 *Technical details of crystal data and structure refinement parameters of 7.*

Compound	**7**
Empirical formula	$C_{18}H_{31}Cl_2NiN_5O_2$
Formula weight	479.07
Temperature	296(2) K
Wavelength	0.71073 Å
Crystal system	Monoclinic
Space group	$P2_1/c$
Unit cell dimensions	a = 9.5980(16) Å b = 15.785(3) Å c = 14.990(3) Å α = 90° β = 92.193(6)° γ = 90°
Volume	2269.5(7) $Å^3$
Z	4
Density (calculated)	1.402 mg/m^3
Absorption coefficient	1.113 mm^{-1}
F(000)	1008
Theta range for data collection	2.720 to 28.328°
Completeness to theta	99.8%
Index ranges	-12≤ h ≤12 -21≤ k≤21 -19≤ l≤19
Reflections collected	33136
Independent reflections	5630(R_{int}= 0.1014)
Refinement method	Full-matrix least-squares on F^2
Absorption correction	Semi- empirical from equivalents
Data/restraints/parameters	5630 / 0 / 281
Goodness-of-fit on F^2	1.137
Final *R*indices[I>2sigma(I)]	R1= 0.0651, wR2= 0.1185
R indices (all data)	R1= 0.1174, wR2= 0.1364
CCDC No.	2386735

3.7 Reactivity of 5-7 with H_2O_2 in presence of TBAH

Compound **5** (0.5 mM in 2 ml) in CH_3CN on reaction with 10 eq. of H_2O_2 in the presence of 5 eq. tetrabutylammonium hydroxide (TBAH) at 15ºC resulted in the formation a new species as evidenced by the appearance of a peak at 326 nm in the UV-Vis spectrum with a colour change from light blue to yellowish green (**Figure 3.45**). The intermediate formed was quite stable at 15ºC. Earlier studies on the Nickel-oxygen species by other researchers had yielded similar findings[101,102].

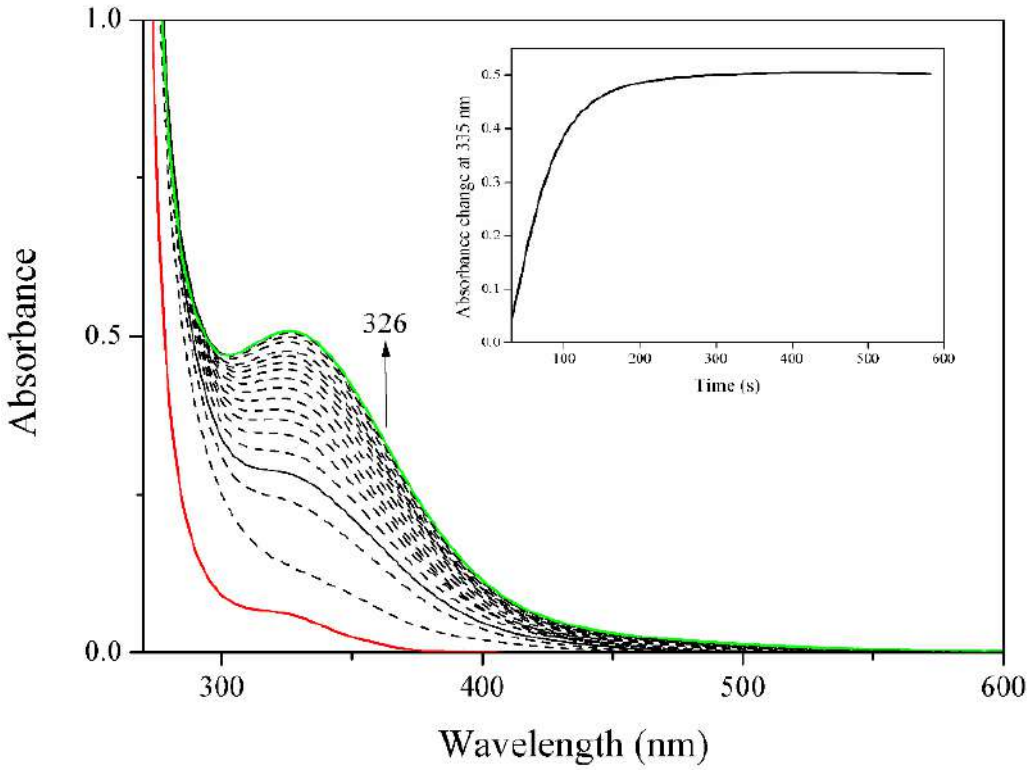

Figure 3.45 *UV-Visible spectral changes for* ***5*** *after addition of 10 eq. of H_2O_2 in presence of 5 eq. of* tetrabutylammonium hydroxide (TBAH) *at 15 °C. Inset shows time trace monitored at 326 nm for the formation of the peak.*

The reactivity of the intermediate was examined with various substrates, and its progress was monitored via UV-Vis spectroscopy. The addition of substrates such as thioanisole, triphenylphosphine, xanthene, benzyl alcohol, and cyclohexane resulted in no spectral changes, with the peak at 326 nm remaining unchanged. The product analysis of the reaction showed that no oxygenated products were formed.

The addition of 2-PPA (2-phenylpropinaldehyde) caused the characteristic UV-Vis band at 326 nm to fade away through a pseudo-first order decay process. We then proceeded to

treat this solution with varying concentrations of 2-phenylpropionaldehyde at a temperature of 15˚C. The spectral variations associated with the 326 nm peak decay were tracked over time as shown in **Figure 3.46**. The peak at 326 nm gradually decreased in intensity following pseudo-first order kinetics, allowing us to determine a pseudo-first order rate constant, k_{obs} of 2.5 x 10^{-2} s^{-1}, as shown in **Figure 3.46**. The values of k_{obs} increased as the concentration of 2-PPA increased, providing us with a second-order rate constant, k_2 = 1.19 M^{-1} S^{-1} (**Figure 3.47**). An examination of the final reaction solution by gas chromatography showed that acetophenone was the predominant product. In the case of **6** and **7**, no clear formation of new species was observed in the reaction with H_2O_2 / TBAH.

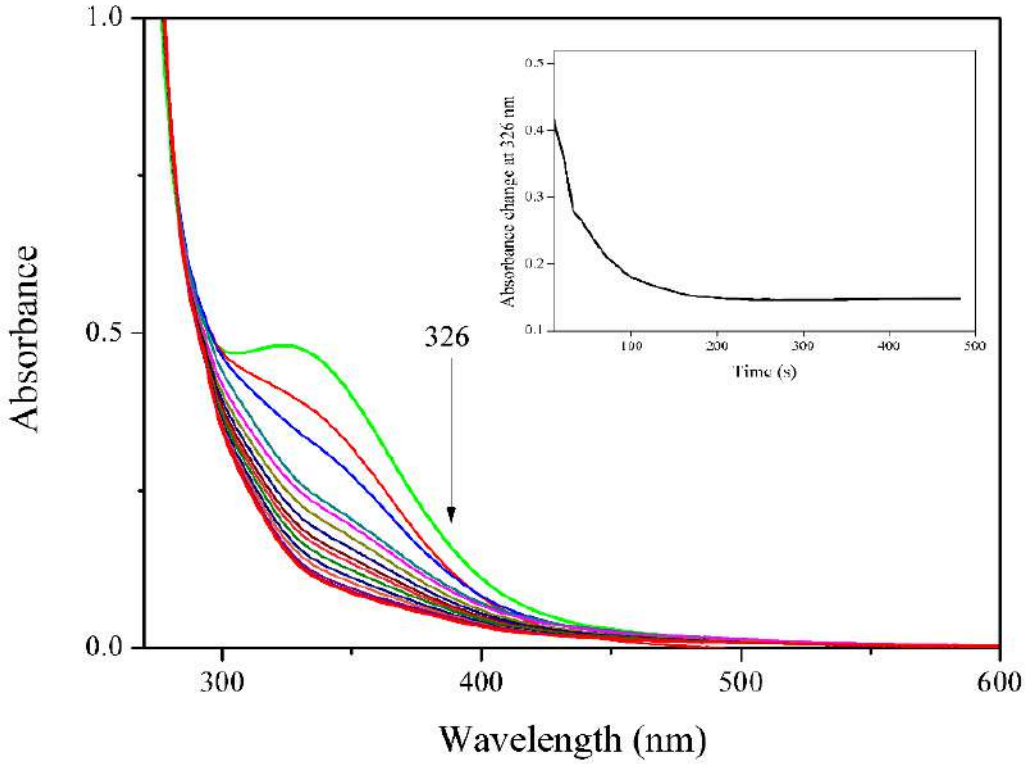

Figure 3.46 *UV-Vis spectral changes occurring at 326 nm on addition of 2-PPA (20 mM). Inset shows the pseudo first order time trace for the decay of peak at 326 nm on addition of 2-PPA.*

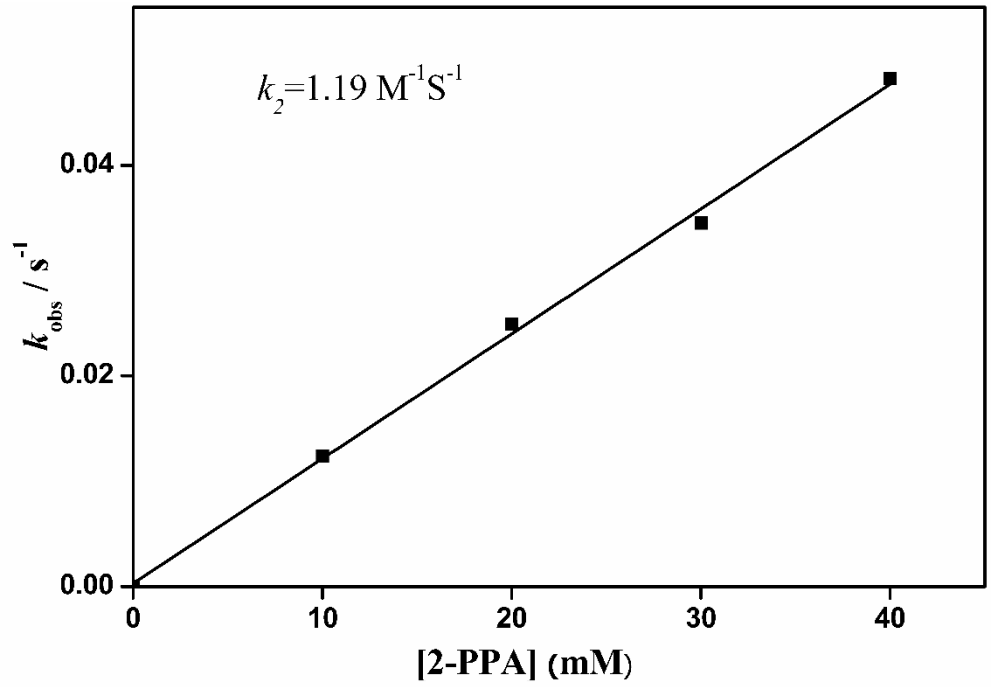

Figure 3.47 *Plot of k_{obs} vs concentration of 2-PPA to determine second-order rate constant (k_2).*

3.8 Conclusion

This study describes the synthesis and characterization of two new Ni(II) compounds, **5** and **7**, stabilized by nonheme ligands **L2** and **L1**, respectively, as well as a Co(II) compound **6** stabilized by **L2**. Compounds **5-7** were characterized via a combination of analytical techniques including C, H, N analysis, infrared (IR), ultraviolet-visible (UV-Vis) and electrospray ionization mass spectrometry (ESI-MS). The compounds were examined using a single-crystal X-ray diffraction technique. The compounds form centrosymmetric monoclinic crystals, which have an octahedral geometry. Compounds **5-7** were tested for the production of reactive intermediates, and the reaction of compound **5** with H_2O_2/TBAH produced a reactive species, as shown by the UV-Vis spectrum, which was subsequently used in a deformylation reaction involving 2-PPA as a substrate. The major product formed was acetophenone following a deformylation reaction.

References

1 E. C. Constable and C. E. Housecroft, *Chem. Soc. Rev.*, 2013, **42**, 1429–1439.

2 H. Taube, H. Myers and R. L. Rich, *J. Am. Chem. Soc.*, 1953, **75**, 4118–4119.

3 H. Taube and H. Myers, *J. Am. Chem. Soc.*, 1954, **76**, 2103–2111.

4 A. Blackman, in *Advances in Heterocyclic Chemistry*, 1993, vol. 58, pp. 123–170.

5 A. G. Blackman, *Polyhedron*, 2019, **161**, 1–33.

6 J. Shen, M. Wang, P. Zhang, J. Jiang and L. Sun, *Chem. Commun.*, 2017, **53**, 4374–4377.

7 B. Das, A. Orthaber, S. Ott and A. Thapper, *ChemSusChem*, 2016, **9**, 1178–1186.

8 Q. Xie, Q. Fu, H.-B. Cui, B.-H. Luo, W.-Q. Liu, R. Qiao, Y.-J. Ren, F. Chen, H.-X. Zhang and J.-Q. Long, *Polyhedron*, 2020, **189**, 114731.

9 J. Shen, M. Wang, T. He, J. Jiang and M. Hu, *Chem. Commun.*, 2018, **54**, 9019–9022.

10 Q. Li, Y. Ren, Q. Xie, M. Wu, H. Feng, L. Zheng, H. Zhang, J. Long and T. Wang, *Appl. Organomet. Chem.*, 2020, **34**, 1–10.

11 Z. Xu, Z. Zheng, Q. Chen, J. Wang, K. Yu, X. Xia, J. Shen and Q. Zhang, *Dalt. Trans.*, 2021, **50**, 10888–10895.

12 S. Hong, Y. M. Lee, K. Bin Cho, K. Sundaravel, J. Cho, M. J. Kim, W. Shin and W. Nam, *J. Am. Chem. Soc.*, 2011, **133**, 11876–11879.

13 R. Mas-Ballesté, M. Costas, T. van den Berg and L. Que, *Chem. – A Eur. J.*, 2006, **12**, 7489–7500.

14 Y. Lu, N. Yeung, N. Sieracki and N. M. Marshall, *Nature*, 2009, **460**, 855–862.

15 M. Rolff, J. Schottenheim, H. Decker and F. Tuczek, *Chem. Soc. Rev.*, 2011, **40**, 4077.

16 M. Zhao, H. B. Wang, L. N. Ji and Z. W. Mao, *Chem. Soc. Rev.*, 2013, **42**, 8360–8375.

17 W. Nam, *Acc. Chem. Res.*, 2015, **48**, 2415–2423.

18 Y.-W. Lin, *Inorg. Chem. Front.*, 2017, **4**, 918–920.

19 S. Fukuzumi, K.-B. Cho, Y.-M. Lee, S. Hong and W. Nam, *Chem. Soc. Rev.*, 2020, **49**, 8988–9027.

20 X.-X. Li, S.-S. Xue, X. Lu, M. S. Seo, Y.-M. Lee, W.-S. Kim, K.-B. Cho and W. Nam, *Inorg. Chem.*, 2021, **60**, 4058–4067.

21 X.-P. Zhang, A. Chandra, Y.-M. Lee, R. Cao, K. Ray and W. Nam, *Chem. Soc. Rev.*, 2021, **50**, 4804–4811.

22 S. E. Allen, R. R. Walvoord, R. Padilla-Salinas and M. C. Kozlowski, *Chem. Rev.*, 2013, **113**, 6234–6458.

23 C. E. Elwell, N. L. Gagnon, B. D. Neisen, D. Dhar, A. D. Spaeth, G. M. Yee and W. B. Tolman, *Chem. Rev.*, 2017, **117**, 2059–2107.

24 D. S. Nesterov, O. V. Nesterova and A. J. L. Pombeiro, *Coord. Chem. Rev.*, 2018, **355**, 199–222.

25 P. Gandeepan, T. Müller, D. Zell, G. Cera, S. Warratz and L. Ackermann, *Chem. Rev.*, 2019, **119**, 2192–2452.

26 R. Trammell, K. Rajabimoghadam and I. Garcia-Bosch, *Chem. Rev.*, 2019, **119**, 2954–3031.

27 S. K. Dey and A. Mukherjee, *Coord. Chem. Rev.*, 2016, **310**, 80–115.

28 V. C.-C. Wang, S. Maji, P. P.-Y. Chen, H. K. Lee, S. S.-F. Yu and S. I. Chan, *Chem. Rev.*, 2017, **117**, 8574–8621.

29 I. A. Koval, P. Gamez, C. Belle, K. Selmeczi and J. Reedijk, *Chem. Soc. Rev.*, 2006, **35**, 814.

30 I. Bento, M. A. Carrondo and P. F. Lindley, *JBIC J. Biol. Inorg. Chem.*, 2006, **11**, 539–547.

31 M. Le Roes-Hill, C. Goodwin and S. Burton, *Trends Biotechnol.*, 2009, **27**, 248–258.

32 U. Hollstein, *Chem. Rev.*, 1974, **74**, 625–652.

33 A. W. Smith, A. Camara-Artigas, M. Wang, J. P. Allen and W. A. Francisco, *Biochemistry*, 2006, **45**, 4378–4387.

34 E. Monzani, L. Quinti, A. Perotti, L. Casella, M. Gullotti, L. Randaccio, S. Geremia, G. Nardin, P. Faleschini and G. Tabbì, *Inorg. Chem.*, 1998, **37**, 553–562.

35 T. Horváth, J. Kaizer and G. Speier, *J. Mol. Catal. A Chem.*, 2004, **215**, 9–15.

36 A. Panja and P. Guionneau, *Dalt. Trans.*, 2013, **42**, 5068.

37 A. Panja, *Dalt. Trans.*, 2014, **43**, 7760.

38 A. Panja, *Polyhedron*, 2014, **80**, 81–89.

39 A. Panja, *RSC Adv.*, 2014, **4**, 37085–37094.

40 M. Garai, D. Dey, H. R. Yadav, A. R. Choudhury, M. Maji and B. Biswas, *ChemistrySelect*, 2017, **2**, 11040–11047.

41 S. Y. Shaban, A. E.-M. M. Ramadan, M. M. Ibrahim, F. I. Elshami and R. van Eldik, *Inorganica Chim. Acta*, 2019, **486**, 608–616.

42 O. V. Nesterova, O. E. Bondarenko, A. J. L. Pombeiro and D. S. Nesterov, *Dalt.*

Trans., 2020, **49**, 4710–4724.

43 T. Dutta, S. Mirdya, P. Giri and S. Chattopadhyay, *Polyhedron*, 2020, **175**, 114164.

44 P. Kumar Mudi, N. Bandopadhyay, M. Joshi, M. Shit, S. Paul, A. Roy Choudhury and B. Biswas, *Inorganica Chim. Acta*, 2020, **505**, 119468.

45 M. Ismael, A.-M. M. Abdel-Mawgoud, M. K. Rabia and A. Abdou, *J. Mol. Struct.*, 2021, **1227**, 129695.

46 W. P. Sohtun, S. Muthuramalingam, M. Sankaralingam, M. Velusamy and R. Mayilmurugan, *J. Inorg. Biochem.*, 2021, **216**, 111313.

47 P. Atkins, T. Overton, J. Rourke, M. Weller and F. Armstron, *Shriver and Atkins' inorganic chemistry*, Oxford University Press, USA, 5th edn., 2010.

48 A. W. Addison, T. N. Rao, J. Reedijk, J. van Rijn and G. C. Verschoor, *J. Chem. Soc., Dalt. Trans.*, 1984, 1349–1356.

49 S. Fukuzumi, Y. Lee and W. Nam, *ChemCatChem*, 2018, **10**, 9–28.

50 S. Hong, Y.-M. Lee, K. Ray and W. Nam, *Coord. Chem. Rev.*, 2017, **334**, 25–42.

51 F. Schwizer, Y. Okamoto, T. Heinisch, Y. Gu, M. M. Pellizzoni, V. Lebrun, R. Reuter, V. Köhler, J. C. Lewis and T. R. Ward, *Chem. Rev.*, 2018, **118**, 142–231.

52 B. Wang, Y.-M. Lee, W.-Y. Tcho, S. Tussupbayev, S.-T. Kim, Y. Kim, M. S. Seo, K.-B. Cho, Y. Dede, B. C. Keegan, T. Ogura, S. H. Kim, T. Ohta, M.-H. Baik, K. Ray, J. Shearer and W. Nam, *Nat. Commun.*, 2017, **8**, 14839.

53 S. Hong, F. F. Pfaff, E. Kwon, Y. Wang, M. Seo, E. Bill, K. Ray and W. Nam, *Angew. Chemie Int. Ed.*, 2014, **53**, 10403–10407.

54 G. E. Martinez, C. Ocampo, Y. J. Park and A. R. Fout, *J. Am. Chem. Soc.*, 2016, **138**, 4290–4293.

55 J. W. Schultz, K. Fuchigami, B. Zheng, N. P. Rath and L. M. Mirica, *J. Am. Chem. Soc.*, 2016, **138**, 12928–12934.

56 K. H. Bok, M. M. Lee, G. R. You, H. M. Ahn, K. Y. Ryu, S. Kim, Y. Kim and C. Kim, *Chem. – A Eur. J.*, 2017, **23**, 3117–3125.

57 L. Wang, L. Duan, R. B. Ambre, Q. Daniel, H. Chen, J. Sun, B. Das, A. Thapper, J. Uhlig, P. Dinér and L. Sun, *J. Catal.*, 2016, **335**, 72–78.

58 M. P. Stewart, M.-H. Ho, S. Wiese, M. Lou Lindstrom, C. E. Thogerson, S. Raugei, R. M. Bullock and M. L. Helm, *J. Am. Chem. Soc.*, 2013, **135**, 6033–6046.

59 A. Das, Z. Han, W. W. Brennessel, P. L. Holland and R. Eisenberg, *ACS Catal.*, 2015, **5**, 1397–1406.

60 S. Hikichi, H. Okuda, Y. Ohzu and M. Akita, *Angew. Chemie Int. Ed.*, 2009, **48**,

188–191.

61 J. Cho, R. Sarangi, J. Annaraj, S. Y. Kim, M. Kubo, T. Ogura, E. I. Solomon and W. Nam, *Nat. Chem.*, 2009, **1**, 568–572.

62 S. Hikichi, C. Kobayashi, M. Yoshizawa and M. Akita, *Chem. – An Asian J.*, 2010, **5**, 2086–2092.

63 J. Kim, B. Shin, H. Kim, J. Lee, J. Kang, S. Yanagisawa, T. Ogura, H. Masuda, T. Ozawa and J. Cho, *Inorg. Chem.*, 2015, **54**, 6176–6183.

64 S. Yun, N. Kwon, S. Kim, D. Jeong, T. Ohta and J. Cho, *Inorg. Chem. Front.*, 2019, **6**, 2112–2117.

65 S. Hikichi, M. Akita and Y. Moro-oka, *Coord. Chem. Rev.*, 2000, **198**, 61–87.

66 M. R. Tiné, *Coord. Chem. Rev.*, 2012, **256**, 316–327.

67 C. L. Bailey and R. S. Drago, *Coord. Chem. Rev.*, 1987, **79**, 321–332.

68 D. E. Hamilton, R. S. Drago and A. Zombeck, *J. Am. Chem. Soc.*, 1987, **109**, 374–379.

69 Y. Jo, J. Annaraj, M. S. Seo, Y.-M. Lee, S. Y. Kim, J. Cho and W. Nam, *J. Inorg. Biochem.*, 2008, **102**, 2155–2159.

70 J. Cho, R. Sarangi, H. Y. Kang, J. Y. Lee, M. Kubo, T. Ogura, E. I. Solomon and W. Nam, *J. Am. Chem. Soc.*, 2010, **132**, 16977–16986.

71 B. Shin, K. D. Sutherlin, T. Ohta, T. Ogura, E. I. Solomon and J. Cho, *Inorg. Chem.*, 2016, **55**, 12391–12399.

72 D. Kim, J. Cho, Y. Lee, R. Sarangi and W. Nam, *Chem. – A Eur. J.*, 2013, **19**, 14112–14118.

73 W. R. Harris, I. Murase, J. H. Timmons and A. E. Martell, *Inorg. Chem.*, 1978, **17**, 889–894.

74 J. A. R. Hartman, A. L. Kammier, R. J. Spracklin, W. H. Pearson, M. Y. Combariza and R. W. Vachet, *Inorganica Chim. Acta*, 2004, **357**, 1141–1151.

75 D. D. Narulkar, A. K. Srivastava, R. J. Butcher, K. M. Ansy and S. N. Dhuri, *Inorganica Chim. Acta*, 2017, **467**, 405–414.

76 K. Nakamoto, *Infrared and Raman Spectra of Inorganic and Coordination Compounds, Part B: Applications in Coordination, Organometallic, and Bioinorganic Chemistry Part 2 of Infrared and Raman Spectra of Inorganic and Coordination Compounds*, John Wiley & Sons, 6th edn., 2009.

77 D. D. Narulkar, A. R. Patil, C. C. Naik and S. N. Dhuri, *Inorganica Chim. Acta*, 2015, **427**, 248–258.

78 S. S. Harmalkar, R. J. Butcher, V. V. Gobre, S. K. Gaonkar, L. R. D'Souza, M. Sankaralingam, I. Furtado and S. N. Dhuri, *Inorganica Chim. Acta*, 2019, **498**, 119020.

79 D. J. Goebbert, E. Garand, T. Wende, R. Bergmann, G. Meijer, K. R. Asmis and D. M. Neumark, *J. Phys. Chem. A*, 2009, **113**, 7584–7592.

80 N. Wei, N. N. Murthy and K. D. Karlin, *Inorg. Chem.*, 1994, **33**, 6093–6100.

81 F. A. Chavez, M. M. Olmstead and P. K. Mascharak, *Inorg. Chem.*, 1996, **35**, 1410–1412.

82 E. V Rybak-Akimova, A. Y. Nazarenko, L. Chen, P. W. Krieger, A. M. Herrera, V. V Tarasov and P. D. Robinson, *Inorganica Chim. Acta*, 2001, **324**, 1–15.

83 L. Yang, D. R. Powell and R. P. Houser, *Dalt. Trans.*, 2007, 955–964.

84 A. G. Blackman, E. B. Schenk, R. E. Jelley, E. H. Krenske and L. R. Gahan, *Dalt. Trans.*, 2020, **49**, 14798–14806.

85 S. Alvarez and M. Llunell, *J. Chem. Soc. Dalt. Trans.*, 2000, 3288–3303.

86 C. F. Macrae, I. Sovago, S. J. Cottrell, P. T. A. Galek, P. McCabe, E. Pidcock, M. Platings, G. P. Shields, J. S. Stevens, M. Towler and P. A. Wood, *J. Appl. Crystallogr.*, 2020, **53**, 226–235.

87 S. Mugiraneza and A. M. Hallas, *Commun. Phys.*, 2022, **5**, 95.

88 B. Kozlevčar, L. Glažar, G. Pirc, Z. Jagličić, A. Golobič and P. Šegedin, *Polyhedron*, 2007, **26**, 11–16.

89 C. M. Buta, M. M. Radu, A. Mischie, C. M. Zălaru, G. Ioniţă and M. Ferbinteanu, *Polyhedron*, 2019, **170**, 771–782.

90 M. Kaushal, T. S. Lobana, L. Nim, R. Bala, D. S. Arora, I. Garcia-Santos, C. E. Duff and J. P. Jasinski, *New J. Chem.*, 2019, **43**, 11727–11742.

91 S. S. Harmalkar, V. R. Chari, R. K. Kunkalekar and S. N. Dhuri, *New J. Chem.*, 2023, **47**, 1852–1860.

92 B. Selvakumaran and M. Murali, *Inorganica Chim. Acta*, 2022, **534**, 120819.

93 S. Kumari, A. K. Mahato, A. Maurya, V. K. Singh, N. Kesharwani, P. Kachhap, I. O. Koshevoy and C. Haldar, *New J. Chem.*, 2017, **41**, 13625–13646.

94 R. Mas-Ballesté, M. Costas, T. van den Berg and L. Que, *Chem. – A Eur. J.*, 2006, **12**, 7489–7500.

95 M. Ayad, R. J. M. Klein Gebbink, Y. Le Mest, P. Schollhammer, N. Le Poul, F. Y. Pétillon and D. Mandon, *Dalt. Trans.*, 2018, **47**, 15596–15612.

96 S. Hong, Y.-M. Lee, K.-B. Cho, K. Sundaravel, J. Cho, M. J. Kim, W. Shin and W.

Nam, *J. Am. Chem. Soc.*, 2011, **133**, 11876–11879.

97 S. Meghdadi, M. Amirnasr, K. Mereiter and M. Karimi Abdolmaleki, *Acta Crystallogr. Sect. E Struct. Reports Online*, 2010, **66**, m332–m333.

98 T. Nagataki, Y. Tachi and S. Itoh, *Chem. Commun.*, 2006, 4016.

99 T. Nagataki, K. Ishii, Y. Tachi and S. Itoh, *Dalt. Trans.*, 2007, 1120.

100 M. Balamurugan, R. Mayilmurugan, E. Suresh and M. Palaniandavar, *Dalt. Trans.*, 2011, **40**, 9413.

101 M. T. Kieber-Emmons, J. Annaraj, M. S. Seo, K. M. Van Heuvelen, T. Tosha, T. Kitagawa, T. C. Brunold, W. Nam and C. G. Riordan, *J. Am. Chem. Soc.*, 2006, **128**, 14230–14231.

102 J. Cho, H. Y. Kang, L. V. Liu, R. Sarangi, E. I. Solomon and W. Nam, *Chem. Sci.*, 2013, **4**, 1502.

CHAPTER 4

CHAPTER 4

Section I: Rational design of bioinspired novel pentadentate Fe(II) compounds: reactivity towards oxidation reactions

4.1 Introduction and literature

Oxygen-activating metalloenzymes sit at the heart of biological redox chemistry, orchestrating an impressive array of reactions under the gentle conditions of living systems[1–3]. In most of these catalysts, an iron centre is anchored by protein residues whose imidazole or carboxylate side chains, typically those of histidine, aspartate, or glutamate, provide neutral or anionic ligation. Yet a sizeable metalloenzymes depend on binding the metal axially or equatorially through cysteine derived sulfur. The nature and geometry of these donor atoms profoundly reshape the electronic landscape of the active site, ultimately governing each enzyme's reactivity and functional spectrum. Notable examples include cytochrome P450 and nitric-oxide synthase, whose crystal structures reveal an iron–heme prosthetic group tethered to the protein backbone via a cysteinate sulfur[4–6]. The thiolate ligand does more than simply secure the cofactor: its strong σ-donor character "pushes" electron density toward the metal-heme core, elevating the basicity and tuning the redox potential of the ensuing metal–oxygen intermediates. This electronic modulation is widely regarded as a key factor in the remarkable efficiency of these enzymes for oxygen-atom transfer chemistry[7–9]. Cytochrome P450s are the most intensively studied monooxygenases which carry out a remarkable breadth of regio- and stereoselective oxidations, notably C–H hydroxylation and olefin epoxidations that drive xenobiotic detoxification in the liver and underpin the biosynthesis of many natural products[10–13]. Their expansive substrate scope and catalytic properties make P450s indispensable oxidative tools throughout biology.

A comparable motif is found among several nonheme iron enzymes in which a cysteinyl residue from the substrate itself coordinates the metal centre, either as a free amino acid or embedded within a peptide backbone. Representative examples include isopenicillin N synthase (IPNS)[14,15], cysteine dioxygenase (CDO)[16–19], the ergothioneine-biosynthetic enzyme EgtB[20], and mercaptopropionate dioxygenase (MDO)[21,22]. Collectively, these enzymes engage molecular oxygen at the iron active site and are thought to carry out the reaction through a Fe(IV)-oxo species. Computational comparisons between wild-type CDO and variants in which a neutral equatorial histidine

is replaced by an anionic donor have illuminated how such ligand swaps reshape reactivity[23]. Introducing an anionic ligand attenuates the strength of the Fe–S bond, a perturbation that dramatically alters the kinetics of the reaction. These findings underscore a central principle in bioinorganic chemistry: the identity and geometry of first coordination sphere fine tune the electronic character of the iron centre and, by extension, dictate its catalytic properties.

Despite the central role that equatorially bound Sulphur donors play in many non-heme metalloenzymes, their precise influence on the geometry and reactivity of Fe(IV)-oxo remain poorly defined. These high valent oxo species are widely recognized as the pivotal intermediates responsible for most biological reactions. To probe how sulfur coordination modulates their electronic structure and oxidative power, numerous research groups have turned to biomimetic chemistry, devising synthetic Fe(IV)-oxo complexes that replicate the enzymatic first sphere[24–26]. Yet, despite intensive synthetic exploration, an iron(IV)−oxo porphyrin bearing a coordinated thiolate has not been reported. In contrast, several non-heme systems that integrate thiolate or thioether donors into their ligand scaffolds have been successfully prepared and characterized. The cationic [Fe IV(O)(TMCS)]$^{+}$ compound reported by Bukowski and co-workers, stands as one of the earliest sulfur ligated iron(IV)–oxo species[26].

Within native non-heme enzymes, the transient Fe(IV)-oxo moieties that drive substrate oxidations are unequivocally high-spin (S = 2). In contrast, nearly all synthetic analogues favour a low-spin configuration, with only a few notable compounds replicating the enzymatic S = 2 state[27–29]. Density functional theory (DFT) predicts that the high spin compounds offer a pronounced kinetic edge in hydrogen atom abstraction relative to low spin[30,31]. For pseudo-octahedral systems, narrowing the crystal-field splitting among equatorial d orbitals promotes population of the higher spin state, a goal often achieved by incorporating weak field donors into pentadentate ligand frameworks[27]. Moreover, multiple studies reveal that even low spin Fe(IV)-oxo species display enhanced oxidative reactivity when the ligand field is deliberately weakened, underscoring the pivotal influence of electronic structure on catalysis[32].

Beyond the metal coordinated sphere that make up the primary coordination sphere (PCS), metalloenzyme function is profoundly shaped by the surrounding secondary coordination sphere (SCS), that delivers subtle non-covalent influences that includes electrostatic fields,

hydrophobic pockets, steric boundaries, and hydrogen bond networks. *De novo* protein scaffolds and re-engineered natural folds have proven invaluable for dissecting these effects in artificial metalloenzymes, offering a controlled platform to probe how SCS architecture governs metal center behaviour[33–38]. Systematic variation of these outer sphere elements has already enabled redox potentials to be shifted over remarkably broad range[39–41]. By contrast, leveraging the same interactions to steer catalytic reactivity remains one of the most challenging and exciting frontiers in contemporary metalloenzyme engineering[42–44].

The literature survey above suggests the diversity of iron(II) compounds that arise from variations in ligand scaffolds; most notably in donor atom type (N and S), denticity, and overall geometry. Motivated by the rich reactivity of nonheme transition metal compounds featuring mixed N/S donors, we set out to engineer ligands that balance electronic effects with steric control. Toward this aim we revisited two pentadentate aminopyridine frameworks previously prepared in our laboratory: N^1-(pyridin-2-ylmethyl)-N^2-(2-((pyridin-2-ylmethyl)amino)ethyl)ethane-1,2-diamine (**L4**) and N^1,N^2-dimethyl-N^1-(2-(methyl(pyridin-2-ylmethyl)amino)ethyl)-N^2-(pyridin-2-ylmethyl)ethane-1,2-diamine (**L5**). To demonstrate how targeted modifications can fine tune both structure and catalytic behaviour, we have now synthesized two new ligands, 2,2'-thiobis(*N*-(pyridin-2-ylmethyl)ethanamine) (**L6**) and 2,2'-thiobis(*N*-methyl-*N*-(pyridin-2-ylmethyl)ethanamine) (**L7**), in which one of the N–H or N-methyl group of **L4** and **L5**, respectively, is strategically replaced by a thioether sulfur donor. This substitution introduces a softer donor site while preserving the pentadentate backbone, providing a platform to probe how subtle electronic and steric adjustments influence iron-centred reactivity.

In this work, four novel Fe(II) compounds supported by the tailored ligands **L5**, **L6**, and **L7** were synthesized and comprehensively characterized. Comparative crystallographic analysis across the series reveals systematic variations in coordination geometry that correlate with the incremental electronic and steric modifications embedded within each ligand framework. To extend these findings to high valent chemistry, the N_4S-coordinated iron(IV)-oxo species (**9a**) was generated and directly compared with its N_5-ligated iron(IV)-oxo analogue (**8a**). Both oxo complexes were obtained under same oxidative conditions, authenticated by a suite of spectroscopic techniques, and subsequently evaluated for their reactivity using representative model substrates. The comparison of **9a** and **8a** thus provides a focused platform for elucidating how equatorial sulfur donors

modulate both the structure and the catalytic profile of non-heme iron(IV)-oxo centres, thereby advancing our understanding of ligand field effects in biomimetic oxidation chemistry.

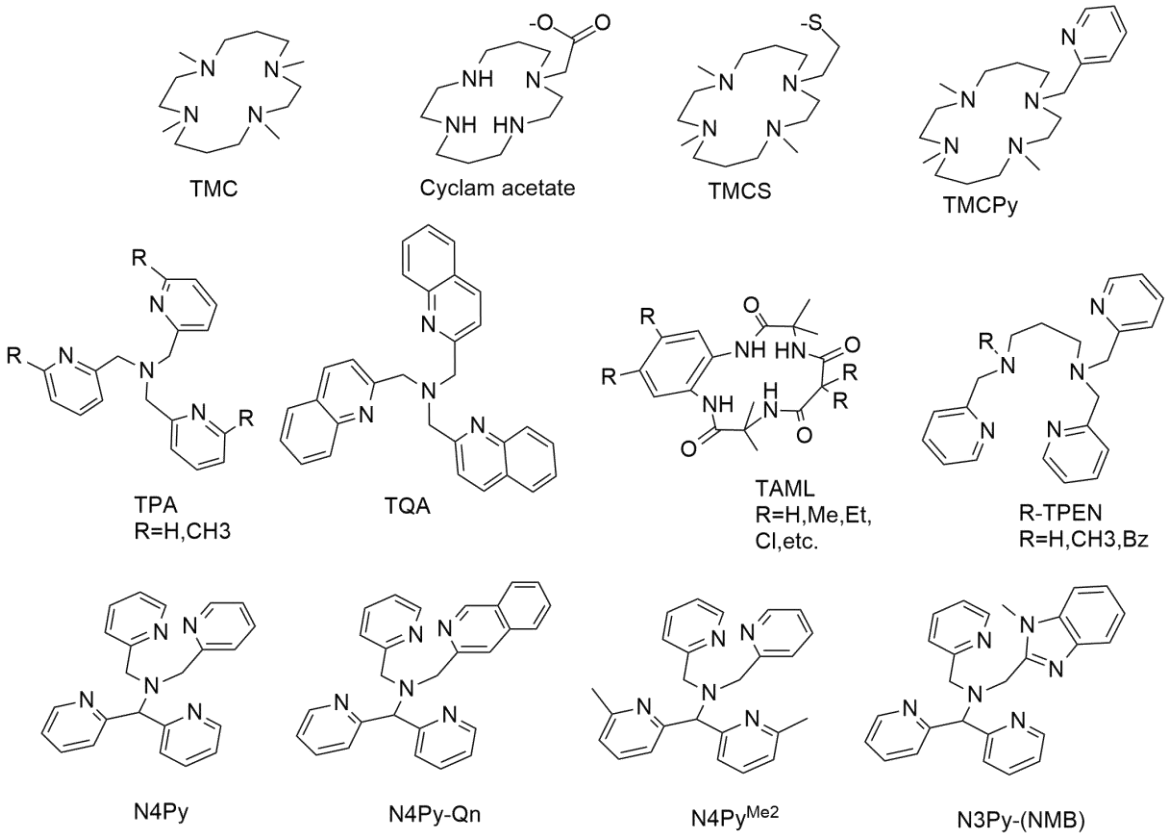

Scheme 4.1 *Ligands Scaffolds that can stabilize iron oxo intermediates.*

Section I

Rational design of bioinspired novel pentadentate Fe(II) compounds : reactivity towards oxidation reactions

4.2 Experimental details

The procedures used to synthesise ligands **L4**, **L5**, **L6**, and **L7**, as well as four Fe(II) compounds, $[Fe(L5)(H_2O)](ClO_4)_2$ **8,** $[Fe(L7)(H_2O)](ClO_4)_2$ **9,** $[Fe(L7)(CH_3CN)](ClO_4)_2$ **10** and $[Fe(L6)(CH_3CN)](ClO_4)_2$ **11** are detailed in this section along with their characterization. The structures of the ligands and the Fe(II) compounds synthesised in this study are depicted in **Scheme 4.2**.

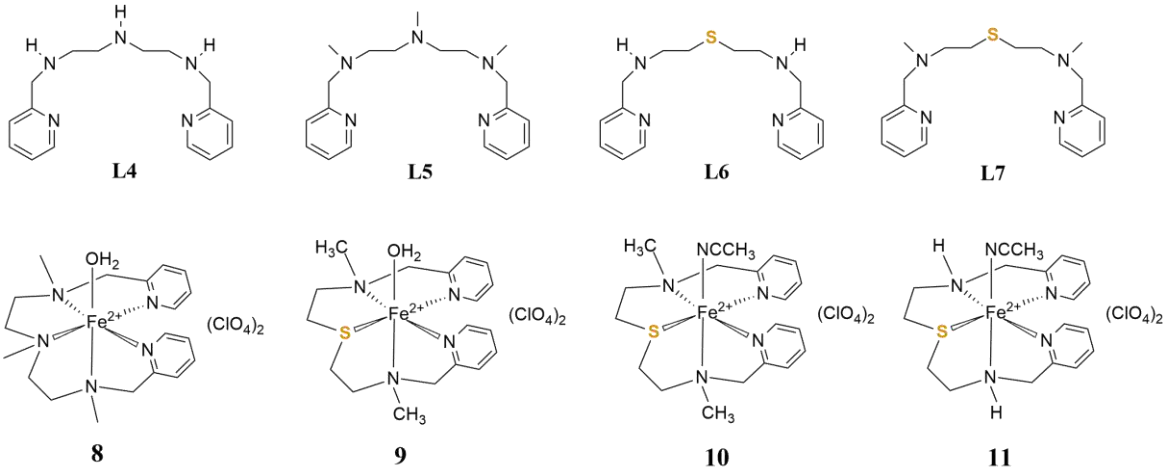

Scheme 4.2 *Structure of the ligands employed in this work and the corresponding Fe(II) compounds.*

4.2.1 Synthesis of ligands L4, L5, L6 and L7

L4 and **L5** were synthesized via our previously reported procedure, which involved the reductive amination of diethylenetriamine and pyridine-2-carboxaldehyde in ethanol, followed by N-methylation with formaldehyde and formic acid[45,46].

L6 was prepared by adding a solution of 2,2'-thiobis(ethylamine) (1.8 g, 14.0 mmol) in 5 mL of ethanol to a solution of pyridine-2-carboxaldehyde (3.0 g, 28.0 mmol) in 15 mL of ethanol. The resulting mixture was refluxed and stirred for approximately 5 h. Following this, the mixture was cooled to room temperature, and then the solvent was evaporated under reduced pressure, resulting in a semisolid imine that was subsequently redissolved in 20 mL of methanol. Slowly, 0.48g of $NaBH_4$ (12.8 mmol) was then added to this methanolic solution, following which the mixture was stirred overnight. The crude

product, which resulted after evaporating the solvent, was then further processed by adding 20 mL of distilled water and extracted with three 30 mL portions of ethyl acetate, ultimately yielding a yellow viscous oil of **L6**. The yield of **L6** was 3.44g (11.4 mmol) 81.2 %. *Anal. Calc.* for **L6** $C_{16}H_{22}N_4S$ (%): C, 63.54; H, 7.33; N, 18.53; S 10.60 *Found:* C, 63.53; H, 7.19; N, 18.32; S 10.35 IR (KBr, cm^{-1}): 3310-3360 υ(NH); 2980-3130 υ(CH); ^{1}H NMR ($CDCl_3$, ppm): δ 8.55 (d, 2H, *J* = 4.4 Hz), δ 7.66 (t, 2H, *J* = 7.6 Hz), δ 7.32 (d, 2H, *J* = 8.0 Hz), δ 7.17 (t, 2H, *J* = 4.8 Hz), δ 3.92 (s, 4H, Ar-CH2), δ 2.86 (t, 4H, N-CH2), δ 2.73 (t, 4H, S-CH2),^{13}C NMR ($CDCl_3$, ppm): δ 159.51, δ 149.26, δ 136.52, δ 122.25, δ 122.0, δ 54.77, δ 48.27, δ 32.17.

L6 (2.6 g and 8.6 mmol) was dissolved in 3.0 mL of water and cooled in an ice bath. Formaldehyde (37 %, 22.0 mL) and formic acid (85 %, 15.0 mL) were then added to the mixture, which was refluxed for 24 h, cooled, and basified to a pH of 12 using 2 M NaOH solution. The crude brown oil resulting from chloroform extraction (20 mL x 4) was dissolved in a HCl solution to a pH of 1. NaOH solution was used to basify the mixture, with the resulting pH being 12; the product was then extracted using diethyl ether, yielding **L7** as an orange oil. The yield of **L7** was 2.28g (6.89 mmol) 80.28%. *Anal. Calc.* for **L7** $C_{18}H_{26}N_4S$ (%): C, 65.42; H, 7.93; N, 16.95; S 9.70 *Found:* C, 65.17; H, 7.19; N, 18.32; S 10.35 IR (KBr, cm^{-1}): 2980-3130 υ(CH); ^{1}H NMR ($CDCl_3$, ppm): δ 8.53 (d, 2H, *J* = 4.0 Hz), δ 7.66 (t, 2H, *J* = 8.0 Hz), δ 7.46 (d, 2H, *J* = 8.0 Hz), δ 7.16 (t, 2H, *J* = 4.0 Hz), δ 3.68 (s, 4H, Ar-CH2), δ 2.70 (m, 8H, N-CH2, S-CH2), δ 2.28 (s, 6H, N-CH3).^{13}C NMR ($CDCl_3$, ppm): δ 159.07, δ 148.95, δ 136.38, δ 123.03, δ 121.95, δ 63.55, δ 57.55, δ 42.30, δ 29.87.

4.2.2 Synthesis of Fe(II) compounds $[Fe(L5)(H_2O)](ClO_4)_2$ 8, $[Fe(L7)(H_2O)](ClO_4)_2$ 9, $[Fe(L7)(CH_3CN)](ClO_4)_2$ 10 and $[Fe(L6)(CH_3CN)](ClO_4)_2$ 11

Compound **8** was synthesized by adding iron(II)-perchlorate (0.5 g, 1.96 mmol) to a Schlenk flask that had been dried and connected to a Schlenk line, and a nitrogen atmosphere was maintained. Acetonitrile was introduced against positive N_2 pressure and allowed to stir at room temperature for 15 minutes. The acetonitrile solution of **L5** (0.64 g, 1.96 mmol) was then added slowly against positive N_2 pressure. The mixture was left to stir at room temperature for 5 hours, then placed in a diethylether bath and stored overnight. Crystallization of compound **8** following slow diffusion resulted in pink

crystals, which were then collected by filtration and dried. The yield of **8** was 0.96 g (1.6 mmol), 82.05 %. *Anal. Calc.* for **8** C_{19} H_{31} Cl_2 Fe N_5 O_9 (%): C, 38.02; H, 5.21; N, 11.67. *Found:* C, 38.30; H, 5.84; N, 11.79. IR (KBr, cm^{-1}): 3490 υ(OH); 1092, 622 υ(ClO_4); UV-Vis data, λ_{max}, CH_3CN/nm (ε/dm^3 mol^{-1} cm^{-1}): 253 (3133), 352 (1016) and 555 (167). ESI-MS: m/z = 191.6 (calc. 191.6) for $[Fe(L5)]^{2+}$ and m/z = 482.1 (calc. 482.1) for $[Fe(L5)(ClO_4)]^{+}$.

Compound **9** was synthesized in a manner analogous to **8** by adding **L7** (0.647 g, 1.96 mmol) dissolved in 2 mL CH_3CN to an iron(II)-perchlorate solution in 2 mL CH_3CN (0.5 g, 1.96 mmol). Whitish pink crystals resulted from the slow diffusion of diethyl ether over a period of two days. The yield of **9** was 0.91 g (1.5 mmol), 77.11 %. *Anal. Calc.* for **9** $C_{18}H_{28}Cl_2FeN_4O_9S$ (%): C, 35.84; H, 4.68; N, 9.29; S 5.32. *Found:* C, 35.46; H, 4.31; N, 9.02; S, 5.18. IR (KBr, cm^{-1}): 3490 υ(OH); 1092, 622 υ(ClO_4); UV-Vis data, λ_{max}, CH_3CN/nm (ε/dm^3 mol^{-1} cm^{-1}): 251 (2978), 341 (1146) and 551 (73). ESI-MS: m/z = 193.1 (calc. 193.1) for $[Fe(L7)]^{2+}$, m/z = 213.1 (calc. 213.4) for $[Fe(L7)(CH_3CN)]^{2+}$ and m/z = 485.0 (calc. 485.0) for $[Fe(L7)(ClO_4)]^{+}$.

Compound **10** was obtained by slow evaporation of acetonitrile solution of compound **9**. The yield of **10** was 1.16 g (1.84 mmol), 95 %. *Anal. Calc.* for **10** C_{20} H_{29} Cl_2 Fe N_5 O_8S (%): C, 38.36; H, 4.67; N, 11.18; S, 5.12. *Found:* C, 38.14; H, 4.33; N, 11.02; S, 4.97. IR (KBr, cm^{-1}): 3053-2816 υ(CH); 1093, 621 υ(ClO_4); UV-Vis data, λ_{max}, CH_3CN/nm (ε/dm^3 mol^{-1} cm^{-1}): 251 (2951), 341 (1105) and 551 (68). ESI-MS: m/z = 213.5 (calc. 213.4) for $[Fe(L7)(CH_3CN)]^{2+}$ and m/z = 485.0 (calc. 485.0) for $[Fe(L7)(ClO_4)]^{+}$.

Compound **11** was obtained using a method analogous to that of compound **9**. **L6** (0.59 g, 1.96 mmol) was dissolved in 2 mL of acetonitrile. To this, iron(II)-perchlorate (0.5 g, 1.96 mmol) in 2 mL acetonitrile was slowly added in a dropwise manner. Whitish pink crystals suitable for single-crystal X-ray diffraction were obtained from the slow diffusion of diethyl ether over a period of two days. The yield of **11** was 1.02 g (1.7 mmol), 87.17 %. *Anal. Calc.* for **11** C_{18} H_{25} Cl_2 Fe N_5 O_8S (%): C, 36.14; H, 4.21; N, 11.71; S, 5.36. *Found:* C, 36.21; H, 4.35; N, 11.93; S, 5.58. IR (KBr, cm^{-1}): 3310 υ(NH); 1093, 621 υ(ClO_4); UV-Vis data, λ_{max}, CH_3CN/nm (ε/dm^3 mol^{-1} cm^{-1}): 278 (2876), 360 (2436) and 547 (1847). ESI-MS: m/z = 199.5 (calc. 199.5) for $[Fe(L6)(CH_3CN)]^{2+}$ and m/z = 457.0 (calc. 457.0) for $[Fe(L6)(ClO_4)]^{+}$.

4.3 Results and discussions

4.3.1 Synthesis and characterization of L4, L5, L6 and L7

Research in bioinspired chemistry has demonstrated that the ligands create an environment for central metal ions which enables the resulting structure to function as a model for enzymatic reactions. Transition metal compounds catalyze oxidation reactions through the formation of a high valent metal-oxygen intermediate, stabilized by highly basic ligands. Pentadentate N-donor ligands used in early research showed that metal compounds were well stabilized in their high-valent oxidation state. The ligand's structure should be sufficiently robust to withstand the catalytic oxidative conditions. The methylation of N-H bonds is a key step, which ensures the ligand's protection against decomposition[47]. The pentadentate ligands **L4** and **L5** were synthesized using a previously established method published by our team[45,46]. **L4** was formed through the reductive amination of diethylenetriamine and pyridine-2-carboxaldehyde in ethanol with sodium borohydride. The *N*-methylated analogue, **L5**, was synthesized by methylation of N-H bonds with formaldehyde and formic acid.

Ray and co-workers suggested that the introduction of sulfur groups increases oxidative reactivity of the ligands. Mandal et al. conducted a comprehensive computational analysis which revealed that enriching sulfur atoms within the ligand framework enhances the C-H activation reactivity of iron(IV)-oxo cyclam compounds[32,48]. Here, two novel ligands, **L6** and **L7**, were synthesized to provide further insights into the enrichment of sulfur atoms into the ligand scaffold. In this case, one of the three amine groups in the parent ligand framework of **L4** and **L5** was replaced by a thioether sulfur group, which significantly altered the chemical properties and reactivity of these compounds. Preparation of **L6** involved the condensation of 2,2'-thiobis(ethylamine) and pyridine-2-carboxaldehyde to form a Schiff base imine, which was subsequently reduced using sodium borohydride (**Scheme 4.3**). Ligand **L7** was synthesized by methylation of N-H bonds of ligand **L6** following Eschweiler-Clarke reaction (**Scheme 4.3**). **L6** and **L7** were characterized using Infrared spectroscopy, ^{1}H, ^{13}C, DEPT NMR spectroscopy.

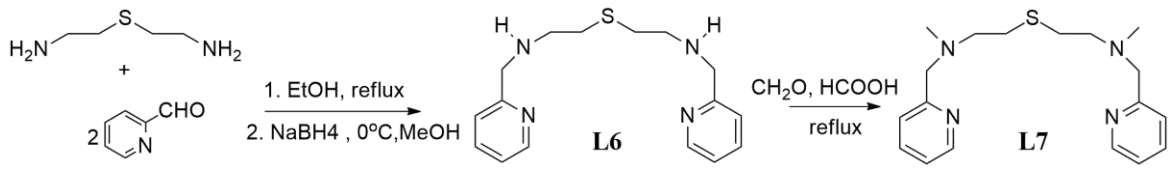

Scheme 4.3 *Synthesis route to ligands* ***L6*** *and* ***L7****.*

The ligands **L6** and **L7** were analyzed by infrared spectroscopy in the region 4000-400 cm^{-1}. In **L6**, peaks occur at 3310-3360 cm^{-1} due to N-H stretching vibrations, whereas a comparable peak was not seen in **L7** because of methylation of secondary amine groups. Medium-to-weak absorption peaks detected between 2980-3130 cm^{-1} were indicative of C-H stretching vibrations in **L6** and **L7**[49].

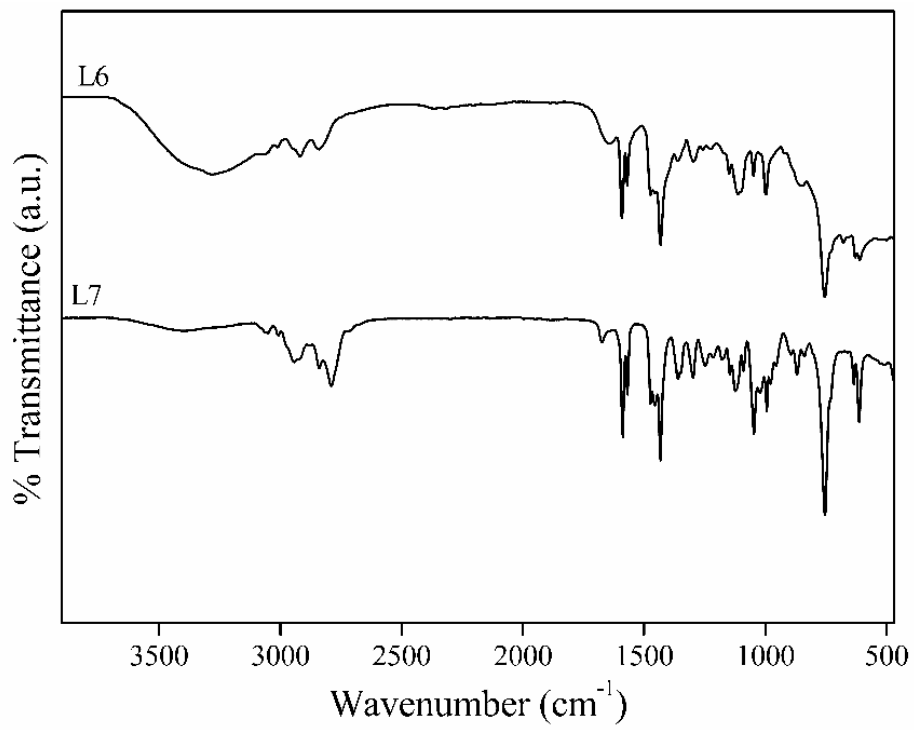

Figure 4.1 *IR spectra of the ligands* ***L6*** *and* ***L7****.*

Confirmation of the **L6** and **L7** structure was achieved through the use of ^{1}H, ^{13}C and DEPT NMR spectroscopy, with the associated peaks identified in the corresponding NMR spectra as shown in **Figure 4.2-4.7**.

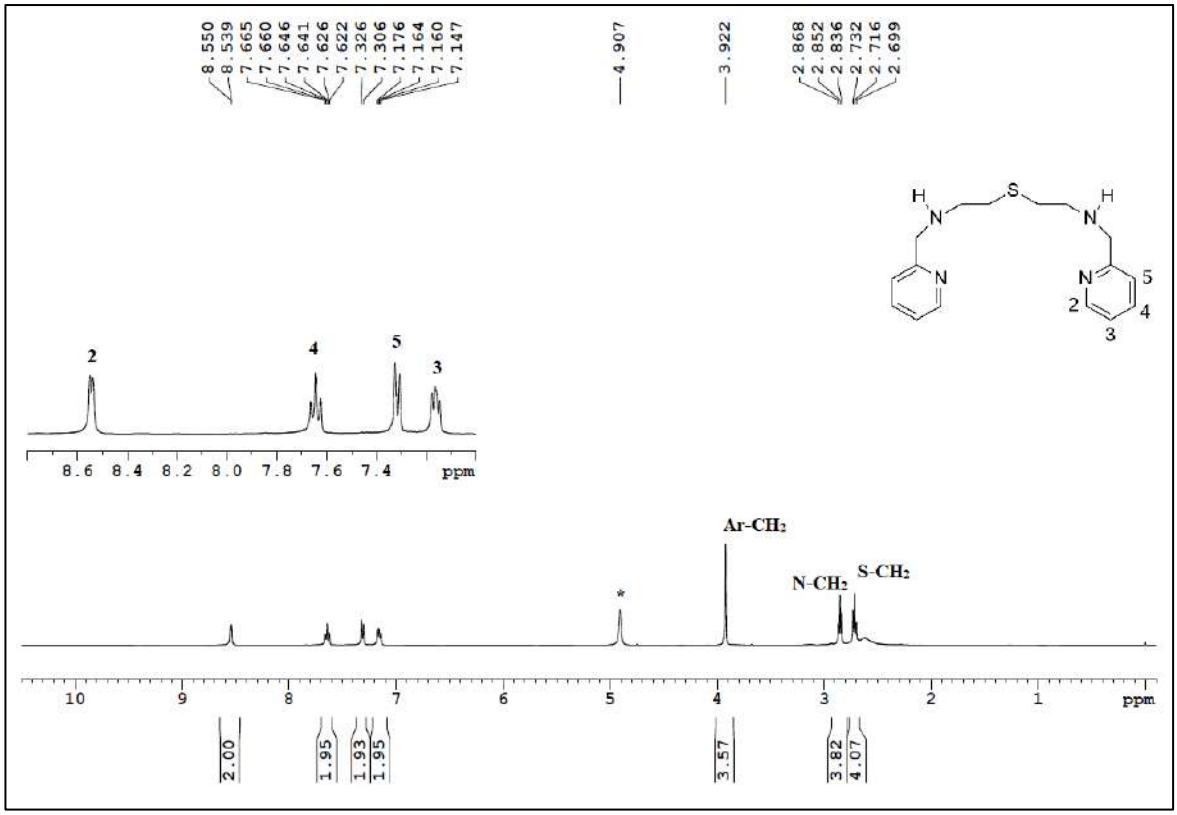

Figure 4.2 *The ^{1}H NMR spectrum of* ***L6*** *recorded in $CDCl_3$ (asterisk (*) stands for residual solvent peak).*

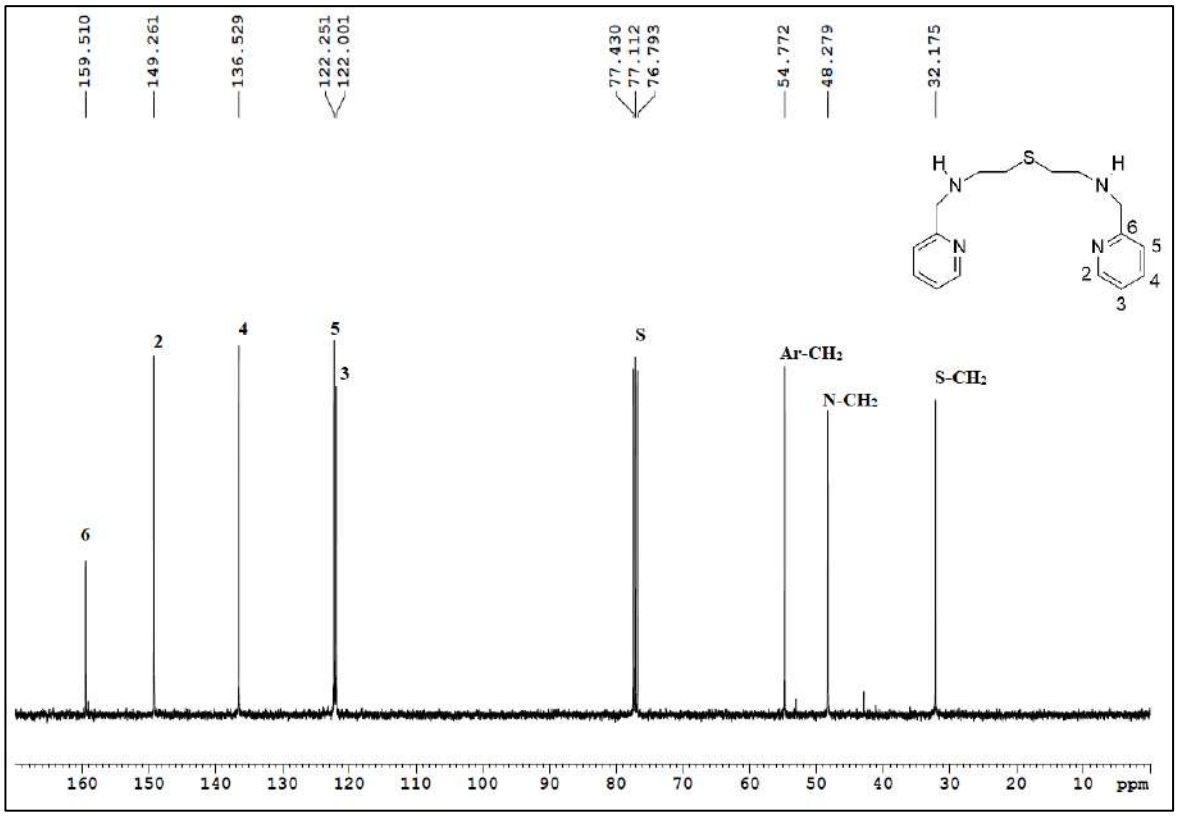

Figure 4.3 *The ^{13}C NMR spectrum of* ***L6*** *recorded in $CDCl_3$ (S stands for solvent peak).*

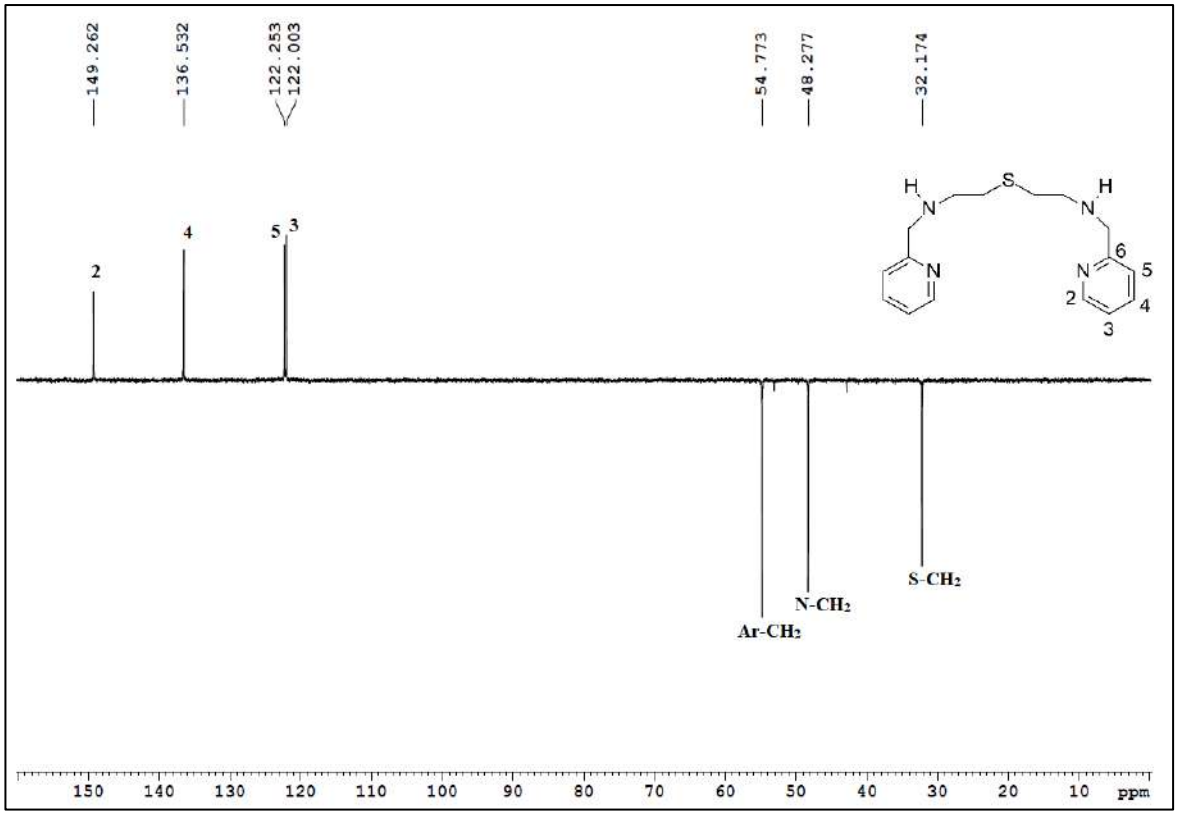

Figure 4.4 *The DEPT spectrum of* ***L6*** *recorded in* $CDCl_3$.

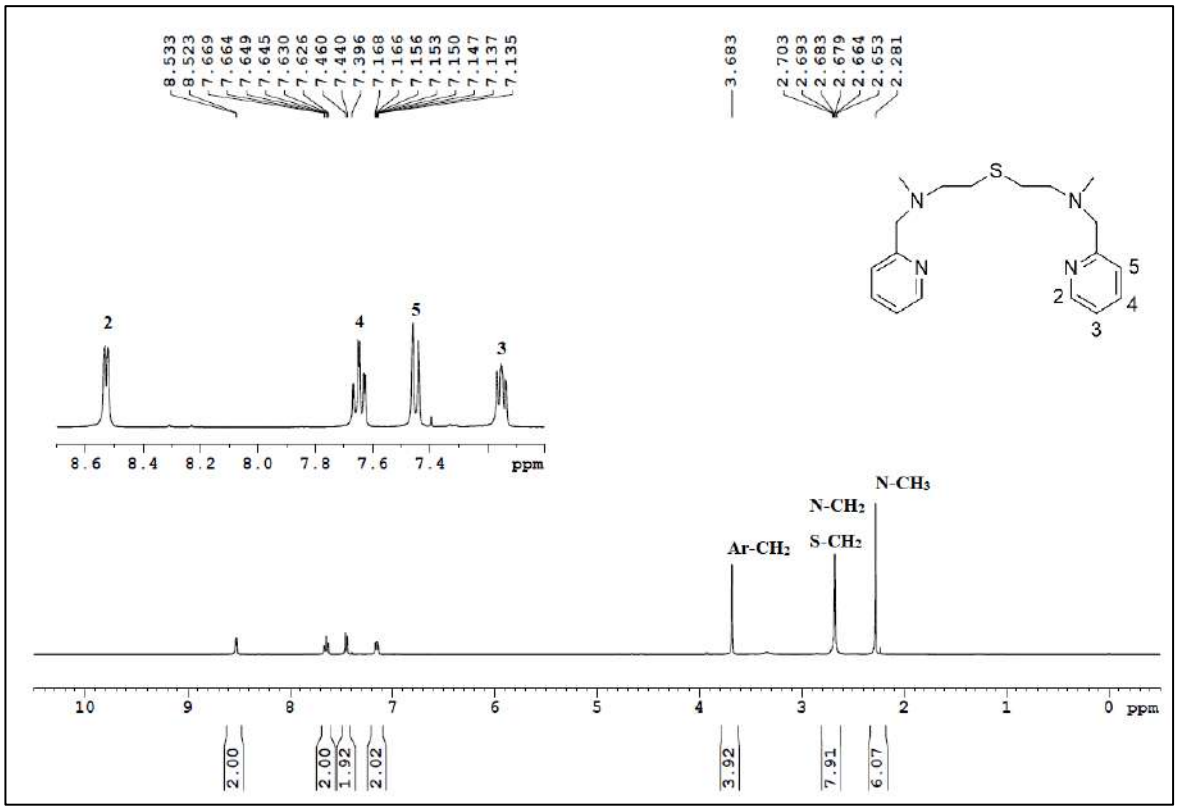

Figure 4.5 *The* ^1H *NMR spectrum of* ***L7*** *recorded in* $CDCl_3$.

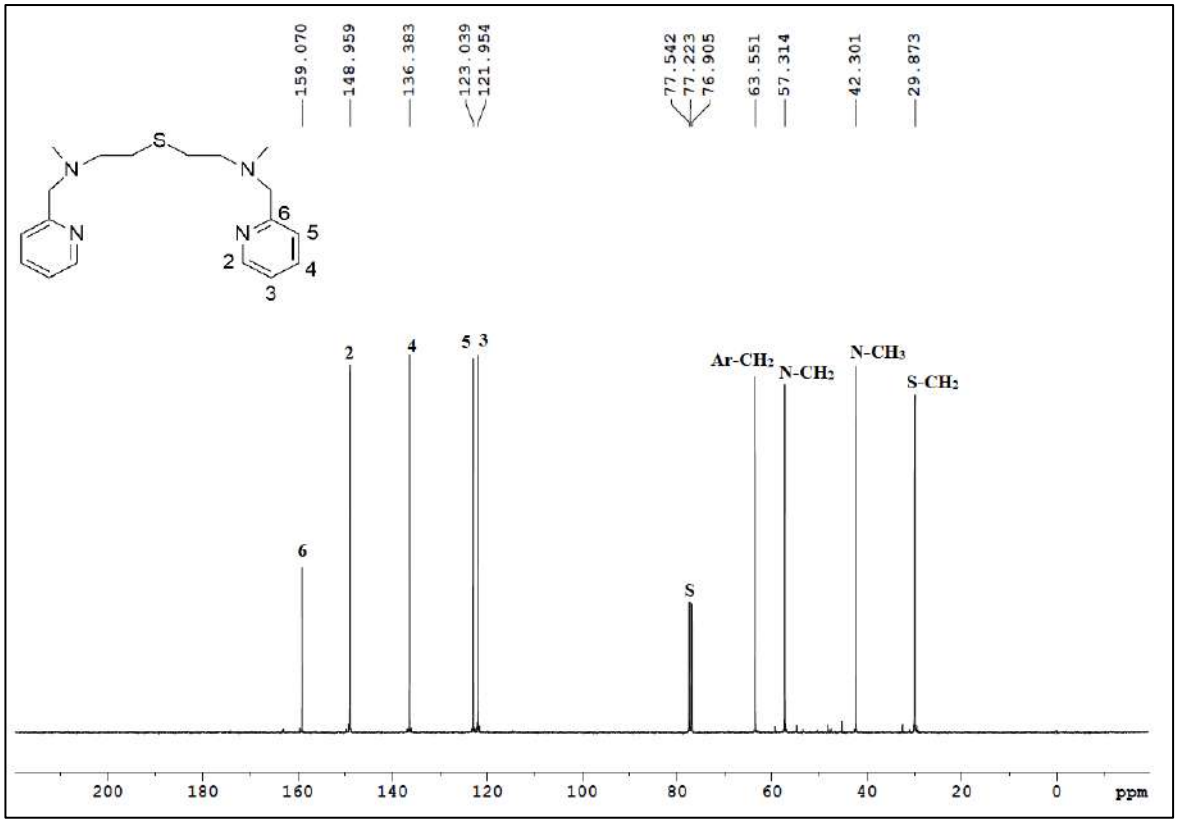

Figure 4.6 *The ^{13}C NMR spectrum of **L7** recorded in $CDCl_3$ (S stands for solvent peak).*

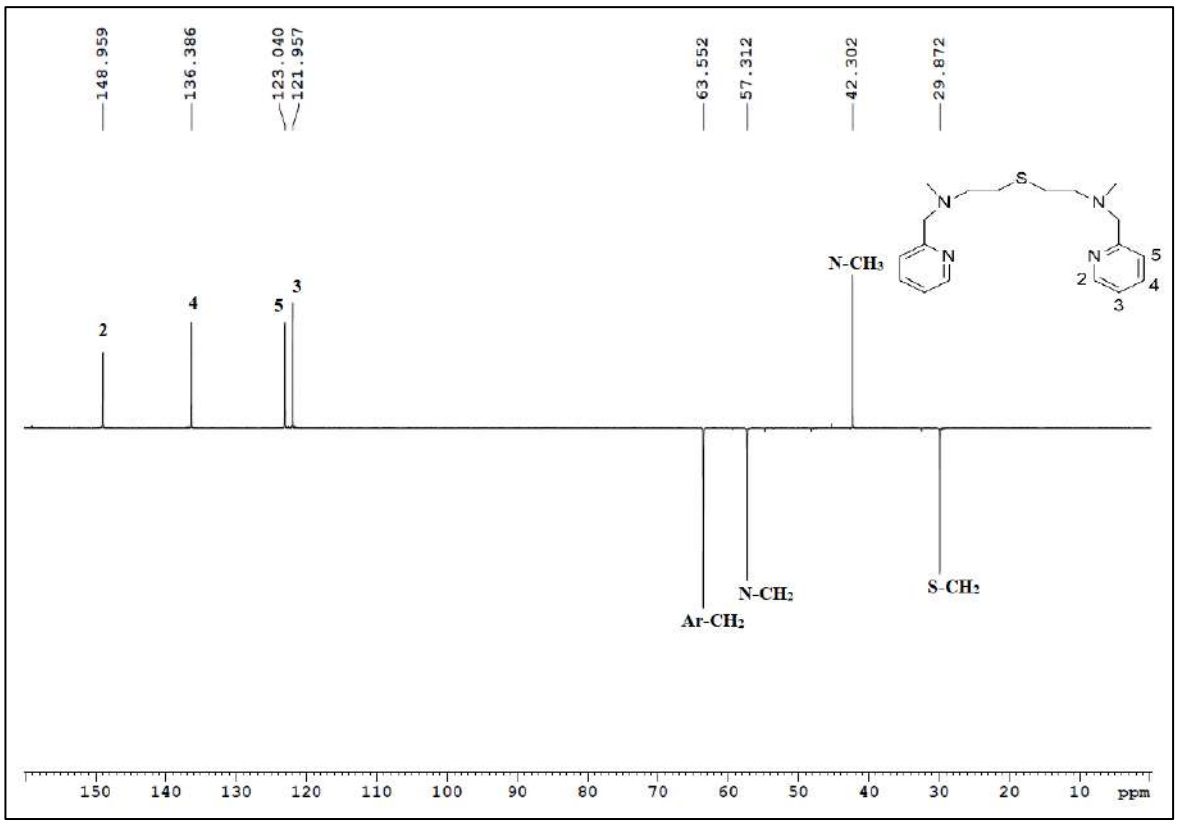

Figure 4.7 *The DEPT spectrum of **L7** recorded in $CDCl_3$.*

4.3.2 Synthesis and characterization of 8 and 9

The reaction of **L5** and **L7** with equimolar concentration of iron(II)-perchlorate (1.96 mmol) in acetonitrile solution at room temperature afforded $[Fe(L5)(H_2O)](ClO_4)_2$ **8** and $[Fe(L7)(H_2O)](ClO_4)_2$ **9** respectively in high yields by following the protocol as illustrated in **section 4.2.2** (**Scheme 4.4**). The reactions were carried out in a Schlenk flask that had been dried and connected to a Schlenk line, and a nitrogen atmosphere was maintained. The compounds have been characterized by CHNS analyzer, Infrared and UV-Vis spectroscopy, ESI-MS and Single crystal X-ray diffraction analysis.

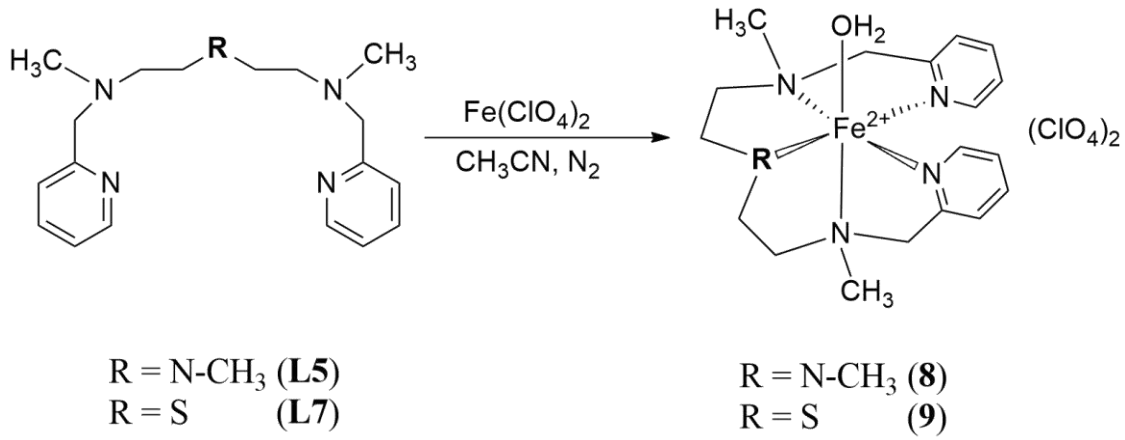

Scheme 4.4 *Synthesis of* $[Fe(L5)(H_2O)](ClO_4)_2$ ***8*** *and* $[Fe(L7)(H_2O)](ClO_4)_2$ ***9***.

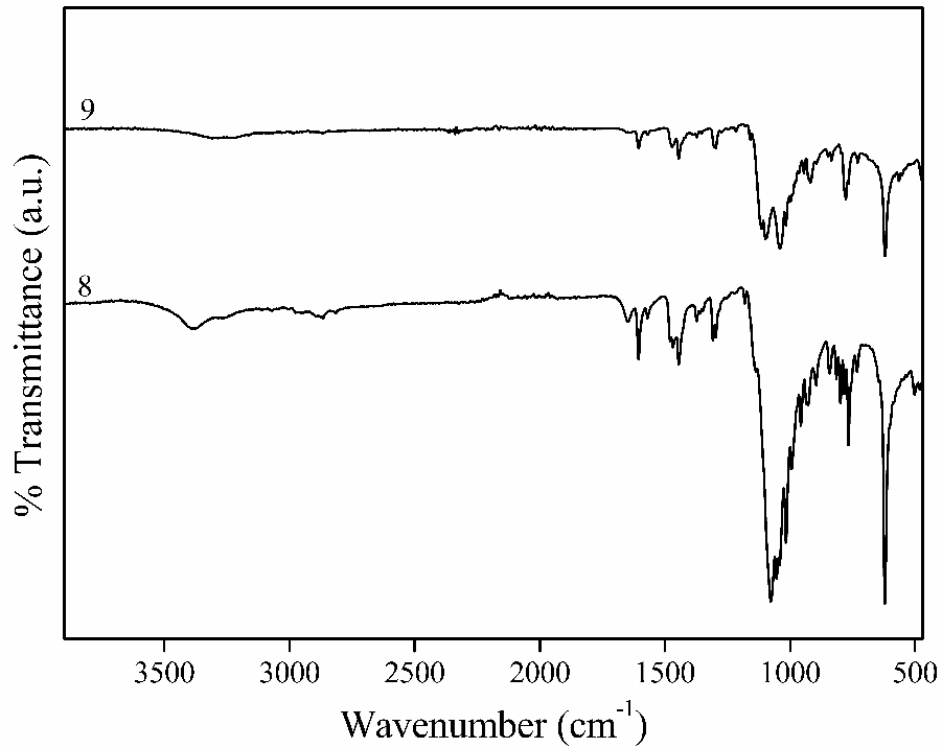

Figure 4.8 *IR spectra of the compounds* ***8*** *and* ***9***.

The infrared spectra of **8** and **9** is illustrated in **Figure 4.8**. IR spectra, indicates the presence of water in compounds **8** and **9** which can be inferred from the broad O-H stretching vibration peaks centred at 3480 cm^{-1}. Further, presence of uncoordinated perchlorate ions was revealed from well pronounced absorption peaks at 1092 cm^{-1} and 622 cm^{-1}[49].

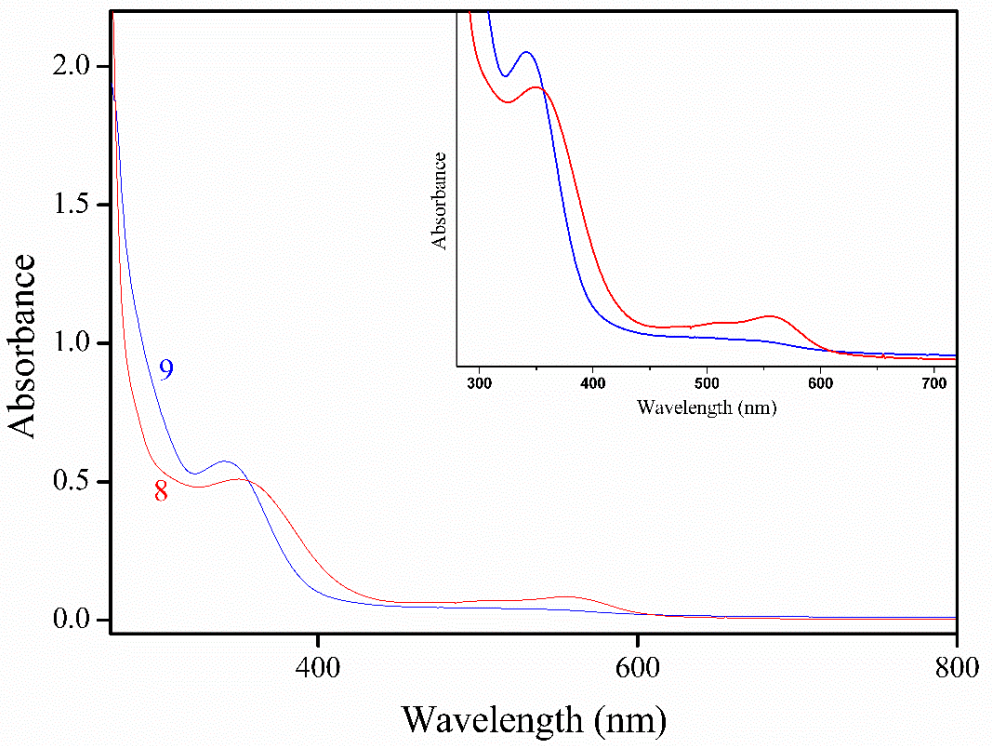

Figure 4.9 *UV/Vis spectra of **8** (red line) and **9** (blue line)(0.5mM each) in acetonitrile; inset shows the expanded region of **8** and **9**.*

The compounds **8** and **9**, which contain Fe(II), show two MLCT bands in their absorption spectra as seen in **Figure 4.9**, with epsilon values that differ distinctly and are comparable to those found for similar compounds in the literature[50,51]. Compound **8** has absorption peaks at 352 nm with ε = 1016 M^{-1} cm^{-1} and at 555 nm with ε = 167 M^{-1} cm^{-1}, whereas compound **9** exhibits peaks at 341 nm with ε = 1146 M^{-1} cm^{-1} and at 551 nm with ε = 73 M^{-1} cm^{-1}.

The compounds $[Fe(L5)(H_2O)](ClO_4)_2$ **8** and $[Fe(L7)(H_2O)](ClO_4)_2$ **9** were investigated by Electrospray ionization mass spectrometry in acetonitrile (**Figure 4.10**). Initial evidence for the formulation of compounds **8** and **9** as iron(II) compounds came from ESI-MS analysis. The ESI-MS spectrum of $[Fe(L5)(H_2O)](ClO_4)_2$ **8**, showed significant mass peaks at m/z values of 191.6 (calc. *m/z* 191.6) and 482.1 (calc. *m/z* 482.1), which are attributed

to $[Fe(L5)]^{2+}$ and $[Fe(L5)(ClO_4)]^{+}$ respectively. On other hand, ESI-MS spectrum of $[Fe(L7)(H_2O)](ClO_4)_2$ **9** reveals three notable mass peaks at at *m/z* values of 193.1 (calc. *m/z* 193.1), 213.1 (calc. *m/z* 213.4) and 485.0(calc. *m/z* 485.0) which denotes the presence of $[Fe(L7)]^{2+}$, $[Fe(L7)(CH_3CN)]^{2+}$ and $[Fe(L7)(ClO_4)]^{+}$ species respectively.

The ESI-MS peak at *m/z* value of 482.1 for compound **8** and *m/z* value of 485.0 for compound **9**, which correspond to the theoretically expected isotope distribution pattern, is shown in the inset of **Figure 4.10**.

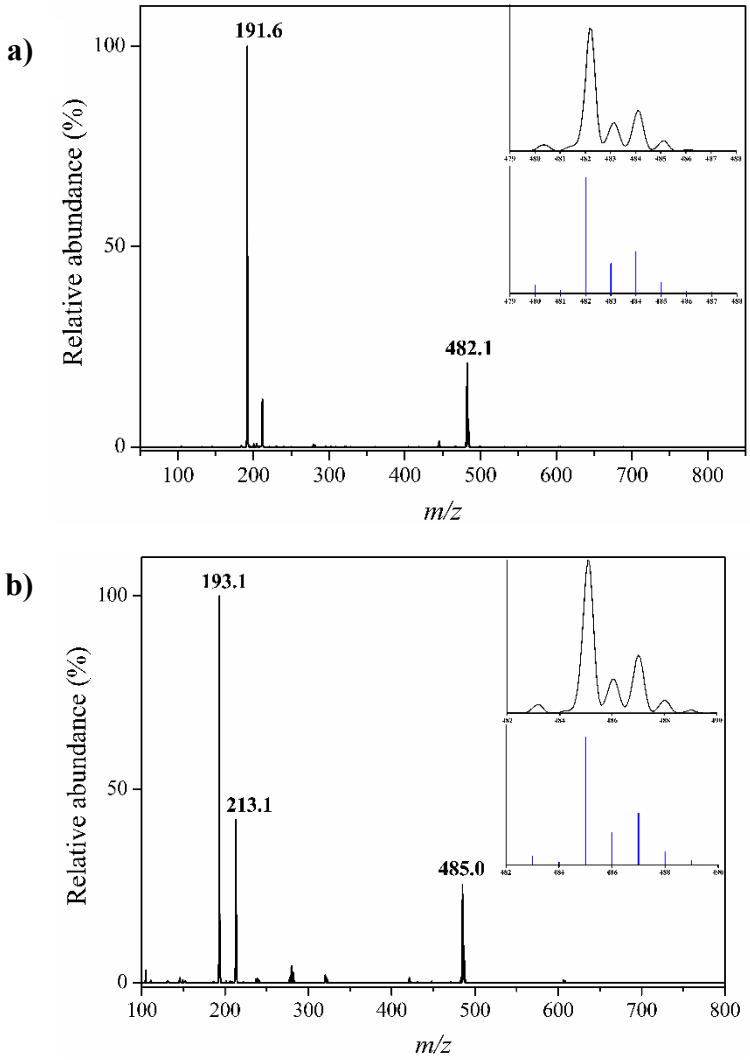

Figure 4.10 *ESI-MS spectrum of* ***8*** *(a) and* ***9*** *(b) recorded in acetonitrile solvent. The inset shows the isotope distribution patterns for the prominent peaks in black with stimulated pattern in blue colour.*

4.3.3 Structural analysis of 8 and 9

Single crystals apt for X-ray diffraction of compounds **8** and **9** could be grown, and their crystal structures were then determined. The molecular structures of compounds **8** and **9** are depicted in **Figure 4.11** and **Figure 4.13**, and chosen bond distances and bond angles are collated in **Table 4.2** and **Table 4.4**. Compounds **8** and **9** crystallize in the centrosymmetric monoclinic space group $P2_1/c$ with all the atoms located at general positions. The crystal structure of compound **8** features an octahedral arrangement around Fe(II) cation, with **L5** acting as a pentadentate ligand, accompanied by a water molecule coordinated to the Fe(II) ion (**Figure 4.11**). Perchlorate ions function as balancing counter anions without coordination. The distances between Fe and the amine nitrogen's N2, N3 and N4 are 2.264(4), 2.210(4), and 2.271(4) Å respectively, whereas the pyridyl nitrogen atoms N1 and N5 are 2.169(4) and 2.2104(4)Å away from Fe(II) ion. The Fe(II) ion is 2.154(4) Å distant to the oxygen of water O1, as documented in **Table 4.2**. The ligand scaffold contains different types of nitrogen-donor atoms, including pyridyl and tertiary amines, as well as oxygen-donor atoms from the water molecule, resulting in a slight distortion of the octahedral unit. The Fe-N and Fe-O bond lengths and N-Fe-N and N-Fe-O bond angles in the compound **8** are all within normal parameters (**Table 4.2**) and match literature standards[52,53]. In this case, the *cis* angles range from 75.08(14) to 109.48(14) Å, whereas the *trans* angles span between 152.22(16) and 174.81(14) Å. This deviation of the cis and trans angles from 90° and 180°, respectively, indicates distortion of the octahedral geometry.

The crystal structure of **9** resembles that of compound **8**, and demonstrates that the pentadentate ligand coordinate as envisaged, with a water molecule occupying the sixth coordination site on the iron ion. In the octahedral (oh) geometry, the N3 and O1 of the **L7** ligand and the water molecule occupy the axial positions, whereas the N1, N2, N4, and S1 of the **L7** ligand hold the equatorial positions. The octahedral $[MN_4SO]^{2+}$ unit shows slight distortion. The Fe−N bond lengths found in the compound range from 2.159(3) and 2.282(3) Å, corresponding to the values observed for **8** and certain previously reported Fe(II) compounds. The replacement of one N-methyl moiety with Sulphur of thioether results in a lengthening of the Fe−S bond distance as compared to $Fe-N_{amine}$ bond distance in **8**. The Fe−S bond distance is 2.5147(11) Å which is in good agreement with the previously reported literature[54–56]. The distortion in the octahedral structure is visibly apparent from the cis angles, which span a range of 81.81(9)- 107.11(11)° in sample **9**, and

similarly, the trans angles vary between 157.44(9) to 175.32(11)° in **9** (**Table 4.4**). Compound **9** has a tilt angle of 158.09(12)°, specifically for O1-Fe-N3, while compound **8** has a tilt angle of 158.41(17)°, for O1-Fe-N3. The perchlorates in compounds **9** function solely as counter anions for the cations $[Fe(L7)]^{2+}$ and do not engage in bonding with iron(II) ion.

Table 4.1 *Technical details and structure refinement parameters of* ***8*** *and* ***9****.*

Compound	**8**	**9**
Empirical formula	C_{19} H_{31} Cl_2 Fe N_5 O_9	C_{18} H_{28} Cl_2 Fe N_4 O_9 S
Formula weight	600.24	603.25
Temperature	296(2) K	296(2) K
Wavelength	0.71073 Å	0.71073 Å
Crystal system	Monoclinic	Monoclinic
Space group	$P2_1/c$	$P2_1/c$
Unit cell dimensions	a = 9.0553(5) Å b = 33.2840(18) Å c = 8.8729(4) Å α = 90° β = 104.994(2)° γ = 90°	a = 9.2165(4) Å b = 33.9838(16) Å c = 8.4299(4)Å α = 90° β = 107.792(2)° γ = 90°
Volume	2583.2(2) $Å^3$	2514.1(2) $Å^3$
Z	4	4
Density (calculated)	1.543 mg/m^3	1.594 mg/m^3
Absorption coefficient	0.848 mm^{-1}	0.950 mm^{-1}
F(000)	1248	1248
Theta range for data collection	2.328 to 28.334°	2.397 to 28.400°
Completeness to theta	100.0%	99.9%
Index ranges	-12≤ h ≤12 -44≤ k≤44 -11≤ l≤11	-12<=h<=12 -45<=k<=45 -11<=l<=11
Reflections collected	75770	74030
Independent reflections	6426(R_{int}= 0.0793)	6284 [R(int) = 0.0570]
Refinement method	Full-matrix least-squares on F^2	Full-matrix least-squares on F^2
Absorption correction	Semi- empirical from equivalents	Semi- empirical from equivalents
Data/restraints/parameters	6426 / 0 / 335	6284 / 0 / 319
Goodness-of-fit on F^2	1.048	1.049
Final *R*indices[I>2sigma(I)]	R1= 0.0775, wR2= 0.2069	R1= 0.0625, wR2= 0.1676
R indices (all data)	R1= 0.1077, wR2= 0.2262	R1= 0.0825, wR2= 0.1798
CCDC No.	2386745	2386752

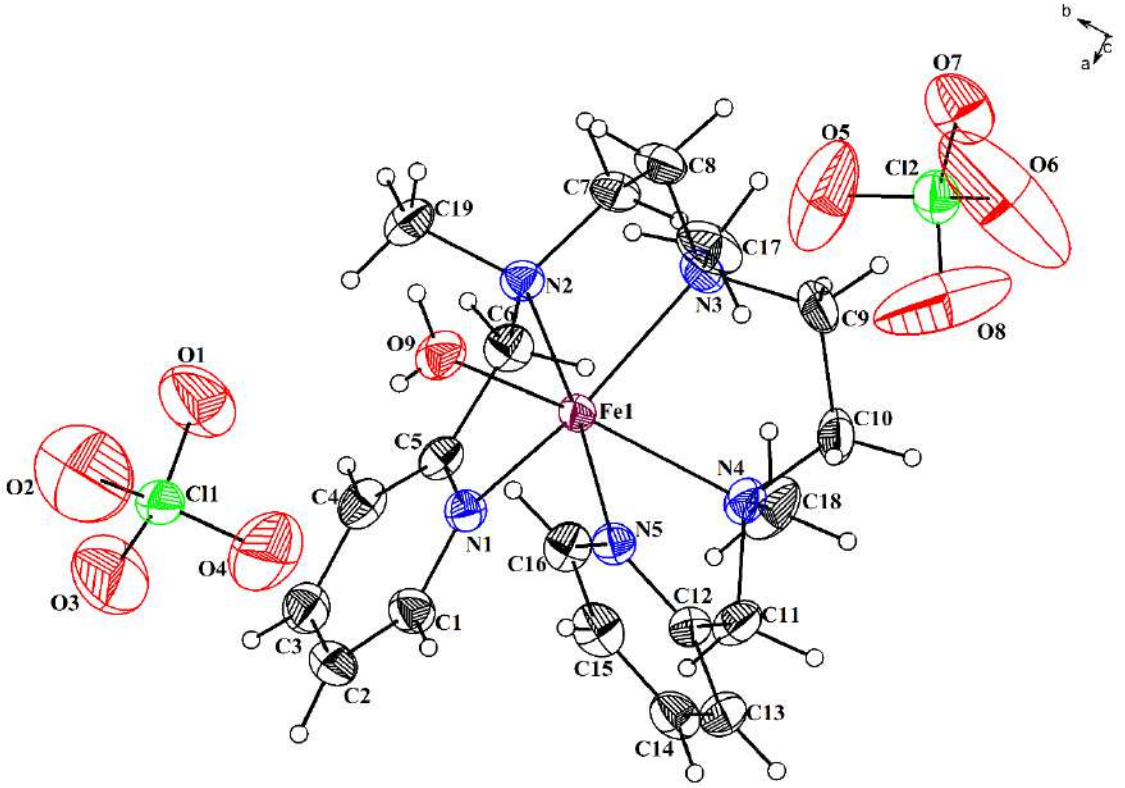

Figure 4.11 *Crystal structure of* ***8*** *showing atom labelling scheme. The thermal ellipsoids are drawn at a 30 % probability level for all the atoms except for the H atoms, which are shown as spheres of arbitrary radii.*

Table 4.2 *Selected bond lengths (Å) and angles (°) for* ***8****.*

Bond lengths (Å)			
Fe(1)-O(9)	2.154(4)	Fe(1)-N(5)	2.210(4)
Fe(1)-N(1)	2.169(4)	Fe(1)-N(2)	2.264(4)
Fe(1)-N(3)	2.210(4)	Fe(1)-N(4)	2.271(4)
Bond angles (°)			
O(9)-Fe(1)-N(1)	96.53(18)	N(1)-Fe(1)-N(2)	75.77(14)
O(9)-Fe(1)-N(3)	97.22(19)	N(3)-Fe(1)-N(2)	79.95(15)
N(1)-Fe(1)-N(3)	152.22(16)	N(5)-Fe(1)-N(2)	174.81(14)
O(9)-Fe(1)-N(5)	84.77(15)	O(9)-Fe(1)-N(4)	158.41(17)
N(1)-Fe(1)-N(5)	101.63(14)	N(1)-Fe(1)-N(4)	95.07(15)
N(3)-Fe(1)-N(5)	103.57(15)	N(3)-Fe(1)-N(4)	80.40(16)
O(9)-Fe(1)-N(2)	91.03(15)	N(5)-Fe(1)-N(4)	75.08(14)
N(2)-Fe(1)-N(4)	109.48(14)		

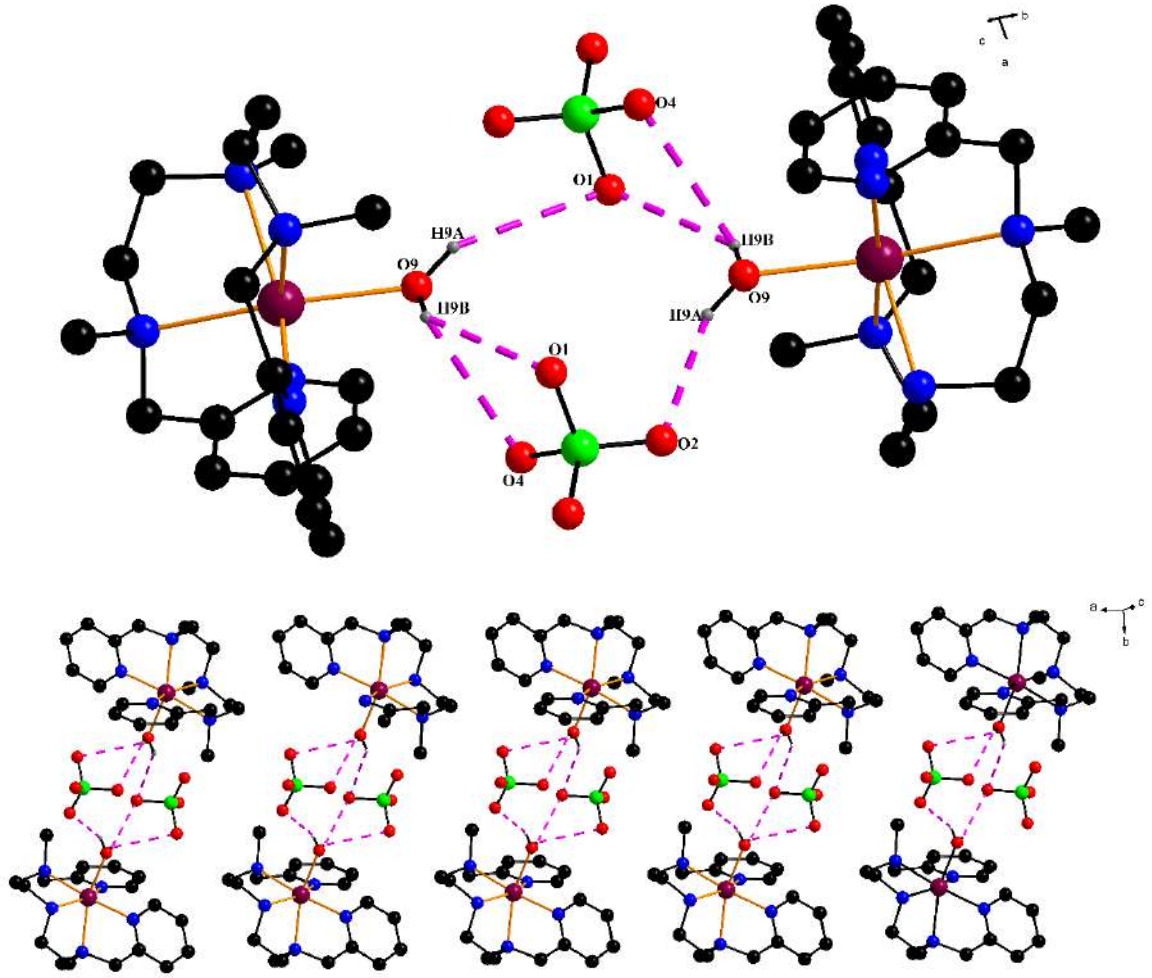

Figure 4.12 *(a) The cyclic structure formed due to hydrogen bonding interactions in* ***8*** *with atom labelling scheme of atoms involved in hydrogen bonding. Hydrogen atoms attached to carbon are omitted for clarity (b) The enlarged view of a network of hydrogen bonding in* ***8*** *showing the symmetric organisation of* $[Fe(L5)(H_2O)]^{2+}$ *cations and perchlorate anions*

In compound **8**, perchlorate counter ions are pivotal in constructing the supramolecular framework. Their oxygen atoms O1, O2 and O4 form weak O···H hydrogen bonds with a lattice water molecule (**Table 4.3**). The ensuing three-dimensional architecture, built from Cl–O···H contacts, cationic $[MN_5O]^{2+}$ units and perchlorate anions, is shown in **Figure 4.12**.

Table 4.3 *Hydrogen bonding parameters (Å, º) for* ***8****.*

D-H···A	D-H/ Å	H···A/ Å	D···A/ Å	D-H···A/º	Symmetry code
O9-H9A···O1	0.844(1)	2.784(1)	3.526(1)	147.60(0)	-x+1, -y+1, -z+1
O9-H9B··· O1	0.668(1)	2.329(0)	2.845(1)	135.57(0)	x, y, z
O9-H9B···O4	0.668(1)	2.760(1)	3.146(0)	119.96(0)	x, y, z

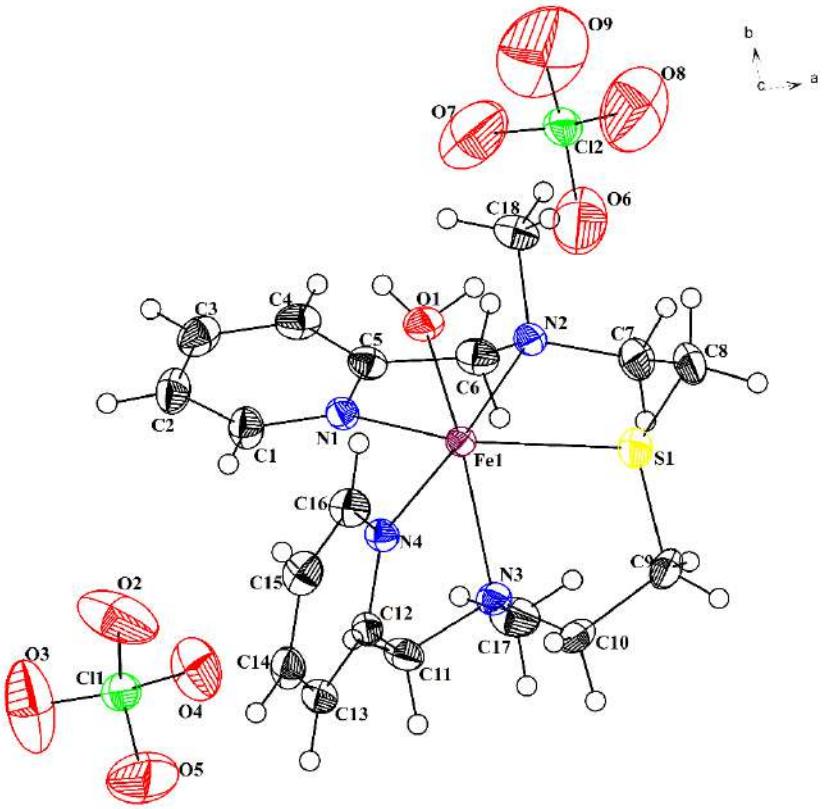

Figure 4.13 *Crystal structure of* ***9*** *showing atom labelling scheme. The thermal ellipsoids are drawn at a 30 % probability level for all the atoms except for the H atoms, which are shown as spheres of arbitrary radii.*

Table 4.4 *Selected bond lengths (Å) and angles (°) for* ***9****.*

Bond lengths (Å)			
S(1)-Fe(1)	2.5147(11)	Fe(1)-N(2)	2.265(3)
Fe(1)-O(1)	2.130(3)	Fe(1)-N(3)	2.282(3)
Fe(1)-N(1)	2.159(3)	Fe(1)-N(4)	2.200(3)
Bond angles (°)			
O(1)-Fe(1)-N(1)	95.12(12)	N(3)-Fe(1)-S(1)	82.97(9)
O(1)-Fe(1)-N(4)	85.07(11)	N(2)-Fe(1)-S(1)	81.81(9)
N(1)-Fe(1)-N(4)	99.14(11)	N(4)-Fe(1)-S(1)	102.64(9)
O(1)-Fe(1)-N(2)	93.36(11)	N(1)-Fe(1)-S(1)	157.44(9)
N(1)-Fe(1)-N(2)	76.59(11)	O(1)-Fe(1)-S(1)	92.56(10)
N(4)-Fe(1)-N(2)	175.32(11)	N(2)-Fe(1)-N(3)	107.11(11)
O(1)-Fe(1)-N(3)	158.09(12)	N(4)-Fe(1)-N(3)	75.11(11)
N(1)-Fe(1)-N(3)	97.12(12)		

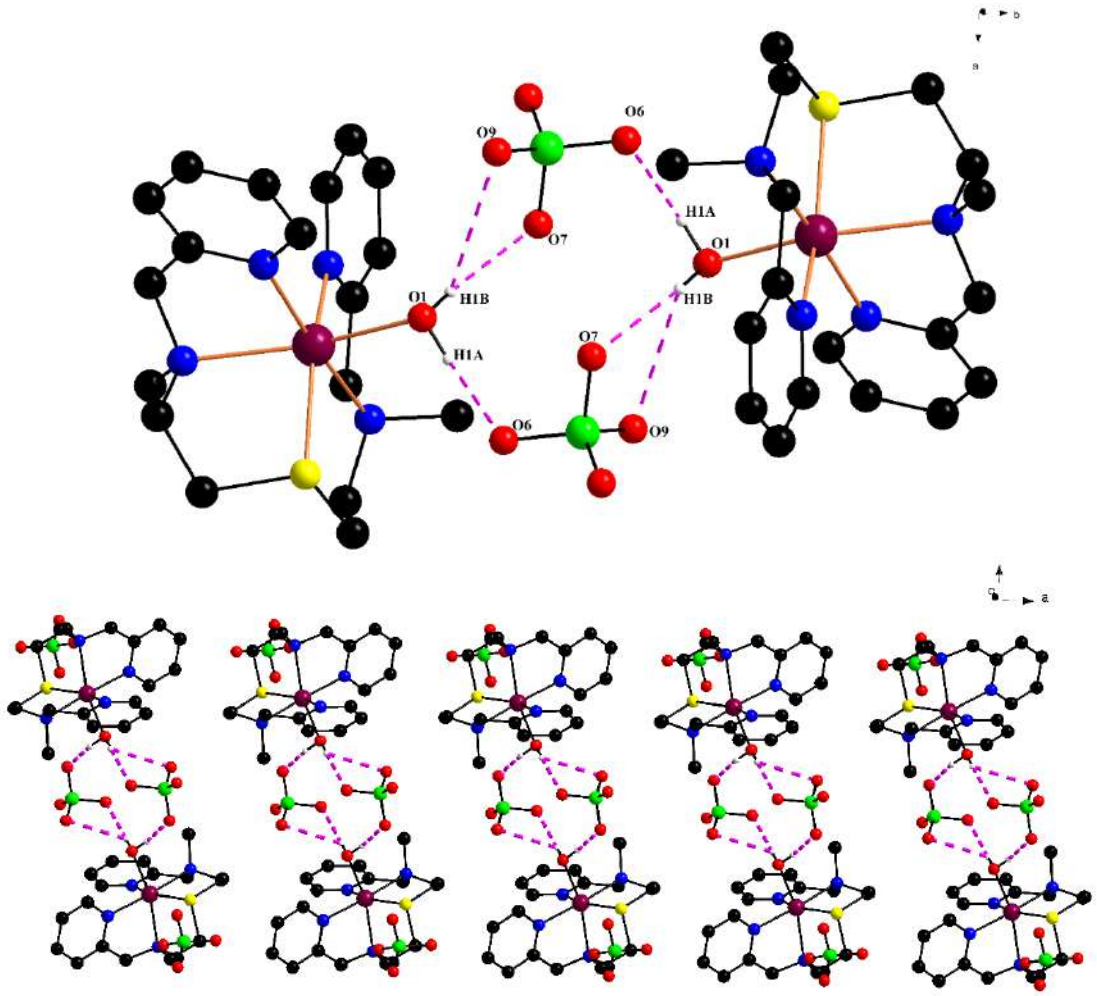

Figure 4.14 *(a) The cyclic structure formed due to hydrogen bonding interactions in* ***9*** *with atom labelling scheme of atoms involved in hydrogen bonding. Hydrogen atoms attached to carbon are omitted for clarity (b) The enlarged view of a network of hydrogen bonding in* ***9*** *showing the symmetric organisation of* $[Fe(L7)(H_2O)]^{2+}$ *cations and perchlorate anions.*

Table 4.5 *Hydrogen bonding parameters (Å, º) for* ***9****.*

D-H···A	D-H/ Å	H···A/ Å	D···A/ Å	D-H···A/º	Symmetry code
O1-H1A···O6	0.854(1)	1.993(2)	2.799(3)	157.03(0)	x, y, z
O1-H1B··· O7	0.854(1)	2.037(1)	2.855(1)	160.32(0)	-x+1, -y+1, -z+1
O1-H1B···O9	0.854(1)	2.668(1)	3.136(0)	115.91(0)	-x+1, -y+1, -z+1

The perchlorate anions contribute significantly to the formation of the extended network via their oxygen atoms, which include O6, O7, and O9 in compound **9**; these oxygen atoms participate in weak hydrogen bonding with a water molecule, as shown in **Table 4.5**. The three-dimensional network structures, which are composed of Cl-O···H contacts, $[MN_4SO]^{2+}$ motifs, and perchlorate anions, is illustrated in **Figure 4.14**.

4.3.4 Generation, characterization and the reactivity of iron(IV)-oxo intermediates 8a and 9a

Compounds **8a** and **9a** (**Scheme 4.5)** were generated *in situ* by oxidizing their iron(II) precursors with PhIO in acetonitrile at –10 °C. The resulting iron-oxo species were confirmed by UV-Vis spectroscopy and ESI-MS. Immediately after the oxidant was introduced, Fe(IV)=O chromophores appeared for both **8a** and **9a**, as evidenced by their UV-Vis profiles, by analogy with earlier reported iron(IV)-oxo intermediate[52,57,58]. Although the spectra for the two iron(IV)-oxo compounds are broadly similar, they exhibit subtle differences in their absorption features (**Figure 4.15**).

The formation of iron(IV)-oxo intermediates **8a** and **9a** was monitored through changes in UV-Vis spectra. Upon adding 1.1 equivalents of iodosylbenzene (PhIO) to a 1 mM solution of compound **8** in acetonitrile at -10 °C, the formation of the new intermediate, $[Fe^{IV}(O)(L5)]^{2+}$, **8a**, is observed, with an absorption band at $\lambda_{max,8a}$ = 780 nm (ε 8a = 294 M^{-1} cm^{-1}) (**Figure 4.16(a)**). Compound **9a** was synthesized using the same method as **8a**, and its characterization via UV-Vis absorption spectroscopy is illustrated in **Figure 4.16(b)**. The UV−Vis absorption spectrum of $[Fe^{IV}(O)(L7)]^{2+}$, **9a**, gives an absorption band at $\lambda_{max,9a}$ = 776 nm (ε 9a = 420 M^{-1} cm^{-1}). These compounds, **8a** and **9a** exhibit absorption values comparable to those found in similar Fe^{IV}-oxo compounds. Replacing one of the the N-methyl group in **L5** with a sulfur atom to form **L7** produced an iron(IV)-oxo species that showed a 4 nm hypsochromic shift of its absorption band, suggesting a change in the metal's first-coordination sphere and indicating sulfur binding to the metal.

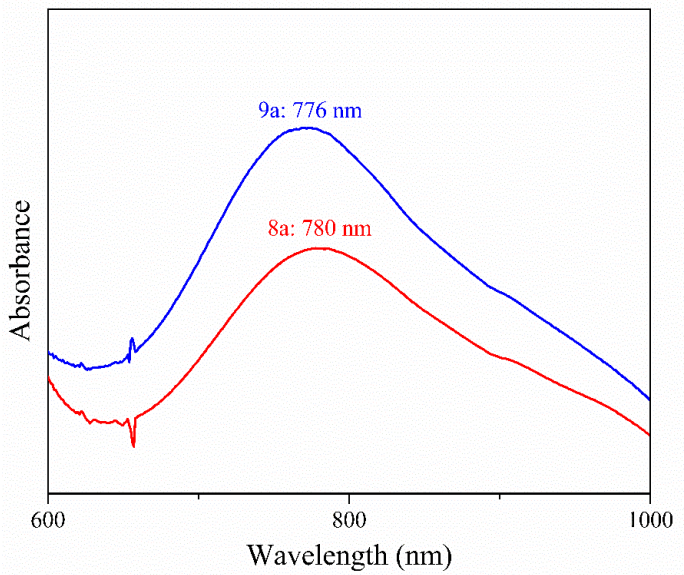

Figure 4.15 *UV-Vis spectra of* ***8a*** *(red) and* ***9a*** *(blue) indicating hypsochromic shift.*

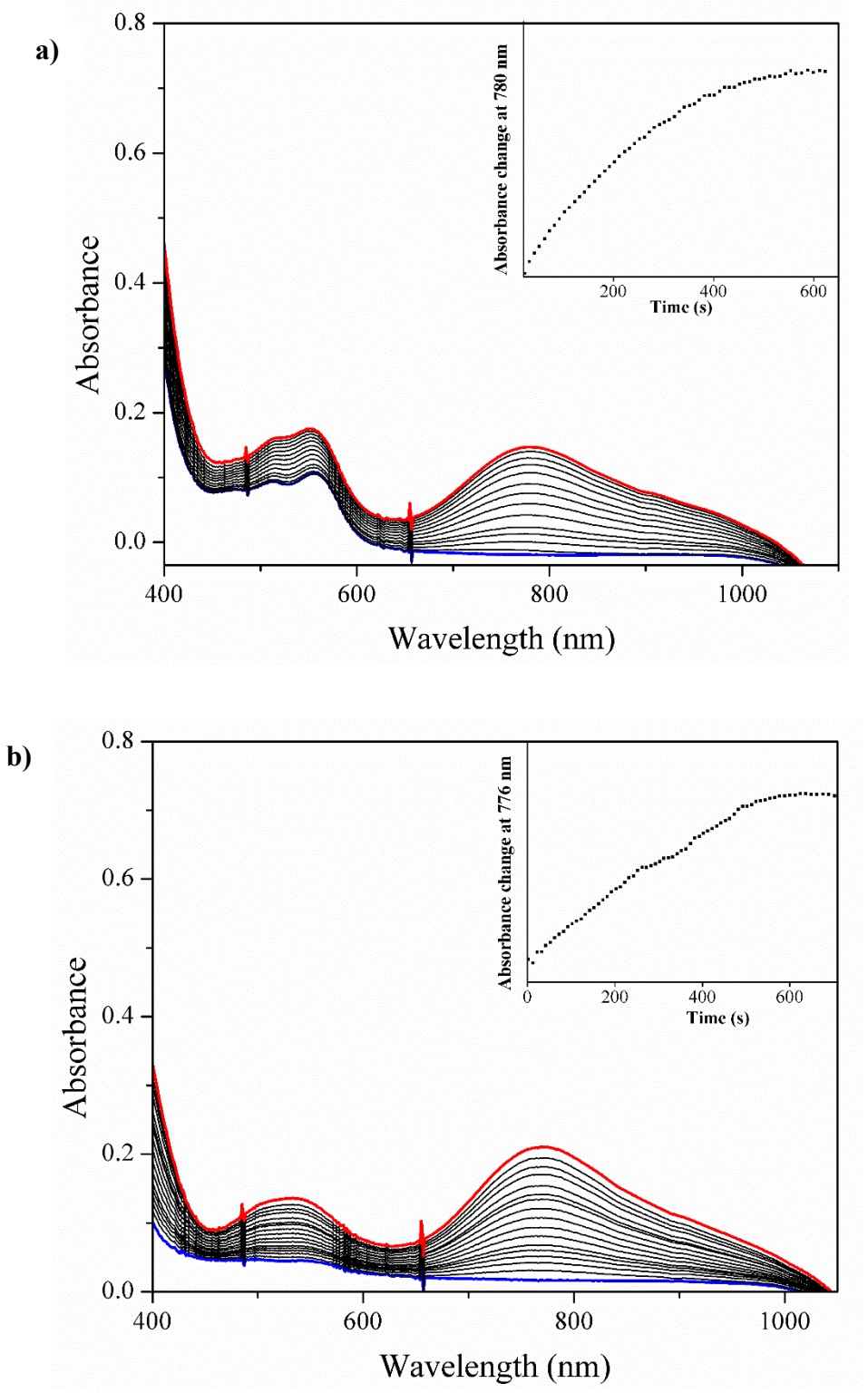

Figure 4.16*(a) UV-Visible spectral changes after the reaction of* ***8*** *(1mM) and PhIO (1.1equiv.) in CH_3CN at -10°C. Inset: time course monitored at 780 nm for the formation of* ***8a****. (b) UV-Visible spectral changes after the reaction of* ***9*** *(1mM) and PhIO (1.1equiv.) in CH_3CN at -10°C. Inset: time course monitored at 776 nm for the formation of* ***9a****.*

Initial evidence for the formulation of compounds **8a** and **9a** as Fe(IV)-oxo compounds came from Electrospray ionization mass spectrometry investigation. The ESI-MS spectrum of **8a**, showed significant mass peaks at *m/z* values of 199.6 (calc. *m/z* 199.6) and 498.1 (calc. *m/z* 498.1), which are attributed to $[Fe^{IV}(O)(L5)]^{2+}$and $[Fe^{IV}(O)(L5)\ (ClO_4)]^{+}$ respectively (**Figure 4.17**). On other hand, ESI-MS spectrum of **9a** reveals two notable mass peaks at *m/z* values of 201.0 (calc. *m/z* 201.0) and 501.0 (calc. *m/z* 501.0) which denotes the presence of $[Fe^{IV}(O)(L7)]^{2+}$and $[Fe^{IV}(O)(L7)(ClO_4)]^{+}$ species respectively (**Figure 4.17**).

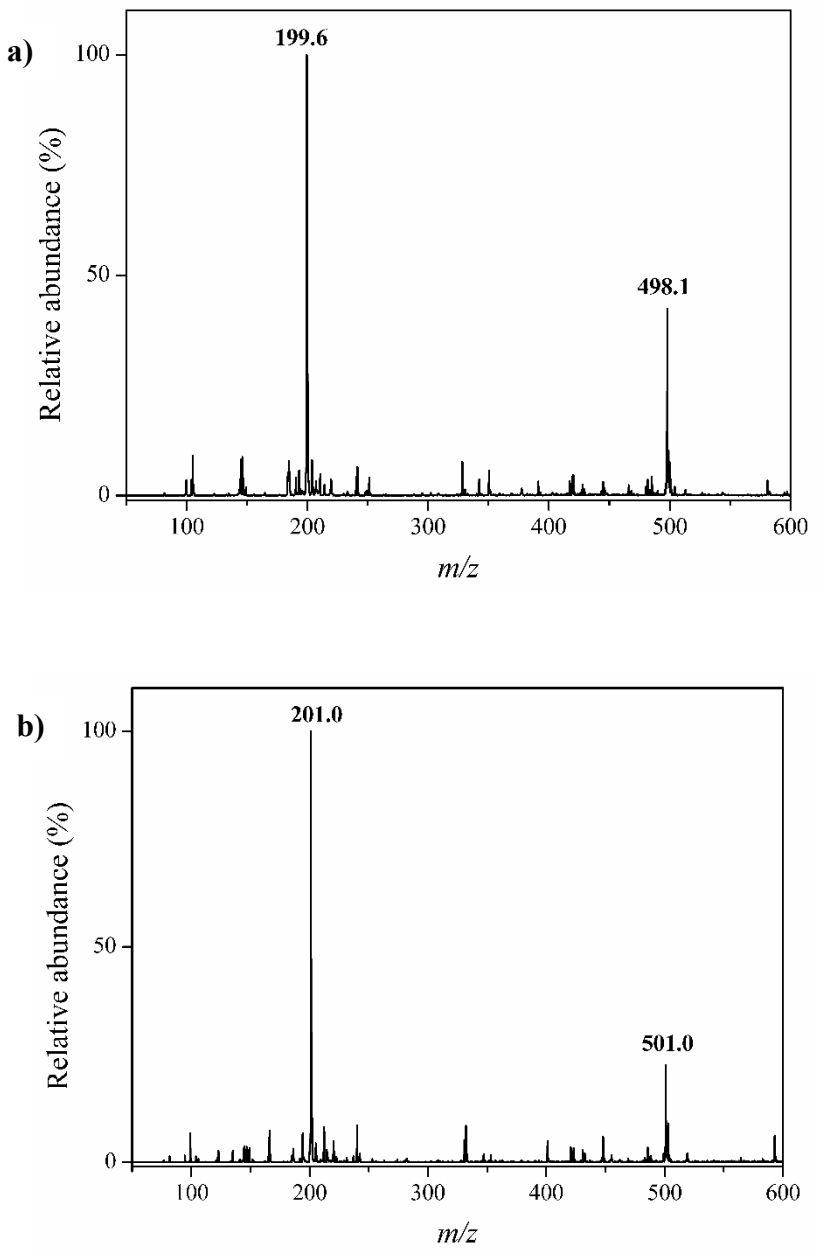

Figure 4.17 *ESI-MS spectrum of* ***8a*** *(a) and* ***9a*** *(b) recorded in acetonitrile solvent.*

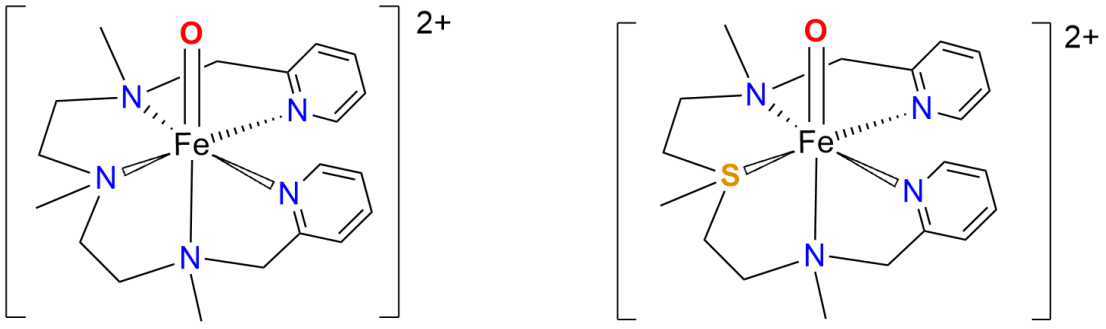

8a **9a**

Scheme 4.5 *Schematic drawings of* $[Fe^{IV}(O)(L5)]^{2+}$ **8a** *and* $[Fe^{IV}(O)(L7)]^{2+}$ **9a**.

4.3.5 Reactivity of iron(IV)-oxo intermediates 8a and 9a

The C-H activation potential of the compounds **8a** and **9a** was probed kinetically. Adding substrates to an acetonitrile solution of **8a** or **9a** induced a first order diminution of the characteristic *d–d* absorption band in their UV-Vis spectra. Pseudo-first-order rate constants (k_{obs}) extracted from these decay traces were plotted against substrate concentration, and the slope of this plot furnished the corresponding second-order rate constant (k_2).

The addition of ethylbenzene to a pre-cooled (-10 °C) acetonitrile solution of compound **8a** produced an immediate and progressive attenuation of its diagnostic UV-Vis band at 780 nm. Because ethylbenzene was employed in large excess, the decay of this absorption followed pseudo first order kinetics, enabling the use of a single exponential fit to extract the observed rate constants (k_{obs}) (**Figure 4.18**). Successive kinetic traces were collected at four substrate concentrations, and the resulting k_{obs} values obtained exhibited proportional increase with increase in concentration. Plotting k_{obs} against substrate concentration afforded a straight line whose slope corresponds to second-order rate constant, k_2 = 1.76 x 10^{-2} M^{-1} s^{-1}, at -10 °C (**Figure 4.20**). This linear relationship verifies that the disappearance of the 780 nm occurs through a single, second order step involving one molecule each of **8a** and ethylbenzene. Final product analysis by gas chromatography revealed that 1-phenylethanol is formed as the major product. Under identical conditions, compound **9a** exhibited second-order rate constant, k_2 = 3.11 x 10^{-2} M^{-1} s^{-1}, at -10 °C (**Figure 4.19** and **Figure 4.21**).

Under identical conditions (263 K), compound **9a** activates C–H bonds substantially faster than **8a**. This rate enhancement trend was again verified using cumene as the H-donor. Plots of k_{obs} versus substrate concentration are linear for both compounds. The resulting Second order rate constant k_2 = 4.78 x 10^{-2} M^{-1} S^{-1} show that **9a** is intrinsically far more competent at C–H activation than **8a** (k_2 = 2.16 x 10^{-2} M^{-1} s^{-1}) at 263 K. Practically, this means that at matched substrate loadings, the diagnostic absorption associated with the reactive intermediate of **9a** decays more rapidly than for **8a**. While a detailed mechanistic analysis lies beyond the present section, the superior kinetics of **9a** are consistent with the changes in electronic environment at the reaction which would lower the barrier for hydrogen atom transfer. The concordant behavior across ethylbenzene and cumene reinforces that the reactivity difference is inherent to the iron(IV)-oxo intermediate rather than a peculiarity of a single substrate.

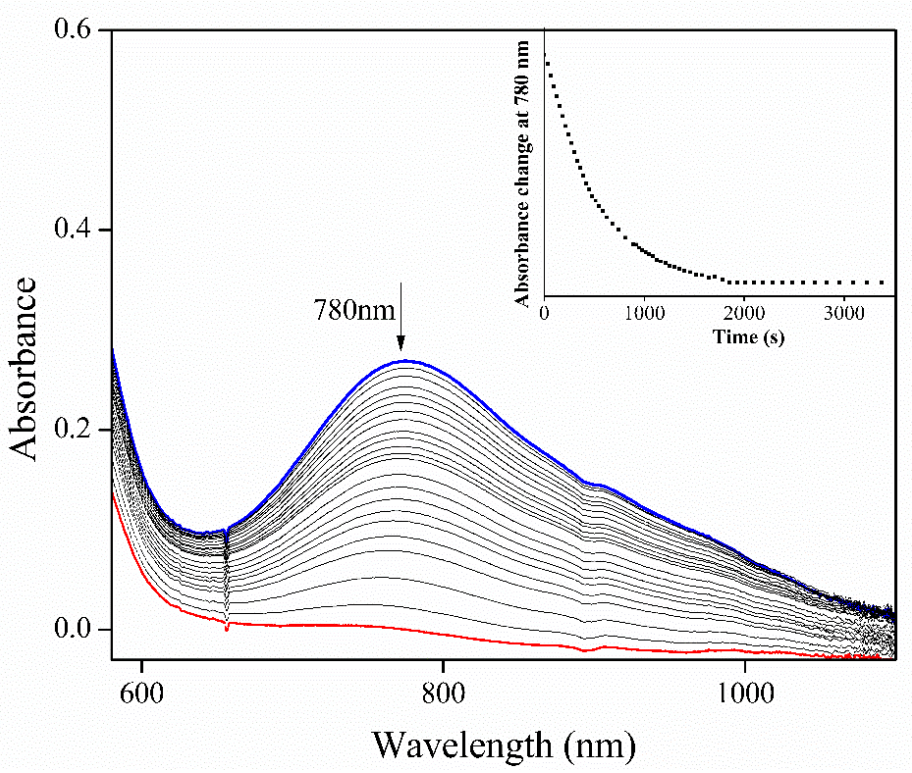

Figure 4.18 *UV-Vis spectral changes occurring at 780 nm on addition of ethylbenzene (200 equivalent) to* ***8a****. Inset shows the pseudo first order time trace for the decay of peak 780 nm on addition of ethylbenzene.*

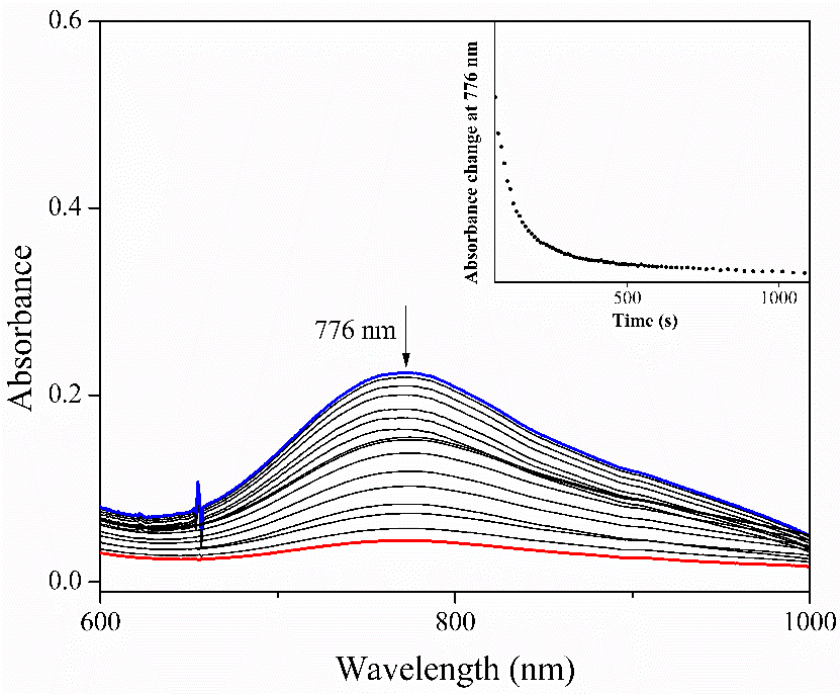

Figure 4.19 *UV-Vis spectral changes occurring at 776 nm on addition of ethylbenzene (200 equivqlent) to* ***9a****. Inset shows the pseudo first order time trace for the decay of peak 776 nm on addition of ethylbenzene.*

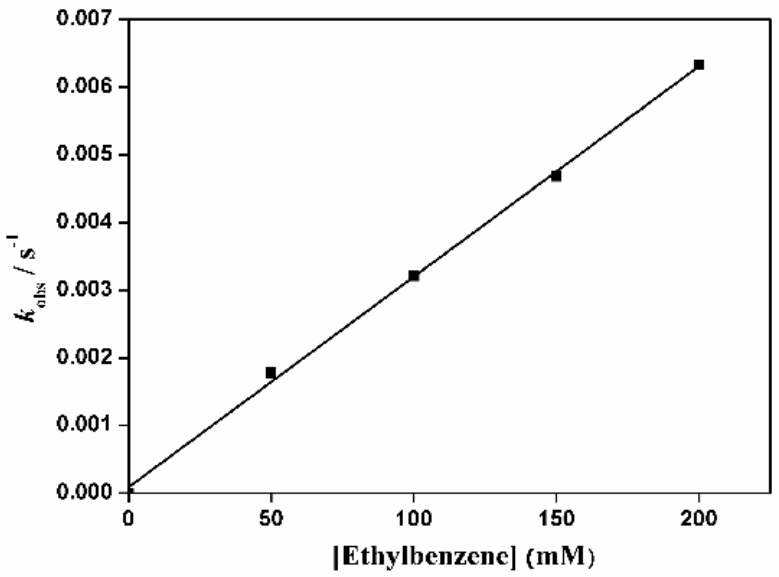

Figure 4.20 *Plot of k_{obs} vs concentration of ethylbenzene to determine second-order rate constant (k_2) for* ***8a****.*

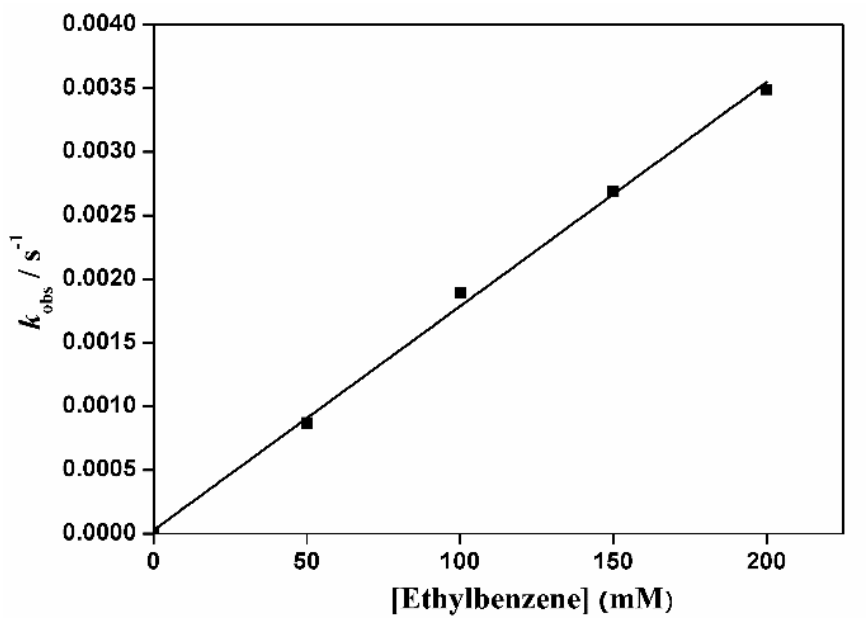

Figure 4.21 *Plot of k_{obs} vs concentration of ethylbenzene to determine second-order rate constant (k_2) for* ***9a****.*

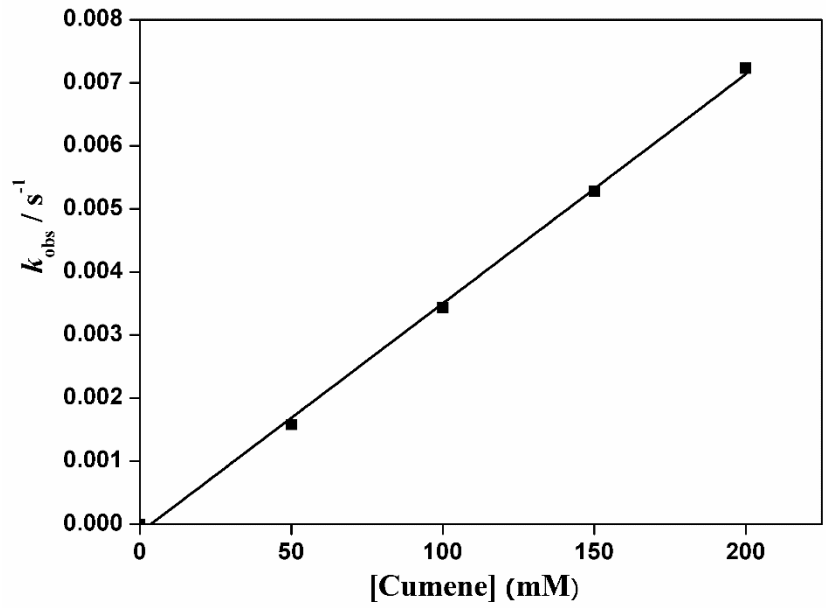

Figure 4.22 *Plot of k_{obs} vs concentration of cumene to determine second-order rate constant (k_2) for* ***9a****.*

4.3.6 Synthesis and characterization of 10 and 11

The complete synthetic protocols for compound **10** and **11** are presented in **Section 4.2.2**. Slow evaporation of an acetonitrile solution of precursor **9** promoted replacement of its weakly bound aqua ligand by an acetonitrile molecule, giving rise to compound **10**. To assess how the presence of methyl substituents influences the geometric parameters around the iron center in **9** and **10**, we also prepared the unmethylated analogue, compound **11**.

The absorption spectra (**Figure 4.23**) reveals that both Fe(II) compounds **10** and **11** display two metal to ligand charge transfer (MLCT) bands, yet their molar-absorptivity (ε) values differ markedly. Compound **10** exhibits much weaker ε values, a diagnostic feature often associated with a high spin electronic configuration[52,53,59]. The reduced intensity can be rationalized by the steric bulk of the N-methyl substituents: crowding around the iron center lengthens Fe–N and Fe–S bonds, diminishes ligand field strength, and consequently attenuates the MLCT transitions. In contrast, compound **11** which lack these sterically demanding N-methyl groups shows significantly higher ε values, consistent with a stronger ligand field and a low spin Fe(II) state, in line with literature reports for analogous systems.

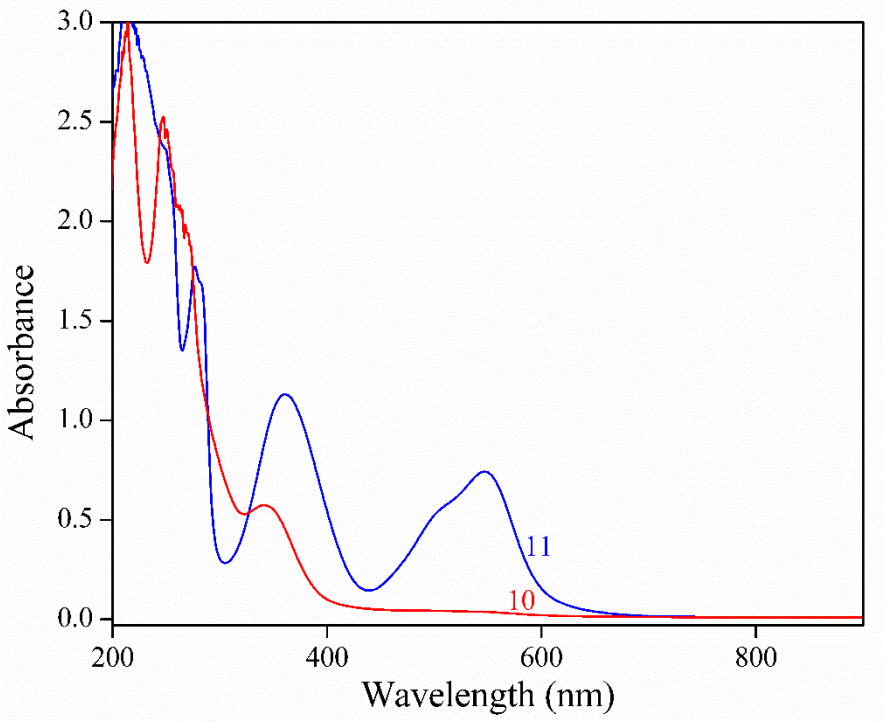

Figure 4.23 *UV-Vis spectra of* ***10*** *(red line) and* ***11*** *(blue line) (0.5mM each) in acetonitrile.*

Electrospray-ionization mass spectrometry (ESI-MS) measurements carried out in acetonitrile provide clear support for the assignment of compounds $[Fe(L7)(CH_3CN)](ClO_4)_2$ **10** and $[Fe(L6)(CH_3CN)](ClO_4)_2$ **11**, as Fe^{2+} species (**Figure 4.24**). For compound **10**, the spectrum displays two dominant signals: an intense peak at *m/z* 213.5 (calc 213.4) attributable to the fragment $[Fe(L7)(CH_3CN)]^{2+}$, and a second peak at *m/z* 485.0 (calc 485.0) corresponding to $[Fe(L7)(ClO_4)]^{+}$. A closely analogous pattern is observed for compound **11**, whose ESI-MS spectrum exhibits peaks at *m/z* 199.5 (calc 199.5) and *m/z* 457.0 (calc 457.0), assigned $[Fe(L6)(CH_3CN)]^{2+}$ and $[Fe(L6)(ClO_4)]^{+}$ species respectively.

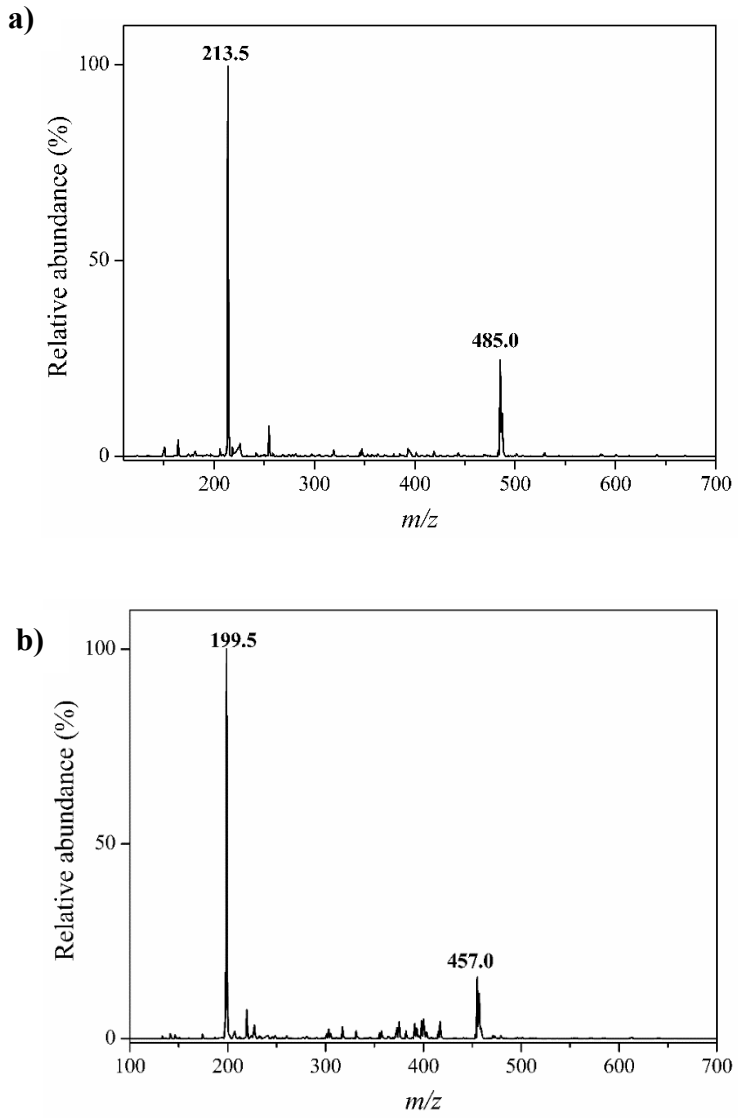

Figure 4.24 *ESI-MS spectrum of* ***10*** *(a) and* ***11*** *(b) recorded in acetonitrile solvent.*

4.3.7 Structural analysis of 10 and 11

Suitable single crystals of compounds **10** and **11** were obtained for X-ray diffraction, enabling full structural elucidation. **Figure 4.25** and **Figure 4.26** illustrates their molecular geometries, while key bond lengths and angles are compiled in **Table 4.6** and **Table 4.7**. Both compounds adopt the centrosymmetric monoclinic space group $P2_1/c$, with every atom occupying a general position. The X-ray data of **10** reveal that the Fe(II), is hexacoordinate in a highly distorted N_5S octahedral environment defined by four nitrogen atoms (N1-N4) and one thioether sulfur atom (S1) from the macrocyclic pentadentate ligand **L6** and a monodentate acetonitrile nitrogen (N5). Fe-N distances range from 2.120(3) to 2.290(3) Å, whereas Fe-S is significantly longer at 2.5321(11) Å, reflecting the larger covalent radius and weaker σ donation of sulphur. The three pseudo trans axes N4-Fe-N2 (175.8°), N5-Fe-N3 (159.5°) and N1-Fe-S1 (155.6°) deviate appreciably from 180°, and the cis angles span 76.2-104.4°, yielding octahedral angular distortion ~102°, a clear gauge of chelate induced strain. Fe–N distances lie between 2.120(3) and 2.290(3) Å, whereas the Fe−S bond distance is slightly elongated to 2.5321(11) Å.

The crystal structure of **11** bears a resemblance to that of compound **10**, and it also shows that the pentadentate ligand **L6** coordinates in the way it was envisioned, with an acetonitrile molecule bound at the sixth coordination site. The distorted octahedral N_5S environment is seen to exhibit two nearly linear *trans* axes, N4-Fe-N2 (175.94°) and N5-Fe-N3 (175.69°), whereas the other nominally *trans* pair, N1-Fe-S1 (168.71°) is appreciably bent. The *cis* angles range from 82.19 to 97.07°. The octahedral angular distortion parameter is approximately 40°. The decreased octahedral angular distortion (~40° in **11**; ~102° in **10**) and smaller *cis* angle span (82.19 to 97.07° in **11**; 76.2 to 104.4° in **10**) in compound **11** indicate moderate octahedral distortion compared with higher distortion in **10**. Fe-N distances range from 1.1952(3) to 2.038(3) Å, whereas Fe-S is at 2.2736(12) Å which is significantly shorter than those in compound **10**.

In compound **11**, perchlorate counter ions are pivotal in constructing the supramolecular framework. Their oxygen atoms O1 and O3 form weak O···H hydrogen bonds with a hydrogen atom bonded to the secondary amine nitrogen donor of the ligand backbone (**Figure 4.27** and **Table 4.8**).

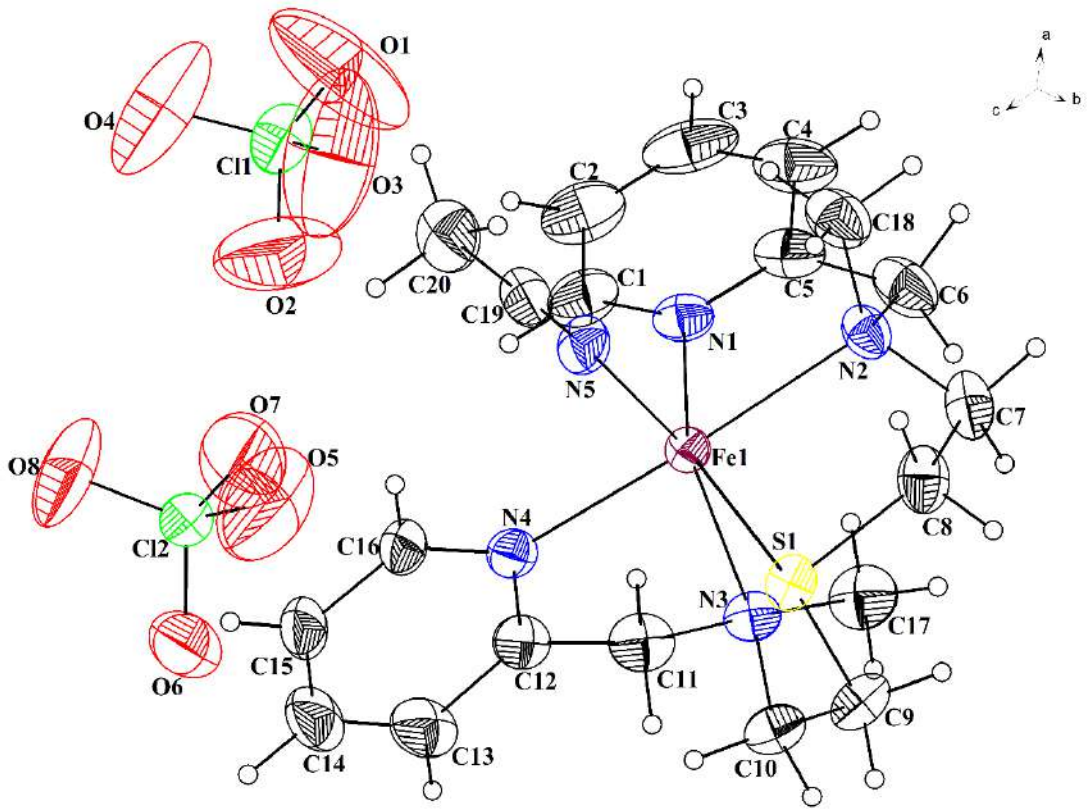

Figure 4.25 *Crystal structure of* ***10*** *showing atom labelling scheme. The thermal ellipsoids are drawn at a 30 % probability level for all the atoms except for the H atoms, which are shown as spheres of arbitrary radii.*

Table 4.6 *Selected bond lengths (Å) and angles (°) for* ***10****.*

Bond lengths (Å)			
N(1)-Fe(1)	2.120(3)	N(4)-Fe(1)	2.190(3)
N(2)-Fe(1)	2.278(3)	N(5)-Fe(1)	2.163(3)
N(3)-Fe(1)	2.290(3)	Fe(1)-S(1)	2.5321(11)
Bond angles (°)			
N(1)-Fe(1)-N(5)	100.23(14)	N(3)-Fe(1)-S(1)	81.51(8)
N(1)-Fe(1)-N(4)	99.59(13)	N(2)-Fe(1)-S(1)	81.32(9)
N(5)-Fe(1)-N(4)	87.49(13)	N(4)-Fe(1)-S(1)	102.89(8)
N(1)-Fe(1)-N(2)	76.23(13)	N(5)-Fe(1)-S(1)	90.25(11)
N(5)-Fe(1)-N(2)	92.68(12)	N(1)-Fe(1)-S(1)	155.56(11)
N(4)-Fe(1)-N(2)	175.79(12)	N(2)-Fe(1)-N(3)	104.45(12)
N(1)-Fe(1)-N(3)	94.75(12)	N(4)-Fe(1)-N(3)	76.25(12)
N(5)-Fe(1)-N(3)	159.53(13)		

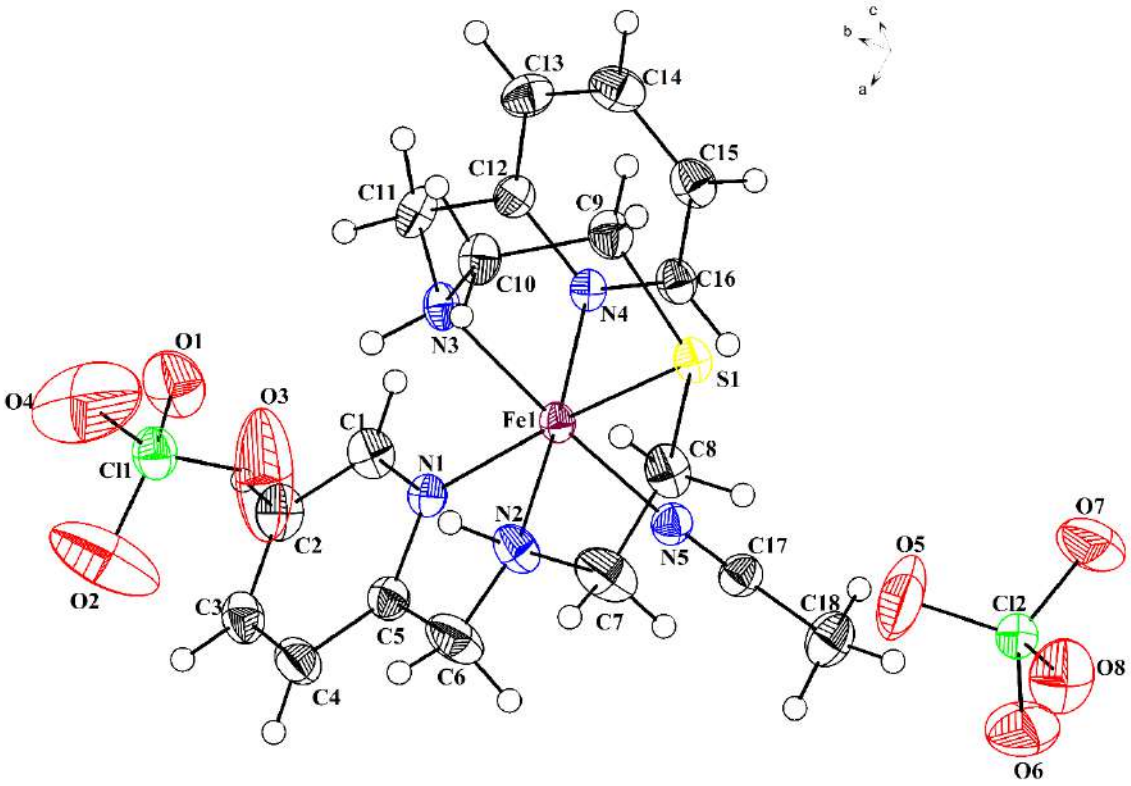

Figure 4.26 *Crystal structure of* ***11*** *showing atom labelling scheme. The thermal ellipsoids are drawn at a 30 % probability level for all the atoms except for the H atoms, which are shown as spheres of arbitrary radii.*

Table 4.7 *Selected bond lengths (Å) and angles (°) for* ***11****.*

Bond lengths (Å)			
N(1)-Fe(1)	1.985(3)	N(4)-Fe(1)	1.982(3)
N(2)-Fe(1)	1.990(3)	N(5)-Fe(1)	1.952(3)
N(3)-Fe(1)	2.038(3)	Fe(1)-S(1)	2.2736(12)
Bond angles (°)			
N(5)-Fe(1)-N(4)	92.41(13)	N(3)-Fe(1)-S(1)	87.71(10)
N(5)-Fe(1)-N(1)	90.43(12)	N(2)-Fe(1)-S(1)	86.80(10)
N(4)-Fe(1)-N(1)	97.07(12)	N(1)-Fe(1)-S(1)	168.71(9)
N(5)-Fe(1)-N(2)	91.59(15)	N(4)-Fe(1)-S(1)	93.74(9)
N(4)-Fe(1)-N(2)	175.94(15)	N(5)-Fe(1)-S(1)	92.37(10)
N(1)-Fe(1)-N(2)	82.19(13)	N(2)-Fe(1)-N(3)	92.72(15)
N(5)-Fe(1)-N(3)	175.69(13)	N(1)-Fe(1)-N(3)	90.32(13)
N(4)-Fe(1)-N(3)	83.28(13)		

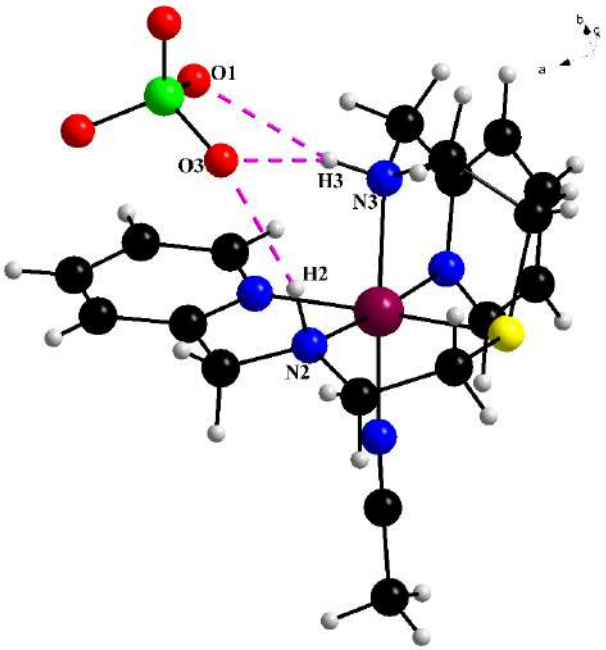

Figure 4.27 *The hydrogen bonding interactions in* ***11*** *with atom labelling scheme of atoms involved in hydrogen bonding.*

Table 4.8 *Hydrogen bonding parameters (Å, º) for* ***11****.*

D-H···A	D-H/ Å	H···A/ Å	D···A/ Å	D-H···A/º	Symmetry code
N2-H2···O3	1.064(0)	2.210(3)	3.168(2)	148.71(2)	x, y, z
N3-H3···O1	0.903(1)	2.312(9)	3.164(9)	157.34(3)	x, y, z
N3-H3···O3	0.903(1)	2.379(6)	3.167(7)	145.84(2)	x, y, z

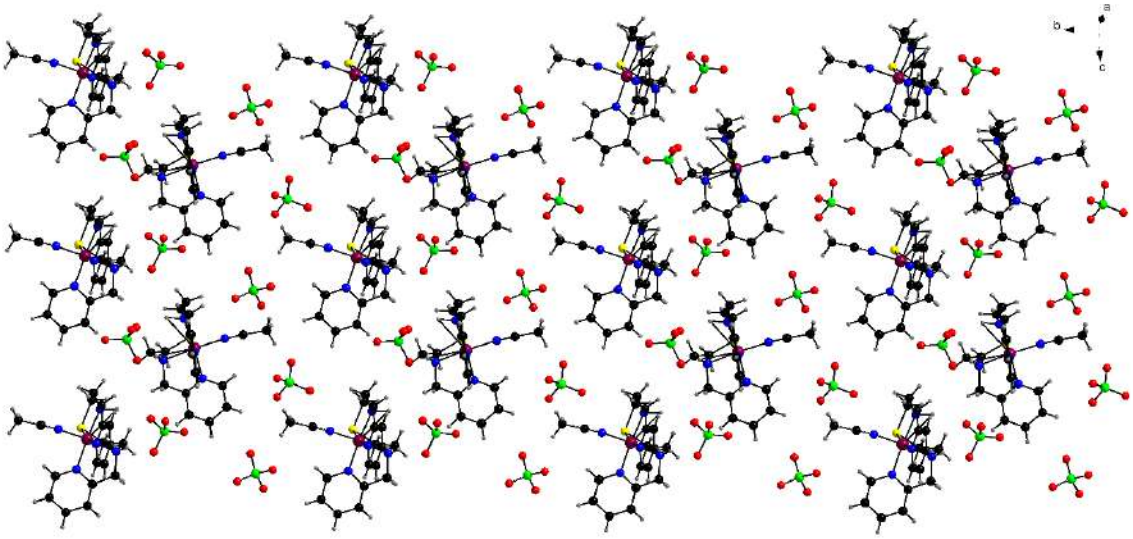

Figure 4.28 *Packing in* ***11*** *view along crystallographic a axis. Colour code: C, black; H, medium grey; N, blue; O, red; Cl, green and Fe, magenta.*

Table 4.9 *Technical details and structure refinement parameters of* ***10*** *and* ***11****.*

Compound	**10**	**11**
Empirical formula	C_{20} H_{29} Cl_2 Fe N_5 O_8 S	C_{18} H_{25} Cl_2 Fe N_5 O_8 S
Formula weight	626.29	598.24
Temperature	296(2) K	296(2) K
Wavelength	0.71073 Å	0.71073 Å
Crystal system	Monoclinic	Monoclinic
Space group	$P2_1/c$	$P2_1/c$
Unit cell dimensions	a = 14.1880(10) Å b = 18.4567(12) Å c = 11.1480(8) Å α = 90° β = 112.934(2)° γ = 90°	a = 13.492(5) Å b = 16.756(6) Å c = 11.254(4) Å α = 90° β = 109.648(10)° γ = 90°
Volume	2688.5(3) $Å^3$	2396.2(15) $Å^3$
Z	4	4
Density (calculated)	1.547 mg/m^3	1.658 mg/m^3
Absorption coefficient	0.890 mm^{-1}	0.995 mm^{-1}
F(000)	1296	1232
Theta range for data collection	2.270 to 28.420°	2.381 to 28.377°
Completeness to theta	99.9%	99.9%
Index ranges	-18<=h<=18 -24<=k<=24 -14<=l<=14	-18<=h<=17 -22<=k<=22 -15<=l<=15
Reflections collected	67841	54482
Independent reflections	6713 [R(int) = 0.0549]	5964 [R(int) = 0.0699]
Refinement method	Full-matrix least-squares on F^2	Full-matrix least-squares on F^2
Absorption correction	Semi- empirical from equivalents	Semi- empirical from equivalents
Data/restraints/parameters	6713 / 0 / 337	5964 / 0 / 323
Goodness-of-fit on F^2	1.039	1.084
Final *R*indices[I>2sigma(I)]	R1= 0.0639, wR2= 0.1793	R1= 0.0592, wR2= 0.1299
R indices (all data)	R1= 0.0886, wR2= 0.1962	R1= 0.0932, wR2= 0.1433
CCDC No.	2386746	2386739

A detailed comparative geometrical analysis of the synthesized Fe(II) compounds was conducted (**Table 4.10**). Strategic replacement of one amine nitrogen donor in the ligand backbone with a softer thioether sulfur donor, while retaining the overall pentadentate structure, resulted in a notable elongation of the metal–donor bond lengths. Longer Fe–donor bonds in iron(IV)-oxo species are generally associated with enhanced reactivity. Additionally, introducing methyl substituents at the secondary amine sites induced steric hindrance, significantly altering the N–Fe–solvent tilt angles. Furthermore, the presence of

methyl groups creates sterically induced, flagpole-like interactions with the solvent molecules (oxygen or nitrogen), potentially indicating the stabilization of the iron(IV)-oxo intermediates through favorable secondary coordination sphere interactions. Such stabilizing interactions are notably absent in analogues lacking methyl substituents.

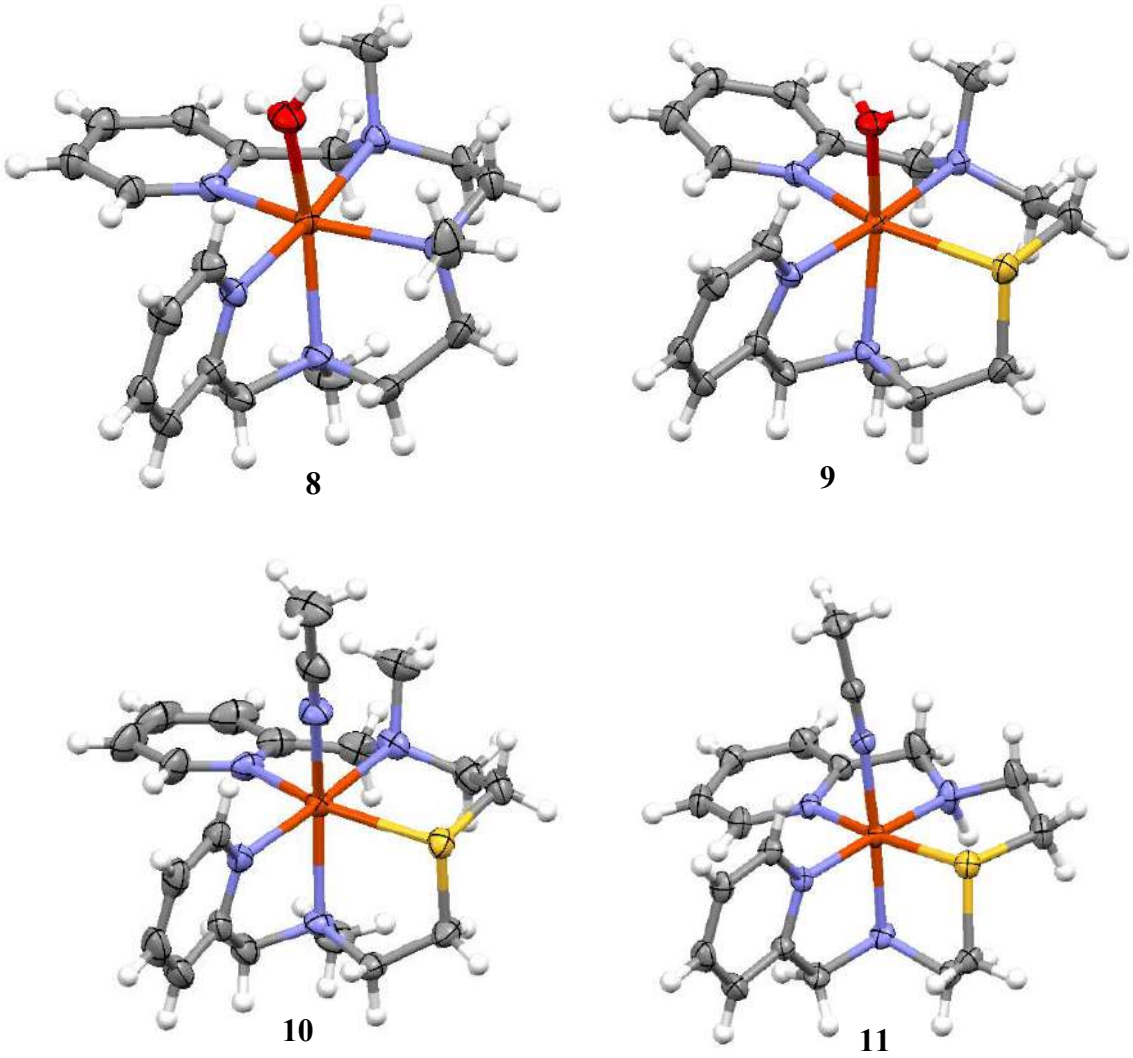

Figure 4.29 *Mercury plots of the molecular structures of the cations of* ***8-11****.*

Table 4.10 *Comparative study of selected bond lengths (Å) and angles (°) for* ***8-11****.*

8			**9**	**10**	**11**
Fe-$O_{solvent}$	2.154(4)	Fe-O/$N_{solvent.}$	2.130(3)	2.163(3)	1.952(3)
Fe-$N(4)_{ax}$	2.271(4)	Fe-N_{ax}	2.282(3)	2.290(3)	2.038(3)
Fe-$N(1)_{Py}$	2.169(4)	Fe-$N(1)_{Py}$	2.159(3)	2.120(3)	1.985(3)
Fe-N(2)	2.264(4)	Fe-N(2)	2.265(3)	2.278(3)	1.990(3)
Fe-N(3)	2.210(4)	Fe-S	2.5147(11)	2.5321(11)	2.2736(12)
Fe-$N(5)_{Py}$	2.210(4)	Fe-$N(4)_{Py}$	2.200(3)	2.190(3)	1.982(3)
∠N_{ax}-Fe-O_{sol}	158.41(17)	N_{ax}-Fe-Solvent	158.09(12)	159.53(13)	175.69(13)

4.4 Conclusion

This study has demonstrated that finely tuned electronic and steric effects imparted by ligand substituents are critical levers for directing the reactivity of non-heme iron(IV)-oxo catalysts. Systematic alterations in both the primary and secondary coordination spheres of mononuclear, octahedral iron(IV)-oxo compound reveal a delicate balance between electronic donation and steric shielding that governs hydrogen atom abstraction (HAA) activity. By designing and characterizing two novel pentadentate ligands (**L6** and **L7**) and four corresponding Fe(II) compounds (**8**-**11**), we have directly compared the behavior of an equatorial sulfur coordinated compound **9** with its nitrogen analogue **8**. Substituting a sulfur donor for an N–CH_3 site dramatically accelerates C–H activation by iron(IV)-oxo compound **9a**, exhibiting the powerful influence of sulfur ligation on the iron-oxo core. Beyond primary sphere modifications, strategic methylation within the ligand periphery further modulates reactivity by introducing steric hindrance and by engaging in secondary sphere interactions as seen in compounds **8**-**10** as compared to **11**.

Collectively, these results illuminate how equatorial sulfur coordination and peripheral methylation cooperate to fine tune iron-oxo reactivity. They provide a set of design principles that can be applied to the development of next generation oxidation catalysts with precisely tailored activity and selectivity. Moreover, the parallels drawn between our synthetic systems and nature's use of *cis* sulfur ligated iron(IV)-oxo intermediates suggest promising avenues for biomimetic catalyst design.

Section II

Synthesis and spectroscopic study of 3d metal compounds bearing N/S-donor ligands

4.5 Introduction

In Section I, we reported the synthesis, characterization, and reactivity of Fe(II) compounds supported by the pentadentate ligands **L5-L7**. In this section, we extend the study to additional 3d metals, Mn(II), Co(II), Ni(II) and Zn(II), and describe the synthesis and comprehensive characterization of their compounds derived from the same pentadentate ligands introduced in **Sections 3.1** and **4.1**.

Interest in catalysts based on earth abundant 3d metals has spurred the development of greener approaches to C–H bond functionalization. Nevertheless, this area remains mechanistically intricate, because 3d metals often operate through pathways that diverge from the well established paradigms of precious metal catalysis. Crucially, transition metal mediated C–H transformations have overturned the long held view of C–H bonds as inherently "inert," enabling retrosynthetic plans that avoid prefunctionalized substrates and thereby streamlining synthetic routes[60–62]. These advances typically reduce step counts and curb the formation of unwanted by-products in total synthesis[63–67]. A persistent challenge, however, is achieving high site selectivity for a chosen C–H bond amid many similar sites within a molecule[68–75]. A common solution is deliberate ligand design: tuning the electronic and steric features of the coordination environment to control catalyst geometry and substrate orientation. In practice, appropriately engineered ligand architectures promote substrate binding at the metal centre and preorganized the assembly so that the targeted C–H bond is proximal to the reactive site, enabling regioselective activation followed by efficient functionalization.

For many years, noble metal compounds, especially palladium, have set the standard in this field, owing to their favourable redox cycling (low barriers for interconversion of oxidation states) and broad compatibility with diverse ligands and oxidants[76–78]. Over roughly the past decade, however, increasing emphasis on sustainability has driven the adoption of abundant, cost-effective first row (3d) transition metals for C(sp^3)–H bond functionalization[79–84]. This shift introduces substantial mechanistic nuance, since 3d

metals can operate through pathways that diverge from those established for precious metals. Consequently, meaningful advances depend critically on parallel progress in the design of new ligand architecture and topology of the reactivity 3d metal catalysts. Hence, in this study we report the synthesis and characterization of seven novel 3d metal compounds which can potentially be used as catalyst.

4.6 Experimental details

The procedures used to synthesise 3d metal compounds, $[Ni(L6)(CH_3CN)](ClO_4)_2$ **12**, $[Ni(L7)(CH_3CN)](ClO_4)_2$ **13**, $[Mn(L6)(ClO_4)](ClO_4)$ **14**, $[Mn(L7)(H_2O)](ClO_4)_2$ **15**, $[Co(L7)(H_2O)](ClO_4)_2$ **16**, $[Zn(L7)(H_2O)](ClO_4)_2$ **17** and $[Zn(L3)](ClO_4)_2$ **18** are detailed in this section along with their characterization. The structures of the 3d compounds synthesised in this study are depicted in **Scheme 4.6**.

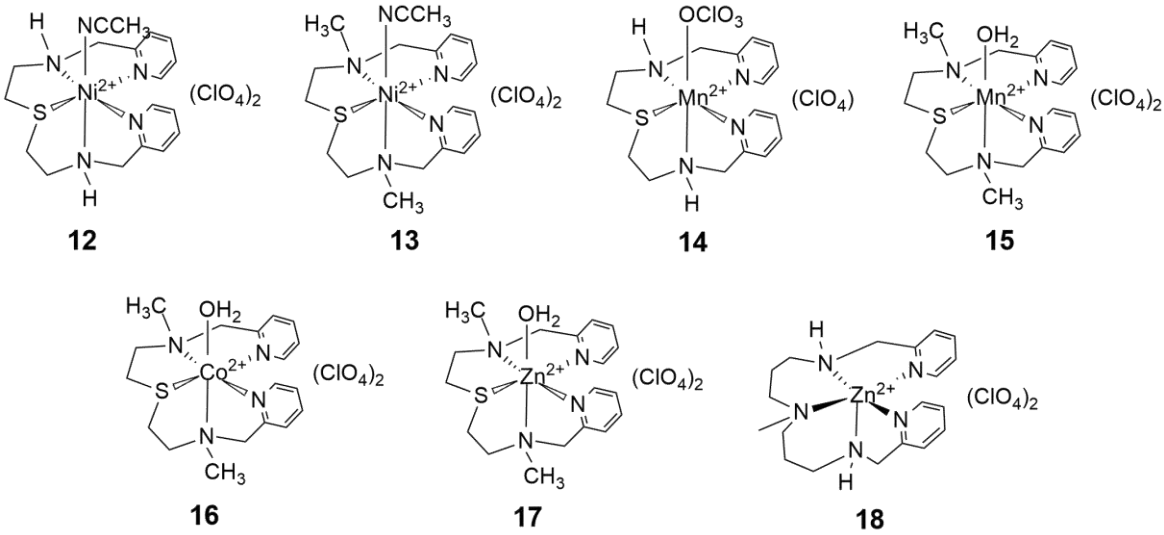

Scheme 4.6 *Structure of compounds* ***12-18*** *under investigation.*

4.6.1 Synthesis of compounds 12-18

$[Ni(L6)(CH_3CN)](ClO_4)_2$ 12

In a nitrogen purged flask connected to a Schlenk line at room temperature, a solution of **L6** in acetonitrile (0.41 g, 1.36 mmol) was introduced gradually into a vigorously stirred acetonitrile solution (2 mL) of $Ni(ClO_4)_2 \cdot 6H_2O$ (0.50 g, 1.36 mmol). Stirring was continued for roughly 5 h, during which the mixture developed an intense pink coloration. Diethyl ether (10 mL) was then added, and the beaker was left undisturbed to allow slow crystallization. After about one day, pink crystals had formed; these were collected by

filtration and air-dried to afford compound **12** in 0.71 g (1.18 mmol) yield, corresponding to 87%. *Anal. Calc.* for **12** C_{18} H_{25} Cl_2 Ni N_5 O_8 S(%): C, 35.97; H, 4.19; N, 11.65; S, 5.33. *Found:* C, 35.12; H, 3.58; N, 11.89; S, 5.04. IR (KBr, cm^{-1}): 3420-3508 υ(NH); 1093, 621 υ(ClO_4); UV-Vis data, λ_{max}, CH_3CN/nm (ε/dm^3 mol^{-1} cm^{-1}): 260 (1835), 510 (48) and 835 (59). ESI-MS: *m/z* = 180.0 (calc. *m/z* 180.0) for $[Ni(L6)]^{2+}$, *m/z* = 200.5 (calc. *m/z* 200.5) for $[Ni(L6)(CH_3CN)]^{2+}$ and *m/z* = 459.0 (calc. *m/z* 459.0) for $[Ni(L6)(ClO_4)]^{+}$.

[Ni(L7)(CH_3CN)](ClO_4)$_2$ 13

Compound **13** was synthesized via a similar protocol as described in **12**; **L7** (0.45 g, 1.36 mmol) was reacted with $Ni(ClO_4)_2 \cdot 6H_2O$ (0.5 g, 1.36 mmol) in acetonitrile under a N_2 atmosphere. The blue crystalline compound **13** was obtained. Blue single crystals formed when diethyl ether was allowed to slowly diffuse into an acetonitrile solution of compound **13**. The yield of **13** was 0.67 g (1.06 mmol), 77.9 %. *Anal. Calc.* for **13** C_{20} H_{29} Cl_2 Ni N_5 O_8 S(%): C, 38.18; H, 4.65; N, 11.13; S, 5.10. *Found:* C, 39.09; H, 5.09; N, 11.6; S, 5.36. IR (KBr, cm^{-1}): 3007-2895 υ(CH); 1093, 621 υ(ClO_4); UV-Vis data, λ_{max}, CH_3CN/nm (ε/dm^3 mol^{-1} cm^{-1}): 260 (2794), 570 (40) and 929 (71). ESI-MS: *m/z* = 194.0 (calc. *m/z* 194.0) for $[Ni(L7)]^{2+}$, *m/z* = 214.5 (calc. *m/z* 214.5) for $[Ni(L7)(CH_3CN)]^{2+}$ and *m/z* = 487.7 (calc. *m/z* 487.7) for $[Ni(L7)(ClO_4)]^{+}$.

[Mn(L6)(ClO_4)](ClO_4) 14

A N_2 purged, dried Schlenk flask was charged with Mn(II) perchlorate (0.50 g, 1.38 mmol). Acetonitrile was added under a gentle positive N_2 flow, and the mixture was stirred at room temperature for 15 min. A separate MeCN solution of **L6** (0.42 g, 1.38 mmol) was then introduced slowly without breaking the inert atmosphere. After a further 5 h of stirring at ambient temperature, the flask was placed in a diethyl-ether bath and left overnight. Slow ether diffusion produced colourless crystals of compound **14**, which were collected by filtration and air-dried. The yield of **14** was 0.59 g (1.06 mmol), 76.6 %. *Anal. Calc.* for **14** C_{16} H_{22} Cl_2 Mn N_4 O_8 S(%): C, 34.55; H, 3.99; N, 10.07; S, 5.76. *Found:* C, 34.82; H, 4.21; N, 10.61; S, 4.83. IR (KBr, cm^{-1}): 3420-3508 υ(NH); 1093, 621 υ(ClO_4); UV-Vis data, λ_{max}, CH_3CN/nm (ε/dm^3 mol^{-1} cm^{-1}): 262 (1926). ESI-MS: *m/z* = 178.5 (calc. *m/z* 178.5) for $[Mn(L6)]^{2+}$and *m/z* = 456.3 (calc. *m/z* 456.0) for $[Mn(L6)(ClO_4)]^{+}$.

$[Mn(L7)(H_2O)](ClO_4)_2$ 15

Compound **15** was prepared using the same approach as compound **14**. A 2 mL acetonitrile solution of **L7** (0.46 g, 1.38 mmol) was slowly combined with an equimolar solution of Mn(II) perchlorate (0.50 g, 1.38 mmol) in 2 mL CH_3CN. The sealed mixture was then exposed to diethyl ether vapour; over roughly 48 hours, slow solvent diffusion produced colourless crystals, which were collected and dried. The yield of **15** was 0.72 g (1.20 mmol), 86.7 %. *Anal. Calc.* for **15** C_{18} H_{28} Cl_2 Mn N_4 O_9 S(%): C, 35.89; H, 4.69; N, 9.30; S, 5.32. *Found:* C, 35.31; H, 5.09; N, 9.63; S, 4.81. IR (KBr, cm^{-1}): 3007-2895 υ(CH); 1093, 621 υ(ClO_4); UV-Vis data, λ_{max}, CH_3CN/nm (ε/dm^3 mol^{-1} cm^{-1}): 279 (2853). ESI-MS: *m/z* = 192.5 (calc. *m/z* 192.5) for $[Mn(L7)]^{2+}$, 213.0 (calc. *m/z* 213.0) for $[Mn(L7)(CH_3CN)]^{2+}$ and *m/z* = 484.0 (calc. *m/z* 484.0) for $[Mn(L7)(ClO_4)]^{+}$.

$[Co(L7)(H_2O)](ClO_4)_2$ 16

A 50 mL dried Schlenk flask was purged with dry nitrogen, charged with $Co(ClO_4)_2 \cdot 6H_2O$ (0.50 g, 1.37 mmol) and treated with 2 mL of anhydrous acetonitrile to give a pale pink solution that was stirred for 10 min at room temperature. While the inert atmosphere was maintained, a separate 2 mL MeCN solution of ligand **L7** (0.45 g, 1.37 mmol) was introduced dropwise; the colour immediately deepened to magenta, and the mixture was allowed to stir for a further 5 h. The resulting solution was transferred to a small vial, loosely sealed with pin-holed Parafilm, and set inside a tightly capped beaker containing 10 mL diethyl ether. Slow ether vapour diffusion over 48 h produced needle shaped pink single crystals, which were collected, washed quickly with cold ether, and vacuum-dried to yield compound **16** as pink microcrystals (0.70 g, 1.15 mmol, 84.3 %). *Anal. Calc.* for **16** C_{18} H_{28} Cl_2 Co N_4 O_9 S(%): C, 35.66; H, 4.65; N, 9.24; S, 5.29. *Found:* C, 35.02; H, 5.09; N, 10.11; S, 5.96. IR (KBr, cm^{-1}): 3007-2895 υ(CH); 1093, 621 υ(ClO_4); UV-Vis data, λ_{max}, CH_3CN/nm (ε/dm^3 mol^{-1} cm^{-1}): 320 (2461), 500 (36). ESI-MS: 194.5 (calc. *m/z* 194.5) for $[Co(L7)]^{2+}$ and m/z 488.0(calc. *m/z* 488.0) for $[Co(L7)(ClO_4)]^{+}$.

$[Zn(L7)(H_2O)](ClO_4)_2$ 17

Compound **17** was synthesised by gradually adding 0.44 g (1.34 mmol) of **L7** to a 5 mL solution of acetonitrile, which was then stirred with 0.5g (1.34 mmol) of $Zn(ClO_4)_2.6H_2O$ (2 mL) at room temperature. The mixture was stirred for approximately 5h. Addition of

diethyl ether to the solution precipitated a white solid, which was collected by filtration, rinsed with fresh ether, and dried under vacuum. Single crystals of **17** suitable for X-ray analysis were subsequently grown by slow evaporation of its acetonitrile solution. The yield of **17** was 0.72 g (1.17 mmol), 87.8 %. *Anal. Calc.* for **17** C_{18} H_{28} Cl_2 Zn N_4 O_9 S(%): C, 35.28; H, 4.61; N, 9.14; S, 5.23. *Found:* C, 34.85; H, 5.09; N, 9.63; S, 4.76. IR (KBr, cm^{-1}): 3007-2895 υ(CH); 1093, 621 υ(ClO_4); ESI-MS: m/z = m/z values of 197.0 (calc. *m/z* 197.0) for $[Zn(L7)]^{2+}$, 217.5 (calc. *m/z* 217.5) for $[Zn(L7)(CH_3CN)]^{2+}$ and 493.0 (calc. *m/z* 493.0) for $[Zn(L7)(ClO_4)]^{+}$

[Zn(L3)]$(ClO_4)_2$ 18

Ligand **L3** (0.44 g, 1.34 mmol) was dissolved in anhydrous acetonitrile (5 mL) under ambient conditions and the solution was added in one portion to a separately prepared solution of $Zn(ClO_4)_2.6H_2O$ (0.50 g, 1.34 mmol) in acetonitrile (2 mL). The homogeneous mixture was stirred at room temperature for 5 h, after which diethyl ether was added slowly with stirring until precipitation was complete. The resulting white solid was collected by vacuum filtration, washed with cold diethyl ether (2 × 5mL), and dried in vacuo to afford compound **18** as a white powder. Single crystals suitable for X-ray diffraction were obtained by slow evaporation of an acetonitrile solution of the purified product. The yield of **18** was 0.62 g (1.05 mmol), 78.5 %. *Anal. Calc.* for **18** C_{19} H_{29} Cl_2 Zn N_5 O_8 (%): C, 38.56; H, 4.94; N, 11.84. *Found:* C, 39.01; H, 4.19; N, 11.63. IR (KBr, cm^{-1}): 3420-3508 υ(NH); 3007-2895 υ(CH); 1093, 621 υ(ClO_4); ESI-MS: m/z = 216.1 (calc. *m/z* 216.1) for $[Zn(L3)(CH_3CN)]^{2+}$, 236.6 (calc. *m/z* 236.6) for $[Zn(L3)(CH_3CN)_2]^{2+}$ and 490.1 (calc. *m/z* 490.1) for $[Zn(L3)(ClO_4)]^{+}$.

4.7 Results and discussions

4.7.1 Infrared spectra of compounds 12-18

The IR spectra of compounds **15**, **16**, and **17** displayed broad bands at 3420-3508 cm^{-1}, which correspond to the O-H vibrations of water. Additionally, the IR spectrum of compounds **12**, **14**, and **18** exhibited N-H stretching vibrations in the region 3350-3430 cm^{-1}, characteristic of compounds with tertiary amine nitrogen. The bands due to O-H vibrations are missing from the IR spectra of compounds **12-14** and **18**, which suggests the absence of a water molecule. The perchlorate anions have been incorporated into all

compounds, as indicated by well-resolved absorption bands at 1093 (s) 621 (m) cm^{-1} (**Figure 4.30** and **Figure 4.31**)[49].

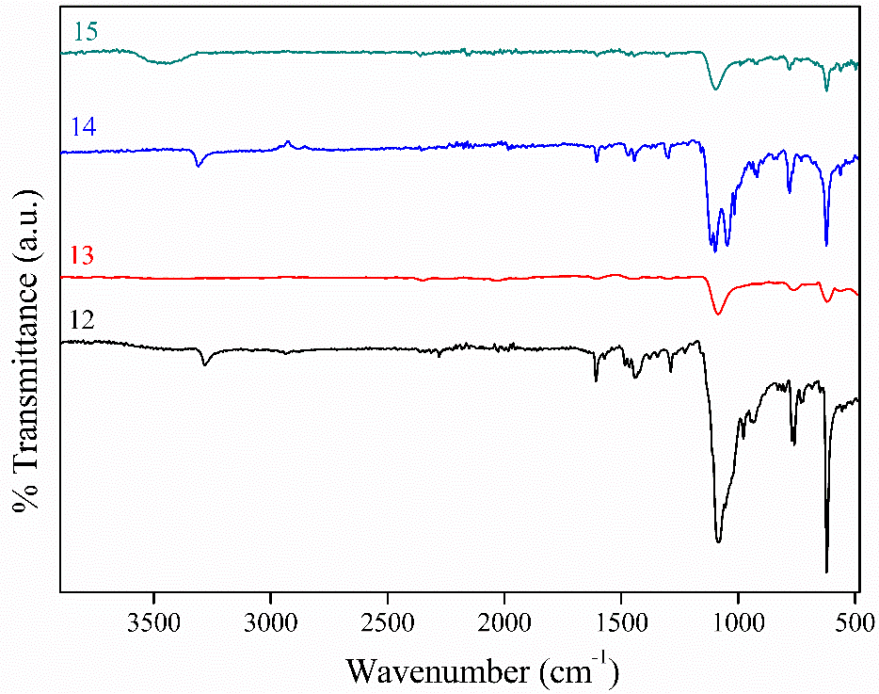

Figure 4.30 *The overlaid infrared spectra of compounds* ***12-15****.*

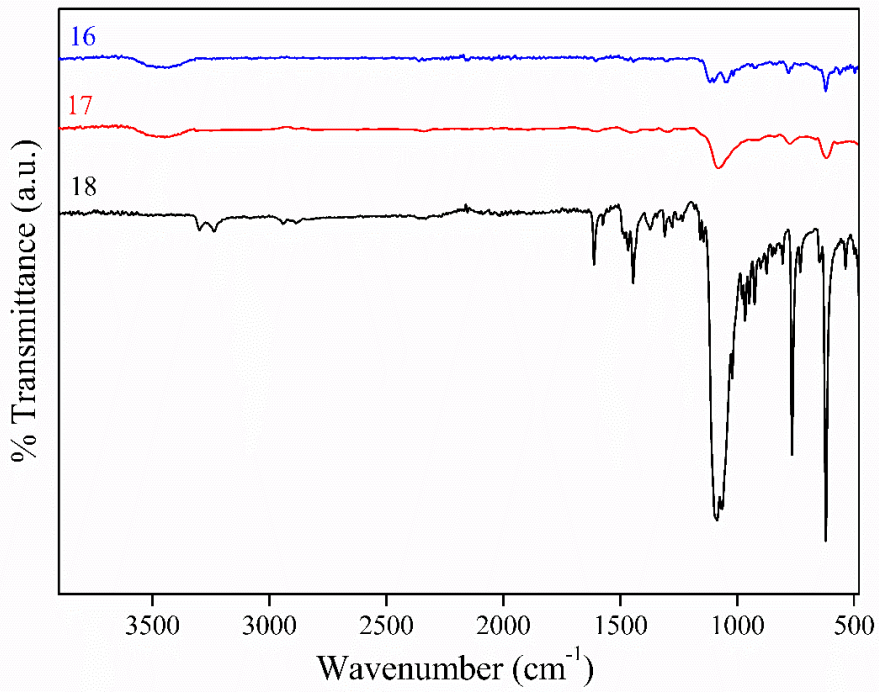

Figure 4.31 *The overlaid infrared spectra of compounds* ***16-18****.*

4.7.2 UV-Vis spectroscopy

Electronic absorption spectra for the compounds were measured in acetonitrile to probe ligand- and Ni^{2+} centered transitions (**Figure 4.32**). Each spectrum displays the characteristically weak, spin-allowed *d–d* features of an octahedral high-spin Ni(II) center in the visible to NIR region. Although three spin-allowed transitions are formally expected from the $^3A_2g(F)$ ground state namely $^3A_2g \rightarrow {}^3T_2g(F)$, $^3A_2g \rightarrow {}^3T_1g(F)$, and $^3A_2g \rightarrow {}^3T_1g(P)$, only two are experimentally resolved. For compound **12**, bands appear at ~510 nm and within the 830–840 nm window; in compound **13** these shift bathochromically to ~570 nm and 929 nm, respectively. The lower-energy (longer-wavelength) feature (~820–930 nm) is assigned to the $^3A_2g \rightarrow {}^3T_2g(F)$ transition, while the higher energy visible band (~450–570 nm) corresponds to $^3A_2g \rightarrow {}^3T_1g(F)$. The third, higher energy $^3A_2g \rightarrow {}^3T_1g(P)$ transition is not distinctly observed because it merges with the more intense charge-transfer absorption toward the ultraviolet. The intense absorption at 260 nm, in the spectra of the Ni(II) compounds is assigned to a ligand centered $\pi \rightarrow \pi^*$ transition of the coordinated aminopyridine ring; its position and high intensity distinguish it from the much weaker, lower energy spin allowed *d–d* transitions[85,86].

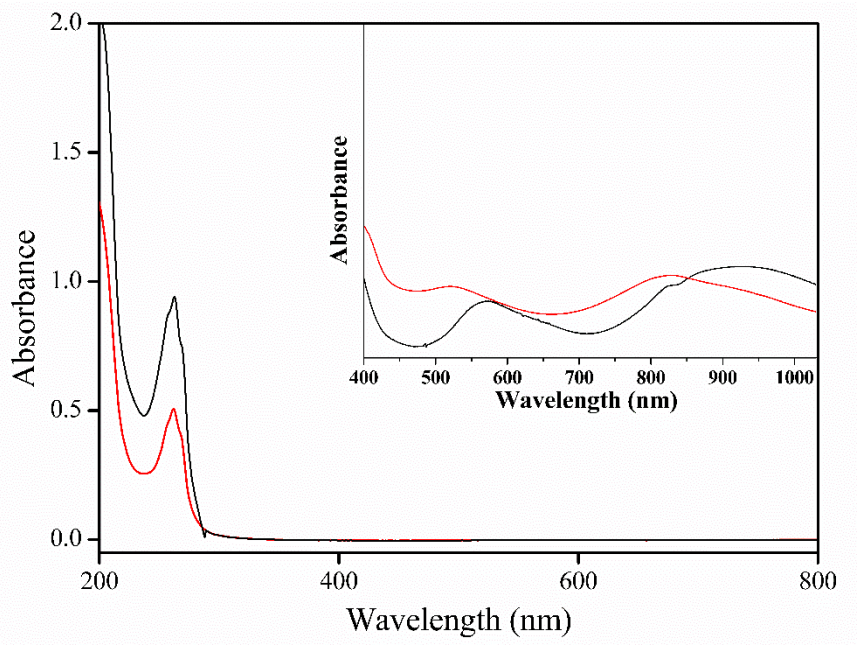

Figure 4.32 *Overlaid UV-Vis spectra of* ***12*** *(red)* and ***13*** *(black) in* CH_3CN. *The inset shows an expanded view of the region 400 to 1100 nm for d-d bands of* ***12*** *and* ***13*** *(5 mM).*

The high-spin, octahedral Mn(II) compounds **14** and **15** exhibits an electronic absorption profile in which strong ligand based π→π* absorptions are exhibited at 200–310 nm region, whereas the spectra from about 350 up to 1100 nm shows no appreciable features (**Figure 4.33**). This lack of bands in the visible to NIR is in line with the very low intensity (or practical absence) of the spin-forbidden d–d excitations characteristic of an octahedral d^5 (high-spin) manganese(II) center[87,88].

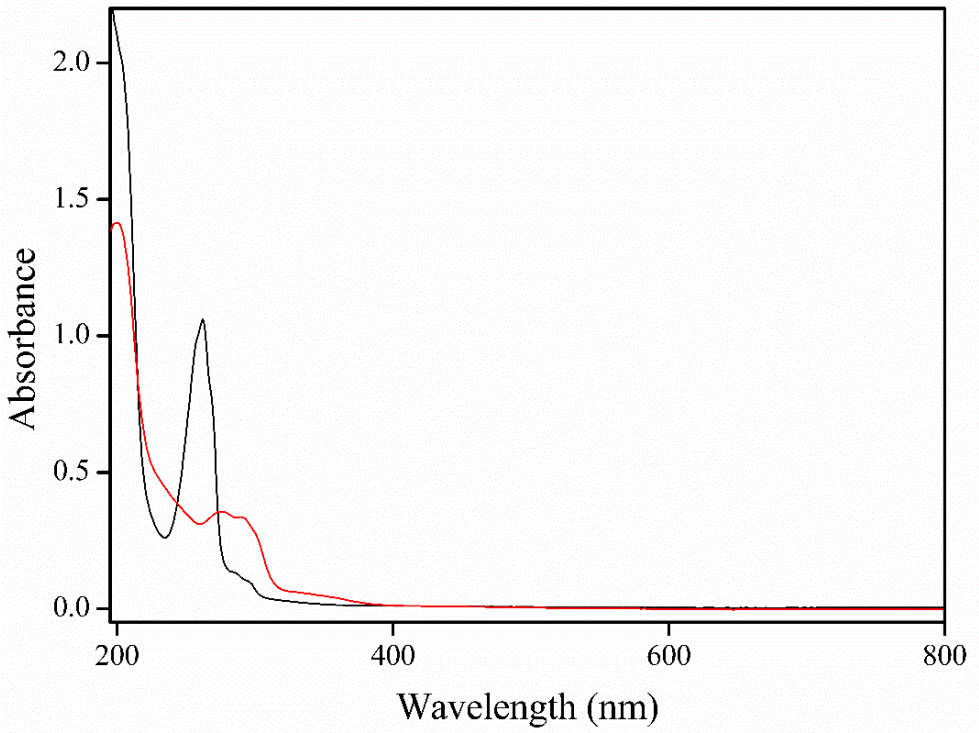

Figure 4.33 *Overlaid UV-Vis spectra of **14** (black)* and ***15*** *(red) in CH_3CN.*

The electronic absorption spectrum (200–1100 nm) of the Co(II) aminopyridine compound **16** displays a single broad visible band centered near ~500 nm with a shoulder toward ~545 nm and a very weak near-IR tail, characteristic of a high-spin octahedral Co(II) center (**Figure 4.34**). These features are assigned to the overlapping spin allowed quartet transitions $^4T_{1g}(F)\rightarrow{}^4A_{2g}(F)$ and $^4T_{1g}(F)\rightarrow{}^4T_{1g}(P)$, while the lowest $^4T_{1g}(F)\rightarrow{}^4T_{2g}(F)$ transition lies as a weak band in the near-IR (only partially captured within the recorded range). Intense ligand centered π→π* absorptions was seen below ~320 nm due to the aminopyridine rings[89–91].

The UV–visible profile of the aminopyridine zinc(II) compounds **17** and **18**, is characterized almost exclusively by strong ligand-based π→π* absorptions, consistent with a d^{10}, diamagnetic Zn^{2+} centre lacking any spin or Laporte allowed *d-d* transitions. Within the 200-310 nm region, two dominant π→π* bands appear at λ_1 = 210 nm and λ_2 = 300 nm, attributable to excitations within the conjugated pyridyl framework[92].

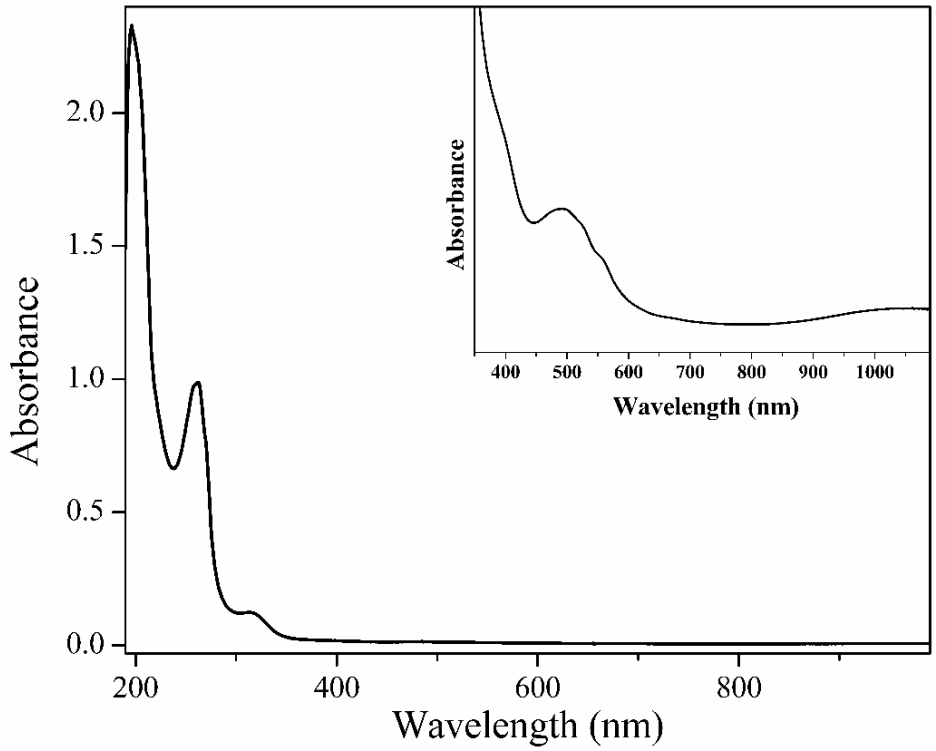

Figure 4.34 *UV-Vis spectra of **16** in CH_3CN. The inset shows an expanded view of the region 400 to 1100 nm for d-d bands of **16** (5 mM).*

4.7.3 ESI-Mass spectrometry

Electrospray mass spectra (ESI-MS) of compounds **12-18** were studied in acetonitrile. ESI-MS spectrum of **12** exhibits mass peaks at *m/z* = 180.0 (calc. *m/z* 180.0) for $[Ni(L6)]^{2+}$, *m/z* = 200.5 (calc. *m/z* 200.5) for $[Ni(L6)(CH_3CN)]^{2+}$ and *m/z* = 459.0 (calc. *m/z* 459.0) for $[Ni(L6)(ClO_4)]^{+}$ fragments. On the other hand, the ESI-MS spectrum of **13** exhibits three mass peaks at *m/z* = 194.0 (calc. *m/z* 194.0), *m/z* = 214.5 (calc. *m/z* 214.5) and *m/z* = 487.7 (calc. *m/z* 487.7) which can be assigned to $[Ni(L7)]^{2+}$, $[Ni(L7)(CH_3CN)]^{2+}$ and $[Ni(L7)(ClO_4)]^{+}$ species, respectively (**Figure 4.35**). Similarly, the ESI-MS spectrum of **14** shows fragmentation peaks at *m/z* = 178.5 (calc. *m/z* 178.5) for $[Mn(L6)]^{2+}$and *m/z* = 456.3 (calc. *m/z* 456.0) for $[Mn(L6)(ClO_4)]^{+}$. The peaks observed at *m/z* = 192.5 (calc. *m/z*

192.5), 213.0 (calc. *m/z* 213.0) and *m/z* = 484.0 (calc. *m/z* 484.0) in ESI-MS spectrum of **15** can be attributed to $[Mn(L7)]^{2+}$, $[Mn(L7)(CH_3CN)]^{2+}$ and $[Mn(L7)(ClO_4)]^{+}$ species respectively (**Figure 4.36**).

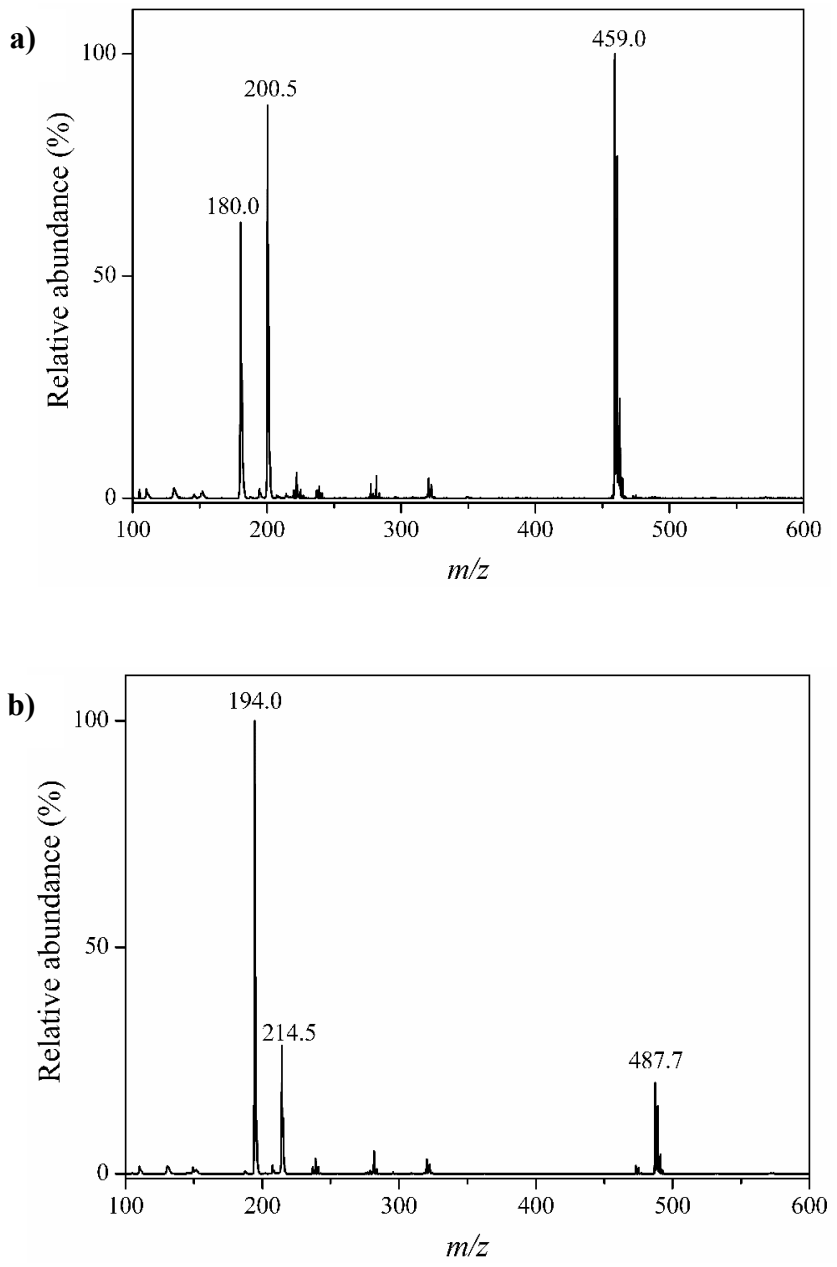

Figure 4.35 *ESI-MS spectrum of* ***12*** *(a) and* ***13*** *(b) recorded in acetonitrile solvent.*

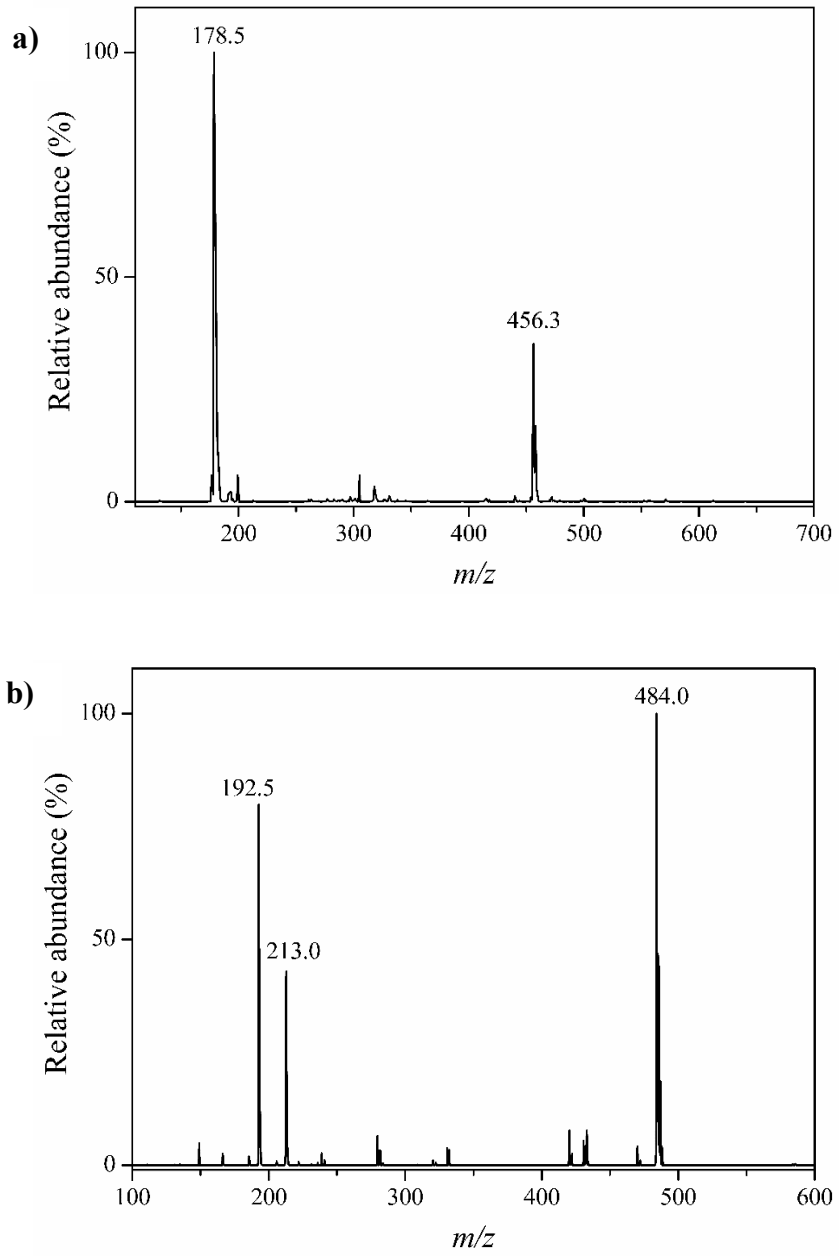

Figure 4.36 *ESI-MS spectrum of* ***14*** *(a) and* ***15*** *(b) recorded in acetonitrile.*

The mass spectrum obtained by electrospray ionization mass spectrometry (ESI-MS) of compound **16** dissolved in acetonitrile exhibited two distinct mass peaks at *m/z* values of 194.5 (calc. *m/z* 194.5) and 488.0(calc. *m/z* 488.0) (**Figure 4.37**). These peaks were attributed to the $[Co(L7)]^{2+}$ and $[Co(L7)(ClO_4)]^{+}$ species respectively. Whereas the peaks observed at m/z values of 197.0 (calc. *m/z* 197.0), 217.5 (calc. *m/z* 217.5) and 493.0 (calc. *m/z* 493.0) can be assigned to $[Zn(L7)]^{2+}$, $[Zn(L7)(CH_3CN)]^{2+}$ and $[Zn(L7)(ClO_4)]^{+}$ species respectively (**Figure 4.37**).

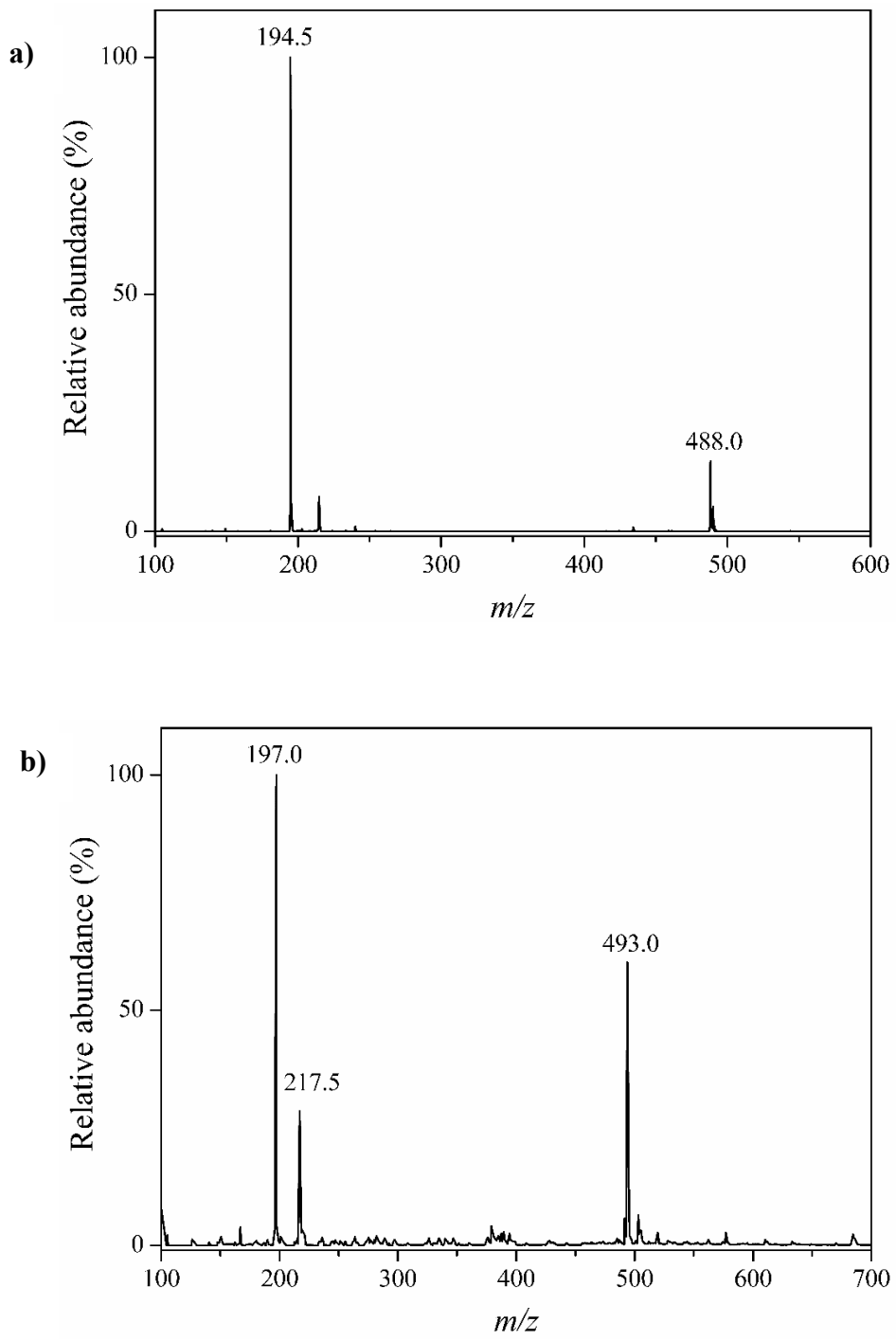

Figure 4.37 *ESI-MS spectrum of* ***16*** *(a) and* ***17*** *(b) recorded in acetonitrile.*

The mass spectrum obtained by electrospray ionization mass spectrometry (ESI-MS) of compound **18** dissolved in acetonitrile exhibited three distinct mass peaks at *m/z* values of 216.1 (calc. *m/z* 216.1), 236.6 (calc. *m/z* 236.6) and 490.1 (calc. *m/z* 490.1) (**Figure 4.38**). These peaks were attributed to the $[Zn(L3)(CH_3CN)]^{2+}$, $[Zn(L3)(CH_3CN)_2]^{2+}$ and $[Zn(L3)(ClO_4)]^{+}$ species respectively.

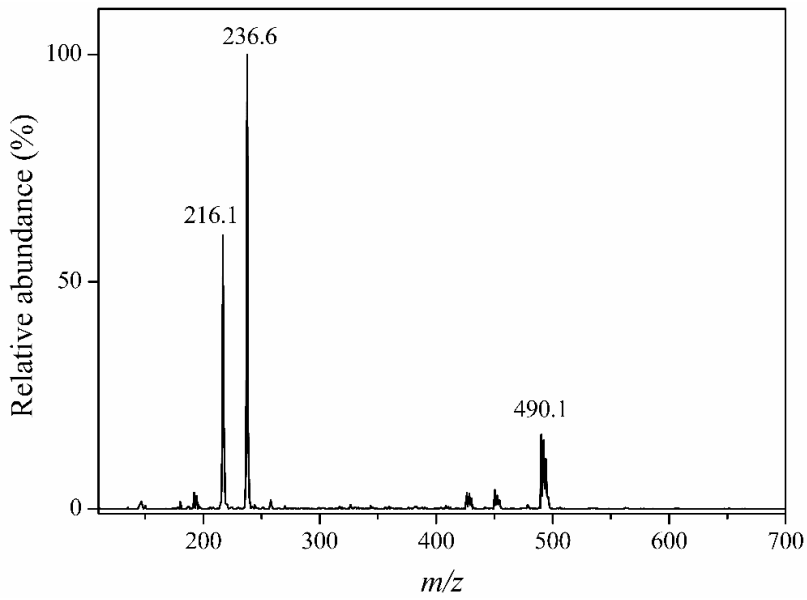

Figure 4.38 *ESI-MS spectrum of* ***18*** *recorded in acetonitrile.*

4.7.4 X-ray powder diffraction

Powder X-ray diffraction (PXRD) patterns were collected for compounds **12–18** to verify that the crystalline samples were phase-pure and representative of the bulk material. The experimental diffractograms were compared with patterns simulated from the single crystal structures using Mercury 4.0[93]. The excellent overlap between measured and calculated traces confirms that the bulk and single-crystal phases are the same (**Figure 4.39–4.41**).

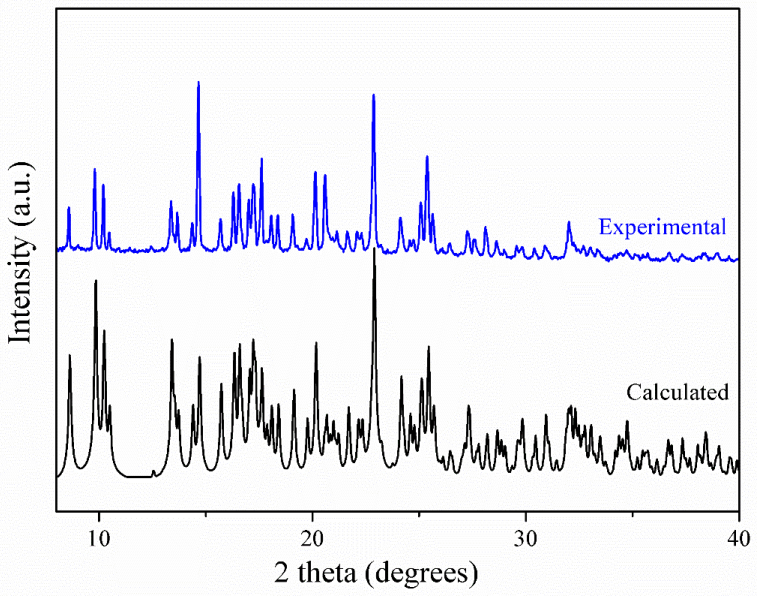

Figure 4.39 *The experimental and calculated PXRD patterns of* ***12****.*

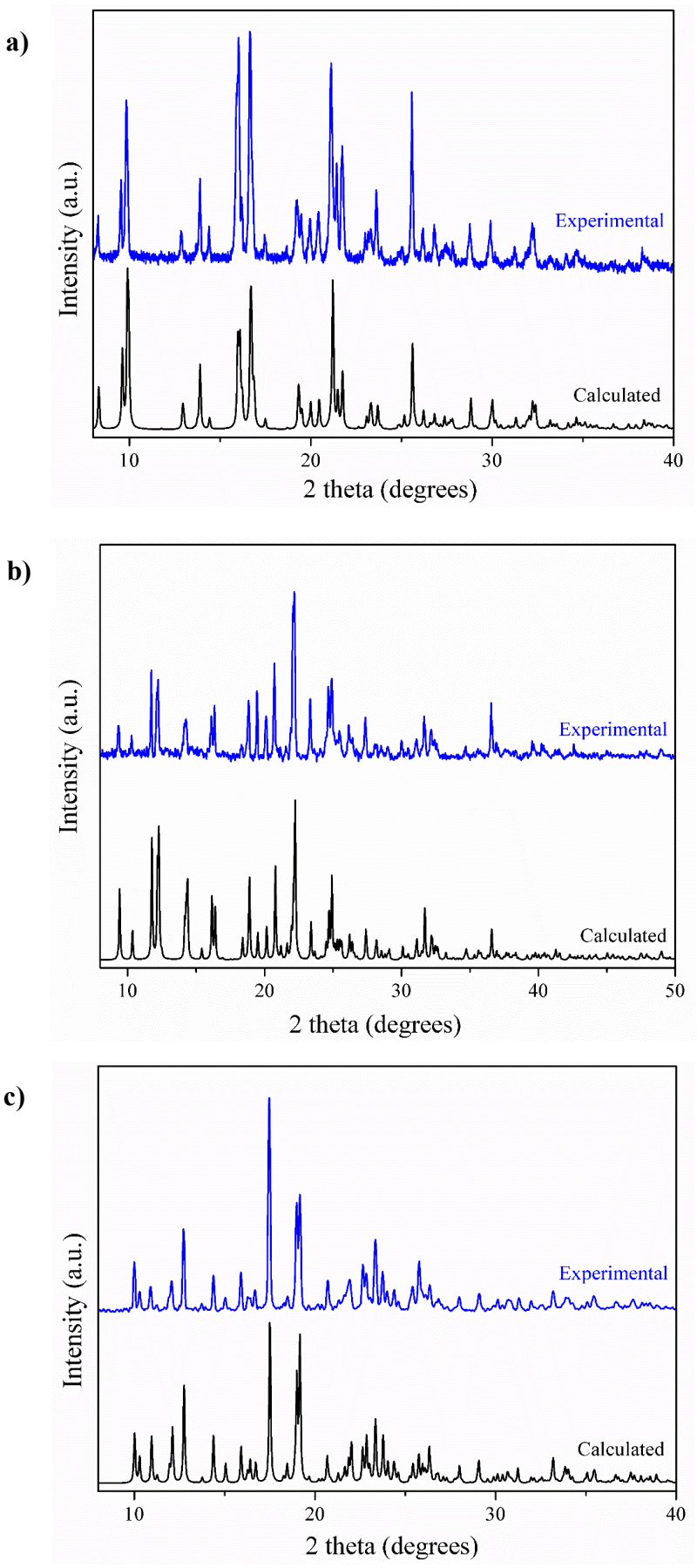

Figure 4.40 *The experimental and calculated PXRD patterns of* ***13*** *(a),* ***14****(b) and* ***15****(c).*

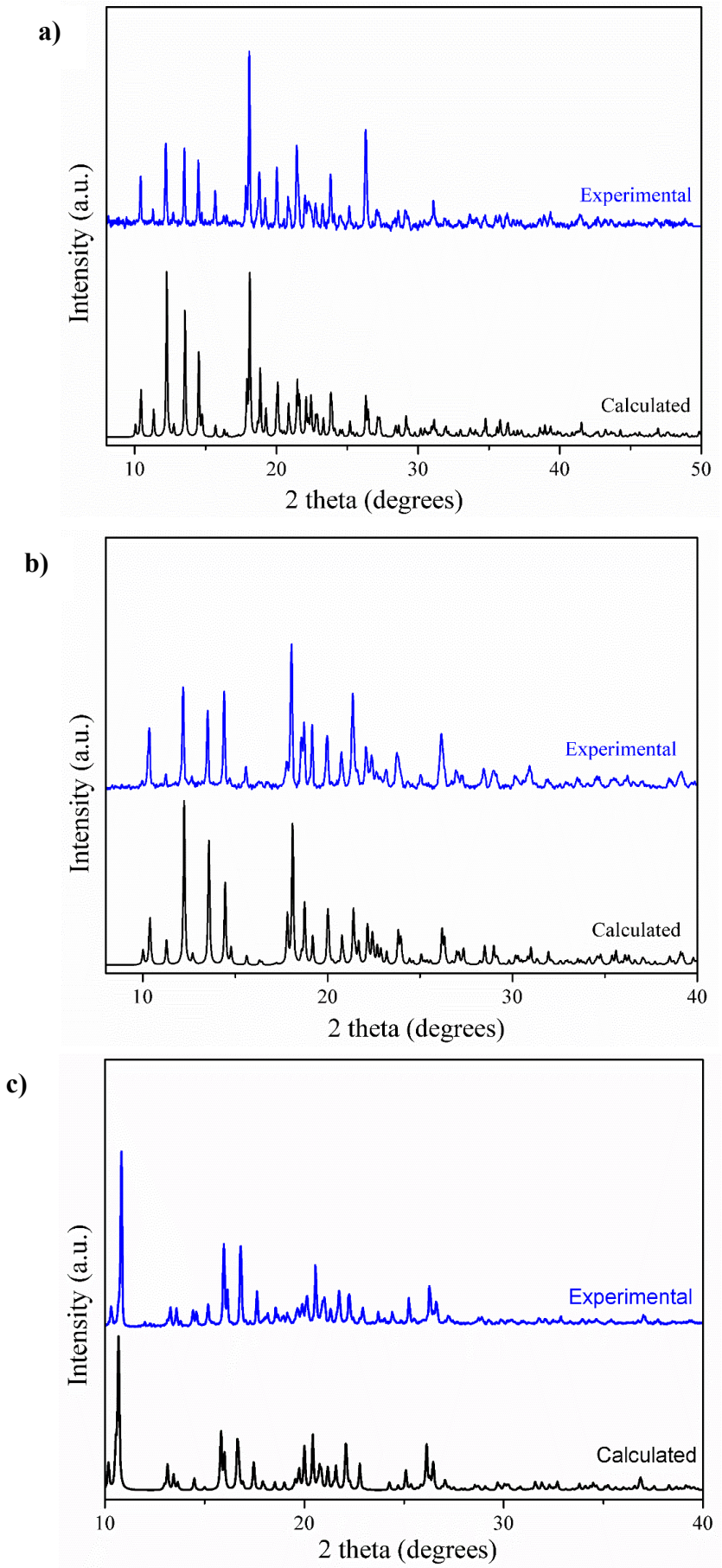

Figure 4.41 *The experimental and calculated PXRD patterns of* ***16*** *(a),* ***17****(b) and* ***18****(c).*

4.7.5 Crystal structures and geometrical analysis

Single crystals of compounds **12** and **13**, suitable for X-ray crystallography, were grown by diffusion of diethyl ether into their solutions of acetonitrile. The technical details of data acquisition and selected refinement results for **12** and **13** are listed in **Table 4.11**. The chosen bond lengths and bond angles for **12** and **13** are collated in **Table 4.12** and **Table 4.14**. In our X-ray structural analysis, both the compounds **12** and **13** are seen to crystallize in monoclinic crystal system with space group $P2_1/c$.

In compound **12**, the asymmetric unit features an octahedral arrangement around Ni(II) cation with, **L6** acting as pentadentate ligand, accompanied by an acetonitrile molecule coordinated to the nickel ion (**Figure 4.42**). Ni(II) is hexacoordinate in a moderately distorted octahedral N_5S environment with two nearly linear *trans* N–Ni–N pairs (N4–Ni–N2 176.24°, N5–Ni–N3 174.01°) and a bent, elongated axis N(1)–Ni–S(1) pair (165.09°, Ni–S 2.439 Å). Average deviation of the three *trans* angles from 180° is (3.76 + 5.99 + 14.91)/3 ~ 8.2°, with the N(1)–S(1) pair dominating. All 12 *cis* angles span from 80.43–99.47°. The octahedral angular distortion parameter Σ (sum of $|90 - \theta|$ over the 12 *cis* angles) ~ 54.9° [94,95]. This reflects a moderate angular distortion, driven mainly by compressed angles, opposite expanded angles imposed by ligand chelation and by the longer Ni–S axis. Ni–N distances vary from 2.063–2.118 Å. Ni–S bond is distinctly longer at 2.439 Å, which is in consistent with the larger covalent radius of sulfur and a softer, more weakly donating thioether donor relative to the amine/pyridyl nitrogens.

The crystal structure of **13** bears a resemblance to that of compound **12**, and it also shows that the pentadentate ligand **L7** coordinates in the way it was envisioned, with an acetonitrile molecule occupying the sixth coordination site on the nickel ion (**Figure 4.44**). The distorted octahedral N_5S environment is seen to exhibit one nearly linear *trans* axis, N1–Ni–N3 (175.13°), whereas the other two nominally *trans* pairs (N5···N2 at 163.22°, N4···S1 at 162.32°) are both appreciably bent. The *cis* angles range from 77.91–104.24°. The octahedral angular distortion parameter is approximately 79°. The increased octahedral angular distortion (~79° in **13**; ~55° in **12**) and larger *cis* angle span (77.9–104.2° in **13**; 80.4–99.5° in **12**) in compound **13** indicate higher octahedral distortion compared with moderate distortion in **12**. Compressed bite angles (~78–79°) in **13** are more acute than any in **12** (~80.4° minimum), implying tighter chelate rings or stronger geometric constraints; this follows opposing *cis* expansions to >100° due to geometric compensation. The simultaneous bending of two *trans* axes in **13** suggests a redistribution

of strain across the coordination sphere rather than localization at a single soft donor axis. Ni–N distances range from 2.052–2.227 Å which indicate a broader range compare to **12**. Ni–S distances are essentially identical (2.439 Å in **12**; 2.441 Å in **13**), so the soft donor itself is not appreciably weakened or strengthened between the structures. The nearly linear *trans* N3–Ni–$N5_{solvent}$ pair in compound **12** (174.01(14)°) is more strongly bent in **13** than the *trans* N2–Ni–$N5_{solvent}$ pair (163.22(11)°). Methylation of the two secondary amine donors to tertiary amines induces pronounced steric and conformational strain elevating the overall octahedral distortion.

Table 4.11 *Details of crystal data and structure refinement parameters of* ***12*** *and* ***13****.*

Compound	**12**	**13**
Empirical formula	C_{18} H_{25} Cl_2 N_5 Ni O_8 S	C_{20} H_{29} Cl_2 N_5 Ni O_8 S
Formula weight	601.08	629.13
Temperature	296(2) K	296(2) K
Wavelength	0.71073 Å	0.71073 Å
Crystal system	Monoclinic	Monoclinic
Space group	$P2_1/c$	$P2_1/c$
Unit cell dimensions	a = 13.7042(10) Å b = 16.8231(11) Å c = 11.2853(7) Å α = 90° β = 110.023(2)° γ = 90°	a = 14.0791(6) Å b = 18.3717(8) Å c = 11.0549(4)Å α = 90° β = 112.3820(10)° γ = 90°
Volume	2444.5(3) $Å^3$	2644.01(19) $Å^3$
Z	4	4
Density (calculated)	1.633 mg/m^3	1.581 mg/m^3
Absorption coefficient	1.152 mm^{-1}	1.069 mm^{-1}
F(000)	1240	1304
Theta range for data collection	2.361 to 28.399°	2.280 to 28.418°
Completeness to theta	99.9%	99.9%
Index ranges	-18<=h<=18 -22<=k<=22 -15<=l<=14	-18<=h<=18 -24<=k<=24 -14<=l<=14
Reflections collected	70401	63322
Independent reflections	6106 [R(int) = 0.0672]	6612 [R(int) = 0.0443]
Refinement method	Full-matrix least-squares on F^2	Full-matrix least-squares on F^2
Absorption correction	Semi- empirical from equivalents	Semi- empirical from equivalents
Data/restraints/parameters	6106 / 0 / 320	6612 / 0 / 337
Goodness-of-fit on F^2	1.034	1.044
Final *R*indices[I>2sigma(I)]	R1= 0.0587, wR2= 0.1473	R1= 0.0548, wR2= 0.1587
R indices (all data)	R1= 0.0930, wR2= 0.1652	R1= 0.0694, wR2= 0.1694
CCDC No.	2386750	2386749

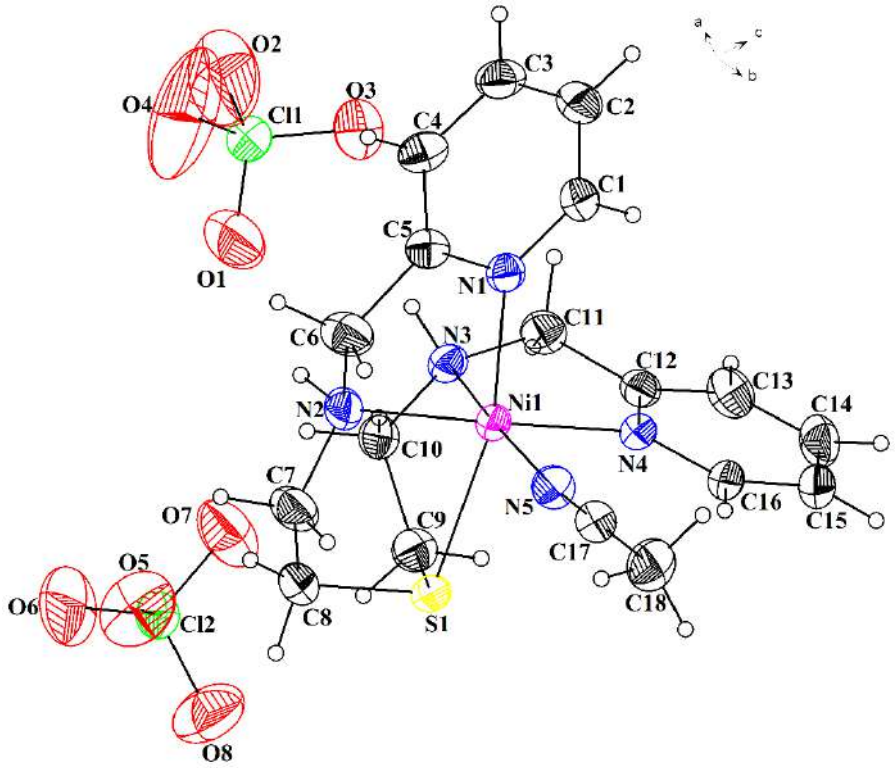

Figure 4.42 *Crystal structure of* ***12*** *showing atom labelling scheme. The thermal ellipsoids are drawn at a 30 % probability level for all the atoms except for the H atoms, which are shown as spheres of arbitrary radii.*

Table 4.12 *Selected bond lengths (Å) and angles (°) for* ***12****.*

Bond lengths (Å)			
N(1)-Ni(1)	2.069(3)	N(4)-Ni(1)	2.063(3)
N(2)-Ni(1)	2.083(3)	N(5)-Ni(1)	2.107(3)
N(3)-Ni(1)	2.118(3)	Ni(1)-S(1)	2.4394(11)
Bond angles (°)			
N(4)-Ni(1)-N(1)	99.47(12)	N(3)-Ni(1)-S(1)	86.33(9)
N(4)-Ni(1)-N(2)	176.24(14)	N(5)-Ni(1)-S(1)	92.67(10)
N(1)-Ni(1)-N(2)	80.43(13)	N(2)-Ni(1)-S(1)	84.85(9)
N(4)-Ni(1)-N(5)	92.60(13)	N(1)-Ni(1)-S(1)	165.09(9)
N(1)-Ni(1)-N(5)	89.97(13)	N(4)-Ni(1)-S(1)	95.07(9)
N(2)-Ni(1)-N(5)	91.16(15)	N(5)-Ni(1)-N(3)	174.01(14)
N(4)-Ni(1)-N(3)	81.62(13)	N(2)-Ni(1)-N(3)	94.63(15)
N(1)-Ni(1)-N(3)	92.50(13)		

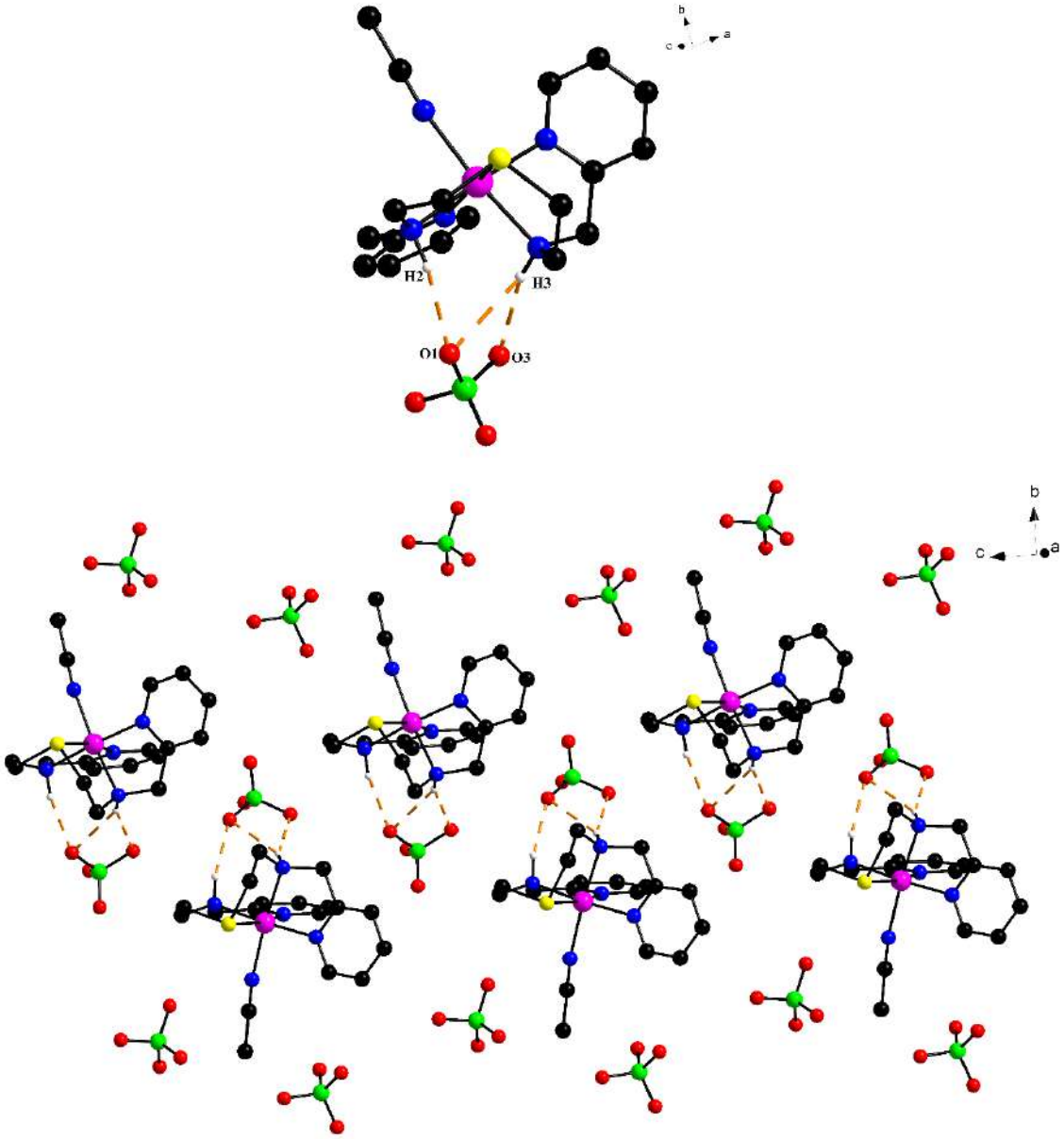

Figure 4.43 *The hydrogen bonding interactions in* ***12*** *with atom labelling scheme of atoms involved in hydrogen bonding; along with the enlarged view of a network of hydrogen bonding in* ***12*** *showing the symmetric organisation of* $[Ni(L6)(CH_3CN)]^{2+}$ *cations and perchlorate anions. Hydrogen atoms attached to carbon are omitted for clarity.*

Table 4.13 *Hydrogen bonding parameters (Å, º) for* ***12****.*

D-H···A	D-H/ Å	H···A/ Å	D···A/ Å	D-H···A/º	Symmetry code
N2-H2···O1	0.980(0)	2.184(1)	3.096(0)	154.15(0)	x, y, z
N3-H3···O1	0.874(0)	2.521(1)	3.271(1)	144.39(1)	x, y, z
N3-H3···O3	0.874(0)	2.353(2)	3.191(2)	160.75(1)	x, y, z

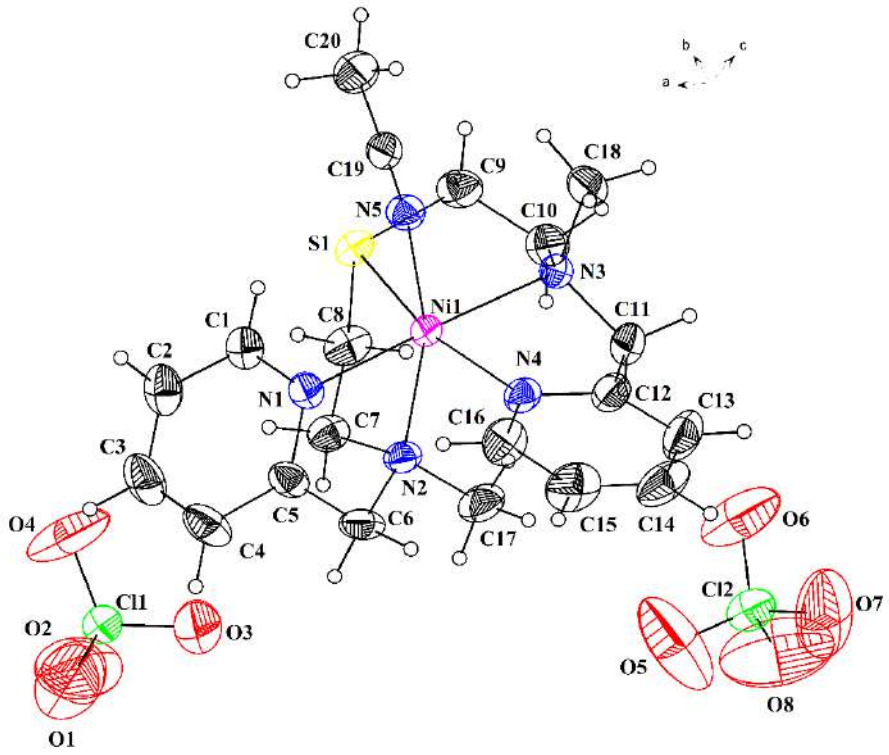

Figure 4.44 *Crystal structure of* ***13*** *showing atom labelling scheme. The thermal ellipsoids are drawn at a 30 % probability level for all the atoms except for the H atoms, which are shown as spheres of arbitrary radii.*

Table 4.14 *Selected bond lengths (Å) and angles (°) for* ***13****.*

Bond lengths (Å)			
N(1)-Ni(1)	2.118(3)	Ni(1)-S(1)	2.4413(9)
N(2)-Ni(1)	2.227(3)	N(5)-Ni(1)	2.105(3)
N(3)-Ni(1)	2.182(3)	N(4)-Ni(1)	2.052(3)
Bond angles (°)			
N(4)-Ni(1)-N(5)	96.41(12)	N(2)-Ni(1)-S(1)	84.00(7)
N(4)-Ni(1)-N(1)	96.29(11)	N(3)-Ni(1)-S(1)	84.16(9)
N(5)-Ni(1)-N(1)	87.96(11)	N(1)-Ni(1)-S(1)	100.47(7)
N(4)-Ni(1)-N(3)	79.27(12)	N(5)-Ni(1)-S(1)	89.80(9)
N(5)-Ni(1)-N(3)	90.56(11)	N(4)-Ni(1)-S(1)	162.32(9)
N(1)-Ni(1)-N(3)	175.13(11)	N(3)-Ni(1)-N(2)	104.24(11)
N(4)-Ni(1)-N(2)	94.12(11)	N(1)-Ni(1)-N(2)	77.91(11)
N(5)-Ni(1)-N(2)	163.22(11)		

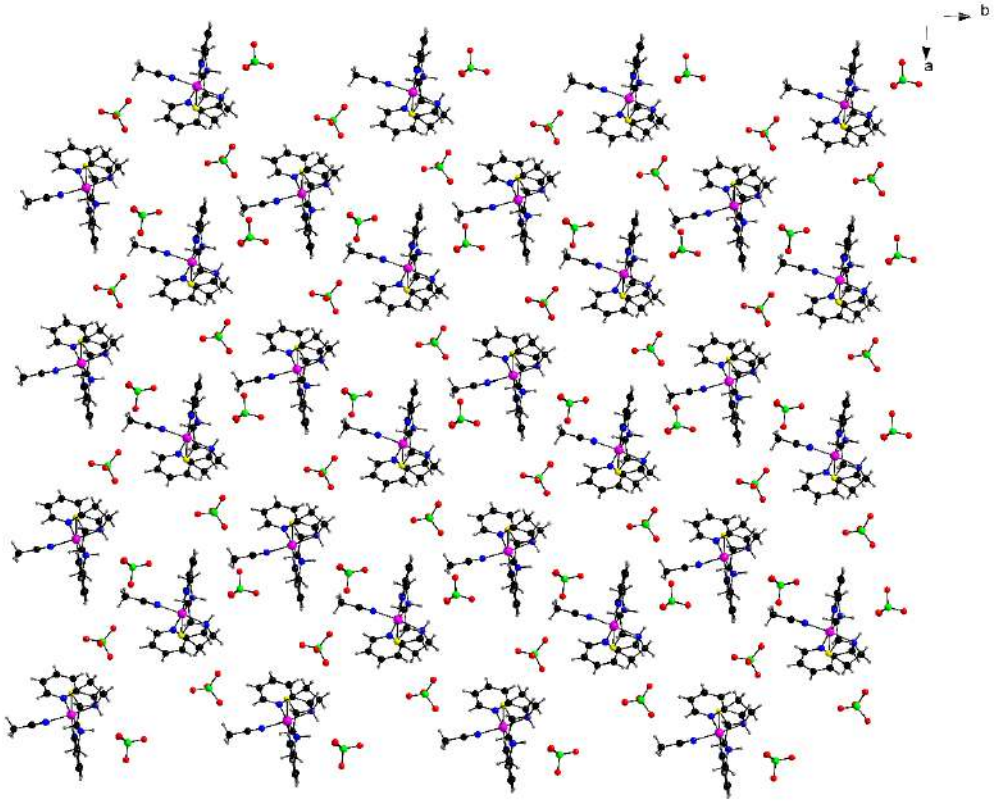

Figure 4.45 *Packing in* ***12*** *view along crystallographic c axis. Colour code: C, black; H, medium grey; N, blue; O, red; Cl, green and Ni, purple.*

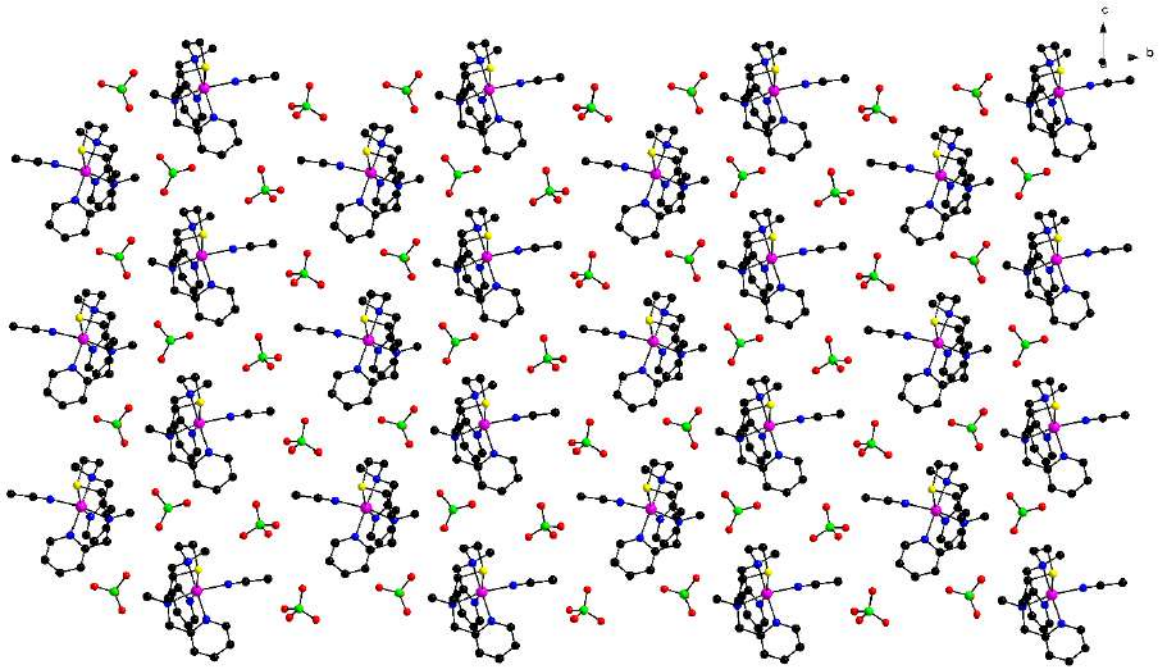

Figure 4.46 *Packing in* ***13*** *view along crystallographic a axis. Colour code: C, black; N, blue; O, red; Cl, green and Ni, purple.*

Single crystals suitable for X-ray analysis were grown for compounds **14** and **15** by the classic vapor diffusion method: an acetonitrile solution of each compound was left undisturbed at 298 K yielding colorless block shaped crystals. A comprehensive summary of the crystallographic experiment is provided in **Table 4.15**. For structural comparison, **Table 4.16** and **Table 4.18** compiles the most pertinent bond lengths and angles that diagnose the coordination geometry in each compound. Single crystal X-ray diffraction of compound **14** revealed that the compound crystallizes in the monoclinic space group $P2_1/n$. The asymmetric unit contains one cation, $[Mn(L6)(ClO_4)]^+$ and one outer sphere perchlorate anion. The X-ray data reveal that the manganese(II) ion, is hexacoordinate in a highly distorted N_4SO octahedral environment defined by four nitrogen atoms (N1–N4) and one thioether sulfur atom (S1) from the macrocyclic pentadentate ligand **L6** and a monodentate perchlorate oxygen (O5) (**Figure 4.47**). Mn–N distances range from 2.194(2) to 2.283(3) Å and Mn–O5 (2.236(2) Å) are typical for Mn^{2+} bound to neutral donors, whereas Mn–S1 is significantly longer at 2.6307(10) Å, reflecting the larger covalent radius and weaker σ donation of sulphur[96–100]. The three pseudo trans axes N4···N2 (170.9°), O5···N3 (156.0°) and S1···N1 (154.0°) deviate appreciably from 180°, and the *cis* angles span 75.4–109.8°, yielding octahedral angular distortion ~119°, a clear gauge of chelate induced strain. The outer-sphere perchlorate participates in weak N–H···O interactions with the cation unit.

Single crystal of compound **15** also adopts the monoclinic space group $P2_1/n$ under identical data collection conditions. The Mn(II) ion retains a distorted N_4SO octahedral environment in compound **15**, where the donor set comprises four nitrogen atoms (N1–N4), one thioether Sulphur (S1) from the ligand **L7**, and one aqua oxygen (O1) instead of coordinated perchlorate ion in **14** (**Figure 4.49**). The asymmetric unit contains one cation, $[Mn(L7)(H_2O)]^{2+}$ and two outer sphere perchlorate anions. The stronger σ donor character of H_2O contracts Mn–O1 to 2.158(3) Å (~ 0.08 Å shorter than Mn–$O(ClO_4)$ in **14** and lengthens its *trans* partner Mn–N3 to 2.324(3) Å. The average Mn–N distance increases slightly, while Mn–S1 elongates to 2.6460(11) Å, consistent with an enhanced trans influence from the opposite nitrogen. Three pseudo *trans* pairs organize the octahedron: N4–Mn–N2 = 174.53(12)°, O1–Mn–N3 = 156.64(14)° and N1–Mn–S1 = 152.93(9)°. None approaches the ideal 180°, signifying notable axial strain. The 12 *cis* angles span 74.85(11)–107.05(9)°. The angular distortion parameter 121.2° demonstrates slightly greater angular distortion than in the perchlorate bound analogue (Σ ~119.2°).

Table 4.15 *Technical details of crystal data and structure refinement parameters of* ***14*** *and* ***15****.*

Compound	**14**	**15**
Empirical formula	C_{16} H_{22} Cl_2 Mn N_4 O_8 S	C_{18} H_{28} Cl_2 Mn N_4 O_9 S
Formula weight	556.28	602.34
Temperature	296(2) K	296(2) K
Wavelength	0.71073 Å	0.71073 Å
Crystal system	Monoclinic	Monoclinic
Space group	$P2_1/n$	$P2_1/n$
Unit cell dimensions	a = 15.7989(6) Å b = 8.3617(3) Å c = 18.5820(6) Å α = 90° β = 113.2530(10)° γ = 90°	a = 8.3617(3) Å b = 17.1671(6) Å c = 17.9947(7) Å α = 90° β = 101.3170(10)° γ = 90°
Volume	2255.39(14) $Å^3$	2532.85(16) $Å^3$
Z	4	4
Density (calculated)	1.638 mg/m^3	1.580 mg/m^3
Absorption coefficient	0.966 mm^{-1}	0.869 mm^{-1}
F(000)	1140	1244
Theta range for data collection	2.712 to 28.468°	2.373 to 28.381°
Completeness to theta	99.9%	99.9%
Index ranges	-21<=h<=19 -11<=k<=11 -24<=l<=24	-11<=h<=11 -22<=k<=22 -24<=l<=24
Reflections collected	53919	62030
Independent reflections	5653 [R(int) = 0.0464]	6322 [R(int) = 0.0466]
Refinement method	Full-matrix least-squares on F^2	Full-matrix least-squares on F^2
Absorption correction	Semi- empirical from equivalents	Semi- empirical from equivalents
Data/restraints/parameters	5653 / 0 / 292	6322 / 3 / 331
Goodness-of-fit on F^2	1.054	1.065
Final *R*indices[I>2sigma(I)]	R1= 0.0512, wR2= 0.1350	R1= 0.0690, wR2= 0.1976
R indices (all data)	R1= 0.0723, wR2= 0.1463	R1= 0.0837, wR2= 0.2098
CCDC No.	2386740	2386744

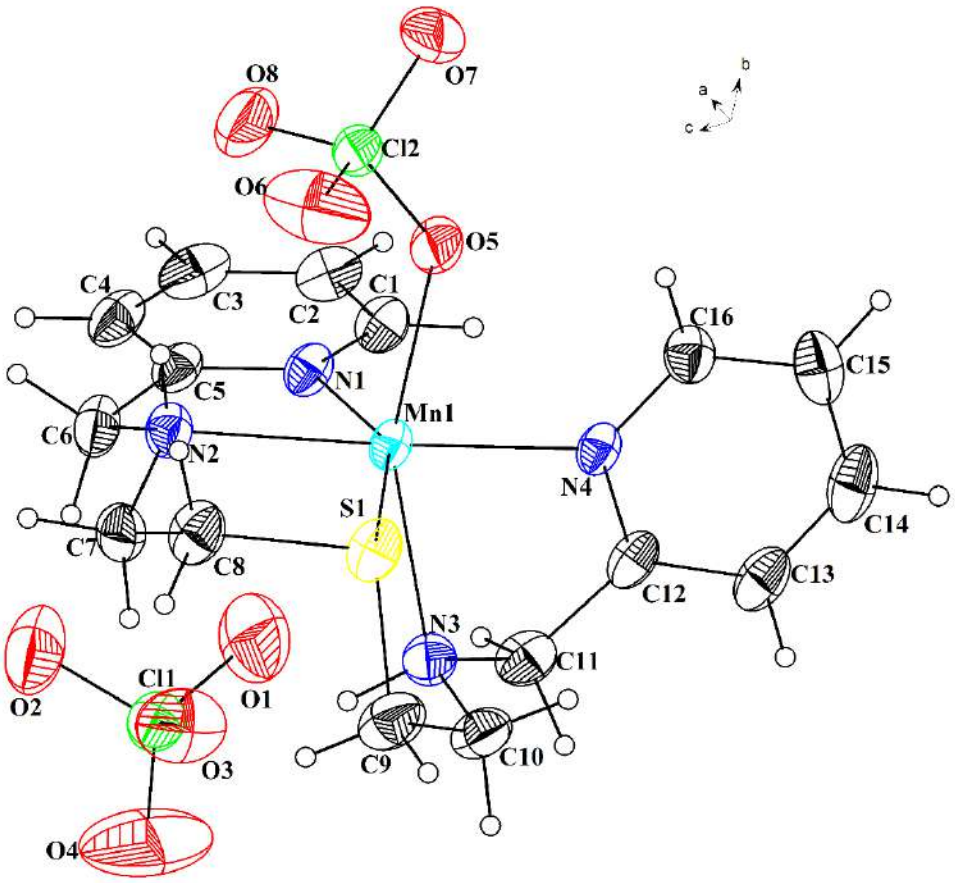

Figure 4.47 *Crystal structure of* ***14*** *showing atom labelling scheme. The thermal ellipsoids are drawn at a 30 % probability level for all the atoms except for the H atoms, which are shown as spheres of arbitrary radii.*

Table 4.16 *Selected bond lengths (Å) and angles (°) for* ***14****.*

Bond lengths (Å)			
N(1)-Mn(1)	2.194(2)	Mn(1)-N(3)	2.267(3)
Mn(1)-N(4)	2.220(2)	Mn(1)-N(2)	2.283(3)
Mn(1)-O(5)	2.236(2)	Mn(1)-S(1)	2.6307(10)
Bond angles (°)			
N(1)-Mn(1)-N(4)	95.53(9)	N(2)-Mn(1)-S(1)	79.18(8)
N(1)-Mn(1)-O(5)	95.05(11)	N(3)-Mn(1)-S(1)	79.54(8)
N(4)-Mn(1)-O(5)	86.50(9)	O(5)-Mn(1)-S(1)	92.20(8)
N(1)-Mn(1)-N(3)	102.22(10)	N(4)-Mn(1)-S(1)	109.82(7)
N(4)-Mn(1)-N(3)	75.43(10)	N(1)-Mn(1)-S(1)	154.01(7)
O(5)-Mn(1)-N(3)	155.98(10)	N(3)-Mn(1)-N(2)	105.58(11)
N(1)-Mn(1)-N(2)	75.36(10)	O(5)-Mn(1)-N(2)	94.78(10)
N(4)-Mn(1)-N(2)	170.88(10)		

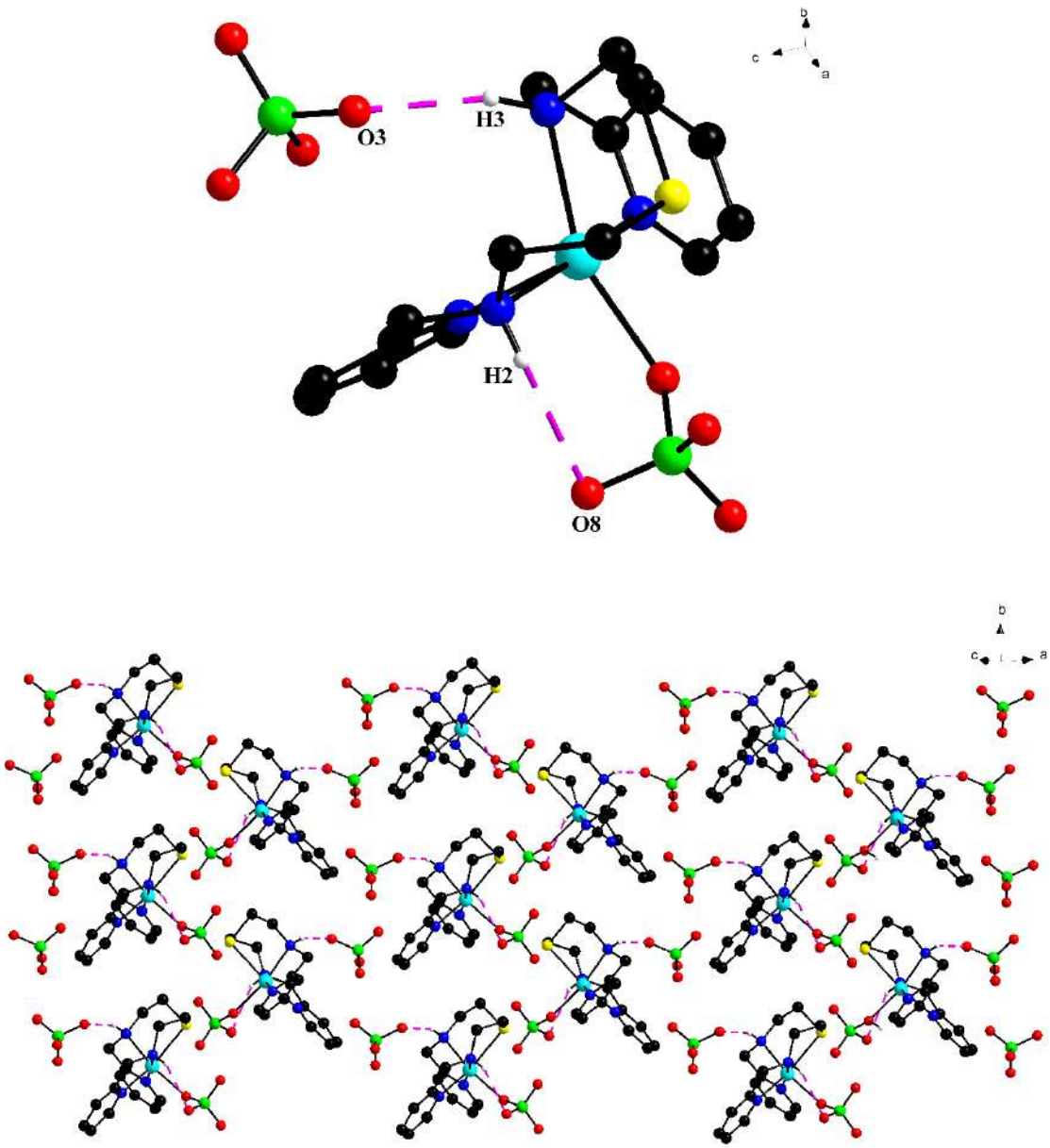

Figure 4.48 *The hydrogen bonding interactions in* ***14*** *with atom labelling scheme of atoms involved in hydrogen bonding; along with the enlarged view of a network of hydrogen bonding in* ***14*** *showing the symmetric organisation of* $[Mn(L6)(ClO_4)]^+$ *cations and perchlorate anions. Hydrogen atoms attached to carbon are omitted for clarity.*

Table 4.17 *Hydrogen bonding parameters (Å, °) for* ***14****.*

D-H···A	D-H/ Å	H···A/ Å	D···A/ Å	D-H···A/°	Symmetry code
N2-H2···O8	0.874(0)	2.509(0)	3.239(0)	141.51(0)	x, y, z
N3-H3···O3	0.980(0)	2.090(0)	3.014(1)	156.39(0)	x, y, z

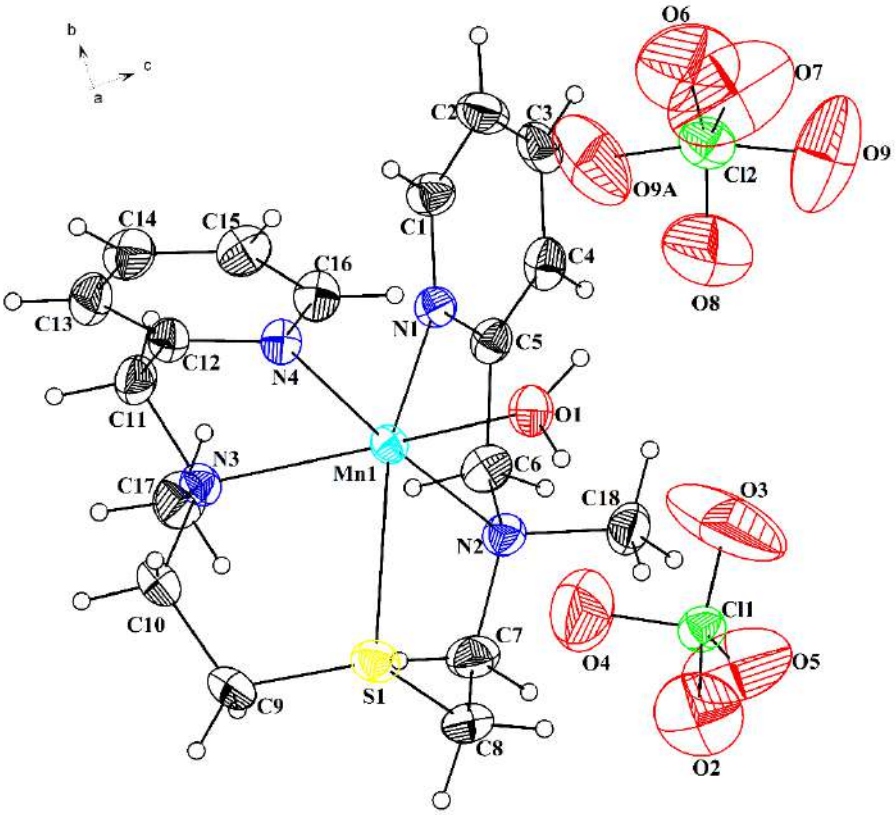

Figure 4.49 *Crystal structure of* ***15*** *showing atom labelling scheme. The thermal ellipsoids are drawn at a 30 % probability level for all the atoms except for the H atoms, which are shown as spheres of arbitrary radii.*

Table 4.18 *Selected bond lengths (Å) and angles (°) for* ***15****.*

Bond lengths (Å)			
N(1)-Mn(1)	2.217(3)	N(4)-Mn(1)	2.254(3)
N(2)-Mn(1)	2.346(3)	O(1)-Mn(1)	2.158(3)
N(3)-Mn(1)	2.324(3)	Mn(1)-S(1)	2.6460(11)
Bond angles (°)			
O(1)-Mn(1)-N(1)	94.36(13)	N(2)-Mn(1)-S(1)	78.41(8)
O(1)-Mn(1)-N(4)	86.64(13)	N(3)-Mn(1)-S(1)	79.66(8)
N(1)-Mn(1)-N(4)	99.45(12)	N(4)-Mn(1)-S(1)	107.05(9)
O(1)-Mn(1)-N(3)	156.64(14)	N(1)-Mn(1)-S(1)	152.93(9)
N(1)-Mn(1)-N(3)	102.51(12)	O(1)-Mn(1)-S(1)	92.64(9)
N(4)-Mn(1)-N(3)	74.85(11)	N(3)-Mn(1)-N(2)	106.30(12)
O(1)-Mn(1)-N(2)	93.49(13)	N(4)-Mn(1)-N(2)	174.53(12)
N(1)-Mn(1)-N(2)	75.09(11)		

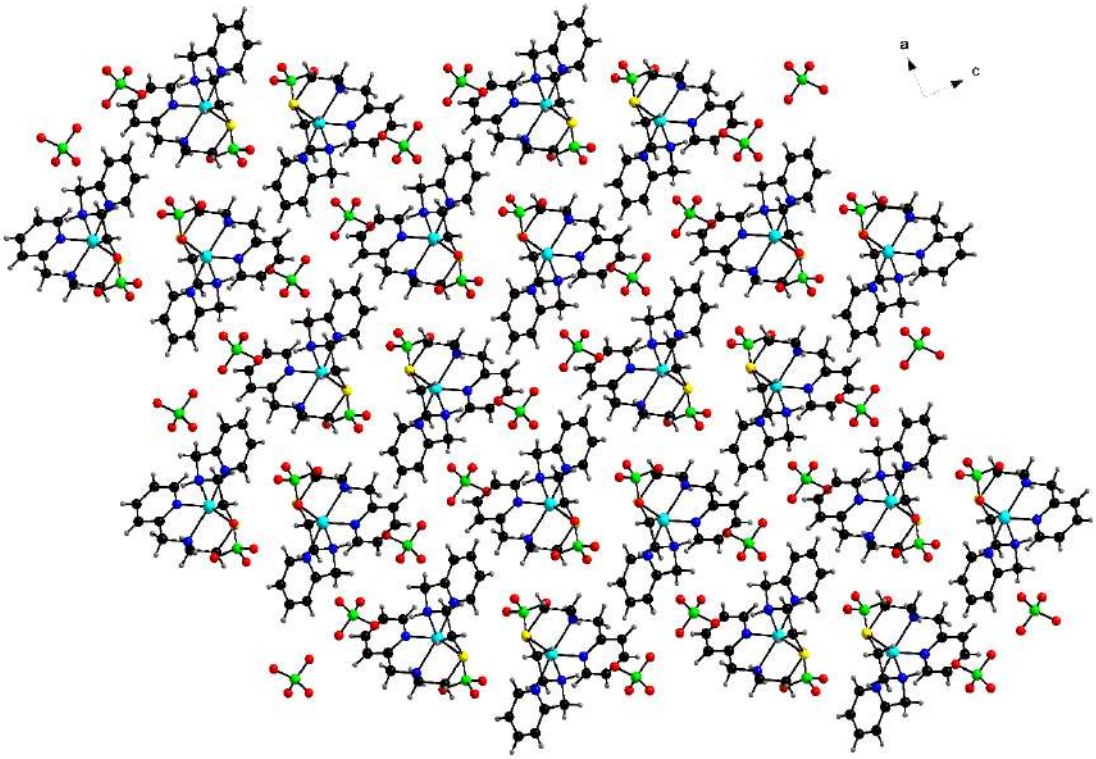

Figure 4.50 *Packing in* ***14*** *view along crystallographic c axis. Colour code: C, black; H, medium grey; N, blue; O, red; Cl, green and Mn, cyan.*

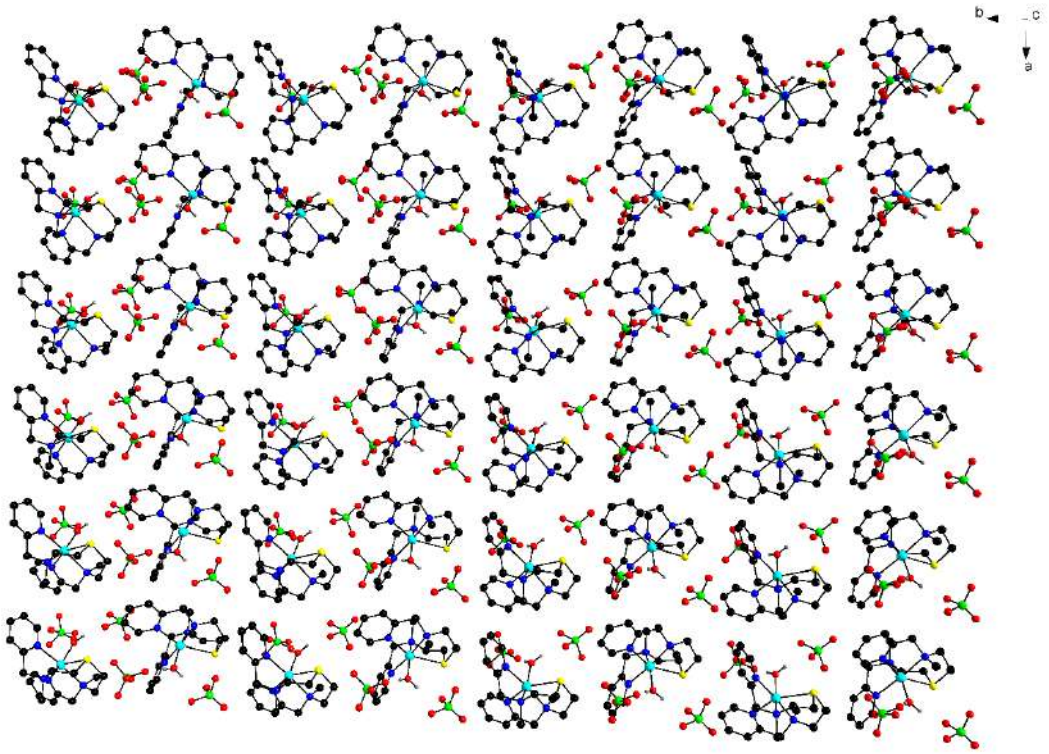

Figure 4.51 *Packing in* ***15*** *view along crystallographic c axis. Colour code: C, black; H, medium grey; N, blue; O, red; Cl, green and Mn, cyan.*

Crystals suitable for X-ray analysis of compounds **16** and **17** were prepared using the traditional vapor diffusion method, where an acetonitrile solution of each compound was left undisturbed at 298 K. The crystallographic experiment results are summarized comprehensively in **Table 4.19**. The data in **Table 4.20** and **Table 4.22** illustrates the key bond lengths and angles necessary for the structural comparison of the coordination geometry in each compound.

Single crystal X-ray diffraction confirms that the aqua ligated cobalt(II) compound **16** crystallizes as pink needles in the monoclinic space group $P2_1/c$ with one crystallographically unique cation and two perchlorate anions per asymmetric unit. In the asymmetric unit the unique mononuclear cation $[Co(L7)(H_2O)]^{2+}$ consist of a pentadentate N_4S chelate wrapped around a Co^{2+} center along with a coordinated water molecule, while two outer sphere perchlorate anions balance the charge (**Figure 4.52**). The metal is hexacoordinate and adopts a markedly distorted octahedral geometry. The distances between Co and the tertiary amine nitrogen's N2 and N3 are 2.225(3) and 2.241(3) Å respectively, whereas the pyridyl nitrogen atoms N1 and N4 are 2.125(3) and 2.164(3)Å away from Co(II) ion. Co-S1 is significantly longer at 2.4675(12) Å, reflecting the larger covalent radius and weaker σ donation of Sulphur. The Co(II) ion is 2.111(3) Å distant to the oxygen of water O1, as documented in **Table 4.20**. Three nearly linear *trans* sets O(1) –Co(1)–N(3) 159.0°, N(4)–Co(1)–N(2) 174.0° and N(1)–Co(1)–S(1) 160.3° define the pseudo-octahedron, while the 12 *cis* angles span from 75.9 to 108.0°. Summing the deviations $|90 - \theta|$ for those *cis* angles gives $\Sigma \sim 95°$, signaling a moderately large distortion that originates from the differing bite angles of five and six membered chelate rings plus the longer Co–S bond.

The inner sphere water ligand is positioned to form hydrogen bonding with neighboring perchlorate oxygens, a motif that usually stabilizes the lattice and can facilitate ligand exchange in solution. The two unique perchlorate ions in compound **16** display an extensive network of hydrogen bonding. The predominant intermolecular H-bonding interactions arising from O1–H1A···O4, O1–H1B···O2 and O1–H1B···O3 renders additional stability to compound **16** (**Figure 4.53** and **Table 4.21**). The oxygen atoms: O1, O2, O3 and O4, of the $(ClO_4)^-$ units are engaged in O–H···O interactions resulting in an extended network in compound **16** (**Figure 4.53**). Two O–Cl–O and two H–O–H molecules are connected to create a 12-membered ring structure through hydrogen bonds within compounds **16**. Structural data clearly indicates that the primary source of hydrogen

bonding is the coexistence of a water molecule and perchlorate counter ions in compounds **16**. The coordinated water in compound **16** can be accounted for despite the use of acetonitrile as the solvent, due to the use of metal perchlorate hexahydrates in the synthesis process. The crystal packing is dominated by an extensive hydrogen bonding ribbon: each coordinated water molecule forms O–H···O interactions to two perchlorate oxygen atoms, while the perchlorate anions participate in supplementary C–H···O contacts that assemble the cationic units into corrugated layers.

X-ray diffraction reveals that compounds **16** and **17** are isostructural, both adopting a $P2_1/c$ monoclinic lattice. The crystal structures of both compounds feature a centrally positioned metal(II) ion, specifically Zinc(II) in compound **17** and cobalt(II) in compound **16**, along with a pentadentate **L7** ligand and a water molecule, as well as two crystallographically independent perchlorate ions, as depicted in **Figure 4.52** and **Figure 4.54**. Zn-N distances range from 2.124(3) to 2.260(3) Å and Zn–O is 2.156(4) Å, whereas Zn–S is significantly longer at 2.5139(13) Å, reflecting the soft donor nature of sulfur atom. The three pseudo *trans* axes N4–Zn–N2 (174.1°), O9–Zn–N3 (158.4°) and S1–Zn–N1 (159.5°) deviate appreciably from 180°, and the *cis* angles span from 76.0–107.8°, yielding octahedral angular distortion ~97°, a clear gauge of chelate induced strain[101]. Comparable metrics in the cobalt analogue confirm that the two compounds are structurally congruent, differing chiefly in the metal donor bond lengths while preserving the same pattern of geometric distortion.

Figure 4.55 reveals that compound **17** assembles into an extended, three-dimensional lattice in which the cationic coordination units, $[ZnN_4SO]^{2+}$, are tethered to their perchlorate counter ions through a network of Cl–O···H hydrogen bonds. A notable feature of this architecture is a cyclic aggregate in which two perchlorate anions and two water molecules engage in reciprocal O–H···O interactions to generate a twelve membered ring. Examination of the crystallographic parameters shows that these water and perchlorate contacts dominate the hydrogen bonding landscape, acting as the principal supramolecular glue that stitches neighboring cations and anions into a robust three-dimensional framework.

Table 4.19 *Technical details of crystal data and structure refinement parameters of* ***16*** *and* ***17****.*

Compound	**16**	**17**
Empirical formula	C_{18} H_{28} Cl_2 Co N_4 O_9 S	C_{18} H_{28} Cl_2 N_4 O_9 S Zn
Formula weight	606.33	612.79
Temperature	296(2) K	296(2) K
Wavelength	0.71073 Å	0.71073 Å
Crystal system	Monoclinic	Monoclinic
Space group	$P2_1/c$	$P2_1/c$
Unit cell dimensions	a = 9.2320(4) Å b = 33.8371(14) Å c = 8.3750(3) Å α = 90° β = 107.7810(10)° γ = 90°	a = 9.2425(5) Å b = 33.9977(18) Å c = 8.3584(4) Å α = 90° β = 107.297(2)° γ = 90°
Volume	2491.24(17) $Å^3$	2507.6(2) $Å^3$
Z	4	4
Density (calculated)	1.617 mg/m^3	1.623 mg/m^3
Absorption coefficient	1.043 mm^{-1}	1.331 mm^{-1}
F(000)	1252	1264
Theta range for data collection	2.611 to 28.342°	2.308 to 28.399°
Completeness to theta	99.9%	100.0%
Index ranges	-12<=h<=12 -45<=k<=45 -11<=l<=11	-12<=h<=12 -45<=k<=45 -11<=l<=11
Reflections collected	71799	63548
Independent reflections	6203 [R(int) = 0.0604]	6265 [R(int) = 0.0604]
Refinement method	Full-matrix least-squares on F^2	Full-matrix least-squares on F^2
Absorption correction	Semi- empirical from equivalents	Semi- empirical from equivalents
Data/restraints/parameters	6203 / 0 / 324	6265 / 0 / 324
Goodness-of-fit on F^2	1.105	1.085
Final *R*indices[I>2sigma(I)]	R1= 0.0658, wR2= 0.1682	R1= 0.0664, wR2= 0.1672
R indices (all data)	R1= 0.0832, wR2= 0.1777	R1= 0.0870, wR2= 0.1789
CCDC No.	2386743	2386742

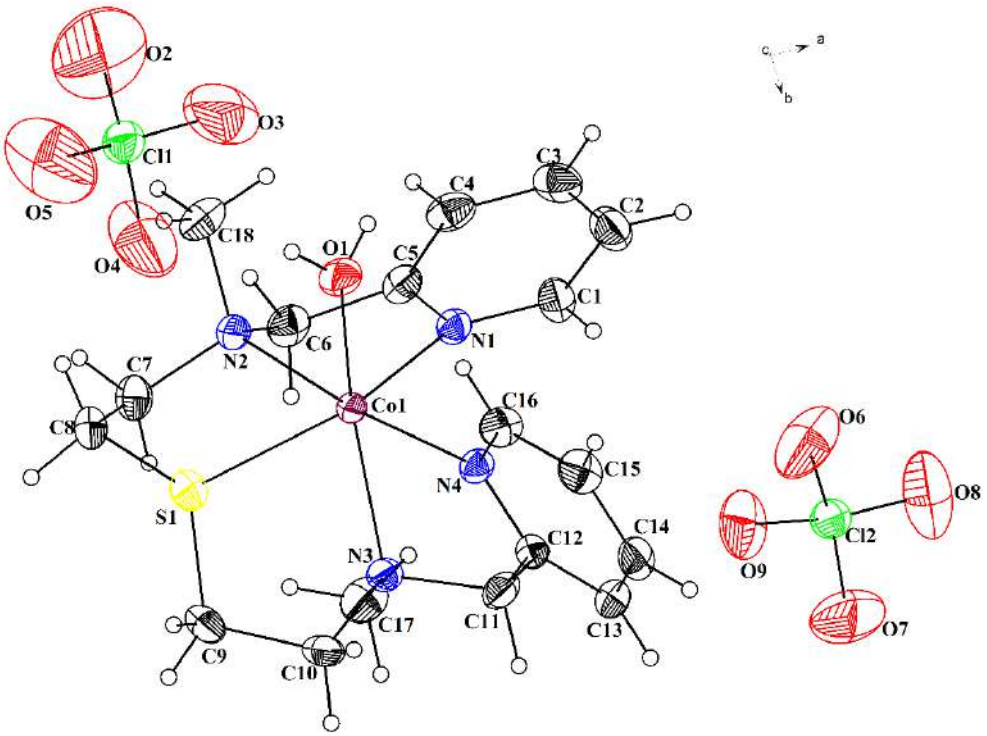

Figure 4.52 *Crystal structure of* ***16*** *showing atom labelling scheme. The thermal ellipsoids are drawn at a 30 % probability level for all the atoms except for the H atoms, which are shown as spheres of arbitrary radii.*

Table 4.20 *Selected bond lengths (Å) and angles (°) for* ***16****.*

Bond lengths (Å)			
N(1)-Co(1)	2.125(3)	N(4)-Co(1)	2.164(3)
N(2)-Co(1)	2.225(3)	S(1)-Co(1)	2.4675(12)
N(3)-Co(1)	2.241(3)	O(1)-Co(1)	2.111(3)
Bond angles (°)			
O(1)-Co(1)-N(1)	94.71(14)	N(3)-Co(1)-S(1)	83.91(9)
O(1)-Co(1)-N(4)	85.41(13)	N(2)-Co(1)-S(1)	82.88(9)
N(1)-Co(1)-N(4)	96.92(13)	N(4)-Co(1)-S(1)	102.32(9)
O(1)-Co(1)-N(2)	91.47(13)	N(1)-Co(1)-S(1)	160.31(9)
N(1)-Co(1)-N(2)	78.16(12)	O(1)-Co(1)-S(1)	90.99(11)
N(4)-Co(1)-N(2)	173.95(12)	N(2)-Co(1)-N(3)	108.00(12)
O(1)-Co(1)-N(3)	159.00(13)	N(4)-Co(1)-N(3)	75.88(11)
N(1)-Co(1)-N(3)	96.90(13)		

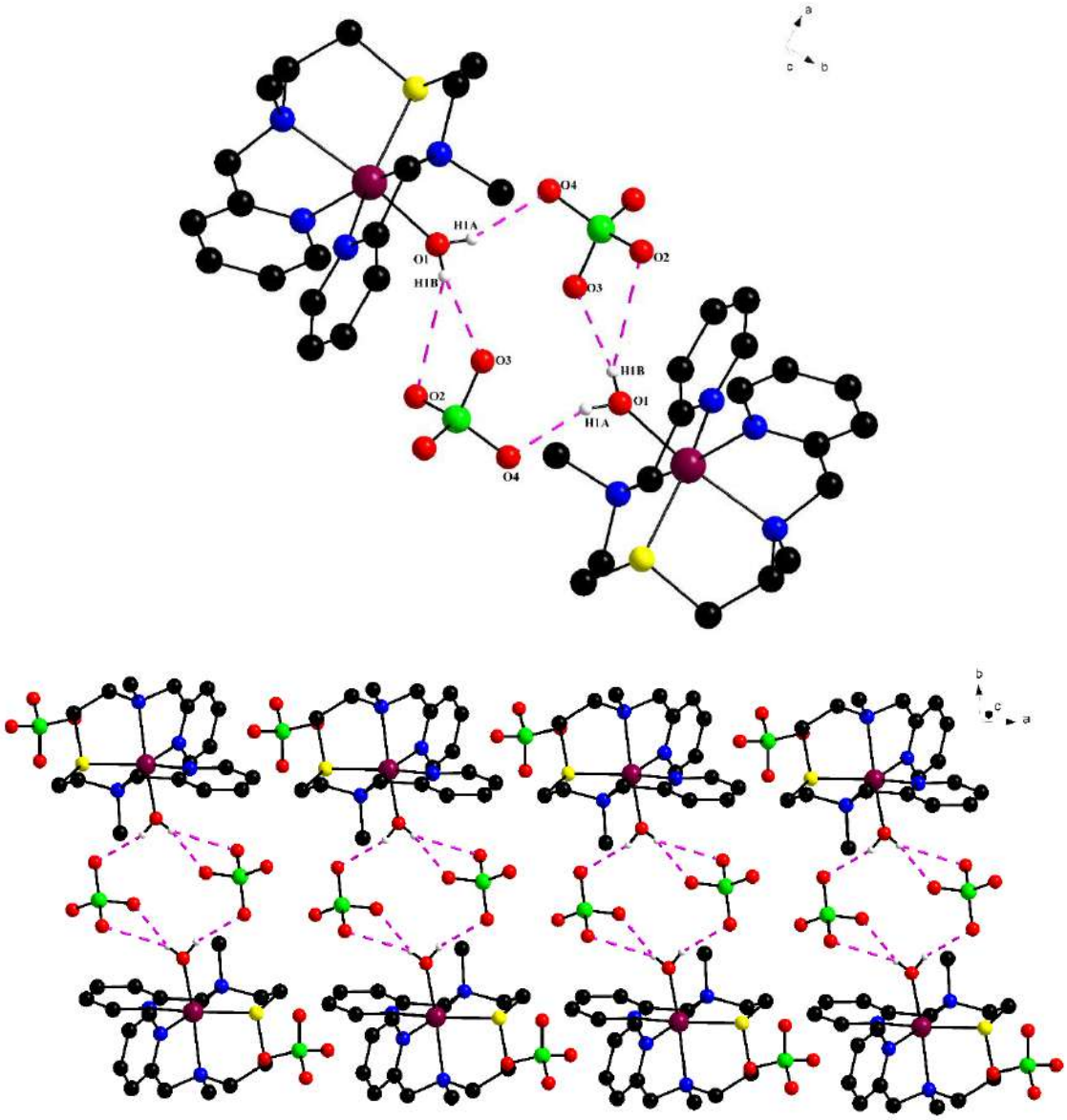

Figure 4.53 *The hydrogen bonding interactions in* ***16*** *with atom labelling scheme of atoms involved in hydrogen bonding; along with the enlarged view of a network of hydrogen bonding in* ***16*** *showing the symmetric organisation of* $[Co(L7)(H_2O)]^{2+}$ *cations and perchlorate anions. Hydrogen atoms attached to carbon are omitted for clarity.*

Table 4.21 *Hydrogen bonding parameters (Å, º) for* ***16****.*

D-H···A	D-H/ Å	H···A/ Å	D···A/ Å	D-H···A/º	Symmetry code
O1-H1A···O4	0.788(0)	2.067(1)	2.818(2)	159.53(0)	x, y, z
O1-H1B···O2	0.784(0)	2.653(0)	3.193(0)	127.65(0)	-x+1, -y+1, -z+1
O1-H1B···O3	0.784(0)	2.077(0)	2.846(1)	166.71(0)	-x+1, -y+1, -z+1

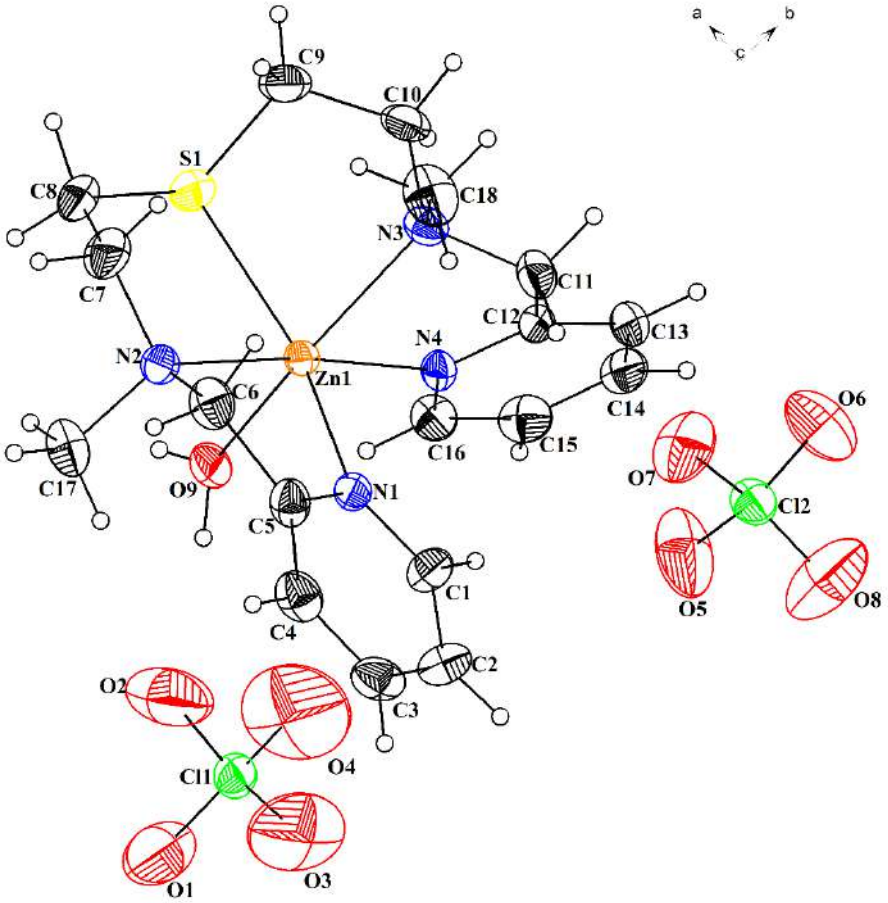

Figure 4.54 *Crystal structure of* ***17*** *showing atom labelling scheme. The thermal ellipsoids are drawn at a 30 % probability level for all the atoms except for the H atoms, which are shown as spheres of arbitrary radii.*

Table 4.22 *Selected bond lengths (Å) and angles (°) for* ***17****.*

Bond lengths (Å)			
N(1)-Zn(1)	2.124(3)	N(4)-Zn(1)	2.172(3)
N(2)-Zn(1)	2.260(3)	Zn(1)-O(9)	2.156(4)
N(3)-Zn(1)	2.258(4)	Zn(1)-S(1)	2.5139(13)
Bond angles (°)			
N(1)-Zn(1)-O(9)	94.54(15)	N(2)-Zn(1)-S(1)	82.32(10)
N(1)-Zn(1)-N(4)	97.57(13)	N(3)-Zn(1)-S(1)	83.83(11)
O(9)-Zn(1)-N(4)	85.36(14)	N(4)-Zn(1)-S(1)	102.75(10)
N(1)-Zn(1)-N(3)	98.56(14)	O(9)-Zn(1)-S(1)	89.87(12)
O(9)-Zn(1)-N(3)	158.44(15)	N(1)-Zn(1)-S(1)	159.49(10)
N(4)-Zn(1)-N(3)	76.03(13)	N(3)-Zn(1)-N(2)	107.83(14)
N(1)-Zn(1)-N(2)	77.55(13)	N(4)-Zn(1)-N(2)	174.08(13)
O(9)-Zn(1)-N(2)	91.64(14)		

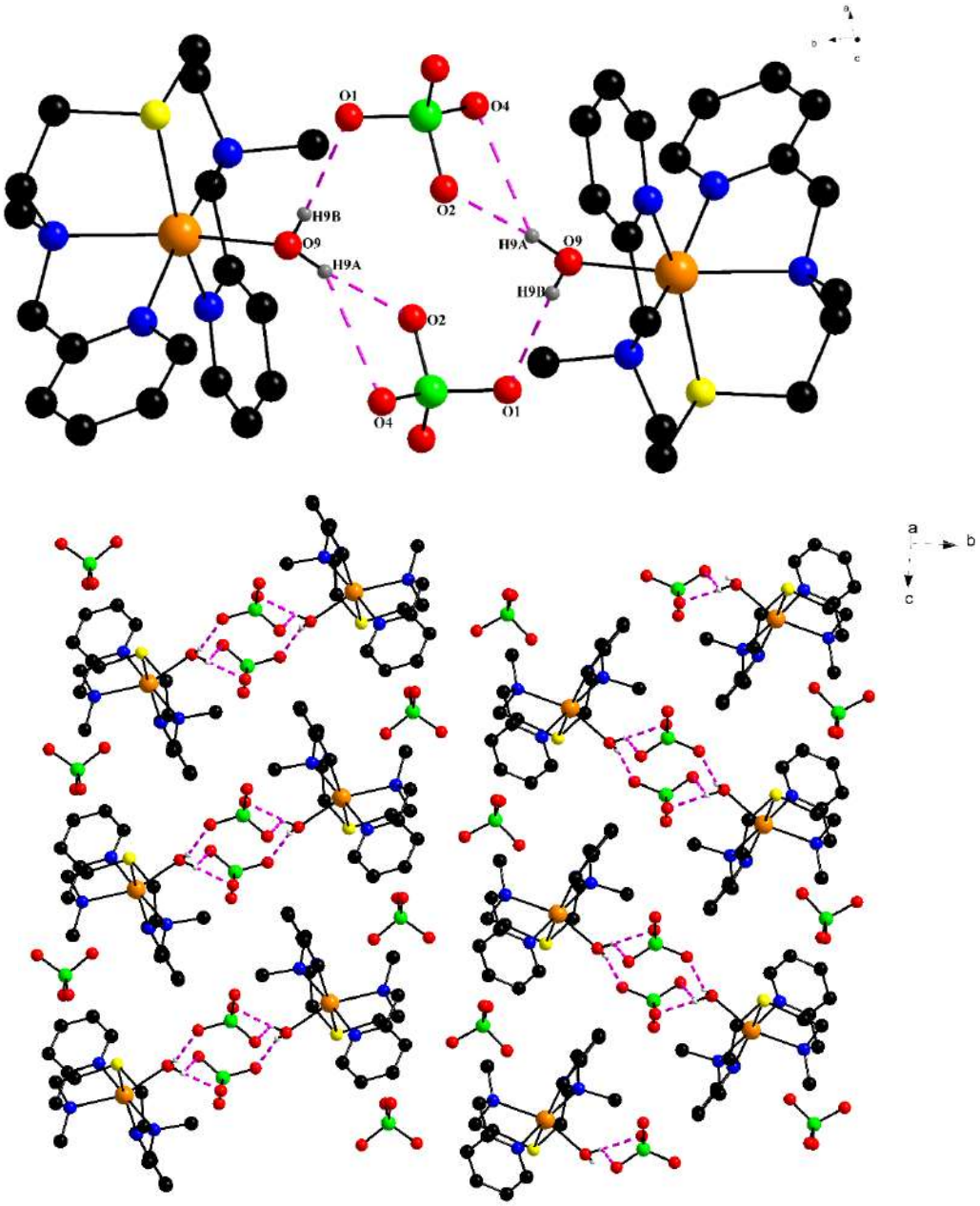

Figure 4.55 *The hydrogen bonding interactions in* ***17*** *with atom labelling scheme of atoms involved in hydrogen bonding; along with the enlarged view of a network of hydrogen bonding in* ***16*** *showing the symmetric organisation of* $[Zn(L7)(H_2O)]^{2+}$ *cations and perchlorate anions. Hydrogen atoms attached to carbon are omitted for clarity.*

Table 4.23 *Hydrogen bonding parameters (Å, º) for* ***17****.*

D-H···A	D-H/ Å	H···A/ Å	D···A/ Å	D-H···A/º	Symmetry code
O9-H9A···O2	0.873(0)	1.976(1)	2.844(1)	173.09(0)	x, y, z
O9-H9A···O4	0.873(0)	2.581(1)	3.234(0)	132.32(0)	x, y, z
O9-H9B···O1	0.659(1)	2.180(3)	2.824(3)	166.36(0)	-x+1, -y+1, -z+1

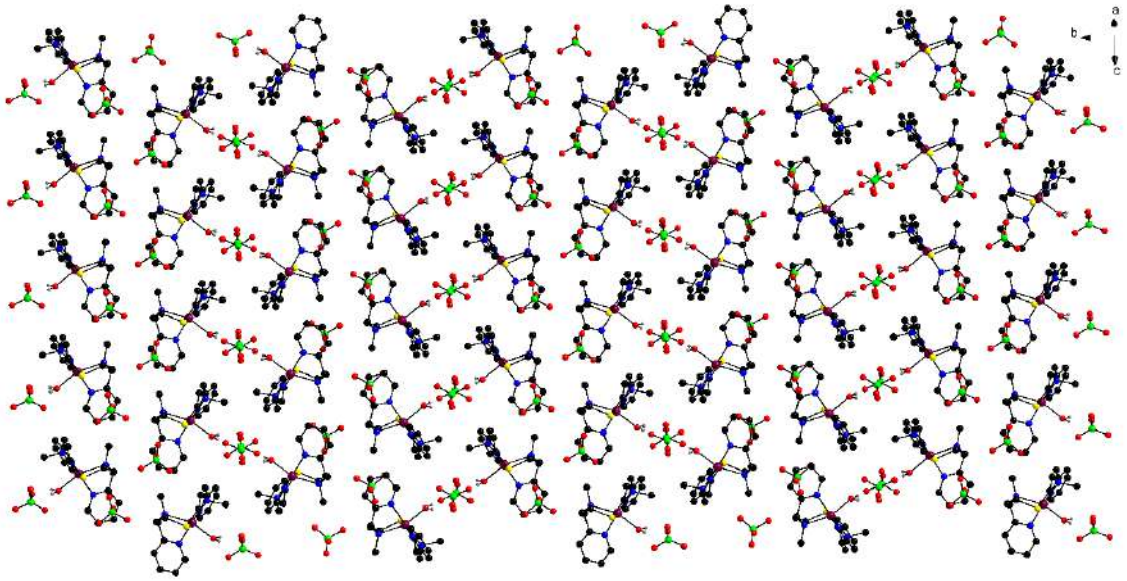

Figure 4.56 *Packing in* ***16*** *view along crystallographic a axis. Colour code: C, black; H, medium grey; N, blue; O, red; Cl, green and Co, magenta.*

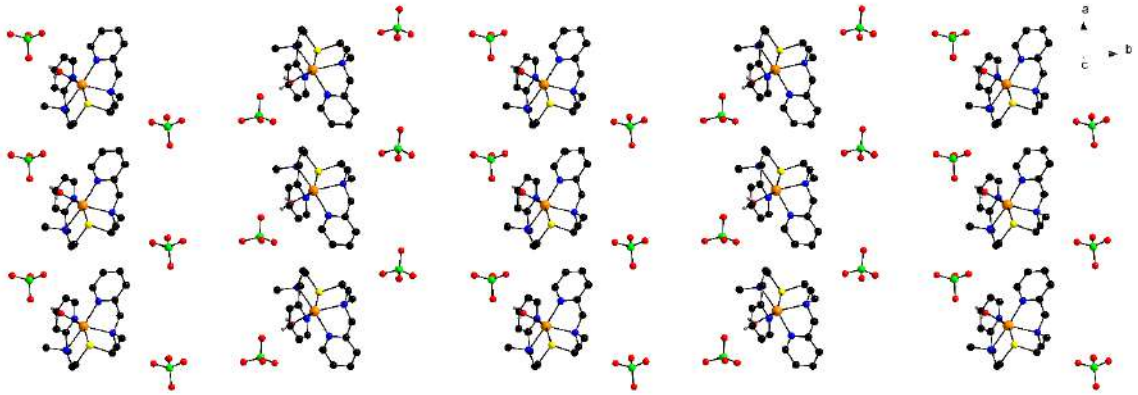

Figure 4.57 *Packing in* ***17*** *view along crystallographic c axis. Colour code: C, black; H, medium grey; N, blue; O, red; Cl, green and Zn, orange.*

Crystals of compound **18** suitable for X-ray diffraction were obtained by allowing a concentrated acetonitrile solution to undergo slow evaporation at 298 K. The full crystallographic parameters are detailed in **Table 4.24**, while the principal bond distances and angles used for evaluating coordination geometries are presented in **Tables 4.25**. Single-crystal X-ray analysis reveals that the Zn(II) compound crystallizes as colorless needle shaped crystals in the monoclinic space group $P2_1/c$, with one unique cation and two perchlorate anions in the asymmetric unit.

Single crystal X-ray diffraction of compound **18** establishes that the Zn^{2+} centre is ligated solely by the five nitrogen atoms of ligand **L3**, while the two perchlorate ions remain outside the coordination sphere (**Figure 4.58**). The metal ion therefore exhibits a five-coordinate [ZnN_5] environment that most closely resembles a distorted trigonal bipyramid. Using the Addison τ_5 descriptor, where $\tau_5 = (\beta - \alpha)/60$, the largest and second-largest N–Zn–N angles ($\beta = 170.06°$; $\alpha = 127.90°$) give $\tau_5 \sim 0.70$; this value places the structure nearer the trigonal bipyramidal limit ($\tau_5 = 1$) than the square pyramidal one ($\tau_5 = 0$)[102–105].The nearly linear N2–Zn–N4 angle of 170.06(12)° defines the axial positions, whereas N1, N3, and N5 occupy the equatorial plane with inter-ligand angles of 127.90(11)°, 119.57(11)° and 112.53(11)°, respectively. Deviation from the ideal 120° arises from the chelate bite constraints of the ligand backbone; the tightest cis angle, N4–Zn–N5 = 78.05(11)°, reflects strain within a five-membered chelate ring.

In compound 18, both crystallographically distinct perchlorate anions are integrated into an extensive hydrogen-bonding framework. Key N–H···O interactions, specifically N2–H1B···O6 and N4–H4···O3, contribute significantly to the stabilization of the structure (**Figure 4.59**; **Table 4.26**). The O3 and O6 atoms of the perchlorate groups further engage in N–H···O contacts, propagating a continuous hydrogen bonded network throughout the crystal lattice (**Figure 4.60**).

Table 4.24 *Technical details of crystal data and structure refinement parameters of* ***18****.*

Compound	**18**
Empirical formula	C_{19} H_{29} Cl_2 Zn N_5 O_8
Formula weight	591.76
Temperature	296(2) K
Wavelength	0.71073 Å
Crystal system	Monoclinic
Space group	$P2_1/c$
Unit cell dimensions	a = 14.1849(14) Å b = 10.6449(11) Å c = 18.0664(18) Å α = 90° β = 111.903(3)° γ = 90°
Volume	2531.1(4) $Å^3$
Z	4
Density (calculated)	1.553 mg/m^3
Absorption coefficient	1.234 mm^{-1}
F(000)	1224
Theta range for data collection	2.266 to 28.418°
Completeness to theta	100.0 %
Index ranges	-18≤ h ≤18 -14≤ k≤14 -24≤ l≤24
Reflections collected	67145
Independent reflections	6328 (R_{int}= 0.0459)
Refinement method	Full-matrix least-squares on F^2
Absorption correction	Semi- empirical from equivalents
Data/restraints/parameters	6328 / 0 / 320
Goodness-of-fit on F^2	1.069
Final *R*indices[I>2sigma(I)]	R1= 0.0545, wR2= 0.1487
R indices (all data)	R1= 0.0741, wR2= 0.1607
CCDC No.	2386741

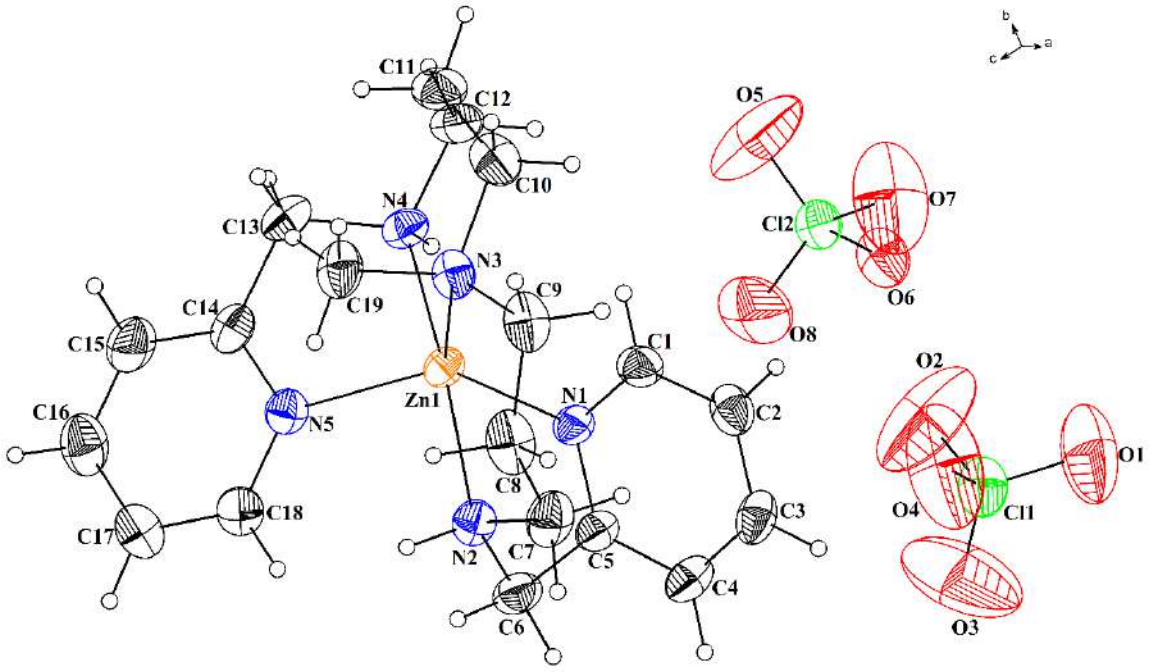

Figure 4.58 *Crystal structure of* ***18*** *showing atom labelling scheme. The thermal ellipsoids are drawn at a 30 % probability level for all the atoms except for the H atoms, which are shown as spheres of arbitrary radii.*

Table 4.25 *Selected bond lengths (Å) and angles (°) for* ***18****.*

Bond lengths (Å)			
Zn(1)-N(1)	2.106(3)	Zn(1)-N(4)	2.145(3)
Zn(1)-N(3)	2.117(3)	Zn(1)-N(5)	2.150(3)
Zn(1)-N(2)	2.142(3)		
Bond angles (°)			
N(1)-Zn(1)-N(3)	127.90(11)	N(2)-Zn(1)-N(4)	170.06(12)
N(1)-Zn(1)-N(2)	79.30(11)	N(1)-Zn(1)-N(5)	112.53(11)
N(3)-Zn(1)-N(2)	96.04(12)	N(3)-Zn(1)-N(5)	119.57(11)
N(1)-Zn(1)-N(4)	96.52(11)	N(2)-Zn(1)-N(5)	95.11(12)
N(3)-Zn(1)-N(4)	93.64(12)	N(4)-Zn(1)-N(5)	78.05(11)

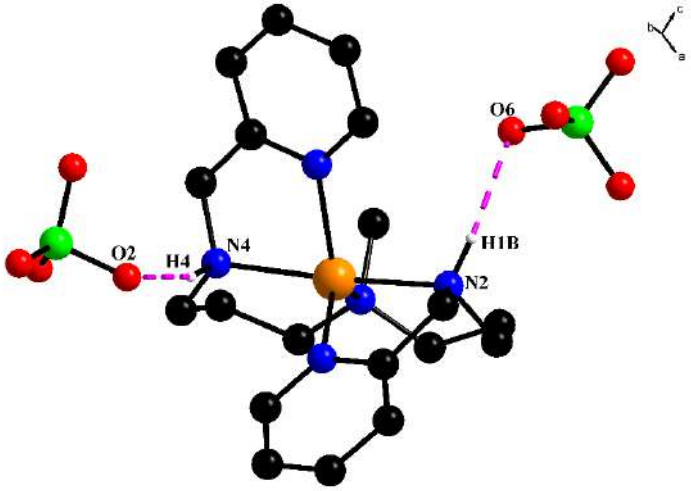

Figure 4.59 *The hydrogen bonding interactions in* ***18*** *with atom labelling scheme of atoms involved in hydrogen bonding. Hydrogen atoms attached to carbon are omitted for clarity.*

Table 4.26 *Hydrogen bonding parameters (Å, º) for* ***18****.*

D-H···A	D-H/ Å	H···A/ Å	D···A/ Å	D-H···A/º	Symmetry code
N2-H1B···O6	0.944(0)	2.349(0)	3.247(0)	158.74(0)	x, 3/2-y, 1/2+z
N4-H4···O3	0.980(0)	2.055(0)	3.013(1)	165.37(0)	-x, 1-y, 1-z

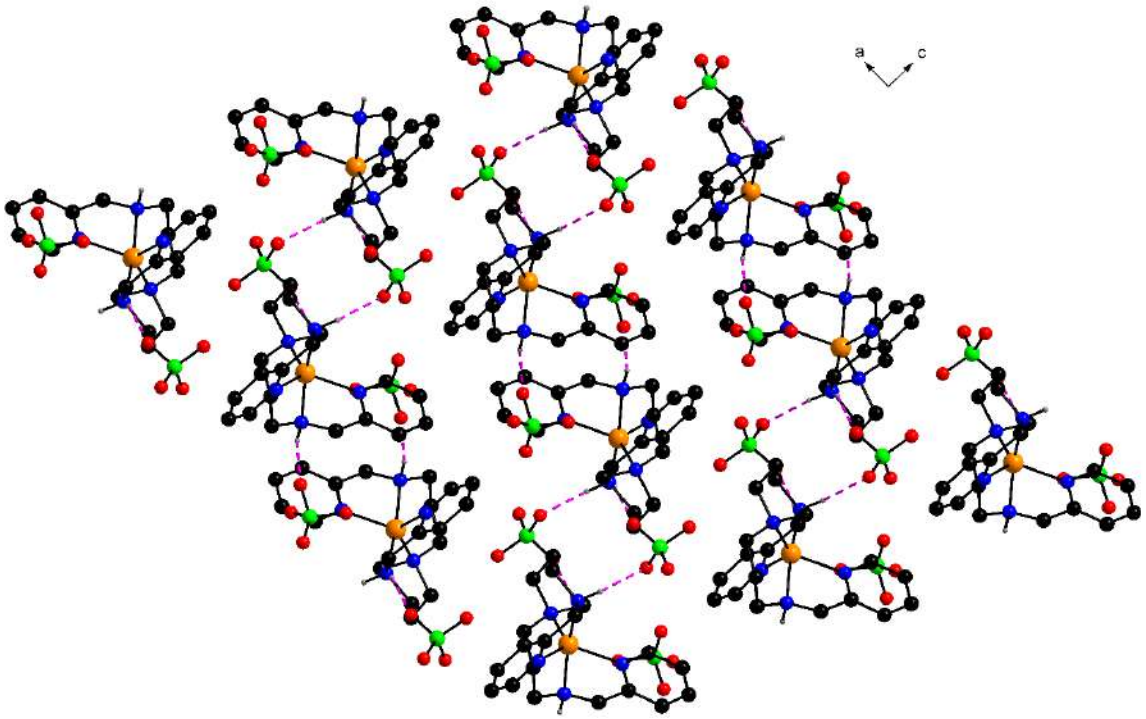

Figure 4.60 *The enlarged view of a network of hydrogen bonding in* ***18*** *showing the symmetric organisation of* $[Zn(L3)]^{2+}$ *cations and perchlorate anions. Hydrogen atoms attached to carbon are omitted for clarity.*

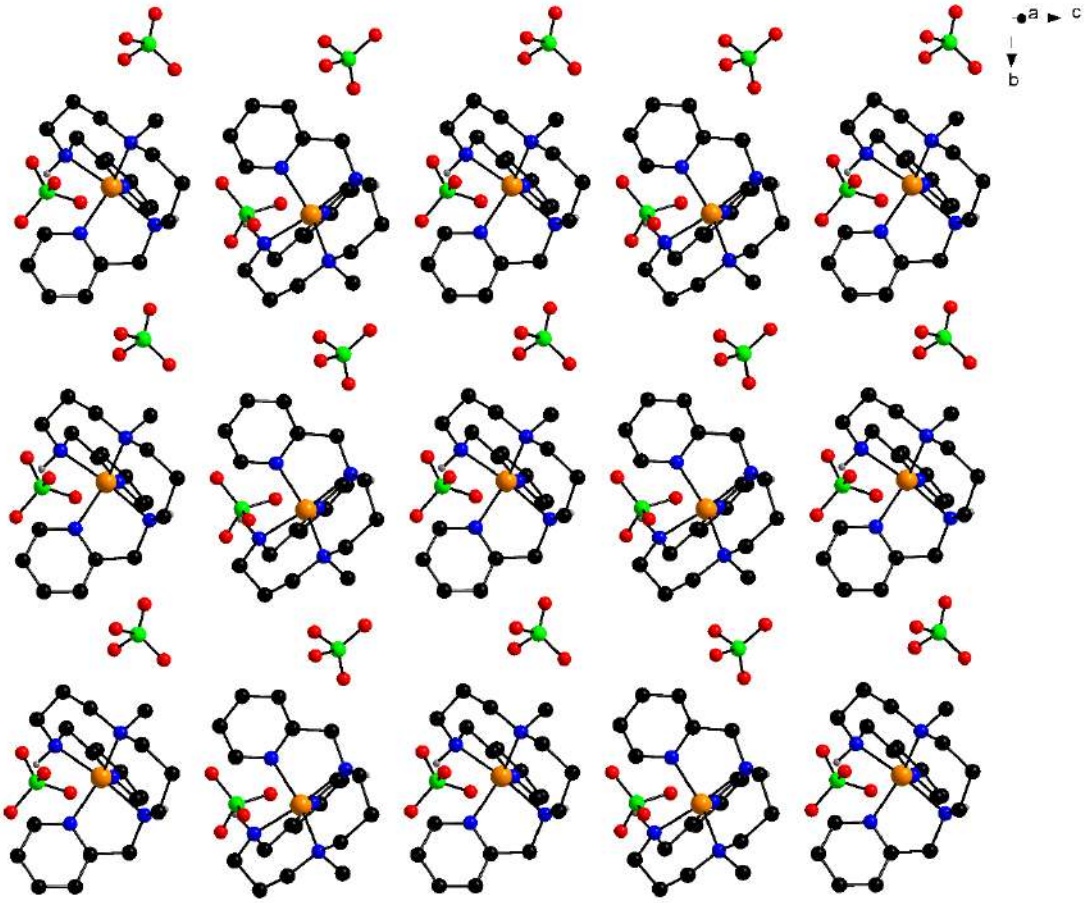

Figure 4.61 *Packing in **17** view along crystallographic c axis. Colour code: C, black; N, blue; O, red; Cl, green and Zn, orange.*

4.8 Conclusion

In this study, we successfully synthesized a series of novel 3d metal compounds, specifically $[Ni(L6)(CH_3CN)](ClO_4)_2$ **12**, $[Ni(L7)(CH_3CN)](ClO_4)_2$ **13**, $[Mn(L6)(ClO_4)](ClO_4)$ **14**, $[Mn(L7)(H_2O)](ClO_4)_2$ **15**, $[Co(L7)(H_2O)](ClO_4)_2$ **16**, $[Zn(L7)(H_2O)](ClO_4)_2$ **17** and $[Zn(L3)](ClO_4)_2$ **18**. The ligands utilized include **L6**, a nonmethylated N_4S aminopyridyl pentadentate ligand containing a thioether donor site, its methylated analogue **L7**, and the aminopyridine based ligand **L3**. These ligands were thoughtfully designed to modulate the electronic and steric environments around the metal centres, aiming to enhance their potential catalytic performance in biomimetic applications.

Comprehensive characterization of these compounds was accomplished using elemental analysis (CHNS), infrared (IR) spectroscopy, ultraviolet-visible (UV-vis) spectroscopy, single crystal X-ray diffraction (SCXRD), powder X-ray diffraction (PXRD), and electrospray ionization mass spectrometry (ESI-MS). The structural analyses confirmed the intended coordination geometries and ligand frameworks, revealing subtle yet meaningful differences arising from methylation and ligand backbone modifications.

Although their catalytic applications have not yet been explored experimentally within this work, the rationale behind their synthesis was supported by literature precedence, which indicates structurally similar compounds as effective biomimetic catalysts. The structural diversity and tunability exhibited by these compounds lay a robust foundation for future investigations into their catalytic behaviours. Thus, this work provides a significant step towards understanding how precise ligand design influences the physicochemical properties and catalytic potentials of 3d metal compounds in biomimetic chemistry.

Section III

Ligand backbone influenced luminescent properties of Zn(II) compounds for detection of nitroaromatic compounds

4.9 Introduction

Chemists are being significantly motivated by sustainable development to design new tools for the selective detection of hazardous substances. Concerns about human health, national security, and the environment have been growing due to the increasing use of nitroaromatic compounds (NACs) in explosive substances[106–108]. Various NACs including nitrobenzene (NB), p-nitrotoluene (p-NT), o-nitrotoluene (o-NT), p-nitrophenol (p-NP), o-nitrophenol (o-NP), 2,4-dinitrophenol (DNP) and 2,4,6-trinitrophenol (TNP) are commonly utilised in industrial applications. TNP is recognized for its extremely high explosive capabilities, rendering it an ideal option for use in destruction[109,110]. The higher solubility and greater use of TNP have resulted in severe, catastrophic water contamination. Consequently, the prompt identification of NACs in wastewater has emerged as a significant area of research in recent times[111–113]. Optical methods employing fluorescent probes have generated considerable attention due to their portability and sensitivity, although other established techniques are widely documented in the literature[114–118]. The luminescent characteristics of these probes primarily depend on the structure, the electron-rich nature of the aromatic ligand, and the metal centre[119,120]. This sensing ability is typically achieved by transferring photoexcited electrons from an electron-rich probe to electron-deficient analytes through quenching of the fluorescence[121].

The compounds of non-transition metals, such as Zn^{2+} and Cd^{2+}, exhibit prominent luminescence over other transition metals, thus making them useful in OLED devices and various emitting appliances. Armaroli *et al.* have accounted for the luminescent properties of zinc, cadmium, and other metal compounds in their recent review[122]. A slight modification to ligand topology in Zn(II) compounds has led to improved stability, enhancement in emission intensity, and changes in emission energies. The mononuclear Zn(II) compounds of varying denticity N-donor ligands have been discovered to exhibit photoluminescent properties[123,124]. Several Zn(II) compounds with varying ligands have been reported as sensors in detecting hazardous NACs[125–127].

Aliphatic coordination polymers of zinc and cadmium, which are diversified topologically and encapsulated with dipyridylamine ligand, have demonstrated the capacity to exhibit a "turn-off" luminescence when sensing NACs[128]. The cadmium ladder-type coordination polymer displayed luminescent properties that were effectively utilised at very low concentrations for the sensing of nitroaromatic compounds[129]. A cadmium-based 3D metal-organic framework has been documented in the detection of possible NAC pollutants[130]. Salen-type ligands' zinc and cadmium compounds have been extensively studied for their capacity to detect nitroaromatics through a turn-off fluorescence response[131]. A 2D and 3D topological cadmium cyclohexyldicarboxylate synthesized through hydrothermal processes with a co-ligand of bis(4-pyridylmethyl)piperazine has been sensibly employed in the quenching of nitroaromatic compounds[132]. Changes in the topological structure of coordinating ligands resulted in altered properties for zinc and cadmium compounds. The versatility of multidentate ligands in cadmium carboxylate coordination polymers has affected their overall structure-function properties, leading to the quenching of nitroaromatics[133].

Multidentate ligands based on aminopyridine have gained acceptance in contemporary coordination chemistry due to their reactivity and stability being regulated by a delicate balance of electronic and structural characteristics[134,135]. Over the past period, we have been consistently making attempts to tune the topology of multidentate N-donor ligands. This has led to a range of compounds of first-row transition metals with amino pyridyl-based ligands, which have been found to have diverse applications, including catalysis and enzyme mimicry[45,136,137].

Recent research has shown a substantial quenching of NACs via the use of quinoline-based ligands and cobalt(II) succinate compounds linked to N-donor ligands[138,139]. Building on our previous work demonstrating the impact of ligand topological effects in metal compounds on their various applications, we have synthesized two Zn(II) compounds, [Zn(L1)](ClO4)2 (1) and [Zn(L2)](ClO4)2 (2), incorporating N1-(pyridin-2-ylmethyl)-N2-(2-((pyridin-2-ylmethyl)amino)ethyl)-ethane-1,2-diamine (**L4**) and N1-(pyridin-2-ylmethyl)-N3-(3-((pyridin-2-ylmethyl)amino)propyl)propane-1,3-diamine (**L1**). The photoluminescent properties of Zn(II) compounds have been described in relation to the effect of extending the carbon chain of ligand **L1** as compared to **L4**.

4.10 Experimental details

4.10.1 Synthesis of $[Zn(L4)](ClO_4)_2$ 19 and $[Zn(L1)](ClO_4)_2$ 20

Compound **19** was synthesised by gradually adding 0.38 g (1.34 mmol) of **L4** to a 5 mL solution of acetonitrile, which was then stirred with 0.5g (1.34 mmol) of $Zn(ClO_4)_2.6H_2O$ (2 mL) at room temperature. The mixture was stirred for approximately five hours. Upon the addition of diethyl ether (10 mL), the reaction mixture yielded a colourless crystalline solid. The slow diffusion of diethyl ether into the CH_3CN solution of compound **19** resulted in white, transparent crystals suitable for single crystal X-ray diffraction analysis. The yield of compound **19** was 0.60 g (1.09 mmol), 82 %. *Anal. Calc.* for **19** $C_{16}H_{23}Cl_2ZnN_5O_8$ (%): C, 34.96; H, 4.22; N, 12.74. *Found:* C, 34.35; H, 4.10; N, 12.43. IR (KBr, cm^{-1}): 3296 υ(NH); 2980-2883 υ(CH); 1078, 619 υ(ClO_4). ESI-MS: *m/z* = 448.15 (*Calc*. 488.07) for $[Zn(L4)(ClO_4)]^+$.

A similar methodology was employed; in this instance, 0.42 g of **L1** (1.34 mmol) was reacted instead of **L4** to yield colorless crystals of compound **20**. The yield of **2** was 0.69 g (1.19 mmol), 89 %. *Anal. Calc.* for **(1)** $C_{18}H_{27}Cl_2ZnN_5O_8$ (%): C, 37.42; H, 4.71; N, 12.12. *Found:* C, 37.54; H, 4.37; N, 12.25. IR (KBr, cm^{-1}): 3298 υ(NH); 2950-2872 υ(CH); 1064, 619 υ(ClO_4). ^1H NMR (D_2O, ppm): δ 8.47 (d, 2H), δ 7.95 (t, 2H), δ 7.44 (m, 4H), δ 4.27-3.84 (m, 4H), δ 3.19-2.42 (m, 8H), δ 1.81-1.71 (m, 4H). ESI-MS: *m/z* = 476.15 (*Calc*. 476.15) for $[Zn(L1)(ClO_4)]^+$.

4.10.2 Photophysical Studies

The photoluminescence properties of compounds **19** and **20** were investigated in an aqueous solution at room temperature. The excitation wavelength was set at 370 nm, with slit widths of 10 nm for both excitation and emission. The experiments were recorded on a Xe flash lamp technology-based Cary Eclipse Fluorescence Spectrophotometer (G9800A), which is manufactured by Agilent Technologies. In a standard experiment, an aqueous solution of 2 mM / 2 mL was placed in a 1 cm quartz cuvette, and spectra were recorded. The fluorescence sensing titrations of compounds **19** and **20** with nitro-aromatic compounds recorded emission intensities following the incremental addition of 1 mM NAC solution.

4.11 Results and discussions

4.11.1 Synthesis of ligands and compounds 19 and 20

Ligands **L4** and **L1** were synthesised from their diamine precursors, then subjected to the standard $NaBH_4$ reduction as previously documented[45,136]. The Zn(II) compounds $[Zn(L4)](ClO_4)_2$ **19** and $[Zn(L1)](ClO_4)_2$ **20** were synthesised by reacting $Zn(ClO_4).6H_2O$ with solutions of the corresponding pentadentate ligands **L4** and **L1** in CH_3CN at a 1:1 mole ratio (**Scheme 4.7**). Single crystals of compounds **19** and **20**, suitable for single crystal X-ray diffraction analysis, were produced through the slow diffusion of diethyl ether into an acetonitrile solution within five hours. In contrast, the reported method involved slow evaporation of an aqueous solution for several days, yielding **19**[140]. Re-examination of **19** was undertaken to compare the effects of an elongated ligand backbone on structural properties with **20** and evaluate its fluorescence characteristics. Single crystal X-ray diffraction examined the spatial arrangement of compounds **19** and **20**. The crystallographic data and results of structural refinement for compounds **19** and **20** are presented in **Table 4.31**, and the chosen bond lengths and angles are listed in **Table 4.27** and **Table 4.29**. The results of elemental analysis for compounds **19** and **20** matched the structural composition determined through single-crystal X-ray diffraction studies.

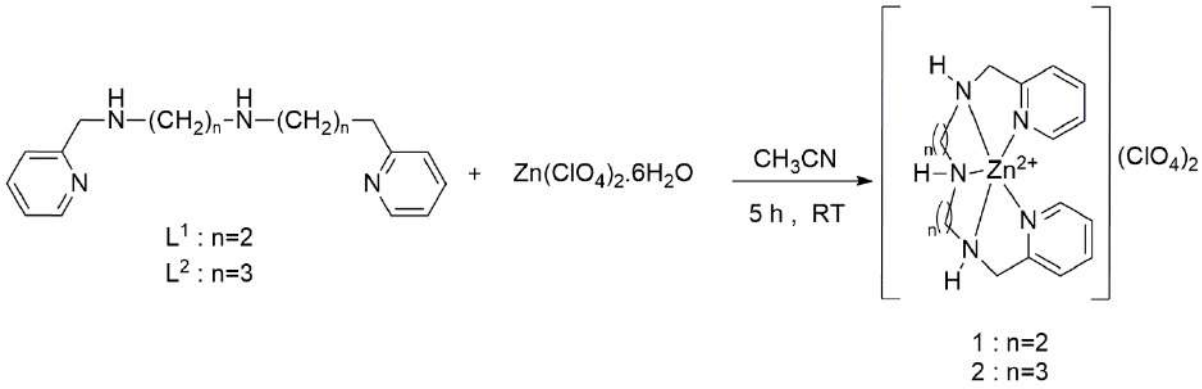

***Scheme 4.7** Synthetic route for preparation of **19** and **20**.*

The Infrared spectra of compounds **19** and **20** (**Figure 4.62**) display moderately strong peaks within the 3290-3298 cm^{-1} range, attributed to the N-H stretching vibrations originating from **L4** and **L1**, respectively. A sharp peak due to pyridyl C=N stretching is observed between 1605-1608 cm^{-1}, in addition. A strong, intense absorption band within the 1063-1079 cm^{-1} range is attributed to the stretching frequencies of $[ClO_4]^-$ ions. The presence of perchlorate ions in crystal lattices causing hydrogen bonding results in the

splitting or broadening of the band. The observed band at approximately 619 cm^{-1} is attributed to the bending mode of vibrational motion for perchlorate ions[141,142].

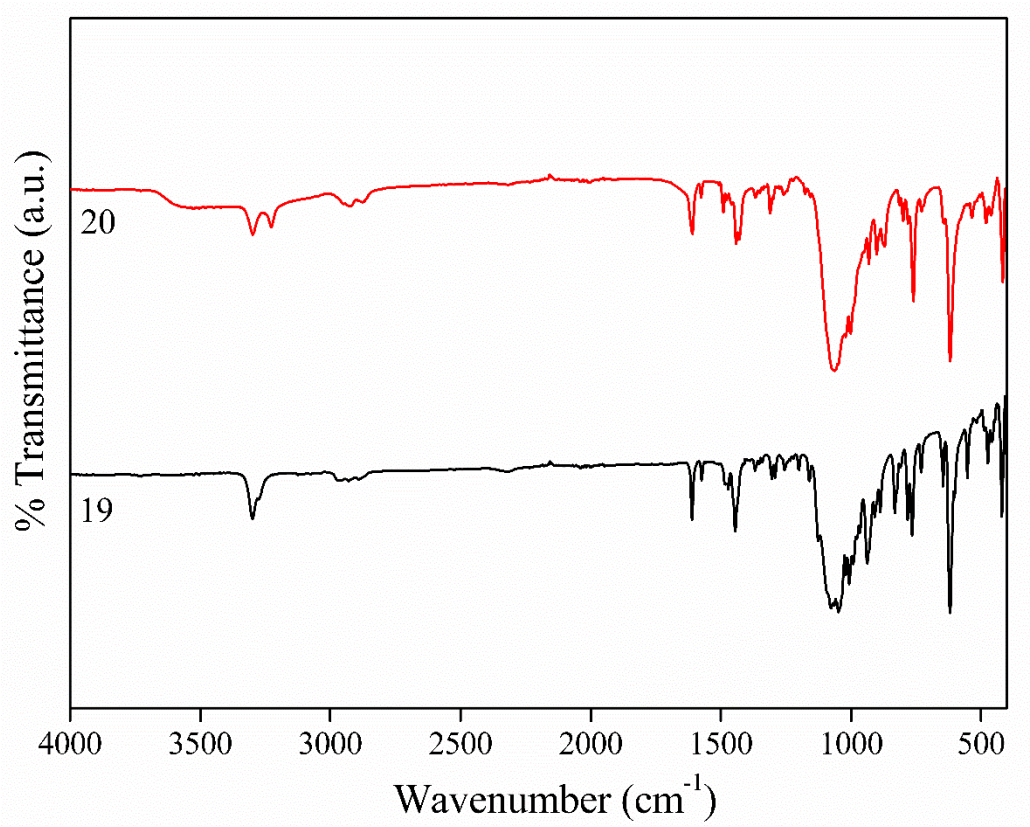

Figure 4.62 *IR spectra of compounds* ***19*** *and* ***20****.*

Powder X-ray diffraction analysis confirmed the overall purity of the synthesized compounds **19** and **20**. The PXRD patterns of compounds **19** and **20** correlate with the results from single crystal X-ray diffraction data obtained using Mercury 4.0 software[93] as shown in **Figure 4.63**.

The stability of compounds **19** and **20** in solution was verified by ESI-MS, which showed that these compounds had mass peaks at *m/z* = 448.1 (calculated *m/z* 448.0) and *m/z* = 195.0 (calculated *m/z* 195.0)for the $[Zn(L4)(ClO_4)]^+$ and $[Zn(L4)(CH_3CN)]^{2+}$ fragments and at *m/z* = 476.1 (calculated *m/z* 476.1) and *m/z* = 209.0 (calculated *m/z* 209.1) for the $[Zn(L1)(ClO_4)]^+$ and $[Zn(L1)(CH_3CN)]^{2+}$ fragment as displayed in **Figure 4.64**.

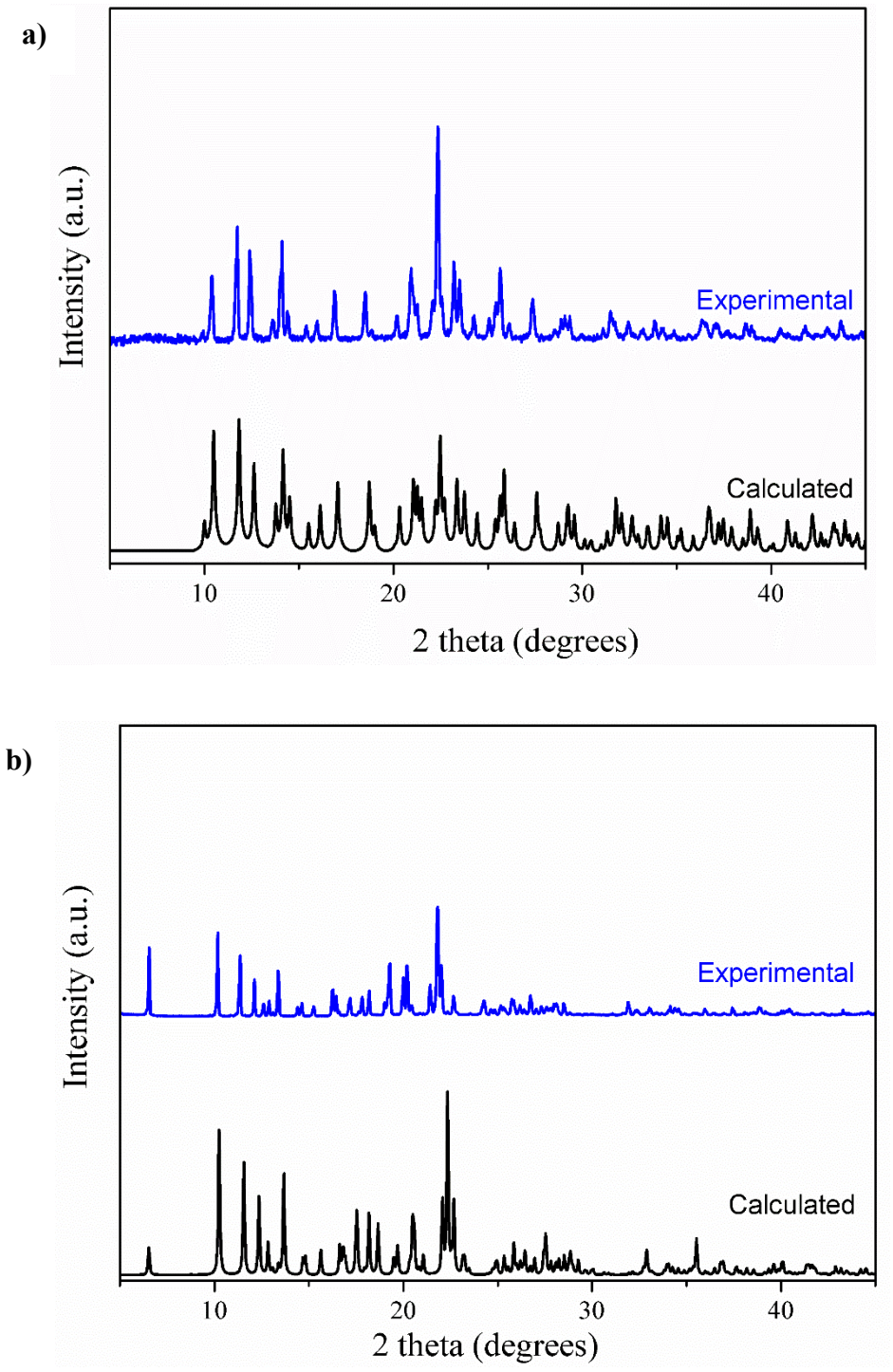

Figure 4.63 *Powder X-ray diffraction patterns for compounds* ***19*** *(a) and* ***20*** *(b).*

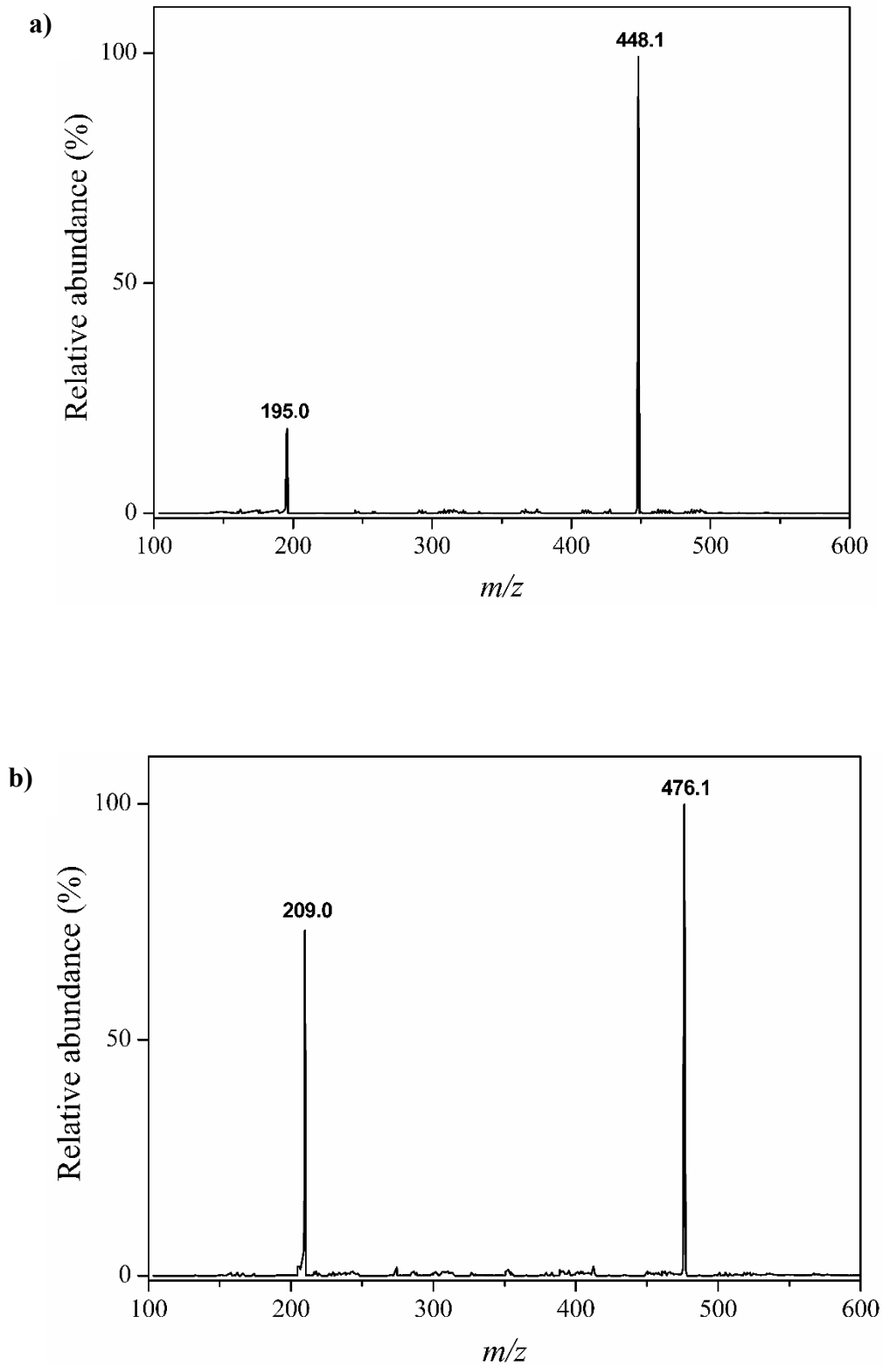

Figure 4.64 *ESI-MS spectrum of* ***19*** *(a) and* ***20*** *(b) recorded in acetonitrile.*

4.11.2 Crystal structures of 19 and 20

Single-crystal X-ray diffraction analysis revealed that compound **19** crystallizes in the tetragonal non-centrosymmetric $P4_1$ space group. The asymmetric unit is built from one crystallographically independent $[Zn(L4)]^{2+}$ cation and two perchlorate anions (**Figure 4.65** and **Figure 4.67**). A unique Zn(II) cation is coordinated by the two N atoms of the flexible pyridyl moiety and three N atoms of the symmetric secondary amine backbone, leading to a five-coordinated square pyramidal geometry. The atoms N1, N2, N3, and N5 formed the base of the square pyramid, while N4 occupies the apical position. The pyridyl nitrogen atoms are disposed *syn* to one another. A careful inspection of bond lengths reveals that Zn–N_{py} bond lengths lie in the range 2.125(3)–2.135(3) Å, which are slightly shorter than Zn–N_{amine} bond distances (2.146–2.148(3) Å) due to the hybridization of sp^2 pyridine and sp^3 amine nitrogen's[143]. The distortion in coordination geometry around the Zn(II) centre can be determined by calculating Addison parameter (τ_5) using the equation $\tau=(\beta-\alpha)/60$, where β alpha are the two most prominent coordinate angles[144–147] The calculated Addison parameter, τ_5 = 0.07, suggested a slight distortion in the square pyramidal geometry of **19**. It is observed that the bond angles of N(1)–Zn(1)–N(3) (157.69°) and N(5)–Zn(1)–N(2) (162.09°) are less than expected 180° in square pyramidal geometry. The perchlorate anions play a significant role in building the supramolecular architecture through its oxygen atoms (O2, O3, O4 and O7), which are involved in non-covalent H-bond interactions (**Figure 4.66**). The predominant intermolecular hydrogen bonds between N–H···O and C–H···O renders additional stability to the crystal structure of **19**. Selected non-covalent H-bonds are summarized in **Table 4.28**. The crystal packing of **19** viewed along the '*ab*' plane (**Figure 4.66**) illustrates the intercalation of perchlorate counterions with the cation species $[Zn(L4)]^{2+}$.

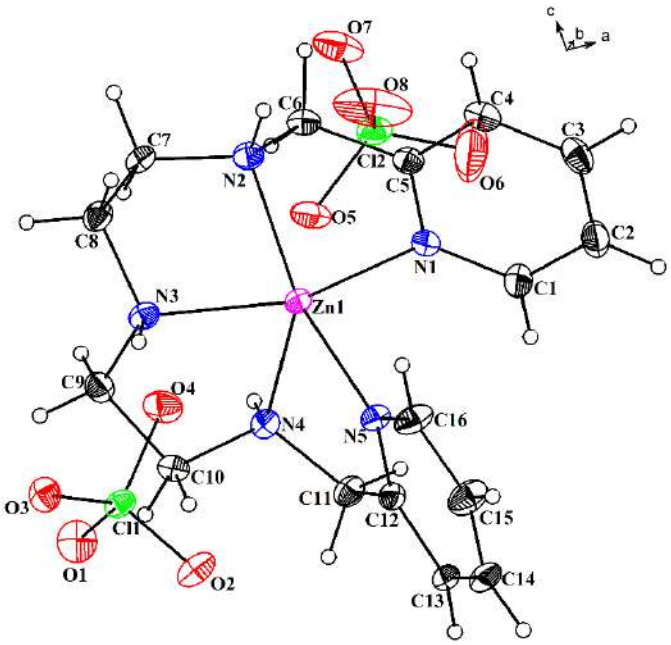

Figure 4.65 *Crystal structure of* ***19*** *showing atom labeling scheme. The thermal ellipsoids are drawn at a 30 % probability level for all the atoms except for the H atoms, which are shown as spheres of arbitrary radii.*

Table 4.27 *Selected bond lengths (Å) and angles (°) for* ***19****.*

Bond lengths (Å)			
Zn(1)-N(5)	2.125(3)	Zn(1)-N(1)	2.135(3)
Zn(1)-N(4)	2.147(3)	Zn(1)-N(3)	2.148(3)
Zn(1)-N(2)	2.146(3)		
Bond angles (°)			
N(5)-Zn(1)-N(1)	94.94(12)	N(5)-Zn(1)-N(2)	162.09(11)
N(1)-Zn(1)-N(2)	78.13(11)	N(5)-Zn(1)-N(4)	78.49(11)
N(2)-Zn(1)-N(4)	118.76(12)	N(5)-Zn(1)-N(3)	107.24(12)
N(1)-Zn(1)-N(3)	157.69(11)	N(2)-Zn(1)-N(3)	81.27(11)
N(4)-Zn(1)-N(3)	82.63(11)	N(1)-Zn(1)-N(4)	99.85(11)

Table 4.28 *Hydrogen bonding parameters for* ***19****.*

D-H···A	**D-H/ Å**	**H···A/ Å**	**D···A/ Å**	**D-H···A/º**	**Symmetry code**
N2-H2···O7	0.980	2.115	3.055	160.11	x, y, z
N3-H3···O4	0.980	2.019	2.978	165.45	x, y, z
N4-H4···O2	0.980	2.428	3.233	139.15	x, y+1, z
N4-H4···O3	0.980	2.197	3.101	152.87	x, y+1, z
C16-H16···O5	0.930	2.432	3.088	127.54	x, y, z

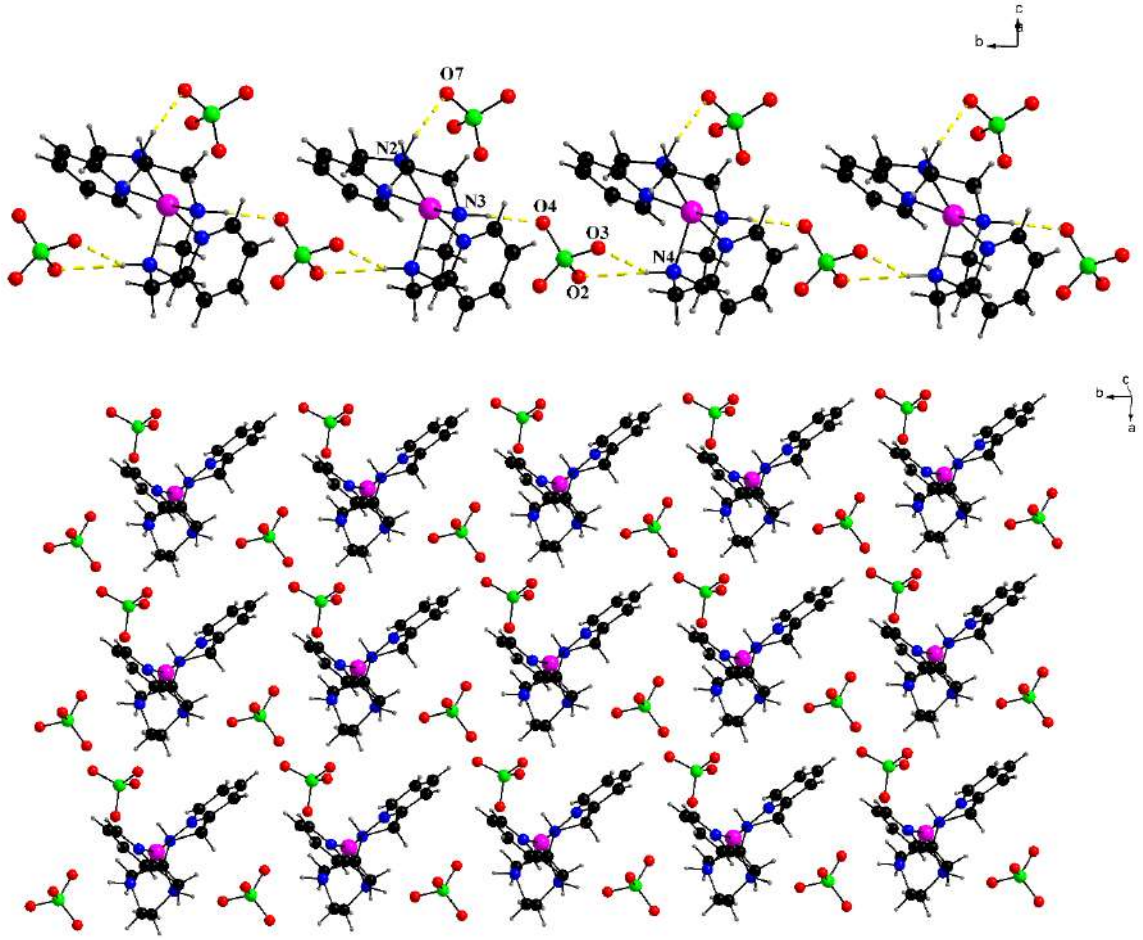

Figure 4.66 *Hydrogen bonding interactions in* ***19*** *with atom labelling scheme of atoms involved in hydrogen bonding and a view of the packing diagram of* ***19*** *along the ab plane.*

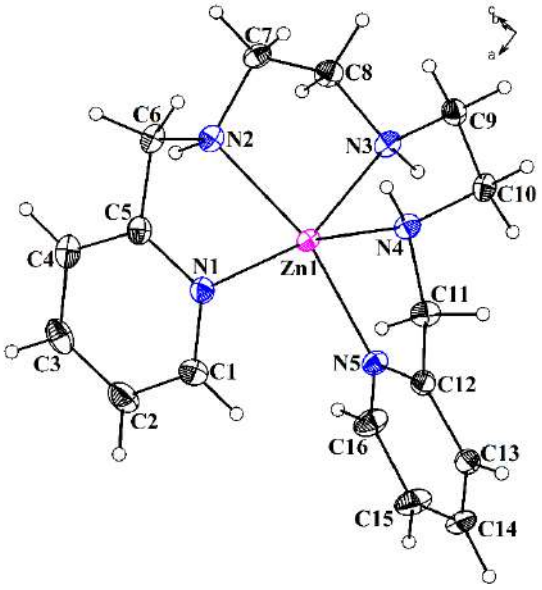

Figure 4.67 *Crystal structure of* $[Zn(L4)]^{2+}$ *showing atom labelling scheme. The thermal ellipsoids are drawn at 30 % probability level for all the atoms except for the H atoms, which are shown as spheres of arbitrary radii. The perchlorate anions have been omitted for the clarity.*

The geometrically related ligand **L1** with a six-carbon secondary amine backbone rather than a four-carbon secondary backbone amine containing **L4** was synthesized and metalated with zinc perchlorate to afford compound **20**. The topology of the ligands **L4** and **L1** has led to interesting structural changes in $[Zn(L4)](ClO_4)_2$ **19** and $[Zn(L1)](ClO_4)_2$ **20**. The single crystal X-ray diffraction study of **20** reveals that it crystallizes in a centrosymmetric monoclinic space group $P2_1/c$. The asymmetric unit consists of a centrally located Zn(II) cation, a pentadentate **L1** ligand, and two crystallographically independent perchlorate anions (**Figure 4.68** and **Figure 4.69**). The carbon atoms C7-C12 and N3 are disordered over two positions, which are modelled with occupancies of 0.64 and 0.36 (**Figure 4.70**). The Zn-N bond lengths are similar in both positions, which lie in the range 2.043(3)-2.174(5). The pyridine rings are *trans* to one another. It displayed a distorted trigonal bipyramidal arrangement compared to **19**, which is confirmed by Addison parameter $\tau_5 = 0.53$ based on two relevant angles N(5)-Zn(1)-N(2) (166.1°) and N(1)-Zn(1)-N(4) (134.0°), α and β respectively. Thus, a more significant distortion was observed from square pyramidal to trigonal bipyramidal in compound **20**. The non-coordinated perchlorate ions form weak non-covalent N-H···O interactions (**Table 4.30**, **Figure 4.71**). The crystal packing of compound **20** depicts the arrangement of the cations and anions into alternating layers along the *a*-axis (**Figure 4.72**).

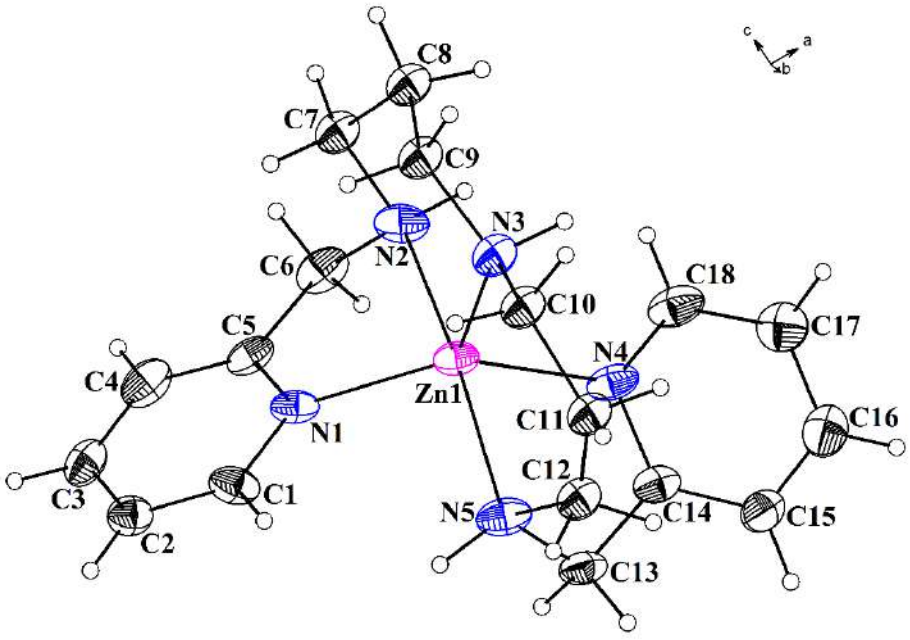

Figure 4.68 *Crystal structure of* $[Zn(L1)]^{2+}$ *showing atom labelling scheme. The thermal ellipsoids are drawn at 30 % probability level for all the atoms except for the H atoms, which are shown as spheres of arbitrary radii. The perchlorate anions have been omitted for the clarity.*

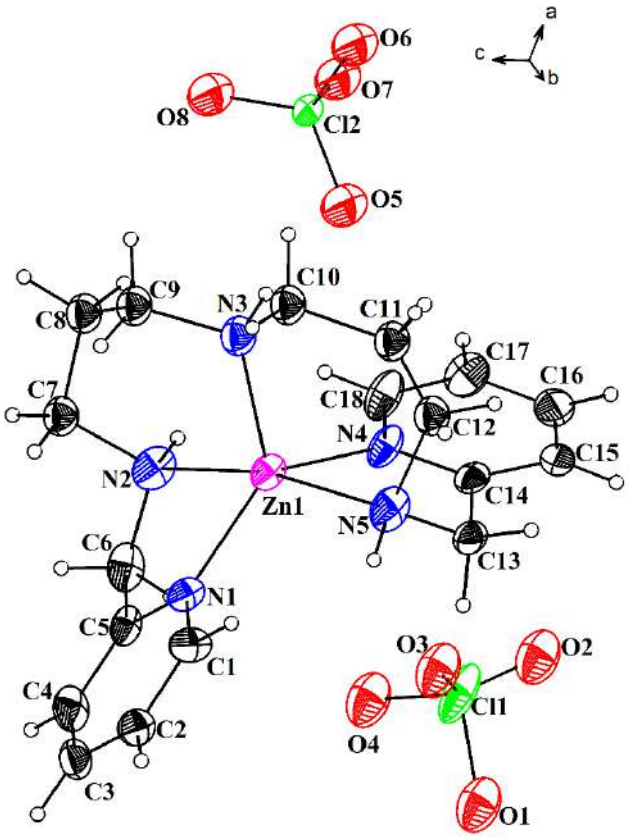

Figure 4.69 *Crystal structure of* ***20*** *showing atom labeling scheme. The thermal ellipsoids are drawn at a 30 % probability level for all the atoms except for the H atoms, which are shown as spheres of arbitrary radii.*

Table 4.29 *Selected bond lengths (Å) and angles (°) for* ***20****.*

Bond lengths (Å)			
Zn(1)-N(3)	2.043(3)	Zn(1)-N(1)	2.090(5)
Zn(1)-N(4)	2.118(5)	Zn(1)-N(5)	2.165(5)
Zn(1)-N(2)	2.174(5)		
Bond angles (°)			
N(3)-Zn(1)-N(1)	123.8(3)	N(3)-Zn(1)-N(4)	102.0(3)
N(1)-Zn(1)-N(4)	134.0(18)	N(3)-Zn(1)-N(5)	100.2(3)
N(1)-Zn(1)-N(5)	95.3(2)	N(4)-Zn(1)-N(5)	79.1(2)
N(3)-Zn(1)-N(2)	93.6(3)	N(1)-Zn(1)-N(2)	77.8(19)
N(4)-Zn(1)-N(2)	96.8(2)	N(5)-Zn(1)-N(2)	166.1(2)

Table 4.30 *Hydrogen bonding parameters for* ***20.***

D-H···A	**D-H/ Å**	**H···A/ Å**	**D···A/ Å**	**D-H···A/º**	**Symmetry code**
N3-H3A ···O5	0.980(0)	2.087(0)	3.059(0)	171.04(0)	x, y, z
N5-H5B ···O4	0.980(0)	2.228(1)	3.179(2)	163.25(0)	x, y, z

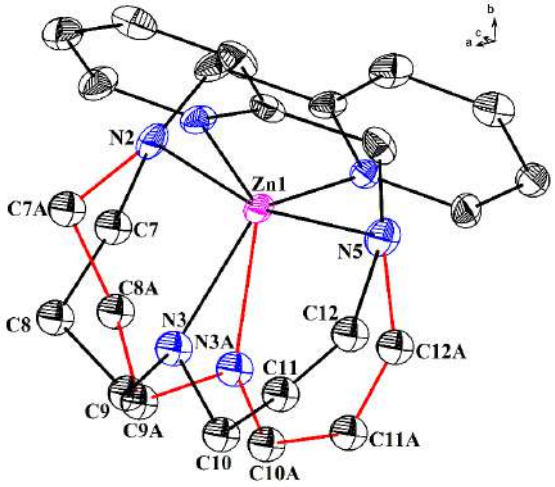

Figure 4.70 *The crystal structure of* ***20*** *showing the modeled disorder. The thermal ellipsoids are drawn at a 30 % probability level for all the atoms. The hydrogen atoms and perchlorate anions have been omitted for clarity.*

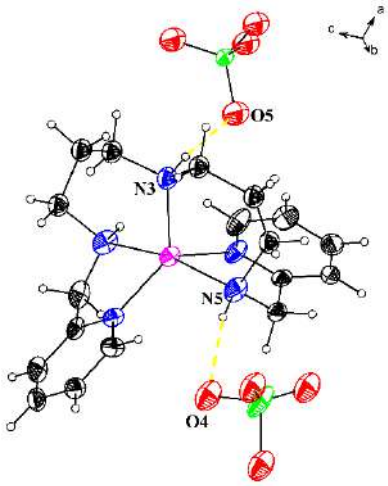

Figure 4.71 *Hydrogen bonding interactions in* ***20*** *with atom labelling scheme of atoms involved in hydrogen bonding*

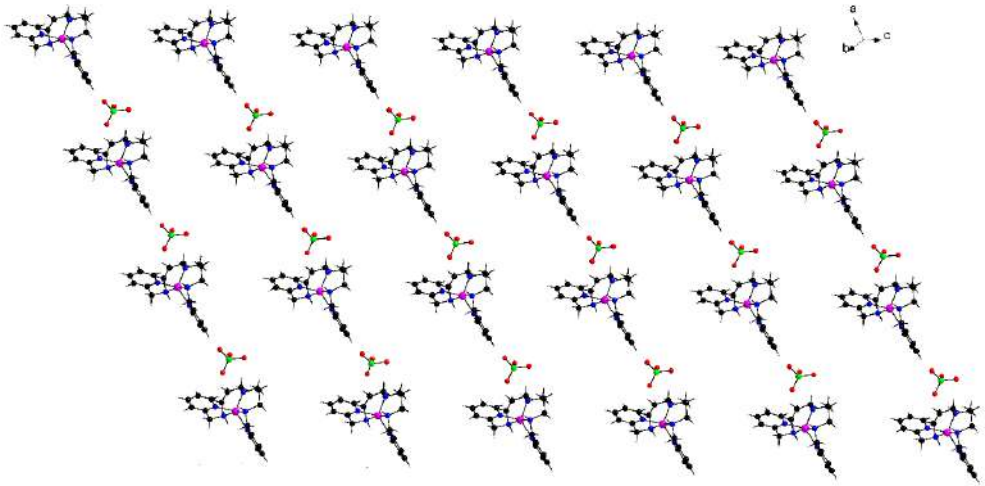

Figure 4.72 *A view of the packing diagram of* ***20****.*

Table 4.31 *Technical details of crystal data and structure refinement parameters of* ***19*** *and* ***20****.*

Compound	**19**	**20**
Empirical formula	C_{16} H_{23} Cl_2 Zn N_5 O_8	C_{18} H_{27} Cl_2 Zn N_5 O_8
Formula weight	549.68	577.74
Temperature	150 K	150 K
Wavelength	0.71073 Å	0.71073 Å
Crystal system	Tetragonal	Monoclinic
Space group	$P4_1$	$P2_1/c$
Unit cell dimensions	a = 8.8375(5) Å b = 8.8375(5) Å c = 28.034(2) Å α = 90° β = 90° γ = 90°	a = 13.6348(7) Å b = 8.4280(4) Å c = 20.3603(10) Å α = 90° β = 97.136(2)° γ = 90°
Volume	2189.5(3) $Å^3$	2321.6(2) $Å^3$
Z	4	4
Density (calculated)	1.668 mg/m^3	1.653 mg/m^3
Absorption coefficient	1.420 mm^{-1}	1.344 mm^{-1}
F(000)	1128	1192
Theta range for data collection	2.305 to 28.277°	2.619 to 28.322°
Completeness to theta	100.0%	99.8%
Index ranges	-11≤ h ≤11 -11≤ k≤11 -37≤ l≤37	-18≤ h ≤18 -11≤ k≤11 -27≤ l≤26
Reflections collected	43081	168996
Independent reflections	5439 [R(int) = 0.0432]	5767 [R(int) = 0.0302]
Refinement method	Full-matrix least-squares on F^2	Full-matrix least-squares on F^2
Absorption correction	Semi- empirical from equivalents	Semi- empirical from equivalents
Data/restraints/parameters	5439 / 1 / 289	5767 / 0 / 288
Goodness-of-fit on F^2	1.052	1.066
Final *R*indices[I>2sigma(I)]	R1= 0.0289, wR2= 0.0665	R1= 0.0913, wR2= 0.2346
R indices (all data)	R1= 0.0367, wR2= 0.0690	R1= 0.0949, wR2= 0.2380
CCDC No.	2309423	2309424

4.11.3 Photophysical properties of 19 and 20

Compound **19** exhibited a notable peak at 470 nm, whereas compound **20** showed a pronounced peak at 460 nm under excitation with a 370 nm wavelength. Emissions are caused by intra-ligand transitions of π*→n and π→π* within the ligands **L4** and **L1**[148]. After identifying the unique emission bands, we chose to examine the sensing properties of compounds **19** and **20** with nitroaromatic compounds (NACs). In this study, the electron-deficient NACs used were nitrobenzene (NB), o-nitrotoluene (o-NT), p-nitrotoluene (p-NT), o-nitrophenol (o-NP), p-nitrophenol (p-NP), 2,4-dinitrophenol (DNP) and 2,4,6-trinitrophenol (TNP).The addition of aqueous solutions of NACs to the aqueous solution of **19** led to the observation of quenching at a wavelength of 470 nm. The emission titration of **19** with TNP is displayed in **Figure 4.73**, and the titration spectra of **19** with remaining NACs are presented in **Figures 4.74- 4.76**. Repeated measurements, at least three times, were conducted to guarantee reliable results, with each instance showing a notable decrease in the initial fluorescence intensity of **19** as NACs were added gradually.

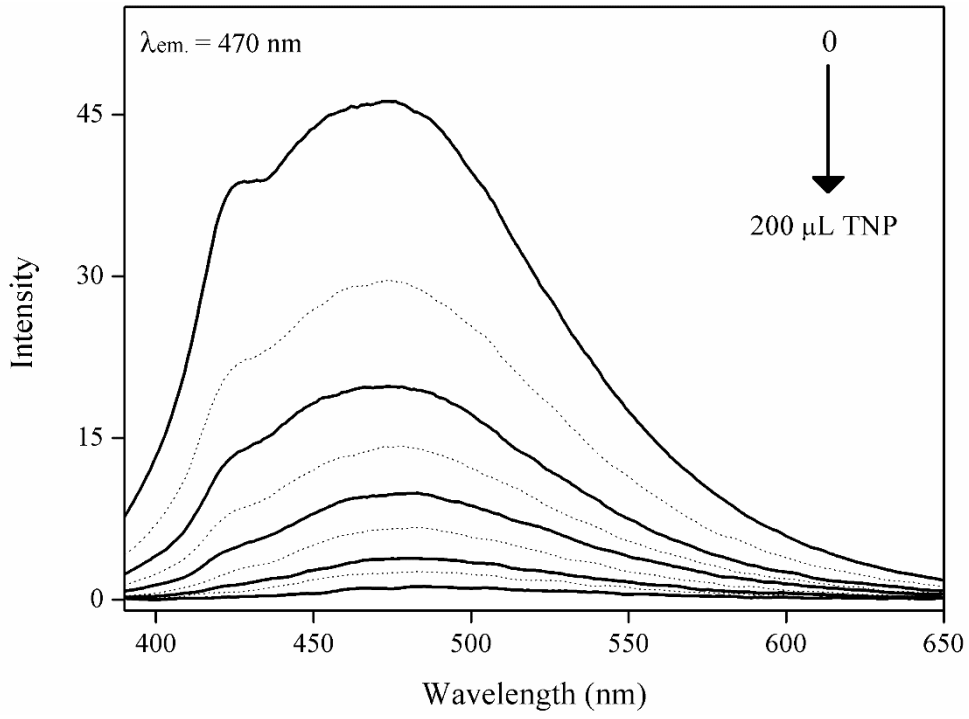

Figure 4.73 *The decay of fluorescence emission peak of* ***19*** *($\lambda_{ex.}$ = 370 nm) upon gradual addition of 1 mM of trinitrophenol (TNP).*

The quenching efficiency (η) was calculated using the equation given below.;

$$[(I_o - I) / I_o] \times 100\ \% \ldots\ldots.(i)$$

where I_o and I are the fluorescence intensities before and after adding the respective NACs. Upon testing all the NACs, we found that with TNP, the initial emission intensity was reduced by almost 98% (η) when 200 μL of TNP was added to a solution of **19**. Upon adding DNP (200 μL), **19** exhibited approximately 96 % quenching of the emission band at 470 nm..The emission intensity fell to 46% for o-NP and 42% for p-NP for other NACs. A sluggish decay of the emission band of **19** was observed with NB, o-NT, and p-NT, resulting in approximately 31- 36 % quenching.

The quenching efficiency was conformed to the sequence: NB < o-NT < p-NT < p-NP < o-NP < DNP < TNP for all examined NACs. The sensitivity of compound **19** towards various NACs is illustrated by their respective quenching efficiencies (%), as shown in **Figure 4.77**. Compound **19** demonstrated significantly greater quenching efficacy towards dinitro and tri-nitrophenols relative to other NAC compounds. The outcomes clearly showed that **19** can be selectively employed as a chemical sensing reagent in identifying TNP and DNP from an aqueous mixture of other NACs.

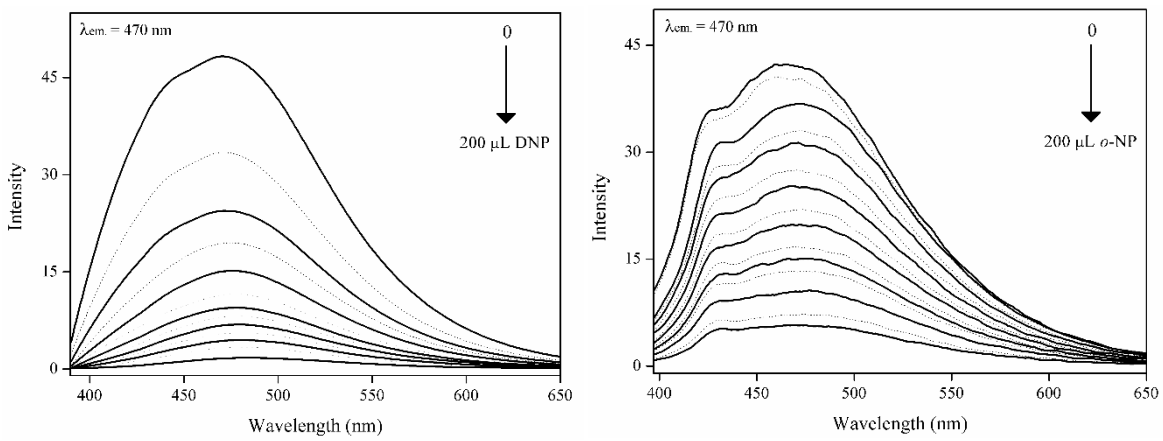

Figure 4.74 *The reduction of fluorescence emission of* ***19*** *($\lambda_{ex.}$ = 370 nm) upon gradual addition of 1mM of dinitrophenol (DNP)(left) and o-nitrophenol (o-NP) (right).*

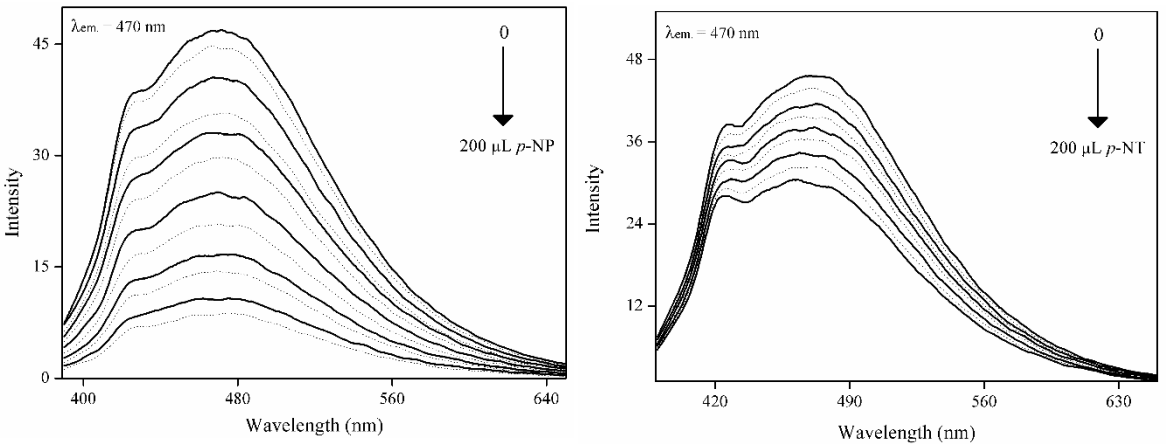

Figure 4.75 *The reduction of fluorescence emission of* ***19*** *($\lambda_{ex.}$ = 370 nm) upon gradual addition of 1mM of p-nitrophenol (p-NP) (left) and p-nitrotoluene (p-NT)(right).*

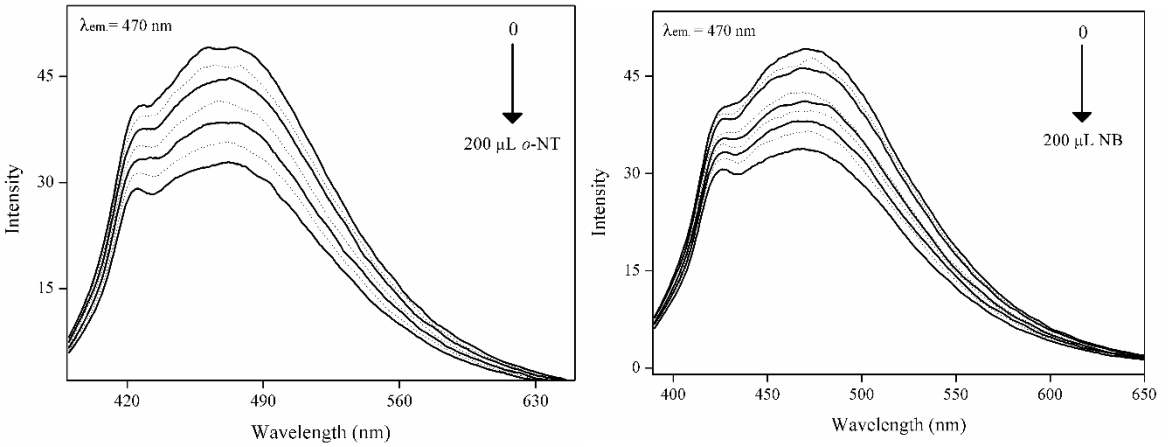

Figure 4.76 *The reduction of fluorescence emission of* ***19*** *($\lambda_{ex.}$ = 370 nm) upon gradual addition of 1mM of o-nitrotoluene (o-NT) (left) and nitrobenzene (NB)(right).*

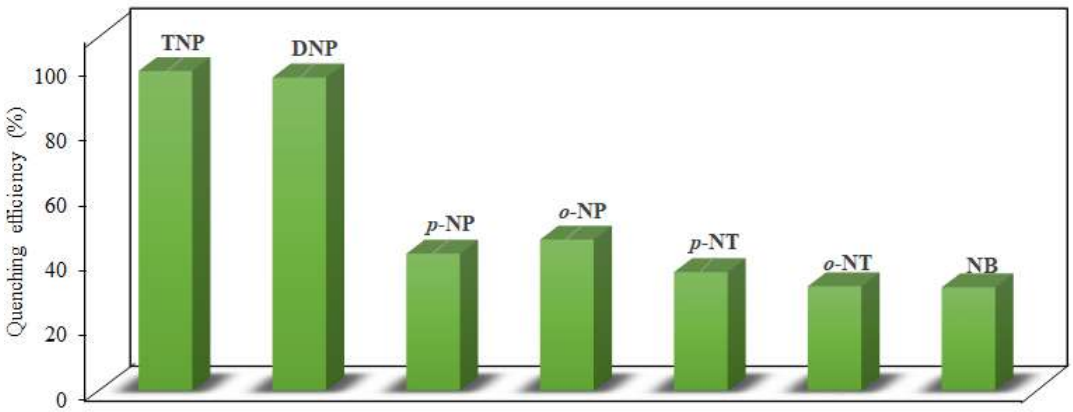

Figure 4.77 *Representation of the quenching efficiency of* ***19*** *towards different NACs.*

The Stern-Volmer quenching constant (K_{sv}) was calculated by examining the normalised fluorescence emission intensity (I_0/I) at various concentrations of the quencher [Q] using the formula $I_0/I = 1 + K_{sv}[Q]$, with I_0 and I representing the emission intensities before and after the addition of NACs respectively, K_{sv} signifying the quenching constant (M^{-1}) and [Q] denoting the molar concentration of NACs. The S-V plots of **19** with the NACs are shown in **Figure 4.78**. The plots demonstrate that the S-V curves for TNP and DNP maintained a straight line at low concentrations but diverged into a curved shape at higher concentrations, and a quenching constant of **19** was obtained from the slope of the equation line, $I_0/I = 1 + K_{sv}[Q]$. The quenching constants for TNP and DNP are greater than those of the other NACs utilised in this study (**Table 4.32**).This highlighted the selective quenching capacity of TNP and DNP towards luminescent **19** in water, amongst other NACs[111,118].

Table 4.32 *The quenching efficiencies upon addition of different NACs to* ***19****.*

Sr. No.	NAC	Quenching efficiency η (%)	S-V constant K_{sv} (M^{-1})
1	NB	31.74	5.023×10^3
2	*o*-NT	32.10	6.950×10^3
3	*p*-NT	36.45	4.652×10^3
4	*o*-NP	46.43	6.541×10^3
5	*p*-NP	42.12	5.321×10^3
6	DNP	96.28	5.547×10^4
7	TNP	98.25	6.443×10^4

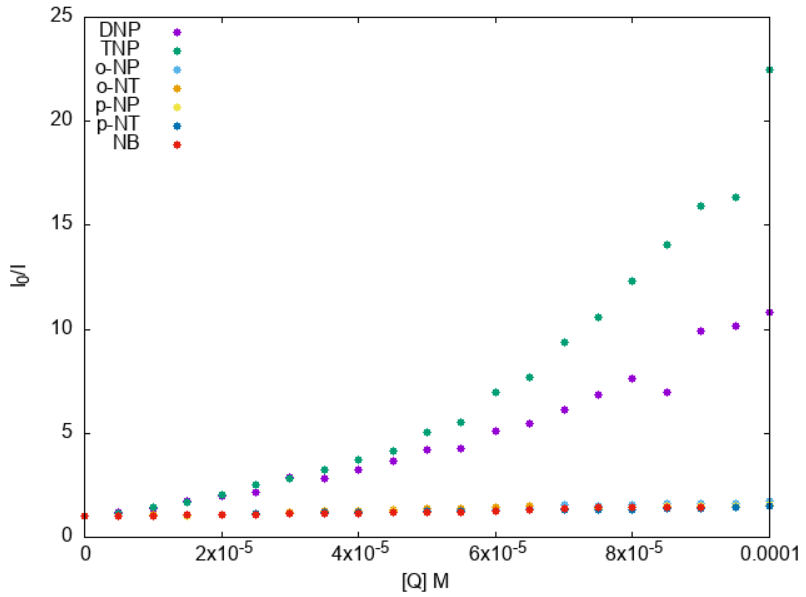

Figure 4.78 *Stern-Volmer plots for NACs added to* ***19*** *in water.*

Fluorescent titrations were also carried out using compound **20** in water. Compound **20** showed emission at 460 nm upon excitation at 370 nm. The best quenching results in screening **20** were achieved for DNP and TNP. The titration of **20** with TNP and DNP is shown in **Figure 4.79**. Calculating the quenching efficiencies (% η), the initial emission intensity of compound **20** was reduced by 87% with 200 µL of DNP and by 92% with 200 µL of TNP. Compound **19** displays Ksv values that are nearly double those of compound **20** for both TNP and DNP.

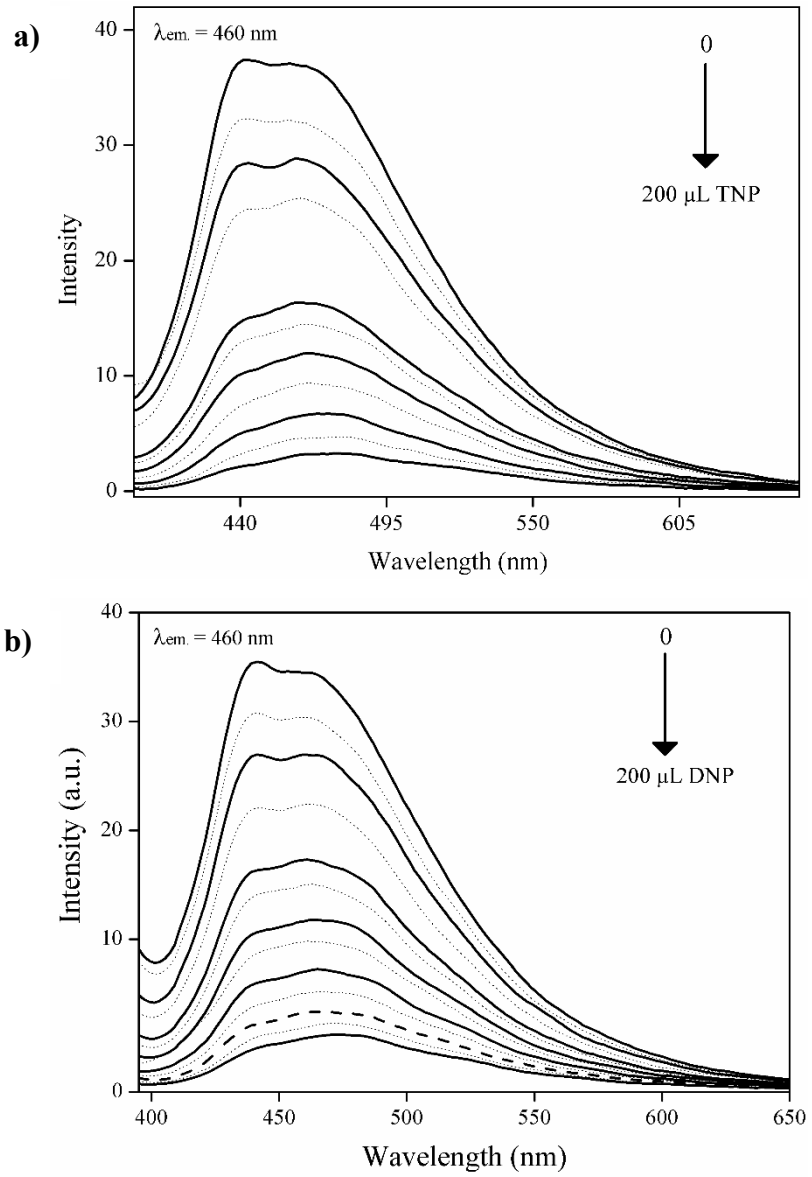

Figure 4.79 *The reduction of fluorescence emission of* ***20*** *($\lambda_{ex.}$ = 370 nm) upon gradual addition of 1mM of trinitrophenol (TNP (a) and dinitrophenol (DNP) (b).*

The Stern-Volmer plots were examined to gain a better understanding of the quenching mechanism displayed by compounds **19** and **20**. Observations revealed a second-order polynomial fit for the S-V plot in the case of TNP and DNP, whereas other NACs displayed a linear response. A non-linear response to the addition of TNP and DNP is observed in compounds **19** and **20**, but a linear relationship is seen in the S-V plot at lower concentrations of the NACs (**Figure 4.80** and **Figure 4.81**). Second-order polynomial fitting for an NAC suggests the presence of both static and dynamic quenching mechanisms within the system[149].

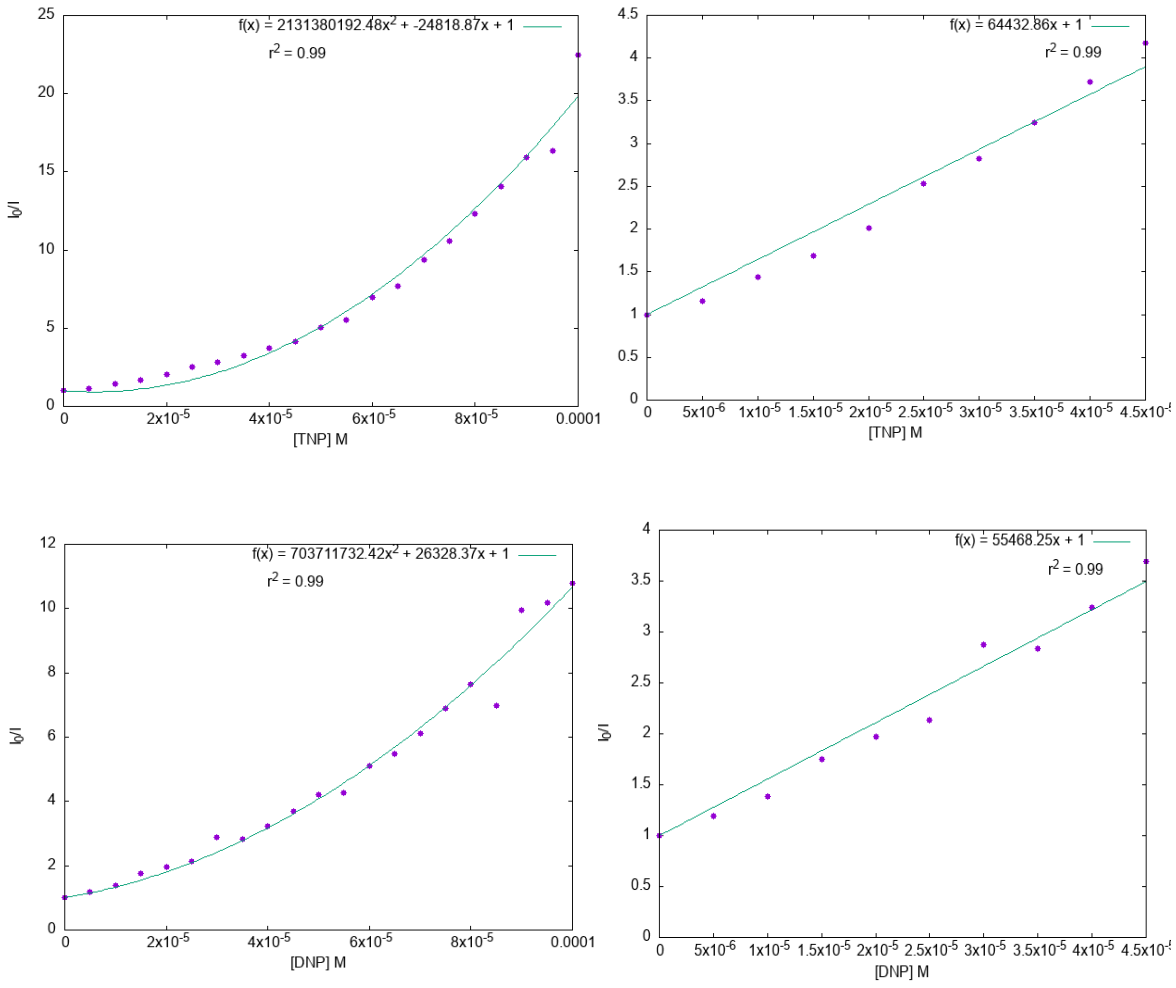

Figure 4.80 *Stern-Volmer plots of **19** exhibiting a non-linear response to addition of TNP and DNP along with a linear relationship at lower concentration.*

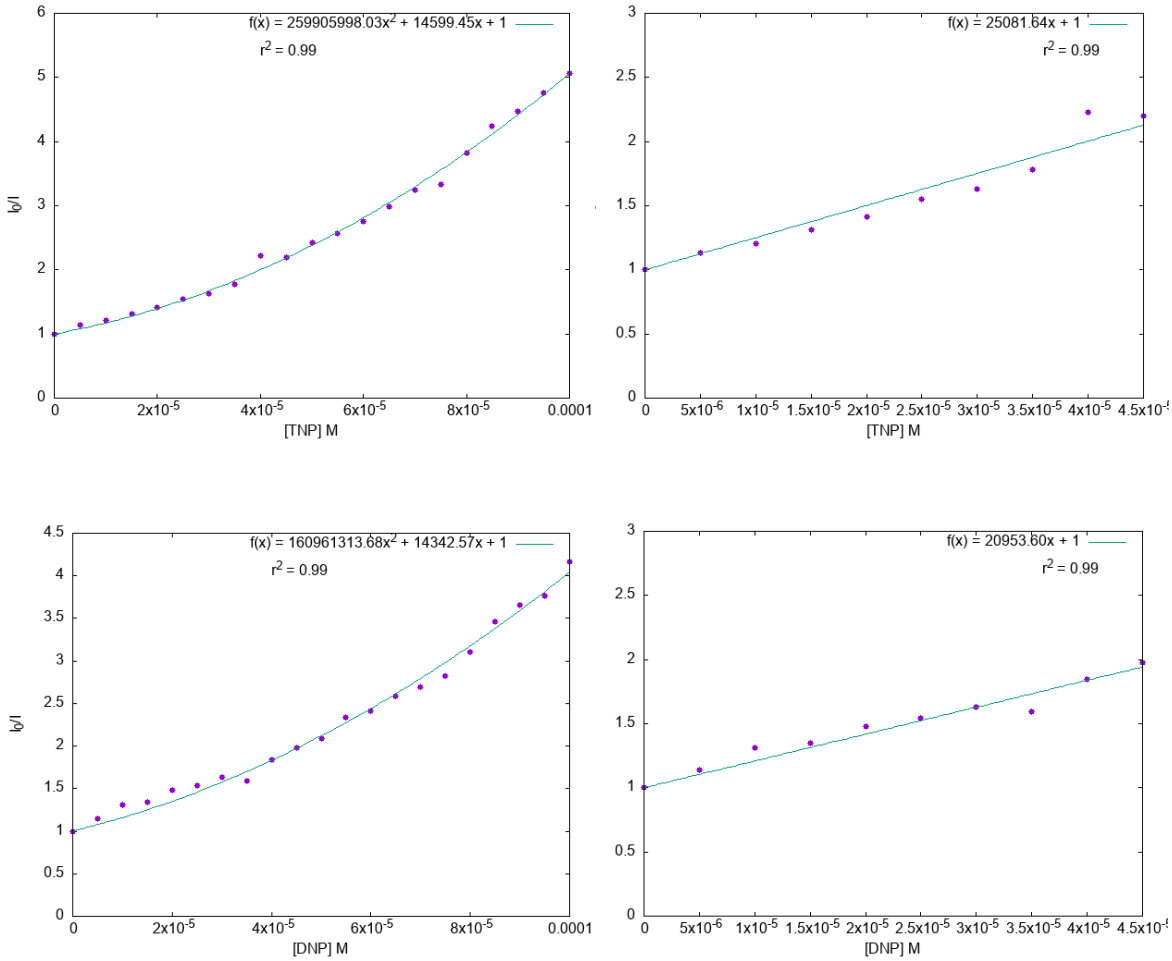

Figure 4.81 *Stern-Volmer plots of **20** exhibiting a non-linear response to addition of TNP and DNP along with a linear relationship at lower concentration.*

The extent of spectral overlap between the absorption band of the NACs and the emission band of the compounds is the determining factor for the likelihood of the resonance energy transfer (RET) mechanism occurring, which leads to increased quenching. The overlap between the absorption spectra of TNP and DNP with the emission spectra of the compound signifies the RET mechanism responsible for enhanced quenching. In contrast, the remaining NACs do not show such overlap as illustrated in the **Figure 4.82(a)**. In contrast to the other NACs, which show minimal spectral overlap, TNP and DNP exhibit significant overlap with the 470 nm emission band, as observed in **Figure 4.82(b)**. As a result, TNP and DNP display stronger quenching reactions than the other NACs. Upon verifying the spectral overlap in relation to compound **20**, specifically in **Figure 4.82(a)**, there was significant overlap between the emission band of **20** and the bands of TNP and

DNP, indicating its potential for effectively quenching TNP and DNP. It was noted that there was a greater overlap in the case of **19** than in the case of **20**. Observations indicate that compound **19** exhibits greater selectivity in detecting TNP and DNP compared to compound **20**, which possesses a longer carbon chain backbone. The topology of ligand **L4** and the structure of compound **19** are the primary factors influencing reactivity with nitroaromatic compounds.

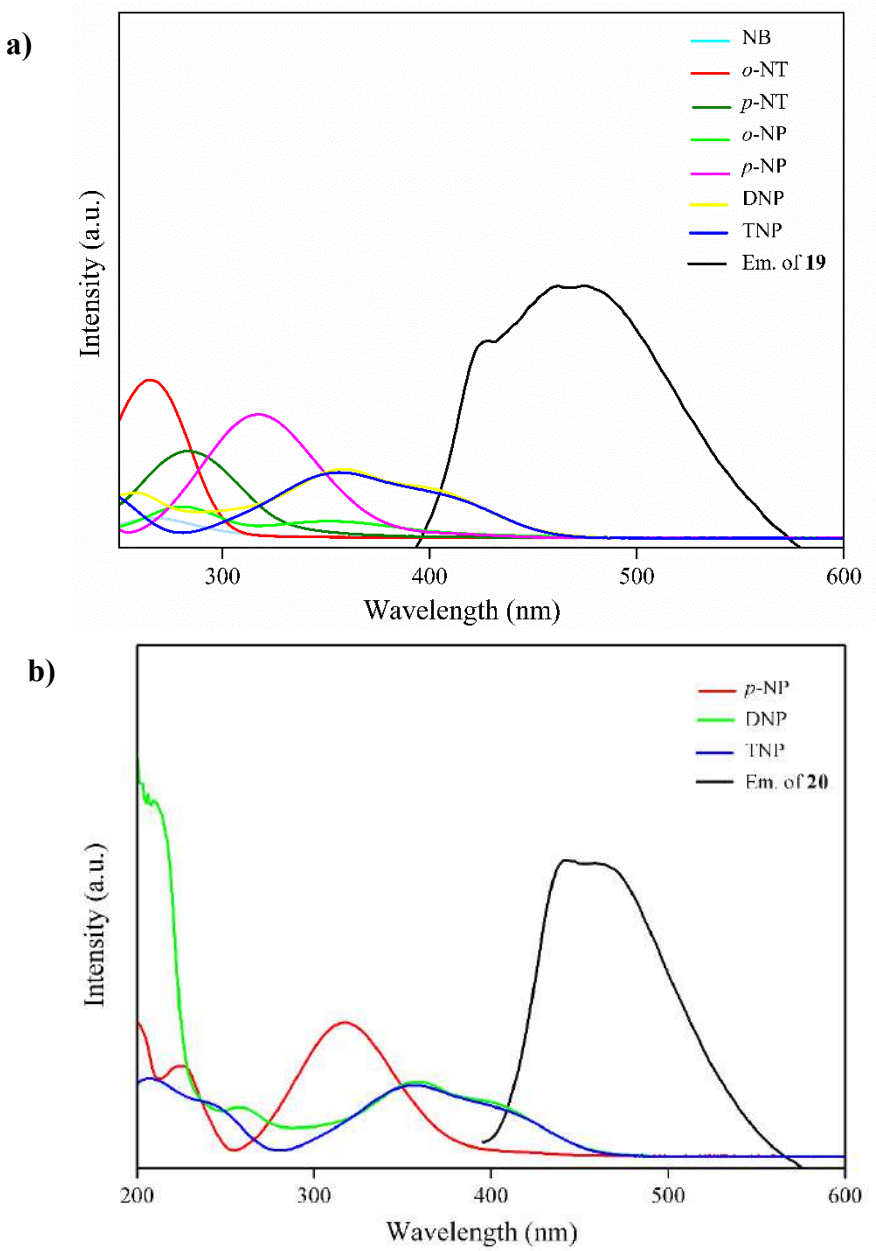

Figure 4.82 *Spectral overlap between the absorption spectra of NACs and the emission spectrum of* ***19*** *(a) in water and* ***20*** *(b) in water.*

4.12 Conclusion

This study examined the structural, spectroscopic, and photophysical characteristics of two Zn(II) compounds, $[Zn(L4)](ClO_4)_2$ **19** and $[Zn(L1)](ClO_4)_2$ **20**. Compound **19** was reevaluated to determine the effect of ligand structure on its electronic property and to compare it with the new compound **20** stabilised by **L1**. The distinct and noticeable influence of the difference in ligand topology was apparent in the reactivity patterns of compounds **19** and **20** with NAC substrates. Compound **19** exhibits superior selectivity for detecting TNP and DNP compared to compound **20**, which possesses a longer carbon chain backbone. The overlap of the absorption band with the emission band is shown, and this overlap is more pronounced in compound **19**.

References

1 A. G. Jarvis, *Curr. Opin. Chem. Biol.*, 2020, **58**, 63–71.

2 A. Das, C. Hessin, Y. Ren and M. Desage-El Murr, *Chem. Soc. Rev.*, 2020, **49**, 8840–8867.

3 A. C. Ghosh, C. Duboc and M. Gennari, *Coord. Chem. Rev.*, 2021, **428**, 213606.

4 T. L. Poulos and A. H. Follmer, *Acc. Chem. Res.*, 2022, **55**, 373–380.

5 D. J. Stuehr, *Biochim. Biophys. Acta - Bioenerg.*, 1999, **1411**, 217–230.

6 C.-C. Wei, B. R. Crane and D. J. Stuehr, *Chem. Rev.*, 2003, **103**, 2365–2384.

7 J. H. Dawson, R. H. Holm, J. R. Trudell, G. Barth, R. E. Linder, E. Bunnenberg, C. Djerassi and S. C. Tang, *J. Am. Chem. Soc.*, 1976, **98**, 3707–3709.

8 T. L. Poulos, *JBIC J. Biol. Inorg. Chem.*, 1996, **1**, 356–359.

9 F. Ogliaro, S. P. de Visser and S. Shaik, *J. Inorg. Biochem.*, 2002, **91**, 554–567.

10 M. Sono, M. P. Roach, E. D. Coulter and J. H. Dawson, *Chem. Rev.*, 1996, **96**, 2841–2888.

11 P. R. Ortiz de Montellano, *Chem. Rev.*, 2010, **110**, 932–948.

12 P. Mondal, I. Ishigami, E. F. Gérard, C. Lim, S.-R. Yeh, S. P. de Visser and G. B. Wijeratne, *Chem. Sci.*, 2021, **12**, 8872–8883.

13 P. Mondal, S. Rajapakse and G. B. Wijeratne, *J. Am. Chem. Soc.*, 2022, **144**, 3843–3854.

14 J. E. Baldwin and M. Bradley, *Chem. Rev.*, 1990, **90**, 1079–1088.

15 M. Lundberg, P. E. M. Siegbahn and K. Morokuma, *Biochemistry*, 2008, **47**, 1031–1042.

16 M. H. Stipanuk, *Annu. Rev. Nutr.*, 2004, **24**, 539–577.

17 C. A. Joseph and M. J. Maroney, *Chem. Commun.*, 2007, 3338.

18 D. Buongiorno and G. D. Straganz, *Coord. Chem. Rev.*, 2013, **257**, 541–563.

19 S. P. de Visser, *Chem. Rec.*, 2018, **18**, 1501–1516.

20 K. V. Goncharenko, A. Vit, W. Blankenfeldt and F. P. Seebeck, *Angew. Chemie Int. Ed.*, 2015, **54**, 2821–2824.

21 M. Fellner, S. Aloi, E. P. Tchesnokov, S. M. Wilbanks and G. N. L. Jameson, *Biochemistry*, 2016, **55**, 1362–1371.

22 N. J. York, M. M. Lockart, S. Sardar, N. Khadka, W. Shi, R. E. Stenkamp, J. Zhang, P. D. Kiser and B. S. Pierce, *J. Biol. Chem.*, 2021, **296**, 100492.

23 S. P. de Visser and G. D. Straganz, *J. Phys. Chem. A*, 2009, **113**, 1835–1846.

24 T. Devi, Y.-M. Lee, W. Nam and S. Fukuzumi, *Coord. Chem. Rev.*, 2020, **410**, 213219.

25 J. Chen, Z. Jiang, S. Fukuzumi, W. Nam and B. Wang, *Coord. Chem. Rev.*, 2020, **421**, 213443.

26 M. R. Bukowski, K. D. Koehntop, A. Stubna, E. L. Bominaar, J. A. Halfen, E. Münck, W. Nam and L. Que, *Science (80-.).*, 2005, **310**, 1000–1002.

27 M. Puri and L. Que, *Acc. Chem. Res.*, 2015, **48**, 2443–2452.

28 A. R. McDonald and L. Que, *Coord. Chem. Rev.*, 2013, **257**, 414–428.

29 K. Warm, A. Paskin, U. Kuhlmann, E. Bill, M. Swart, M. Haumann, H. Dau, P. Hildebrandt and K. Ray, *Angew. Chemie Int. Ed.*, 2021, **60**, 6752–6756.

30 S. Shaik, H. Chen and D. Janardanan, *Nat. Chem.*, 2011, **3**, 19–27.

31 C. Geng, S. Ye and F. Neese, *Angew. Chemie Int. Ed.*, 2010, **49**, 5717–5720.

32 J. Deutscher, P. Gerschel, K. Warm, U. Kuhlmann, S. Mebs, M. Haumann, H. Dau, P. Hildebrandt, U.-P. Apfel and K. Ray, *Chem. Commun.*, 2021, **57**, 2947–2950.

33 C. Van Stappen, Y. Deng, Y. Liu, H. Heidari, J.-X. Wang, Y. Zhou, A. P. Ledray and Y. Lu, *Chem. Rev.*, 2022, **122**, 11974–12045.

34 K. J. Koebke, T. B. J. Pinter, W. C. Pitts and V. L. Pecoraro, *Chem. Rev.*, 2022, **122**, 12046–12109.

35 F. Schwizer, Y. Okamoto, T. Heinisch, Y. Gu, M. M. Pellizzoni, V. Lebrun, R. Reuter, V. Köhler, J. C. Lewis and T. R. Ward, *Chem. Rev.*, 2018, **118**, 142–231.

36 S. A. Kerns, A. Biswas, N. M. Minnetian and A. S. Borovik, *JACS Au*, 2022, **2**, 1252–1265.

37 F. Rosati and G. Roelfes, *ChemCatChem*, 2010, **2**, 916–927.

38 A. F. Peacock, *Curr. Opin. Chem. Biol.*, 2013, **17**, 934–939.

39 A.-F. Miller, *Acc. Chem. Res.*, 2008, **41**, 501–510.

40 N. M. Marshall, D. K. Garner, T. D. Wilson, Y.-G. Gao, H. Robinson, M. J. Nilges and Y. Lu, *Nature*, 2009, **462**, 113–116.

41 A. Singha, A. Sekretareva, L. Tao, H. Lim, Y. Ha, A. Braun, S. M. Jones, B. Hedman, K. O. Hodgson, R. D. Britt, D. J. Kosman and E. I. Solomon, *J. Am. Chem. Soc.*, 2023, **145**, 13284–13301.

42 M. W. Drover, *Chem. Soc. Rev.*, 2022, **51**, 1861–1880.

43 N. Vereshchuk, R. Matheu, J. Benet-Buchholz, M. Pipelier, J. Lebreton, D. Dubreuil, A. Tessier, C. Gimbert-Suriñach, M. Z. Ertem and A. Llobet, *J. Am. Chem. Soc.*, 2020, **142**, 5068–5077.

44 W. Liu, P. J. Das, H. M. Colquhoun and J. F. Stoddart, *CCS Chem.*, 2022, **4**, 755–784.

45 D. D. Narulkar, A. K. Srivastava, R. J. Butcher, K. M. Ansy and S. N. Dhuri, *Inorganica Chim. Acta*, 2017, **467**, 405–414.

46 J. L. Viegas, V. R. Chari and S. N. Dhuri, *ChemistrySelect*, DOI:10.1002/slct.202402704.

47 A. McAuley and C. Xu, *Inorg. Chem.*, 1992, **31**, 5549–5554.

48 L. Kaur and D. Mandal, *Inorg. Chem.*, 2022, **61**, 14582–14590.

49 P. Bhowmik, M. G. B. Drew and S. Chattopadhyay, *Inorganica Chim. Acta*, 2011, **366**, 62–67.

50 G. Mukherjee, A. Alili, P. Barman, D. Kumar, C. V. Sastri and S. P. de Visser, *Chem. – A Eur. J.*, 2019, **25**, 5086–5098.

51 S. Jana, P. De, C. Dey, S. G. Dey, A. Dey and S. Sen Gupta, *Chem. Sci.*, 2023, **14**, 10515–10523.

52 S. Munshi, A. Sinha, S. Yiga, S. Banerjee, R. Singh, M. K. Hossain, M. Haukka, A. F. Valiati, R. D. Huelsmann, E. Martendal, R. Peralta, F. Xavier, O. F. Wendt, T. K. Paine and E. Nordlander, *Dalt. Trans.*, 2022, **51**, 870–884.

53 Y. Li, R. Singh, A. Sinha, G. C. Lisensky, M. Haukka, J. Nilsson, S. Yiga, S. Demeshko, S. J. Gross, S. Dechert, A. Gonzalez, G. Farias, O. F. Wendt, F. Meyer and E. Nordlander, *Inorg. Chem.*, 2023, **62**, 18338–18356.

54 J. Annaraj, S. Kim, M. S. Seo, Y.-M. Lee, Y. Kim, S.-J. Kim, Y. S. Choi, H. G. Jang and W. Nam, *Inorganica Chim. Acta*, 2009, **362**, 1031–1034.

55 J. B. Gordon, A. C. Vilbert, I. M. DiMucci, S. N. MacMillan, K. M. Lancaster, P.

Moënne-Loccoz and D. P. Goldberg, *J. Am. Chem. Soc.*, 2019, **141**, 17533–17547.

56 G. Villar-Acevedo, P. Lugo-Mas, M. N. Blakely, J. A. Rees, A. S. Ganas, E. M. Hanada, W. Kaminsky and J. A. Kovacs, *J. Am. Chem. Soc.*, 2017, **139**, 119–129.

57 J.-U. Rohde, J.-H. In, M. H. Lim, W. W. Brennessel, M. R. Bukowski, A. Stubna, E. Münck, W. Nam and L. Que, *Science (80-.).*, 2003, **299**, 1037–1039.

58 J. Rohde and L. Que, *Angew. Chemie Int. Ed.*, 2005, **44**, 2255–2258.

59 A. F. Vailati, R. D. Huelsmann, E. Martendal, A. J. Bortoluzzi, F. R. Xavier and R. A. Peralta, *New J. Chem.*, 2020, **44**, 2514–2526.

60 J. A. M. Simoes and J. L. Beauchamp, *Chem. Rev.*, 1990, **90**, 629–688.

61 X.-S. Xue, P. Ji, B. Zhou and J.-P. Cheng, *Chem. Rev.*, 2017, **117**, 8622–8648.

62 K. M. Altus and J. A. Love, *Commun. Chem.*, 2021, **4**, 173.

63 D. J. Abrams, P. A. Provencher and E. J. Sorensen, *Chem. Soc. Rev.*, 2018, **47**, 8925–8967.

64 O. Baudoin, *Angew. Chemie Int. Ed.*, 2020, **59**, 17798–17809.

65 L. Guillemard, N. Kaplaneris, L. Ackermann and M. J. Johansson, *Nat. Rev. Chem.*, 2021, **5**, 522–545.

66 R. Jana, H. M. Begam and E. Dinda, *Chem. Commun.*, 2021, **57**, 10842–10866.

67 J. H. Docherty, T. M. Lister, G. Mcarthur, M. T. Findlay, P. Domingo-Legarda, J. Kenyon, S. Choudhary and I. Larrosa, *Chem. Rev.*, 2023, **123**, 7692–7760.

68 D. Balcells, E. Clot and O. Eisenstein, *Chem. Rev.*, 2010, **110**, 749–823.

69 H. M. L. Davies and D. Morton, *ACS Cent. Sci.*, 2017, **3**, 936–943.

70 Y. Wei, P. Hu, M. Zhang and W. Su, *Chem. Rev.*, 2017, **117**, 8864–8907.

71 M. Bietti, *Angew. Chemie Int. Ed.*, 2018, **57**, 16618–16637.

72 T. Rogge, N. Kaplaneris, N. Chatani, J. Kim, S. Chang, B. Punji, L. L. Schafer, D. G. Musaev, J. Wencel-Delord, C. A. Roberts, R. Sarpong, Z. E. Wilson, M. A. Brimble, M. J. Johansson and L. Ackermann, *Nat. Rev. Methods Prim.*, 2021, **1**, 43.

73 S. K. Sinha, S. Guin, S. Maiti, J. P. Biswas, S. Porey and D. Maiti, *Chem. Rev.*, 2022, **122**, 5682–5841.

74 J. Grover, A. T. Sebastian, S. Maiti, A. C. Bissember and D. Maiti, *Chem. Soc. Rev.*, 2025, **54**, 2006–2053.

75 P. Bellotti, H.-M. Huang, T. Faber and F. Glorius, *Chem. Rev.*, 2023, **123**, 4237–4352.

76 G. Saini and M. Kapur, *Chem. Commun.*, 2021, **57**, 1693–1714.

77 A. Das and B. Maji, *Chem. – An Asian J.*, 2021, **16**, 397–408.

78 W. Ali, G. A. Oliver, D. B. Werz and D. Maiti, *Chem. Soc. Rev.*, 2024, **53**, 9904–9953.

79 S. Rej, Y. Ano and N. Chatani, *Chem. Rev.*, 2020, **120**, 1788–1887.

80 B. Liu, A. M. Romine, C. Z. Rubel, K. M. Engle and B.-F. Shi, *Chem. Rev.*, 2021, **121**, 14957–15074.

81 P. Gandeepan, T. Müller, D. Zell, G. Cera, S. Warratz and L. Ackermann, *Chem. Rev.*, 2019, **119**, 2192–2452.

82 S. St John-Campbell and J. A. Bull, *Adv. Synth. Catal.*, 2019, **361**, 3662–3682.

83 J. Loup, U. Dhawa, F. Pesciaioli, J. Wencel-Delord and L. Ackermann, *Angew. Chemie Int. Ed.*, 2019, **58**, 12803–12818.

84 L. Ackermann, *Acc. Chem. Res.*, 2020, **53**, 84–104.

85 R. Ivaniková, R. Boča, L. Dlháň, H. Fuess, A. Mašlejová, V. Mrázová, I. Svoboda and J. Titiš, *Polyhedron*, 2006, **25**, 3261–3268.

86 M. Akbar Ali, A. H. Mirza, F. H. Bujang, M. H. S. A. Hamid and P. V. Bernhardt, *Polyhedron*, 2006, **25**, 3245–3252.

87 R. L. Shook and A. S. Borovik, *Inorg. Chem.*, 2010, **49**, 3646–3660.

88 R. A. Geiger, S. Chattopadhyay, V. W. Day and T. A. Jackson, *Dalt. Trans.*, 2011, **40**, 1707.

89 I. García-Santos, J. Sanmartín, A. M. García-Deibe, M. Fondo and E. Gómez, *Inorganica Chim. Acta*, 2010, **363**, 193–198.

90 J. Jin, Y. Gong, L. Li, X. Han, Q. Meng, Y. Liu and S. Niu, *Spectrochim. Acta Part A Mol. Biomol. Spectrosc.*, 2015, **137**, 856–863.

91 V. P. Daya, R. Jagan and D. K. Chand, *J. Chem. Sci.*, 2022, **134**, 54.

92 V. Borghesani, M. L. Zastrow, A. E. Tolbert, A. Deb, J. E. Penner-Hahn and V. L. Pecoraro, *Chem. – A Eur. J.*, DOI:10.1002/chem.202304367.

93 C. F. Macrae, I. Sovago, S. J. Cottrell, P. T. A. Galek, P. McCabe, E. Pidcock, M. Platings, G. P. Shields, J. S. Stevens, M. Towler and P. A. Wood, *J. Appl. Crystallogr.*, 2020, **53**, 226–235.

94 M. K. Wojnar, K. Kundu, A. Kairalapova, X. Wang, A. Ozarowski, T. C. Berkelbach, S. Hill and D. E. Freedman, *Chem. Sci.*, 2024, **15**, 1374–1383.

95 P. Insiti, P. Jitthiang, P. Harding, K. Chainok, R. Chotima, J. Sirirak, S. Blackwood, A. Alkaş, S. G. Telfer and D. J. Harding, *Polyhedron*, 2016, **114**, 242–248.

96 N. Saravanan, M. Sankaralingam and M. Palaniandavar, *RSC Adv.*, 2014, **4**, 12000–12011.

97 X. Wu, M. S. Seo, K. M. Davis, Y.-M. Lee, J. Chen, K.-B. Cho, Y. N. Pushkar and W. Nam, *J. Am. Chem. Soc.*, 2011, **133**, 20088–20091.

98 A. Murphy, G. Dubois and T. D. P. Stack, *J. Am. Chem. Soc.*, 2003, **125**, 5250–5251.

99 S. Yu, C.-X. Miao, D. Wang, S. Wang, C. Xia and W. Sun, *J. Mol. Catal. A Chem.*, 2012, **353**–**354**, 185–191.

100 J. W. de Boer, W. R. Browne, J. Brinksma, P. L. Alsters, R. Hage and B. L. Feringa, *Inorg. Chem.*, 2007, **46**, 6353–6372.

101 S. Noor, S. Suda, T. Haraguchi, F. Khatoon and T. Akitsu, *Acta Crystallogr. Sect. E Crystallogr. Commun.*, 2021, **77**, 542–546.

102 A. W. Addison, T. N. Rao, J. Reedijk, J. van Rijn and G. C. Verschoor, *J. Chem. Soc., Dalt. Trans.*, 1984, 1349–1356.

103 J. A. R. Hartman, A. L. Kammier, R. J. Spracklin, W. H. Pearson, M. Y. Combariza and R. W. Vachet, *Inorganica Chim. Acta*, 2004, **357**, 1141–1151.

104 A. G. Blackman, E. B. Schenk, R. E. Jelley, E. H. Krenske and L. R. Gahan, *Dalt. Trans.*, 2020, **49**, 14798–14806.

105 S. Alvarez and M. Llunell, *J. Chem. Soc. Dalt. Trans.*, 2000, 3288–3303.

106 J. S. Caygill, F. Davis and S. P. J. Higson, *Talanta*, 2012, **88**, 14–29.

107 E. A. Naumenko, B. Ahlemeyer and E. Baumgart-Vogt, *Environ. Toxicol.*, 2017, **32**, 989–1006.

108 T. M. Mallon, J. M. Ortiz, W. H. Candler, G. Rogers and R. Hillburn, *Mil. Med.*, 2014, **179**, 1374–1383.

109 G. He, H. Peng, T. Liu, M. Yang, Y. Zhang and Y. Fang, *J. Mater. Chem.*, 2009, **19**, 7347.

110 Y. Peng, A.-J. Zhang, M. Dong and Y.-W. Wang, *Chem. Commun.*, 2011, **47**, 4505.

111 Y. Meng, N. Zhang, J. Li, Y. Xu, Q. Yang, Y. Yuan, X. Zhang, J. Wu and L. Zhao, *Spectrochim. Acta Part A Mol. Biomol. Spectrosc.*, 2022, **266**, 120419.

112 S. S. Nagarkar, A. V. Desai, P. Samanta and S. K. Ghosh, *Dalt. Trans.*, 2015, **44**, 15175–15180.

113 Y. Deng, N. Chen, Q. Li, X. Wu, X. Huang, Z. Lin and Y. Zhao, *Cryst. Growth Des.*, 2017, **17**, 3170–3177.

114 D. S. Moore, *Rev. Sci. Instrum.*, 2004, **75**, 2499–2512.

115 S.-P. Wang and H.-J. Chen, *J. Chromatogr. A*, 2002, **979**, 439–446.

116 H. Ebrahimzadeh, Y. Yamini and F. Kamarei, *Talanta*, 2009, **79**, 1472–1477.

117 R. Wilson, C. Clavering and A. Hutchinson, *Anal. Chem.*, 2003, **75**, 4244–4249.

118 A. Jana, J. Mandal, S. Sekhar Mondal, R. Patra and A. Bhunia, *Inorganica Chim. Acta*, 2023, **549**, 121409.

119 A. Gusev, V. Shul'gin, E. Braga, E. Zamnius, M. Kryukova and W. Linert, *Dye. Pigment.*, 2020, **183**, 108626.

120 X.-Q. Song, Y.-Q. Peng, G.-Q. Cheng, X.-R. Wang, P.-P. Liu and W.-Y. Xu, *Inorganica Chim. Acta*, 2015, **427**, 13–21.

121 S. Shanmugaraju and P. S. Mukherjee, *Chem. – A Eur. J.*, 2015, **21**, 6656–6666.

122 A. Barbieri, G. Accorsi and N. Armaroli, *Chem. Commun.*, 2008, 2185.

123 M. Shyamal, A. Panja and A. Saha, *Polyhedron*, 2014, **69**, 141–148.

124 V. Amani, *J. Mol. Struct.*, 2018, **1155**, 477–483.

125 Y. Ma, G. Xu, F. Wei, Y. Cen, Y. Song, M. Shi, X. Xu, M. Sohail and Q. Hu, *New J. Chem.*, 2018, **42**, 5162–5167.

126 T. Chatterjee, E. Hossain, S. Khan, S. Roy, S. M. Wabaidur, M. A. Islam, S. M. Alam and M. H. Mir, *J. Mol. Struct.*, 2023, **1271**, 134011.

127 A. S. Burlov, V. G. Vlasenko, Y. V. Koshchienko, N. I. Makarova, A. A. Zubenko, Y. D. Drobin, G. S. Borodkin, A. V. Metelitsa, Y. V. Zubavichus and D. A. Garnovskii, *Polyhedron*, 2018, **144**, 249–258.

128 Z. I. Contejean and R. L. LaDuca, *J. Solid State Chem.*, 2018, **266**, 44–53.

129 B. Dutta, S. Paul and S. Halder, *Heliyon*, 2023, **9**, e13504.

130 J.-L. Du, X. Lu, T.-L. Shen, C.-P. Li, Y.-J. Mu and L.-J. Li, *Mater. Lett.*, 2015, **158**, 225–228.

131 S. Roy, I. Mondal, K. Harms and S. Chattopadhyay, *Polyhedron*, 2019, **159**, 265–274.

132 A. R. LaDuca and R. L. LaDuca, *CrystEngComm*, 2018, **20**, 5677–5687.

133 X.-Z. Guo, S.-S. Chen, W.-D. Li, S.-S. Han, F. Deng, R. Qiao and Y. Zhao, *ACS Omega*, 2019, **4**, 11540–11553.

134 A. G. Blackman, *Polyhedron*, 2019, **161**, 1–33.

135 W. K. C. Lo, C. J. McAdam, A. G. Blackman, J. D. Crowley and D. A. McMorran, *Inorganica Chim. Acta*, 2015, **426**, 183–194.

136 J. L. Viegas and S. N. Dhuri, *J. Mol. Struct.*, 2023, **1288**, 135719.

137 D. D. Narulkar, K. Devulapally, A. K. U., S. N. Dhuri, V. M. Dhavale, A. K. Vardhaman and L. Giribabu, *Sustain. Energy Fuels*, 2020, **4**, 2656–2660.

138 S. S. Harmalkar, A. V. Naik, M. K. Nilajakar and S. N. Dhuri, *ChemistrySelect*,

2020, **5**, 8447–8454.

139 L. R. D'souza, N. N. Harmalkar and S. N. Dhuri, *ChemistrySelect*, DOI:10.1002/slct.202203016.

140 J. Lin, N. Wang, X. Chen, X. Yang, L. Hong, Z. Ruan, H. Ye, Y. Chen and X. Liang, *Sustain. Energy Fuels*, 2022, **6**, 1312–1318.

141 A. Panja, *Dalt. Trans.*, 2014, **43**, 7760.

142 S. S. Harmalkar, R. J. Butcher, V. V. Gobre, S. K. Gaonkar, L. R. D'Souza, M. Sankaralingam, I. Furtado and S. N. Dhuri, *Inorganica Chim. Acta*, 2019, **498**, 119020.

143 W. P. Sohtun, S. Muthuramalingam, M. Velusamy and R. Mayilmurugan, *Inorg. Chem. Commun.*, 2019, **110**, 107608.

144 A. W. Addison, T. N. Rao, J. Reedijk, J. van Rijn and G. C. Verschoor, *J. Chem. Soc., Dalt. Trans.*, 1984, 1349–1356.

145 L. Yang, D. R. Powell and R. P. Houser, *Dalt. Trans.*, 2007, 955–964.

146 A. G. Blackman, E. B. Schenk, R. E. Jelley, E. H. Krenske and L. R. Gahan, *Dalt. Trans.*, 2020, **49**, 14798–14806.

147 S. Alvarez and M. Llunell, *J. Chem. Soc. Dalt. Trans.*, 2000, 3288–3303.

148 D. Das, B. G. Chand, J. Dinda and C. Sinha, *Polyhedron*, 2007, **26**, 555–562.

149 A. S. Tanwar, R. Parui, R. Garai, M. A. Chanu and P. K. Iyer, *ACS Meas. Sci. Au*, 2022, **2**, 23–30.

CHAPTER 5

CHAPTER 5

Section I: Synthesis and characterization of novel tetradentate Cu(II) compounds and its reactivity

5.1 Introduction and literature

Copper(II) compounds have long attracted attention in bioinorganic chemistry due to their pivotal roles in mimicking metalloenzyme functions and mediating small-molecule transformations relevant to biological processes. In nature, copper centres are integral to enzymes such as nitrite reductases (CuNiRs), laccases, and cytochrome c oxidase, where they participate in electron transfer, substrate activation, and redox catalysis under mild conditions. Nitric oxide (NO) is a gaseous secondary messenger with diverse biological functions, including neurotransmission, vascular regulation, platelet disaggregation, and immune responses in mammals[1–4] as well as plant growth and stress regulation[5]. Inadequate NO production has been linked to conditions such as atherosclerosis, diabetic hypertension, and other pathologies[6], while excessive NO or its oxidized derivatives, peroxynitrite ($ONOO^-$)[7,8] and nitrogen dioxide ($\bullet NO_2$)[9], can lead to cytotoxic effects and oxidative damage[10,11].

In living systems, NO is produced primarily by nitric oxide synthases (NOSs) and nitrite reductases (NiRs)[12,13]. NOSs, which are heme-containing enzymes, catalyse the oxidation of L-arginine to L-citrulline with NO release[14]. Under hypoxic conditions, NOS activity can be suppressed, and nitrite (NO_2^-) becomes an alternative NO source via NiR-mediated reduction[15]. In bio-physiological processes, copper containing NiRs (CuNiRs) catalyse the electron, H^+ reduction of nitrite to NO, while in mammals, hemoglobins and other metalloproteins exhibit NiR-like activity[4,16,17].

CuNiRs contain two mononuclear Cu sites: a type 1 (T1) electron transfer centre with a $(His)_2(Met)Cu(Cys)$ motif and a type 2 (T2) catalytic site with a $(His)_3Cu–OH_2$ coordination environment. Proton responsive residues such as Asp98 and His255, positioned near the T2 site, facilitate proton transfer and promote N–O bond cleavage in the bound nitrite[18,19].

The fleeting nature of Cu–HONO intermediates and the complexity of the protein matrix hinder direct mechanistic elucidation. Consequently, numerous synthetic models have been developed to replicate aspects of CuNiR chemistry, capturing key nitrite binding

modes (κ^2-O,O′ vs κ^1-N)[20–27] and enabling studies on proton coupled electron transfer (PCET) and metal nitrosyl formation.

Acid induced reduction of Cu(II)–nitrite compounds has been shown to produce NO along with either H_2O or H_2O_2, depending on the amount of proton source used. Mechanistic proposals frequently involve the formation of a Cu–HONO intermediate, followed by N–O bond homolysis. Secondary sphere proton donors or hydrogen bonding functionalities have been demonstrated to enhance nitrite activation, accelerate reaction kinetics, and stabilise reactive intermediates[28–30].

Despite significant progress, catalytic H^+ driven NO generation from Cu(II)–nitrite compounds remain relatively unexplored, and the mechanistic basis for divergent product formation is still unclear. Furthermore, the bidirectional interconversion between NO_2^- and NO mimicking the dual NiR and nitric oxide oxidase (NOO) activities found in biology has only recently been demonstrated in mononuclear Cu(II) systems[31,32]. This reactivity is influenced not only by the Cu(II)/Cu(I) redox potential but also by ligand induced geometric preferences that dictate substrate binding and electron transfer pathways[33].

In this chapter, we present the design, synthesis, and characterization of novel tetradentate ligand architecture, *N^1,N^3,2,2-tetramethyl-N^1,N^3-bis(pyridin-2-ylmethyl)propane-1,3-diamine* (**L8**), along with reactivity of new biomimetic Cu(II) compounds $[Cu(L8)](ClO_4)_2$ **21** and $[Cu(L8)(NO_2)](ClO_4)$ **22**, that emulate the active site chemistry of CuNiR enzymes. This compounds incorporate ligand architectures that combine robust primary coordination with strategically placed secondary sphere H-bonding sites to facilitate controlled proton delivery to bound nitrite. Through systematic variation of ligand structure and reaction conditions, we investigate acid induced nitrite reduction, thereby contributing to a potential mimic of Cu-mediated NO_2^-/NO interconversion.

5.2 Experimental details

5.2.1 Synthesis of ligand L8

A solution of 2,2-dimethyl-1,3-propanediamine (1.4 g, 14.0 mmol) in 5 mL ethanol was added dropwise to a stirred solution of pyridine-2-carboxaldehyde (3.0 g, 28.0 mmol) in 15 mL ethanol. The reaction mixture was heated under reflux with stirring for 5 h. After cooling to ambient temperature, the solvent was removed under reduced pressure to afford a semisolid imine, which was redissolved in 20 mL methanol. Sodium borohydride (0.48 g, 12.8 mmol) was then introduced portionwise, and the mixture was stirred overnight. Removal of the methanol yielded a crude residue that was suspended in 20 mL water and extracted three times with 30 mL portions of ethyl acetate, providing an orange viscous oil (2.6 g, 8.6 mmol). This oil was dissolved in 3 mL water and cooled in an ice bath, after which 22 mL of 37 % formaldehyde solution and 15 mL of 85 % formic acid were added. The resulting mixture was refluxed for 24 h, then cooled and adjusted to pH 12 with 2 M NaOH. The brown oil obtained by extracting with chloroform (4 × 20 mL) was subsequently dissolved in aqueous HCl (pH 1) and then basified again to pH 12 using NaOH. A final extraction with diethyl ether afforded **L8** as a yellow oil. The yield of **L8** was 3.8g (12.30 mmol), 88%. *Anal. Calc.* for **L8** $C_{19}H_{28}N_4$ (%): C, 73.04; H, 9.03; N, 17.93; *Found:* C, 73.59; H, 9.48; N, 17.98; IR (KBr, cm^{-1}): 2863-3060 υ(CH); 1590 υ(C=C); 1570 υ(C=N); ^{1}H NMR ($CDCl_3$, ppm): δ 8.50 (d, 2H, *J* = 4.4 Hz), δ 7.65 (t, 2H, *J* = 7.6 Hz), δ 7.56 (d, 2H, *J* = 8.0 Hz), δ 7.15 (t, 2H, *J* = 5.6 Hz), δ 3.74 (s, 4H), δ 2.40 (s, 4H), δ 2.27 (s, 6H), δ 0.92 (s, 6H).^{13}C NMR ($CDCl_3$, ppm): δ 160.74, δ 148.73, δ 136.44, δ 122.55, δ 121.75, δ 67.50, δ 66.61, δ 45.67, δ 38.88, δ 24.57.

5.2.2 Synthesis of Cu(II) compound $[Cu(L8)](ClO_4)_2$ 21

L8 (0.42 g, 1.35 mmol) was dissolved in 5 mL of acetonitrile and added dropwise to a stirred solution of $Cu(ClO_4)_2 \cdot 6H_2O$ (0.50 g, 1.35 mmol) in 2 mL of acetonitrile at ambient temperature. After stirring for approximately 5 h, 10 mL of diethyl ether was carefully introduced to the deep blue reaction mixture, which was then left stationary to allow crystallization. Over the course of 24 h, blue crystals formed, were collected by filtration, and air dried to give compound **21** in 80 % yield (0.62 g, 1.07 mmol). *Anal. Calc.* for **21** C_{19} H_{28} Cl_2 Cu N_4 O_8 (%): C, 39.69; H, 4.91; N, 9.75. *Found:* C, 38.78; H, 5.23; N, 8.98. IR (KBr, cm^{-1}): 2898-2996 υ(CH);1096, 621 υ(ClO_4); UV-Vis data, λ_{max}, CH_3CN/nm

(ε/dm^3 mol^{-1} cm^{-1}): 570 (136). ESI-MS: m/z = 188.0 (calc. 188.0) for $[Cu(L8)]^{2+}$ and m/z = 476.2 (calc. 476.2) for $[Cu(L8)(ClO_4)]^+$.

5.2.3 Synthesis of Cu(II) compound $[Cu(L8)(NO_2)](ClO_4)$ 22

To a 20 ml CH_3CN solution of $[Cu(L8)](ClO_4)_2$ (574.9 mg, 1.0 mmol), 1.0 mL aqueous solution of $NaNO_2$ (69 mg, 1.0 mmol) was added slowly with constant stirring and the colour of the reaction mixture changes from blue to cyan-green. The mixture was stirred for 1 hour at 298 K. The volume of the reaction mixture was decreased to 10 mL under reduced pressure and then layered with diethyl ether and kept for crystallization at 298 K. Compound **22** gave 92 % yield (479.7 mg, 0.91 mmol). *Anal. Calc.* for **22** C_{19} H_{28} Cl Cu N_5 O_6 (%): C, 43.76; H, 5.41; N, 13.43. *Found:* C, 43.97; H, 5.64; N, 13.71. UV-Vis data, λ_{max}, CH_3CN/nm (ε/dm^3 mol^{-1} cm^{-1}): 365 (797) and 683 (172). ESI-MS: m/z = m/z = 422.0 (calc. 422.0) for $[Cu(L8)(NO_2)]^+$.

5.3 Results and discussions

5.3.1 Synthesis and characterization of L8

The tetradentate N-methylated pyridylamine ligand (**L8**) was prepared in two steps from its non-methylated precursor (**Scheme 5.1**). First, 2,2-dimethyl-1,3-propanediamine was condensed with pyridine-2-carboxaldehyde, and the resulting imine intermediate was reduced with $NaBH_4$ to furnish the secondary amine ligand (reductive amination). In the second step, exhaustive N-methylation was achieved using the Eschweiler-Clarke protocol (formaldehyde/formic acid)[34], converting the secondary amines to their N-methyl derivatives and affording **L8** in good yield.

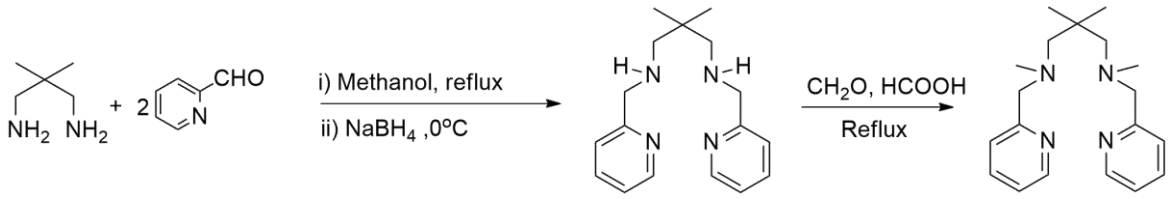

Scheme 5.1 *Synthesis route to ligand **L8**.*

IR spectrum of ligand **L8** was recorded in the region 4000 – 400 cm^{-1}. The IR spectrum (**Figure 5.1**) show features attributed to the ligand formation. The IR spectrum of **L8** exhibits the expected features for a pyridyl appended, tertiary amine macrocycle. A weak aromatic ν(C–H) bands at 3060–3000 cm^{-1} and aliphatic ν(C–H) absorptions at ~2945 and

2863 cm^{-1}. The ring stretching region is dominated by strong pyridyl ν(C=C/C=N) bands at ~1590 and ~1570 cm^{-1}[35].

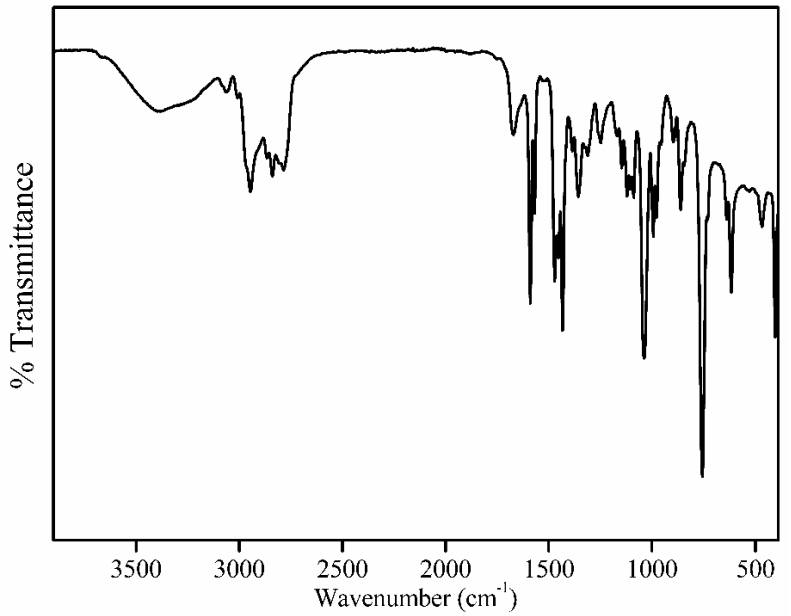

Figure 5.1 *IR spectrum of the ligand* ***L8.***

The structure of the ligands was confirmed by ^{1}H and ^{13}C NMR spectroscopy and the corresponding peaks were assigned in the corresponding NMR spectra as depicted in **Figure 5.2**.

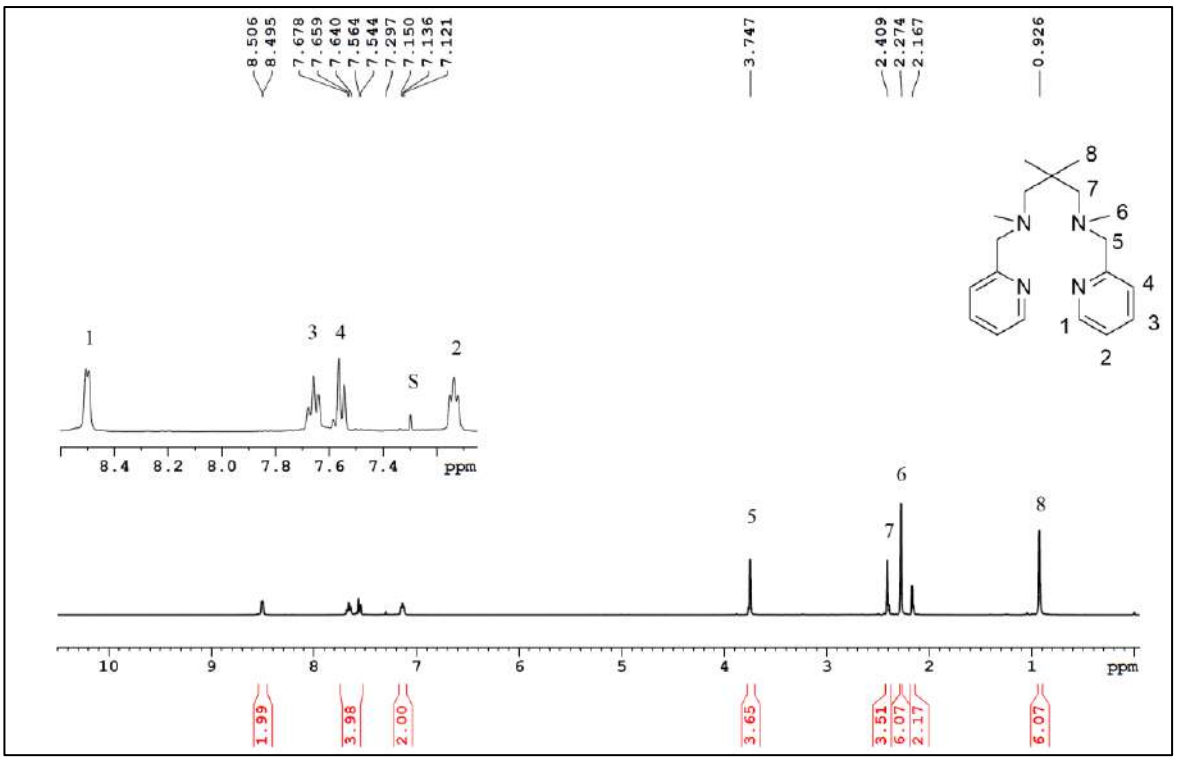

Figure 5.2 *The ^{1}H NMR spectrum of* ***L8*** *recorded in $CDCl_3$ (S stands for solvent peak).*

5.3.2 Synthesis and characterization of 21

An equimolar reaction of **L8** with copper(II) perchlorate (1.96 mmol) in acetonitrile at room temperature furnished the compound $[Cu(L8)](ClO_4)_2$ **21** in high yield, following the procedure described in **Section 5.2.2** (**Scheme 5.2**). The compound was characterized by elemental (C, H, N, S) analysis, IR and UV–Vis spectroscopy, ESI-MS, VSM, PXRD and single crystal X-ray diffraction.

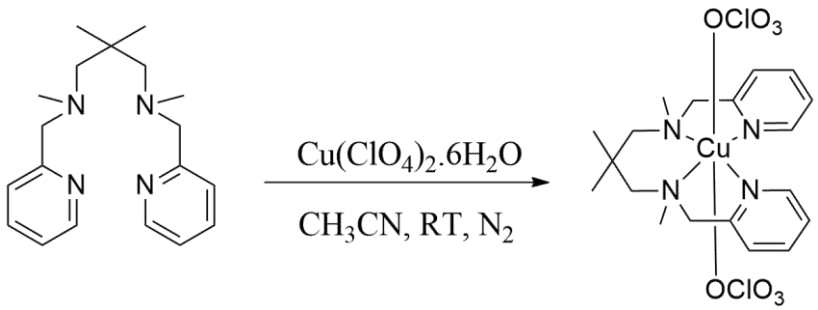

Scheme 5.2 *Synthesis route to Cu(II) compound* ***21****.*

The infrared spectrum of compound **21** (**Figure 5.3**) shows weak aliphatic C–H stretching features at 2898–2996 cm^{-1}. The aromatic region is dominated by intense pyridyl ring bands assigned to ν(C=C)/ν(C=N) at ~1612 and ~1471 cm^{-1}. Further, presence of perchlorate ions was revealed from well pronounced absorption peaks at 1096 cm^{-1} and 621 cm^{-1}[36,37].

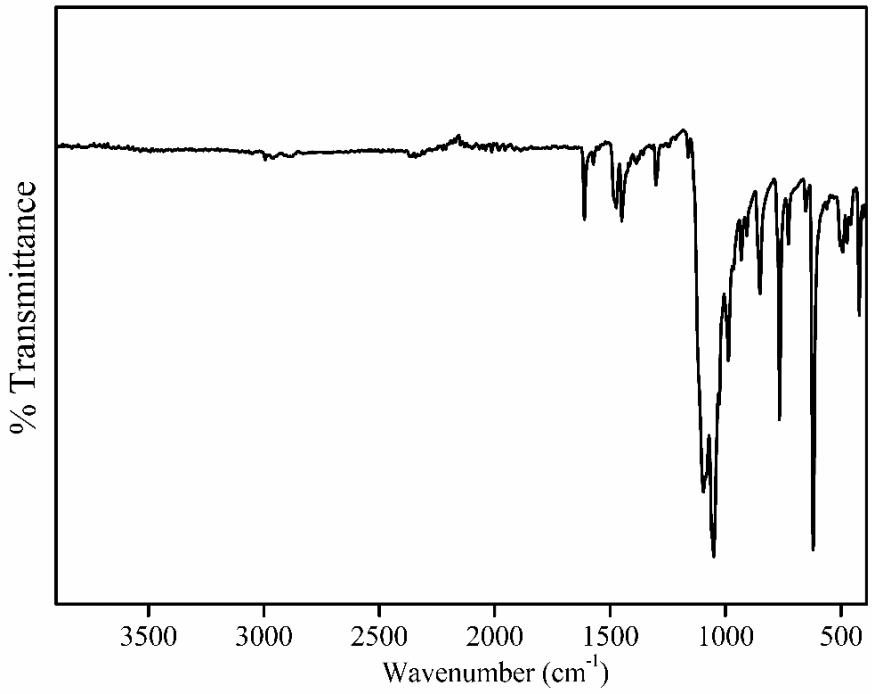

Figure 5.3 *IR spectrum of the compound* ***21****.*

Electrospray ionization mass spectrometry (ESI-MS) of **21** in acetonitrile revealed two dominant ions at *m/z* 188.0 (calc. *m/z* 188.0) and 476.2 (calc. *m/z* 476.2), assignable to the cation $[Cu(L8)]^{2+}$ and the perchlorate adduct $[Cu(L8)(ClO_4)]^{+}$, respectively (**Figure 5.4**), consistent with the proposed formulation.

Temperature dependent magnetic susceptibility was measured on finely ground sample of compound **21** under a field of 100 Oe over 60–350 K. Zero-field-cooled/field-cooled (ZFC/FC) protocols were employed: for ZFC, the sample was cooled to 60 K in zero field, after which the field was applied and data were collected on warming; for FC, cooling and warming were performed under the applied field. The magnetization (emu g^{-1}) is higher at 60 K and decreases progressively toward room temperature, and the FC curve lies above the ZFC trace across the measured range (**Figure 5.5**). The enhanced FC signal is consistent with field induced alignment of unpaired spins, whereas the reduced ZFC response reflects spin randomization in the absence of field during cooling. Overall, the M–T behavior indicates simple paramagnetism with no evidence of long-range ordering in this temperature window[38].

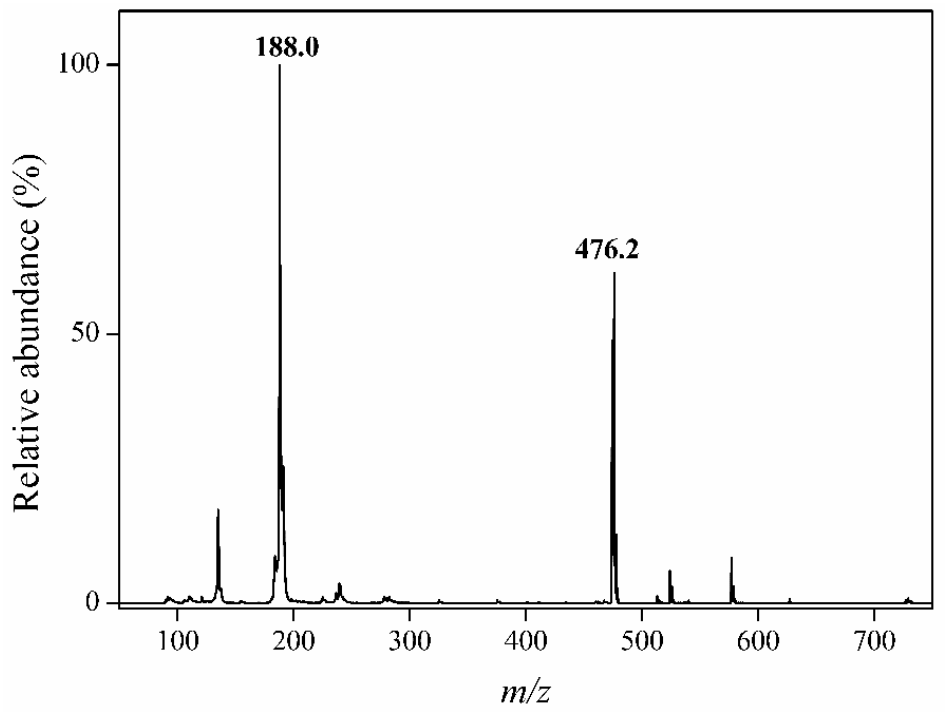

***Figure 5.4** ESI-MS spectrum of **21** recorded in acetonitrile solvent.*

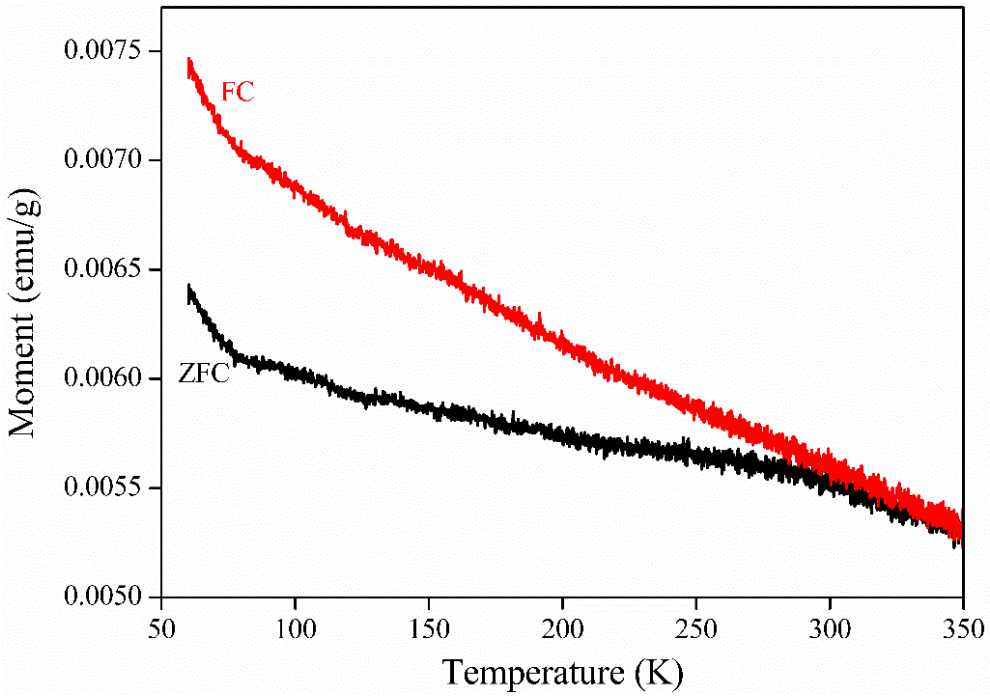

Figure 5.5 *Plot of Magnetic moment vs. Temperature for* ***21*** *under an applied field of 100 Oe between 60 to 300 K.*

Powder X-ray diffraction (PXRD) was used to verify that the bulk sample of **21** corresponds to the single-crystal phase. The experimental PXRD pattern was compared with a simulated pattern generated from the single crystal structure of **21** (Mercury 4.0)[39]. The close correspondence of peak positions confirms phase purity and equivalence of the bulk and single crystal material (**Figure 5.6**).

The UV-Vis spectrum of compound **21** was recorded in CH_3CN. The intense band observed in the high energy region are assigned to the Cu(II)-pyridine charge transfer band (276 nm). The weaker *d-d* band is observed as a broad band centered at 570 nm (**Figure 5.7**).

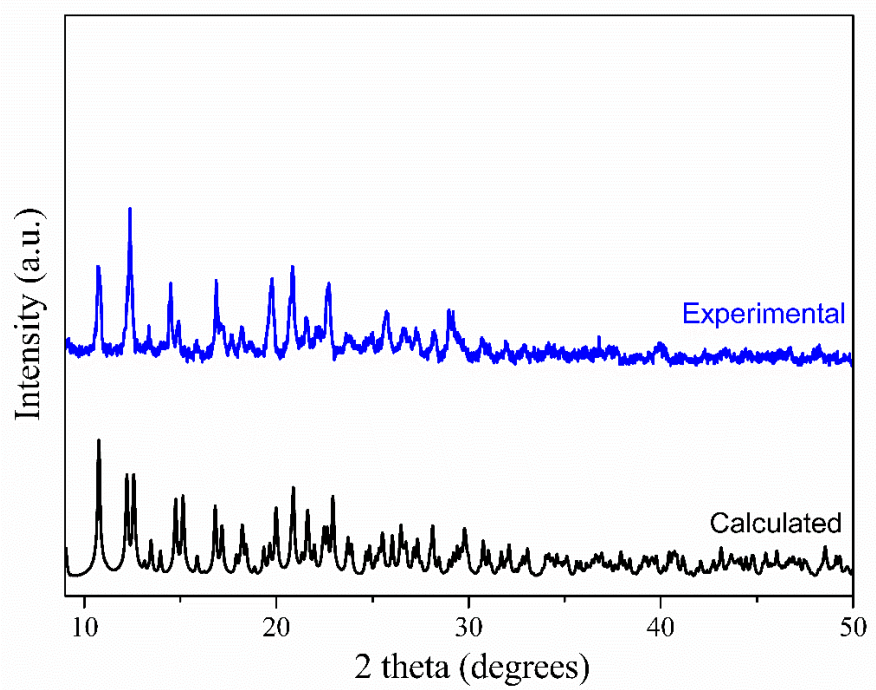

Figure 5.6 *The experimental and calculated PXRD pattern of* ***21****.*

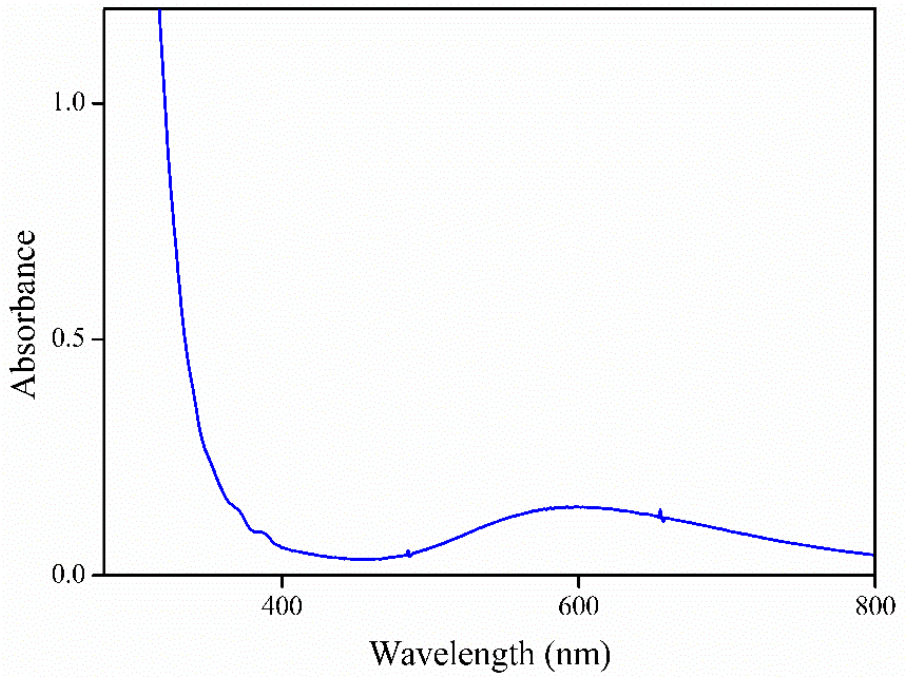

Figure 5.7 *UV-Vis spectrum of* ***21*** *in acetonitrile solvent.*

5.3.3 Structural analysis of 21

Data collection and refinement parameters of compound **21** are summarized in **Table 5.2**, and selected bond lengths and angles are provided in **Table 5.1**. Compound **21** crystallizes in the monoclinic space group $P2_1/n$. The Cu(II) center is hexacoordinate, with four nitrogen donors from ligand **L8** forming the equatorial plane and two perchlorate oxygen atoms occupying mutually *trans* axial positions (**Figure 5.8**). The coordination environment is octahedral but exhibits a pronounced tetragonal elongation arising from the Jahn–Teller effect. Consistent with weak axial coordination, the apical Cu–O separations are long (Cu1–O1 = 2.510 Å; Cu1–O7 = 2.463 Å). A survey of the Cambridge Structural Database (CSD) indicates an average Cu^{2+}–O separation of ~2.40 Å, supporting the conclusion that the perchlorate bind only weakly in **21** [40]. The Cu–N bond lengths fall in the range 2.025–2.049 Å. Notably, the Cu–N(pyridyl) contacts are shorter (2.025–2.035 Å) than the Cu–N(amine) contacts (2.046–2.049 Å), indicating stronger coordination by the sp^2 hybridized pyridyl donor. This likely reflects its enhanced backbonding relative to the sp^3 aliphatic amine. The N-methyl substituents on the amine donors are arranged *trans* across the N_4 equatorial plane.

Within the N_4 equatorial set, the two chelate bite angles are tight: N(4)–Cu(1)–N(3) = 81.45(15)° and N(1)–Cu(1)–N(2) = 81.68(14)°, as expected for five-membered chelate rings. The nitrogens of the ligand are arranged approximately *trans* to one another, with N(1) and N(3) nearly colinear [N(1)–Cu(1)–N(3) = 175.02(15)°] and N(4) opposite N(2) [175.32(15)°]. The remaining N–Cu–N *cis* angles deviate moderately from 90° [N(3)–Cu(1)–N(2) = 93.90(14)°, N(1)–Cu(1)–N(4) = 102.94(15)°], reflecting the chelate constraints.

The two axial perchlorate donors are close to *trans* [O(1)–Cu(1)–O(7) = 165.83°], and their interactions with the equatorial nitrogens show typical octahedral distortions (e.g., O(1)–Cu(1)–N(1) = 81.71°, O(1)–Cu(1)–N(3) = 96.67°, O(7)–Cu(1)–N(1) = 85.69°, O(7)–Cu(1)–N(3) = 96.41°, O(7)–Cu(1)–N(2) = 86.89°, O(7)–Cu(1)–N(4) = 94.17°). The octahedral angular distortion parameter is approximately 81°.

The molecular packing of compound **21** along crystallographic axes a and c illustrates the alternate arrangement of Cu(II) cationic unit and the weakly bound perchlorate anions (**Figure 5.9**).

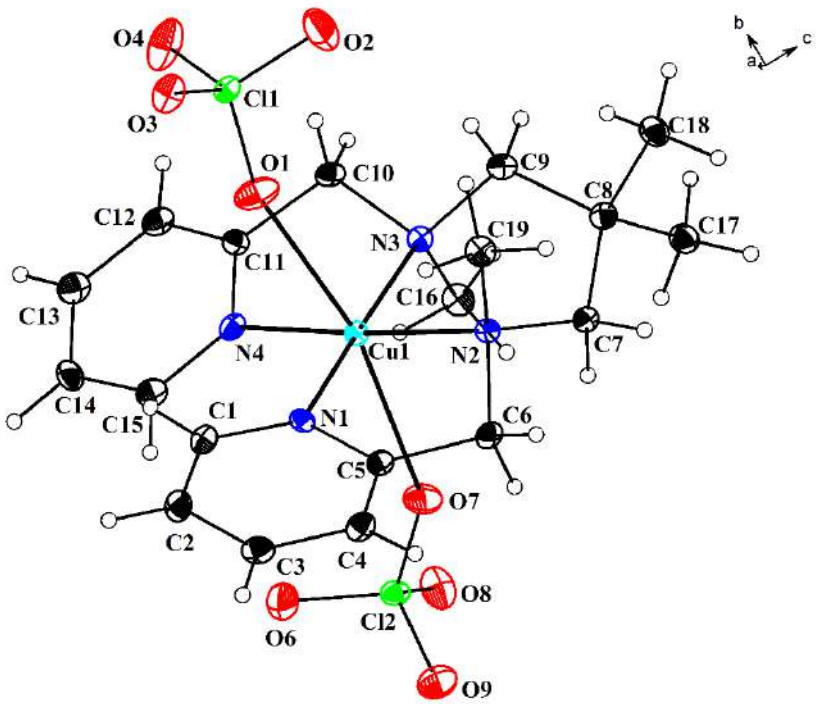

Figure 5.8 *Crystal structure of* ***21*** *showing atom labelling scheme. The thermal ellipsoids are drawn at a 30 % probability level for all the atoms except for the H atoms, which are shown as spheres of arbitrary radii.*

Table 5.1 *Selected bond lengths (Å) and angles (°) for* ***21****.*

Bond lengths (Å)			
Cu(1)-N(1)	2.025(3)	Cu(1)-N(4)	2.035(4)
Cu(1)-N(3)	2.046(4)	Cu(1)-N(2)	2.049(4)
Cu(1)-O(1)	2.510(0)	Cu(1)-O(7)	2.463(0)
Bond angles (°)			
N(1)-Cu(1)-N(4)	102.94(15)	N(1)-Cu(1)-N(3)	175.02(15)
N(4)-Cu(1)-N(3)	81.45(15)	N(1)-Cu(1)-N(2)	81.68(14)
N(4)-Cu(1)-N(2)	175.32(15)	N(3)-Cu(1)-N(2)	93.90(14)
O(1)-Cu(1)-O(7)	165.83(0)	O(2)-Cu(1)-N(4)	82.43(0)
O(1)-Cu(1)-N(3)	96.67(0)	O(1)-Cu(1)-N(1)	81.71(0)
O(1)-Cu(1)-N(2)	97.62(0)	O(7)-Cu(1)-N(1)	85.69(0)
O(7)-Cu(1)-N(4)	94.17(0)	O(7)-Cu(1)-N(3)	96.41(0)
O(7)-Cu(1)-N(2)	86.89(0)		

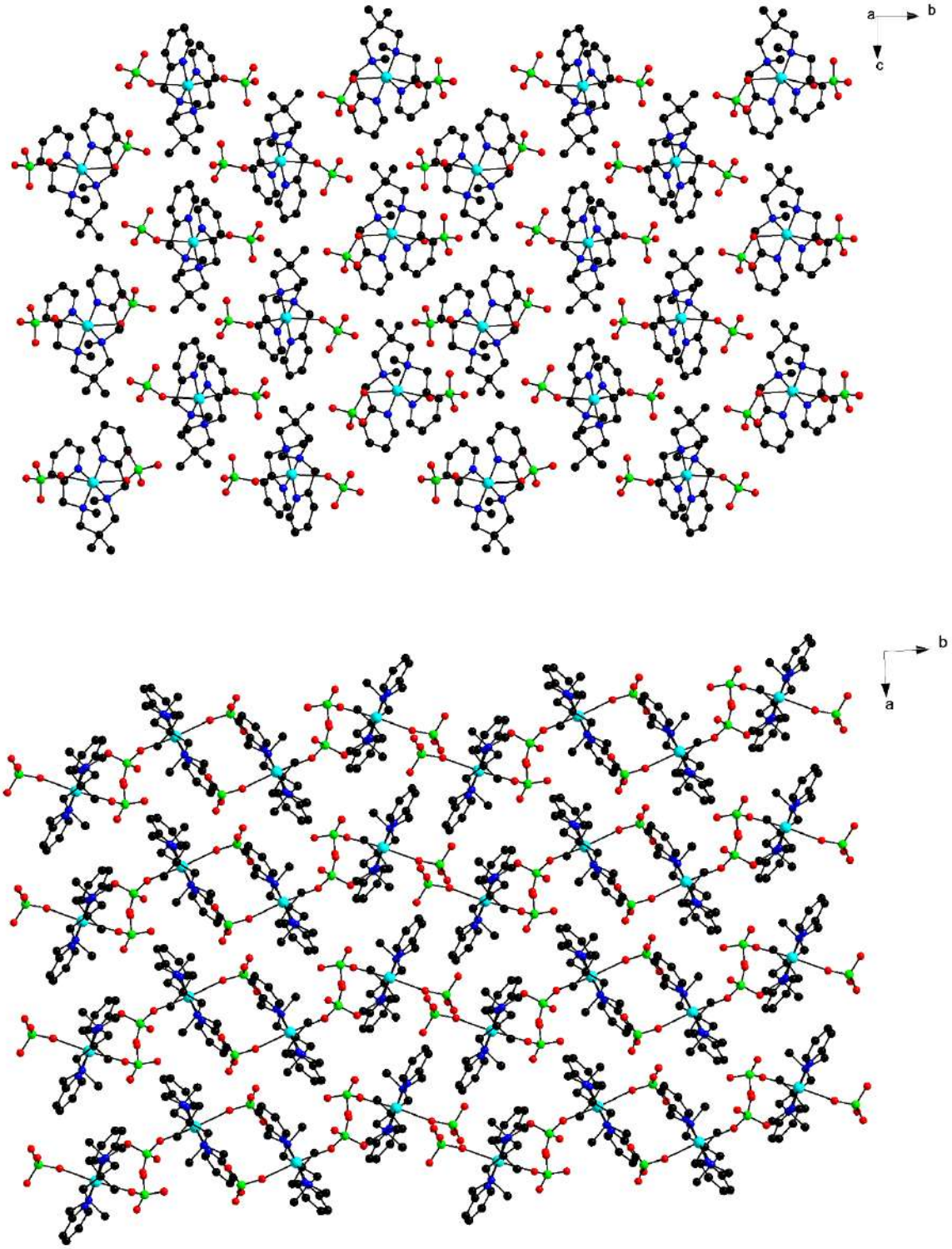

Figure 5.9 *Packing in* ***21*** *view along crystallographic a and c axis. Colour code: C, black; N, blue; O, red; Cl, green and Cu, cyan.*

Table 5.2 *Technical details of crystal data and structure refinement parameters of* ***21****.*

Compound	**21**
Empirical formula	C_{19} H_{28} Cl_2 Cu N_4 O_8
Formula weight	574.90
Temperature	296(2) K
Wavelength	0.71073 Å
Crystal system	Monoclinic
Space group	$P2_1/n$
Unit cell dimensions	a = 8.4809(8) Å b = 26.264(2) Å c = 10.7320(10) Å α = 90° β = 101.007(2)° γ = 90°
Volume	2346.5(4) $Å^3$
Z	4
Density (calculated)	1.627 mg/m^3
Absorption coefficient	1.212 mm^{-1}
F(000)	1188
Theta range for data collection	2.479 to 28.361°
Completeness to theta	99.2%
Index ranges	-11≤ h≤11 -35≤ k≤ 26 -9≤ l≤14
Reflections collected	9714
Independent reflections	5806 (R_{int}= 0.0329)
Refinement method	Full-matrix least-squares on F^2
Absorption correction	Semi- empirical from equivalents
Data/restraints/parameters	5806 / 0 / 318
Goodness-of-fit on F^2	1.182
Final *R*indices[I>2sigma(I)]	R1= 0.0694, wR2= 0.1293
R indices (all data)	R1= 0.0889, wR2= 0.1351
CCDC No.	2375642

5.3.4 Optimized geometrical features of 21

Geometry optimization of the Cu(II) complex with ligand L8 was performed using the TPSSH functional with the def2-TZVP basis set[41,42]. Subsequent frequency calculations confirmed that the optimized geometry corresponded to a true local minimum on the potential energy surface (**Figure 5.10**). All theoretical calculations were carried out with the Gaussian 16 software package[43]. The optimized structure indicated that the Cu(II) center is coordinated by two amine and two pyridyl nitrogen donors, with the pyridyl nitrogens forming slightly shorter bonds [2.00–2.02 Å] than the amine nitrogens

[2.05–2.06 Å]. This difference arises from the sp^2 hybridization of the pyridyl nitrogens, which allows additional back-donation to the metal center. The Cu(II) atom lies in an essentially planar environment imposed by the fused 5–6–5 chelate ring system, with the central six-membered ring adopting a chair conformation, contributing to the shorter Cu–N(pyridyl) distances (~2.00 Å). Two geometric isomers, *cis* and *trans*, were theoretically possible: in the *cis* isomer, both NCH_3 substituents lie on the same side of the plane, whereas in the *trans* isomer, the substituents are positioned opposite each other (**Figure 5.10**). The calculated energy difference (ΔE = 2 kcal mol^{-1}) indicated that the *trans* isomer is significantly more stable than the *cis* form, such that no *cis–trans* equilibrium is expected. Furthermore, the *trans* isomer maintains a chair conformation for the central ring, whereas the *cis* isomer adopts a boat conformation, consistent with the larger chelate cavity of the 5–6–5 ring system favoring the trans geometry.

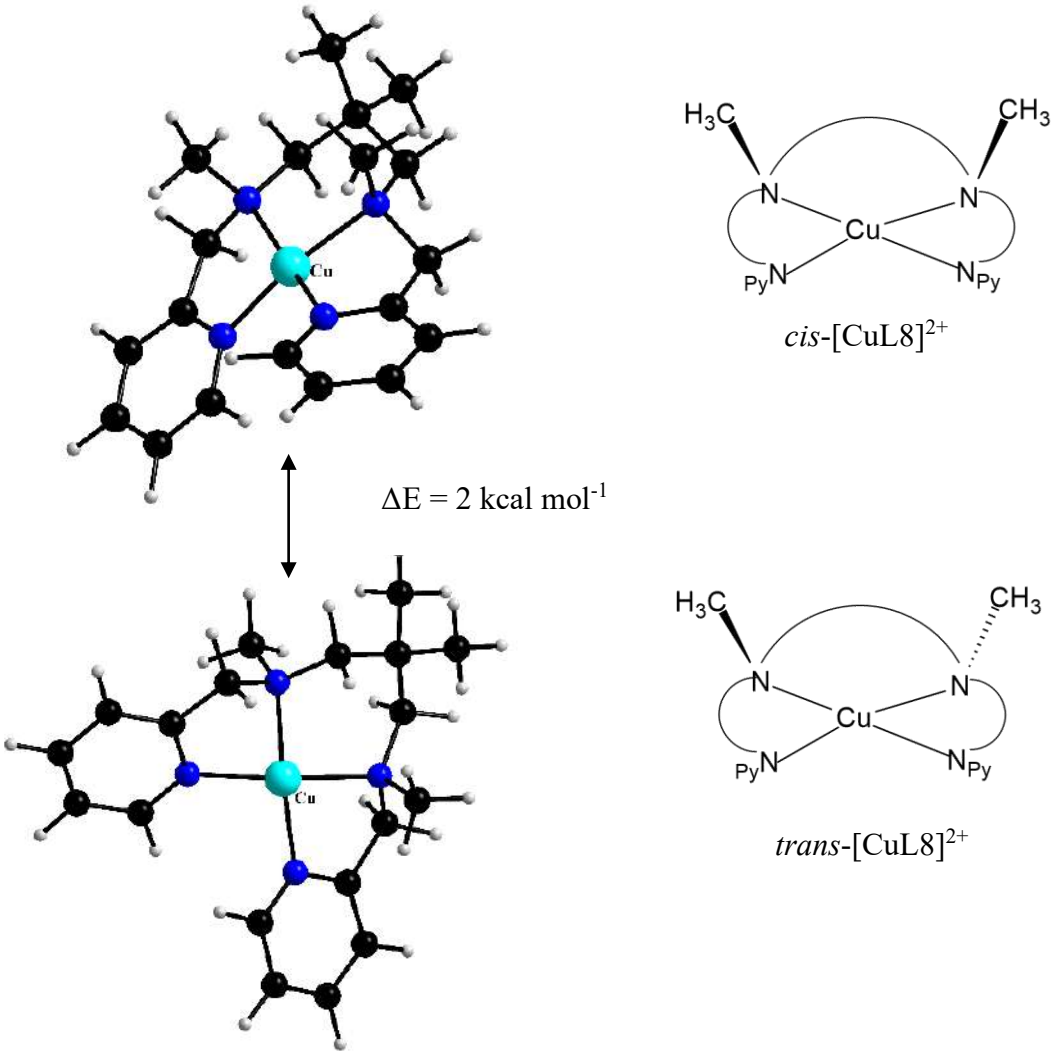

Figure 5.10 *Optimized geometry of* Cu^{II} *with* ***L8*** *and its presence in the cis and trans isomers.*

5.4 Modelling of the NO_x reactivity at the mononuclear Cu(II) site

Copper nitrite reductases demonstrate that a single Cu center, embedded in an N-donor field, can bind and transform NO_x species with high chemoselectivity. To emulate this in a controllable, spectroscopically tractable way, we employed the tetradentate aminopyridine ligand **L8**, which furnished a N_4 square planar platform around Cu(II) while leaving axial sites available for exogenous donors.

The precursor salt, $[Cu(L8)](ClO_4)_2$, was intentionally formulated so that both perchlorate anions are only weakly associated with the cationic core. In practice, ClO_4^- serves as a labile, weakly coordinating placeholder at the axial sites, ensuring that the Cu center remains geometrically pre-organized yet substitution ready. This lability is a feature, not a bug: it enables direct displacement by incoming NO_x ligands without perturbing the N_4 scaffold.

Introducing nitrite under mild conditions furnished the targeted model compound, $[Cu(L8)(NO_2)](ClO_4)$ **22**, by substituting the weakly bound perchlorate donors at the open coordination site (**Scheme 5.3**). In the isolated nitrito adduct, ClO_4^- now primarily plays its conventional role as non-coordinating counter ion that balance charge, while NO_2^- occupied the Cu coordination sphere (κ^2-*O,O'*), completing a weakly hexacoordinate environment. This conversion transformed a "latent" Cu(II) compound into a purpose-built probe for NO_x chemistry; one that allows us to define nitrite binding mode and map proton-dependent product formation.

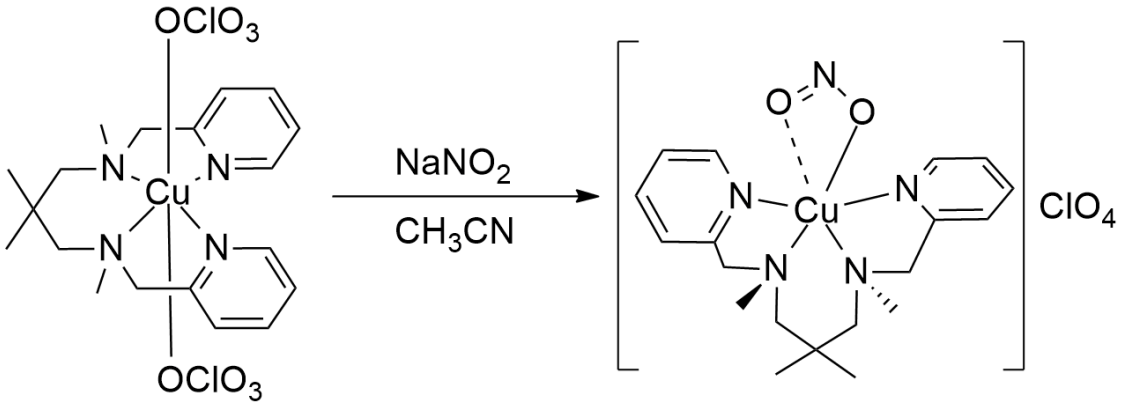

Scheme 5.3 *Synthesis route to compound* ***22****.*

5.4.1 Structural analysis and characterization of 22

Structurally characterized copper(II)–nitrite compounds most often display nitrite coordination through κ^2-*O,O'* or κ^1-*O,* binding modes whereas copper(I)–nitrite species preferentially bind nitrite via a κ^1-*N* linkage[21–24]. Data collection and refinement parameters of compound **22** are summarized in **Table 5.4**, and selected bond lengths and angles are provided in **Table 5.3**. Compound **22** crystallizes in the monoclinic space group *Pn*. The molecular structure of compound **22** obtained from X-ray diffraction analysis discloses a copper(II) site featuring nitrite bound in an unsymmetrical κ^2-*O,O'* fashion (Cu1−O1 2.057(6) Å, Cu1···O2 2.587 Å). The crystal structure of **22** shows a hexa-coordinated Cu(II) center in a distorted octahedral geometry defined by two pyridyl nitrogen donors [Cu–N(4) = 2.027(6) Å, Cu–N(1) = 2.179(6) Å], two amine nitrogen donors [Cu–N(2) = 2.050(6) Å, Cu–N(3) = 2.082(5) Å], and two oxygen atoms from a chelating κ²-(O,O′)-nitrito ligand [Cu–O(1) = 2.057(6) Å, Cu–O(2) = 2.587(1) Å] (**Figure 5.11**). The longer Cu–N(1) bond is consistent with its position trans to the strongly bound nitrito oxygen O(1), reflecting a pronounced trans influence. The nitrite group binds asymmetrically, with the coordinated N–O bond [N(5)–O(1) = 1.262(1) Å] elongated relative to the non-coordinated N=O bond [N(5)–O(2) = 1.229(1) Å]; the O–N–O angle is 113.13(1)°, typical of O,O′-chelating nitrite. The tetradentate chelate bite angles remain tight [N(4)–Cu–N(3) = 81.9(2)°, N(2)–Cu–N(1) = 81.1(2)°], while non-bite cis angles show greater deviations, such as N(3)–Cu–N(1) = 113.5(2)°. The N(4)–Cu–N(2) trans angle remains nearly linear [175.1(2)°], whereas O(1)–Cu–N(3) is significantly bent at 154.1(2)°, indicating distortion from the ideal octahedral arrangement. Overall, the coordination sphere differs markedly from the symmetric Jahn–Teller elongated octahedron observed in the perchlorate analogue, instead showing a highly asymmetric axial environment imposed by κ²-nitrite coordination.

The ESI-MS spectrum of compound **22** depicts a *m/z* peak at 422.0 (*calc. m/z* for $[Cu(L8)(NO_2)]^+$ = 422.0) (**Figure 5.12**). The UV-vis spectrum of **22** in acetonitrile exhibits a new band at 365 nm and shifting of *d-d* transition feature at 683 nm, which is similar to the previously reported square-planar copper(II)-nitrite compounds (**Figure 5.13**).

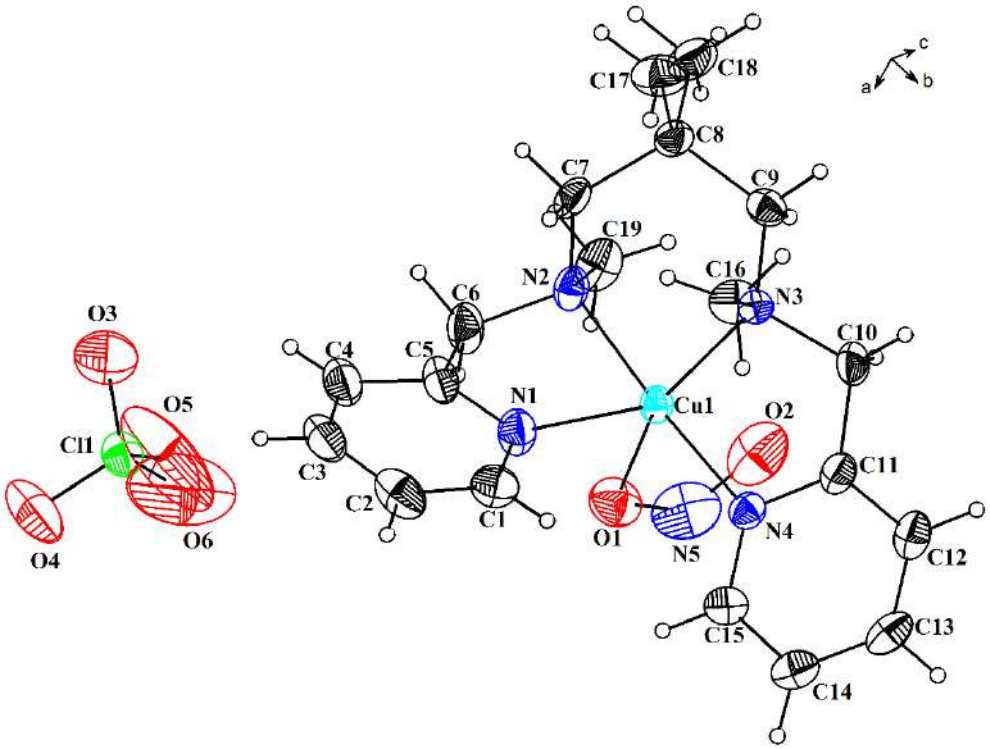

Figure 5.11 *Crystal structure of* ***22*** *showing atom labelling scheme. The thermal ellipsoids are drawn at a 30 % probability level for all the atoms except for the H atoms, which are shown as spheres of arbitrary radii.*

Table 5.3 *Selected bond lengths (Å) and angles (°) for* ***22****.*

Bond lengths (Å)			
Cu(1)-N(4)	2.027(6)	Cu(1)-N(3)	2.082(5)
Cu(1)-N(2)	2.050(6)	Cu(1)-N(1)	2.179(6)
Cu(1)-O(1)	2.057(6)	Cu(1)-O(2)	2.587(1)
N(5)-O(1)	1.262(1)	N(5)-O(2)	1229(1)
Bond angles (°)			
N(4)-Cu(1)-N(2)	175.1(2)	O(1)-Cu(1)-N(3)	154.1(2)
N(4)-Cu(1)-O(1)	91.7(2)	N(4)-Cu(1)-N(1)	100.1(2)
N(2)-Cu(1)-O(1)	93.0(2)	N(2)-Cu(1)-N(1)	81.1(2)
N(4)-Cu(1)-N(3)	81.9(2)	O(1)-Cu(1)-N(1)	92.3(3)
N(2)-Cu(1)-N(3)	93.2(2)	N(3)-Cu(1)-N(1)	113.5(2)
O(1)-N(5)-O(2)	113.13(1)		

Table 5.4 *Technical details of crystal data and structure refinement parameters of* ***22****.*

Compound	**22**
Empirical formula	C_{19} H_{28} Cl Cu N_5 O_6
Formula weight	521.46
Temperature	296(2) K
Wavelength	0.71073 Å
Crystal system	Monoclinic
Space group	*Pn*
Unit cell dimensions	*a* = 11.7230(10) Å *b* = 8.1416(7) Å *c* = 12.0118(10) Å α = 90° β = 94.181(2)° γ = 90°
Volume	1143.40(17) $Å^3$
Z	2
Density (calculated)	1.515 mg/m^3
Absorption coefficient	1.117 mm^{-1}
F(000)	542
Theta range for data collection	2.344 to 28.340°
Completeness to theta	100.0 %
Index ranges	-15≤ h ≤15 -10≤ k≤10 -16≤ l≤16
Reflections collected	25463
Independent reflections	5676 (R_{int}= 0.0660)
Refinement method	Full-matrix least-squares on F^2
Absorption correction	Semi- empirical from equivalents
Data/restraints/parameters	5676 / 2 / 293
Goodness-of-fit on F^2	1.023
Final *R*indices[I>2sigma(I)]	R1= 0.0528, wR2= 0.1103
R indices (all data)	R1= 0.0948, wR2= 0.1527
CCDC No.	2375643

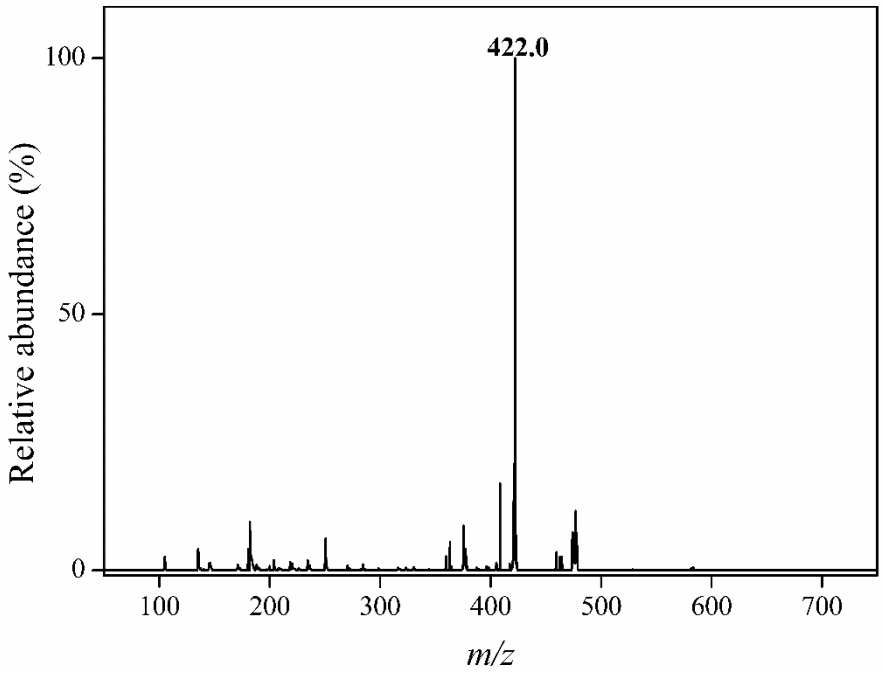

Figure 5.12 *The ESI-MS spectrum of* ***22*** *in acetonitrile solution.*

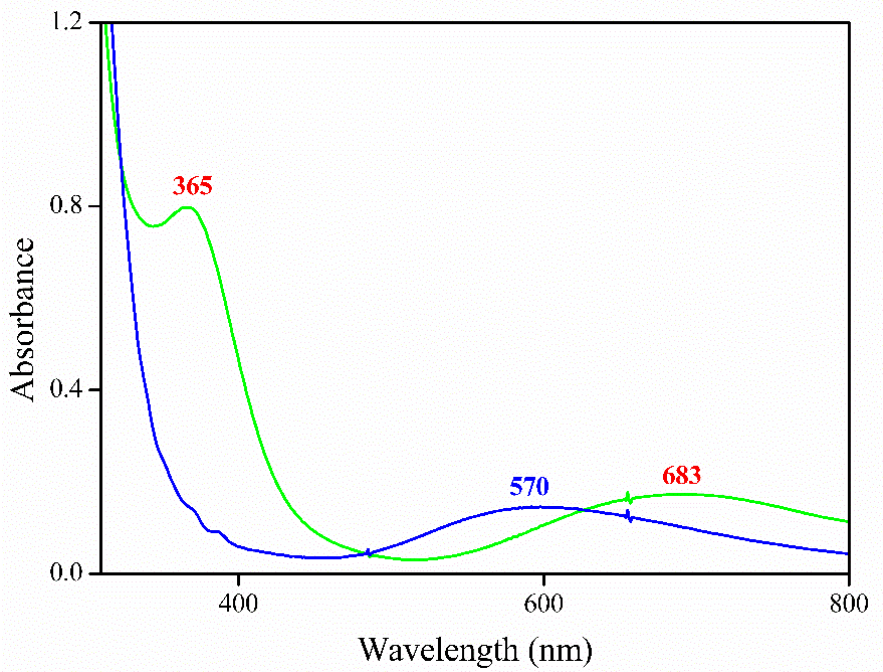

Figure 5.13 *The UV-vis spectra of* ***21*** *(1.0 mM, blue line) and* ***22****(1.0 mM, green line).*

To gain further insight into the H^+ catalyzed conversion of coordinated nitrite (NO_2^-) to nitric oxide (NO) at the Cu(II) center in compound **22**, its reactivity toward perchloric acid ($HClO_4$) was examined, using the latter as a proton source. Upon addition of H^+, the solution color changed from cyan green to deep blue, and UV–Vis spectroscopy revealed the appearance of a new absorption band at 570 nm, matching that of the parent Cu(II) compound **21**. This observation is consistent with a rapid acid promoted transformation of coordinated NO_2^- into NO(g), in agreement with literature reports[28,29] (**Figure 5.14**). The identity of the product as **21** was confirmed by spectroscopic analysis and single crystal X-ray diffraction. In the absence of H^+, **22** remained stable in CH_3CN at 298 K, showing no spectral changes over time.

The catalytic nature of NO generation was established by cycling between compounds **21** and **22** in the presence of H^+. First, compound **21**, obtained after the initial acid reaction, was treated with one equivalent of $NaNO_2$ to regenerate **22**; the yield, determined from the absorption at 365 nm relative to an authentic sample, was 96%. Subsequent treatment of **22** with acid regenerated **21** and released NO(g). After purging with N_2, re-addition of $NaNO_2$ restored **22**, with each cycle monitored by the absorbance at 365 nm. This process was repeated for five consecutive cycles, with regeneration yields of ~94% even after the fifth run, demonstrating that the Cu(II) centre in **22** can repeatedly catalyze the proton-mediated conversion of NO_2^- to NO(g) with high efficiency.

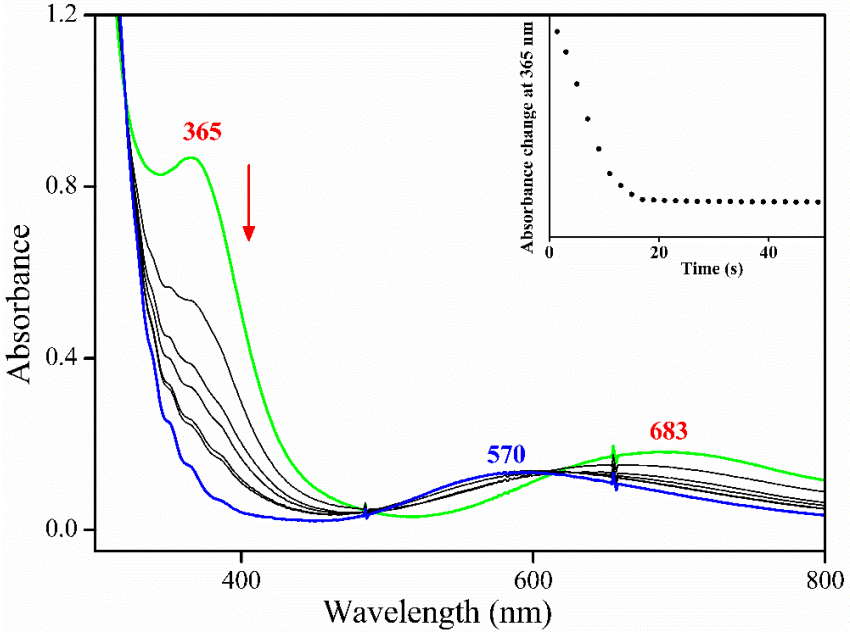

Figure 5.14 *The UV-Vis spectral changes of **22** (1.0 mM, green line) upon the addition of one equivalent of H^+ in CH_3CN at 298K. Inset: the time course of the reaction of **22** monitored at 365 nm upon the addition of one equivalent of H^+.*

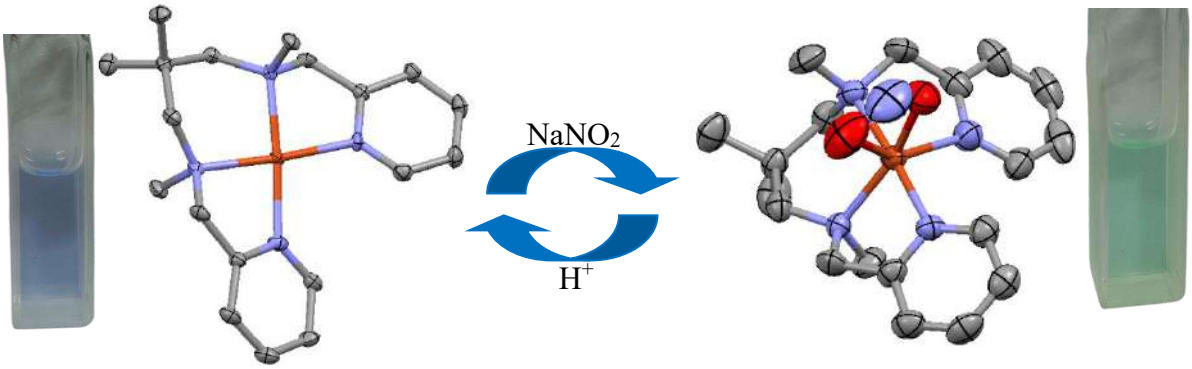

Figure 5.15 *The colour change observed during the catalytic cycle of* ***21*** *(blue) to* ***22*** *(cyan green) in CH_3CN at 298K.*

5.5 Conclusion

This chapter established a biomimetic Cu(II)–aminopyridyl systems designed to model nitrite reductase chemistry, as framed in the introduction. Single crystal data showed that the tetradentate N_4 donor set (two pyridyl, two amine) enforces a distorted octahedral Cu(II) environment. The perchlorate adduct displays a typical Jahn–Teller elongated N_4O_2 octahedron with two weak axial Cu–O contacts, whereas substitution by a κ^2-(O,O′)-nitrito ligand produces a more asymmetric octahedron with pronounced axial inequivalence and larger angular deviations. Complementary spectroscopic data supported these observations, and in the case of nitrite-bound species, indicated the potential for small molecule reactivity at the Cu(II) site.

Crucially, the same coordination features that tune geometry also enable function of the compound. In the presence of acid, the nitrite compound **22** catalyzes NO(g) formation and cleanly converts to the parent species **21**, evidenced by the diagnostic color change and growth of the 365 nm band. Cycling between **22** and **21** with $NaNO_2/H^+$ demonstrates robust regenerability and stability of **22** in the absence of H^+, establishing an efficient H^+ mediated nitrite to NO transformation at Cu(II) centre. Together, these results fulfill the objective of synthesizing new model to study NO(g) releasing reactivity in a biomimetic platform, and they provide a firm basis for subsequent kinetic, spectroscopic, and mechanistic studies.

Section II: Synthesis and spectroscopic study of tetradentate quinoline based Zn(II) compounds

5.6 Introduction and literature

Zinc(II) compounds have long attracted attention in coordination chemistry because of their rich structural diversity, functional versatility, and broad relevance in catalysis, sensing, and bioinorganic modelling[44–49]. As a d^{10} ion, Zn(II) is redox-inert under most conditions[50] but exhibits high Lewis acidity, enabling it to adopt a variety of coordination geometries depending on ligand set, denticity, and steric/electronic environment. This geometric adaptability is a key factor in its roles within metalloenzymes, supramolecular assemblies, and functional materials[51–53].

Ligand backbone architecture is central to this adaptability. Diamine containing multidentate ligands offer strong nitrogen donors while simultaneously enforcing defined bite angles and conformations, which influence metal–ligand bond distances, *cis*/*trans* relationships, and overall octahedral distortion[54,55]. Varying the length and rigidity of the diamine backbone, from rigid cyclohexane scaffolds to flexible polymethylene chains, provides a systematic means to modulate the chelate geometry and thus fine-tune stability, reactivity, and ligand exchange kinetics[56,57].

Backbone modification is not purely structural; it also affects functional behavior. As demonstrated in related Zn(II)–tetradentate ligand systems, shorter and more rigid backbones tend to yield compounds with more constrained coordination spheres, favoring selectivity and stability in catalysis and sensing applications[58,59]. In contrast, longer, more flexible backbones permit increased geometric adaptability, which can enhance dynamic binding and stimuli-responsive properties, but may reduce overall structural rigidity[60]. Minor adjustments to ligand topology in Zn(II) compounds can enhance stability, boost photoluminescence intensity, and shift emission energies. Mononuclear Zn(II) systems bearing N-donor ligands of differing denticity are well documented to display photoluminescent behavior[61–69].

Aminoquinoline-based multidentate ligands are especially attractive in contemporary coordination chemistry, as their reactivity and stability arise from a delicate balance of electronic and structural factors. Building on this premise, we have systematically tuned the topology of multidentate N-donor frameworks, generating a broad family of first-row transition metal compounds of quinoline-derived ligands with functions spanning catalysis

and enzyme mimetic chemistry[70–72]. We have also shown pronounced quenching of nitroaromatic compounds (NACs) using quinoline-based ligands[73].

In this chapter, we present a series of Zn(II) compounds containing an aminoquinoline-based tetradentate ligand framework, with systematic variation of the diamine backbone: cyclohexane-1,2-diamine, ethane-1,2-diamine, propane-1,3-diamine and butane-1,4-diamine. By integrating these experimental results with prior literature on Zn(II) diamine systems, this study develops a structure function framework that links backbone flexibility and auxiliary ligand type to potential applications across catalysis, sensing, biomimetic chemistry, and materials science. Such understanding supports rational ligand design strategies for tailoring Zn(II) compounds toward targeted scientific and technological roles.

5.7 Experimental details

The synthesis of ligands **L9-L12** are detailed in this section along with their Zn(II) compounds $[Zn(L9)(H_2O)(CH_3CN)](ClO_4)_2$ **23**, $[Zn(L10)(H_2O)(CH_3CN)](ClO_4)_2$ **24**, $[Zn(L9)(CH_3CN)(ClO_4)](ClO_4)$ **25**, $[Zn(L9)(H_2O)(ClO_4)](ClO_4)$ **26** synthesised in this study are depicted in **Scheme 5.4**.

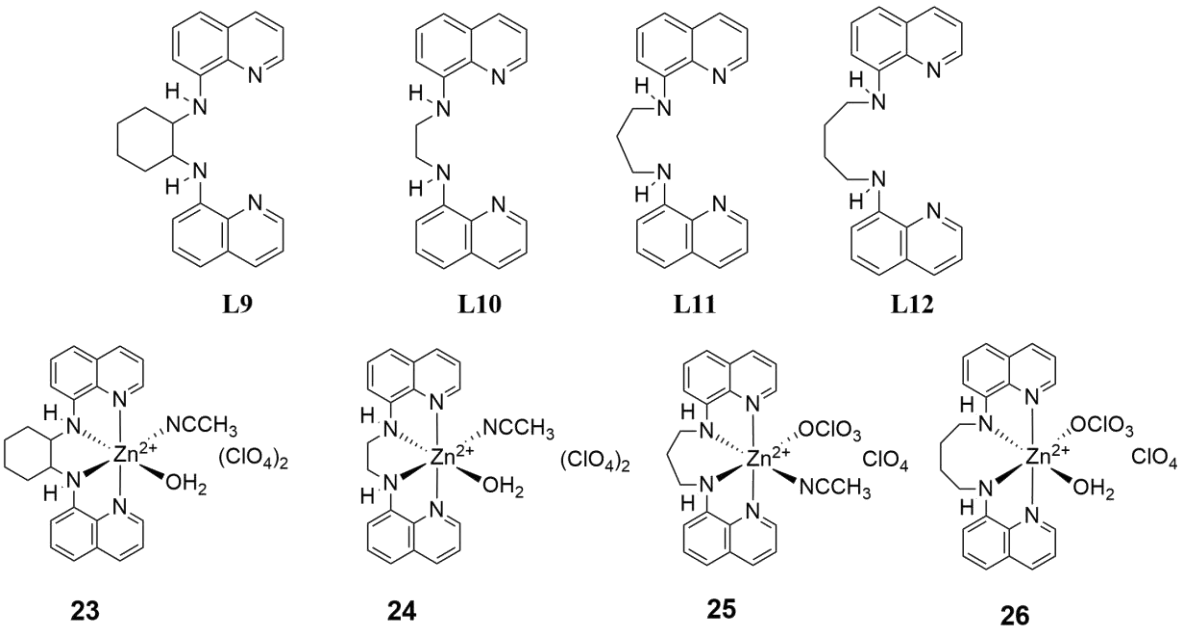

Scheme 5.4 *Structure of ligands* ***L9-L12*** *and Zn(II) compounds* ***23-26*** *under investigation.*

5.7.1 Synthesis of ligand L9-L12

Ligands **L9**, **L10**, and **L11** were synthesized following the procedure previously reported by Britovsek, whereas **L12** was prepared for the first time by our group using a similar synthetic strategy. A mixture of 8-hydroxyquinoline (25.0 g, 172.0 mmol), the appropriate diamine (86.0 mmol), and sodium metabisulphite (32.8 g, 172.0 mmol) was suspended in distilled water (200 mL) and refluxed at 110 °C for approximately eight days. Upon completion, the reaction mixture was allowed to cool to room temperature and subsequently basified to pH 12.0 with aqueous sodium hydroxide. The mixture was extracted with dichloromethane (3 × 100 mL), and the combined organic phases were dried over anhydrous sodium sulphate. Removal of the solvent under reduced pressure afforded the crude ligand, which was purified by recrystallization from ethanol or ethanol–water mixtures to yield the desired product. Ligands **L9–L12** were synthesized using the same general procedure, with the respective diamines, (±)-trans-1,2-diaminocyclohexane, ethylenediamine, 1,3-diaminopropane and 1,4-diaminobutane, employed as the amine backbones for **L9**, **L10**, **L11** and **L12** respectively.

N,N′-Bis(8-quinolyl)cyclohexane-1,2-diamine(**L9**)

Prepared according to the general procedure using (±)-trans-1,2-diaminocyclohexane (9.82 g, 86.0 mmol) as the diamine backbone. The product was obtained as a pale yellow crystalline solid after recrystallization from ethanol. **Yield:** 15.20 g (48 %). *Anal. Calc.* for **L9** C_{24} H_{24} N_4(%): C, 78.23; H, 6.57; N, 15.21; *Found:* C, 78.41; H, 6.64; N, 15.36. IR (KBr, cm^{-1}): 3387 υ(NH); 3103-2769 υ(CH).

N,N′-Bis(8-quinolyl)ethane-1,2-diamine(**L10**)

Synthesized as per the general procedure with ethylenediamine (5.74 mL, 86.0 mmol) as the diamine backbone. The product crystallized as yellow plates upon slow cooling from ethanol–water. **Yield:** 13.0 g (56 %). *Anal. Calc.* for **L10** C_{20} H_{18} N_4(%): C, 76.41; H, 5.77; N, 17.82; *Found:* C, 76.58; H, 5.92; N, 17.93. IR (KBr, cm^{-1}): 3387 υ(NH); 3103-2769 υ(CH).

N,N′-Bis(8-quinolyl)propane-1,3-diamine(**L11**)

Prepared according to the general procedure using 1,3-diaminopropane (7.17 mL, 86.0 mmol) as the diamine backbone. The ligand was isolated as light-yellow crystals after

ethanol recrystallization. **Yield:** 15.13 g (54 %). *Anal. Calc.* for **L11** C_{21} H_{20} N_4(%): C, 76.80; H, 6.14; N, 17.06; *Found:* C, 76.86; H, 6.21; N, 17.15. IR (KBr, cm^{-1}): 3361 υ(NH); 3072-2740 υ(CH).

N,N′-Bis(8-quinolyl)butane-1,4-diamine(**L12**)

Synthesized for the first time in this work following the general procedure with 1,4-diaminobutane (8.64 mL, 86.0 mmol) as the diamine backbone. The pale yellow crystalline product was obtained after recrystallization from ethanol. **Yield:** 16.8 g (57%). *Anal. Calc.* for **L12** C_{22} H_{22} N_4(%): C, 77.16; H, 6.48; N, 16.36; *Found:* C, 77.31; H, 6.62; N, 16.45. IR (KBr, cm^{-1}): 3404 υ(NH); 3145-2777 υ(CH).

5.7.2 Synthesis of Zn(II) compounds 23-26

The Zn(II) compounds **23-26** were synthesized by direct metal–ligand coordination under inert conditions in dry acetonitrile. Each ligand was reacted with an equimolar amount of $Zn(ClO_4)_2 \cdot 6H_2O$ at room temperature under a nitrogen atmosphere, affording pale yellow to colorless solutions. The compound precipitated upon addition of diethyl ether, were collected by filtration, and purified by washing with cold ether. All compounds were obtained in good yields as microcrystalline solids, stable to air and moisture under ambient conditions. The synthetic approach is versatile, requiring no post synthetic modification, and consistently furnished analytically pure materials suitable for spectroscopic and crystallographic characterization. Slow vapor diffusion of diethyl ether into an acetonitrile solution of each complex afforded single crystals of sufficient quality for X-ray diffraction, enabling direct comparison of coordination geometries arising from variations in the ligand amine backbone.

A solution of ligand **L9** (0.49 g, 1.34 mmol) in dry DCM (10 mL) was prepared under a nitrogen atmosphere. To this, a solution of $Zn(ClO_4)_2 \cdot 6H_2O$ (0.5 g, 1.34 mmol) in dry CH_3CN (2 mL) was added dropwise with stirring at room temperature. The mixture was stirred for 3 h, then filtered to remove any insoluble material. The filtrate was concentrated, and diethyl ether (20 mL) was added to precipitate the product. The solid was collected by filtration, washed with cold ether (2 × 5 mL), and dried in vacuo to give $[Zn(L9)(H_2O)(CH_3CN)](ClO_4)_2$ as a pale yellow crystalline solid. The yield of **23** was 0.74 g (1.07 mmol) 79.5 %. *Anal. Calc.* for **23** C_{26} H_{29} Cl_2 Zn N_5 O_9 (%): C, 45.14; H,

4.23; N, 10.12. *Found:* C, 45.28; H, 4.36; N, 10.29. IR (KBr, cm^{-1}): 3400-3420 υ(OH) υ(NH); 3007-2895 υ(CH); 1093, 621 υ(ClO_4).

Compound **24** was prepared following the same protocol. The yield of $[Zn(L10)(H_2O)(CH_3CN)](ClO_4)_2$ **24** was 0.72 g (1.13 mmol), 83.7 %. *Anal. Calc.* for **24** C_{22} H_{23} Cl_2 Zn N_5 O_9 (%): C, 41.43; H, 3.64; N, 10.98. *Found:* C, 41.52; H, 3.74; N, 11.06. IR (KBr, cm^{-1}): 3400-3420 υ(OH) υ(NH); 3007-2895 υ(CH); 1075, 624 υ(ClO_4).

Compound **25** was prepared following the same protocol. The yield of $[Zn(L9)(CH_3CN)(ClO_4)](ClO_4)$ **25** was 0.69 g (1.13 mmol), 84.1 %. *Anal. Calc.* for **25** C_{23} H_{23} Cl_2 Zn N_5 O_8 (%): C, 43.59; H, 3.66; N, 11.05. *Found:* C, 43.71; H, 3.83; N, 11.22. IR (KBr, cm^{-1}): 3400-3420 υ(NH); 3007-2895 υ(CH); 1094, 625 υ(ClO_4).

Compound **26** was prepared following the same protocol. The yield of $[Zn(L9)(H_2O)(ClO_4)](ClO_4)$ **26** was 0.73 g (1.17 mmol), 86.9 %. *Anal. Calc.* for **26** C_{22} H_{24} Cl_2 Zn N_4 O_9 (%): C, 42.30; H, 3.87; N, 8.97. *Found:* C, 42.53; H, 3.96; N, 9.04 IR (KBr, cm^{-1}): 3400-3420 υ(OH) υ(NH); 3007-2895 υ(CH); 1094, 625 υ(ClO_4).

5.8 Results and discussions

5.8.1 Synthesis of ligands L9-L12

The topology and conformational flexibility of a ligand framework significantly influence the stability, coordination geometry, and reactivity of 3d transition metal compounds. To systematically investigate the effect of backbone structure, a series of quinoline-based diamine ligands was synthesized, differing only in the nature of the diamine spacer. This was achieved by substituting ethylenediamine in the parent ligand with (±)-trans-1,2-diaminocyclohexane, 1,3-diaminopropane or 1,4-diaminobutane, thereby introducing variations in both rigidity and length of the amine backbone. These modifications were designed to modulate the steric and electronic properties of the coordination environment while maintaining a common quinoline donor motif for comparative studies.

All ligands were prepared following a generalized synthetic route based on a modified Bucherer reaction, first described by Nielsen and co-workers[74] (**Scheme 5.5**). In this transformation, 8-hydroxyquinoline undergoes condensation with the selected diamine in the presence of sodium metabisulphite under refluxing aqueous conditions, affording the target non-methylated secondary amines. The products were isolated via basification of the reaction mixture to pH 12, extraction with dichloromethane, and drying over

anhydrous sodium sulphate, followed by solvent removal to yield the desired ligands as crystalline solids.

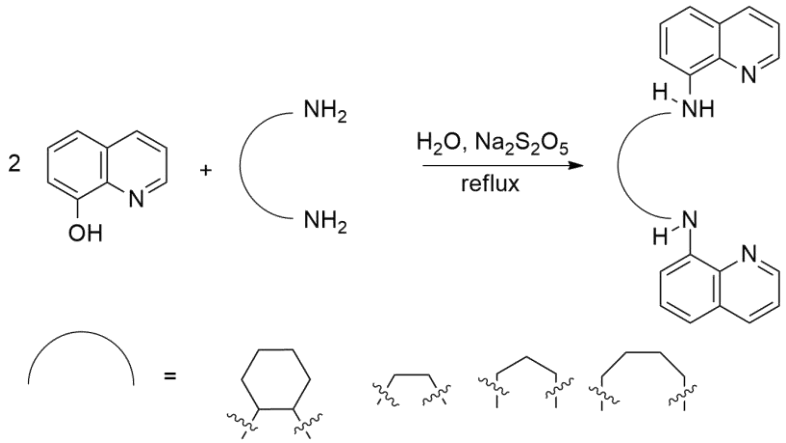

Scheme 5.5 *Synthetic route employed to synthesis of quinoline-based ligands* ***L9-L12****.*

5.8.2 Infrared spectra of compounds 23-26.

The IR spectra of compounds **23-26** exhibit characteristic absorptions consistent with their proposed formulations (**Figure 5.16**). Broad bands in the 3400–3420 cm^{-1}region are assigned to O–H stretching vibrations from coordinated water molecules and possible N–H stretches from the ligand backbone. Compounds **23**, **24** and **26** display medium bands at ~1620–1625 cm^{-1}, corresponding to the δ(H–O–H) bending mode of bound water. Strong absorptions in the 1580–1600 cm^{-1}range are attributed to aromatic C=C and C=N stretches of the quinoline moieties. All compounds show intense bands between 1070–1115 cm^{-1} and 615–625 cm^{-1}, diagnostic of ClO_4^- anions[36,37].

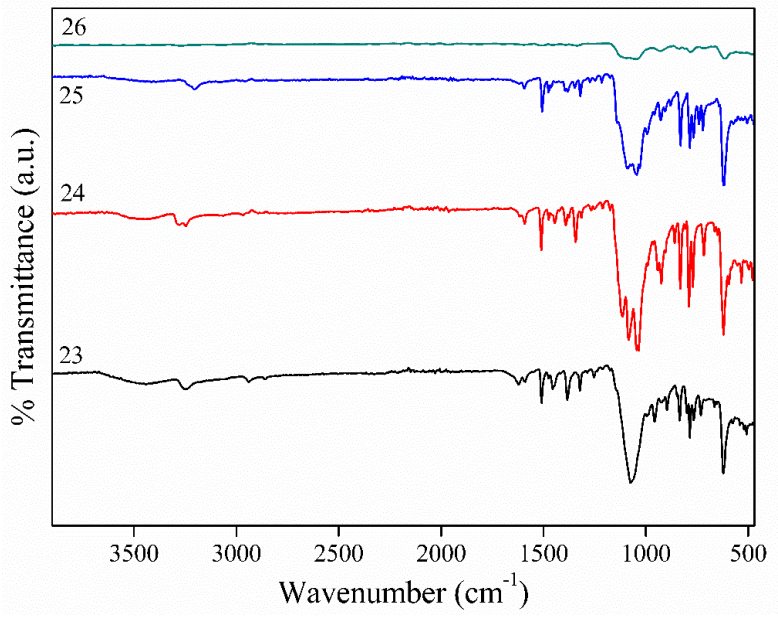

Figure 5.16 *The overlaid infrared spectra of compounds* ***23-26****.*

5.8.3 Crystal structure and geometrical analysis of compounds 23- 26

All four Zn(II) compounds, **23–26**, were obtained as crystalline solids. Single crystals suitable for X-ray diffraction analysis of $[Zn(L9)(H_2O)(CH_3CN)](ClO_4)_2$ **23**, $[Zn(L10)(H_2O)(CH_3CN)](ClO_4)_2$ **24**, $[Zn(L11)(CH_3CN)(ClO_4)](ClO_4)$ **25** and $[Zn(L11)(H_2O)(ClO_4)](ClO_4)$ **26** were prepared by slow diffusion of diethyl ether into acetonitrile solutions of the respective compounds. The experimental conditions for data acquisition and selected refinement parameters for compounds **23** and **24** are summarised in **Table 5.8**, while those for compounds **25** and **26** are provided in **Table 5.13.** Key bond lengths and angles are presented in **Tables 5.5, 5.6, 5.9** and **5.11** for compounds **23–26**, respectively. Compounds **23**-**25** crystallise in the monoclinic crystal system in space groups *C*2/*c*, $P2_1/n$ and $P2_1/c$ respectively, whereas **26** crystalize in triclinic space group *P*-1. In all cases, the atoms occupy general positions.

The asymmetric units of compounds **23** and **24** each comprise a single Zn(II) ion coordinated by a discrete tetradentate aminoquinoline ligand (**L9** in **23**; **L10** in **24**), one coordinated water molecule, and one acetonitrile ligand, together with two independent perchlorate counter anions. The perchlorate anions act solely as charge balancing species and do not coordinate directly to the Zn(II) centre (**Figures 5.17–5.18**). Although the asymmetric units of **23** and **24** are superficially similar, variation in the diamine backbone results in discernible differences in their coordination geometries, which are further discussed in the subsequent structural analysis.

In compound **23**, Zn(II) ion is coordinated by the tetradentate aminoquinoline ligand **L9** through two quinoline nitrogen donors (N1, N4) and two secondary amine nitrogen donors (N2, N3). The Zn(II) center is six-coordinate and best described as a distorted octahedron. Choosing the N1···N4 axis as the axial pair (N1–Zn–N4 = 176.31(11)°). The equatorial plane is formed by N2, N3, O1(H_2O) and N5(MeCN), arranged as two equatorial *trans* pairs: O1···N2 = 167.47(15)° and N3···N5 = 163.61(13)°. Bond distances are: Zn–O1 = 2.100(3) Å; Zn–N5 = 2.185(3) Å; Zn–N(chelate) = 2.147(3)–2.185(3) Å. The compressed chelate bites (e.g., N2–Zn–N1 = 77.97(11)°; N3–Zn–N4 = 76.84(10)°) reflect the cyclohexanediamine constraint, while the two neutral equatorial donors (H_2O, MeCN) sit *cis* to each other.

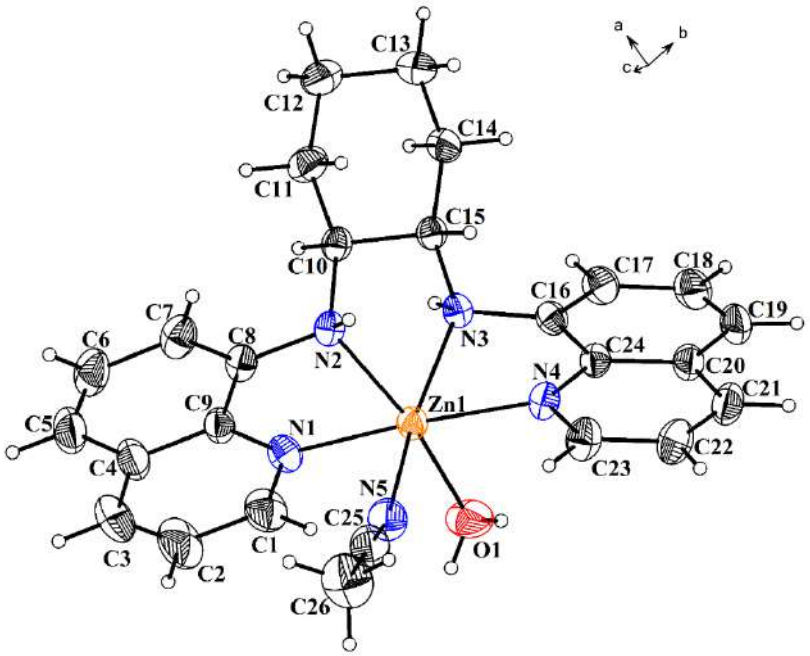

Figure 5.17 *Crystal structure of* $[Zn(L9)(H_2O)(CH_3CN)]^{2+}$***23*** *showing atom labelling scheme. The thermal ellipsoids are drawn at 30 % probability level for all the atoms except for the H atoms, which are shown as spheres of arbitrary radii. The uncoordinated perchlorate anions have been omitted for the clarity.*

Table 5.5 *Selected bond lengths (Å) and angles (°) for* ***23****.*

Bond lengths (Å)			
Zn(1)-O(1)	2.100(3)	Zn(1)-N(5)	2.185(3)
Zn(1)-N(3)	2.147(3)	Zn(1)-N(4)	2.185(3)
Zn(1)-N(2)	2.149(3)	Zn(1)-N(1)	2.150(3)
Bond angles (°)			
O(1)-Zn(1)-N(3)	96.37(14)	N(4)-Zn(1)-N(5)	89.74(12)
O(1)-Zn(1)-N(2)	167.47(15)	N(1)-Zn(1)-N(5)	88.54(13)
N(3)-Zn(1)-N(2)	83.97(10)	N(2)-Zn(1)-N(5)	90.69(13)
O(1)-Zn(1)-N(1)	89.91(15)	N(3)-Zn(1)-N(5)	163.61(13)
N(3)-Zn(1)-N(1)	105.38(11)	O(1)-Zn(1)-N(5)	92.19(17)
N(2)-Zn(1)-N(1)	77.97(11)	N(1)-Zn(1)-N(4)	176.31(11)
O(1)-Zn(1)-N(4)	86.90(15)	N(2)-Zn(1)-N(4)	105.31(11)
N(3)-Zn(1)-N(4)	76.84(10)		

In compound **24**, Zn(II) is coordinated by **L10** in a similar tetradentate mode. A distorted octahedral environment is again observed. Defining N4···N1 as the axial pair (N4–Zn–N1 = 172.66(16)°), the equatorial donors are N2, N3, O9(H_2O) and N5(MeCN). Within that

plane, the equatorial trans relationships are O9···N2 = 171.35(16)° and N5···N3 = 172.36(16)°, giving an almost perfectly balanced equatorial set. Bond lengths: Zn–O9 = 2.167(4) Å; Zn–N5 = 2.142(4) Å; Zn–N(chelate) = 2.139(4)–2.171(4) Å. The shorter, more flexible ethylenediamine backbone yields the most regular octahedron in the series, with both equatorial *trans* pairs close to linear.

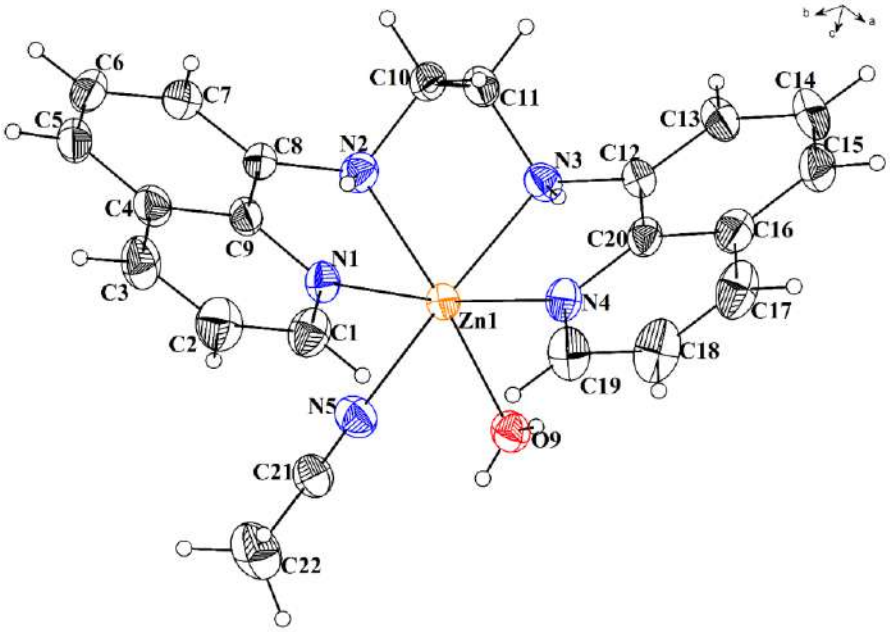

Figure 5.18 *Crystal structure of* $[Zn(L10)(H_2O)(CH_3CN)]^{2+}$***24*** *showing atom labelling scheme. The thermal ellipsoids are drawn at 30 % probability level for all the atoms except for the H atoms, which are shown as spheres of arbitrary radii. The uncoordinated perchlorate anions have been omitted for the clarity.*

Table 5.6 *Selected bond lengths (Å) and angles (°) for* ***24****.*

Bond lengths (Å)			
Zn(1)-N(4)	2.139(4)	Zn(1)-N(3)	2.171(4)
Zn(1)-N(5)	2.142(4)	Zn(1)-N(1)	2.169(4)
Zn(1)-N(2)	2.149(4)	Zn(1)-O(9)	2.167(4)
Bond angles (°)			
N(4)-Zn(1)-N(5)	93.19(17)	N(1)-Zn(1)-N(3)	94.89(15)
N(4)-Zn(1)-N(2)	95.70(16)	O(9)-Zn(1)-N(3)	97.02(15)
N(5)-Zn(1)-N(2)	94.81(17)	N(2)-Zn(1)-N(3)	84.02(16)
N(4)-Zn(1)-O(9)	92.93(16)	N(5)-Zn(1)-N(3)	172.36(16)
N(5)-Zn(1)-O(9)	85.28(16)	N(4)-Zn(1)-N(3)	79.45(15)
N(2)-Zn(1)-O(9)	171.35(16)	O(9)-Zn(1)-N(1)	92.40(16)
N(4)-Zn(1)-N(1)	172.66(16)	N(2)-Zn(1)-N(1)	78.96(16)
N(5)-Zn(1)-N(1)	92.28(17)		

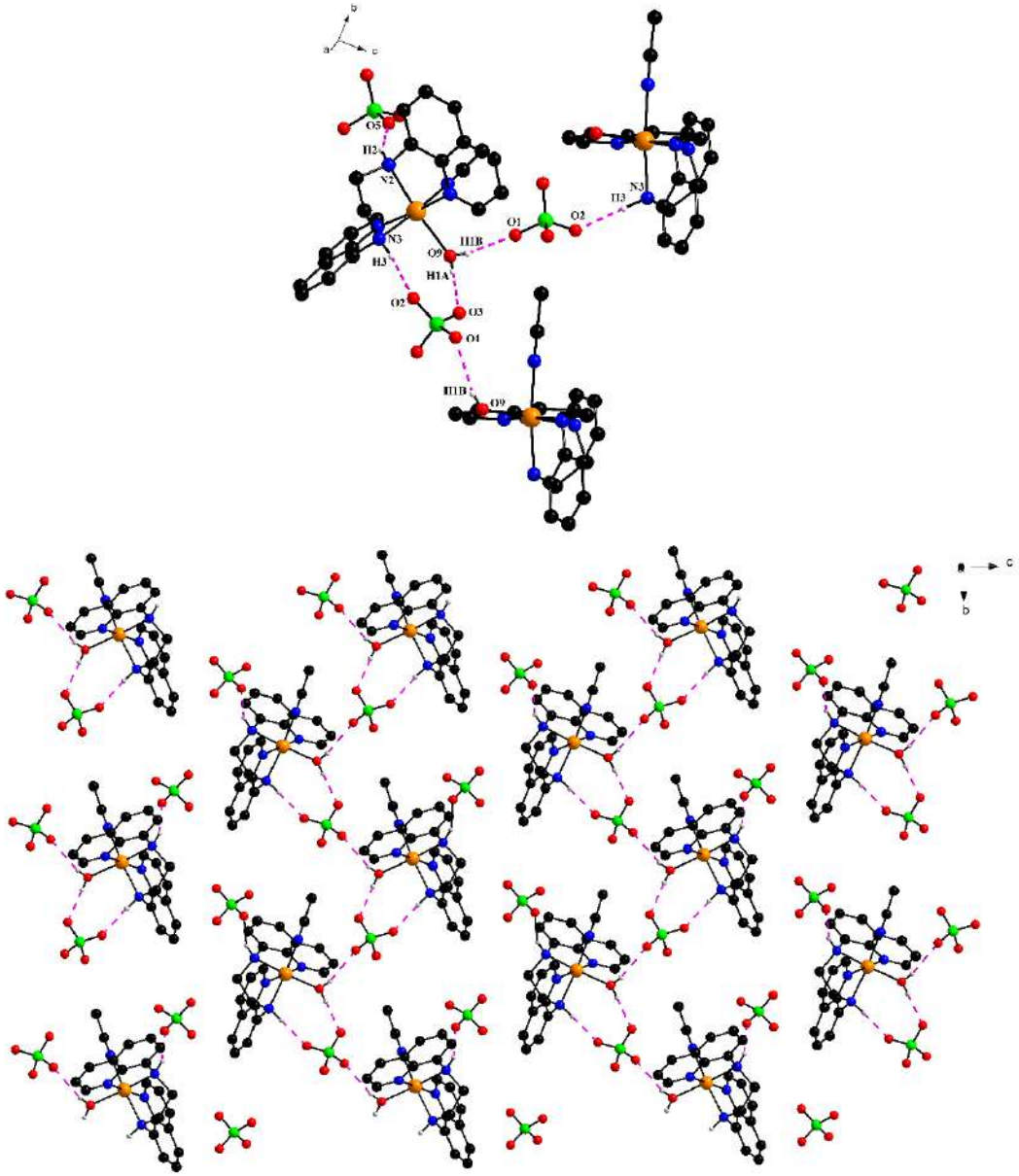

Figure 5.19 *The hydrogen bonding interactions in* ***24*** *with atom labelling scheme of atoms involved in hydrogen bonding; along with the enlarged view of a network of hydrogen bonding in* ***24*** *showing the symmetric organisation of* $[Zn(L10)(H_2O)(CH_3CN)]^{2+}$ *cations and perchlorate anions. Hydrogen atoms attached to carbon are omitted for clarity.*

Table 5.7 *Hydrogen bonding parameters (Å, º) for* ***24****.*

D-H···A	D-H/ Å	H···A/ Å	D···A/ Å	D-H···A/º	Symmetry code
O9-H1A···O3	0.789(0)	1.984(0)	2.773(0)	177.20(0)	x, y, z
O9-H1B···O1	0.705(0)	2.242(0)	2.930(1)	165.75(0)	-x+3/2, y+1/2, -z+3/2
N2-H2···O5	0.980(0)	1.947(0)	2.877(0)	157.53(0)	-x+3/2, y+1/2, -z+1/2
N3-H3···O2	0.980(0)	2.016(0)	2.987(0)	170.38(0)	x, y, z

Table 5.8 *Technical details of crystal data refinement parameters of* ***23*** *and* ***24****.*

Compound	**23**	**24**
Empirical formula	C_{26} H_{29} Cl_2 N_5 O_9 Zn	C_{22} H_{23} Cl_2 N_5 O_9 Zn
Formula weight	691.83	637.74
Temperature	296(2) K	296(2) K
Wavelength	0.71073 Å	0.71073 Å
Crystal system	Monoclinic	Monoclinic
Space group	*C*2/*c*	$P2_1/n$
Unit cell dimensions	*a* = 17.9224(9) Å	*a* = 13.7417(6) Å
	b = 20.0291(10) Å	*b* = 12.3424(5) Å
	c = 17.0966(8) Å	*c* = 15.8481(7) Å
	α = 90°	α = 90°
	β = 96.028(2)°	β = 100.5640(10)°
	γ = 90°	γ = 90°
Volume	6103.2(5) $Å^3$	2642.4(2) $Å^3$
Z	8	4
Density (calculated)	1.506 mg/m^3	1.603 mg/m^3
Absorption coefficient	1.039 mm^{-1}	1.192 mm^{-1}
F(000)	2848	1304
Theta range for data collection	2.740 to 28.315°	2.169 to 28.333°
Completeness to theta	99.9%	100.0 %
Index ranges	-23<=h<=23	-18<=h<=18
	-26<=k<=26	-16<=k<=16
	-22<=l<=22	-21<=l<=21
Reflections collected	44097	60466
Independent reflections	7572 [R(int) = 0.0362]	6583 [R(int) = 0.0745]
Refinement method	Full-matrix least-squares on F^2	Full-matrix least-squares on F^2
Absorption correction	Semi- empirical from equivalents	Semi- empirical from equivalents
Data/restraints/parameters	7572 / 0 / 403	6583 / 0 / 359
Goodness-of-fit on F^2	1.049	1.002
Final *R*indices[I>2sigma(I)]	R1= 0.0591, wR2= 0.1822	R1= 0.0720, wR2= 0.1869
R indices (all data)	R1= 0.0771, wR2= 0.2059	R1= 0.1141, wR2= 0.2127
CCDC No.	2386738	2386751

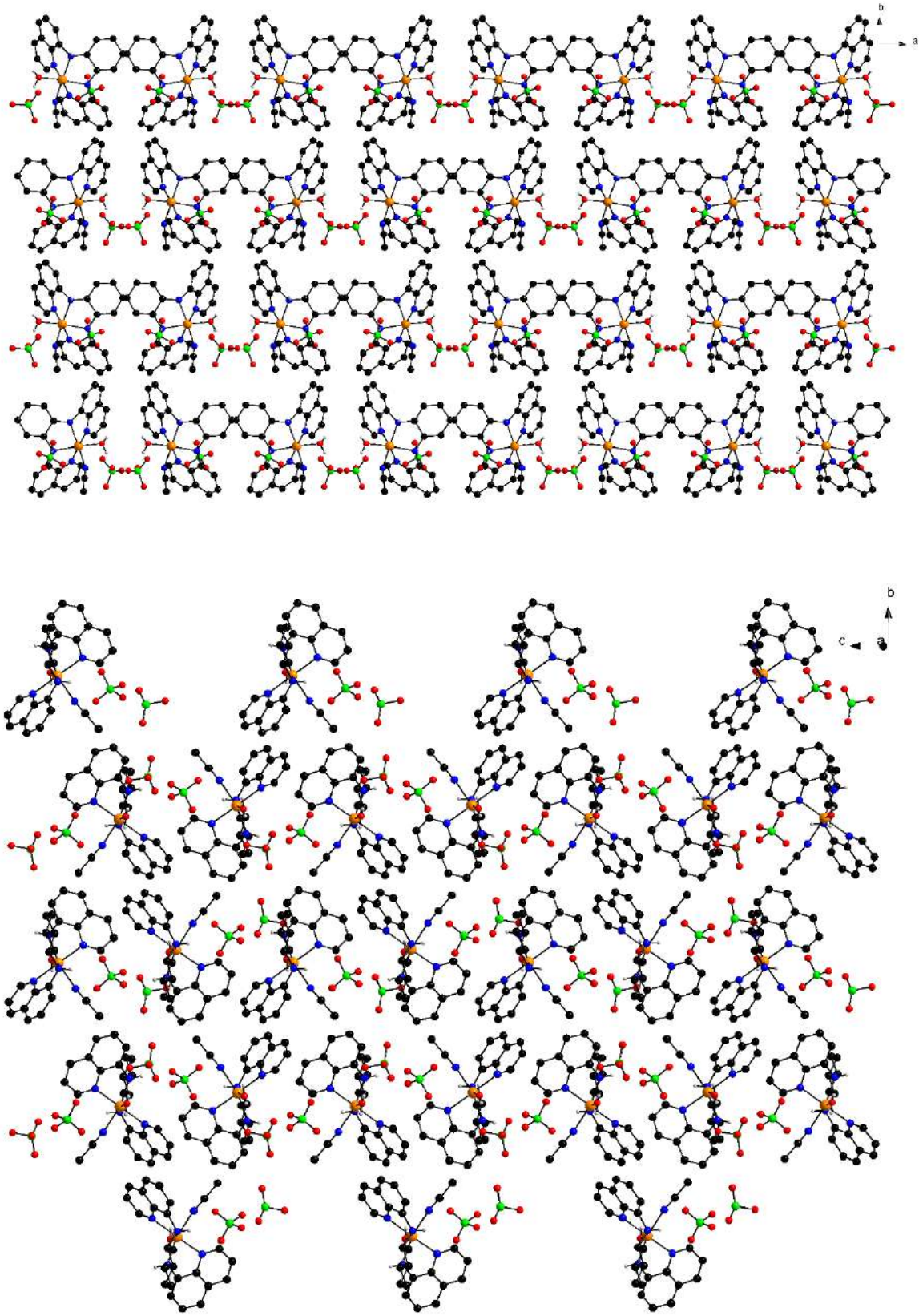

Figure 5.20 *Packing in* ***23*** *view along crystallographic a and c axes. Colour code: C, black; N, blue; O, red; Cl, green and Zn, orange.*

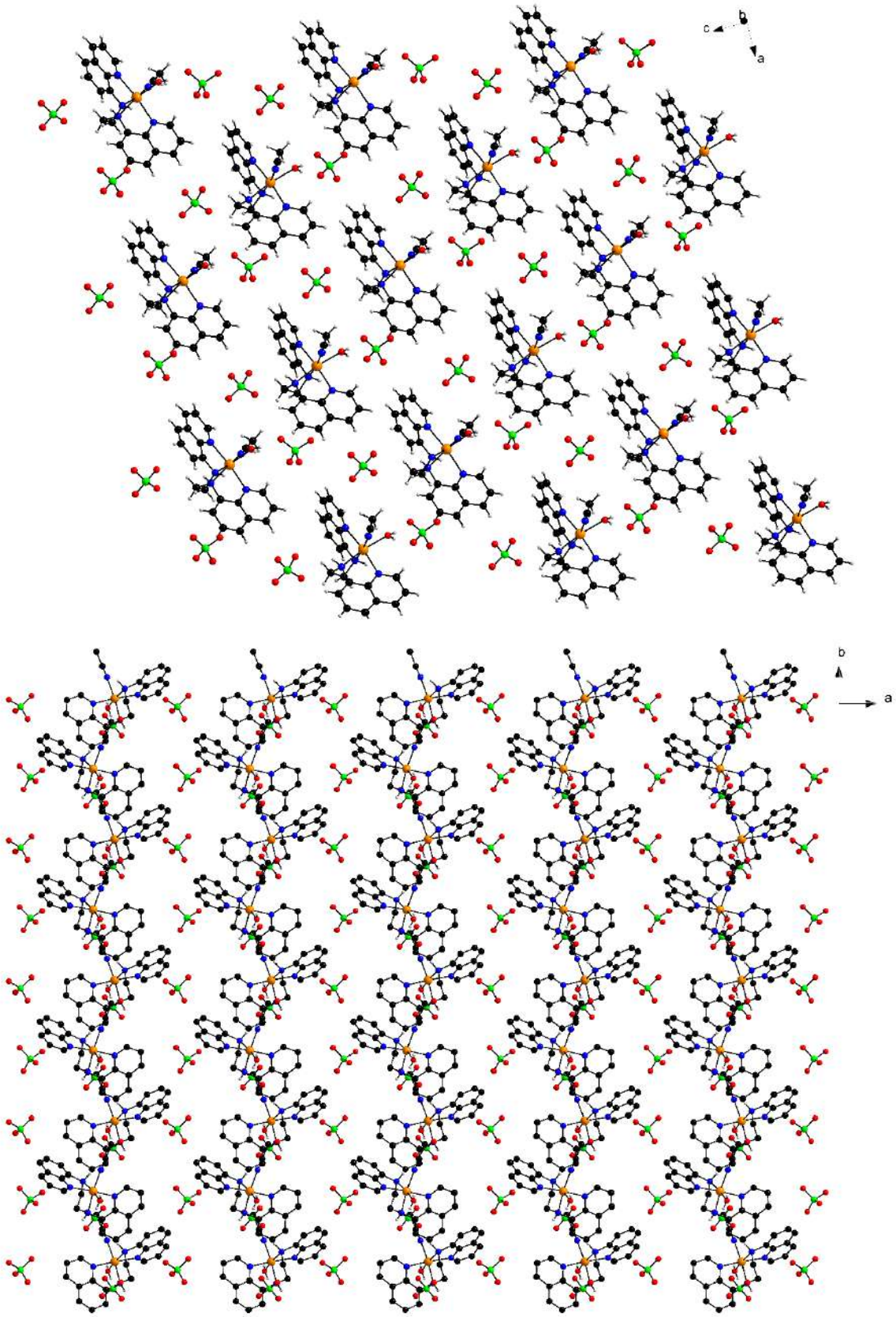

Figure 5.21 *Packing in* ***24*** *view along crystallographic b and c axes. Colour code: C, black; N, blue; O, red; Cl, green and Zn, orange.*

The asymmetric units of **25** and **26** each contain a single Zn(II) centre chelated by a tetradentate aminoquinoline ligand (**L11** in **25**; **L12** in **26**), together with one coordinated solvent molecule (CH_3CN in **25** and H_2O in **26**) and one monodentate perchlorate ligand; charge balance is provided by an additional, independent non-coordinating perchlorate counter anion (**Figures 5.22–5.24**). Despite their similar formulations, variations in the diamine backbone and the identity of the solvent donor give rise to subtle differences in coordination geometry, which are examined in the subsequent structural analysis.

In compound **25** the axial direction is defined by the chelate N4···N2 pair (N4–Zn–N2 = 171.00(15)°). The equatorial plane therefore contains N1, N3, N5(MeCN) and O5(ClO_4^-), with equatorial *trans* pairs N1···O5 = 167.01(16)° and N5···N3 = 163.78(14)° indicating notable deviation from linearity. The bond distances are Zn–O5 = 2.342(4) Å (weak, elongated); Zn–N5 = 2.163(4) Å and Zn–N(chelate) = 2.088(4)–2.187(3) Å. The Zn–O($ClO3^-$) distance is the longest in the coordination sphere, reflecting weak axial binding. The flexible propane-1,3-diamine backbone introduces greater angular distortion in the *cis* angles.

In **26**, taking N4···N1 as the axial pair (N4–Zn–N1 = 172.26(9)°), the equatorial donors are N2, N3, O7(ClO_4^-) and O9(H_2O), with equatorial trans pairs N2···O7 = 168.80(10)° and N3···O9 = 159.47(11)°. The bond distances are Zn–O7 = 2.446(3) Å for weakly bound perchlorate oxygen, Zn–O9 = 2.193(3) Å for water molecule and Zn–N(chelate) = 2.100(2)–2.147(2) Å. The butanediamine backbone allows the largest angular freedom; with both H_2O and ClO_4^- at equatorial position, and the markedly bent N3···O9 and very long Zn–O(ClO_4^-) define the most anisotropic octahedral distortion across the series.

All four structures are distorted octahedra in which the axial axis is defined by a near-linear intrachelate N···N pair from the tetradentate ligand: N1···N4 in **23** (176.31°) and **24** (172.66°), N4···N2 in **25** (171.00°) and N4···N1 in **26** (172.26°). The remaining four donors form the equatorial plane. In **23** and **24**, both H_2O and MeCN are equatorial and *cis*, with well-balanced equatorial *trans* pairs (**23**: O1···N2 = 167.47°, N3···N5 = 163.61°; **24**: O9···N2 = 171.35°, N5···N3 = 172.36°), giving **24** the most regular geometry in the series. By contrast, **25** and **26** each contain one coordinated perchlorate O-donor in the equatorial plane (with an additional outer sphere ClO_4^- for charge balance). This weak anionic donor produces long Zn–O(ClO_4^-) contacts (2.342 Å in **25**; 2.446 Å in **26**) and compresses adjacent *cis* angles (**25**: 82–87°; **26**: 78–86°), while the equatorial *trans* pairs

become noticeably bent (**25**: N5···N3 = 163.78°, N1···O5 = 167.01°; **26**: N3···O9 = 159.47°, N2···O7 = 168.80°).

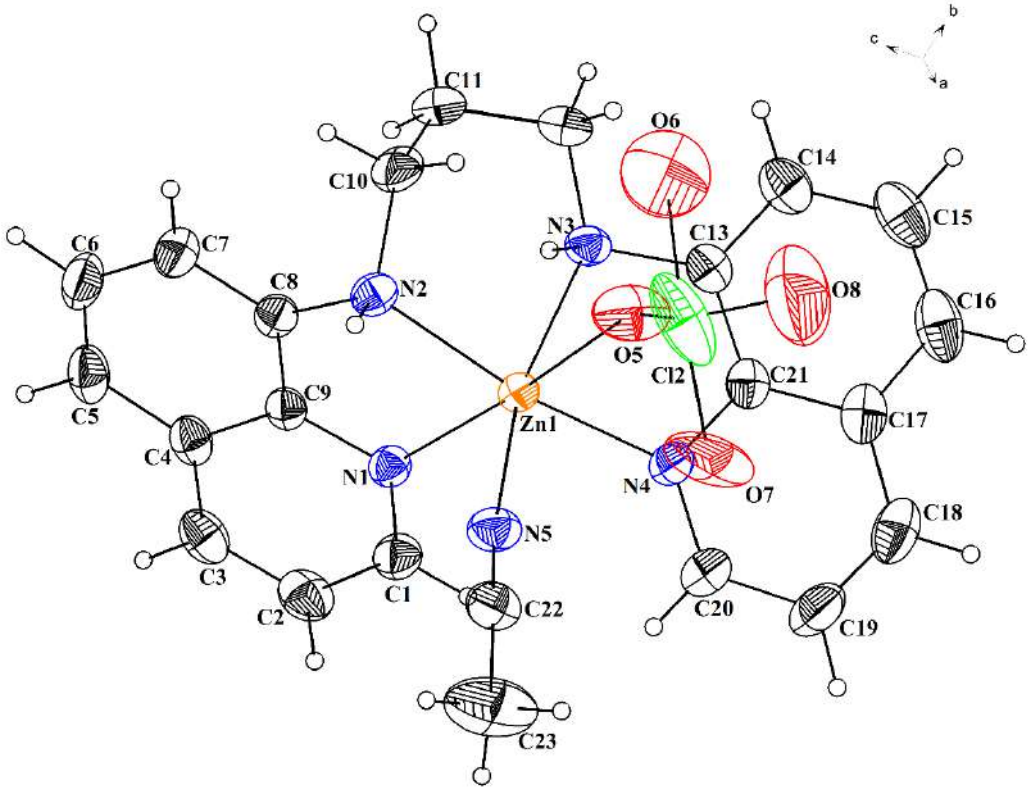

Figure 5.22 *Crystal structure of* $[Zn(L11)(CH_3CN)(ClO_4)]^{2+}$ ***25*** *showing atom labelling scheme. The thermal ellipsoids are drawn at 30 % probability level for all the atoms except for the H atoms, which are shown as spheres of arbitrary radii. The uncoordinated perchlorate anions have been omitted for the clarity.*

Table 5.9 *Selected bond lengths (Å) and angles (°) for* ***25****.*

Bond lengths (Å)			
Zn(1)-N(4)	2.088(4)	Zn(1)-O(5)	2.342(4)
Zn(1)-N(1)	2.089(3)	Zn(1)-N(3)	2.187(3)
Zn(1)-N(2)	2.120(4)	Zn(1)-N(5)	2.163(4)
Bond angles (°)			
N(4)-Zn(1)-N(1)	103.33(13)	N(3)-Zn(1)-O(5)	82.98(14)
N(4)-Zn(1)-N(2)	171.00(15)	N(5)-Zn(1)-O(5)	82.28(15)
N(1)-Zn(1)-N(2)	80.82(13)	N(2)-Zn(1)-O(5)	89.74(16)
N(4)-Zn(1)-N(5)	93.67(15)	N(1)-Zn(1)-O(5)	167.01(16)
N(1)-Zn(1)-N(5)	89.51(14)	N(4)-Zn(1)-O(5)	87.31(16)
N(2)-Zn(1)-N(5)	94.36(16)	N(5)-Zn(1)-N(3)	163.78(14)
N(4)-Zn(1)-N(3)	78.90(13)	N(2)-Zn(1)-N(3)	92.31(14)
N(1)-Zn(1)-N(3)	106.15(13)		

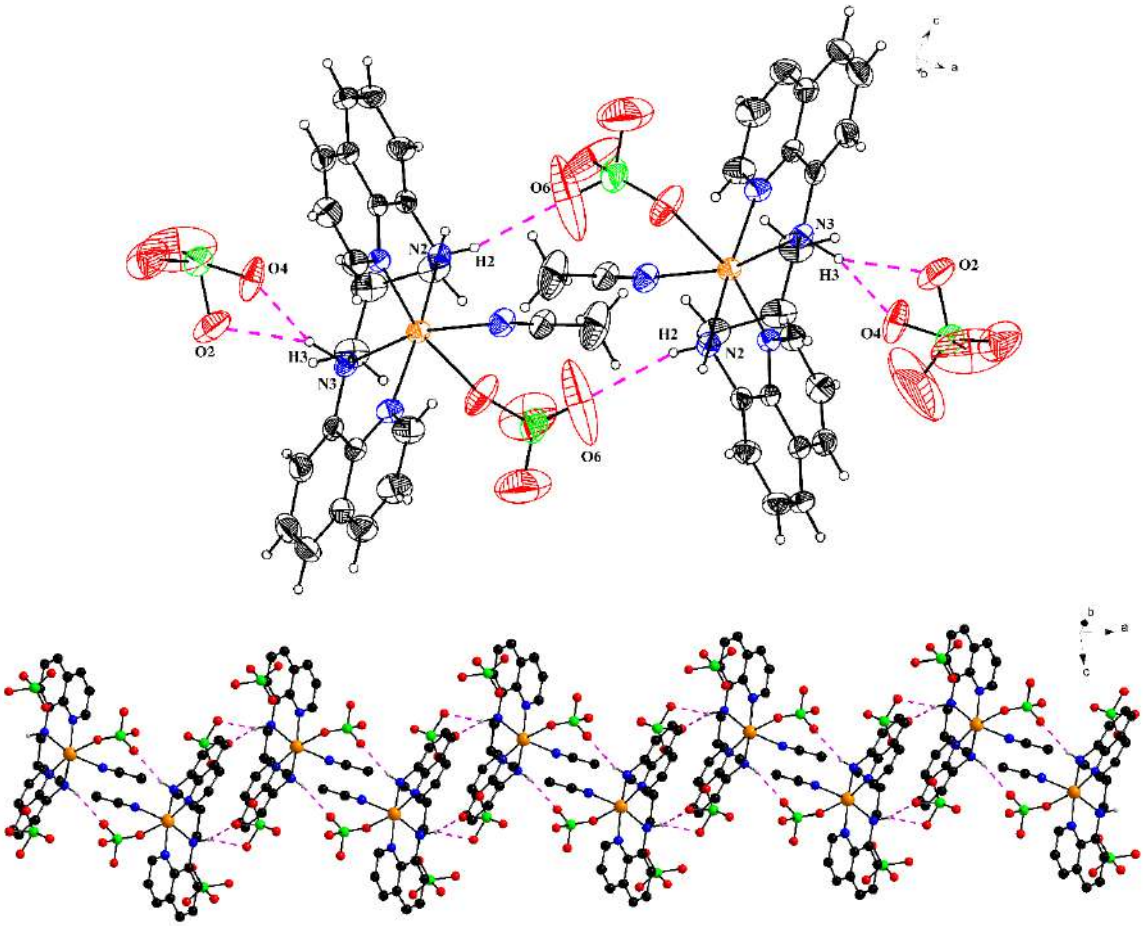

Figure 5.23 *The hydrogen bonding interactions in* ***25*** *with atom labelling scheme of atoms involved in hydrogen bonding; along with the enlarged view of a network of hydrogen bonding in* ***25*** *showing the symmetric organisation of* $[Zn(L11)(H_2O)(ClO_4)]^{2+}$ *cations and perchlorate anions. Hydrogen atoms attached to carbon are omitted for clarity.*

Table 5.10 *Hydrogen bonding parameters (Å, º) for* ***25****.*

D-H···A	D-H/ Å	H···A/ Å	D···A/ Å	D-H···A/º	Symmetry code
N3-H3···O2	0.980(0)	2.140(1)	3.045(1)	152.98(0)	x, y, z
N3-H3···O4	0.980(0)	2.057(0)	3.004(0)	161.82(0)	x, y, z
N2-H2···O6	0.797(1)	2.298(2)	3.061(3)	160.68(0)	-x+1, -y+1, -z+1

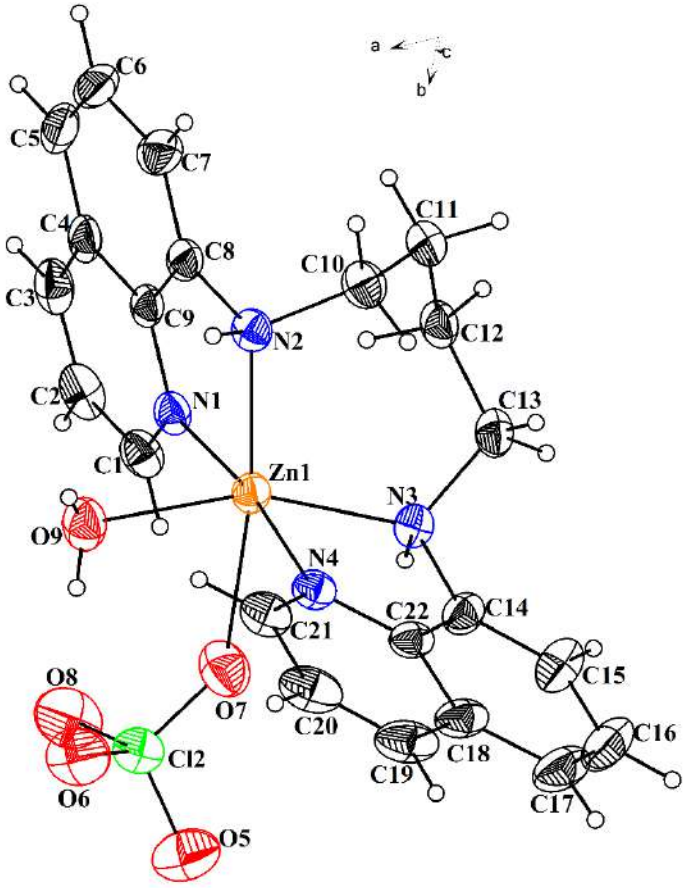

Figure 5.24 *Crystal structure of* $[Zn(L11)(H_2O)(ClO_4)]^{2+}$ ***26*** *showing atom labelling scheme. The thermal ellipsoids are drawn at 30 % probability level for all the atoms except for the H atoms, which are shown as spheres of arbitrary radii. The uncoordinated perchlorate anions have been omitted for the clarity.*

Table 5.11 *Selected bond lengths (Å) and angles (°) for* ***26****.*

Bond lengths (Å)			
O(9)-Zn(1)	2.193(3)	Zn(1)-N(1)	2.116(2)
Zn(1)-N(2)	2.100(2)	Zn(1)-N(3)	2.147(2)
Zn(1)-N(4)	2.100(2)		
Bond angles (°)			
N(2)-Zn(1)-N(4)	104.72(9)	O(9)-Zn(1)-O(7)	84.16(11)
N(4)-Zn(1)-O(9)	88.62(10)	N(3)-Zn(1)-O(7)	77.86(10)
N(2)-Zn(1)-O(9)	92.25(11)	N(1)-Zn(1)-O(7)	87.94(10)
N(1)-Zn(1)-N(3)	102.85(9)	N(4)-Zn(1)-O(7)	85.84(10)
N(2)-Zn(1)-N(1)	81.22(9)	N(2)-Zn(1)-O(7)	168.80(10)
N(4)-Zn(1)-N(3)	80.33(9)	N(3)-Zn(1)-O(9)	159.47(11)
N(2)-Zn(1)-N(3)	107.22(10)	N(1)-Zn(1)-O(9)	86.18(9)
N(4)-Zn(1)-N(1)	172.26(9)		

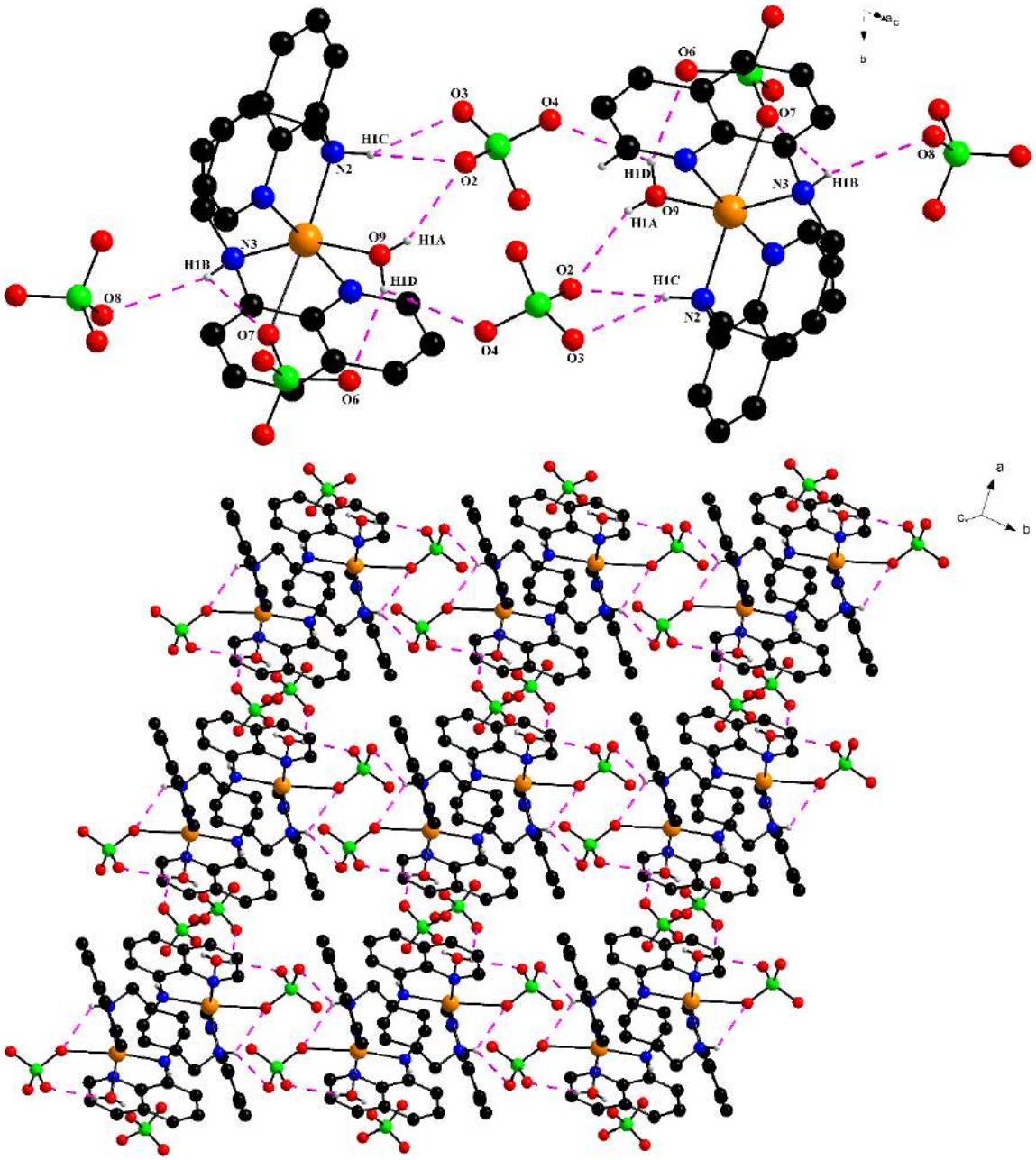

Figure 5.25 *The hydrogen bonding interactions in* ***26*** *with atom labelling scheme of atoms involved in hydrogen bonding; along with the enlarged view of a network of hydrogen bonding in* ***26*** *showing the symmetric organisation of* $[Zn(L11)(H_2O)(ClO_4)]^{2+}$ *cations and perchlorate anions. Hydrogen atoms attached to carbon are omitted for clarity.*

Table 5.12 *Hydrogen bonding parameters (Å, o) for* ***26****.*

D-H···A	D-H/ Å	H···A/ Å	D···A/ Å	D-H···A/º	Symmetry code
O9-H1A···O2	0.713(1)	2.266(1)	2.926(2)	154.68(0)	x, y, z
O9-H1D···O4	0.779(0)	2.501(1)	2.967(1)	119.90(0)	-x+2, -y+1, -z+2
O9-H1D···O6	0.779(0)	2.233(1)	2.939(1)	151.22(0)	x, y, z
N2-H1C···O2	0.856(1)	2.334(1)	3.150(2)	159.65(0)	x, y, z
N2-H1C···O3	0.856(1)	2.462(2)	3.177(2)	141.59(0)	x, y, z
N3-H1B···O8	0.835(1)	2.516(2)	3.209(3)	141.05(0)	-x+1, -y+2, -z+1
N3-H1B···O7	0.835(1)	2.569(1)	2.895(1)	104.66(0)	x, y, z

Table 5.13 *Technical details of crystal data and refinement parameters of* ***25*** *and* ***26****.*

Compound	**25**	**26**
Empirical formula	$C_{23}H_{23}Cl_2ZnN_5O_8$	$C_{22}H_{24}Cl_2N_4O_9Zn$
Formula weight	633.74	624.74
Temperature	296(2) K	296(2) K
Wavelength	0.71073 Å	0.71073 Å
Crystal system	Monoclinic	Triclinic
Space group	$P2_1/c$	P -1
Unit cell dimensions	a = 12.7114(7) Å b =14.6528(7) Å c = 14.2674(7)Å α = 90° β = 91.898(2)° γ = 90°	a = 10.4830(4) Å b = 11.5153(5) Å c = 11.6511(5) Å α = 76.3600(10)° β = 82.1070(10)° γ = 66.4010(10)°
Volume	2656.0(2) $Å^3$	1251.03(9) $Å^3$
Z	4	2
Density (calculated)	1.585 mg/m^3	1.658 mg/m^3
Absorption coefficient	1.183 mm^{-1}	1.256 mm^{-1}
F(000)	1296	640
Theta range for data collection	2.528 to 28.388°	2.389 to 28.342°
Completeness to theta	99.9%	99.9%
Index ranges	-16<=h<=16 -19<=k<=19 -19<=l<=19	-13<=h<=13 -15<=k<=15 -15<=l<=15
Reflections collected	64072	51476
Independent reflections	6629 (R(int) = 0.0656)	6235 [R(int) = 0.0466]
Refinement method	Full-matrix least-squares on F^2	Full-matrix least-squares on F^2
Absorption correction	Semi- empirical from equivalents	Semi- empirical from equivalents
Data/restraints/parameters	6629 / 2 / 377	6235 / 0 / 355
Goodness-of-fit on F^2	1.045	1.042
Final Rindices[I>2sigma(I)]	R1= 0.0664, wR2= 0.1558	R1= 0.0468, wR2= 0.1289
R indices (all data)	R1= 0.1024, wR2= 0.1740	R1= 0.0612, wR2= 0.1389
CCDC No.		2386747

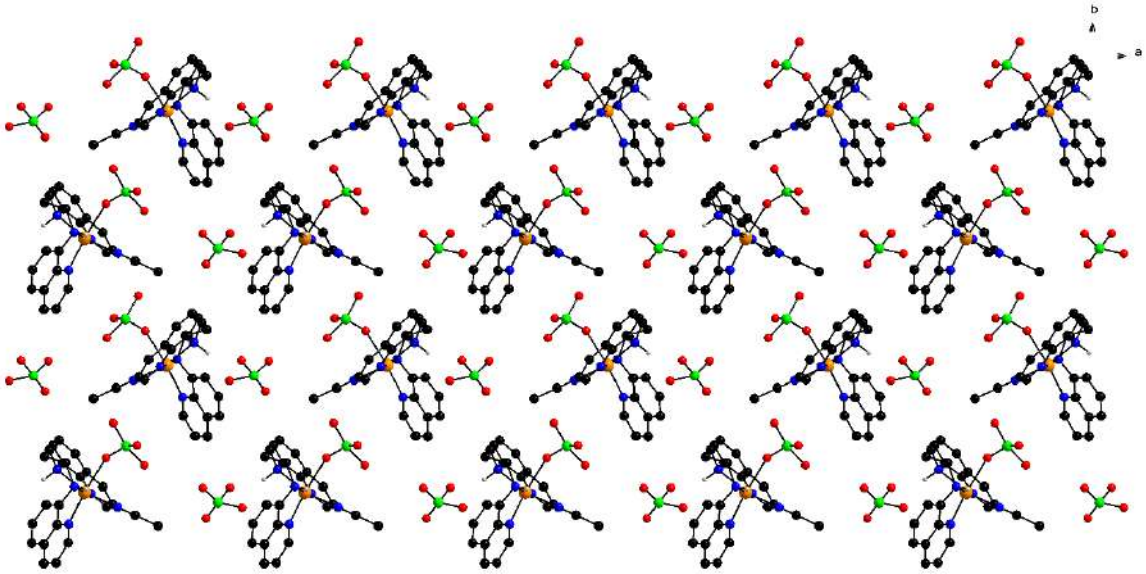

Figure 5.26 *Packing in* ***25*** *view along crystallographic c axis. Colour code: C, black; N, blue; O, red; Cl, green and Zn, orange.*

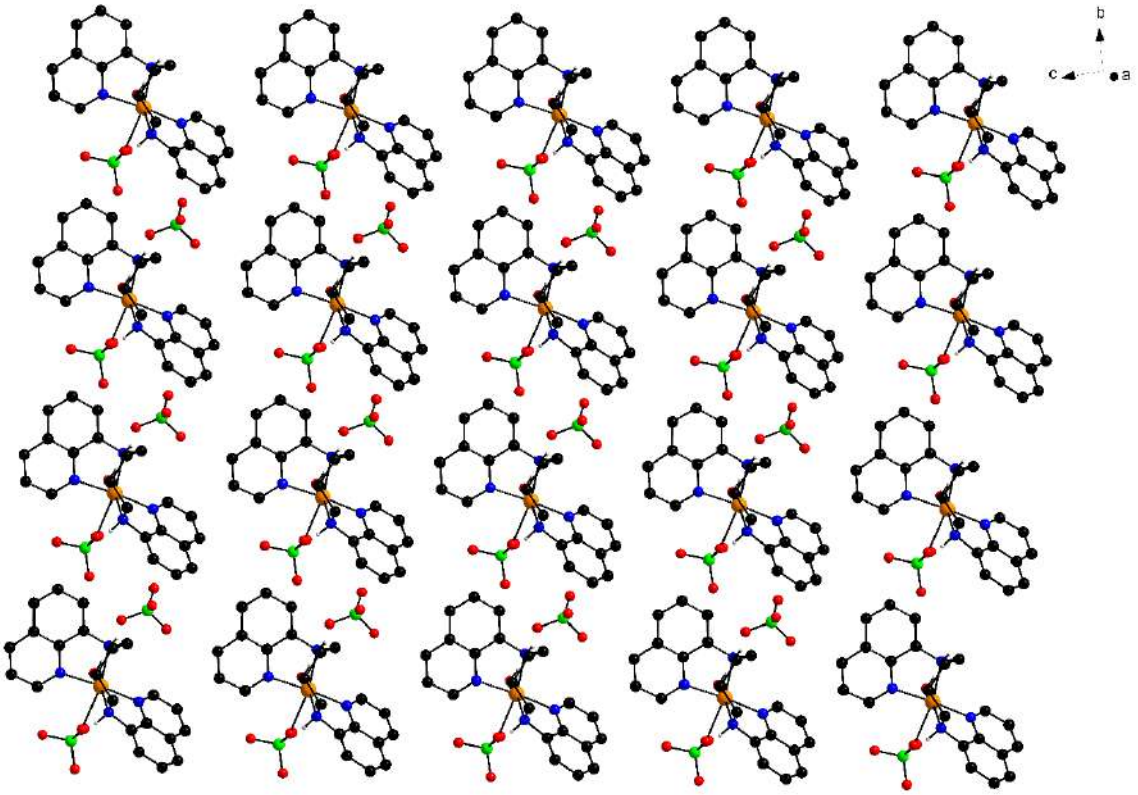

Figure 5.27 *Packing in* ***26*** *view along crystallographic a axis. Colour code: C, black; N, blue; O, red; Cl, green and Zn, orange.*

Chelate bite distance and bite angle are known to tune the geometry and function of the compounds[54,75]. The chelate bite angle N2–Zn–N3 widens systematically with backbone length as seen in **23**: 83.97°; **24**: 84.02°; **25**: 92.31°; **26**: 107.22° and the corresponding N2···N3 bite distance grows in parallel (2.873, 2.891, 3.107, 3.419 Å for **23–26**), evidencing the backbone-controlled expansion of the "natural bite." Within this framework, donor strength modulates the degree of equatorial anisotropy: MeCN gives short Zn–N (**23**: 2.185 Å; **24**: 2.142 Å; **25**: 2.163 Å), H_2O is moderately short (**23**: 2.100 Å; **24**: 2.167 Å; **26**: 2.193 Å), whereas ClO_4^- is distinctly weak (**25**: 2.342 Å; **26**: 2.446 Å). Overall, **24** (ethylenediamine) exhibits the most symmetric octahedron; **23** (cyclohexanediamine) is slightly more strained but still regular; introduction of a coordinated perchlorate together with longer, more flexible backbones in **25–26** yields the largest equatorial distortions and the greatest axial bond-length disparity, with **26** the most anisotropic member of the series.

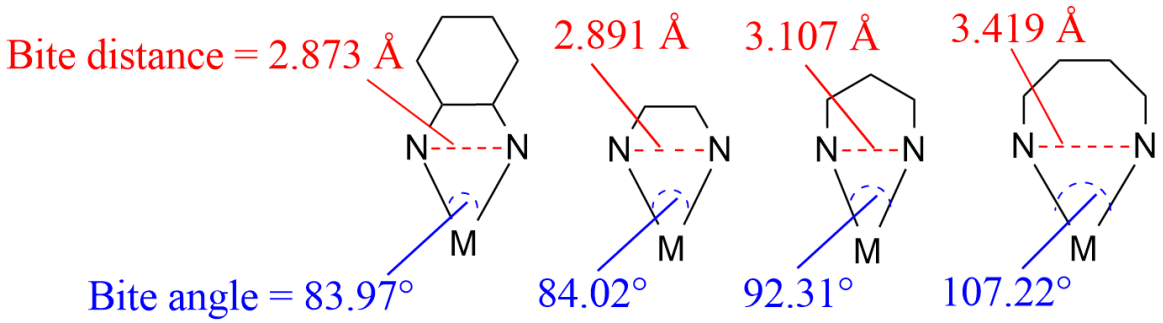

Scheme 5.6 *Schematic illustration of bite distance and bite angle in compounds* ***23-26****.*

5.8.4 X-ray powder diffraction

Powder X-ray diffraction (PXRD) patterns were collected for compounds **23–26** to verify that the crystalline samples were phase-pure and representative of the bulk material. The experimental diffractograms were compared with patterns simulated from the single crystal structures using Mercury 4.0[39]. The excellent overlap between measured and calculated traces confirms that the bulk and single-crystal phases are the same (**Figure 5.28** and **Figure 5.29**).

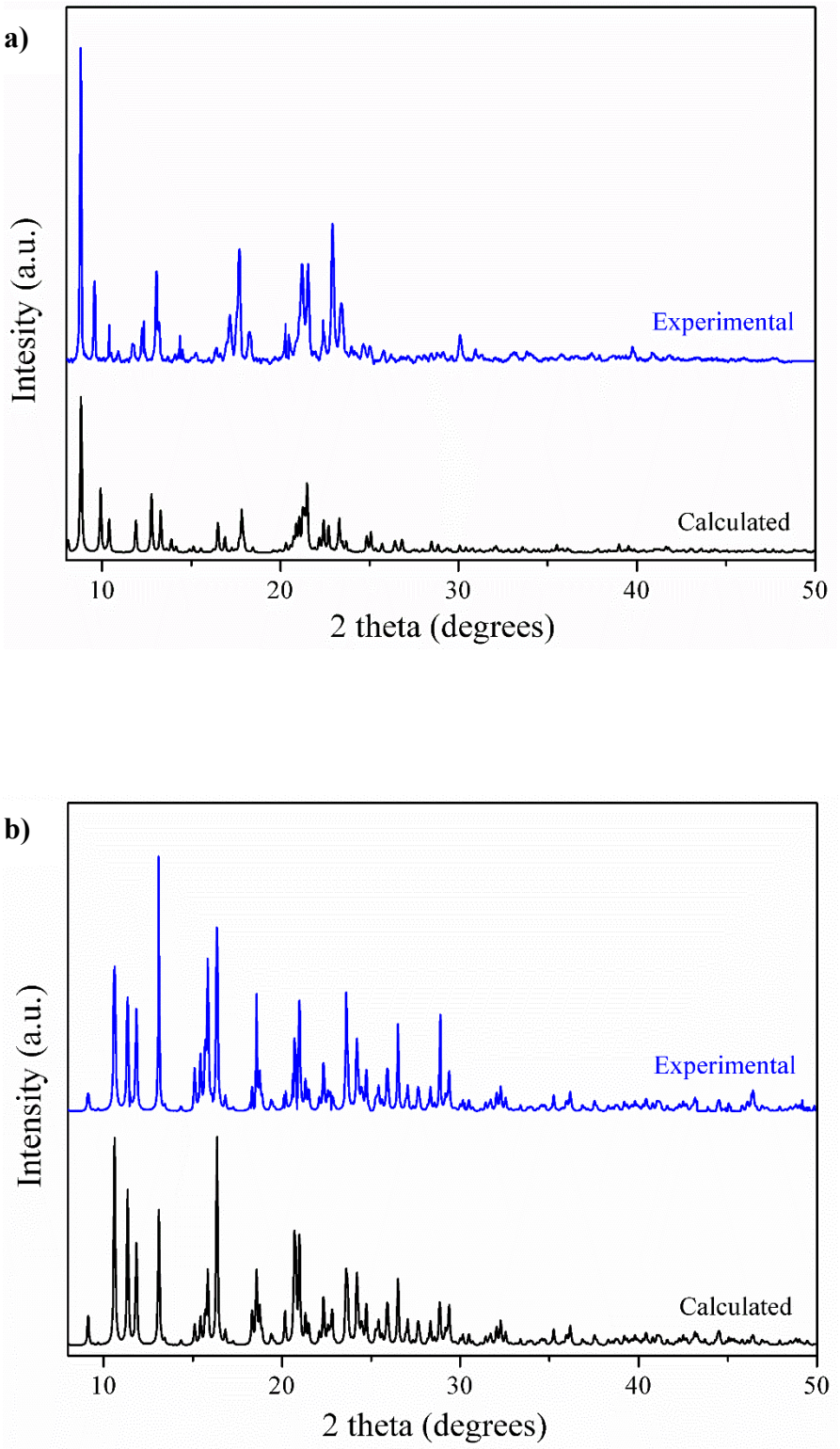

Figure 5.28 *The experimental and calculated PXRD patterns of* ***23*** *(a) and* ***24*** *(b).*

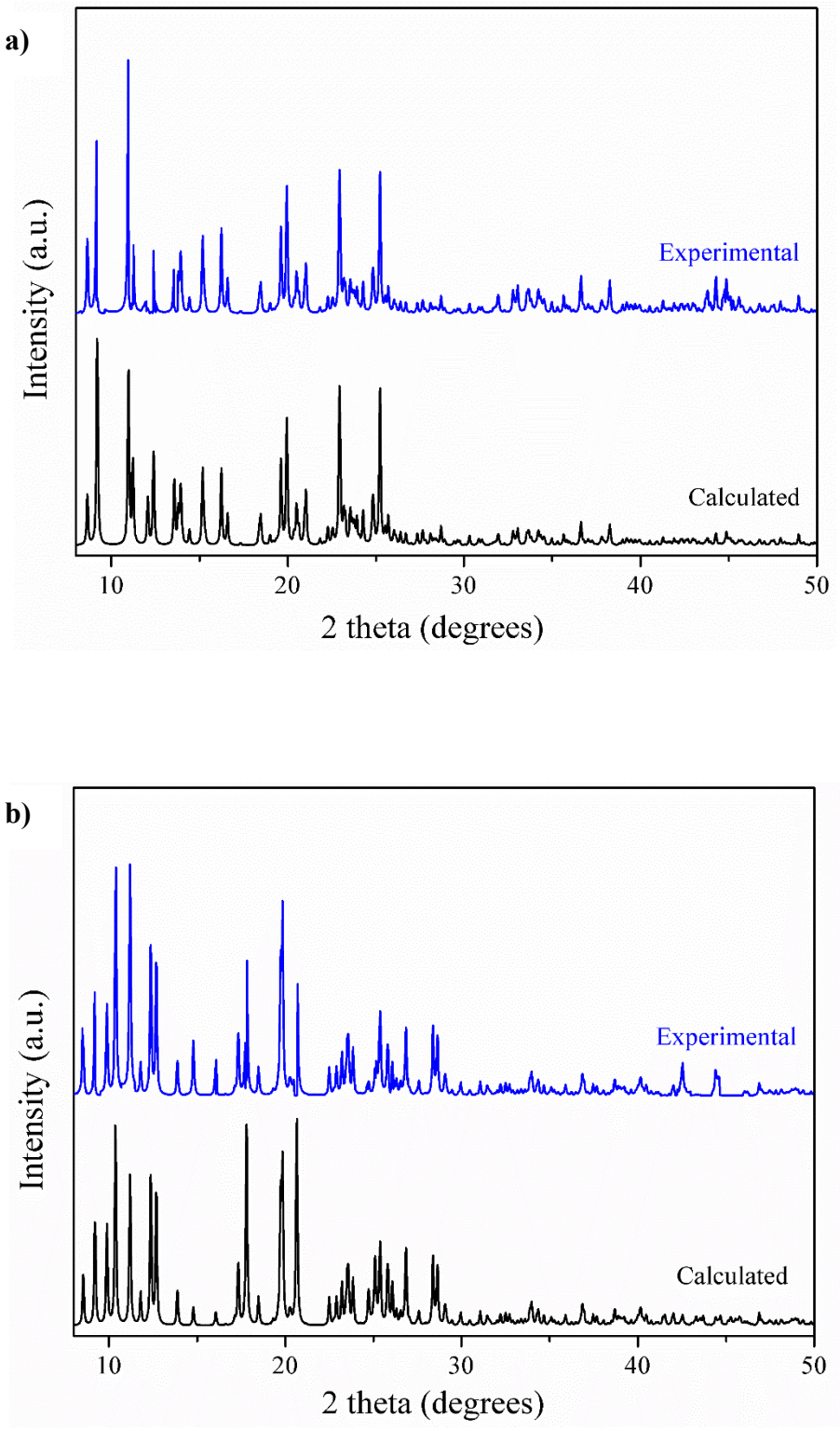

Figure 5.29 *The experimental and calculated PXRD patterns of* ***25*** *(a) and* ***26*** *(b).*

5.9 Conclusion

This chapter establishes how diamine backbone length and rigidity dictate the coordination geometry of aminoquinoline-based Zn(II) complexes in the solid state. Across **23–26**, the chelate bite angle N2–Zn–N3 and bite distance N2···N3 increase monotonically from cyclohexanediamine and ethylenediamine to propanediamine and butanediamine, shifting the structures from more preorganized, near-regular octahedra to more anisotropic, distorted environments. The axial axis in each compound is defined by a near-linear intrachelate N···N pair, while equatorial donors (H_2O, MeCN and in **25–26**, coordinated ClO_4^-) tune the extent of equatorial distortion; notably, Zn–O(ClO_3^-) is elongated, marking perchlorate as a weak, geometry loosening donor. Within this series, the ethylenediamine analogue **24** is the most symmetric, whereas the butanediamine analogue **26** shows the greatest equatorial bending and axial disparity.

These results provide design rules rather than demonstrated functions: shorter, more rigid backbones favor stable, well-defined coordination pockets, while longer, flexible backbones enable adaptive, labile coordination that accommodates weak donors. Although no applications were tested here, the structural trends offer a clear framework for prospective uses i.e. choosing rigid backbones when geometric regularity is paramount and flexible backbones where responsiveness or substitution lability could be advantageous.

References

1 R. F. Furchgott, *Angew. Chemie Int. Ed.*, 1999, **38**, 1870–1880.

2 G. B. Richter-Addo, P. Legzdins and J. Burstyn, *Chem. Rev.*, 2002, **102**, 857–860.

3 I. M. Wasser, S. de Vries, P. Moënne-Loccoz, I. Schröder and K. D. Karlin, *Chem. Rev.*, 2002, **102**, 1201–1234.

4 N. Lehnert, E. Kim, H. T. Dong, J. B. Harland, A. P. Hunt, E. C. Manickas, K. M. Oakley, J. Pham, G. C. Reed and V. S. Alfaro, *Chem. Rev.*, 2021, **121**, 14682–14905.

5 R. B. S. Nabi, R. Tayade, A. Hussain, K. P. Kulkarni, Q. M. Imran, B.-G. Mun and B.-W. Yun, *Environ. Exp. Bot.*, 2019, **161**, 120–133.

6 F. Vargas, J. M. Moreno, R. Wangensteen, I. Rodríguez-Gómez and J. García-Estañ, *Eur. J. Endocrinol.*, 2007, **156**, 1–12.

7 P. Pacher, J. S. Beckman and L. Liaudet, *Physiol. Rev.*, 2007, **87**, 315–424.

8 C. Prolo, M. N. Álvarez and R. Radi, *BioFactors*, 2014, **40**, 215–225.

9 C. H. Lim, P. C. Dedon and W. M. Deen, *Chem. Res. Toxicol.*, 2008, **21**, 2134–2147.

10 B. Kalyanaraman, *Proc. Natl. Acad. Sci.*, 2004, **101**, 11527–11528.

11 P. C. Dedon and S. R. Tannenbaum, *Arch. Biochem. Biophys.*, 2004, **423**, 12–22.

12 B. A. Averill, *Chem. Rev.*, 1996, **96**, 2951–2964.

13 E. I. Tocheva, F. I. Rosell, A. G. Mauk and M. E. P. Murphy, *Science (80-.).*, 2004, **304**, 867–870.

14 R. G. Knowles and S. Moncada, *Biochem. J.*, 1994, **298**, 249–258.

15 L. Ma, L. Hu, X. Feng and S. Wang, *Aging Dis.*, 2018, **9**, 938.

16 N. Benjamin, F. O'Driscoll, H. Dougall, C. Duncan, L. Smith, M. Golden and H. McKenzie, *Nature*, 1994, **368**, 502–502.

17 J. O. Lundberg, E. Weitzberg, J. M. Lundberg and K. Alving, *Gut*, 1994, **35**, 1543–1546.

18 G. G. Martirosyan, A. A. Hovhannisyan, L. S. Harutyunyan, A. G. Aleksanyan, A. V. Iretskii and P. C. Ford, *Inorg. Chem.*, 2025, **64**, 741–750.

19 J. Martinez Fernandez, A. Haji Seyed Javadi, S. J. Teat, T. R. Cundari and T. D. Tilley, *J. Am. Chem. Soc.*, 2024, **146**, 34962–34969.

20 S. Ghosh, A. Dey, Y. Sun, C. P. Scholes and E. I. Solomon, *J. Am. Chem. Soc.*, 2009, **131**, 277–288.

21 A. C. Merkle and N. Lehnert, *Dalt. Trans.*, 2012, **41**, 3355–3368.

22 Y.-L. Chang, Y.-F. Lin, W.-J. Chuang, C.-L. Kao, M. Narwane, H.-Y. Chen, M. Y. Chiang and S. C. N. Hsu, *Dalt. Trans.*, 2018, **47**, 5335–5341.

23 Z. Sakhaei, S. Kundu, J. M. Donnelly, J. A. Bertke, W. Y. Kim and T. H. Warren, *Chem. Commun.*, 2017, **53**, 549–552.

24 K. Chand, Y.-C. Chu, T.-W. Wang, C.-L. Kao, Y.-F. Lin, M.-L. Tsai and S. C. N. Hsu, *Dalt. Trans.*, 2022, **51**, 3485–3496.

25 Y. Kametani, K. Ikeda, K. Yoshizawa and Y. Shiota, *Inorg. Chem.*, 2023, **62**, 13765–13774.

26 A. Mondal, K. P. Reddy, S. Som, D. Chopra and S. Kundu, *Inorg. Chem.*, 2022, **61**, 20337–20345.

27 S. Gupta, S. Vijayan, J. A. Bertke and S. Kundu, *Inorg. Chem.*, 2022, **61**, 8477–8483.

28 P. Bhardwaj, Kulbir, T. Devi and P. Kumar, *Inorg. Chem. Front.*, 2023, **10**, 7285–7295.

29 Kulbir, S. Das, T. Devi, S. Ghosh, S. Chandra Sahoo and P. Kumar, *Chem. Sci.*, 2023, **14**, 2935–2942.

30 S. Gupta, S. Arora, A. Mondal, S. C. E. Stieber, P. Gupta and S. Kundu, *Eur. J. Inorg. Chem.*, DOI:10.1002/ejic.202200105.

31 S. Zhang, M. M. Melzer, S. N. Sen, N. Çelebi-Ölçüm and T. H. Warren, *Nat. Chem.*, 2016, **8**, 663–669.

32 S. Tian, J. Liu, R. E. Cowley, P. Hosseinzadeh, N. M. Marshall, Y. Yu, H. Robinson, M. J. Nilges, N. J. Blackburn, E. I. Solomon and Y. Lu, *Nat. Chem.*, 2016, **8**, 670–677.

33 R. L. Lieberman, D. M. Arciero, A. B. Hooper and A. C. Rosenzweig, *Biochemistry*, 2001, **40**, 5674–5681.

34 D. D. Narulkar, A. K. Srivastava, R. J. Butcher, K. M. Ansy and S. N. Dhuri, *Inorganica Chim. Acta*, 2017, **467**, 405–414.

35 K. Nakamoto, *Infrared and Raman Spectra of Inorganic and Coordination Compounds, Part B: Applications in Coordination, Organometallic, and Bioinorganic Chemistry Part 2 of Infrared and Raman Spectra of Inorganic and*

Coordination Compounds, John Wiley & Sons, 6th edn., 2009.

36 D. D. Narulkar, A. R. Patil, C. C. Naik and S. N. Dhuri, *Inorganica Chim. Acta*, 2015, **427**, 248–258.

37 S. S. Harmalkar, R. J. Butcher, V. V. Gobre, S. K. Gaonkar, L. R. D'Souza, M. Sankaralingam, I. Furtado and S. N. Dhuri, *Inorganica Chim. Acta*, 2019, **498**, 119020.

38 S. Mugiraneza and A. M. Hallas, *Commun. Phys.*, 2022, **5**, 95.

39 C. F. Macrae, I. Sovago, S. J. Cottrell, P. T. A. Galek, P. McCabe, E. Pidcock, M. Platings, G. P. Shields, J. S. Stevens, M. Towler and P. A. Wood, *J. Appl. Crystallogr.*, 2020, **53**, 226–235.

40 F. H. Allen, *Acta Crystallogr. Sect. B Struct. Sci.*, 2002, **58**, 380–388.

41 A. Hoffmann and S. Herres-Pawlis, *Phys. Chem. Chem. Phys.*, 2016, **18**, 6430–6440.

42 F. Weigend and R. Ahlrichs, *Phys. Chem. Chem. Phys.*, 2005, **7**, 3297.

43 A. E. Reed, R. B. Weinstock and F. Weinhold, *J. Chem. Phys.*, 1985, **83**, 735–746.

44 K. A. McCall, C. Huang and C. A. Fierke, *J. Nutr.*, 2000, **130**, 1437S-1446S.

45 W. Maret and Y. Li, *Chem. Rev.*, 2009, **109**, 4682–4707.

46 C. Andreini and I. Bertini, *J. Inorg. Biochem.*, 2012, **111**, 150–156.

47 M. Cassandri, A. Smirnov, F. Novelli, C. Pitolli, M. Agostini, M. Malewicz, G. Melino and G. Raschellà, *Cell Death Discov.*, 2017, **3**, 17071.

48 A. S. Nakashima and R. H. Dyck, *Brain Res. Rev.*, 2009, **59**, 347–373.

49 B. K. Y. Bitanihirwe and M. G. Cunningham, *Synapse*, 2009, **63**, 1029–1049.

50 W. N. Lipscomb and N. Sträter, *Chem. Rev.*, 1996, **96**, 2375–2434.

51 S. H. Kwon, S. Lee, J. Tessarolo and H. Lee, *RSC Adv.*, 2024, **14**, 32655–32660.

52 N. Kumar, Roopa, V. Bhalla and M. Kumar, *Coord. Chem. Rev.*, 2021, **427**,

213550.

53 G. M. Romano, Y. T. Simonini Steiner, F. Bartoli, L. Conti, E. Macedi, C. Bazzicalupi, P. Rossi, P. Paoli, M. Innocenti, A. Bencini and M. Savastano, *Dalt. Trans.*, 2025, **54**, 1689–1702.

54 M. M. Major, Z. Császár, A. C. Bényei, S. Balogh, J. Bakos and G. Farkas, *J. Organomet. Chem.*, 2020, **921**, 121332.

55 A. M. Abu-Dief and I. M. A. Mohamed, *Beni-Suef Univ. J. Basic Appl. Sci.*, 2015, **4**, 119–133.

56 L. Cheng, Y.-Y. Sun, Y.-W. Zhang and G. Xu, *Acta Crystallogr. Sect. E Struct. Reports Online*, 2008, **64**, m1246–m1246.

57 T. J. Roberts, T. F. Mehari, Z. Assefa, T. Hamby and R. E. Sykora, *Acta Crystallogr. Sect. E Crystallogr. Commun.*, 2015, **71**, m240–m241.

58 M. A. Alotaibi, A. I. Alharthi, W. Zierkiewicz, M. Akhtar, M. N. Tahir, M. Mazhar, A. A. Isab and S. Ahmad, *J. Mol. Struct.*, 2017, **1133**, 271–277.

59 A. Barbieri, G. Accorsi and N. Armaroli, *Chem. Commun.*, 2008, 2185.

60 I. Pietro Oliveri and S. Di Bella, *Chemistry (Easton).*, 2023, **5**, 119–137.

61 M. Shyamal, A. Panja and A. Saha, *Polyhedron*, 2014, **69**, 141–148.

62 V. Amani, *J. Mol. Struct.*, 2018, **1155**, 477–483.

63 Y. Ma, G. Xu, F. Wei, Y. Cen, Y. Song, M. Shi, X. Xu, M. Sohail and Q. Hu, *New J. Chem.*, 2018, **42**, 5162–5167.

64 T. Chatterjee, E. Hossain, S. Khan, S. Roy, S. M. Wabaidur, M. A. Islam, S. M. Alam and M. H. Mir, *J. Mol. Struct.*, 2023, **1271**, 134011.

65 A. S. Burlov, V. G. Vlasenko, Y. V. Koshchienko, N. I. Makarova, A. A. Zubenko, Y. D. Drobin, G. S. Borodkin, A. V. Metelitsa, Y. V. Zubavichus and D. A. Garnovskii, *Polyhedron*, 2018, **144**, 249–258.

66 D. Mukherjee, K. Sarkar, S. Reja, Md. Bakibillah, S. Guha, N. K. Mandal, J. P. Naskar and R. K. Das, *J. Fluoresc.*, 2024, **34**, 2335–2347.

67 Z. I. Contejean and R. L. LaDuca, *J. Solid State Chem.*, 2018, **266**, 44–53.

68 S. Roy, I. Mondal, K. Harms and S. Chattopadhyay, *Polyhedron*, 2019, **159**, 265–274.

69 X.-Z. Guo, S.-S. Chen, W.-D. Li, S.-S. Han, F. Deng, R. Qiao and Y. Zhao, *ACS Omega*, 2019, **4**, 11540–11553.

70 D. D. Narulkar, A. R. Patil, C. C. Naik and S. N. Dhuri, *Inorganica Chim. Acta*, 2015, **427**, 248–258.

71 S. S. Harmalkar, D. D. Narulkar, R. J. Butcher, M. S. Deshmukh, A. Kumar Srivastava, M. Mariappan, P. Lama and S. N. Dhuri, *Inorganica Chim. Acta*, 2019, **486**, 425–434.

72 S. S. Harmalkar, R. J. Butcher, V. V. Gobre, S. K. Gaonkar, L. R. D'Souza, M. Sankaralingam, I. Furtado and S. N. Dhuri, *Inorganica Chim. Acta*, 2019, **498**, 119020.

73 S. S. Harmalkar, A. V. Naik, M. K. Nilajakar and S. N. Dhuri, *ChemistrySelect*, 2020, **5**, 8447–8454.

74 J. England, G. J. P. Britovsek, N. Rabadia and A. J. P. White, *Inorg. Chem.*, 2007, **46**, 3752–3767.

75 R. D. Hancock and L. J. Bartolotti, *Polyhedron*, 2013, **52**, 284–293.

APPENDIX I

List of publications (Appended to thesis):

1. Synthesis and characterization of a copper (II) compound with a new N3Py2 core ligand: Influence of methyl substitution on structural parameters and catalytic mimicking activity. **Jeffrey, L. V**.; Sunder, N. D.; ***J. Mol. Struct.,*** **2023**, *1288,* 135719.
2. Ligand Backbone Influenced Luminescent Properties of Mononuclear Zn(II)-N3Py2 Compounds: Synthesis, Structures and Nitroaromatics Detection. **Jeffrey, L. V**.; Vishnu R. C.; Sunder, N. D.; ***J. Mol. Struct.,*** **2024**, *9, e202402704*.
3. A three-component reaction of 4-hydroxycoumarin, 2-aminopyridine and aryl aldehydes: Synthesis of enolate salts of 2-aminopyridinium biscoumarins. *ChemistrySelect* (Accepted August 2025)

Manuscripts under preparation

1. Synthesis, characterization and catalytic application of tetradentate amino-pyridyl appended Cu(II) compounds.
2. Influence of equatorial sulfur coordination in nonheme Fe(II) compounds on the reactivity.

Papers presented at conferences/workshops:

1. "Synthesis, characterization and catalytic application of pentadentate copper (II) compounds." at International Conference on "Advance Materials: Properties and Applications" held on 20-24 February, 2023, organised by Goa University.

2. “Synthesis, characterization and catalytic fate of copper(II) compounds towards oxidation reaction.” at International Conference on “Modern Trends in Inorganic Chemistry” held on 14-17 December, 2023, organised by IISc Bangalore.
3. “Synthesis, characterization and reactivity of non-heme manganese compound” at 6th symposium on “Advanced Biological Inorganic Chemistry” held on 7-11 January, 2024, organised by IACS-Kolkata and TFIR-Mumbai.
4. “Tuning the reactivity of copper(II) compounds as biomimetic catalysts”, National conference on Advances in material science, organized by Department of Chemistry & Cluster research centre of Government college of Arts and Science and Commerce, Khandola, Feb. 09-10, 2024.

Seminars/webinars/activities attended:

1. Attended two-day workshop on Raman Spectroscopy organized by School of Chemical Sciences and School of Physical and Applied Sciences Goa University on 26-27 August 2024.
2. Attended Webinar on “Unlock the Potential of the CSD to Teach Chemistry and Crystallography” by CCDC on 6 June 2024.
3. Attended Workshop on “Innovating, Designing, Modeling, Characterization and Simulation of Materials and Bio-Molecule using in Silico Solution Suite, Atomistic Simulation Advanced Platform (ASAP) and J-OCTA” jointly organized by Goa University, Directorate of Research Development and Resource Mobilization (DRDRM) and Directorate of Internships, Incubation and Industry Partnership (DI3P) from 18- 19 January 2024.
4. Attended one day seminar on “Recent Advances in Bio-Inorganic Chemistry” organized by BITS Pilani KK Birla Goa Campus, on 29 December 2023.
5. Attended workshop on “Materials Characterization using Powder X-ray Diffraction” organized by School of Chemical Sciences Goa University on 7-8 December 2023.
6. Attended the one-day National Seminar on Recent Trends in Applied Organic Synthesis at the School of Chemical sciences, Goa University on 26 November 2022.

7. Attended a three- day workshop on X-ray Crystallography at the School of Chemical Sciences, Goa University from 21-23 July 2022.
8. Attended the 2D-SAGE webinar talk by Prof. Giulia Grancini at SCS, Goa University through Google meet on 10 March 2022.
9. Attended the 2D-SAGE webinar talk by Dr. Aditya Sadhanala at SCS, Goa University through Google meet on 21 January 2022.
10. Attended one-day Seminar on "Recent Advances in Chemical Sciences" organized by School of Chemical Sciences, Goa University on 17 December 2019.
11. Attended two- day Workshop on Material Science organized by University of Porto, University of Coimbra and Goa University held from 18- 19 November 2019.
12. Attended the one-day seminar on "Recent trends in Structural Chemistry" organized by the Department of Chemistry, Goa University on 16 February 2019.

Journal of Molecular Structure 1288 (2023) 135719

Contents lists available at ScienceDirect

Journal of Molecular Structure

journal homepage: www.elsevier.com/locate/molstr

Synthesis and characterization of a copper (II) compound with a new N3Py2 core ligand: Influence of methyl substitution on structural parameters and catalytic mimicking activity

Jeffrey L. Viegas [a,b], Sunder N. Dhuri [a,*]

[a] School of Chemical Sciences, Goa University, Plateau, Taleigao, Goa 403 206 India
[b] Carmel College of Arts, Science and Commerce for Women, Nuvem, Goa 403 604 India

ARTICLE INFO

Keywords:
Copper(II)
Crystal structure
Nonheme
Distortion
Phenoxazinone synthase
Catacholase

ABSTRACT

A mononuclear copper (II) compound $[Cu(L^1)](ClO_4)_2$ **1** containing nonheme N3Py2 pentadentate ligand N^1,N^3-dimethyl-N^1-(3-(methyl(pyridin-2-ylmethyl)amino)propyl)-N^3-(pyridin-2-ylmethyl)propane-1,3-diamine) have been synthesized and characterized by several methods. A new ligand L^1 has been prepared by methylation of secondary -NH of L^2 (N^1-(pyridin-2-ylmethyl)-N^3-(3-((pyridin-2-ylmethyl)amino)propyl)propane-1,3-diamine) at and characterized by NMR spectroscopy. Compound **1** has been characterized by single-crystal X-ray crystallography and spectroscopic techniques. It crystallizes in a centrosymmetric space group $P2_1/n$ and adopts a distorted square-pyramidal geometry with τ_5= 0.13. We also prepared compound $[Cu(L^2)](ClO_4)_2$ **2,** and its structural properties were compared with **1**. The geometry of **1** is nearly SP, while compound **2** is intermediate between SP and TBP. We then investigated the applications of **1** and **2** in phenoxazinone synthase and catecholase activity. The results suggest compound **1** was more effective in both activities than **2**.

1. Introduction

The transition metalloenzymes play critical roles in biological processes. Several reports on biomimetic model compounds containing N-donor coordination suppliers have shown an insight into the structure-function properties [1–8]. The impetus to design novel ligands and transition metal compounds appears from their potential to understand the correlation of their geometric and electronic structure with their reactivity. The copper-based coordination compounds are known for their diverse applications [9–12]. Several copper compounds have been known as biomimetic models of metalloenzymes [13,14]. The coinage transition metal copper is a well-known essential element in biology. Its compounds can catalyze various biochemical redox reactions such as methane monooxygenase, catechol oxidase, superoxide dismutase, and phenoxazinone synthase [15–18]. Phenoxazinone synthase (PHS) is a multicopper oxidase enzyme produced by *Streptomyces antibioticus*. A hexameric copper active site can catalyze an oxidative coupling of substituted 2-aminophenols to phenoxazinone chromophore in the biosynthesis of actinomycin D, a naturally synthesized antineoplastic agent [19,20]. The design and development of numerous small molecule catalysts bearing amine and polypyridyl ligands have helped the bioinorganic chemist to understand the structure-activity synergy at the active site [21–26]. The metal compounds, ligand architecture, and coordination geometry, are known to control the reactivity and stability of such compounds [27–33]. In our endeavor to design new N3Py2 type N-donor ligands, we herein report the synthesis and characterization of a new ligand L^1 = N^1,N^3-dimethyl-N^1-(3-(methyl(pyridin-2-ylmethyl) amino)propyl)-N^3-(pyridin-2-ylmethyl)propane-1,3-diamine) prepared by methylation of L^2 = N^1-(pyridin-2-ylmethyl)-N^3-(3-((pyridin-2-ylmethyl)amino)propyl)propane-1,3-diamine at normal laboratory conditions. Copper(II) ions tend to form common tetrahedral, octahedral, square pyramidal, and trigonal bipyramidal geometry compounds, all of which are tetragonally distorted [34]. The pentadentate N-donor ligands form square pyramidal and trigonal bipyramidal copper(II) compounds. Addison and co-workers showed connectivity between SP and TBP with intermediate geometries in copper compounds [35]. Recently we have reported copper(II) compounds of tetradentate ligands and a coordinated solvent molecule exhibiting five-coordinate geometries and enormous distortions [36]. In this work, we are presenting a thoroughly characterized copper (II) compound, $[Cu(L^1)](ClO_4)_2$ **1** stabilized by L^1 showing the influence of ligand architecture on the phenoxazinone synthase and catecholase-like

* Corresponding author.
E-mail address: sndhuri@unigoa.ac.in (S.N. Dhuri).

https://doi.org/10.1016/j.molstruc.2023.135719
Received 25 February 2023; Received in revised form 14 April 2023; Accepted 3 May 2023
Available online 4 May 2023

activity. To understand the reactivity pattern with non-methylated ligands, we have also reinvestigated $[Cu(L^2)](ClO_4)_2$ **2** [37] stabilized by ligand L^2.

2. Experimental section

2.1. Material and methods

All reagents used for synthesis and reactivity studies were purchased from commercial sources and used without further purification. The solvents were distilled and dried under N_2 atmosphere before their use. The infrared (IR) spectra were recorded on Shimadzu (IR-Prestige-21) FTIR spectrometer by diluting the compounds in KBr powder in the region of 4000–400 cm^{-1}. The C, H and N analyses was carried out using Elementar Variomicro Cube CHNS Analyser. Thermogravimetric studies were conducted on a Perkin Elmer Thermogravimetric Analyser (TGA 4000). ^1H and ^{13}C-NMR spectra were measured on a Bruker Avance III, 400 MHz, NMR spectrometer using $CDCl_3$. The single crystal X-ray structures of **1** and **2** were determined using Bruker D8 Quest Eco X-ray diffractometer. Intensity data were collected at room temperature (RT) using monochromated (MoKα = 0.7107 Å) radiation. The program suite APEX3 (Version 2018.1) was used to integrate the frames, perform absorption correction, and determine the unit cell. The structures of **1** and **2** were solved with SHELXS., and subsequent refinements were performed with SHELXL [38]. The phase purity of powdered samples was confirmed using powder X-ray diffraction (PXRD) measurements carried out on a Bruker D8 Advance X-ray diffractometer using Cu $k_{\alpha 1}$. (λ = 1.5406 Å) with a nickel filter. The UV–Vis spectra were recorded on Agilent diode array 8453 UV–Vis spectrophotometer. The electrospray ionization mass spectra (ESI-MS) of **1** and **2** in CH_3CN were recorded using Applied Biosystem Matrix-assisted Laser Desorption Ionization Time-of-flight (MALDI-TOF) spectrometer. The X-band EPR measurements were performed on a JEOL X-band spectrometer (JESFA100). The field-dependent magnetic studies were performed between 5 and 300 K under an applied field of 100 Oe (M-T) with SQUID magnetometer, Cryogenic Limited.

2.2. Synthesis of L^1 and L^2

Ligand L^1 was synthesized by methylation of the reported L^2 [37]. The ice-cold aqueous solution of L^2 (3 g, 9.5 mmol) was combined with formaldehyde solution (37%, 22.0 mL) and formic acid (85%, 15.0 mL) and refluxed for ~ 24 h. An aqueous NaOH (2.0 M) was added until the pH was above 12. A brown oil was extracted with three 30 mL aliquots of chloroform and dissolved in HCl solution (pH ~ 1). The acidic mixture was basified with aqueous NaOH, and the reddish-brown product L^1 was then extracted with six 20 mL aliquots of diethyl ether. The yield of L^1 was 2.7 g (7.59 mmol) 79%. *Anal. Calc.* for (L^1) $C_{21}H_{33}N_5$ (%): C, 70.95; H, 9.36; N, 19.70. *Found:* C, 70.04; H, 8.95; N, 19.03. IR (KBr, cm^{-1}): 3007–2895 υ(CH); ^1H NMR ($CDCl_3$, ppm): δ 8.54 (d, 2H, J = 4.8 Hz), δ 7.65 (t, 2H, J = 7.6 Hz), δ 7.42 (d, 2H, J = 8.0 Hz), δ 7.15 (t, 2H, J = 6.0 Hz), δ 3.64 (s, 4H), δ 2.44 (t, 4H), δ 2.36 (t, 4H), δ 2.24 (s, 6H), δ 2.20 (s, 3H), δ 1.70 (qui, 4H),^{13}C NMR ($CDCl_3$, ppm): δ 159.4, δ 149.0, δ 136.4, δ 123.0, δ 121.9, δ 63.9, δ 55.9, δ 55.6, δ 42.4, δ 42.2, δ 25.1.

The synthesis of L^2 was reported elsewhere, followed with modifications [39]. A solution of bis(3-aminopropyl) amine (1.8 g, 14.0 mmol) in ethanol (5 mL) was added dropwise to a solution of pyridine-2-carboxaldehyde (3.0 g, 28.0 mmol) in ethanol (15 mL) and refluxed, with stirring, for ~ 5 h. The mixture was cooled to room temperature and evaporated under reduced pressure to produce semi-solid imine. The imine was redissolved in ice-cold methanol (20 mL) and to this solution $NaBH_4$ (0.48 g, 12.8 mmol) was added slowly, after which the mixture was stirred overnight. The solvent was then removed under vacuum, and the distilled water (20 mL) was added to the crude product flask. Yellow viscous oil of L^2 was extracted with three 30 mL of ethyl acetate. The yield of L^2 was 3.6 g (11.48 mmol) 85%. *Anal. Calc.* for (L^2) $C_{18}H_{27}N_5$ (%): C, 68.97; H, 8.63; N, 22.34. *Found:* C, 68.26; H, 8.45; N, 21.92. IR (KBr, cm^{-1}): 3298 υ(NH); 3053–2816 υ(CH).

2.3. Synthesis of $[Cu(L^1)](ClO_4)_2$ (1)

A solution of L^1 (0.48 g, 1.37 mmol) in acetonitrile (5 mL) was added slowly to the stirring solution of $Cu(ClO_4)_2{\cdot}6H_2O$ (0.5 g, 1.37 mmol) in acetonitrile (2 mL) at room temperature. The mixture was stirred for ~ 8 h. Diethyl ether (10 mL) was added to the resulting dark blue color solution, and the mixture was kept undisturbed for crystallization. The blue crystals formed after two days were isolated by filtration and dried in the air. The yield of **1** was 0.64 g (1.03 mmol) 77.0%. *Anal. Calc.* for (**1**) C_{21} H_{33} Cl_2 Cu N_5 O_8 (%): C, 40.82; H, 5.38; N, 11.33. *Found:* C, 40.58; H, 5.05; N, 11.95. IR (KBr, cm^{-1}):3007–2895 υ(CH); 1093, 621 $\upsilon(ClO_4)$; UV–Vis data, λ_{max}, CH_3CN/nm (ε/dm^3 mol^{-1} cm^{-1}): 275 (2665) and 610 (45).ESI-MS: m/z = 209.1 (calc. 209.1) for $[Cu(L^1)]^{2+}$ and m/z = 517.0 (calc. 517.0) for $[Cu(L^1)(ClO_4)]^+$.

2.4. Synthesis of $[Cu(L^2)](ClO_4)_2$ (2)

$[Cu(L^2)](ClO_4)_2$(**1**) was synthesized with a modification of the reported procedure [37]. A solution of L^2 (0.42 g, 1.37 mmol) in acetonitrile (5 mL) was added slowly to the stirring solution of $Cu(ClO_4)_2{\cdot}6H_2O$ (0.5 g, 1.37 mmol) in acetonitrile (2 mL) at room temperature. The mixture was stirred for ~8 h. Diethyl ether (10 mL) was added to the resulting dark blue color solution, and the mixture was kept undisturbed for crystallization. The blue crystals formed after two days were isolated by filtration and dried in the air. The yield of **2** was 0.62 g (1.07 mmol) 80%. *Anal. Calc.* for (**2**) C_{18} H_{27} Cl_2 Cu N_5 O_8 (%): C, 37.54; H, 4.73; N, 12.16. *Found:* C, 37.10; H, 3.95; N, 12.23. IR (KBr, cm^{-1}):3217 υ(NH); 3053–2816 υ(CH); 1093, 621 $\upsilon(ClO_4)$; UV–Vis data, λ_{max}, CH_3CN/nm (ε/dm^3 mol^{-1} cm^{-1}): 280 (2722) and 690 (75). ESI-MS: m/z = 188.0 (calc. 188.0) for $[Cu(L^2)]^{2+}$ and m/z = 475.1 (calc. 475.1) for $[Cu(L^2)(ClO_4)]^+$.

Caution! *Although we have not experienced any issues, perchlorate salts are potentially explosive and should be handled in small quantities and with extreme care.*

2.5. Catalytic oxidation of 2-aminophenol (OAP) and 3,5-di-tert-butylcatechol (3,5-DTBC)

Compounds **1** and **2** were tested in the oxidation of model substrates 2-aminophenol (OAP) and 3,5-di-tert-butylcatechol (3,5-DTBC). In a typical catalytic reaction, the compound (1×10^{-4}) dissolved in dioxygen-saturated methanolic solution was reacted with OAP (1×10^{-3}) at 25 °C for 2 h. The time dependent reaction progress was monitored using UV–Vis spectrophotometer. After two hours, the evaporation of the solvent yielded a reddish-brown residue which was then infused on Shimadzu GC 2014 equipped with HP capillary column (30 m x 0.25 mm x 2.5 μM) and an FID detector using methanol as eluent. The oxidation of 3,5-DTBC was examined spectrophotometrically by reacting 100 equivalents of 3,5-DTBC with catalyst (1×10^{-4}) in methanol for two hours. The quinone was purified by column chromatography using a 10% mixture of ethyl acetate and hexane as eluent.

3. Results and discussion

3.1. Synthesis and characterization of ligands

We have reported the synthesis of a new pentadentate N-methylated pyridyl amine ligand $\mathbf{L^1}$ prepared from the non-methylated precursor L^2 via the Eschweiler-Clarke reaction (Scheme 1) [40]. The ligand L^1 was characterized by ^1H and ^{13}C NMR spectroscopy (SI, Figs. S1–S3). Martell and co-workers first synthesized the bis-pyridine ligand $\mathbf{L^2}$ in 1978, wherein the Schiff base was subsequently hydrogenated with a palladium catalyst. A similar diimine reduction method with Zn has also been

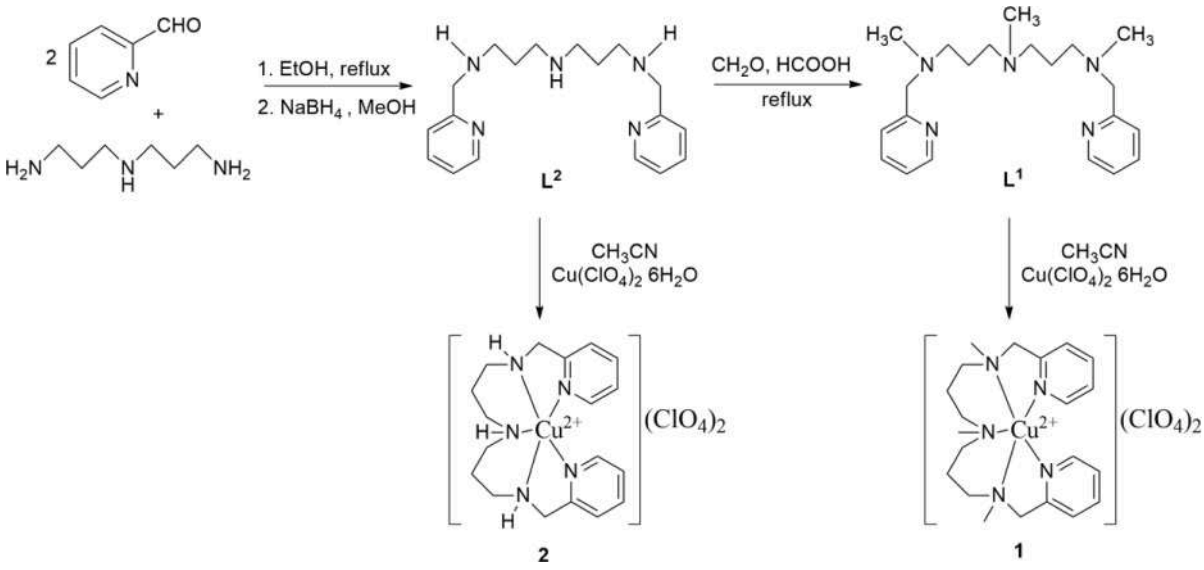

Scheme 1. Synthetic route for preparation of L^1, L^2, **1** and **2**.

reported [41]. In the current work, we have synthesized L^2 starting from its diimine precursor, followed by the standard $NaBH_4$ reduction (Scheme 1). IR spectra of ligands L^1 and L^2 were recorded in the region 4000 – 400 cm^{-1}. The overlaid IR spectra (SI, Fig. S4) show features attributed to the ligands and compound formation. The IR spectrum of L^2 exhibits N-H stretching vibration in the region 3290–3350 cm^{-1}, while similar peaks were not observed in the IR spectrum of methylated analog L^1. Medium-to-weak absorptions observed between 2890 and 3040 cm^{-1} were characteristic of C-H stretching vibrations of organic ligands [42].

3.2. Synthesis and spectroscopic characterization compounds 1 and 2

Compounds **1** and **2** were synthesized by reacting L^1 and L^2 with equimolar concentrations of $Cu(ClO_4)_2.6H_2O$ in acetonitrile, respectively (Scheme 1). The slow diffusion of diethyl ether in acetonitrile solution yielded crystals suitable for single-crystal X-ray diffraction. In the reported literature, compound **2** was prepared by refluxing in ethanol [37]; however, we carried out the reaction at room temperature using acetonitrile. Compounds **1** and **2** were formulated as $[Cu(L^1)](ClO_4)_2$ (**1**) and $[Cu(L^2)](ClO_4)_2$ (**2**) based on various characterized techniques such as C, H, N analysis, thermogravimetric analysis, IR, UV–Visible spectroscopy and ESI-MS. The crystal structure of **1** was obtained using single-crystal X-ray diffraction. We have reinvestigated the crystal structure of **2** [37] to compare the structural differences with **1** in terms of the τ_5 parameter. In addition, for the first time, we have also focused on phenoxazinone synthase and catecholase activity by these compounds. The bands due to O-H vibrations are absent in the IR spectra of compounds **1** and **2,** indicating the absence of water molecules, thus giving the first hint of pentadentate coordination with copper (II). Compound **2** showed N—H stretching vibration in the region 3290–3350 cm^{-1} due to incorporating L^2. In both **1** and **2,** the well-resolved absorption bands at ~ 1090 cm^{-1} and ~ 620 cm^{-1} are observed for uncoordinated perchlorate anions [43,44] (SI, Fig. S4).

UV–Vis spectra for compounds **1** and **2** were recorded in CH_3CN. The pentadentate ligand-based Cu(II) compounds with a typical square pyramidal geometry exhibit $d_{xz}, d_{xy} \rightarrow d_{z^2}$ transition bands in the 550–670 nm region, i.e., a high-energy peak with a low-energy shoulder. The intense band observed in the high energy region are assigned to the Cu (II)-pyridine charge transfer band (260–315 nm) [45]. The weaker *d-d* bands observed in the 500–1000 nm region and their patterns can suggest the exact nature of pentacoordinate geometry [46,47]. The high-intensity band at ~ 610 nm and shoulder at ~ 850 nm could be attributed to the effects of distortion in compound **1**. A broad band centered at ~690 nm in compound **2** indicates a significant distortion (SI, Fig. S5).

3.3. ESI-Mass spectrometry

Electrospray mass spectra (ESI-MS) of compounds **1** and **2** were studied in acetonitrile. ESI-MS spectrum of **1** exhibits mass peaks at m/z = 209.1 for $[Cu(L^2)]^{2+}$ and m/z = 517.0 for $[Cu(L^2)(ClO_4)]^+$ fragments (SI, Fig. S6a). On the other hand, the ESI-MS spectrum of **2** exhibits two major mass peaks at m/z = 188.0 and m/z = 475.1, which can be assigned to $[Cu(L^1)]^{2+}$ and $[Cu(L^1)(ClO_4)]^+$ species, respectively (SI, Fig. S6b).

3.4. Crystal structure and geometrical analyses of 1 and 2

Single crystals of $[Cu(L^1)](ClO_4)_2$ **1** and $[Cu(L^2)](ClO_4)_2$ **2** suitable for structure determination were obtained by slow diffusion of diethyl ether into the CH_3CN solution of the respective compounds. Our CSD search indicated that the crystal structure of **2** was earlier reported [37]. However, for comparing the crystal structure data of **1**, we have reinvestigated the crystal structure of compound **2** prepared by our method. The summary of technical details of data acquisition and selected

Table 1
Selected bond lengths (Å) and angles (°) for **1** and **2**.

Compound **1**
Cu(1)-N(1) 2.064(4) Cu(1)-N(4) 2.067(4)
Cu(1)-N(2) 2.302(4) Cu(1)-N(5) 2.042(4)
Cu(1)-N(3) 2.088(4)
N(5)-Cu(1)-N(1) 91.47(16) N(5)-Cu(1)-N(4) 80.64(17)
N(1)-Cu(1)-N(4) 162.05(16) N(5)-Cu(1)-N(3) 169.90(17)
N(1)-Cu(1)-N(3) 91.62(16) N(4)-Cu(1)-N(3) 93.64(17)
N(5)-Cu(1)-N(2) 96.28(16) N(1)-Cu(1)-N(2) 79.39(15)
N(4)-Cu(1)-N(2) 117.31(15) N(3)-Cu(1)-N(2) 93.74(17)
Compound **2**
Cu(1)-N(1) 2.017(2) Cu(1)-N(2) 2.023(2)
Cu(1)-N(3) 2.028(2) Cu(1)-N(5) 2.032(2)
Cu(1)-N(4) 2.225(2)
N(1)-Cu(1)-N(2) 82.97(9) N(1)-Cu(1)-N(3) 153.78(10)
N(2)-Cu(1)-N(3) 91.94(10) N(1)-Cu(1)-N(5) 93.25(8)
N(2)-Cu(1)-N(5) 175.72(9) N(3)-Cu(1)-N(5) 92.34(10)
N(1)-Cu(1)-N(4) 106.05(9) N(2)-Cu(1)-N(4) 98.62(9)
N(3)-Cu(1)-N(4) 100.14(10) N(5)-Cu(1)-N(4) 80.47(9)

refinement results for **1** and **2** are given in SI, Table S1. At the same time, the desired bond lengths and angles are provided in Table 1 for **1**. Both compounds **1** and **2** crystallize in the centrosymmetric monoclinic space group $P2_1/n$ with all the atoms located at general positions. An asymmetric unit of **1** and **2** is made up of one unique Cu(II) ion, a discrete pentadentate ligand (L^1 in **1**; L^2 in **2**), and two independent perchlorate ions. The independent perchlorate anions balance the charge neutrality of the cationic core without coordinating with the Cu(II) ion. Despite of apparent resemblance in their asymmetric unit, they show different coordination geometries due to changes at N-donor. Crystallographic analysis of compound **2** revealed it to be identical to the previously published structure [37]. The geometries of five-coordinated metal compounds lie on a continuum between a square pyramid and a trigonal bipyramid.

Addison and co-workers clearly defined and quantified this continuum using the geometric parameter τ, according to the equation $\tau = (\beta - \alpha)/60$, where $\beta > \alpha$ are the two most prominent coordinate angles [35]. Since such structural parameters were also calculated for four-coordinate compounds, the symbol τ was modified to τ_5 [48]. For perfect square pyramidal, τ_5 is 0, while it becomes 1.0 for ideal trigonal bipyramidal geometry; however, Allan and co-workers have also presented τ_5 values greater than 1.0 [49,50]. The calculated τ_5 values for compounds **1** compared with **2** suggest a significant structural change induced upon the coordination center by methylation of amine nitrogen atoms.

In compound **1** (Fig. 1) the equatorial positions of square pyramidal geometry are occupied by N1, N3, N4, and N5, while N2 occupies the axial position. The τ_5 value calculated from the bond angles N5-Cu1-N3 (169.90°) and N1-Cu1-N4 (162.05°) was found to be 0.13, which indicates a slight divergence from the ideal square pyramidal geometry. In compound **2**, N4 is the apical bond, and the atoms N1, N2, N3, and N5 form the base of the square pyramid. The basal Cu-N bond lengths lie in the range (2.017–2.032 Å), whereas the apical Cu-N4 bond is slightly longer, 2.225 Å, as is typical for SP Cu(II) geometries (Fig. 2 & Table 1). Based on the calculation, the two relevant angles β and α. are N2-Cu1-N5 (175.72°) and N1-Cu1-N3 (153.78°), respectively, which gave $\tau_5 = 0.36$. Thus, we can say that **2** has a greater extent of distortion compared to **1**.

The oxygen atoms: O1, O2, O3, O4, O5, and O7 of the tetrahedral $(ClO_4)^-$ units are involved in C—H···O interactions resulting in an extended network in compound **1** (Fig. 3 & SI, Table S2). Similarly, the two unique perchlorate ions in compound **2** display an extensive network of hydrogen bonding. The predominant intermolecular H-bonding interactions arising from N3-H6···O4 and N4-H5···O8, accompanied by several C-H···O interactions, renders additional stability to compound **2** (SI, Table S2). The crystal packing of compounds **1** and **2** along the a-axis illustrates the arrangement of the cations and anions into alternating layers (SI Figs. S7, S8).

3.5. X-ray powder diffraction, thermogravimetric, EPR, and magnetic studies of 1 and 2

We recorded their powder X-ray diffraction patterns to confirm the phase purity of the crystalline compounds 1 and 2 with that of the bulk material. The experimental powder pattern of **1** was compared with the simulated PXRD pattern obtained from single crystal structure data of **1** using Mercury 4.0 software [51]. The experimental and simulated powder patterns of **1** exactly matched, suggesting that the bulk and single crystal phase are identical (SI Fig. S9). The evidence for their purity was further provided by profile fitting of the powder patterns using the Le Bail method with the help of FullProf software. Similarly, the experimental and simulated PXRD patterns of **2** matched, thus confirming the phase purity of **2** in bulk and single crystals (SI Fig. S10). Pure samples **1** and **2** were used for their characterization and reactivity studies.

Thermogravimetric (TG) plots of compounds **1** and **2** obtained between 30 and 400 °C under a nitrogen atmosphere are displayed in SI Figs. S11, S12. The slight difference in the thermal stability of compounds **1** and **2** can be attributed to the nature of the ligands (L^1 and L^2) coordinated with the copper (II) ion. The decrease in weight observed above 200 °C indicates the absence of lattice water or solvent in its formula unit and the decomposition of the ligand.

The EPR spectra for Compounds **1** and **2** were recorded as frozen acetonitrile solutions at 77 K. Both **1** and **2** showed a broad pseudo isotropic band at 312 mT (SI Fig. S13), with g_{iso}values of 2.07 and 2.06, respectively, and no observable hyperfine structure. Similar observations were reported for the known square-pyramid compounds [37, 52–54].

The magnetic properties of compound **1** and **2** were studied by temperature-dependent magnetic susceptibility (χM) measurements on the finely powdered samples under an applied magnetic field of 100 Oe in the temperature range of 5 −300 K. The resulting magnetization (emu/g) vs. temperature plots for compounds **1** and **2** revealed simple paramagnetic behavior (SI Fig. S14, S15).

3.6. Catalytic activity

As compounds **1** and **2** were phase pure, thermal stable, and structurally different in terms of τ_5 values, we considered investigating their enzyme-mimicking properties using 2-aminophenol (OAP) and 3,5-di-*tert*-butylcatechol (3,5-DTBC) for phenoxazinone synthase and

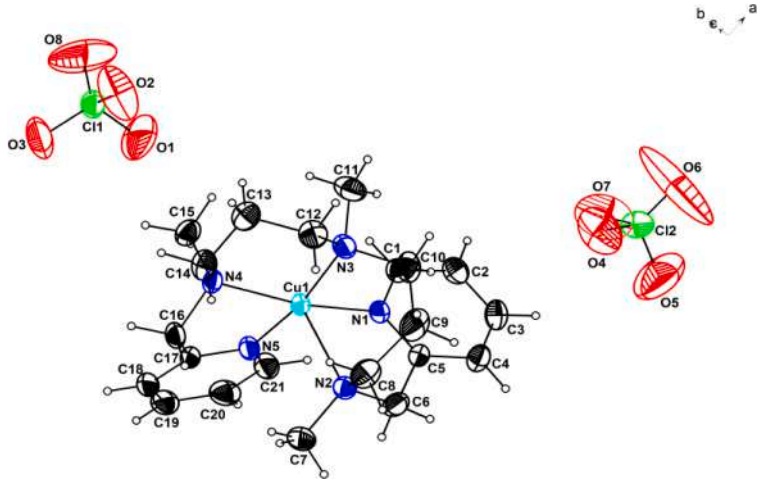

Fig. 1. Crystal structure of **1** showing atom labeling scheme. The thermal ellipsoids are drawn at 30% probability level for all the atoms except for the H atoms, which are shown as spheres of arbitrary radii.

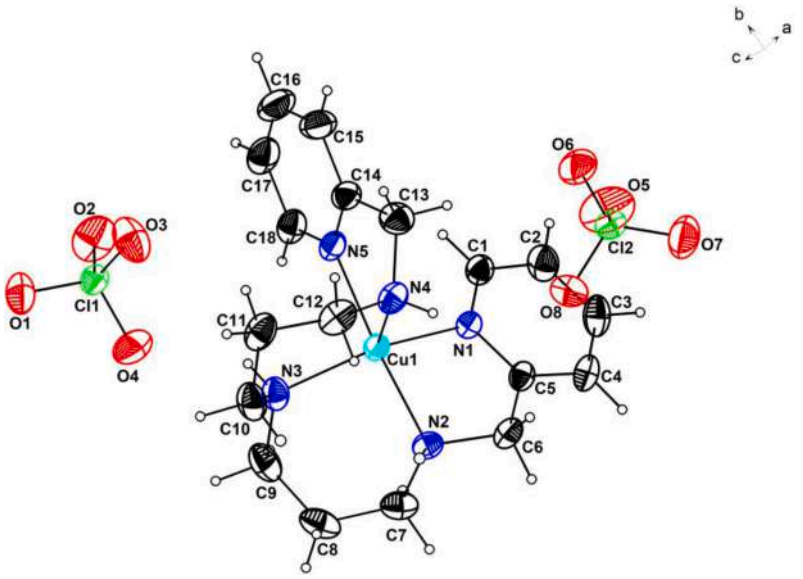

Fig. 2. Crystal structure of **2** showing atom labeling scheme. The thermal ellipsoids are drawn at a 30% probability level for all the atoms except for the H atoms, which are shown as spheres of arbitrary radii.

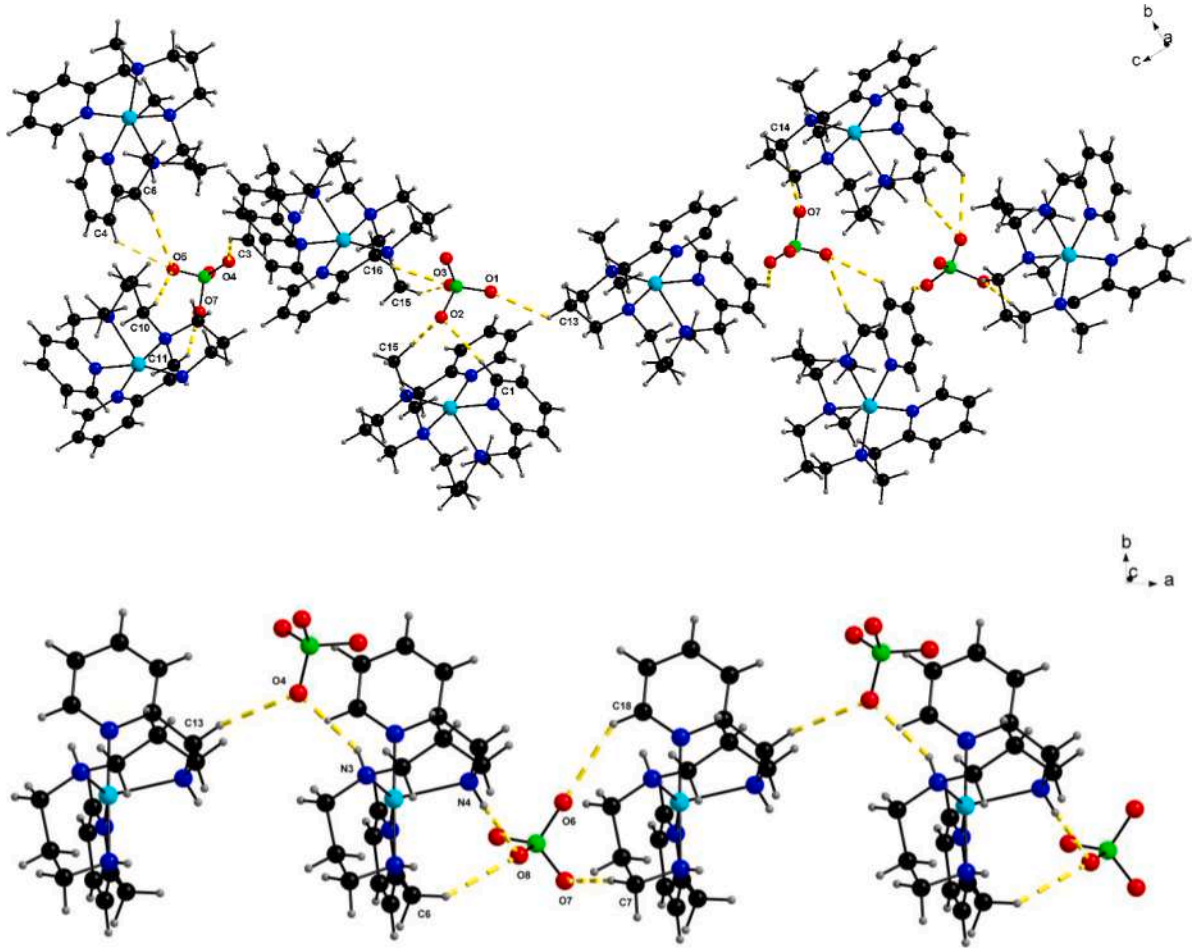

Fig. 3. Hydrogen bonding interactions in **1** (top) and **2** (bottom) with atom labeling scheme of atoms involved in hydrogen bonding.

catecholase activity. The dioxygen-saturated methanolic solutions (1×10^{-4}) of **1** and **2** were treated with OAP (1×10^{-3}) at 25 °C. The time-dependent spectrophotometrically studies exhibited a gradual growth of the signature peak at 432 nm, indicating the formation of phenoxazinone chromophore [36]. The colorless solution of OAP changing to intense brown reveal its catalytic oxidation to the corresponding 2-aminophenoxazine-3-one (APX). The oxidation product was quantified by gas chromatography, and the yields were 73% (±5) and 30

(±3)% for compounds **1** and **2,** respectively (Table 2). The appearance of a base peak at *m/z* 213.0 in ESI-MS spectrometry and the ^{1}H NMR ($CDCl_3$, ppm): δ 7.77 (d, 1H), δ 7.46–7.35 (m, 3H), δ 6.48 (s, 1H), δ 6.42 (s, 1H), δ 5.13 (br,s, 2H), (SI, Fig. S17) analysis of the product helped in confirming the formation of APX product. The comparative experiments without a catalyst do not show significant peak intensity growth at 432 nm under identical conditions. Similarly, under similar catalytic reaction conditions, the oxidation of OAP with copper perchlorate salt was very slow, and only 10% APX product formed. The reaction mixtures of **1** and **2** with OAP were subjected to EPR and ESI-MS studies to check the stability **1** and **2** after the end of catalytic reaction. EPR spectra after the reaction mixtures were found to be the same as that of the parent compounds **1** and **2** (SI, Fig. S18). ESI-MS of reaction mixtures of **1** and **2** exhibited *m/z* peaks identical to those observed in the parent compounds (SI, Fig. S6). Both these results suggest that the catalysts **1** and **2** are stable in the solution after the end of reactions.

The kinetic experiments have been performed to understand the catalytic efficacy of copper (II) compounds **1** (Fig. 4) and **2** (Fig. 5) in the oxidation of OAP. For this study, a fixed concentration of 1×10^{-4} M solutions of **1** and **2** was reacted with varying substrate concentrations in methanol to maintain the pseudo-first-order kinetics. All the kinetic studies were carried out at 25 °C. The experiments were monitored at a wavelength of 432 nm for a time span of 10 min. The non-linear plot of the initial rate of a reaction (v_o) versus substrate concentration indicates rate saturation kinetics for both compounds **1** (Fig. 6) and **2** (Fig. 7).

The Michealis-Menten approach was used to analyze the data and obtain the kinetic parameters like maximum rate of reaction (V_{max}), Michealis binding constant (K_m), and turnover number (K_{cat}), which are listed in Table 3.

Comparing compound **1** with **2**, we observed a higher catalytic efficiency K_{cat} (4.34×10^5 h^{-1}) for **1** than **2** K_{cat} (3.67×10^4 h^{-1}) in methanol.

For catecholase activity studies, we have examined the efficiency of **1** and **2** in the oxidation of 3,5-di-*tert*-butylcatechol (3,5-DTBC). 3,5-DTBC is known to form a very stable oxidized product 3,5-di-*tert*-butyl-*o*-quinone (3,5-DTBQ) due to low quinone-catechol reduction potential [55]. The time-dependent spectral changes for a period of 2 h after the addition of catalyst (1×10^{-4} M concentration) and 100 equivalents of 3,5-DTBC in methanol were monitored by UV–Visible spectroscopy. The growth of the characteristic peak of 3,5- DTBQ at 398 nm in methanol was observed (Fig. 8 & SI Fig. S16), which is due to the oxidation of 3,5-DTBC in presence of the catalyst (**1** and **2**) [56]. The color of the solution gradually turned deep brown that indicated the formation of 3,5-DTBQ. However, the oxidative conversion of 3,5-DTBC substrate alone in methanol was found to be negligible. The first-order catalytic reaction was observed with an initial rate of 2.7×10^{-3} s^{-1} for compound **1** and 3.4×10^{-5} s^{-1} for compound **2.**

The 3,5-DTBQ was purified by column chromatography, and the product was isolated as a solid. The melting point (110 °C) of the isolated *o*-quinone product was the same as that reported literature [56]. The ^{1}H NMR spectrum in $CDCl_3$ of the isolated *o*-quinone product same as reported [56]. The yields for **1** and **2** were 85 (±5) and 35 (±2)%, respectively.

Thus, the product yields and reactivity studies of **1** and **2** with OAP and 3,5-DTBC was clearly visible based on the topology of ligands L1 and L2 in **1** and **2,** respectively. In L1 all three N's are methylated, making it sterically hindered and more reactive; on the other hand, L2 has all three secondary N's making it topologically a different environment around the Cu(II) ion. Ligand topology in various metal compounds has always been a factor in olefin oxidation, C-H activation, and other oxygenation reactions [57–59].

Table 2
% yield of 2-aminophenoxazine-3-one (APX) in phenoxazinone synthase-like activity.

Compound	% Yield (APX)
No catalyst	—
$Cu(ClO_4)_2{\cdot}6H_2O$	10
Compound 1	73
Compound 2	30

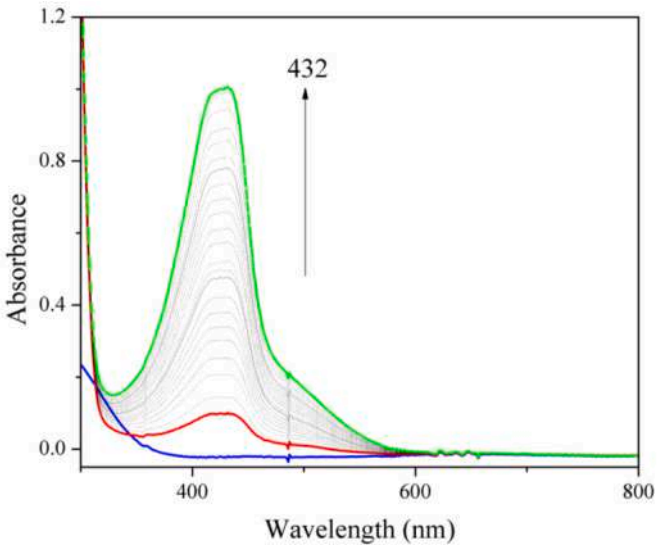

Fig. 4. The UV–Vis spectral profile exhibiting the growth of phenoxazine band (432 nm) over time upon addition of 10^{-3}M 2-aminophenol to 10^{-4} M methanolic solution of compound **1** at 25 °C.

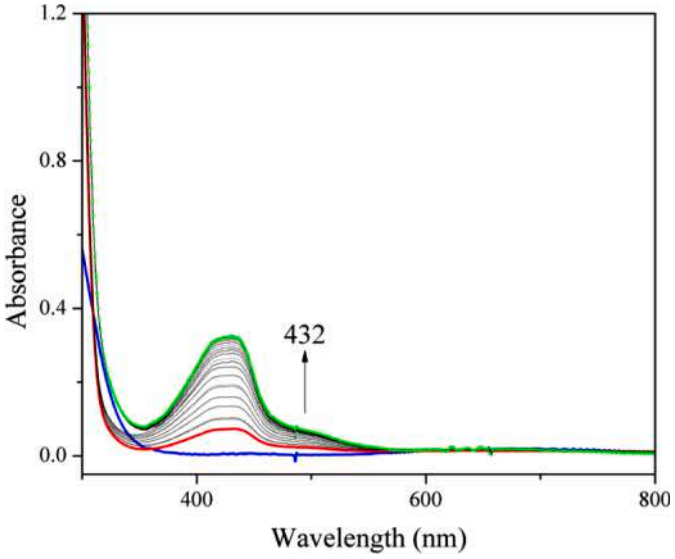

Fig. 5. The UV–Vis spectral profile exhibiting the growth of phenoxazine band (432 nm) over time upon addition of 10^{-3} M 2-aminophenol to 10^{-4} M methanolic solution of compound **2** at 25 °C.

4. Conclusion

The synthesis and characterization of a new copper(II) compound namely, $[Cu(L^1)](ClO_4)_2$ **1** stabilized by first time synthesized nonheme ligand N^1,N^3-dimethyl-N^1-(3-(methyl(pyridin-2-ylmethyl)amino)propyl)-N^3-(pyridin-2-ylmethyl)propane-1,3-diamine) has been reported in this work. Compound **2** is also reinvestigated to compare the structural properties and reactivities with compound **1**. Both compounds crystallize in a centrosymmetric space group $P2_1/n$ and adopt a distorted square-pyramidal geometry with different distortion parameter values,

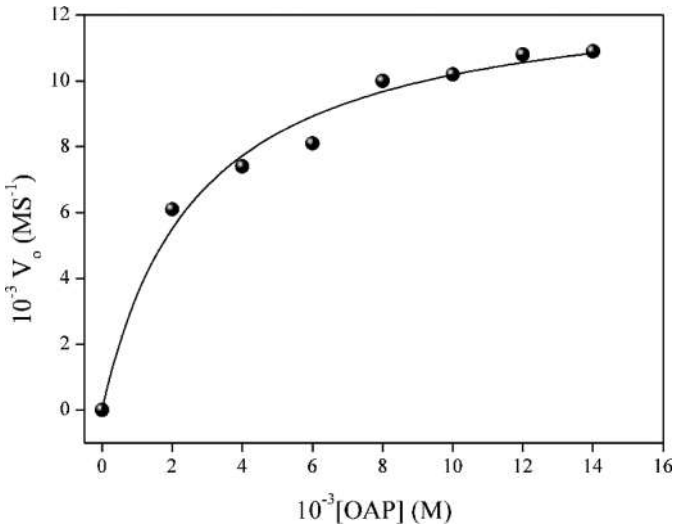

Fig. 6. Plot of rate vs [OAP] in the presence of **1** in methanol.

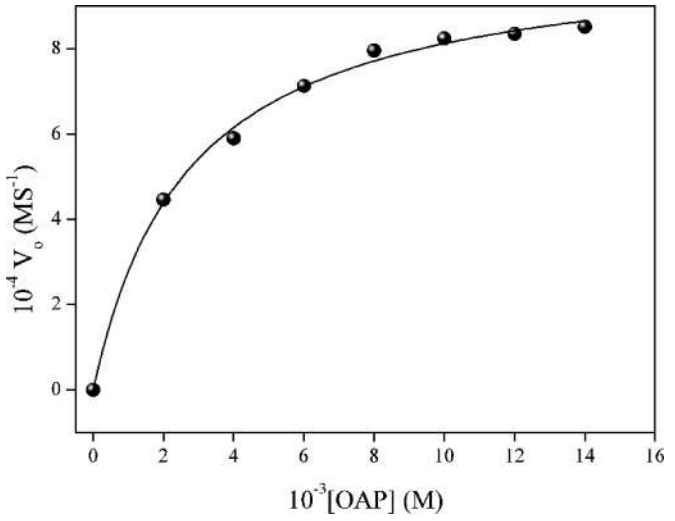

Fig. 7. Plot of rate vs. [OAP] in the presence of **2** in methanol.

Table 3
Kinetic parameters comparison for phenoxazinone synthase-like activity of compounds **1** and **2**.

Compound	V_{max} (Ms^{-1})	K_m (M)	K_{cat} (h^{-1})
1	10.21×10^{-4}	2.62×10^{-4}	3.67×10^{4}
2	12.06×10^{-3}	2.05×10^{-3}	4.34×10^{5}

τ_5= 0.13 and 0.36 respectively for **1** and **2**. Thus geometry of **1** is closer to a square-pyramid. The phenoxazinone synthase and catecholase-like mimicking reactivities of **1** and **2** were studied by using OAP and 3,5-DTBC. The ligand topology of L^1 and L^2 has shown influence in the reactivity of **1** and **2**.

Supplementary Material

The supplementary material file contains additional figures (Fig. S1–S12) and table (Table S1). The crystal cif structure data and checkcif of compounds 1 and 2 are also given in supplementary material. CCDC No. 2244555 (1) and 2244556 (2), contains the supplementary crystallographic data for this paper. These data can be obtained free of charge via http://www.ccdc.cam.ac.uk/-conts/retrieving.html (or from the Cambridge Crystallographic Data centre, 12, Union Road, Cambridge CB2 1EZ, UK; fax: +44 1223 336033).

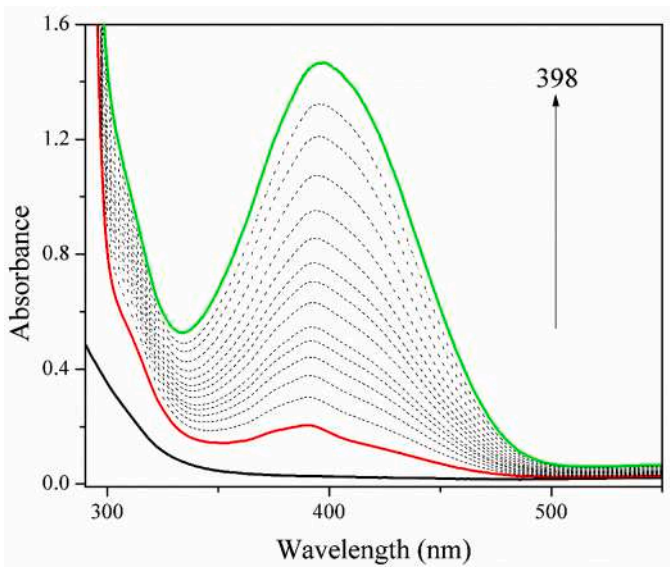

Fig. 8. The UV–Vis spectral profile showing an increase of 3,5-DTBQ band at 398 nm on addition of 100 equivalents of 3,5-DTBC to the solution of **1** in MeOH.

Credit author statement

Jeffrey L Viegas – conceptualization, data curation, formal analysis, investigation, writing and editing.

Sunder N. Dhuri– conceptualization, funding acquisition, project administration, resources, supervision, writing – review & editing of the manuscript, submission

Declaration of Competing Interest

The authors declare that they have no known competing financial interests or personal relationships that could have appeared to influence the work reported in this paper.

Data availability

Data will be made available on request.

Acknowledgment

SND acknowledge the Council of Scientific and Industrial Research, New Delhi (No. 01(2923)/18/EMR-II) for financial support. JLV thank Govt. of Goa for Study Leave. Authors greatly acknowledge support of DST-FIST (SR/FST/CSII-034/2014(C) and UGC-SAP (F.504/14/DSA-I/2015) to the School of Chemical Sciences, Goa University.

Supplementary materials

Supplementary material associated with this article can be found, in the online version, at doi:10.1016/j.molstruc.2023.135719.

References

[1] Y. Lu, N. Yeung, N. Sieracki, N.M. Marshall, design of functional metalloproteins, Nature 460 (2009) 855–862, https://doi.org/10.1038/nature08304.
[2] M. Rolff, J. Schottenheim, H. Decker, F. Tuczek, Copper-O2reactivity of tyrosinase models towards external monophenolic substrates: molecular mechanism and comparison with the enzyme, Chem. Soc. Rev. 40 (2011) 4077–4098, https://doi.org/10.1039/c0cs00202j.
[3] M. Zhao, H.B. Wang, L.N. Ji, Z.W. Mao, Insights into metalloenzyme microenvironments: biomimetic metal complexes with a functional second

coordination sphere, Chem. Soc. Rev. 42 (2013) 8360–8375, https://doi.org/10.1039/c3cs60162e.
[4] W. Nam, Synthetic Mononuclear Nonheme Iron-Oxygen Intermediates, Acc. Chem. Res. 48 (2015) 2415–2423, https://doi.org/10.1021/acs.accounts.5b00218.
[5] Y.W. Lin, Understanding the choice of copper by heme-copper oxidase using biosynthetic models in myoglobin, Inorg. Chem. Front. 4 (2017) 918–920, https://doi.org/10.1039/c6qi00603e.
[6] S. Fukuzumi, K. Bin Cho, Y.M. Lee, S. Hong, W. Nam, Mechanistic dichotomies in redox reactions of mononuclear metal-oxygen intermediates, Chem. Soc. Rev. 49 (2020) 8988–9027, https://doi.org/10.1039/d0cs01251c.
[7] X.X. Li, S.S. Xue, X. Lu, M.S. Seo, Y.M. Lee, W.S. Kim, K. Bin Cho, W. Nam, Ligand architecture perturbation influences the reactivity of nonheme Iron(V)-oxo tetraamido macrocyclic ligand complexes: a combined experimental and theoretical study, Inorg. Chem. 60 (2021) 4058–4067, https://doi.org/10.1021/acs.inorgchem.1c00110.
[8] X.P. Zhang, A. Chandra, Y.M. Lee, R. Cao, K. Ray, W. Nam, Transition metal-mediated O-O bond formation and activation in chemistry and biology, Chem. Soc. Rev. 50 (2021) 4804–4811, https://doi.org/10.1039/d0cs01456g.
[9] S.E. Allen, R.R. Walvoord, R. Padilla-salinas, M.C. Kozlowski, Aerobic copper-catalyzed organic reactions, Chem. Rev. 113 (2013) 6234–6458.
[10] C.E. Elwell, N.L. Gagnon, B.D. Neisen, D. Dhar, A.D. Spaeth, G.M. Yee, W. B. Tolman, Copper-oxygen complexes revisited: structures, spectroscopy, and reactivity, Chem. Rev 117 (2017) 2059–2107, https://doi.org/10.1021/acs.chemrev.6b00636.
[11] D.S. Nesterov, O.V. Nesterova, A.J.L. Pombeiro, Homo- and heterometallic polynuclear transition metal catalysts for alkane C–H bonds oxidative functionalization: recent advances, Coord. Chem. Rev. 355 (2018) 199–222, https://doi.org/10.1016/j.ccr.2017.08.009.
[12] P. Gandeepan, T. Müller, D. Zell, G. Cera, S. Warratz, L. Ackermann 3d, Transition metals for C-H activation, Chem. Rev. 119 (2019) 2192–2452, https://doi.org/10.1021/acs.chemrev.8b00507.
[13] R. Trammell, K. Rajabimoghadam, I. Garcia-Bosch, Copper-promoted functionalization of organic molecules: from biologically relevant Cu/O 2 model systems to organometallic transformations, Chem. Rev. 119 (2019) 2954–3031, https://doi.org/10.1021/acs.chemrev.8b00368.
[14] S.K. Dey, A. Mukherjee, Catechol oxidase and phenoxazinone synthase: biomimetic functional models and mechanistic studies, Coord. Chem. Rev. 310 (2016) 80–115, https://doi.org/10.1016/j.ccr.2015.11.002.
[15] V.C.C. Wang, S. Maji, P.P.Y. Chen, H.K. Lee, S.S.F. Yu, S.I. Chan, Alkane oxidation: methane monooxygenases, related enzymes, and their biomimetics, Chem. Rev. 117 (2017) 8574–8621, https://doi.org/10.1021/acs.chemrev.6b00624.
[16] I.A. Koval, P. Gamez, C. Belle, K. Selmeczi, J. Reedijk, Synthetic models of the active site of catechol oxidase: mechanistic studies, Chem. Soc. Rev. 35 (2006) 814–840, https://doi.org/10.1039/b516250p.
[17] I. Bento, M.A. Carrondo, P.F. Lindley, Reduction of dioxygen by enzymes containing copper, J. Biol. Inorg. Chem. 11 (2006) 539–547, https://doi.org/10.1007/s00775-006-0114-9.
[18] M. Le Roes-Hill, C. Goodwin, S. Burton, Phenoxazinone synthase: what's in a name? Trends Biotechnol. 27 (2009) 248–258, https://doi.org/10.1016/j.tibtech.2009.01.001.
[19] U. Hollstein Actinomycin, Chemistry and mechanism of action, Chem. Rev. 74 (1974) 625–652, https://doi.org/10.1021/cr60292a002.
[20] A.W. Smith, A. Camara-Artigas, M. Wang, J.P. Allen, W.A. Francisco, Structure of phenoxazinone synthase from Streptomyces antibioticus reveals a new type 2 copper center, Biochemistry 45 (2006) 4378–4387, https://doi.org/10.1021/bi0525526.
[21] E. Monzani, L. Quinti, A. Perotti, L. Casella, M. Gullotti, L. Randaccio, S. Geremia, G. Nardin, P. Faleschini, G. Tabbì, Tyrosinase models. Synthesis, structure, catechol oxidase activity, and phenol monooxygenase activity of a dinuclear copper complex derived from a triamino pentabenzimidazole ligand, Inorg. Chem. 37 (1998) 553–562, https://doi.org/10.1021/ic970996n.
[22] T. Horváth, J. Kaizer, G. Speier, Functional phenoxazinone synthase models: kinetic studies on the copper-catalyzed oxygenation of 2-aminophenol, J. Mol. Catal. A Chem. 215 (2004) 9–15, https://doi.org/10.1016/j.molcata.2004.01.006.
[23] A. Panja, P. Guionneau, The first example of a centro-symmetrical bis(imido)-bridged dinuclear cobalt(iii) complex: synthesis via oxidative dehydrogenation and phenoxazinone synthase activity, Dalton Trans. 42 (2013) 5068–5075, https://doi.org/10.1039/c3dt32788d.
[24] A. Panja, Exclusive selectivity of multidentate ligands independent on the oxidation state of cobalt: influence of steric hindrance on dioxygen binding and phenoxazinone synthase activity, J. Chem. Soc. Dalton Trans. 43 (2014) 7760–7770, https://doi.org/10.1039/c3dt53546k.
[25] A. Panja, Syntheses and structural characterizations of cobalt(II) complexes with N4-donor Schiff base ligands: influence of methyl substitution on structural parameters and on phenoxazinone synthase activity, Polyhedron 80 (2014) 81–89, https://doi.org/10.1016/j.poly.2014.02.004.
[26] A. Panja, Metal ionic size directed complexation in manganese(II) coordination chemistry: efficient candidates showing phenoxazinone synthase mimicking activity, RSC Adv. 4 (2014) 37085–37094, https://doi.org/10.1039/c4ra03427a.
[27] M. Garai, D. Dey, H.R. Yadav, A.R. Choudhury, M. Maji, B. Biswas, Catalytic fate of two copper complexes towards phenoxazinone synthase and catechol dioxygenase activity, ChemistrySelect 2 (2017) 11040–11047, https://doi.org/10.1002/slct.201702113.
[28] S.Y. Shaban, A.E.M.M. Ramadan, M.M. Ibrahim, F.I. Elshami, R. van Eldik, Square planar versus square pyramidal copper(II) complexes containing N3O moiety: synthesis, structural characterization, kinetic and catalytic mimicking activity, Inorg. Chim. Acta 486 (2019) 608–616, https://doi.org/10.1016/j.ica.2018.11.024.
[29] O.V. Nesterova, O.E. Bondarenko, A.J.L. Pombeiro, D.S. Nesterov, Phenoxazinone synthase-like catalytic activity of novel mono- And tetranuclear copper(ii) complexes with 2-benzylaminoethanol, Dalton Trans. 49 (2020) 4710–4724, https://doi.org/10.1039/d0dt00222d.
[30] T. Dutta, S. Mirdya, P. Giri, S. Chattopadhyay, Synthesis and characterization of a double oximato bridged dimeric copper(II) complex and its use in oxidative dimerisation of o-aminophenol, Polyhedron 175 (2020), 114164, https://doi.org/10.1016/j.poly.2019.114164.
[31] P. Kumar Mudi, N. Bandopadhyay, M. Joshi, M. Shit, S. Paul, A.Roy Choudhury, B. Biswas, Schiff base triggering synthesis of copper(II) complex and its catalytic fate towards mimics of phenoxazinone synthase activity, Inorg. Chim. Acta 505 (2020), 119468, https://doi.org/10.1016/j.ica.2020.119468.
[32] M. Ismael, A.M.M. Abdel-Mawgoud, M.K. Rabia, A. Abdou, Synthesis, characterization, molecular modeling and preliminary biochemical evaluation of new copper (II) mixed-ligand complexes, J. Mol. Struct. 1227 (2021), 129695, https://doi.org/10.1016/j.molstruc.2020.129695.
[33] W.P. Sohtun, S. Muthuramalingam, M. Sankaralingam, M. Velusamy, R. Mayilmurugan, Copper(II) complexes of tripodal ligand scaffold (N3O) as functional models for phenoxazinone synthase, J. Inorg. Biochem. 216 (2021), 111313, https://doi.org/10.1016/j.jinorgbio.2020.111313.
[34] P.W. Atki, T.L. Overton, J.P. Rourke, M.T. Weller, F.A. Armstrong, Shriver and Atkins' Inorganic Chemistry, Oxford University Press, 2009 fifth ed.
[35] A.W. Addison, T.N. Rao, J. Reedijk, J. van Rijn, G.C. Verschoor, Synthesis, structure, and spectroscopic properties of Copper(II) compounds containing nitrogen-sulphur donor ligands ; the crystal and molecular structure of Aqua[l,7-bis (N-methylbenzimidazol-2'-yl)- 2,6-dithiaheptane]copper(II) Perchlorate, J. Chem. Soc., Dalton Trans. (1984) 1349–1356, https://doi.org/10.1016/S0277-5387(98)00128-4.
[36] S.S. Harmalkar, V.R. Chari, R.K. Kunkalekar, S.N. Dhuri, Structure–function correlation of mononuclear nonheme copper(II) compounds based on a ligand backbone effect and phenoxazinone synthase activity, New J. Chem. 47 (2023) 1852–1860.
[37] R.A.J. Hartman, A.L. Kammier, R.J. Spracklin, W.H. Pearson, M.Y. Combariza, R. W. Vachet, A comparison of the gas, solution, and solid state coordination environments for the Cu (II) complexes of a series of linear aminopyridine ligands with varying ratios of 5- and 6-membered chelate rings, Inorg. Chim. Acta 357 (2004) 1141–1151, https://doi.org/10.1016/j.ica.2003.09.030.
[38] G.M. Sheldrick, Crystal structure refinement with SHELXL, Acta Crystallogr. Sect. C Struct. Chem 71 (2015) 3–8, https://doi.org/10.1107/S2053229614024218.
[39] W.R. Harris, I. Murase, J.H. Timmons, A.E. Martell, Chelating tendencies of pyridyl-containing polyamines and oxygenation of the, Inorg. Chem. 17 (1978) 889–894, https://doi.org/10.1021/ic50182a019.
[40] D.D. Narulkar, A.K. Srivastava, R.J. Butcher, K.M. Ansy, S.N. Dhuri, Synthesis and characterization of N3Py2 ligand-based cobalt(II), nickel(II) and copper(II) catalysts for efficient conversion of hydrocarbons to alcohols, Inorg. Chim. Acta 467 (2017) 405–414, https://doi.org/10.1016/j.ica.2017.08.027.
[41] A.G. Blackman, The coordination chemistry of acyclic pentadentate pentaamine ligands, Polyhedron 161 (2019) 1–33, https://doi.org/10.1016/j.poly.2018.12.004.
[42] K. Nakamoto, Infrared and Raman Spectra of Inorganic and Coordination Compounds, Part B: Applications in Coordination, Organometallic, and Bioinorganic Chemistry, John Wiley, 2009 sixth ed.
[43] D.D. Narulkar, A.R. Patil, C.C. Naik, S.N. Dhuri, Synthesis, characterization, cis-ligand substitution and catalytic alkane hydroxylation by mononuclear nickel(II) complexes stabilized with tetradentate tripodal ligands, Inorg. Chim. Acta 427 (2015) 248–258, https://doi.org/10.1016/j.ica.2015.01.009.
[44] S.S. Harmalkar, R.J. Butcher, V.V. Gobre, S.K. Gaonkar, L.R. D'Souza, M. Sankaralingam, I. Furtado, S.N. Dhuri, Synthesis, characterization and antimicrobial properties of mononuclear copper(II) compounds of N,N′-di (quinolin-8-yl)cyclohexane-1,2-diamine, Inorg. Chim. Acta 498 (2019), 119020, https://doi.org/10.1016/j.ica.2019.119020.
[45] N. Wei, N.N. Murthy, K.D. Karlin, Chemistry of pentacoordinate [LCuII-Cl]+ complexes with quinolyl containing tripodal tetradentate ligands L, Inorg. Chem. 33 (1994) 6093–6100, https://doi.org/10.1021/ic00104a018.
[46] F.A. Chavez, M.M. Olmstead, P.K. Mascharak, Synthesis, structure, and properties of {N,N'-Bis[2-(2-pyridyl)ethyl]pyridine-2,6-dicarboxamido}copper(II), Inorg. Chem. 35 (1996) 1410–1412, https://doi.org/10.1021/ic9512136.
[47] E.V. Rybak-Akimova, A.Y. Nazarenko, L. Chen, P.W. Krieger, A.M. Herrera, V. V. Tarasov, P.D. Robinson, Synthesis, characterization, redox properties, and representative X-ray structures of four- and five-coordinate copper(II) complexes with polydentate aminopyridine ligands, Inorg. Chim. Acta 324 (2001) 1–15, https://doi.org/10.1016/S0020-1693(01)00495-9.
[48] L. Yang, D.R. Powell, R.P. Houser, Structural variation in copper(i) complexes with pyridylmethylamide ligands: structural analysis with a new four-coordinate geometry index, 4, J. Chem. Soc. Dalton Trans. (2007) 955–964, https://doi.org/10.1039/b617136b.
[49] A.G. Blackman, E.B. Schenk, R.E. Jelley, E.H. Krenske, L.R. Gahan, Five-coordinate transition metal complexes and the value of: τ 5: observations and caveats, Dalton Trans. 49 (2020) 14798–14806, https://doi.org/10.1039/d0dt02985h.
[50] S. Alvarez, M. Llunell, Continuous symmetry measures of penta-coordinate molecules: berry and non-Berry distortions of the trigonal bipyramid, J. Chem. Soc. Dalton Trans. (2000) 3288–3303, https://doi.org/10.1039/b004878j.
[51] C.F. MacRae, I. Sovago, S.J. Cottrell, P.T.A. Galek, P. McCabe, E. Pidcock, M. Platings, G.P. Shields, J.S. Stevens, M. Towler, P.A. Wood, Mercury 4.0: from

visualization to analysis, design and prediction, J. Appl. Crystallogr. 53 (2020) 226–235, https://doi.org/10.1107/S1600576719014092.
[52] L. Glaz, Diverse coordination of two ligands in ferromagnetic [Cu(μ-HCO2)2(3-pyOH)]n and [Cu2(μ-HCO2)2(μ-3-pyOH)2(3-pyOH)2(HCO2)2]n, Polyhedron 26 (2007) 11–16, https://doi.org/10.1016/j.poly.2006.07.025.
[53] M.C. Buta, G. Ionita, M.M. Radu, A. Mischie, C.M. Zalaru, M. Ferbinteanu, Experimental and computational characterization of structural and spectroscopic features of mixed ligand copper complexes-prototypes for square-pyramidal stereochemistry, Polyhedron 170 (2019) 771–782, https://doi.org/10.1016/j.poly.2019.06.046.
[54] M. Kaushal, T.S. Lobana, L. Nim, R. Bala, D.S. Arora, I. Garcia-santos, C.E. Duff, J. P. Jasinski, Synthesis of 2-acetylpyridine-N-substituted thiosemicarbazonates of copper(II) with high antimicrobial activity against methicillin resistant S. aureus, K. pneumoniae 1 and C. albicans, New J. Chem. 43 (2019) 11727–11742, https://doi.org/10.1039/C9NJ01459D.
[55] S. Kumari, A.K. Mahato, A. Maurya, V.K. Singh, N. Kesharwani, P. Kachhap, I. O. Koshevoy, C. Haldar, Syntheses and characterization of monobasic tridentate Cu (II) Schiff-base complexes for efficient oxidation of 3,5-di-: tert -butylcatechol and oxidative bromination of organic substrates, New J. Chem. 41 (2017) 13625–13646, https://doi.org/10.1039/c7nj00957g.
[56] B. Selvakumaran, M. Murali, Functional mimic for amine and catechol oxidases: structural, spectral, electrochemical and catalytic properties of mononuclear copper(II) complex, Inorganica Chim. Acta 534 (2022), 120819, https://doi.org/10.1016/j.ica.2022.120819.
[57] R. Mas-Ballesté, M. Costas, T. van den Berg, L. Que Jr., Ligand topology effects on olefin oxidations by bio-inspired [FeII(N2Py2)] catalysts, Chem. Eur. J. 12 (2006) 7489–7500, https://doi.org/10.1002/chem.200600453.
[58] M. Ayad, R.J.M. Klein Gebbink, Y.Le Mest, P. Schollhammer, N.L. Poul, F. Y. Pétillon, D. Mandon, Mononuclear iron(ii) complexes containing a tripodal and macrocyclic nitrogen ligand: synthesis, reactivity and application in cyclohexane oxidation catalysis, Dalton Trans. 47 (2018) 15596–15612, https://doi.org/10.1039/C8DT02952K.
[59] S. Hong, Y.-.M. Lee, K.-.B. Cho, K. Sundaravel, J. Cho, M.J. Kim, W. Shin, W. Nam, Ligand topology effect on the reactivity of a mononuclear nonheme iron(IV)-Oxo complex in oxygenation reactions, J. Am. Chem. Soc. 133 (2011) 11876–11879, https://doi.org/10.1021/ja204008u.

ChemistrySelect

Research Article
doi.org/10.1002/slct.202402704

Chemistry Europe
European Chemical Societies Publishing

www.chemistryselect.org

Ligand Backbone Influenced Luminescent Properties of Mononuclear Zn(II)-N3Py2 Compounds: Synthesis, Structures and Nitroaromatics Detection

Jeffrey L. Viegas,[a, b] Vishnu R. Chari,[a] and Sunder N. Dhuri*[a]

Mononuclear Zn(II) compounds, $[Zn(L^1)](ClO_4)_2$ (**1**) and $[Zn(L^2)](ClO_4)_2$ (**2**), embedded with ligands, $L^1 = N^1$-(pyridin-2-ylmethyl)-N^2-(2-((pyridin-2-ylmethyl)amino)ethyl)ethane-1,2-diamine and $L^2 = N^1$-(pyridin-2-ylmethyl)-N^3-(3-((pyridin-2-ylmethyl)amino)propyl)propane-1,3-diamine are synthesized. Compound **1** is revisited, and structure-function relation is compared with new compound **2**. Single crystal X-ray analysis revealed that compound **1** crystallizes in the tetragonal non-centrosymmetric $P4_1$ space group while **2** crystallizes in a centrosymmetric monoclinic space group $P2_1/c$. The asymmetric unit consists of a crystallographically independent $[Zn(L^1)]^{2+}$ cation in **1** while $[Zn(L^2)]^{2+}$cation in **2** and two unique perchlorate anions in both. IR spectra of **1** and **2** confirmed the vibrations due to organic ligands and tetrahedral perchlorates. PXRD confirmed the phase purity of powdered samples compared with theoretical PXRD patterns obtained from single-crystal X-ray diffraction data. NMR and ESI-MS data suggested the phase purity and stability of compounds **1** and **2** in solution. Photoluminescence properties of compounds **1** and **2** have been investigated, considering their application in sensing explosive nitroaromatic compounds. Our results suggest that compound **1** is very selective in the chemical sensing of trinitrophenol (TNP) and dinitrophenol (DNP) in an aqueous medium compared to the reactivity of compound **2**. The existence of spectral overlap in the absorption spectra of 2,4-dinitrophenol (DNP) and 2,4,6-trinitrophenol (TNP) with the emission spectrum of **1** or **2** indicates the operation of the resonance electron transfer (RET) mechanism.

1. Introduction

Sustainable development has significantly stimulated chemists to design new tools for the selective detection of hazardous materials. The utilization of nitroaromatic compounds (NACs) as explosive substances has aroused widespread concern for human health, national security, and the environment in recent years.[1–3] There are several NACs such as nitrobenzene (NB), *p*-nitrotoluene (*p*-NT), *o*-nitrotoluene (*o*-NT), *p*-nitrophenol (*p*-NP), *o*-nitrophenol (*o*-NP), 2,4-dinitrophenol (DNP) and 2,4,6-trinitrophenol (TNP) which are widely used in the industry. TNP is known for its high explosivity rate, thus making it a superior choice for use in destruction over other NACs.[4,5] The larger use and higher solubility in water of TNP has led to severe, catastrophic contamination in water bodies. Therefore, the rapid detection of NACs in aqueous effluents has become a highlighted topic of research.[6–8] The portability and sensitivity of optical approaches involving fluorescent probes have garnered significant interest despite many other techniques being well-known in the literature.[9–13] The luminescent properties of the probes mainly depend on the structure, the electron-rich nature of the aromatic ligand, and the metal center.[14,15] The sensing ability by quenching the fluorescence is generally realized by transferring the photoexcited electrons from an electron-rich probe to the electron-deficient analytes.[16]

The compounds of non-transition metals, such as $Zn^{2+}$and Cd^{2+}, exhibit prominent luminescence over other transition metals, thus making them useful in OLED devices and various emitting appliances. Armaroli *et al.* has well-documented the luminescent properties of zinc, cadmium, and other metal compounds in their recent review.[17] A slight modification to ligand topology in Zn(II) compounds has led to improved stability, enhancement in emission intensity, and changes in emission energies. The mononuclear Zn(II) compounds of varying denticity N-donor ligands have been discovered to exhibit photoluminescent properties.[18,19] Several Zn(II) compounds with varying ligands have been reported as sensors in detecting hazardous NACs.[20–23] The topologically diverse aliphatic coordination polymers of zinc and cadmium encapsulated with dipyridylamine ligand have shown the "turn-off" luminescence ability in sensing NACs.[24] The ladder-type coordination polymer of cadmium exhibited luminescent properties, which were effectively used in nitroaromatic sensing at very low concentrations.[25] A 3D metal-organic framework of cadmium has been reported in the detection of potential NAC pollutants.[26] The zinc and cadmium compounds of salen-type ligands have been well studied due to their ability to detect nitroaromatics *via* turn-off fluorescence response.[27] The hydrothermally synthesized 2D, 3D topological cadmium cyclohexyldicarboxylate with co-ligand bis(4-pyridylmethyl)piperazine has been sensibly used in nitroaromatic quenching.[28] The

[a] J. L. Viegas, V. R. Chari, S. N. Dhuri
School of Chemical Sciences, Goa University, Taleigao Plateau, Goa 403 206, India
E-mail: sndhuri@unigoa.ac.in

[b] J. L. Viegas
Carmel College of Arts, Science and Commerce for Women, Nuvem, Goa 403 604, India

Supporting information for this article is available on the WWW under https://doi.org/10.1002/slct.202402704

topological changes in coordinating ligands were experienced, altering the properties of zinc and cadmium compounds. The versatility of multidentate ligands in cadmium carboxylate coordination polymers has influenced overall structure-function properties, resulting in the quenching of nitroaromatics.[29]

The aminopyridine-based multidentate ligands are proven more acceptable in modern coordination chemistry due to their reactivity and stability being controlled by a subtle interplay of electronic and structural properties.[30,31] In recent times, we have been continuously making efforts to tune the topology of multidentate N-donor ligands. This has resulted in a series of first-row transition metal compounds of amino pyridyl-based ligands that showed diverse applications ranging from catalysis to mimicking enzymes.[32–34] We have also demonstrated a significant quenching of NACs using quinoline-based ligands and N-donor ligand-linked cobalt(II) succinate compounds in our recent work.[35,36] In continuation to our efforts in showcasing the ligand topological effects in metal compounds on their various applications, herein, we have synthesized two Zn(II) compounds, $[Zn(L^1)](ClO_4)_2$ (**1**) and $[Zn(L^2)](ClO_4)_2$ (**2**), containing *N*^{1}-(pyridin-2-ylmethyl)-*N*^{2}-(2-((pyridin-2-ylmethyl)amino)ethyl)-ethane-1,2-diamine (L^1) and *N*^{1}-(pyridin-2-ylmethyl)-*N*^{3}-(3-((pyridin-2-ylmethyl)amino)propyl)propane-1,3-diamine (L^2) (Chart 1). The effect of extrapolating the carbon chain of ligand L^2 compared to L^1 on the photoluminescent properties of Zn(II) compounds has been described.

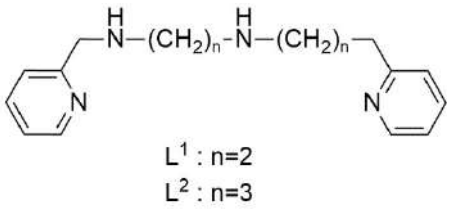

Chart 1: Chemical structures L^1 and L^2 used in this work.

Experimental Section

Material and Methods

Reagents for synthesis and reactivity investigations were bought from commercial sources and did not require further purification. The solvents being used were distilled and dried in a N_2 environment before use. Ligands L^1 and L^2 were prepared following our recent reports.[32,33] Infrared (IR) spectra were recorded on the Shimadzu (IR-Prestige-21) FTIR spectrometer by diluting the compounds in KBr powder in the 4000–400 cm^{-1} region. C, H and N content were obtained using Elementar Variomicro Cube CHNS Analyser. Single crystal X-ray structures of **1** and **2** were determined using Bruker D8 Quest Eco X-ray diffractometer. Intensity data were collected at room temperature (RT) using monochromated (MoKα = 0.7107 Å) radiation. The program suite APEX4 (Version 2021.10-0) was used to integrate the frames, perform absorption correction, and determine the unit cell. The structures were solved with SHELXS, and subsequent refinements were performed with SHELXL.[37] The phase purity of powdered samples was confirmed using powder X-ray diffraction (PXRD) measurements carried out on a Bruker D8 Advance X-ray diffractometer using Cu $k_{\alpha 1}$ (λ = 1.5406 Å) with a nickel filter. The solution state fluorescence spectra were recorded on the Cary Eclipse fluorescence spectrophotometer. ^{1}H NMR spectra were recorded on a Bruker Avance III, 400 MHz, NMR spectrometer using D_2O. The electrospray ionization mass spectra (ESI-MS) of **1** and **2** were recorded using Shimadzu LCMS-2020.

Syntheses of the Zn(II) Compounds

Synthesis of $[Zn(L1)](ClO_4)_2$ (1)

Compound **1** was prepared by slowly adding L^1 (0.38 g, 1.34 mmol) in acetonitrile (5 mL) to the stirring CH_3CN solution of $Zn(ClO_4)_2.6H_2O$ (0.5 g, 1.34 mmol) (2 mL) at room temperature. The mixture was stirred for ~ 5 h. The reaction mixture afforded a colorless crystalline solid upon adding diethyl ether (10 mL). The slow diffusion of diethyl ether into the CH_3CN solution of **1** resulted in white transparent crystals suitable for single crystal x-ray diffraction analysis. The yield of compound **1** was 0.60 g (1.09 mmol) 82 %. *Anal. Calc.* for (**1**) $C_{16}H_{23}Cl_2ZnN_5O_8$ (%): C, 34.96; H, 4.22; N, 12.74. *Found:* C, 34.35; H, 4.10; N, 12.43. IR (KBr, cm^{-1}): 3296 υ(NH); 2980–2883 υ(CH); 1078, 619 υ(ClO_4). ESI-MS: *m/z* = 448.15 (*Calc.* 488.07) for $[Zn(L^1)(ClO_4)]^+$.

Synthesis of [Zn(L2)](ClO4)2 (2)

As mentioned for **1**, a similar methodology was used by reacting L^2 (0.42 g, 1.34 mmol) instead of L^1 to afford colorless crystals of **2**. The yield of **2** was 0.69 g (1.19 mmol), 89 %. *Anal. Calc.* for (**1**) $C_{18}H_{27}Cl_2ZnN_5O_8$ (%): C, 37.42; H, 4.71; N, 12.12. *Found:* C, 37.54; H, 4.37; N, 12.25. IR (KBr, cm^{-1}): 3298 υ(NH); 2950–2872 υ(CH); 1064, 619 υ(ClO_4). ^{1}H NMR (D_2O, ppm): δ 8.47 (d, 2H), δ 7.95 (t, 2H), δ 7.44 (m, 4H), δ 4.27–3.84 (m, 4H), δ 3.19–2.42 (m, 8H), δ 1.81–1.71 (m, 4H). ESI-MS: *m/z* = 476.15 (*Calc.* 476.15) for $[Zn(L^2)(ClO_4)]^+$.

***Caution**! Although we have not experienced accidents, perchlorate salts are potentially explosive in dry states and should be handled in small quantities and with extreme care.*

Photophysical Studies

The photoluminescence properties of compounds **1** and **2** were investigated in the aqueous solution at room temperature. The excitation wavelength was fixed to 370 nm with slit widths (for both excitation and emission) of 10 nm. The experiments were recorded on a Xe flash lamp technology-based Cary Eclipse Fluorescence Spectrophotometer (G9800 A) from Agilent Technologies. In a typical experiment, a 2 mM / 2 mL aqueous solution of **1** or **2** was placed in a 1 cm quartz cuvette, and emission spectra were recorded. For fluorescence sensing titrations of **1** and **2** with the nitroaromatic compounds (NACs), the emission intensities were recorded after the incremental addition of 1 mM NAC solution.

2. Results and Discussion

2.1. Synthesis of Ligands and Compounds 1 and 2

Ligands L^1 and L^2 (Chart 1) were prepared from their diamine precursors, followed by the standard $NaBH_4$ reduction as per our recent reports.[32,33] The Zn(II) compounds, $[Zn(L^1)](ClO_4)_2$ (**1**) and $[Zn(L^2)](ClO_4)_2$ (**2**), were synthesized by reacting $Zn(ClO_4).6H_2O$ with a corresponding CH_3CN solution of the pentadentate ligand (L^1 and L^2) in a 1 : 1 mole ratio (Scheme 1).

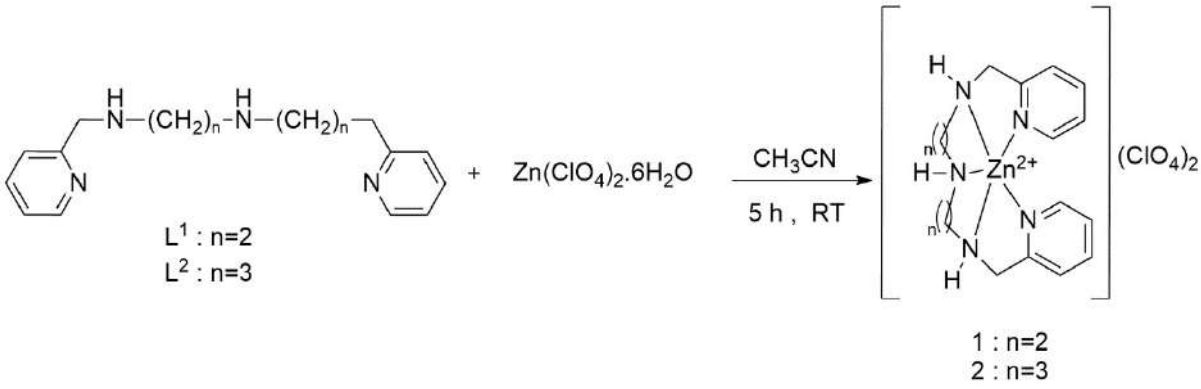

Scheme 1. Synthetic route for preparation of **1** and **2**.

Crystals of compounds **1** and **2**, suitable for single crystal X-ray diffraction analysis, were obtained by slow diffusion of diethylether into the acetonitrile solution in 5 hr. In contrast, in the reported method, **1** was obtained by slow evaporation of aqueous solution after many days.[38] We reinvestigated **1** to compare the influence of increased ligand backbone on the structural parameters with **2** and study its fluorescence properties. A single crystal X-ray diffraction technique was used to determine the spatial structures of **1** and **2**. The summary of crystallographic data and structural refinement results for **1** and **2** are given in Table 1, while the selected bond lengths and angles for both compounds are listed in Table 2. Elemental analysis of **1** and **2** was consistent with the structural composition obtained from single-crystal X-ray diffraction studies.

2.2. Crystal structures of 1 and 2

2.1.1. Crystal Structure of $[Zn(L^1)](ClO_4)_2$ (1)

Single-crystal X-ray diffraction analysis revealed that compound **1** crystallizes in the tetragonal non-centrosymmetric $P4_1$ space group. The asymmetric unit is built from one crystallographically independent $[Zn(L^1)]^{2+}$ cation and two perchlorate anions (Fig. 1, SI Fig. S1). A unique Zn(II) cation is coordinated by the two N atoms of the flexible pyridyl moiety and three N atoms of the symmetric secondary amine backbone, leading to a five-coordinated square pyramidal geometry. The atoms N1, N2, N3, and N5 formed the base of the square pyramid, while N4 occupies the apical position. The pyridyl nitrogen atoms are disposed *syn* to one another. A careful inspection of bond lengths reveals that Zn-N_{py} bond lengths lie in the range 2.125(3)-2.135(3) Å, which are slightly shorter than Zn-N_{amine} bond distances (2.146–2.148(3) Å) due to the hybridization of sp^2 pyridine and sp^3 amine nitrogens.[39] The distortion in coordination geometry around the Zn(II) center can be determined by calculating Addison parameter (τ_5) using the equation $\tau = (\beta - \alpha)/60$, where β and α are the two most prominent coordinate angles.[40–43] The calculated Addison parameter, $\tau_5 = 0.07$, suggested a slight distortion in the square

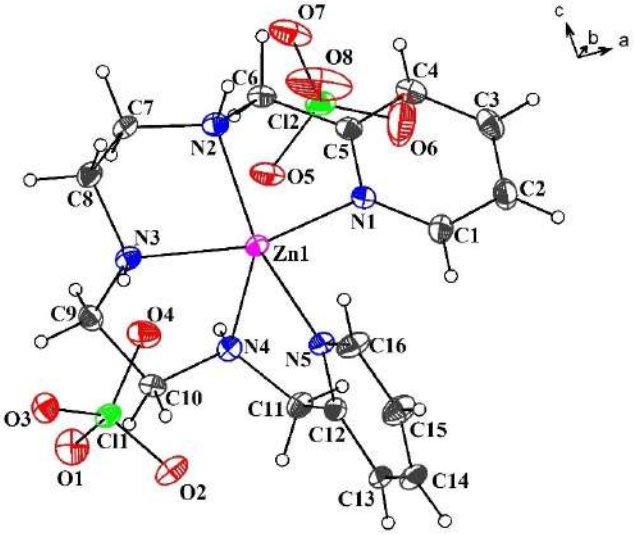

Figure 1. Crystal structure of **1** showing atom labeling scheme. The thermal ellipsoids are drawn at a 30% probability level for all the atoms except for the H atoms, which are shown as spheres of arbitrary radii.

pyramidal geometry of **1**. It is observed that the bond angles of N(1)-Zn(1)-N(3) (157.69°) and N(5)-Zn(1)-N(2) (162.09°) are less than expected 180° in square pyramidal geometry. The perchlorate anions play a significant role in building the supramolecular architecture through its oxygen atoms (O2, O3, O4, and O7), which are involved in non-covalent H-bond interactions (Fig. 2). The predominant intermolecular hydrogen bonds between N–H···O and C–H···O renders additional stability to the crystal structure of **1**. Selected non-covalent H-bonds are summarized in Table 3. The crystal packing of **1** viewed along the *'ab'* plane (SI Fig. S2) illustrates the intercalation of perchlorate counterions with the cation species $[Zn(L^1)]^{2+}$.

Table 1. Crystal data and structure refinement parameters for **1** and **2**.

Empirical formula	$C_{16}H_{23}Cl_2ZnN_5O_8$ (**1**)	$C_{18}H_{27}Cl_2ZnN_5O_8$ (**2**)
Formula weight (g mol^{-1})	549.68	577.74
Temperature (K)	150	150
Wavelength (Å)	0.71073	0.71073
Crystal system	Tetragonal	Monoclinic
Space group	$P4_1$	$P2_1/c$
a (Å)	8.8375(5)	13.6348(7)
b(Å)	8.8375(5)	8.4280(4)
c (Å)	28.034(2)	20.3603(10)
α (°)	90	90
β (°)	90	97.136(2)
γ (°)	90	90
Volume ($Å^3$)	2189.5(3)	2321.6(2)
Z	4	4
Calc. Density (mg/m^3)	1.668	1.653
Absorption coefficient (mm^{-1})	1.420	1.344
F(000)	1128	1192
Diffractometer	Bruker D8 Quest Eco	Bruker D8 Quest Eco
Theta range for data collection (°)	2.305 to 28.277	2.619 to 28.322°
Completeness to theta	100.0	99.8
Index ranges	$-11 \le h \le 11$	$-18 \le h \le 18$
	$-11 \le k \le 11$	$-11 \le k \le 11$
	$-37 \le l \le 37$	$-27 \le l \le 26$
Reflections collected	43081	168996
Independent reflections	5439 [R(int) - = 0.0432]	5767 [R(int) - = 0.0302]
Refinement method	Full-matrix least-squares on F^2	Full-matrix least-squares on F^2
Absorption correction	Semi-empirical from equivalents	Semi-empirical from equivalents
Data/restraints/parameters	5439/1/289	5767/0/288
Goodness-of-fit on F^2	1.052	1.066
Final *R*indices [I > 2sigma(I)]	R1 = 0.0289, wR2 = 0.0665	R1 = 0.0913, wR2 = 0.2346
R indices (all data)	R1 = 0.0367, wR2 = 0.0690	R1 = 0.0949, wR2 = 0.2380
CCDC No.	2309423	2309424

Table 2. Selected bond lengths (Å) and angles (°) for **1** and **2**.

Compound **1**
Zn(1)-N(5) 2.125(3) Zn(1)-N(1) 2.135(3)
Zn(1)-N(4) 2.147(3) Zn(1)-N(3) 2.148(3)
Zn(1)-N(2) 2.146(3)
N(5)-Zn(1)-N(1) 94.94(12) N(5)-Zn(1)-N(2) 162.09(11)
N(1)-Zn(1)-N(2) 78.13(11) N(5)-Zn(1)-N(4) 78.49(11)
N(2)-Zn(1)-N(4) 118.76(12) N(5)-Zn(1)-N(3) 107.24(12)
N(1)-Zn(1)-N(3) 157.69(11) N(2)-Zn(1)-N(3) 81.27(11)
N(4)-Zn(1)-N(3) 82.63(11) N(1)-Zn(1)-N(4) 99.85(11)
Compound **2**
Zn(1)-N(3) 2.043(3) Zn(1)-N(1) 2.090(5)
Zn(1)-N(4) 2.118(5) Zn(1)-N(5) 2.165(5)
Zn(1)-N(2) 2.174(5)
N(3)-Zn(1)-N(1) 123.8(3) N(3)-Zn(1)-N(4) 102.0(3)
N(1)-Zn(1)-N(4) 134.0(18) N(3)-Zn(1)-N(5) 100.2(3)
N(1)-Zn(1)-N(5) 95.3(2) N(4)-Zn(1)-N(5) 79.1(2)
N(3)-Zn(1)-N(2) 93.6(3) N(1)-Zn(1)-N(2) 77.8(19)
N(4)-Zn(1)-N(2) 96.8(2) N(5)-Zn(1)-N(2) 166.1(2)

2.1.2. Crystal Structure of $[Zn(L^2)](ClO_4)_2$ (2)

The geometrically-related ligand L^2 with a six-carbon secondary amine backbone rather than a four-carbon secondary backbone amine containing L^1 was synthesized and metallated with zinc perchlorate to afford compound **2**. The topology of the ligands L^1 and L^2 has led to interesting structural changes in $[Zn(L^2)](ClO_4)_2$ **1** and $[Zn(L^2)](ClO_4)_2$ **2**. The single crystal X-ray diffraction study of **2** reveals that it crystallizes in a centrosymmetric monoclinic space group $P2_1/c$. The asymmetric unit consists of a centrally located Zn(II) cation, a pentadentated L^2 ligand, and two crystallographically independent perchlorate anions (Fig. 3, SI Fig. S3). The carbon atoms C7-C12 and N3 are disordered over two positions, which are modeled with occupancies of 0.64 and 0.36 (SI Fig. S4). The Zn–N bond lengths are similar in both positions, which lie in the range 2.043(3)–2.174(5). The pyridine rings are *trans* to one another. It displayed a distorted trigonal bipyramidal arrangement compared to **1**, which is confirmed by Addison parameter $\tau_5 = 0.53$ based on two relevant angles N(5)-Zn(1)-N(2) (166.1 °) and N(1)-Zn(1)-N(4) (134.0 °), β and α respectively. Thus, a more significant distortion was observed from square pyramidal to trigonal bipyramidal in compound **2**. The non-coordinated perchlorate ions form weak non-covalent N–H···O interactions (Table 3, SI Fig. S5). The crystal packing of compound **2** depicts the arrangement of the cations and anions into alternating layers along the *a*-axis (SI Fig. S6).

2.2. IR spectra, PXRD, ESI-MS, and ^{1}H NMR

The IR spectra of compounds **1** and **2** (SI Fig. S7) exhibit moderately strong peaks in the 3290–3298 cm^{-1} range, assigned to the N–H stretching vibrations arising from L^1 and L^2, respectively. In addition, a sharp peak due to pyridyl C=N stretching is observed between 1605–1608 cm^{-1}. A robust, intense absorption band in the range of 1063–1079 cm^{-1} is assigned to the stretching frequencies of $[ClO_4]^-$ ions. The involvement of hydrogen bonding of perchlorate ions in the

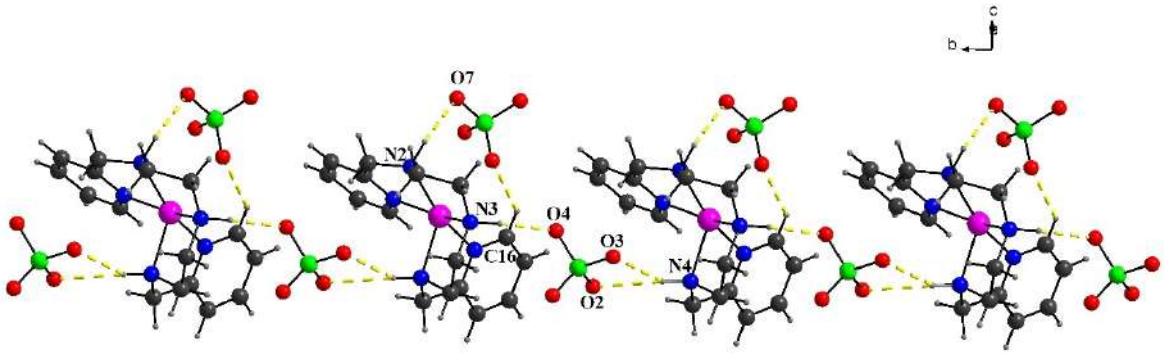

Figure 2. Hydrogen bonding interactions in **1** with atom labeling scheme of atoms involved in hydrogen bonding.

Table 3. Hydrogen bonding parameters for **1** and **2**.

D-H···A	D-H/Å	H···A/Å	D···A/Å	D-H···A/°	Symmetry code
1					
N2-H2···O7	0.980	2.115	3.055	160.11	x, y, z
N3-H3···O4	0.980	2.019	2.978	165.45	x, y, z
N4-H4···O2	0.980	2.428	3.233	139.15	x, y+1, z
N4-H4···O3	0.980	2.197	3.101	152.87	x, y+1, z
C16-H16···O5	0.930	2.432	3.088	127.54	x, y, z
2					
N3-H3A···O5	0.980(0)	2.087(0)	3.059(0)	171.04(0)	x, y, z
N5-H5B ···O4	0.980(0)	2.228(1)	3.179(2)	163.25(0)	x, y, z

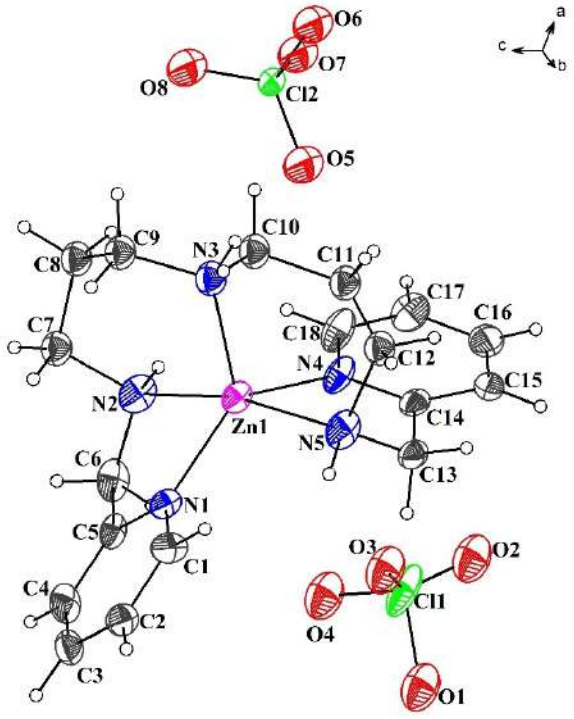

Figure 3. Crystal structure of **2** showing atom labeling scheme. The thermal ellipsoids are drawn at a 30% probability level for all the atoms except for the H atoms, which are shown as spheres of arbitrary radii.

crystal lattices leads to splitting or broadening of the band. The strong band at ~619 cm^{-1} is observed due to the bending mode of vibration for perchlorate ions.[44,45]

Analysis *via* powder X-ray diffraction confirmed the overall purity of synthesized compounds **1** and **2**. The PXRD patterns of **1** and **2** match the findings from single crystal X-ray diffraction data generated with Mercury 4.0 software (Fig. 4).[46]

The stability of compounds **1** and **2** in solution was confirmed by electrospray mass-spectra (ESI-MS), where **1** and **2** exhibits mass peaks at $m/z = 448.15$ (*Calc.* 488.07) for $[Zn(L^1)(ClO_4)]^+$ and $m/z = 476.15$ (*Calc.* 476.15) for $[Zn(L^2)(ClO_4)]^+$ fragments respectively (SI Fig. S8,S9). Compound **2** was further characterized by ^{1}H NMR spectroscopy (SI Fig. S10).

2.3. Photophysical properties of 1 and 2

Compound **1** displayed a prominent peak at 470 nm, whereas compound **2** showed a strong peak at 460 nm when excited with a 370 nm wavelength. These emissions are due to the intra-ligand transitions of $\pi^* \rightarrow n$ and $\pi \rightarrow \pi^*$ of the ligands L^1 and L^2.[47] Once the distinct emission bands were identified, we decided to investigate the sensing properties of **1** and **2** with nitroaromatic compounds (NACs). The electron-deficient NACs employed in this study were nitrobenzene (NB), *o*-nitrotoluene (*o*-NT), *p*-nitrotoluene (*p*-NT), *o*-nitrophenol (*o*-NP), *p*-nitrophenol (*p*-NP), 2,4-dinitrophenol (DNP) and 2,4,6- trinitrophenol

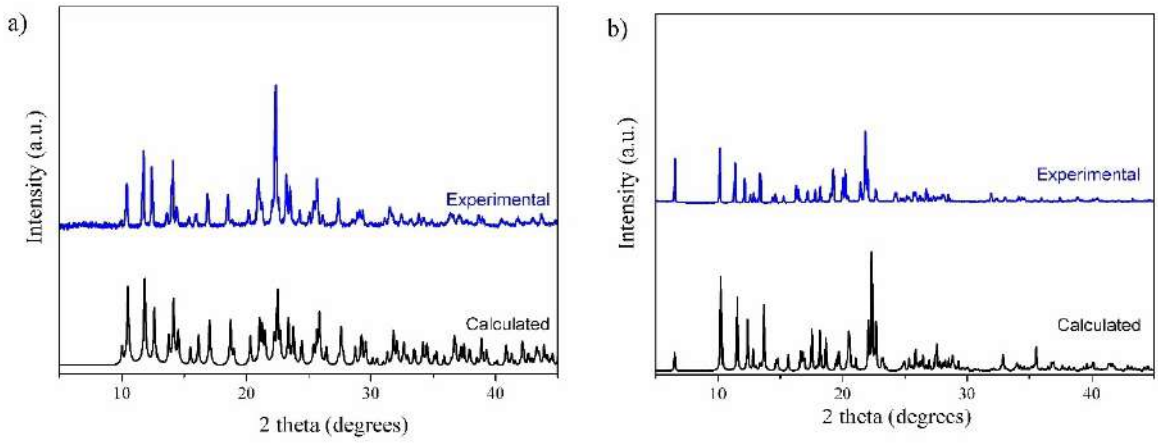

Figure 4. Powder X-ray diffraction patterns for compounds **1 (a)** and **2 (b).**

(TNP). On addition of aqueous solutions of NACS to the aqueous solution of **1**, quenching was observed at 470 nm. The emission titration of **1** with TNP is displayed in Figure 5, and the titration spectra of **1** with remaining NACs are presented in SI Fig. S11-S16. The fluorescence measurements were carried out repeatedly, a minimum of three times, to ensure consistent results. In every instance, adding NACs gradually led to a significant reduction in the initial fluorescence intensity of **1**. The quenching efficiency (η) was determined using the equation provided below;

$$[(I_0 - I)/I_0]x100\% \quad \text{(i)}$$

where I_0 and I are the fluorescence intensities before and after adding the respective NACs. Among all the NACs tested, we observed that in the case of TNP, the initial emission intensity was quenched by almost 98% (η) on adding 200 μL TNP to the solution of **1**. Similarly, on adding DNP (200 μL) to **1**, there was about 96% quenching of the emission band at 470 nm. For other NACs, the emission intensity dropped to 46% for *o*-NP and 42% for *p*-NP. A very sluggish decay of the emission band of **1** was observed with NB, *o*-NT, and *p*-NT, leading to about 31–36% quenching.

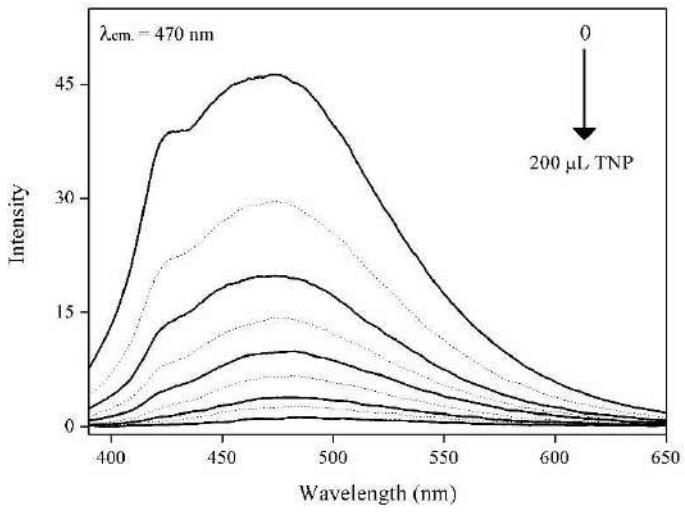

Figure 5. The decay of fluorescence emission peak of **1** ($\lambda_{ex.}$ = 370 nm) upon gradual addition of 1 mM of trinitrophenol (TNP).

Thus, the quenching efficiency followed the order: NB < *o*-NT < *p*-NT < *p*-NP < *o*-NP < DNP < TNP for all tested NACs. The sensing ability of **1** towards the different NACs is plotted in terms of their quenching efficiencies (%), as depicted in Figure 6. Compound **1** showed remarkably higher quenching efficiency towards dinitro and tri-nitrophenols over other NACs. The results unambiguously indicated that **1** could be selectively used as a chemical sensing reagent in detecting TNP and DNP from an aqueous mixture of other NACs.

Furthermore, the Stern-Volmer (S–V) quenching constant (K_{sv}) was determined by analyzing the normalized fluorescence emission intensity (I_0/I) at different quencher concentrations [Q] using the equation; $I_0/I = 1 + K_{sv}$ [Q] where I_0 and I are the emission intensities of **1**, before and after addition of NACs respectively, K_{sv} is the quenching constant (M^{-1}) and [Q] is the molar concentration of NACs. The S–V plots of **1** with the NACs are shown in Figure 7 (SI Fig. S18). The plots illustrate that the S–V curves for TNP and DNP followed a straight line at low concentrations but diverged into a curved shape at higher concentrations. The quenching constant (K_{sv}) of **1** was obtained from the slope of the equation line, $I_0/I = 1 + K_{sv}$ [Q]. The quenching constants for TNP and DNP are more significant than the other NACs used in this work (SI Table S1). This signified the exclusive quenching ability of TNP and DNP towards luminescent **1** in water, amongst other NACs.[6,13]

Similarly, the fluorescent titrations were performed with compound **2** in water. Compound **2** exhibited emission at 460 nm upon excitation at 370 nm. On screening **2** with the NACs mentioned earlier, the best quenching results were obtained for DNP and TNP. The titration of **2** with TNP is shown in Figure 8, while the titration with DNP is provided in the Supporting Information (SI Fig. S17). On calculating the quenching efficiencies (% η), the initial emission intensity of **2** was

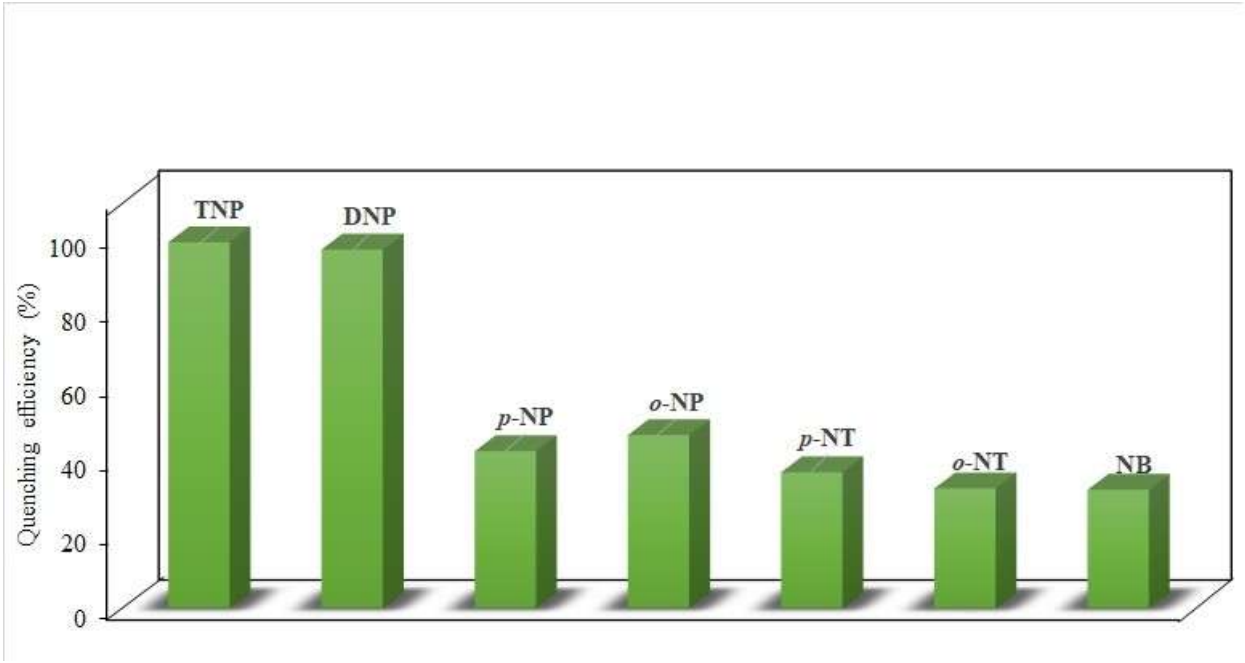

Figure 6. Representation of the quenching efficiency of **1** towards different NACs.

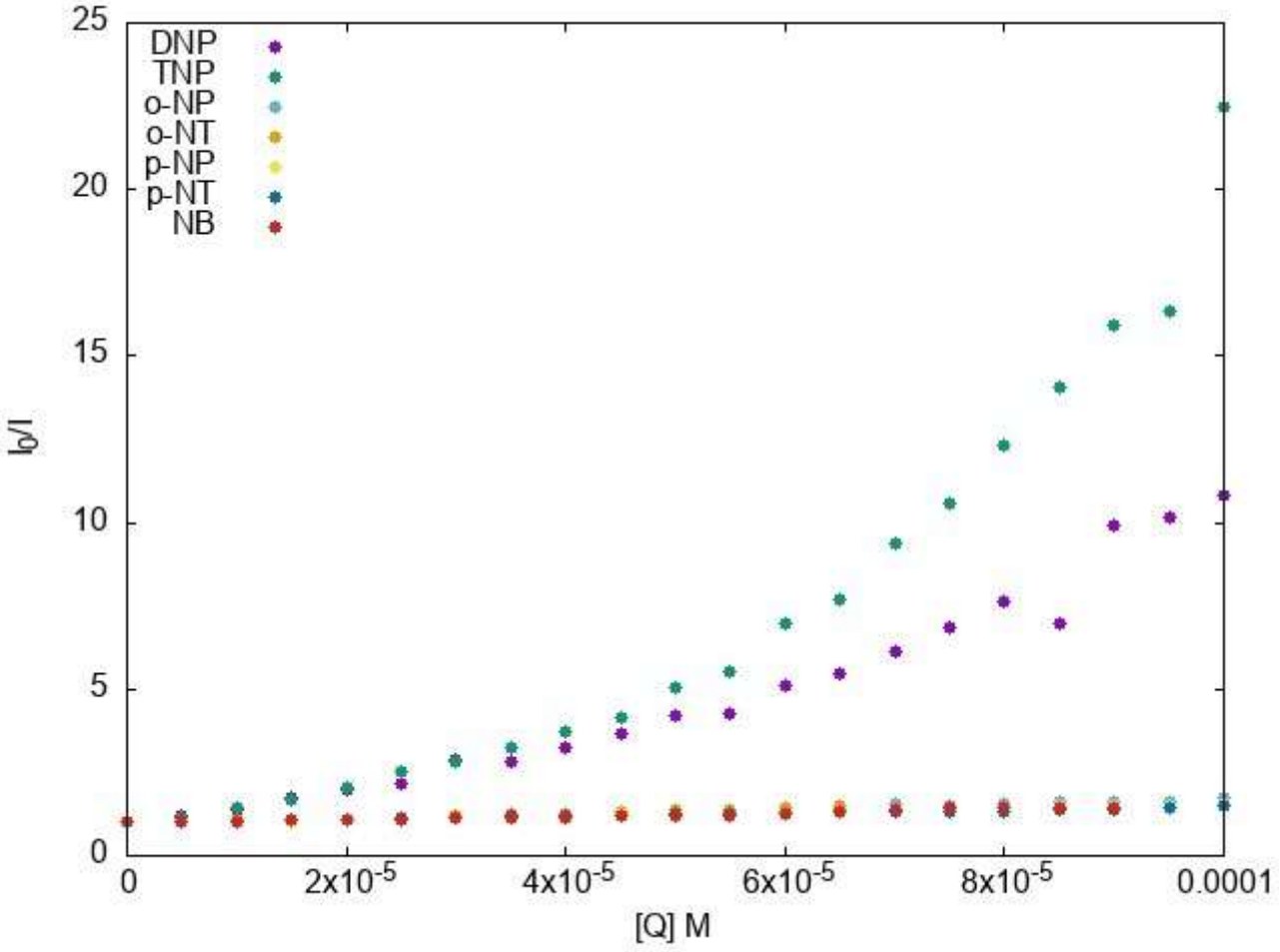

Figure 7. Stern-Volmer plots for NACs added to **1** in water.

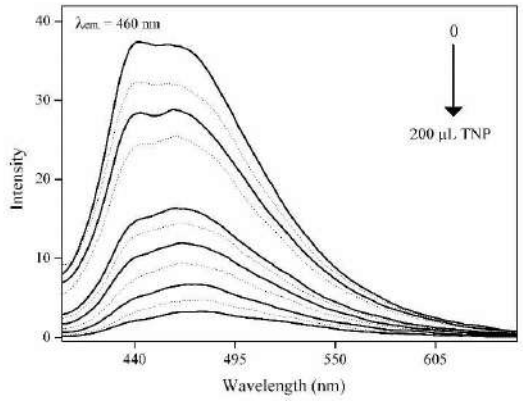

Figure 8. The reduction of fluorescence emission of **2** ($\lambda_{ex.}$ = 370 nm) upon gradually adding 1 mM of 2,4,6- trinitrophenol (TNP).

quenched by 87% for 200 µL of DNP while 92% after 200 µL of TNP. Compound **1** exhibits K_{sv} values almost twice as high as **2** for TNP and DNP.

To gain more insight into the quenching mechanism exhibited by compounds **1** and **2**, the Stern-Volmer plots were investigated. It was observed that the TNP and DNP showed a second-order polynomial fit for the S–V plot, whereas other NACs showed a linear response. While both **1** and **2** exhibit a non-linear response to the addition of TNP and DNP, a linear relationship is observed in the S–V plot at lower concentrations of the NACs (SI Fig. S19 and S20). Second-order polynomial fitting for an NAC indicates the presence of static and dynamic quenching mechanisms in the system.[48]

The degree of spectral overlap between the absorption band of the NACs and the emission band of the compounds determines the likelihood of the resonance energy transfer (RET) mechanism for increased quenching. The existence of spectral overlap in the absorption spectra of TNP and DNP with the emission spectra of the compound indicates the RET mechanism for enhanced quenching. In contrast, the remaining NACs do not exhibit such overlap (SI, Fig S21). As seen (SI, Fig. S21a), in contrast to the other NACs, which exhibit little to no spectral overlap, the absorption spectra of TNP and DNP exhibit significant overlap with the 470 nm emission band of **1**. Consequently, TNP and DNP exhibit higher quenching reactions in comparison to the remaining NACs. Similarly, on verifying the spectral overlap concerning **2** (SI, Fig. S21b), there was considerable overlap between the emission band of **2** with TNP and DNP, thereby suggesting the practical quenching ability of **2** towards TNP and DNP. However, it was observed that the adequate overlap was more in the case of **1** as compared to **2**. These observations suggest that **1** demonstrates superior selectivity towards TNP and DNP sensing over **2**, which has a more extended carbon chain backbone. Thus, the topology of ligand L^1 and the structure of compound **1** dominate the reactivity with nitroaromatic compounds.

3. Conclusions

This study investigated structural, spectroscopic and photophysical properties two Zn(II) compounds, $[Zn(L^1)](ClO_4)_2$ (**1**) and $[Zn(L^2)](ClO_4)_2$ (**2**). Compound **1** was revisited to understand the influence of ligand structure on the electronic property of **1** and compare it with a new compound 2 stabilized by L^2. The distinct and noticeable influence of the difference in ligand topology was seen in the reactivity patterns of **1** and **2** with NAC substrates. Compound **1** demonstrates superior selectivity towards sensing of TNP and DNP over compound **2**, which has a longer carbon chain backbone. This has been demonstrated by the overlap of the absorption band with the emission band, and the overlap is more prominent in compound **1**.

Supporting Information Summary

The supplementary material contains additional figures (Figure S1–S21) and table (Table S1). The crystal cif structure data and check if of compounds **1** and **2** are also given in supplementary material. Crystal structure Deposition Number(s): CCDC 2309423 (for **1**) and 2309424 (for **2**), contain(s) the supplementary crystallographic data for this paper. These data are provided free of charge by the joint Cambridge Crystallographic Data Centre and Fachinformationszentrum Karlsruhe Access Structures service "http://www.ccdc.cam.ac.uk/structures".

Acknowledgements

SND acknowledged the Council of Scientific and Industrial Research, New Delhi (No. 01(2923)/18/EMR-II) and Goa State Research Foundation, Goa (GSRF/Schemes/MajorGR /13/2023/187/ii) for research support. JLV thanks the government of Goa for the Study Leave. Authors greatly acknowledge the support from the Department of Science and Technology, New Delhi (SR/FST/CSII-034/2014(C), and SR/PURSE/2023/198 to the School of Chemical Sciences, Goa University. The authors also thank the University Grants Commission, New Delhi, for supporting the School of Chemical Sciences, Goa University, under the UGC-SAP program (F.504/14/DSA-I/2015).

Conflict of Interests

The authors declare no conflict of interest.

Data Availability Statement

The data that support the findings of this study are available from the corresponding author upon reasonable request.

Keywords: Zinc · Pentadendate · Nitrogen donor · Crystal structure · Nitroaromatics

[1] J. S. Caygill, F. Davis, S. P. J. Higson, *Talanta* **2012**, *88*, 14–29.
[2] E. A. Naumenko, B. Ahlemeyer, E. Baumgart-vogt, *Environ. Toxicol.* **2017**, *3*, 989–1006.
[3] T. M. Mallon, J. M. Ortiz, W. H. Candler, G. Rogers, R. Hillburn, *Mil. Med.* **2014**, *179*, 1374–1383.
[4] G. He, H. Peng, T. Liu, M. Yang, Y. Zhang, Y. Fang, *J. Mater. Chem.* **2009**, *19*, 7347–7353.
[5] Y. Peng, A.-J. Zhang, M. Dong, Y.-W. Wang, *Chem. Commun.* **2011**, *47*, 4505–4507.
[6] Y. Meng, N. Zhang, J. Li, Y. Xu, Q. Yang, Y. Yuan, X. Zhang, J. Wub, L. Zhao, *Spectrochim. Acta Part A* **2022**, *266*, 120419.
[7] S. S. Nagarkar, A. V Desai, P. Samanta, S. K. Ghosh, *Dalton Trans.* **2015**, *44*, 15175–15180.
[8] Y. Deng, N. Chen, Q. Li, X. Wu, X. Huang, Z. Lin, Y. Zhao, *Cryst. Growth Des.* **2017**, *17*, 3170–3177.
[9] D. S. Moore, *Rev. Sci. Instrum.* **2004**, *75*, 2499–2511.
[10] S. Wang, H. Chen, *J. Chromatogr. A.* **2002**, *979*, 439–446.
[11] H. Ebrahimzadeh, Y. Yamini, F. Kamarei, *Talanta* **2009**, *79*, 1472–1477.
[12] R. Wilson, C. Clavering, A. Hutchinson, *Anal. Chem.* **2003**, *75*, 4244–4249.
[13] A. Jana, J. Mandal, S. S. Mondal, R. Patra, A. Bhunia, *Inorg. Chim. Acta.* **2023**, *549*, 121409.
[14] A. Gusev, V. Shul'gin, E. Braga, E. Zamnius, M. Kryukova, W. Linert, *Dyes Pigm.* **2020**, *183*, 108626.
[15] X. Song, Y. Peng, G. Cheng, X. Wang, P. Liu, W. Xu, *Inorg. Chim. Acta.* **2015**, *427*, 13–21.
[16] S. Shanmugaraju, P. S. Mukherjee, *Chem. Eur. J.* **2015**, *21*, 6656–6666.
[17] A. Barbieri, G. Accorsi, N. Armaroli, *Chem. Commun.* **2008**, *19*, 2185–2193.
[18] M. Shyamal, A. Panja, A. Sah, *Polyhedron* **2014**, *69*, 141–148.
[19] V. Amani, *J. Mol. Struct.* **2018**, *1155*, 477–483.
[20] Y. Ma, G. Xu, F. Wei, Y. Cen, Y. Song, M. Shi, X. Xu, M. Sohail, Q. Hu, *New J. Chem.* **2018**, *42*, 5162–5167.
[21] T. Chatterjee, E. Hossain, S. Khan, S. Roy, S. M. Wabaidur, M. A. Islam, S. M. Alam, M. H. Mir, *J. Mol. Struct.* **2023**, *1271*, 134011.
[22] A. S. Burlov, V. G. Vlasenko, Y. V Koshchienko, N. I. Makarova, A. A. Zubenko, Y. D. Drobin, G. S. Borodkin, A. V Metelitsa, Y. V Zubavichus, D. A. Garnovskii, *Polyhedron* **2018**, *144*, 249–258.
[23] D. Mukherjee, K. Sarkar, S. Reja, M. Bakibillah, S. Guha, N. K. Mandal, J. P. Naskar, R. K. Das, *J. Fluoresc.* **2023**.
[24] Z. I. Contejean, R. L. LaDuca, *J. Solid State Chem.* **2018**, *266*, 44–53.
[25] B. Dutta, S. Paul, S. Halder, *Heliyon* **2023**, *9*, e13504.
[26] J.-L. Du, X. Lu, T.-L. Shen, C.-P. Li, Y.-J. Mu, L.-J. Li, *Mater. Lett.* **2015**, *158*, 225–228.
[27] S. Roy, I. Mondal, K. Harms, S. Chattopadhyay, *Polyhedron* **2019**, *159*, 265–274.
[28] A. R. LaDuca, R. L. LaDuca, *CrystEngComm* **2018**, *20*, 5677–5687.
[29] X. -Z. Guo, S. -S. Chen, W. -D. Li, S. -S. Han, F. Deng, R. Qiao, Y. Zhao, *ACS Omega* **2019**, *4*, 11540–11553.
[30] A. G. Blackman, *Polyhedron* **2019**, *161*, 1–33.
[31] W. K. C. Lo, C. J. McAdam, A. G. Blackman, J. D. Crowley, D. A. McMorran, *Inorg. Chim. Acta.* **2015**, *426*, 183–194.
[32] D. D. Narulkar, A. K. Srivastava, R. J. Butcher, K. M. Ansy, S. N. Dhuri, *Inorg. Chim. Acta.* **2017**, *467*, 405–414.
[33] J. L. Viegas, S. N. Dhuri, *J. Mol. Struct.* **2023**, *1288*, 135719.
[34] D. D. Narulkar, K. Devulapally, A. K. U. S. N. Dhuri, *Sustain. Energy Fuels* **2020**, *4*, 2656–2660.
[35] S. S. Harmalkar, A. V. Naik, M. K. Nilajakar, S. N. Dhuri, *ChemistrySelect* **2020**, *5*, 8447–8454.
[36] L. R. D'souza, N. N. Harmalkar, S. S. Harmalkar, S. B. Tayade, S. N. Dhuri, *ACS Omega* **2022**, *7*, 5698–5712.
[37] G. M. Sheldrick, *Acta Crystallogr. Sect. C* **2015**, *71*, 3–8.
[38] J. Lin, N. Wang, X. Chen, X. Yang, L. Hong, Z. Ruan, H. Ye, Y. Chen, X. Liang, *Sustain. Energy Fuels* **2022**, *6*, 1312–1318.
[39] W. P. Sohtun, S. Muthuramalingam, M. Velusamy, R. Mayilmurugan, *Inorg. Chem. Commun.* **2019**, *110*, 107608.
[40] A. W. Addison, T. N. Rao, J. Reedijk, J. van Rijn, G. C. Verschoor, *Dalton Trans.* **1984**, *7*, 1349–1356.
[41] L. Yang, D. R. Powell, R. P. Houser, *Dalton Trans.* **2007**, *9*, 955–964.
[42] A. G. Blackman, E. B. Schenk, R. E. Jelley, E. H. Krenske, L. R. Gahan, *Dalton Trans.* **2020**, *49*, 14798–14806.
[43] S. Alvarez, M. Llunell, *Dalton Trans.* **2000**, *19*, 3288–3303.
[44] A. Panja, *Dalton Trans.* **2014**, *43*, 7760–7770.
[45] S. S. Harmalkar, R. J. Butcher, V. V. Gobre, S. K. Gaonkar, L. R. D'Souza, M. Sankaralingam, I. Furtado, S. N. Dhuri, *Inorg. Chim. Acta.* **2019**, *498*, 119020.
[46] C. F. MacRae, I. Sovago, S. J. Cottrell, P. T. A. Galek, P. McCabe, E. Pidcock, M. Platings, G. P. Shields, J. S. Stevens, M. Towler, P. A. Wood, *J. Appl. Crystallogr.* **2020**, *53*, 226–235.
[47] D. Das, B. G. Chand, J. Dinda, C. Sinha, *Polyhedron* **2007**, *26*, 555–562.
[48] A. S. Tanwar, R. Parui, R. Garai, M. A. Chanu, P. K. Iyer, *ACS Meas. Sci. Au.* **2022**, *2*, 23–30.

Manuscript received: June 5, 2024

ChemistrySelect

Research Article
doi.org/10.1002/slct.202503672

Chemistry Europe
European Chemical Societies Publishing

www.chemistryselect.org

A Three-Component Reaction of 4-Hydroxycoumarin, 2-Aminopyridine, and Aryl Aldehydes: Synthesis of Enolate Salts of 2-Aminopyridinium Biscoumarins

Madhuri M. Gaikwad,[a] Santosh G. Tilve,*[a] Jeffrey L. Viegas,[a] Sunder N. Dhuri,[a] Shrikant A. Shete,[b] and Bhanu Manjunath[b]

Dedicated to Prof. S.K. Paknikar on his 90th birthday on 26-06-2025

Multicomponent reaction (MCR) of aryl aldehydes, 4-hydroxycoumarin, and 2-aminopyridine gave the corresponding 2-aminopyridinium enolate salts of biscoumarins in the presence of zirconyl oxynitrate as a catalyst. This differs from other reports that claim the formation of chromeno[4,3-*d*]pyrido[1,2-*a*]pyrimidin-6-ones and 3-[aryl(pyridin-2-ylamino)methyl]-2*H*-chromen-2-ones. Spectroscopic methods confirmed the chemical structures of all the novel compounds. Moreover, single-crystal X-ray diffraction confirms the molecular structure of the product 2-aminopyridin-1-ium-3((4-fluorophenyl)(4-hydroxy-2-oxo-2*H*-chromen-3-yl)methyl)2-oxo-2*H*-chromen-4-olate. These salts' NMR and IR data closely resemble the previously reported data on chromeno[4,3-*d*]pyrido[1,2-*a*]pyrimidin-6-ones and 3-[aryl(pyridin-2-ylamino)methyl]-2*H*-chromen-2-ones. This study suggests new structural assignments for previous reports and proposes a re-examination of the described multicomponent reaction.

1. Introduction

The remarkable medicinal properties displayed by coumarins and their hybrids have drawn the attention of organic and medicinal chemists to design their synthesis in more efficient and greener ways.[1] Multicomponent reactions (MCRs) have aided in designing more complex structures with simplicity. 4-Hydroxycoumarin has been an excellent component with two reactive positions, the C-4 hydroxyl functionality and the electron rich C-3 position in MCRs.[2] A large variety of hybrid heterocyclic structures using 4-hydroxycoumarins have been prepared and tested for their pharmacological activities.[3] One such fused heterocycle is chromeno[4,3-*d*]pyrido[1,2-*a*]pyrimidin-6-one. The pathway for the synthesis of this heterocycle is a multicomponent reaction between aldehyde, 4-hydroxycoumarin and 2-aminopyridine using an acidic catalyst. The synthesis of chromeno [4,3-*d*]pyrido[1,2-*a*]pyrimidin-6-ones has been carried out using catalysts such as sulfamic acid,[4] $NiFe_2O_4$@SiO_2 grafted di(3-propylsulfonic acid),[5] Fe_3O_4@SiO_2 functionalized sulfonic acid,[6] sulfonated rice husk,[7] and ionic liquid [CMMIM][BF_4^-].[8] The same combination of the three components is also reported to give 3-[aryl(pyridin-2-ylamino)methyl]-2*H*-chromen-2-ones in the presence of a catalytic amount of formic acid in acetonitrile under refluxing conditions[9] (Scheme 1).

Though Lewis acids $FeCl_3.6H_2O$, $ZnCl_2$, SiO_2-$FeCl_3$, $MgCl_2$, $NiCl_2.6H_2O$, SiO_2-BF_3, $AlCl_3$, $Fe(NO_3)_3.6H_2O$, $CaCl_2$, $SnCl_2$, $SnCl_4$, SiO_2-$ZnCl_2$, $Bi(NO_3)_3.6H_2O$, SiO_2-$MgCl_2$, SiO_2-$NiCl_2$, $Zn(NO_3)_2.6H_2O$, $FeSO_4$, $NiSO_4$, and SiO_2-$AlCl_3$ were unable to give any product,[5] we were interested in using zirconyl oxynitrate[10] as a novel catalyst for the synthesis of chromeno[4,3-*d*]pyrido[1,2-*a*]pyrimidin-6-ones. A series of fifteen compounds was prepared at room temperature using ethanol-water as the solvent. The melting point and spectroscopic data of the synthesized derivatives matched with those of the reported compounds.[4–8] However, the disproportionate ratio of protons seen in ^{1}H NMR spectra did not match the corresponding structures, which intrigued us. Also, in the ^{13}C NMR spectrum, the single sp^3 carbon appearing at around ~36 ppm, assigned to the allylic carbon next to nitrogen, baffled us the most. We expected that signal to be in the range from 60 to 70 ppm. Interestingly, the sp^3 carbon in the case of 4-fluorobiscoumarin appears at 35.79 ppm.[11] This prompted us to re-examine our compounds' NMR data as well as literature data, and carry out further studies to clarify our doubts.

In-depth spectroscopic studies revealed that the reaction only produced the 2-aminopyridinium enolate salt of biscoumarin, and not the previously believed chromeno[4,3-*d*]pyrido[1,2-*a*]pyrimidin-6-one. Since 4-hydroxycoumarin is very reactive, there is a favourable chance that the corresponding biscoumarin will be produced as a byproduct.[12]

In this study, we report that the MCR reaction between aldehydes, 4-hydroxycoumarin, and 2-aminopyridine leads to the formation of 2-aminopyridinium enolate salt of biscoumarins.

[a] *M. M. Gaikwad, Prof. Dr. S. G. Tilve, J. L. Viegas, Prof. Dr. S. N. Dhuri*
School of Chemical Sciences, Goa University, Taleigao Plateau, Goa 403 206, India
E-mail: stilve@unigoa.ac.in

[b] *S. A. Shete, Dr. B. Manjunath*
Syngenta Biosciences Pvt. Ltd, Corlim Ilhas, Goa 403 110, India

Supporting information for this article is available on the WWW under https://doi.org/10.1002/slct.202503672

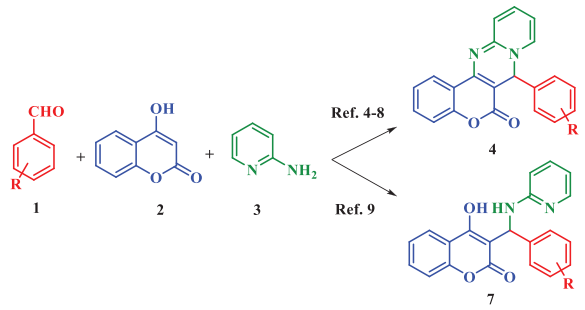

Scheme 1. Literature synthesis of chromeno[4,3-*d*]pyrido[1,2-*a*] pyrimidin-6-ones and 3-[aryl(pyridin-2-ylamino)methyl]-2*H*-chromen-2ones.

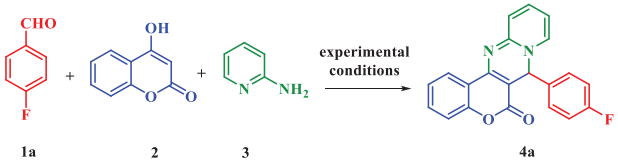

Scheme 2. Optimization of reaction conditions for the synthesis of chromeno[4,3-*d*]pyrido[1,2-*a*] pyrimidin-6-one (**4a**).

2. Results and Discussion

Initially, to synthesize chromeno[4,3-*d*]pyrido[1,2-*a*] pyrimidin-6-one **4a**, we undertook the reaction of 4-fluorobenzaldehyde **1a**, 4-hydroxycoumarin **2** and 2-aminopyridine **3** in the presence of 10 mol % of zirconyl oxynitrate as the catalyst and 1:1 ethanol-water as the solvent system (Scheme 2). After 24 h, a white solid precipitated in the reaction flask was filtered off. The yield of the product was 52% on assumed structure **4a**. The melting point of this obtained product, which was assumed to be **4a** matched perfectly with the one reported in the literature.[8] The NMR data of this compound was in agreement with the literature.[4]

Further optimization studies were carried out using different solvents and catalyst concentrations to get the maximum yield of the product (Table 1).

Having optimized conditions in hand, we extended this reaction to other aromatic aldehydes. A series of ten known and five novel chromeno[4,3-*d*]pyrido[1,2-*a*]pyrimidin-6-ones were synthesized (Table 2). For the newly synthesized compounds (Table 2), entries 11–15 were subjected to HRMS studies for further confirmation. However, in none of these cases we could get the desired mass for the expected compounds. Instead, the presence of biscoumarin was confirmed.

This prompted us to relook at the data of all the compounds and to literature data. It was observed that, all the compounds showed excess protons in the aromatic region in their proton NMR spectra. After careful examination of the ^{1}H NMR spectra of the obtained products, we concluded that the products formed in the reaction mixture were 2-aminopyridinium enolate salts of biscoumarins **5** and not chromeno[4,3-*d*]pyrido[1,2-*a*]pyrimidin-6-ones **4** (Scheme 3). In the ^{1}H NMR spectrum of the compound **5a**, two protons at 17.62 and 13.28 ppm (exchangeable with D_2O) were seen, four protons were merged as a multiplet at 7.94–7.90 ppm which comprises of two NH_2 protons (exchangeable with D_2O, Figure S68) and two protons of pyridine ring (α & γ protons of pyridine). The phenyl and coumarin ring protons appeared in the region from 7.52–6.84 ppm. The methine proton appeared at 6.24 ppm. Initially, the presence of three extra protons, one of hydroxyl proton and two amino protons indicated formation of the enolate salt.

However, four exchangeable protons were expected for the assigned enolate salt, and only three were observed. This prompted us to rerecord the spectrum, as the hydrogen present on pyridinium nitrogen could still be downfield than 15 ppm (the normal scan of a ^{1}H NMR spectrum is up to 15 ppm). As expected, we could observe one more proton at 17.62 ppm, which balanced the proton count for the assigned structure of the salt. We attributed the two exchangeable protons at 17.62

Table 1. Optimization of reaction conditions with respect to solvent and catalyst loading.[a)]

Entry	Solvent	Temperature (°C)	Reaction Time (h)	Catalyst (x mol %)	Yield[b)] (%)
1	H_2O: EtOH (1:1 v/v)	r.t.	24	10	52
2	H_2O	r.t.	24	10	53
3	EtOH	r.t.	24	10	47
4	CH_3OH	r.t.	24	10	44
5	IPA	r.t.	24	10	20
6	CH_3CN	r.t.	24	10	NR
7[c)]	H_2O: EtOH (1:1 v/v)	r.t.	9	15	63
8[c)]	H_2O: EtOH (1:1 v/v)	r.t.	7.5	20	78
9[c)]	H_2O: EtOH (1:1 v/v)	r.t.	6	25	83
10[c)]	H_2O: EtOH (1:1 v/v)	r.t.	6	27	81
11[c)]	H_2O: EtOH (1:1 v/v)	80	4	25	79

[a)] Reaction Conditions: mixture of 4-fluorobenzaldehyde (1 mmol), 4-hydroxycoumarin (1 mmol), 2-aminopyridine (1 mmol), and catalyst zirconyl oxynitrate was stirred in 10 mL of the respective solvent at room temperature (r.t.).
[b)] Yields of isolated products based on 4-hydroxycoumarin.
[c)] Reaction conditions for entries 7–11: mixture of 4-fluorobenzaldehyde (1 mmol), 4-hydroxycoumarin (1 mmol), 2-aminopyridine (1 mmol), and zirconyl oxynitrate was stirred in 10 mL of 1:1 ethanol-water as a solvent under room temperature/reflux reaction conditions.

Table 2. Synthesis of substituted chromeno[4,3-*d*]pyrido[1,2-*a*]pyrimidin-6-ones.[a)]

Entry	Aldehyde	Product	Time (h)	Yield[b)] (%)	Melting point (°C)	
					Observed	Reported
1	4F-C_6H_4	5a	3	76	224–228	224–225[4]
2	C_6H_5	5b	6	83	208–212	211–212[4]
3	4OCH_3-C_6H_4	5c	7	78	220–222	223–225[8]
4	4CH_3-C_6H_4	5d	4.5	87	222-224	225-227[8]
5	4OH-C_6H_4	5e	8	80	156–158	156–158[8]
6	4Br-C_6H_4	5f	5	76	242–244	240–242[4]
7	2F-C_6H_4	5g	5	75	116–118	112–113[4]
8	4Cl-C_6H_4	5h	4	80	236–240	236–238[8]
9	2-Furyl	5i	9	77	174–176	171–173[4]
10	3,4-$(OCH_3)_2C_6H_3$	5j	10	75	212–214	215–216[4]
11	Piperonal	5k	10	76	228–230	–
12	2,5-$(OCH_3)_2C_6H_3$	5l	7	77	220–224	–
13	3-Furyl	5m	12	81	176–180	–
14	2,4,5-$(OCH_3)_3C_6H_2$	5n	4.5	75	206–208	–
15	2,3-$(OH)_2C_6H_3$	5o	7	83	180–182	–

[a)] Reaction conditions: A mixture of aldehyde (0.5 mmol), 4-hydroxycoumarin (1 mmol), 2-aminopyridine (1 mmol), and zirconyl oxynitrate (25 mol%) was stirred in 10 mL of 1:1 ethanol-water at room temperature.
[b)] Yields of isolated products based on aldehydes.

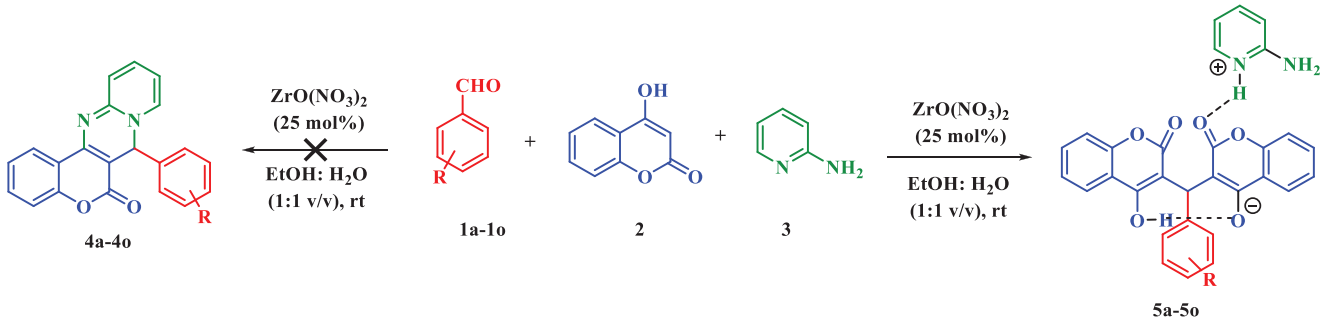

Scheme 3. Zirconyl oxynitrate-assisted one-pot synthesis of a 2-aminopyridinium salt of biscoumarins.

and 13.26 ppm to the pyridinium hydrogen and the hydroxyl hydrogen of biscoumarin, respectively. Figure 1 displays the reported ^{1}H NMR spectrum[4] of compound **4a** and the observed ^{1}H NMR spectrum of compound **5a**. While reporting the data of the compound **4a**, there appears to be an error in the proton count may be because during the integration, a proton was assigned a value in fraction (0.74). Also, the spectrum does not display the important downfield exchangeable protons of biscoumarin and pyridinium N-H.

The IR studies provided further support for the assigned structure **5a**. The IR spectra of all the obtained compounds showed strong and broad absorption band between 2600 and 3400 cm^{-1}, indicating the presence of pyridinium hydrogen, NH_2 and OH functional groups (Figure S4), which are unexpected for the desired compound **4a** as it lacks these groups. (Incidentally, literature references[4,8] did provide IR spectra and have these bands). All this data was taken as evidence that the compound has been assigned a probably incorrect structure in earlier reports and that it is the corresponding 2-aminopyridinium enolate salt of biscoumarin and not chromeno[4,3 *d*]pyrido [1,2 a]pyrimidin-6-one. Further, in the ^{13}C NMR spectrum, the single sp^3 carbon appeared at 36.03 ppm, which appears at 35.94 ppm. It was expected that if the compound formed in the reaction was **4a**, the sp^3 is quite similar to that of 4-fluorobiscoumarin (Figure S70), in which this carbon would have been observed at 60–70 ppm due to the inductive effect of the neighbouring nitrogen atom. Similarly, for all the remaining compounds, the structures were confirmed as **5b–5o** (Figure 2).

Having the optimized reaction conditions in hand, we further explored the utility of this three-component reaction for the series of aliphatic aldehydes and substituted amino pyridines. Aliphatic aldehydes such as propionaldehyde, butyraldehyde, heptaldehyde, and iso-valeraldehyde failed to produce desired enolate salts even after refluxing the reaction for 24 h. Substituted amino pyridine, such as 4-methyl-2-amino pyridine, also offered a very low yield of the products.

High-resolution mass spectrometry was performed for derivatives **5k**, **5l**, **5m**, **5n,** and **5o**, in which the molecular ion

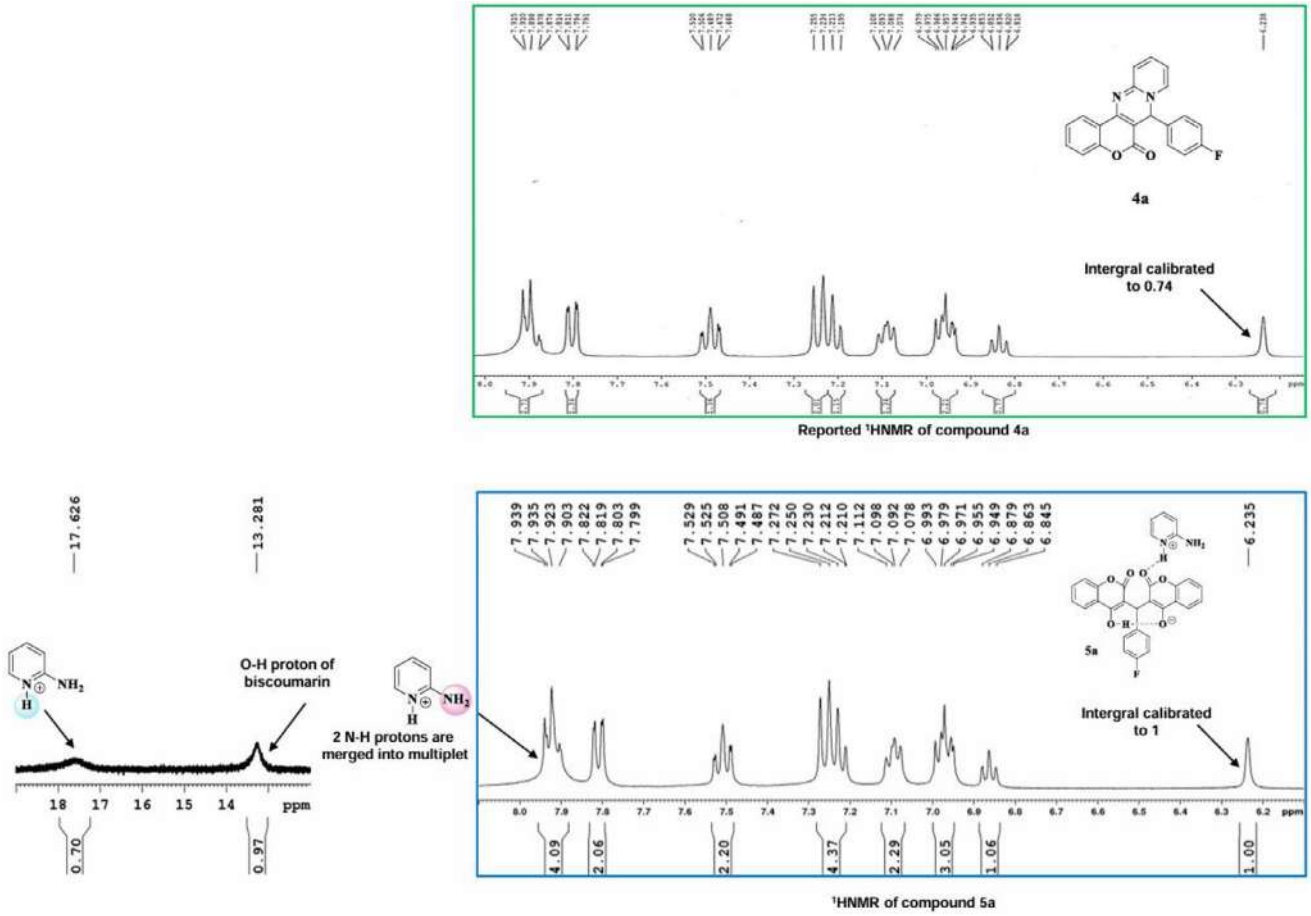

Figure 1. [1]HNMR spectrum of reported compound **4a** and enolate salt **5a**.

peak for the expected product **4** was not seen at all. Molecular ion peaks for biscoumarin and 2-aminopyridine were seen instead (Figures S66 and S67). This showed that these two molecules combine to form an enolate salt and stay in the reaction mixture as a single product, and gets separated on the HPLC column of the LC-MS. In the mass spectrum of derivative **5l**, which is displayed in Figure 3, notable peaks include the protonated biscoumarin at *m/z* 473, the protonated Knoevenagel intermediate at *m/z* 311, and 2-aminopyridine at *m/z* 95.

When the compounds were subjected to the electrospray ionization mass spectrometry (ESI-MS) via direct injection, the molecular ion peak corresponding to enolate salt was observed in case of all fifteen derivatives, thus confirming the formation of enolate salts.

2.1. Description of the Molecular Structure of 5a in the Crystal

Compound **5a** has been characterized by single crystal X-ray diffraction technique. Compound **5a** crystallizes in the polar monoclinic space group *Cc*, with all atoms located at general positions. The asymmetric unit of **5a** consists of a 2-aminopyridinium cation intramolecularly H-bonded with a deprotonated 3,3′-((4-fluorophenyl)methylene)bis(4-hydroxy-2*H*-chromen-2-one) (Figure 4). Technical details of data acquisition and selected refinement results for **5a** are summarized in Table S1. The oxygen atoms O2, O4, and O6 of the bis(coumarin) anion unit are involved in N—H···O interactions with the 2-amino pyridinium cation, while O6 forms an O—H···O H-bond with O3, resulting in a supramolecular assembly. The molecular structure is stabilized by a combination of intra- and intermolecular hydrogen bonds, resulting in an extensive network (Figure 5).

Interestingly, Shemchuk and coworkers[13] have reported the isolation of such enol salts of bis-*N*-ethyl-1*H*-2,1-benzothiazine-4(3*H*)-one 2,2-doixide with triethyl amine, DMAP, and DBU during the attempted MCR reaction of *N*-ethyl-1*H*-2,1-benzothiazine-4(3*H*)-one 2,2-doixide, ethyl cyanoacetate, and benzaldehydes.

2.2. Reinvestigation of the Selected Published Reports and Attempted Experiments Toward Synthesis of 4a

To reinvestigate the synthesis of compound **4a**, the reaction of 4-fluorobenzaldehyde, 4-hydroxycoumarin, and 2-aminopyridine was repeated using several established catalysts, which were employed for the synthesis of **4a**. Initially, catalytic use of sulfamic acid, which is reported for the synthesis of chromeno[4,3-*d*]pyrido[1,2-*a*]pyrimidin-6-ones, was studied. The reactions were performed in aqueous ethanol at room temperature, under ultrasonication, and under refluxing conditions. In all cases, the enolate salt **5a** was obtained as the sole product (entry 1–3, Table 3).

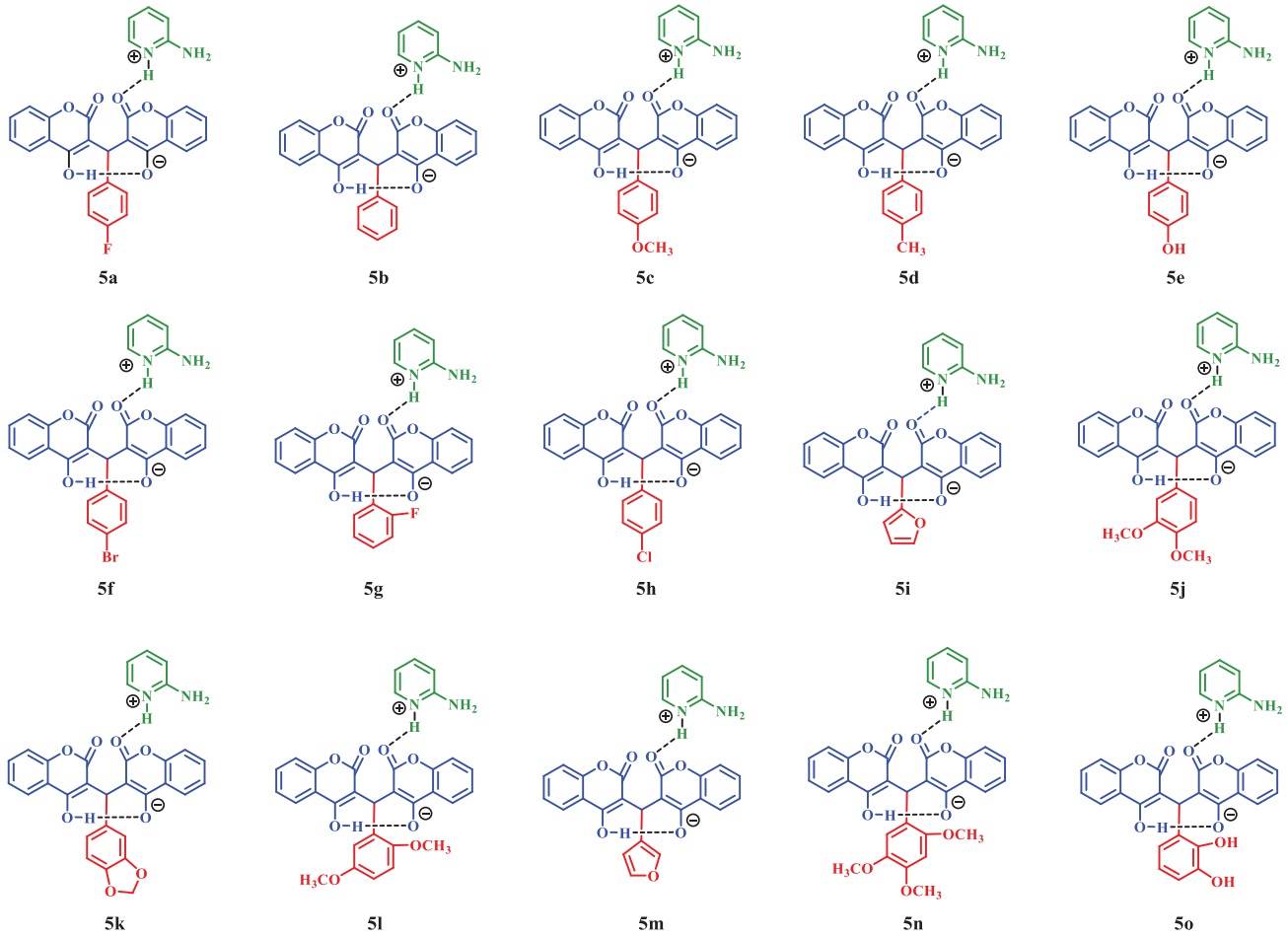

Figure 2. 2-Aminopyridinium salts of substituted biscoumarins.

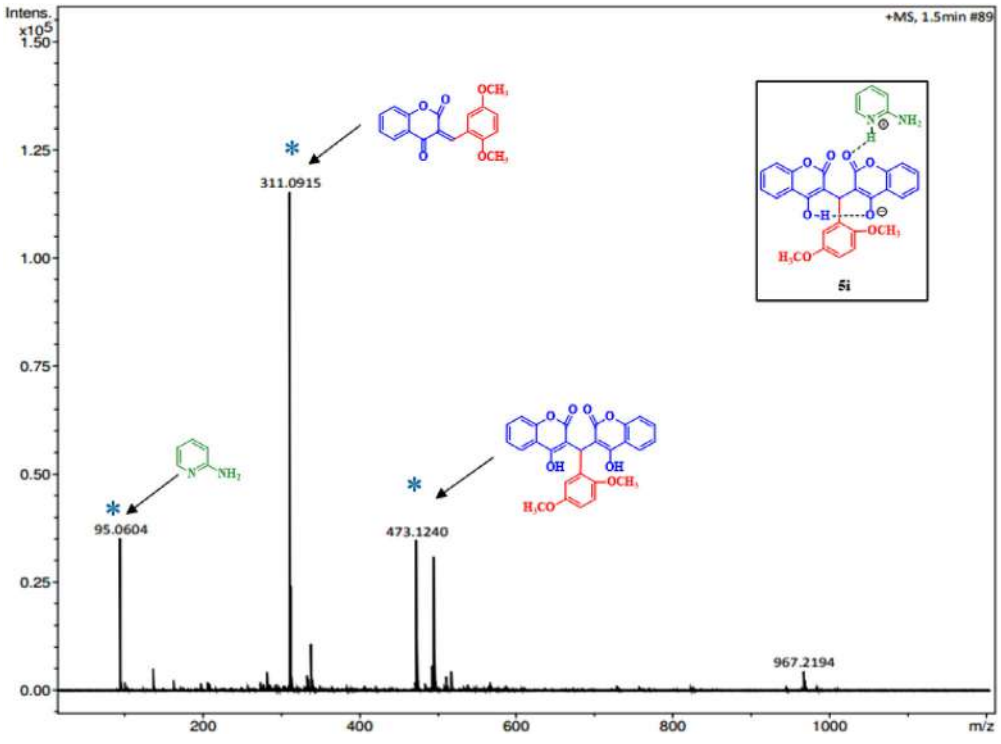

Figure 3. High resolution ESI (+)-MS characterization of the derivative **5l**.

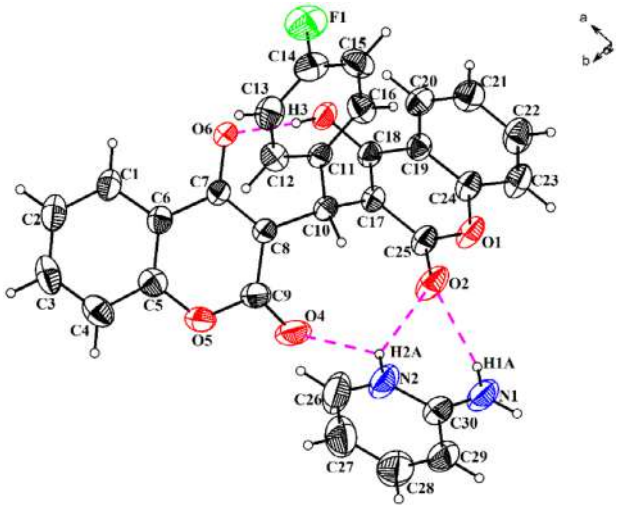

Figure 4. Crystal structure of **5a** showing atom labeling scheme. The thermal ellipsoids are drawn at a 50% probability level for all the atoms except for the H atoms, which are shown as spheres of arbitrary radii. The intramolecular H-bond is shown by broken lines.

So also was the case with catalysts such as H_2SO_4, L-proline, iodine, acetic acid, *p*-TSA, and formic acid (see entries 4–8, Table 3). Solvent-free reaction in triflic acid and triflic acid/P_2O_5 at room temperature led to charring of the reaction mixture and provided the exclusively biscoumarin **6a**. Upon neutralizing the reaction mixture with base, recovery of 2-aminopyridine was confirmed. Table 4 highlights the comparison of the spectroscopic characterization data of reported compound **4a** as published in the literature with the observed enolate salt **5a**.

Next, to avoid the formation of biscoumarin, the reaction of two equivalents of 4-fluorobenzaldehyde **1a** and 1 equiv of 4-hydroxycoumarin **2** was carried out under solvent-free conditions at 150 °C and 10 bar pressure in a monowave reactor. After consumption of 4-hydroxycoumarin as indicated by TLC, 2 equiv of 2-aminopyridine **3** were added to the same reaction mixture, and the reaction was continued till the consumption of 2-aminopyridine was seen. The reaction mixture was diluted with ethyl acetate, and the mass of the crude sample was recorded, which did not show the required molecular ion peak corresponding to product **4a**.

The formation of **5a** was also confirmed by conducting a separate reaction of biscoumarin **6a** and 2-aminopyridine **3** in ethanol: water (1:1 v/v), ethanol, and solvent-free conditions at ambient temperature. Biscoumarin, when it came in contact with 2-aminopyridine, "slowly started dissolving, forming a homogenous phase" (Scheme 4).

It was concluded that the three-component reaction between 4-hydroxy coumarin, aryl aldehyde, and 2-amino pyridine follows a path of first base-catalyzed bis-coumarin formation followed by 2-amino pyridine-mediated deprotonation, leading to enolate salt **5**.

3. Conclusion

In summary, we have assessed the multicomponent reaction between aldehydes, 4-hydroxycoumarin and 2-aminopyridine, which led us to the reinvestigation and examination of some of the previously published literature reports, along with their spec-

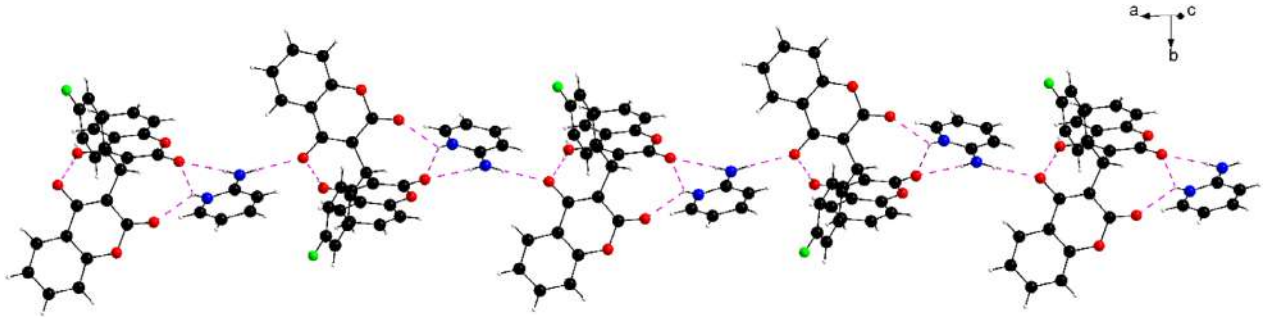

Figure 5. Hydrogen bonding interactions involved in **5a**.

Table 3. Catalysts screened for the synthesis of chromeno[4,3-*d*]pyrido[1,2-*a*]pyrimidin-6-ones.

Entry	Catalyst	Reaction Conditions	Reaction Time (h)	Catalyst (x mol%)	Yield (%) of Enolate Salt 5a
1	Sulfamic acid	H_2O- EtOH (1:1), r.t.	24	10	72
2	Sulfamic acid	US, H_2O- EtOH (1:1), r.t.	2	10	53
3	Sulfamic acid	H_2O- EtOH (1:1), reflux	24	10	80
4	H_2SO_4	H_2O- EtOH (1:1), reflux	24	–	79
5	I_2	CH_3CN, r.t.	24	10	65
6	L-proline	H_2O- EtOH (1:1), reflux	24	10	75
7	*p*-TSA	H_2O- EtOH (1:1), reflux	24	10	89
8	HCOOH	CH_3CN, reflux	24	10	82

Table 4. Comparative table displaying the characterization data of compounds 4a and 5a.

Reported Characterization Data of Compound 4a	Observed Characterization Data of Compound 5a
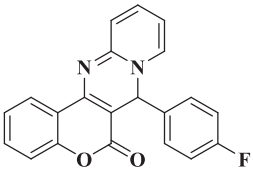	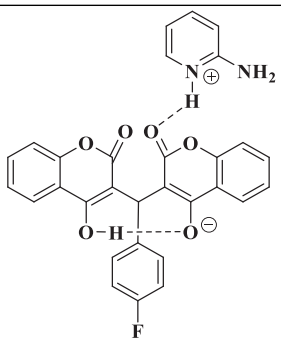
White amorphous powder.	White solid.
Melting point: 224–225 °C.	Melting point: 224–228 °C.
IR: 3180, 2925, 1685, 1662, 1603, 1544, 1507, 1408, 1330, 1228, 1184, 1106, 1056, 1037, 998, 860, 760 cm^{-1}.	IR: **3361, 3190**, 1676, 1598, 1531, 1396, 1215, 754 cm^{-1}.
^1H NMR (400 MHz, DMSO-d_6): δ 7.92–7.87 (m, 3H), 7.80 (dd, 1H, J = 8.0 and J = 1.2 Hz), 7.49 (dt, 1H, J = 7.6 and 1.6 Hz), 7.24 (d, 2H, J = 8.4 Hz), 7.20 (d, 1H, J = 7.2 Hz), 7.11–7.07 (m, 1H); 6.98–6.94 (m, 2H), 6.85–6.82 (m, 1H), 6.24(s, 1H) ppm.	^1H NMR (400 MHz, DMSO-d_6): δ **17.62 (brs, 1H, NH)**, **13.28 (brs, 1H, OH)**, 7.94–7.90 (m, 4H), 7.81 (dd, 2H, J = 7.8, 1.6 and 1.2 Hz), 7.51 (dt, 2H, J = 7.6 and J = 1.6 Hz), 7.27–7.21 (m, 4H), 7.11–7.08 (m, 2H), 6.99–6.95 (m, 3H), 6.86 (t, 1H J = 7.2 and 6.4 Hz), 6.24 (s, 1H) ppm.
^{13}C NMR (100 MHz, DMSO-d_6): δ 167.70, 164.48, 161.31, 158.92, 153.88, 152.49, 144.09, 138.24, 138.21, 136.04, 130.95, 128.34, 128.27, 124.10, 122.89, 119.85, 115.45, 114.34, 114.14, 113.38, 112.11, 103.37, 35.57 ppm.	^{13}C NMR (100 MHz, DMSO-d_6): δ 168.19, 164.96, 159.40, 154.43, 152.97, 144.50, 138.72, 136.67, 131.45, 128.81, 128.74, 124.59, 123.38, 120.32, 115.94, 114.83, 114.63, 113.79, 112.61, 103.84, 36.03 ppm

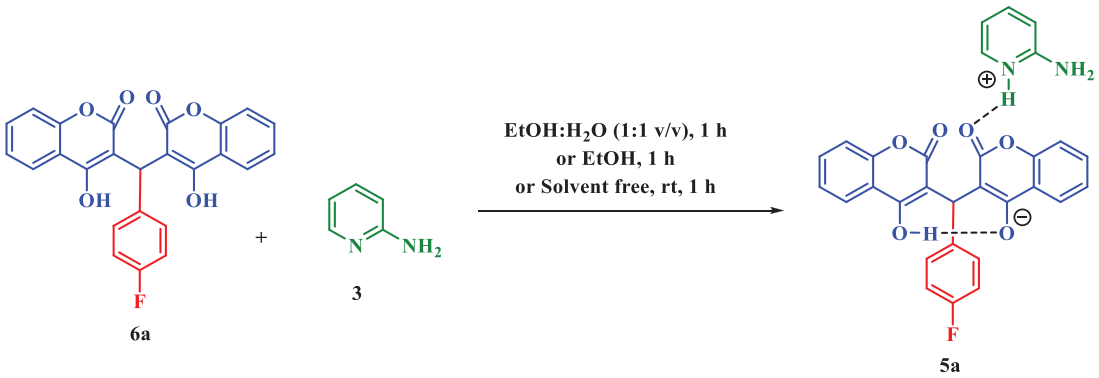

Scheme 4. Reaction of biscoumain and 2-aminopyridine at room temperature.

troscopic data. It has been observed that the structure of the product obtained from this reaction has been assigned improperly. Biscoumarin enolate salts were likely forming instead of the expected products. The present study suggests that the formation of biscoumarin is rapid in the presence of a stronger organic bases and further the biscoumrin formed undergoes deprotonation to generate the enolate salt of it. The structure of the salt **5a** has been confirmed through single crystal X-ray analysis. The construction of fused chromeno-pyrimidin-6-one by other routes is the topic of future studies.

Supporting Information

The Supporting Information contains experimental section, NMR, FTIR, and ESI-MS spectra of compounds.

Acknowledgments

The authors thank Prof. B.R. Srinivasan for useful discussion on X-ray analysis. S.G.T. thank to University Grant Commission, New Delhi for the award of BSR Faculty Fellowship (F.No.26–13/2020) and M.M.G. for Junior Research Fellowship (NET).

Conflict of Interests

The authors declare no conflict of interest.

Data Availability Statement

The data that support the findings of this study are available in the Supporting Information of this article.

Keywords: Biscoumarin-aminopyridine enolate salts · Chromeno[4,3-d]pyrido [1,2-a]pyrimidin-6-one derivatives · Multicomponent synthesis · Reinvestigation · Single crystal X-ray diffraction · Zirconyl oxynitrate

[1] a) K. N. Venugopala, V. Rashmi, B. Odhav, *BioMed. Res. Int.* **2013**, 963248; b) M. Lončarić, D. Gašo-Sokač, S. Jokić, M. Molnar, *Biomolecules* **2020**, *10*, 151.
[2] a) F. Salehian, H. Nadri, L. Jalili-Baleh, L. Youseftabar-Miri, S. N. A. Bukhari, A. Foroumadi, T. T. Küçükkilinç, M. Sharifzadeh, M. Khoobi, *Eur. J. Med. Chem.* **2021**, *212*, 113034; b) S. Pasricha, K. Mittal, P. Gahlot, H. Kaur, N. Avasthi, Shweta, *J. Iran Chem. Soc.* **2022**, *19*, 4035–4092.
[3] a) M. Facompre, C. Tardy, C. Bal-Mahieu, P. Colson, C. Perez, I. Manzanares, C. Cuevas, C. Bailly, *Cancer Res.* **2003**, *63*, 7392–7399; b) R. Zhang, Z. Xu, W. Yin, P. Liu, W. Zhang, *Synth. Commun.* **2014**, *44*, 3257–3263; c) H. M. Hosni, M. M. Abdulla, *Acta. Pharm.* **2008**, *58*, 175–186.
[4] G. Brahmachari, I. Karmakar, N. Khondekar, *ACS Sustainable Chem. Eng.* **2018**, *6*, 11018–11028.
[5] M. Khalaj, M. Taherkhani, M. Kalhor, *New J. Chem.* **2021**, *45*, 10718–10724.
[6] M. Khalaj, M. Taherkhani, M. S. Kazemi, M. Kalhor, G. T. Dehkordy, *Polycycl. Aromat. Compd.* **2022**, *42*, 7354–7367.
[7] S. Dey, P. Basak, S. Sarkar, P. Ghosh, *Asian J. Green Chem.* **2022**, *6*, 24–39.
[8] S. D. Pasuparthy, B. Maiti, *ACS Omega* **2022**, *7*, 39147–39158.
[9] A. Olyaei, E. Dortaj, R. Khoeiniha, F. Rajabi, *J. Heterocyclic Chem.* **2018**, *55*, 2971–2976.
[10] A. Hasaninejad, M. Shekouhy, M. R. Mohammadizadeh, A. Zareb, *RSC Adv.* **2012**, *2*, 6174.
[11] J. Soni, N. Sahiba, A. Sethiya, P. Teli, D. K. Agarwal, A. Manhas, P. C. Jha, D. Joshi, S. Agarwal, *Polycycl. Aromat. Compd.* **2022**, *42*, 2970–2990.
[12] P. S. Beck, A. G. Leitao, Y. B. Santana, J. R. Correa, C. V. S. Rodrigues, D. F. S. Machado, G. D. R. Matos, L. M. Ramos, C. C. Gatto, S. C. C. Oliveira, C. K. Z. Andrade, B. A. D. Neto, *Org. Biomol. Chem.* **2024**, *22*, 3630–3651.
[13] G. V. Grygoriv, D. A. Lega, V. P. Chernykh, L. Zaprutko, A. K. Gzella, A. Pawełczyk, L. A. Shemchuk, *RSC Adv.* **2018**, *8*, 37295–37302.

Manuscript received: June 24, 2025